



# Lawrence Berkeley Laboratory

UNIVERSITY OF CALIFORNIA

## EARTH SCIENCES DIVISION

RECEIVED  
LAWRENCE  
BERKELEY LABORATORY

APR 15 1983

LIBRARY AND  
DOCUMENTS SECTION

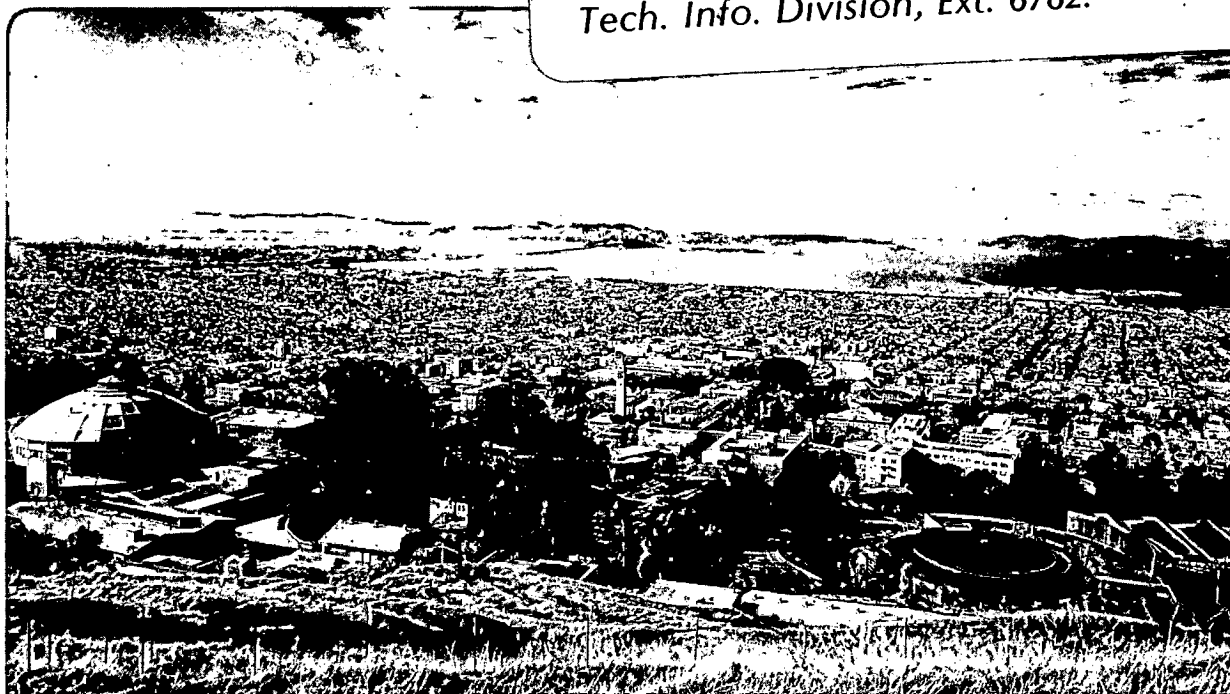
AN INVESTIGATION OF THE CONDUCTIVITY DISTRIBUTION  
IN THE VICINITY OF A CASCADE VOLCANO

Edward Clarence Mozley  
(Ph.D. Thesis)

November 1982

### TWO-WEEK LOAN COPY

*This is a Library Circulating Copy  
which may be borrowed for two weeks.  
For a personal retention copy, call  
Tech. Info. Division, Ext. 6782.*



LBL-15671  
*c.2*

## **DISCLAIMER**

This document was prepared as an account of work sponsored by the United States Government. While this document is believed to contain correct information, neither the United States Government nor any agency thereof, nor the Regents of the University of California, nor any of their employees, makes any warranty, express or implied, or assumes any legal responsibility for the accuracy, completeness, or usefulness of any information, apparatus, product, or process disclosed, or represents that its use would not infringe privately owned rights. Reference herein to any specific commercial product, process, or service by its trade name, trademark, manufacturer, or otherwise, does not necessarily constitute or imply its endorsement, recommendation, or favoring by the United States Government or any agency thereof, or the Regents of the University of California. The views and opinions of authors expressed herein do not necessarily state or reflect those of the United States Government or any agency thereof or the Regents of the University of California.

## **DISCLAIMER**

This document was prepared as an account of work sponsored by the United States Government. While this document is believed to contain correct information, neither the United States Government nor any agency thereof, nor the Regents of the University of California, nor any of their employees, makes any warranty, express or implied, or assumes any legal responsibility for the accuracy, completeness, or usefulness of any information, apparatus, product, or process disclosed, or represents that its use would not infringe privately owned rights. Reference herein to any specific commercial product, process, or service by its trade name, trademark, manufacturer, or otherwise, does not necessarily constitute or imply its endorsement, recommendation, or favoring by the United States Government or any agency thereof, or the Regents of the University of California. The views and opinions of authors expressed herein do not necessarily state or reflect those of the United States Government or any agency thereof or the Regents of the University of California.

AN INVESTIGATION OF THE CONDUCTIVITY  
DISTRIBUTION IN THE VICINITY OF A CASCADE VOLCANO

Edward Clarence Mozley

(Ph.D. thesis)

Earth Sciences Division  
and  
Department of Materials Science and  
Mineral Engineering  
University of California  
Berkeley, California 94720

November 1982

This work was supported by the Assistant Secretary for Conservation and Renewable Energy, Office of Renewable Technology, Division of Geothermal and Hydro-power Technologies of the U. S. Department of Energy under Contract No. DE-AC03-76SF00098.

**AN INVESTIGATION OF THE CONDUCTIVITY  
DISTRIBUTION IN THE VICINITY OF A CASCADE VOLCANO**

**Edward Clarence Mozley**

**Earth Sciences Division  
and  
Department of Materials Science and  
Mineral Engineering  
University of California  
Berkeley, California 94720**

**ABSTRACT**

Magnetotelluric and telluric data were acquired in the vicinity of Mount Hood Oregon as part of a multidisciplinary exploration program to evaluate the geothermal potential of this stratocone volcano. Eleven field components were acquired simultaneously over the frequency band of 50.-.001 hertz. These data consisted of one five component magnetotelluric base site, two sets of two component remote electric field measurements and one set of remote horizontal magnetic field measurements. The data were recorded digitally in the field and processed later using the remote electric and magnetic signals to obtain unbiased tensor impedance and geomagnetic transfer function (tipper) estimates.

The effects on the surface field measurements of the rugged topographic relief were evaluated using forward simulations. A distortion removal scheme based on a linear relation between the topographically distorted fields and distant reference fields indicated that this distortion could be easily removed when a forward solution of the topographic model was available. This procedure, based on a three-dimensional integral equation solution of Laplace's equation, was applied to selected data. This analysis indicated that the topographic effects were responsible for only a small

component of the total field response observed.

These data were interpreted using one- and two-dimensional parameterized fitting schemes in conjunction with simple three-dimensional simulations. The data were divided into five bands based on the frequency characteristics exhibited by various transfer functions throughout the survey area. Polar diagrams for apparent resistivity, impedance phase and the complex geomagnetic transfer functions were generated over each band. The shape and orientation of these diagrams were used to choose appropriate forward simulations. The models obtained from various data subsets were combined into a composite three-dimensional model. This model indicated that at least two near surface conductors probably associated with saturated pyroclastic debris were located under the slopes of this Cascade volcano. The conductivities from near surface to depths of 10-15 kilometers were dominated by a large resistive zone possibly related to a Pliocene intrusive. The main component of the model consisted of a large conductor with a finite cross-section buried 10-15 kilometers and striking north 20 degrees west. This conductive body may represent a partial melt zone in the lower crust.

## ACKNOWLEDGEMENTS

My first and most sincere thanks go to Dr. Frank Morrison, who presented the problem and provided both academic and personal advise throughout this study. His support and friendship have made my stay at Berkeley a very memorable experience.

The data acquisition and processing phase of the project was successfully completed through the efforts of a number of people. Mr. Ramsey Haught whose expertise in the field was a major factor in acquiring the high quality data obtained during the second phase of the field work. I am also indebted to Mr. Victor Labson, Dr. Thomas Gamble and Dr. Wolf Goubau for their assistance with the data processing aspect of the study.

The interpretation of the data depended heavily on a number of programs which were generously provided by several people. My special thanks to Dr. Gary Oppliger, Dr. Keeva Vozoff and Dr. Kiha Lee for providing and in some cases aiding in the modification of the various programs used in this thesis. The interpretation phase of this project was greatly aided by several conversations with Dr. Francis Bostick and by the computational support provided by the Lawrence Berkeley Laboratory. Specifically I wish to thank Dr. Norm Goldstein for his patient support.

I also sincerely appreciate the help provided by my committee members, Dr. Alex Becker and Dr. Lane Johnson, in finishing this thesis within the required time frame.

Finally, I wish to thank my wife Joan, the one person most responsible for the successful completion of this thesis. Whose patience and understanding during the research period and whose typing and editing skills applied to the thesis are very much appreciated.

This work was supported by the Assistant Secretary for Conservation and Renewable Energy, Office of Renewable Technology, Division of Geothermal and Hydropower Technologies of the U.S. Department of Energy under Contract No. DE-AC03-76SF00098.

## Table of Contents

<b>Chapter 1</b>	<b>The Quest for a Magma Chamber</b>	
	[I] Introduction	Page 1
	[II] Regional Geologic and Tectonic Setting	Page 2
	[III] Geologic and Structural Setting of Mount Hood	Page 5
	[IV] The Relevance of Electromagnetic Induction Studies	Page 7
<b>Chapter 2</b>	<b>Data Acquisition and Processing Procedures</b>	
	[I] Field Operations and Equipment	Page 9
	[II] Data Acquisition	Page 13
	[III] Evaluation of the Remote Telluric Impedance Estimates	Page 16
	[IV] Data Processing Procedures	Page 24
	[V] A Comparison of Two Processing Techniques for Bias Removal	Page 33

<b>Chapter 3</b>	<b>Topographic Effects at Mount Hood</b>	
	<b>[I] An Evaluation of the Topographic Effect on Magnetotelluric Data</b>	<b>Page 39</b>
	<b>[II] The Evaluation of a Distortion Removal Technique</b>	<b>Page 44</b>
	<b>[III] A Three Dimensional Extension and Application of the Stripping Technique</b>	<b>Page 49</b>
<b>Chapter 4</b>	<b>Numerical Preliminaries Required for the Three Dimensional Model Studies</b>	
	<b>[I] Introduction to a Hybrid Modeling Technique</b>	<b>Page 59</b>
	<b>[II] The Modified Hybrid Algorithm</b>	<b>Page 61</b>
	<b>[III] Numerical Checks on the Modified Algorithm</b>	<b>Page 68</b>
<b>Chapter 5</b>	<b>Data Interpretation</b>	
	<b>[I] Introduction</b>	<b>Page 78</b>
	<b>[II] Constraints, Objectives and Presentation Techniques</b>	<b>Page 82</b>
	<b>[III] A Qualitative Interpretation of the Near Surface Conductivity Distribution</b>	<b>Page 88</b>

[IV]	Principal Directions Defined by the Residual Phase	Page 106
[V]	Induction Arrows: A Sensitivity Study	Page 135
[VI]	The Composite Model	Page 165
Chapter 6	The End of the Quest	
[I]	The Conductivity Model in Relation to Other Geophysical Information	Page 169
[II]	Conclusions	Page 182
Bibliography		Page 186
Appendix A	Field Data as a Function of Frequency and Rotation Angle	Page 191
Appendix B	Field Data as a Function of Frequency at a Constant Rotation Angle of -20. Degrees	Page 226
Appendix C	Polar Diagrams of the Field Data	Page 251
Appendix D	Polar Diagrams of the Three-Dimensional Model Results	Page 293

## Chapter 1

### The Quest for a Magma Chamber

#### [ I ] Introduction

A series of geological, geochemical and geophysical studies sponsored by the U. S. Department of Energy, U. S. Geological Survey, U. S. Forest Service and the Oregon Department of Geology and Mineral Industries were initiated in 1977 to assess the geothermal potential of the Mount Hood region. Mount Hood was chosen as the site for this multidisciplinary investigation because it is one of the largest most recently active stratovolcanos in the Cascades which was readily accessible for research. Furthermore, Mount Hood is located 80 kilometers from a metropolitan center, Portland Oregon, which would provide a ready market for any geothermal resource discovered. The presence of the chain of active volcanos, high regional heat flow, coupled with its tectonic setting, indicate that the High Cascades of north central Oregon should have a significantly large geothermal potential. The dominant economic factor however is associated with the discovery of localized near surface heat sources. An active volcano with a historic record of eruptive activity is a logical place to begin such an exploration effort.

Lawrence Berkeley Laboratory under contract with the Department of Energy was responsible for the electrical studies undertaken at Mount Hood. Due to the rugged terrain which limited accessibility and the probable existence of high near surface conductivities, the magnetotelluric-remote telluric sounding method was chosen as the most practical means to investigate this hostile environment. These data were supplemented by controlled source electromagnetic soundings at several locations.

The loop soundings were used in conjunction with the high frequency magnetotelluric impedance estimates to interpret the near surface conductivity distribution at several locations. The results are described in detail by Goldstein, Mozley and Wilt (1982).

## [ II ] Regional Geologic and Tectonic Setting

The regional tectonics of northern Oregon are intimately related to the Juan de Fuca ridge and the associated interaction of the Juan de Fuca plate with the North American plate. The relative position of these plates are shown in Figure 1.1. It was magnetic anomaly data acquired in this area in the 1960's that introduced an era of rapid evolution in the geologic sciences, resulting in the general acceptance of plate tectonics. It is therefore ironic that the tectonics in this region are so poorly understood.

The chain of High Cascade volcanos are commonly attributed to the subduction of the Juan de Fuca plate under the continental margin of Washington and Oregon. Whether this subduction is currently occurring is unclear. The absence of deep to intermediate focus seismic activity and the featureless bathymetry characterizing the Cascadia plain, which indicates the absence of a trench, have convinced some scientists that subduction is not presently occurring, (Hollister, 1979). However there is some evidence from P wave residual inversion studies in northern Oregon by Iyer, Rite, and Green (1982) and from P wave conversion studies in western Oregon by Langston (1981), that a south eastern dipping subduction zone exists under northern Oregon. Furthermore, Geodetic evidence for the aseismic subduction of the Juan de Fuca plate was presented by Ando and Balazs (1979).

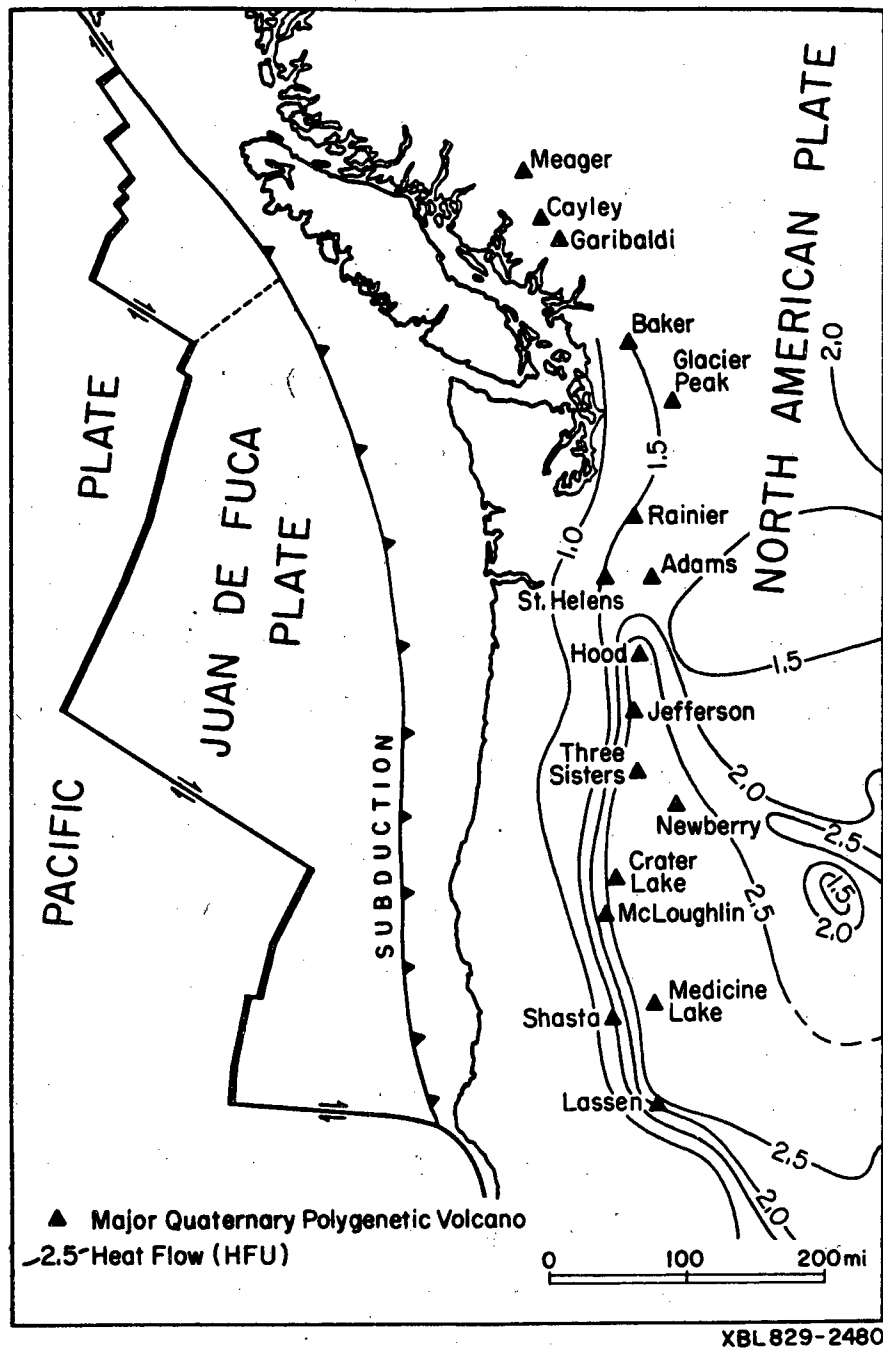


Figure 1.1 Tectonic structure, location of volcanos, and heat flow data for the Cascade Range (after Bacon 1981; Blackwell 1978; and Blackwell, Hull, Bowen, and Steele 1978).

Superimposed on the volcanic activity associated with the past or present subduction of the Juan de Fuca plate is a less obvious major north-south structural change in the crust which is located in the vicinity of Mount Hood. Evidence for this crustal change is both geological and geophysical in nature. Andesitic volcanism dominated all other eruptive rock types prior to 15 million years before present in the Cascades. Since this period, the andesitic volcanism decreased relative to the volume of basaltic lavas occurring south of Mount Hood. The volcanism which has occurred north of Mount Hood is older and dominately andesitic. The factors associated with this transition in type and age of the volcanism which occurs in the vicinity of Mount Hood have been considered by Williams, Hull, Ackermann and Beeson, (1982). The crust beneath the central Cascades in southern Washington and northern Oregon is younger, thinner and made up of mafic materials. In contrast the crust in the Cascades of northern Washington and California consists of older crust. A second factor, may be the close association of the Cascades south of Mount Hood with the hot extended crust in the Basin and Range Province.

The most striking geophysical evidence to support this north-south transition at Mount Hood is the regional heat flow shown in Figure 1.1, which is adapted from Blackwell (1978); Blackwell, Hull, Bowen and Steele (1978). An additional indication of this transition is found in the long range refraction seismic studies of eastern Washington and Oregon by Hill (1972). These data indicate that the crust thins from 35 kilometers in north eastern Washington to 25 kilometers under the Columbia plateau of southern Washington, then thickens again in east central Oregon. Deep resistivity measurements in Washington, Oregon and California, by Cantwell and Orange (1965), indicate that the crust in northern Washington and southern Oregon is underlain by a resistive basement which is missing in southern Washington and northern Oregon. This geological and geophysical evidence provides an incomplete but complex picture of the region in the vicinity of Mount Hood, implying that the lateral changes in the

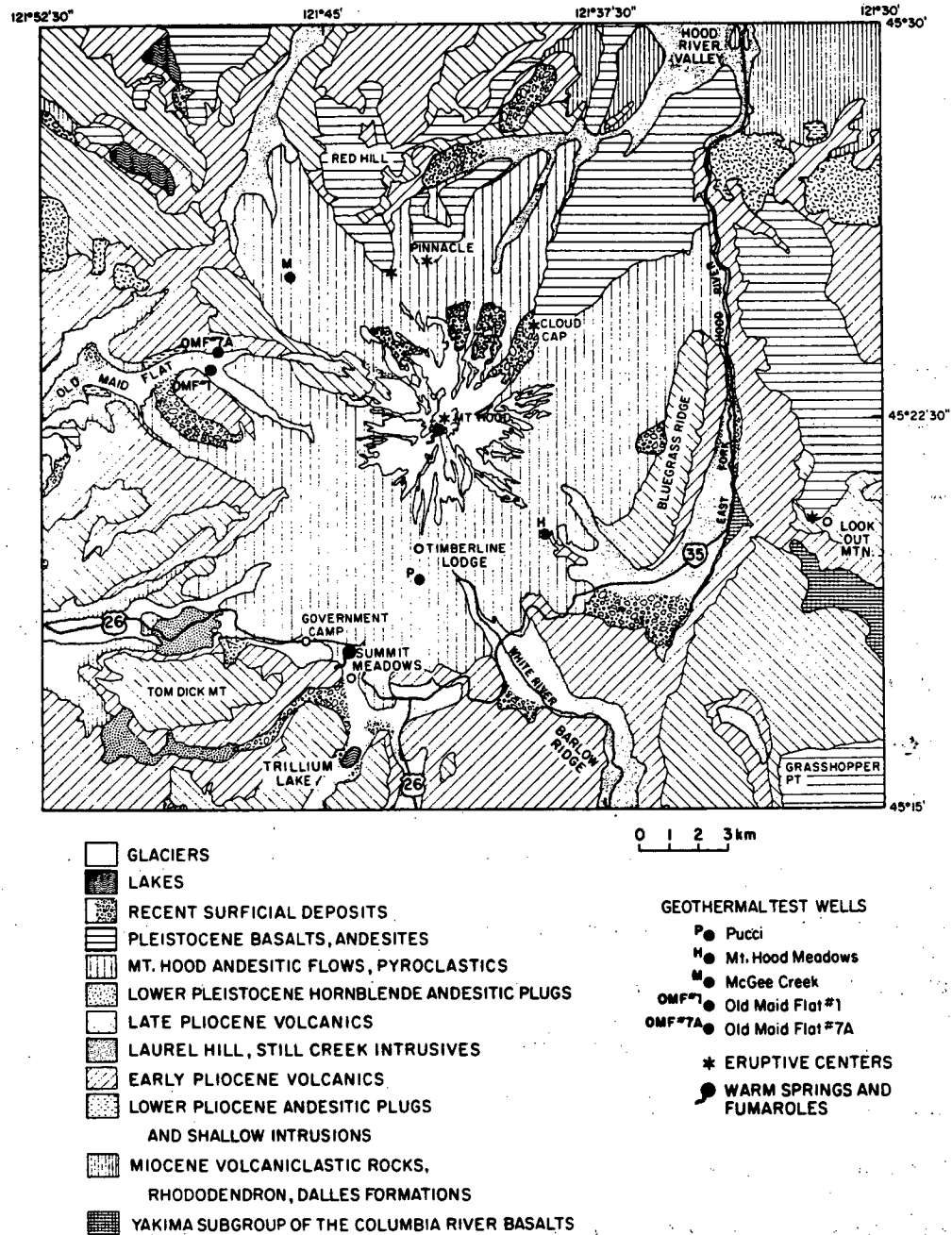
lower crust and upper mantle are three dimensional in character.

### [ III ] Geologic and Structural

#### Setting of Mount Hood

Mount Hood is one of the major Pleistocene composite volcanos occurring midway along the Cascade volcanic chain which extends from northern California to British Columbia as shown in Figure 1.1. A geologic study by Wise (1969), was the earliest work devoted to a detailed understanding of the evolution of Mount Hood. The simplified geologic map shown in Figure 1.2 was based on the results of this study.

The volcano consists of approximately 180 cubic kilometers of dominately andesitic flows and pyroclastic debris. Approximately ninety percent of the cone was formed between 15,000 - 700,000 years ago. This main phase of the cone building era was followed by a post glacial period which has been characterized by dacitic eruptions from the Mount Hood crater and olivine andesite lava flows from vents on the lower flanks of the cone. The youngest of these satellite vent lavas has been radiocarbon dated at 6,900 years ago. Three principal eruptive periods of dacitic volcanism have been recognized by Crandell (1980). The earliest of these periods was between 12,000 and 15,000 years ago. Pyroclastic debris and mudflows avalanched down the flanks of the cone into glaciated valleys as dacitic domes were extruded from the summit. The next period of activity, between 1,500 and 1,800 years ago, resulted in additional pyroclastic flows and mudflows which were restricted to the southern and southwestern flank of the cone. This material was derived from a dacite dome which was extruded within the crater. The missing south rim of the crater directed the debris which resulted as the dome collapsed onto the southern slope of the cone. The last period of activity occurred 200 - 300 years ago, which resulted in the extrusion of



XBL 808-7288

Figure 1.2 A simplified geologic map of the Mount Hood area (after Wise 1969).

the Crater Rock dome. This dacite plug dominates the south facing crater of Mount Hood and is associated with extensive fumarolic activity.

The Mount Hood volcanics erupted through the upper Miocene Columbia River basalts. These basalt flows were extruded onto a surface characterized by low relief. The region near Mount Hood was subsequently subjected to stresses which resulted in the development of folds and thrust faults oriented northeast-southwest. Uplift and volcanism associated with Pliocene intrusives culminated in the development of the complex basement structure under Mount Hood.

Present tectonic activity has superimposed on this complex setting, a series of right-lateral strike-slip faults oriented northwest-southeast. In addition, linear features have been interpreted as subsidence patterns which indicate block faulting associated with the development of a graben structure around Mount Hood. The older volcanics in this vicinity have been deeply eroded and covered with recent pyroclastic debris, which has hidden many geologic features. This complex structure and the various means of inquiry used to unravel its intricacies are summarized by Williams, Hull, Ackermann and Beeson (1982).

#### [ IV ] The Relevance of Electromagnetic

##### Induction Studies

Complex multistage fractionational models of andesitic-dacitic volcanic centers based on petrological evidence have been developed. Based on these models which are described in detail by Hildreth (1981), a complex distribution of magma and partial melt zones may be expected in the crust and upper mantle under a composite stratovolcano. An upper limit of 8-10 kilometers for these melt zones under Mount Hood has been provided by geothermometers discussed by White (1980). A lower

limit on the depth to a partial melt zone of 15 kilometers may be reached by a simple extrapolation for a heat flow of 2.5 HFU or a thermal gradient of 60 C/km in the vicinity of Mount Hood (Williams, Hull, Ackermann and Beeson 1982; Blackwell and Steele 1979).

Two phase model studies of Waff (1974) indicated that the bulk electrical conductivity of a partial melt was dominated by the fraction of melt and the connectivity of liquid paths. This would indicate that the conductivity was a strong function of temperature. Experimental studies by Waff and Weill (1975) showed that compositional variations at fixed temperatures within the magmatic range caused changes in electrical conductivity of less than an order of magnitude. However, thermal variations providing partial melt conditions could change the conductivities by two to four orders of magnitude. These studies support the earlier findings of Watanabe (1970) and Watanabe (1972), which indicated that increases in conductivity by two orders of magnitude occurred at the time of melting under high pressure conditions. This strong dependence of electrical conductivity on temperature has endowed the induction methods with the ability to detect geothermal targets in complex environments where other techniques may be unreliable.

## Chapter 2

### Data Acquisition and Processing Procedures

#### [ I ] Field Operations and Equipment

The data in this study were acquired in two stages by Geonometrics Inc. under contract with Lawrence Berkeley Laboratory. The first phase of the program commenced in June 1977 and resulted in the measurement of magnetotelluric data at eight locations supplemented by remote telluric measurements at an additional eleven sites. The second phase of the acquisition resulted in the completion of an additional seven magnetotelluric and thirteen remote telluric measurements. The onset of inclement weather required the premature termination of the survey in early November 1977.

The survey was designed to use the remote reference scheme introduced by Gamble, Goubau, and Clark (1978) for obtaining unbiased estimates of the tensor impedance. The general field procedure used to implement this scheme is shown in Figure 2.1. The details describing the system components used are shown in the block diagram in Figure 2.2. The two component remote magnetic measurements were acquired for the remote reference data processing procedure. The requirements on these remote data are that they must be coherent with the magnetotelluric field components measured at the base station and that they must have independent noise properties. Remote electric fields acquired simultaneously could be used in place of the remote magnetic measurements since these data should also have independent noise properties. However, the electric field measurements were expected to provide a less reliable reference signal than the magnetic measurements because in regions characterized by near surface lateral changes in conductivity the electric fields may be linearly

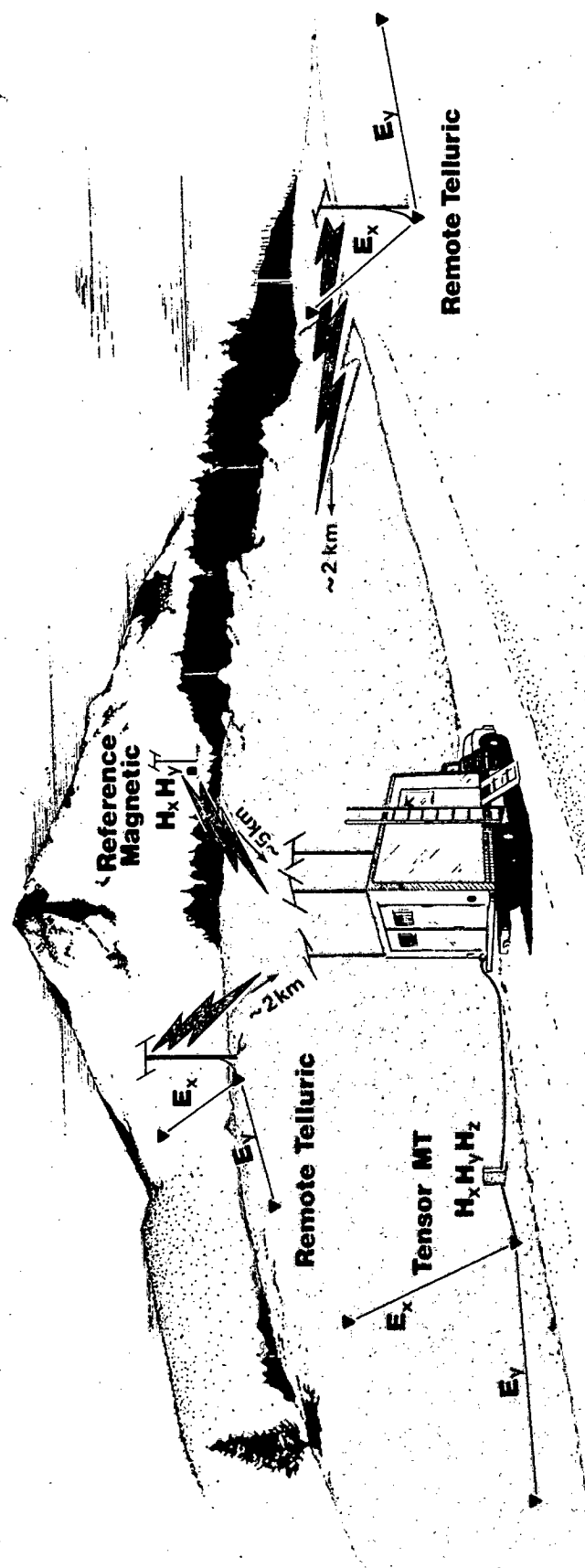


**Figure 2.1** A pictorial diagram of the magnetotelluric-remote telluric data acquisition system with a reference magnetometer.

CBB 770-12413

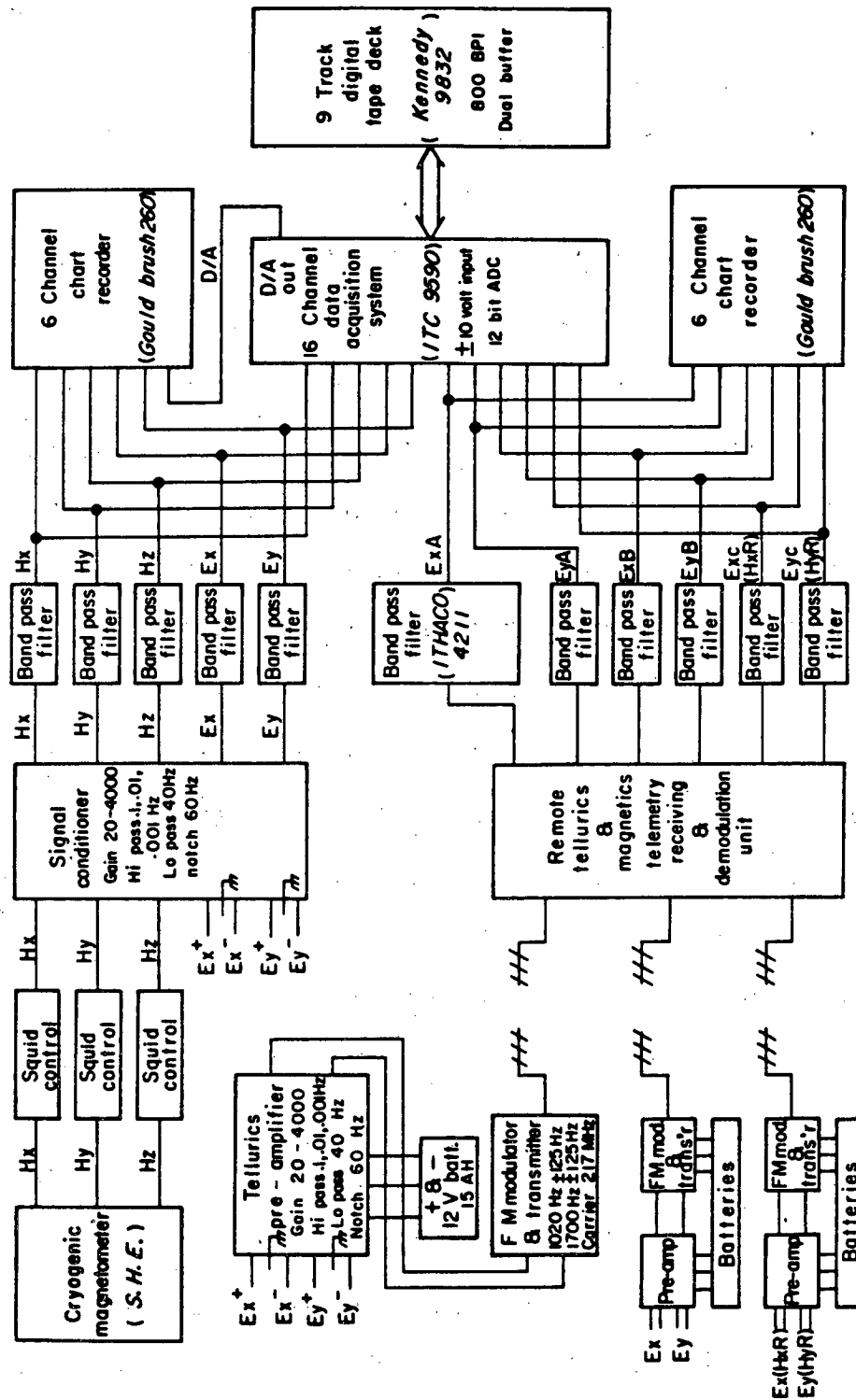


Figure 2.2 A block schematic of the data acquisition system.

polarized. In the remote reference processing technique, described in detail later, two independent field quantities must be measured at the remote site. Impedances cannot be calculated if the coherence of the two fields is unity. A strong linear field polarization implies a linear dependence and therefore results in a high coherence measurement. The geologic information available indicated that the near surface conductivity distribution could be quite complex in the vicinity of Mount Hood. Based on this information it was deemed prudent to acquire the remote magnetic data.

Near surface inhomogeneities give rise to rapid spatial variations and broad band distortions in the resulting transfer functions. These characteristics greatly impede quantitative interpretation of the data. In such an environment, a large number of measurements are required to provide sufficient information for a quantitative estimation of the conductivity distribution. The two sets of remote horizontal electric field measurements were acquired to supplement the magnetotelluric data, thus proving an economic means of effectively increasing our observation density.

The electric field inputs to the differential mode preamplifiers, depicted in Figure 2.2, were provided by an orthogonal pair of grounded electric dipoles. The dipole lengths were 150 meters and copper-copper sulfate electrodes were used to prevent electrode polarization effects. Some measurement locations in the survey area were characterized by high contact impedance values and several electrodes wired in parallel were used to reduce the source impedance. A second difficulty encountered on the upper slopes of the volcanic cone were self potential voltages so large that the D.C. bucking circuit was unable to cancel them. When this phenomenon occurred the measurement dipoles were rotated to minimize the effects.

Eleven field components were amplified, filtered and monitored for data quality. These data were then digitized and recorded on nine track magnetic tapes. The data were acquired in five to six overlapping bands providing a total frequency coverage of 40.-0.001 hertz. The data in each band were recorded serially, thus requiring a total

record time of approximately twenty hours per site to acquire a sufficient number of time series to estimate accurate impedance and geomagnetic transfer functions.

## [ II ] Data Acquisition

During the initial phase of the field work the measurement locations were confined to an eight square kilometer region on the southern slope of the volcanic peak between Timberline Lodge and Trillium Lake which are shown on the geologic map in Figure 1.2. There are two thermal manifestations in the region; the first and most evident is the fumarole activity in the Crater Rock area located on the summit of Mount Hood. The other thermal manifestation, Swim Warm Springs, is located in the survey area. Throughout this phase of the field work, the remote magnetic measurement position was relocated only once to satisfy the line of sight requirements of the telemetry.

Extensive commercial development in this region provided a great deal of electromagnetic noise associated with sixty hertz power lines and switching transients with broad band frequency characteristics. This extensive cultural noise combined with equipment malfunctions resulted in the acquisition of a great deal of poor quality data. Even remote reference signal processing techniques were unable to improve the results significantly at most sites. Only three magnetotelluric sites and one remote telluric site were used during the interpretation stage. These sites are designated as 11, 13, 14, and 15a in Figure 2.3. Most of the measurements in this area were characterized by a north-south polarization of the electric fields.

The next phase of field work consisted of obtaining data in four regions surrounding the volcanic peak. The initial acquisition plan called for two magnetotelluric sites and four remote telluric sites in each region. A magnetotelluric and a remote

# SITE LOCATIONS

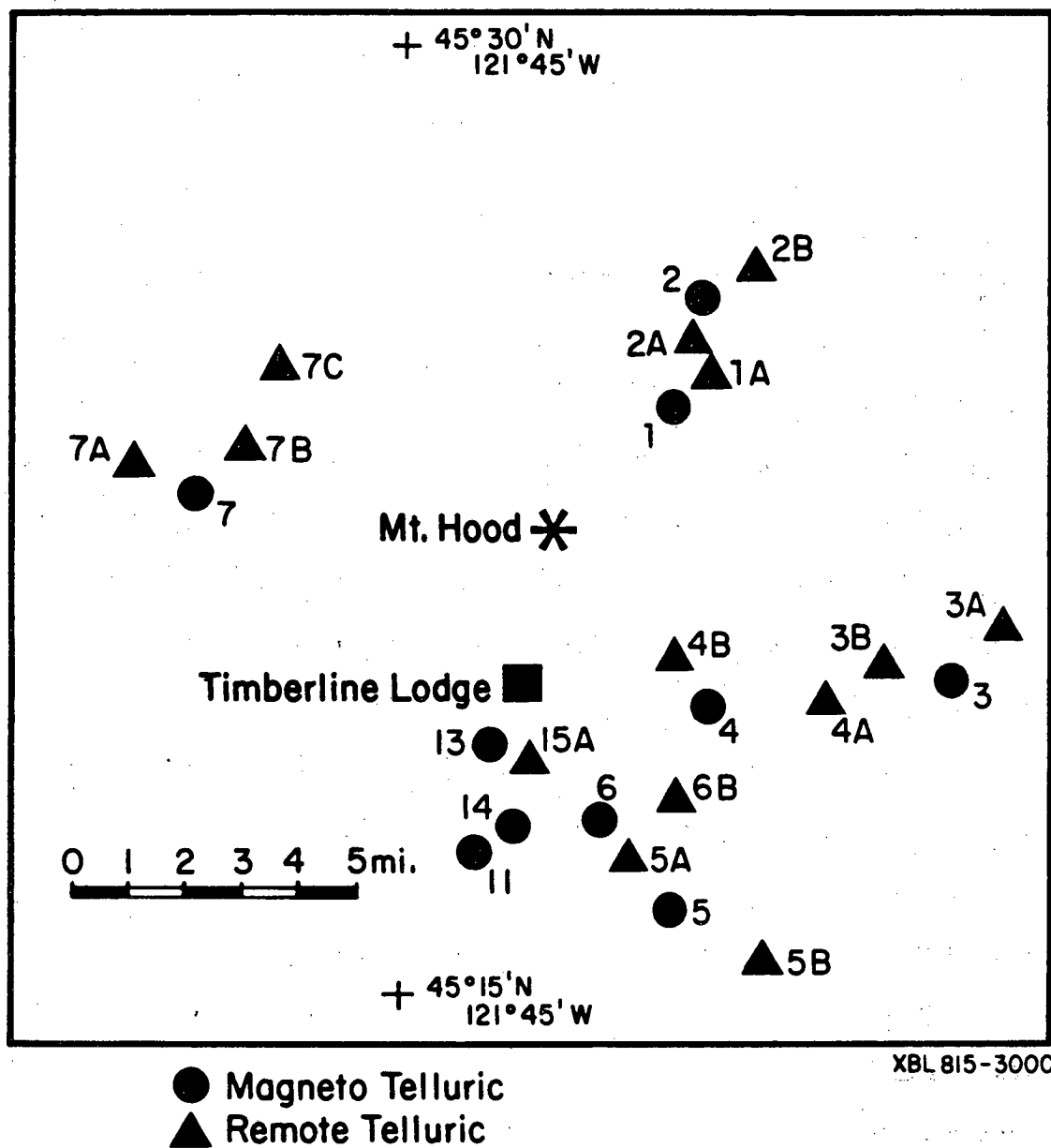


Figure 2.3 Magnetotelluric sites are numerically designated, as an example site 2 with the remote telluric sites measured at the same time indicated by 2A and 2B.

telluric sounding was to be made at the same location in each of the areas. Good quality data were obtained during this phase of the project. The location of these data sites are indicated in Figure 2.3.

The first cluster was located approximately three miles north-east of the volcanic peak, in the vicinity of an olivine andesite satellite vent with an estimated age of 12-16,000 years before present. Magnetotelluric data were acquired at sites 1 and 2, with site 2 being the location of a previously measured remote telluric data set. Three remote telluric sites provided additional control on the near surface conductivity variations in this area.

The next group of measurements acquired provided an east-west profile across the Hood River. This profile consisted of magnetotelluric sites 3 and 4 supplemented by four remote telluric measurements. The sites on the eastern end of the profile were located in an area of rugged topographic relief. The profile was made across the expected fault trace delineating the eastern boundary of a north-south trending graben structure within which Mount Hood may be located.

The third group of measurements consisted of magnetotelluric sites 5 and 6 with three remote telluric measurements. As in the first cluster of sites, one magnetotelluric site was located at the same point as a previously recorded remote telluric measurement. These data were acquired in an area south-east of Mount Hood and east of the area where the initial data were collected. This region was covered with a relatively high density of measurements with the hope that the resulting information would delineate the conductivity distribution responsible for the strong north-south polarization of the electric fields in the area south of Mount Hood.

The last area covered in the survey was near Old Maid Flat on the western flank of Mount Hood. This cluster of measurements consisted of the magnetotelluric site 7 and three remote telluric sites. Due to equipment malfunctions and several inches of snow, the survey was prematurely ended. This group of sites completed the survey

goal of obtaining a reasonable distribution of field measurements around the volcano.

### [ III ] Evaluation of the Remote Telluric Impedance Estimates

In order to increase the density of measurements and minimize time and cost factors, remote telluric measurements were used to supplement the magnetotelluric data. These remote electric measurements are used in conjunction with the horizontal magnetic fields measured at the magnetotelluric site to calculate an impedance tensor. This tensor estimate will be correct if the horizontal magnetic fields do not vary appreciably between the two measurement locations. The distortion of the horizontal fields and their effects on the impedances calculated from remote telluric data are well described using two and three dimensional models by Stodt, Hohmann, and Ting (1981). Their results indicated the distortion of the horizontal magnetic fields caused by near surface conductors could result in significant changes in the resulting impedance values. This effect was most pronounced for two dimensional models; the distortion due to the presence of a three dimensional scatterer was less but still appreciable at higher frequencies.

In order to minimize the effects of these spatial variations in the horizontal magnetic fields, the remote telluric sites were located less than five kilometers from the corresponding magnetotelluric site. The field procedures used during the survey provided six checks on this possible source of error. The measurement of remote telluric data at the same location as a magnetotelluric sounding was initially planned for each cluster of measurements. This check was actually implemented twice during the survey, initially at site 1B - 2 and later at site 5 - 6A. A second check for this type of error was made by placing the remote magnetometer at the same location as one of

the remote electric field measurements. These sites were then processed as both a remote telluric and magnetotelluric measurement. This dual processing procedure was implemented at sites 2A, 3A, 4A and 5A. These data provided an additional four locations to check for variations in the horizontal magnetic fields.

The results of the six magnetotelluric-remote telluric data sets are presented in Figures 2.4 through 2.9. The apparent resistivities calculated from the off-diagonal components of the impedance tensors, plotted as a function of the square root of period, are shown; the vertical bars indicate a 50 percent confidence interval based on a Normal distribution as described by Gamble, Goubau and Clark (1979).

These results were nearly the same at five of the locations. These sites were distributed throughout the survey area and consequently were subjected to a variety of near surface conditions. The apparent resistivities at sites 2, 5, 2A, 4A and 5A are shown in Figures 2.4, 2.5, 2.6, 2.7, and 2.8 respectively. These figures indicate that both apparent resistivities below 1.0 second period are coincident within the statistical errors. They also show spatial variations in the horizontal magnetic field components throughout the survey area in the frequency range above 1.0 hertz. The resulting high frequency distortions in these apparent resistivities could affect their interpretation. However, this would be a second order affect since the general frequency characteristics are similar. The major limitations on the interpretation are provided by the sparse spatial sampling and limited frequency range of the entire data set collected at Mount Hood.

The only dual processed field measurement which indicated a significant amount of distortion due to lateral variations of the horizontal magnetic fields was at site 3A. These data, shown in Figure 2.9, clearly show different frequency characteristics from 0.1 to 0.02 seconds. This implies that the horizontal magnetic fields vary appreciably over lateral dimensions as small as two kilometers. These magnetic fields measured at site 3, were associated with highly polarized electric fields. The resulting apparent

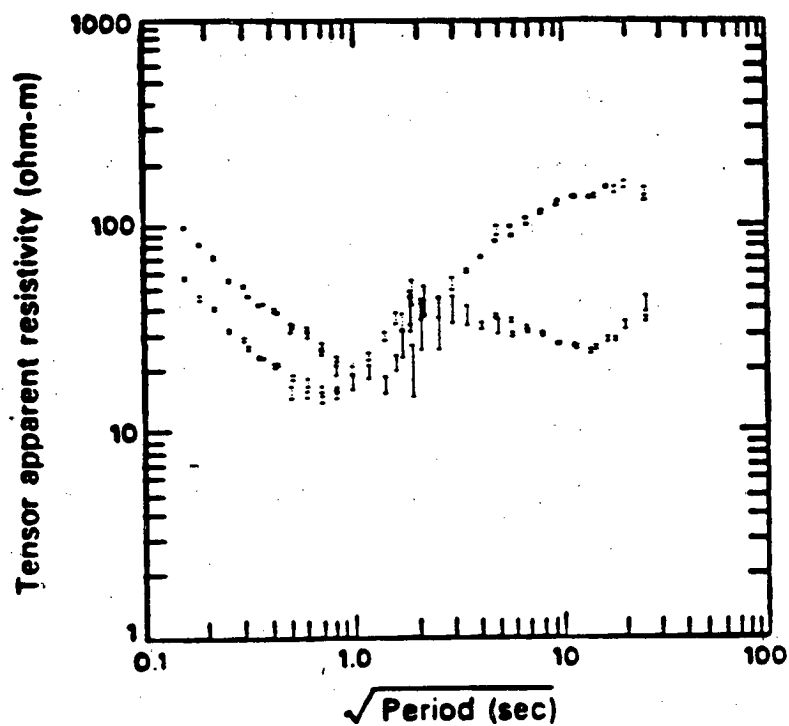


Figure 2.4(a) Magnetotelluric site 2 processed using the remote magnetic signals.

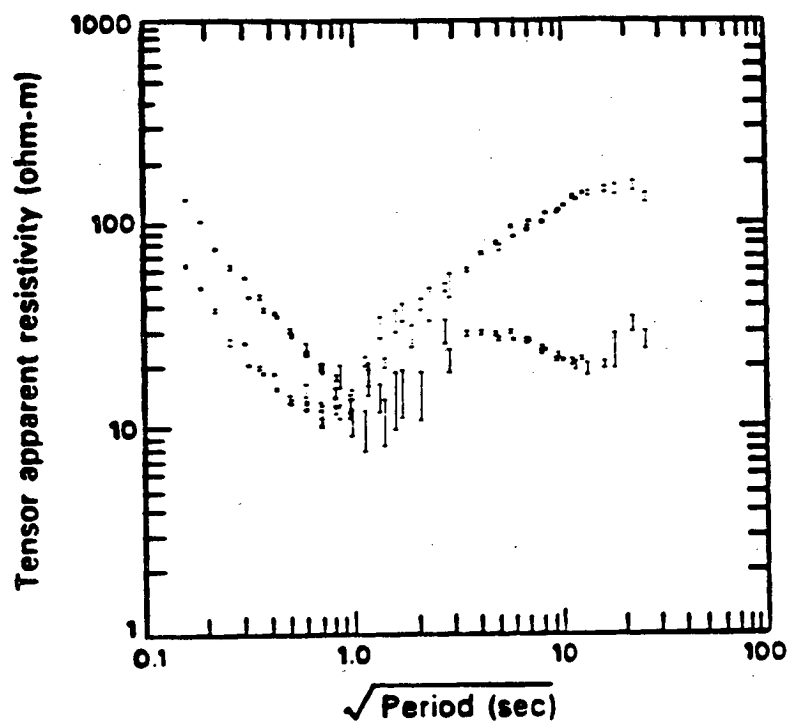


Figure 2.4(b) Remote telluric site 1B measured at the same location as the magnetotelluric site 2 and processed using the remote magnetic signals.

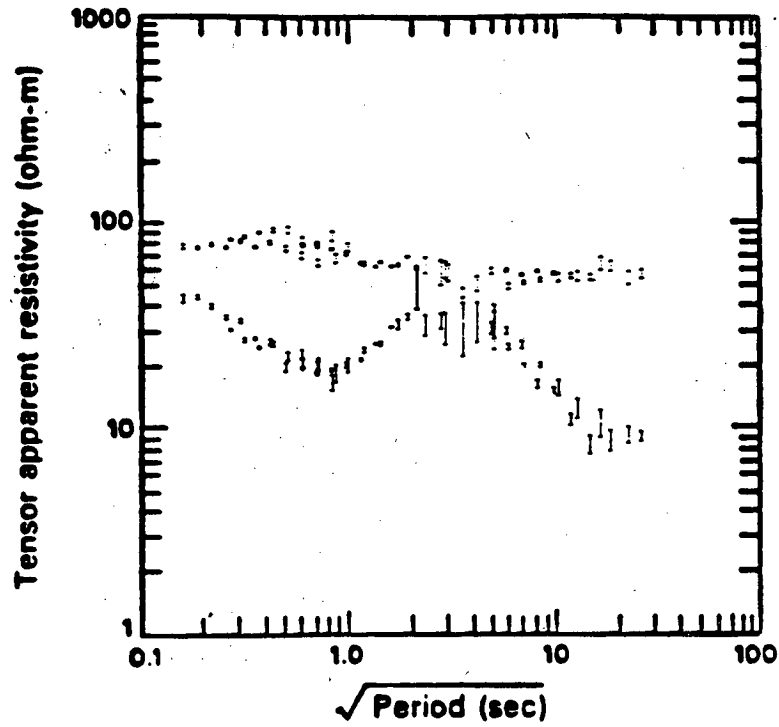


Figure 2.5(a) Magnetotelluric site 5 processed using the remote magnetic signals.

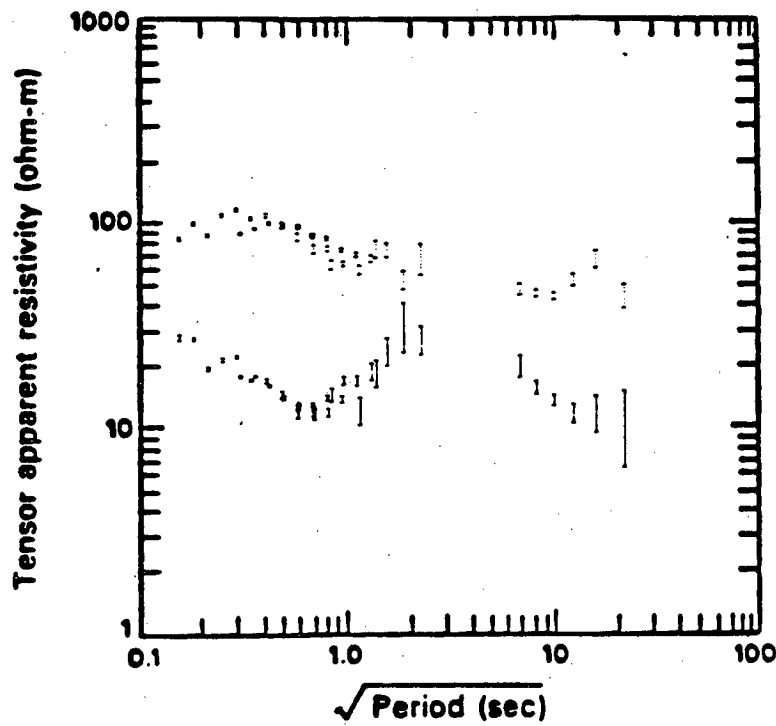


Figure 2.5(b) Remote telluric site 6A measured at the same location as the magnetotelluric site 5 and processed using the remote magnetic signals.

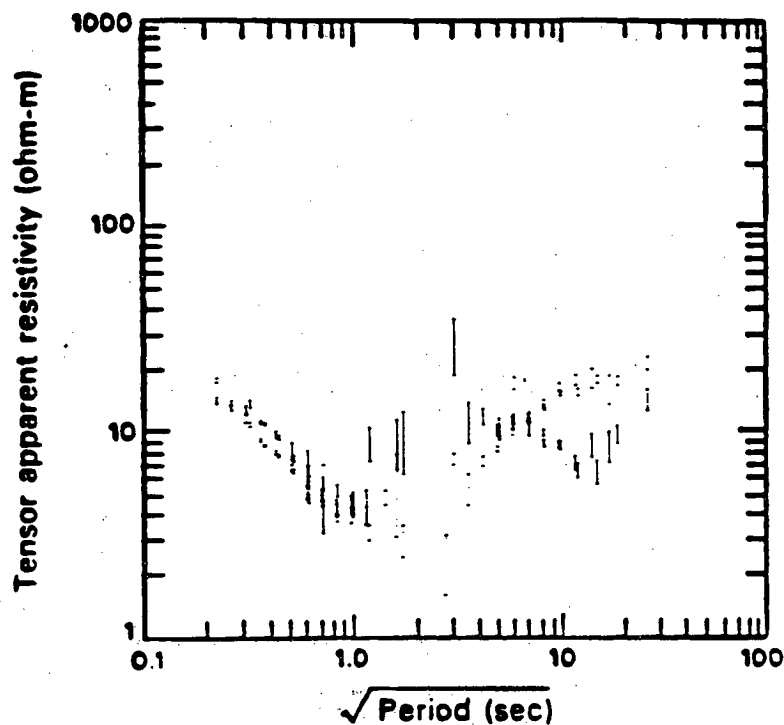


Figure 2.6(a) Remote telluric and magnetic data both measured at site 2A processed as a magnetotelluric measurement using the base magnetic as the reference signal.

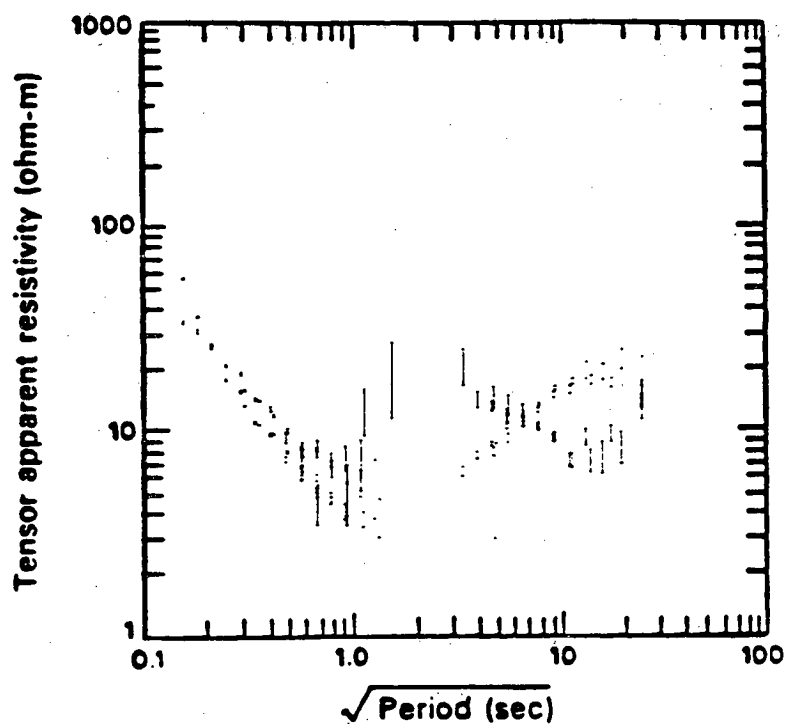


Figure 2.6(b) Remote telluric site 2A processed as a remote measurement using a remote electric (2B) as a reference signal.

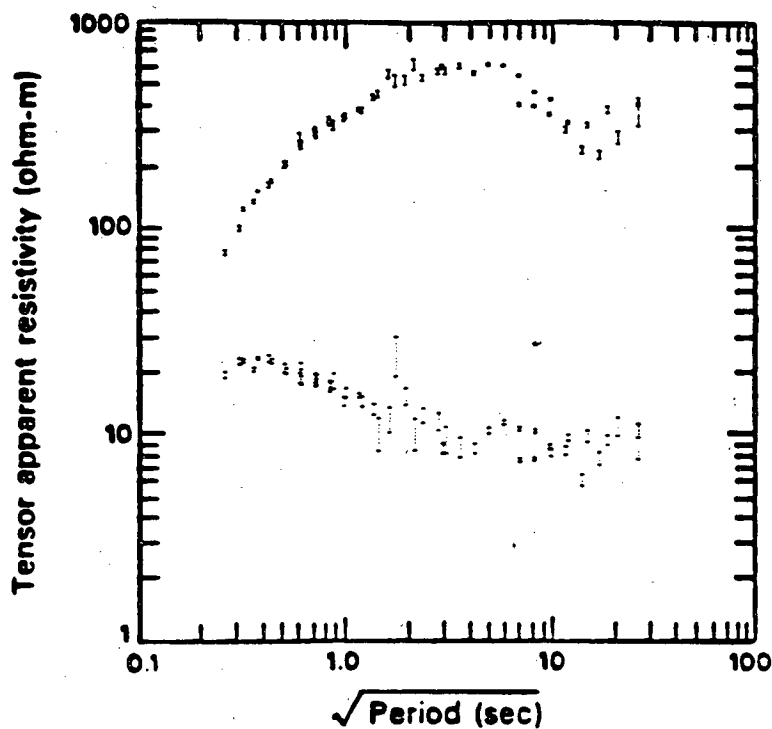


Figure 2.7(a) Remote telluric and magnetic data both measured at site 4A, processed as a magnetotelluric measurement using the base magnetic as the reference signal.

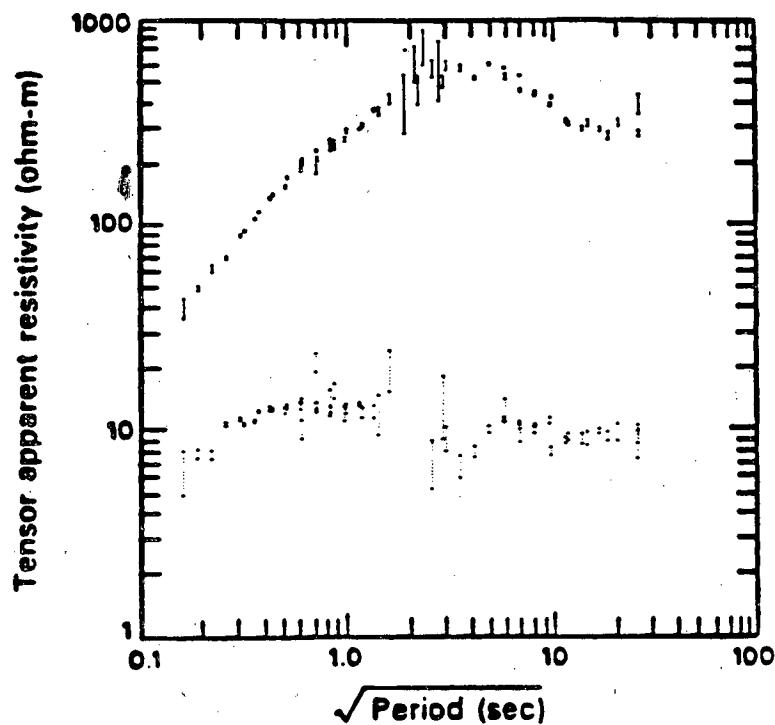


Figure 2.7(b) Remote telluric site 4A processed as a remote measurement using a remote electric (4B) as a reference signal.

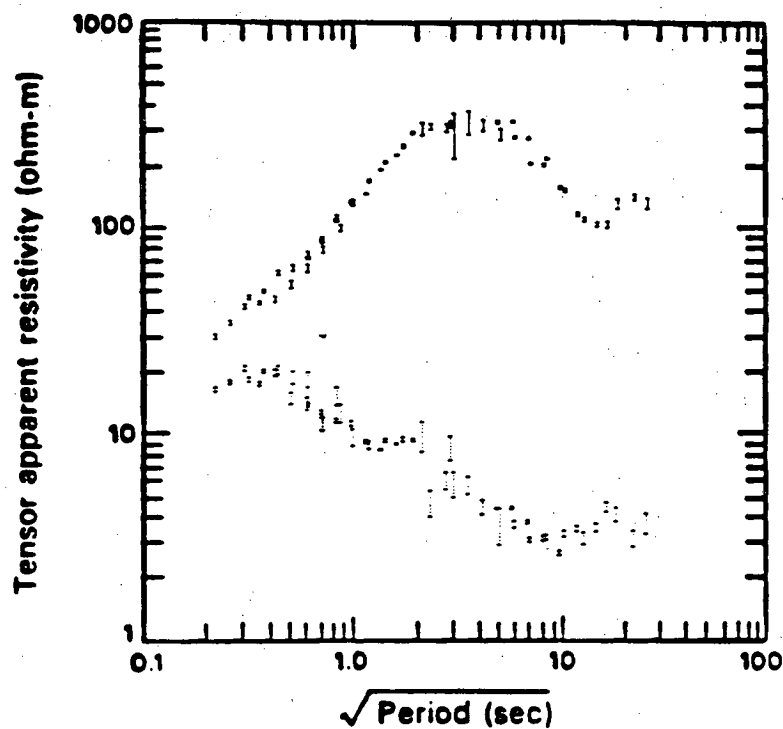


Figure 2.8(a) Remote telluric and magnetic data both measured at site 5A, processed as a magnetotelluric measurement using the base magnetic as the reference signal.

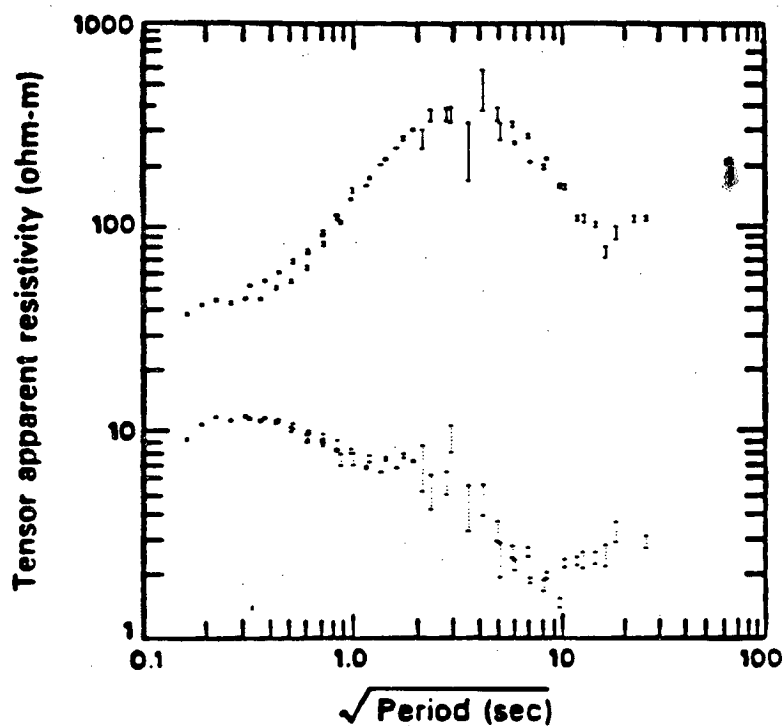


Figure 2.8(b) Remote telluric site 5A processed as a remote measurement using a remote electric (5B) as a reference signal.

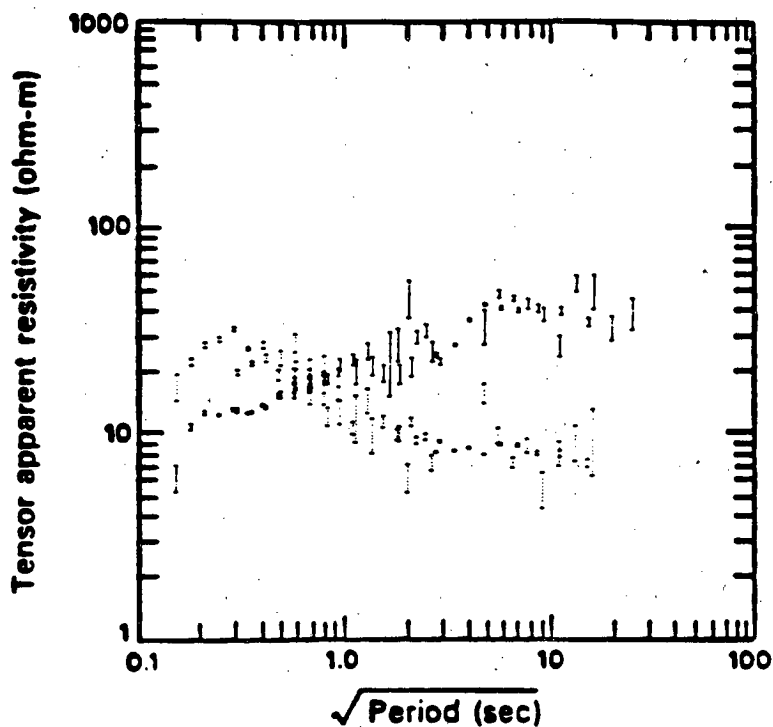


Figure 2.9(a) Remote telluric and magnetic data both measured at site 3A, processed as a magnetotelluric measurement using the base magnetic as the reference signal.

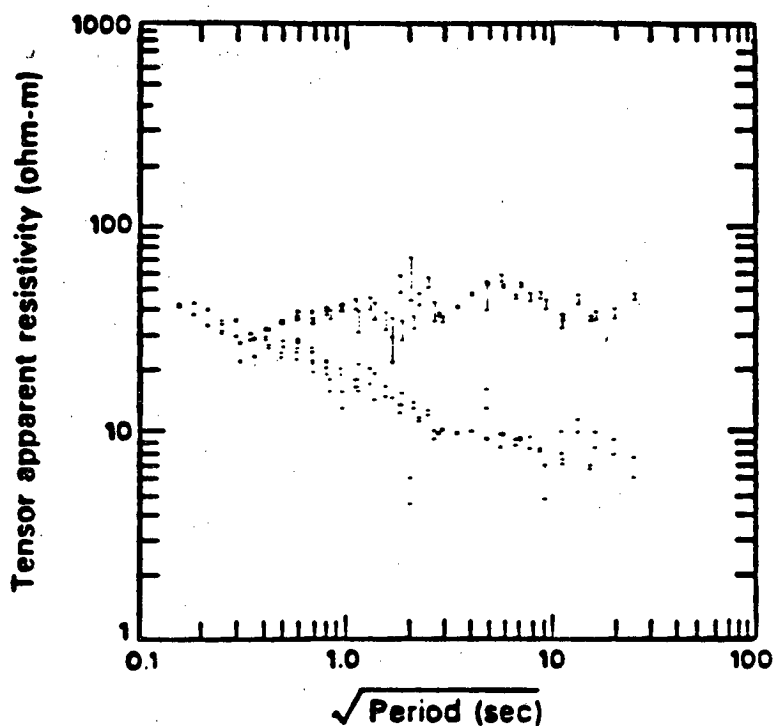


Figure 2.9(b) Remote telluric site 3A processed as a remote measurement using a remote electric (3B) as a reference signal.

resistivities in the principle directions were separated by nearly four orders of magnitude and the tensor skew values were greater than 0.5. A qualitative interpretation of the geomagnetic data in conjunction with other impedance estimates in this area indicate that site 3 is located near the edge of a near surface three dimensional conductivity distribution possibly associated with a Pliocene intrusive center. In addition, sites 3 and 3A are located in some of the most rugged topography in the survey area. It is interesting to note that even in the extremely inhomogeneous environment provided by this example, the magnetic fields are appreciably distorted only at periods less than 10. seconds.

The reason such small lateral changes in the horizontal magnetic fields were observed was probably related to the small separations used between the magnetotelluric sites and the associated remote telluric measurements. The near surface inhomogeneities which were encountered on this scale were three dimensional in nature and therefore had characteristics similar to the TM response of a two dimensional scatterer. This resulted in small horizontal magnetic field variations over distances less than 5 kilometers.

#### [ IV ] Data Processing Procedures

The five to six bands of the various electric and magnetic time series were visually edited to exclude any segments where poor correlation existed between appropriate field components. The remaining time series were tapered and Fourier transformed. Autopower and cross power estimates were then averaged over all the available time series. Additional smoothing of the spectral estimates was obtained by averaging the harmonics over constant Q windows. The first three harmonics in each band were excluded to minimize the effects of the distortion in the spectral estimates

caused by the tapered windows.

These various auto and cross spectral estimates were then used to calculate an estimate of the impedance tensor which provides a measure of the conductivity of the earth as a function of frequency for each measurement location and which is independent of source polarization. When the electric and magnetic field components are measured in the presence of noise, the impedance tensor may be systematically distorted depending on the distribution of the noise in the various field components. The most popular schemes for estimating the impedance tensor  $\mathbf{Z}$  have been various types of least squares estimates which are summarized by Sims, Bostick and Smith (1971). The least squares  $\mathbf{H}$  field estimate of the impedance may be written as,

$$[\mathbf{E}\mathbf{H}^*] = \mathbf{Z}_H [\mathbf{H}\mathbf{H}^*]$$

where the \* implies complex conjugate,  $\langle \rangle$  indicates spectral averages, and the notation is defined as follows.

$$[\mathbf{E}\mathbf{H}^*] = \begin{bmatrix} \langle \mathbf{E}_x \mathbf{H}_x^* \rangle & \langle \mathbf{E}_x \mathbf{H}_y^* \rangle \\ \langle \mathbf{E}_y \mathbf{H}_x^* \rangle & \langle \mathbf{E}_y \mathbf{H}_y^* \rangle \end{bmatrix}$$

$$\mathbf{Z}_H = [\mathbf{E}\mathbf{H}^*] [\mathbf{H}\mathbf{H}^*]^{-1}$$

Two simple cases are provided to illustrate the problem associated with noisy data. First assume that only the magnetic field components  $\mathbf{H}$  have a noise component  $\mathbf{H}_n$ ,

$$\mathbf{H} = \mathbf{H}_s + \mathbf{H}_n$$

$$\mathbf{H}\mathbf{H}^* = |\mathbf{H}|^2 = |\mathbf{H}_s + \mathbf{H}_n|^2 > |\mathbf{H}_s|^2$$

then the estimate of  $\mathbf{Z}_H$  would be biased down since  $\mathbf{Z}_H$  has autopowers of  $\mathbf{H}$  in its denominator. A second example of the effects of noise may be clearly seen in the least squares  $\mathbf{E}$  field estimate of the impedance which is given by:

$$\mathbf{Z}_E = [\mathbf{E}\mathbf{E}^*] [\mathbf{H}\mathbf{E}^*]^{-1}$$

If in this case, one assumes that only the electric fields have a noise component  $\mathbf{E}_n$ ,

$$\mathbf{E} = \mathbf{E}_s + \mathbf{E}_n$$

$$\mathbf{E}\mathbf{E}^* = |\mathbf{E}|^2 = |\mathbf{E}_s + \mathbf{E}_n|^2 > |\mathbf{E}_s|^2$$

then the estimate of  $\mathbf{Z}_E$  is biased up since the autopowers of  $\mathbf{E}$  are in the numerator of  $\mathbf{Z}_E$ .

A technique which provided an unbiased impedance tensor in the presence of correlated noise was developed by Gamble, Goubau and Clark (1978). The method utilizes an additional vector measurement of the electric or magnetic field at a remote location. These remote measurements must be coherent but have uncorrelated noise characteristics with respect to the magnetotelluric measurements. Using this reference signal, an impedance may be estimated using the following equation;

$$[\mathbf{E}\mathbf{R}^*] = \mathbf{Z}_R [\mathbf{H}\mathbf{R}^*]$$

$$\mathbf{Z}_R = [\mathbf{E}\mathbf{R}^*] [\mathbf{H}\mathbf{R}^*]^{-1}$$

where  $\mathbf{R}$  represents the remote reference signal. Since by definition the noise in all of the above cross-spectra are uncorrelated and no autopowers are used, then as the signals are averaged the impedance error will tend to zero and the bias problem is eliminated. An additional advantage in using the remote reference scheme is that it provides an accurate estimate of the signal and noise powers. These powers may then be used to calculate accurate error bounds for the impedance estimates. The details of these calculations are provided in the Ph.D. dissertation by Gamble (1978). An example illustrates the signal estimation procedure. Assume that only the electric field  $\mathbf{E}$  has a noise component  $\mathbf{E}_n$ .

$$\mathbf{E} = \mathbf{E}_s + \mathbf{E}_n$$

First calculate  $\mathbf{Z}_R$  as described earlier, then calculate the predicted electric field  $\mathbf{E}^p$  using  $\mathbf{Z}_R$  and the measured  $\mathbf{H}$  fields.

$$[\mathbf{E}^p \mathbf{E}^*] = \mathbf{Z}_R [\mathbf{H} \mathbf{E}^*] = [\mathbf{E} \mathbf{R}^*] [\mathbf{H} \mathbf{R}^*]^{-1} [\mathbf{H} \mathbf{E}^*]$$

The expectation of  $[\mathbf{E}^p \mathbf{E}^*]$  is given by the following equation,

$$[\mathbf{E}_s \mathbf{E}_s^*] = \begin{bmatrix} |\mathbf{E}_{x_s}|^2 & \mathbf{E}_{x_s} \mathbf{E}_{y_s}^* \\ \mathbf{E}_{y_s} \mathbf{E}_{x_s}^* & |\mathbf{E}_{y_s}|^2 \end{bmatrix}$$

which is a Hermitian matrix. Due to the existence of noise on the various field components  $[\mathbf{E}^p \mathbf{E}^*]$  is not Hermitian. However, the Hermitian component of  $[\mathbf{E}^p \mathbf{E}^*]$  may be estimated by the following relation.

$$[\mathbf{E}_s \mathbf{E}_s^*]^p = \frac{1}{2} \left( [\mathbf{E}^p \mathbf{E}^*] + [\mathbf{E}^p \mathbf{E}^*]^T \right) = \frac{1}{2} \left( [\mathbf{E}^p \mathbf{E}^*] + [\mathbf{E}^* \mathbf{E}^p] \right)$$

Once the signal components have been estimated the noise component is easily found.

$$\mathbf{E}_n = \mathbf{E} - \mathbf{E}_s$$

This procedure may be used for all field components from which the variance of the impedance estimates may be calculated.

The remote reference scheme requires only that the remote signal be coherent and have independent noise characteristics. Since two sets of remote electric fields were acquired as well as a remote magnetic, the magnetotelluric data could be processed using any of these signals. To estimate the relative effect of various types of reference signals, impedance estimates were calculated using both electric and magnetic references. This comparison at five locations are shown in Figures 2.10 through 2.14. The upper plot in each figure represents the apparent resistivities calculated

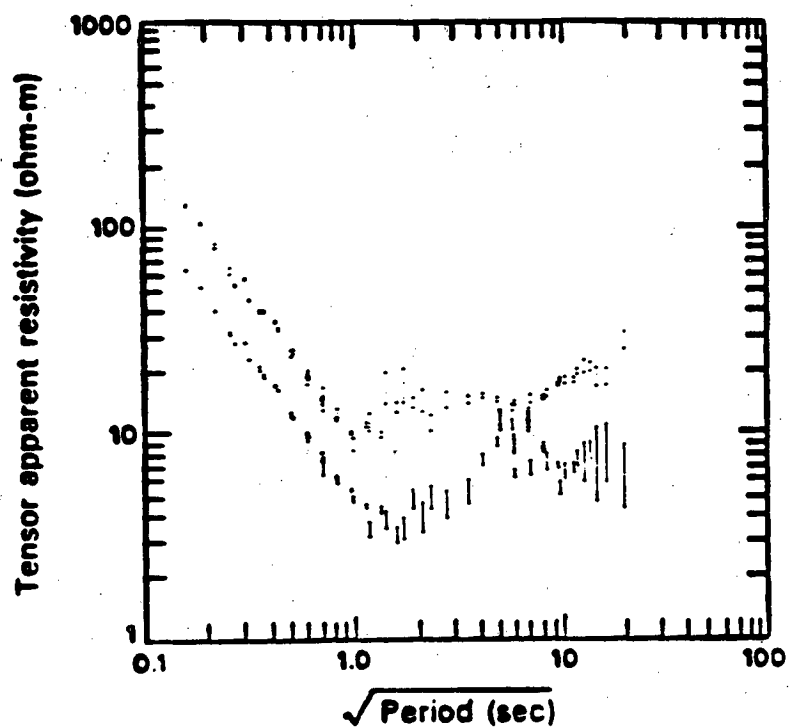


Figure 2.10(a) Magnetotelluric site 1 processed using the remote magnetics as the reference signal.

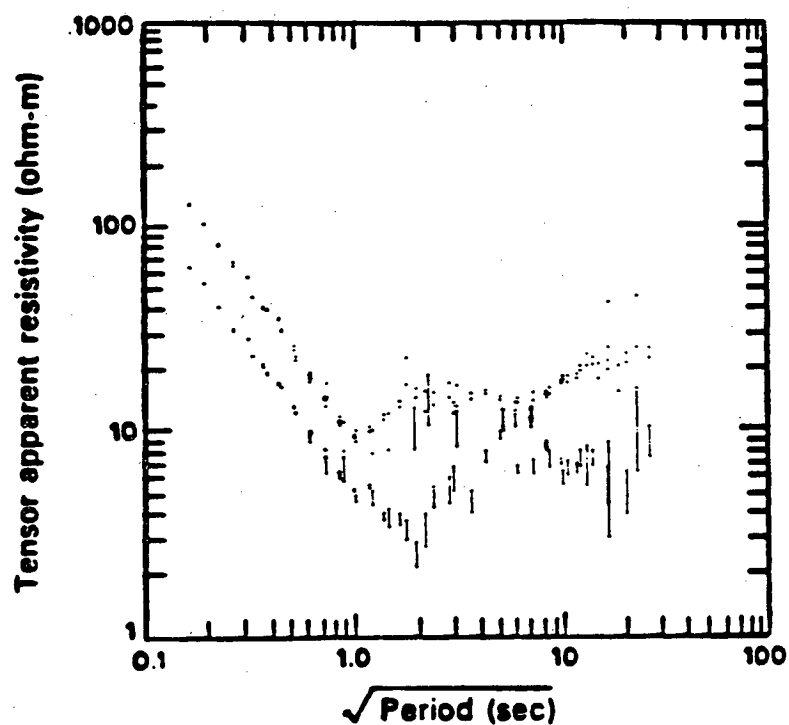


Figure 2.10(b) Magnetotelluric site 1 processed using the remote electric (1B) as the reference signal.

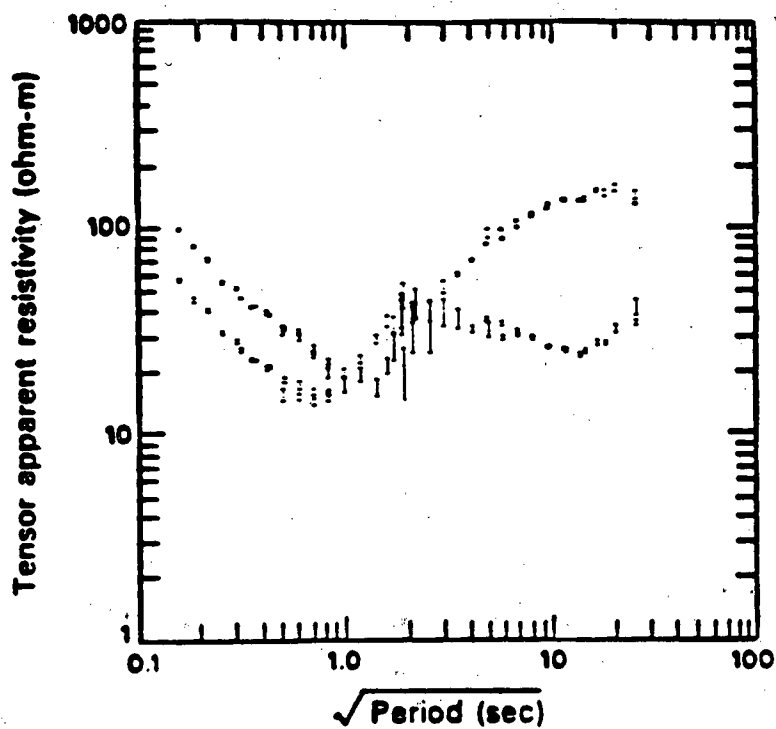


Figure 2.11(a) Magnetotelluric site 2 processed using the remote magnetics as the reference signal.

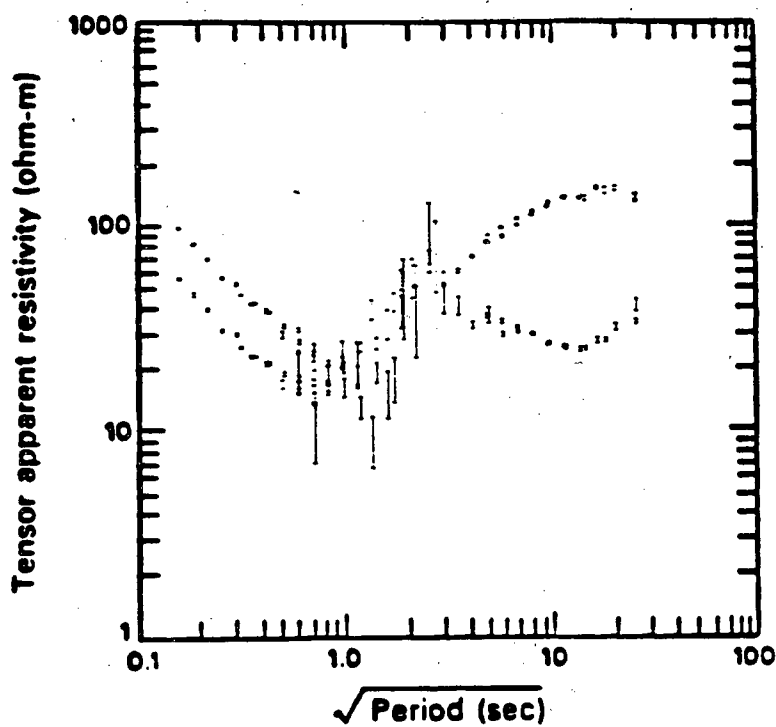


Figure 2.11(b) Magnetotelluric site 2 processed using the remote electric (2B) as the reference signal.

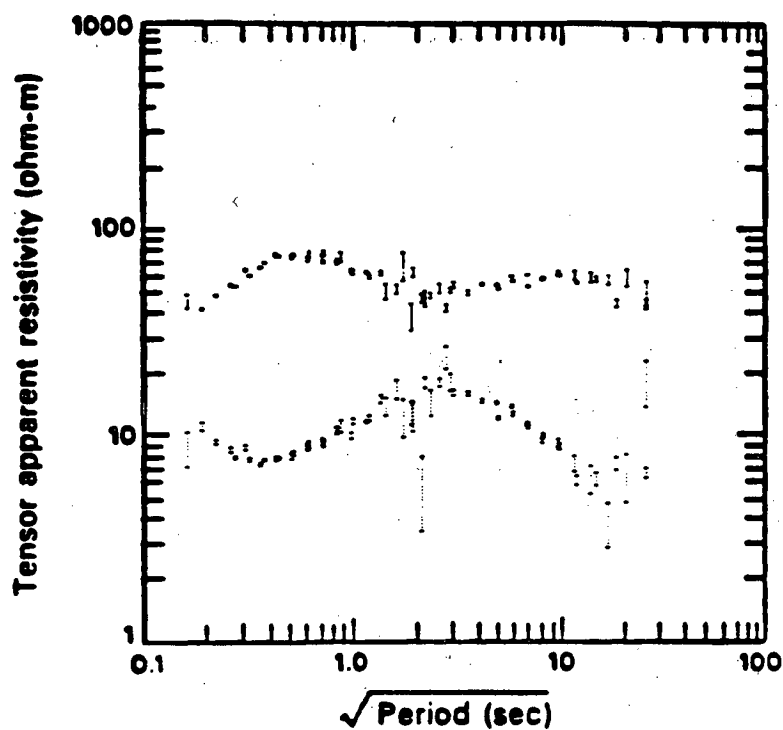


Figure 2.12(a) Magnetotelluric site 4 processed using the remote magnetics as the reference signal.

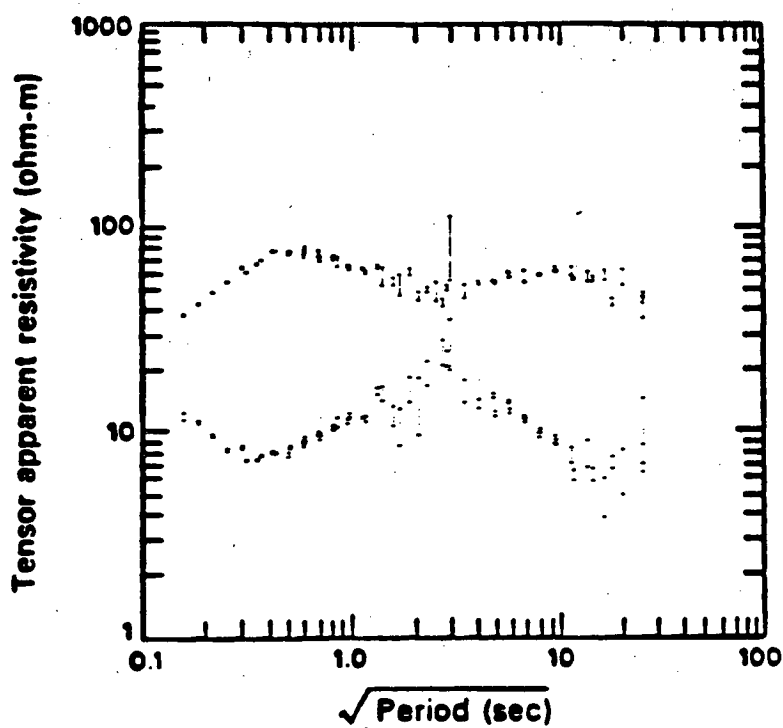


Figure 2.12(b) Magnetotelluric site 4 processed using the remote electric (4A) as the reference signal.

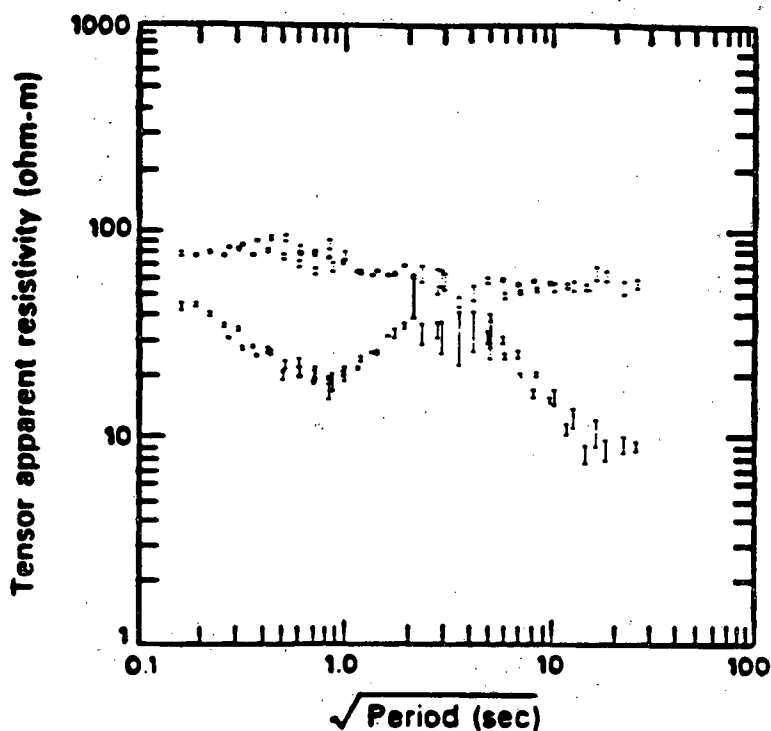


Figure 2.13(a) Magnetotelluric site 5 processed using the remote magnetic as the reference signal.

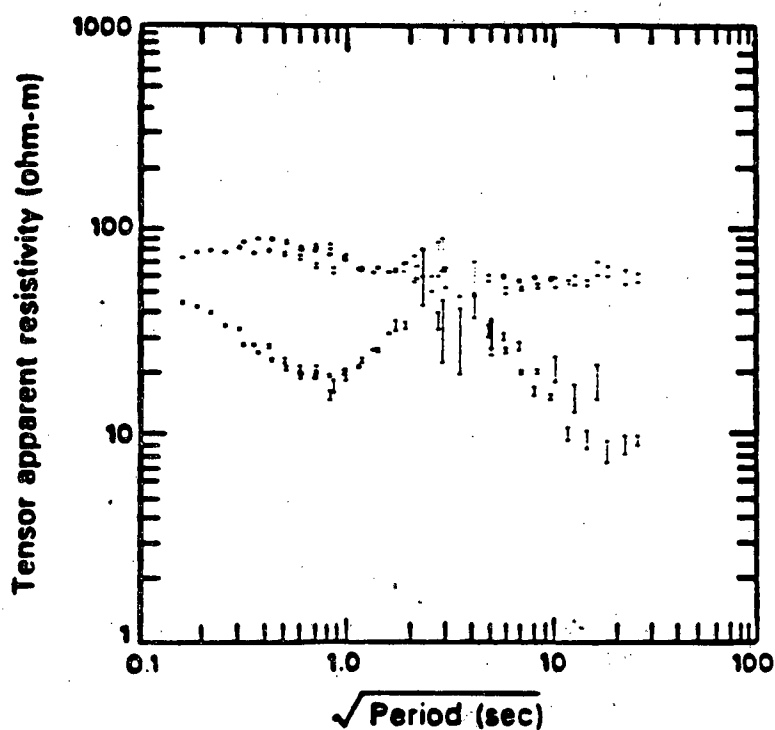


Figure 2.13(b) Magnetotelluric site 5 processed using the remote electric (5B) as the reference signal.

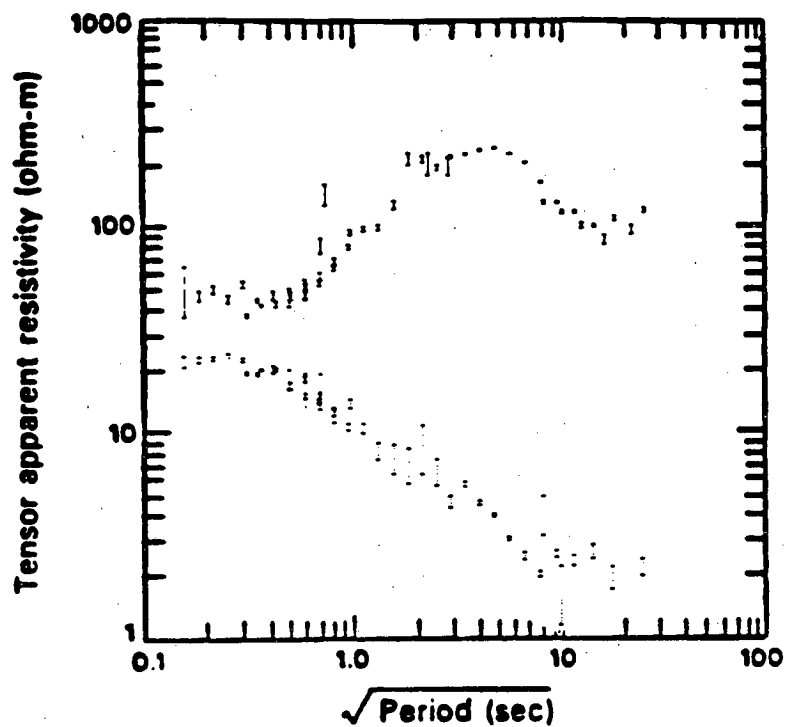


Figure 2.14(a) Magnetotelluric site 6 processed using the remote magnetics as the reference signal.

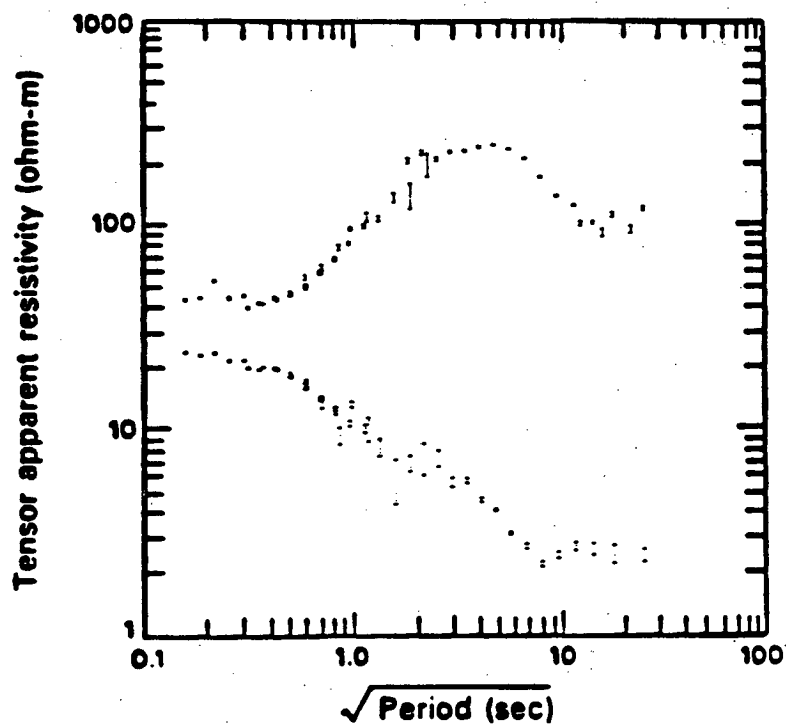


Figure 2.14(b) Magnetotelluric site 6 processed using the remote electric (6B) as the reference signal.

from the off-diagonal elements of the impedance tensor using the remote magnetic signals as the reference. The lower plot indicates the same information with remote electric fields used to process the data. All five figures indicate that the apparent resistivities calculated with either electric or magnetic reference signals provide comparable impedance estimates.

When the field survey was planned, the choice was made to use a horizontal magnetic field measurement as the remote reference signal. Magnetic fields were chosen because they are less susceptible to the distorting effects of near surface inhomogeneities than the electric fields. This decision was made at the expense of losing the additional information regarding the subsurface conductivity which may have been obtained by using the remote electric signals. The results depicted in Figures 2.10 through 2.14 indicate that the increased spatial sampling provided by the substitution of an additional remote telluric for the remote magnetic measurement would have been a wise decision. If remote electric signal processing had been incorporated into the survey plan, unbiased impedance estimates could have been calculated along with an additional six measurement sites. This procedure was inadvertently used in the cluster of measurements at Old Maid Flat, sites 7, 7A, 7B, 7C. The remote magnetometer malfunctioned and was replaced by an additional remote telluric site. These data were processed using remote electric fields and resulted in excellent impedance estimates.

#### [ V ] A Comparison of Two Processing Techniques for Bias Removal

Various techniques have been developed to reduce the effects of noise on the impedance estimates, using only local field measurements ( Kao and Rankin 1977;

Jupp 1978). These techniques have the advantage of requiring no additional information and thus simplifying the acquisition requirements. The relative merit of these techniques compared to the remote reference scheme has not been shown when data are characterized by low predicted coherencies or correlated noise components. However, a comprehensive study of bias removal using data with these characteristics, indicated that a successful bias reduction scheme would require additional information with uncorrelated noise properties with respect to the local measurements, Goubau, Gamble and Clarke (1978).

An opportunity to compare directly a local field bias reduction scheme and the remote reference technique on the same data sets was provided by this survey. The data were initially processed by the contractor using a bias reduction scheme which required only local field measurements. This approach used multiple coherence estimates to develop a system of nonlinear equations which were solved in an iterative fashion. A detailed description of this procedure was published by Lienert, Whitcomb, Phillips, Reddy and Taylor (1980).

This iterative method may be easily summarized. Initially one assumes a signal to noise ratio ( $sn$ ) for the magnetic field components and calculates the multiple coherence functions from the auto and cross-spectral estimates. Utilizing the relationship between the signal to noise ratio  $sn$  of the various components and the multiple coherence ( $\gamma_{ijk}$ ) of the  $i^{th}$  field component in terms of the  $j^{th}$  and  $k^{th}$  components, one obtains the following nonlinear equations.

$$\gamma_{ijk} = \left( \frac{sn_i}{1 + sn_i} \right) \left( \frac{sn_j + sn_k}{1 + sn_j + sn_k} \right)$$

Using the multiple coherence value based on the field measurements and the assumed  $sn$  value for the magnetic field components, one solves the system of equations for the signal to noise ratio of the electric field components. Next, calculate the signal to

noise estimates for the magnetic fields using the electric field ratios previously obtained. Adjust the various autopowers  $P$  using these estimated signal to noise ratios.

$$P_{i,\text{adjusted}} = P_{i,\text{measured}} \left( \frac{sn_i}{1 + sn_i} \right)$$

These adjusted autopowers are used to calculate an updated multiple coherence estimate. This iterative procedure continues until the updated multiple coherence values equal or exceed unity. The adjusted autopowers are then used to obtain a least squares estimate of the impedance tensor.

Two examples are provided to compare the results using the iterative technique with those provided by the remote reference method. The first comparison is shown in Figure 2.15. The upper portion of this figure indicates the apparent resistivities calculated from the off-diagonal components of the impedance tensor rotated into its principle direction, using the iterative method. The lower portion provides the apparent resistivities based on the same data calculated using remote electric reference signals. Large differences in the two sets of impedance estimates are quite evident, the largest departure occurring in the spectral range above 0.1 second period. This portion of the power spectra was characterized by a low signal to noise ratio. The rapid variations as a function of period indicated in the iterative impedance estimates are physically unlikely. The iterative apparent resistivities calculated at all the sites in this area were characterized by a great deal of spatial variability. In contrast, the impedance estimates calculated by the remote reference technique produced smoothly varying apparent resistivities at site 7 which provided a high degree of spatial coherency with respect to the other measurements in the area.

A second example is shown in Figure 2.16. The upper plots indicate the apparent resistivities calculated using the iterative scheme and the lower plots depict the results

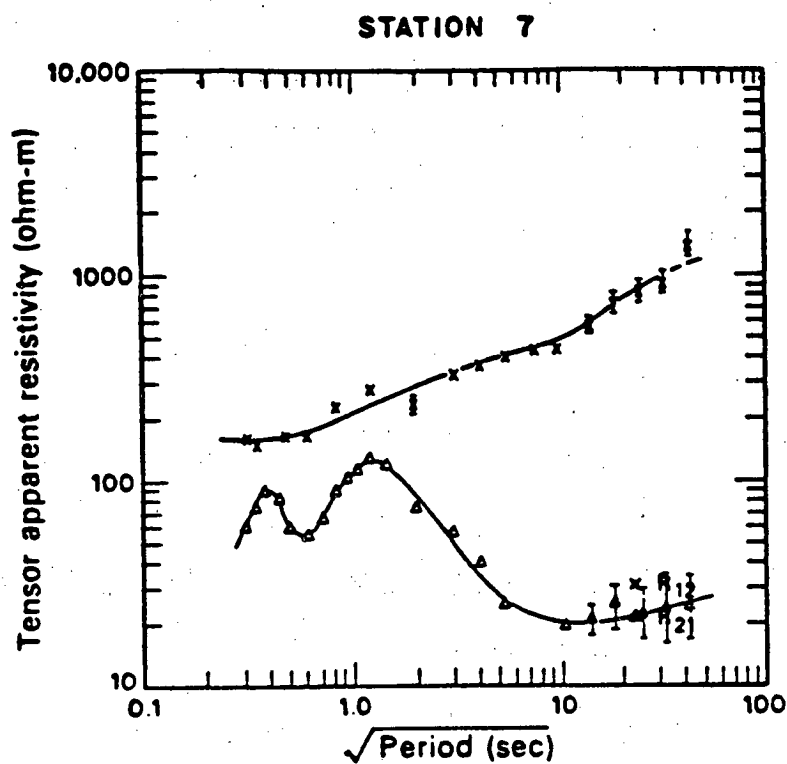


Figure 2.15(a) Magnetotelluric site 7 processed using only local measurements with the iterative bias removal technique.

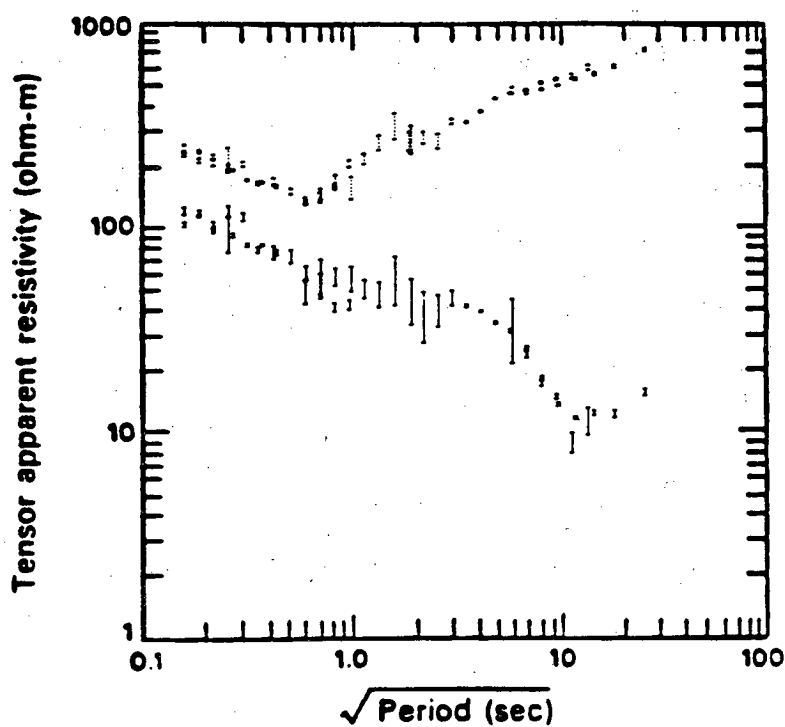


Figure 2.15(b) Magnetotelluric site 7 processed using the remote reference technique.

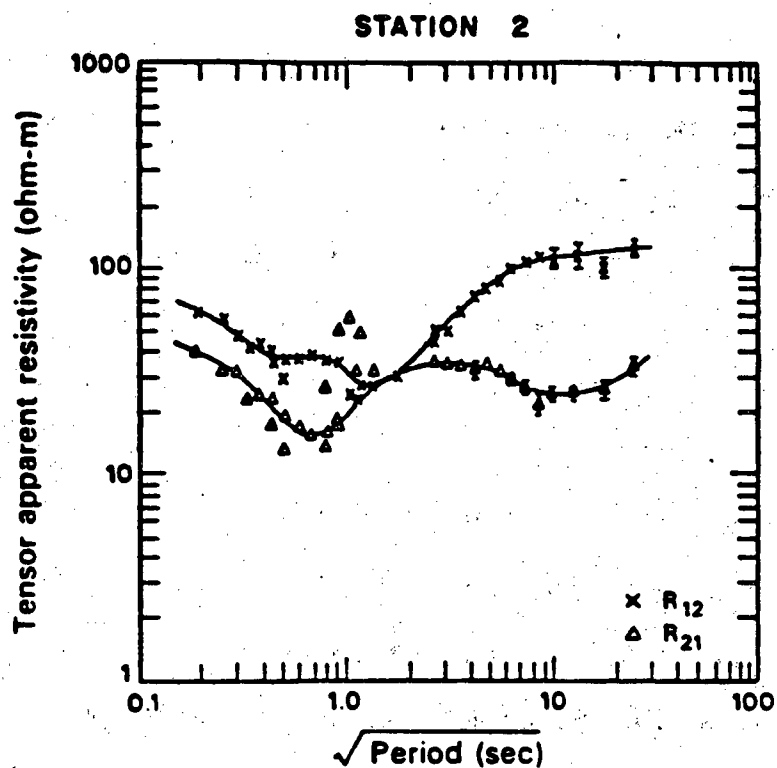


Figure 2.16(a) Magnetotelluric site 2 processed using only local measurements with the iterative bias removal technique.

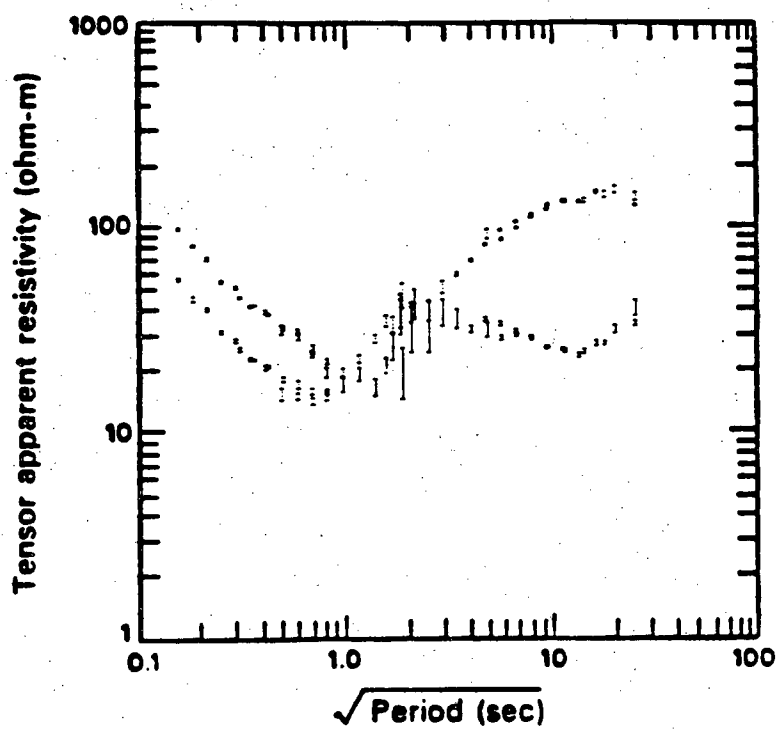


Figure 2.16(b) Magnetotelluric site 2 processed using the remote reference technique.

obtained using the same data with a remote signal processing. The discrepancies between the two sets of apparent resistivities are not as pronounced as in the first example. The only significant departure in these results occur in the vicinity of 1.0 second period. This portion of the spectra was again characterized by a low signal to noise ratio. The smooth variations of the apparent resistivities calculated using the remote reference technique, coupled with their high spatial coherency with other measurement sites in the array, provide evidence supporting the accuracy of these estimates. This indicates that the iterative method fails to provide accurate impedance estimates when the signal to noise ratios are low.

In summary, the remote reference technique provided impedance estimates with smoother frequency characteristics and higher spatial coherencies than the iterative method throughout the entire data set. This improved data quality provided by the remote reference method, proved to be an invaluable aid for interpreting these data.

## Chapter 3

### Topographic Effects at Mount Hood

#### [ I ] An Evaluation of the Topographic Effect on Magnetotelluric Data

The Interpretational complexities associated with magnetotelluric data may be compounded by the distortion of the surface field measurements caused by near surface inhomogeneities. The degree of this distortion depends on the relative conductivity contrast with respect to the background media, the size, and the shape of the anomalous zone. The most obvious source of field distortion in a mountainous region would be the topography. This problem was considered in detail since the topographic relief in the region around Mount Hood ranged from 3400 meters on the peak to as low as 600 meters in the surrounding valleys over lateral dimensions on the order of tens of kilometers.

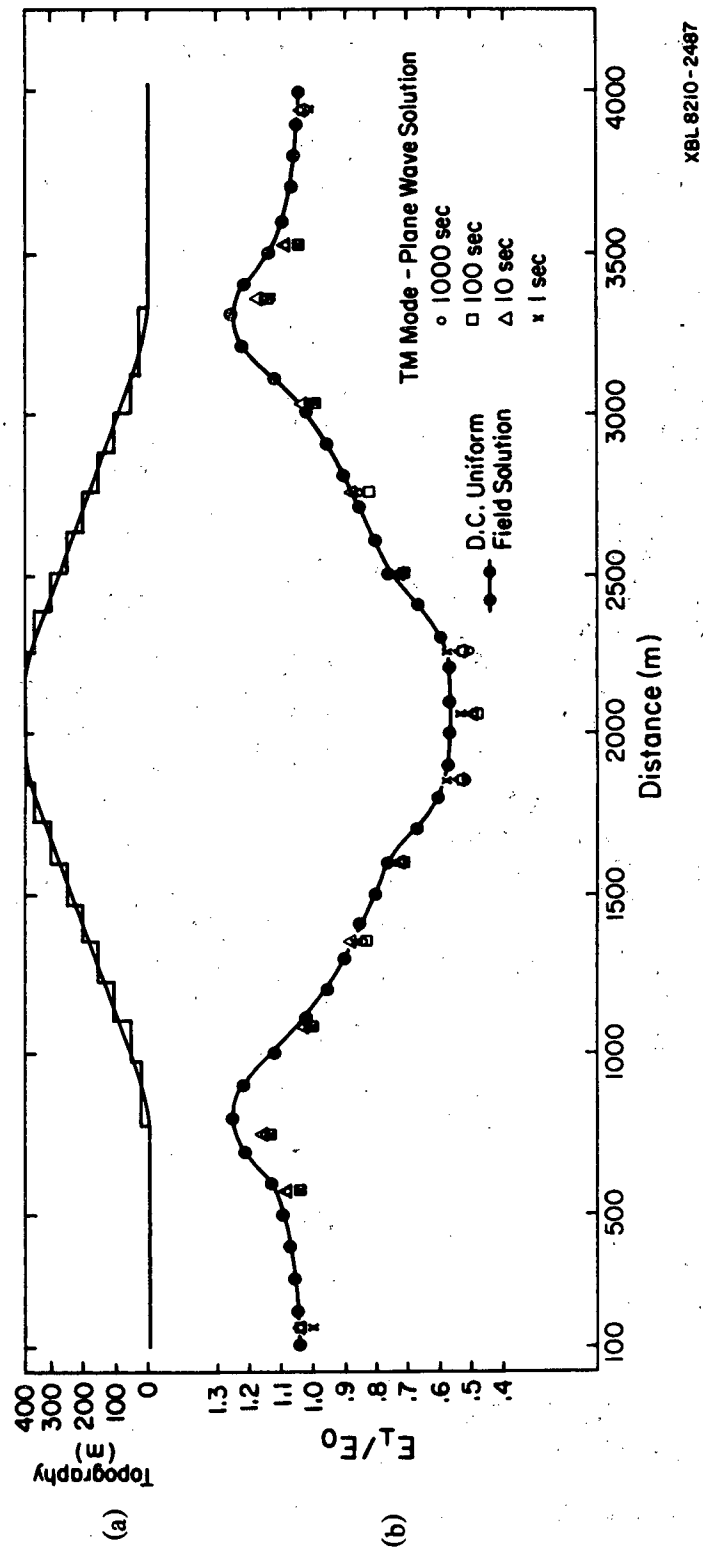
To estimate the effects of this type of "geologic noise", a set of two dimensional topographic models were calculated using a half-space resistivity of 100 Ohm-m. The lateral dimensions were approximately 2500 meters with a height of 375 meters. These dimensions were appropriate to simulate the effects on local measurements caused by the mountains in the survey area.

The magnetotelluric response was simulated using a two dimensional modeling program which provided a solution to Maxwell's equations through the use of the transmission system and network analogies. The program, developed by T. Madden, was modified and provided to the author by K. Vozoff. The modeling results indicated that the only field component which was significantly affected by the topographic

model was the electric field directed perpendicular to the strike of the model. This transverse magnetic (TM) mode response was compared to the direct current solution developed by Oppliger (1982). This solution was calculated using a three dimensional integral equation solution of Laplace's equation. The topography was modeled by rectangular cells oriented parallel to the local terrain. Each cell provided a constant surface charge distribution which simulated the potential distortion caused by the non-planar surface. The comparison was made by using an elongate three dimensional structure to simulate the two dimensional model. A uniform current source was provided by placing the source electrode a large distance, on the order of fifty model dimensions, from the center of the model. The electrode was positioned such that the resulting current flow was perpendicular to the strike direction.

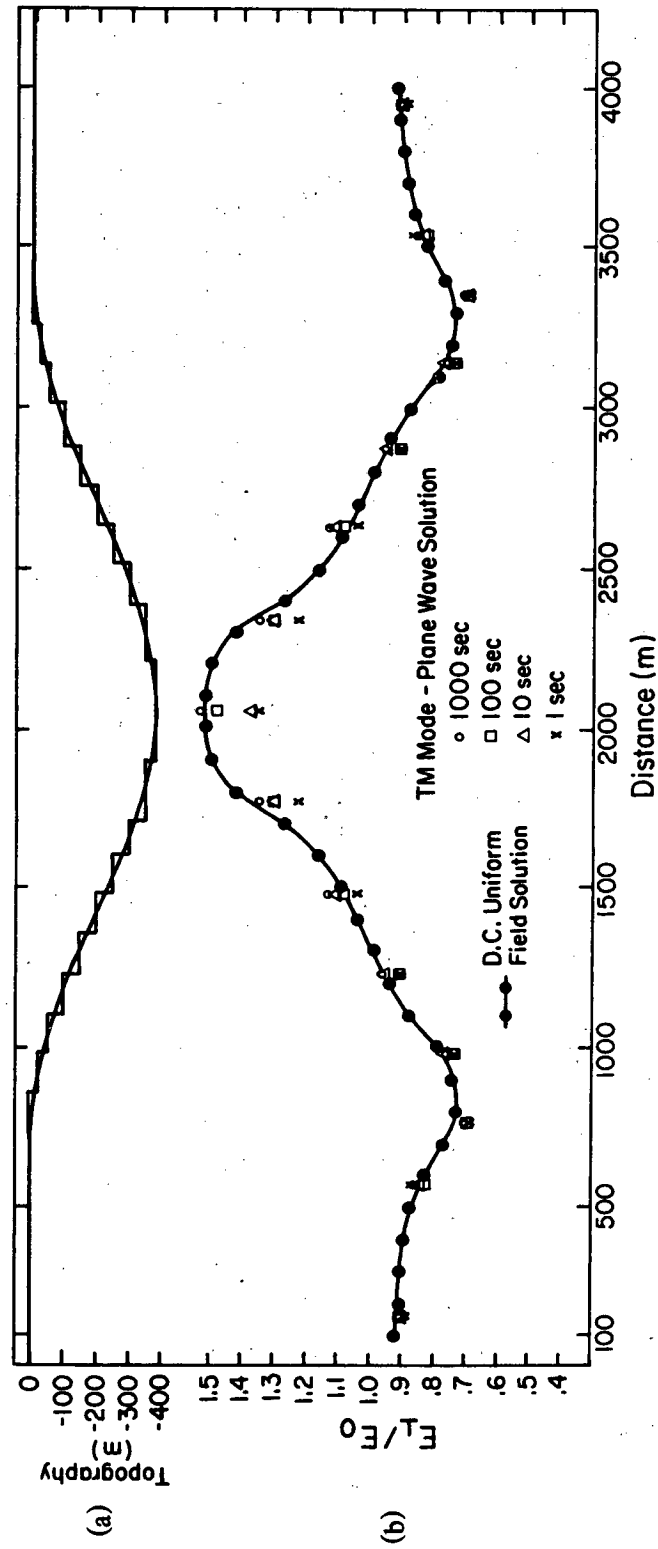
The first model considered was a simple ridge with a twenty degree slope, which is shown in Figure 3.1(a). The steps indicate the electromagnetic model which approximates the topographic feature with rectangular cells. The solid smooth line indicates the tangentially oriented cells which provides the integral equation solution to Laplace's equation. The comparison between the electromagnetic response over a band width of three decades (1.0-0.001 hertz) and the direct current solution is shown in Figure 3.1(b). The similarity of the field responses indicates that the magnetotelluric distortion below 1.0 hertz for this model may be well approximated by the D.C. solution. In this figure the total electric field perpendicular to strike is normalized by the undistorted field. The field distortion is over 40 percent at some positions along the profile. A distortion of this magnitude would have a significant effect on the resulting apparent resistivities.

The next simulation considered was a valley with 20 degree slopes which is shown in Figure 3.2(a). Both the electromagnetic response from 1.0 to 0.001 hertz and the direct current solution are presented in Figure 3.2(b). As in the previous case, the results are similar; indicating that electromagnetic distortion below 1.0 hertz



XBL 8210-2487

Figure 3.1 (a) Topographic ridge model (b) electric field perpendicular to strike normalized by the undistorted field for the TM mode plane wave and D.C. responses.



XBL 8210-2488

Figure 3.2 (a) Topographic valley model (b) electric field perpendicular to strike normalized by the undistorted field for the TM mode plane wave and D.C. responses.

may be well approximated by the D.C. solution.

These two models represent extreme examples of two dimensional topography which could significantly affect the field measurements. The results indicate that the electric fields in the frequency range considered may be approximated by the D.C. solutions. The phase of the impedance for the TM mode was less than four degrees at 1.0 hertz. The plane wave response for transverse electric (TE) source polarizations (electric field parallel to strike) was less than ten percent in amplitude and one degree in phase. The amplitude of the TM mode electric field was the only field component which suffered a significant distortion. This was expected since the maximum dimension of the model (2500 meters) was less than the half space skin depth of approximately 5000 meters. The size of the electromagnetic scatterer with respect to the skin depth is related to the relative dominance of the two mechanisms responsible for the induced fields. The following representation for the electric field (**E**) and the magnetic induction (**B**) as a function of a scalar potential (*p*) and a vector potential (**A**) is a convenient form to visualize this bimodal nature of the induced electromagnetic fields.

$$\mathbf{E} = -\left[\nabla p + \frac{\partial \mathbf{A}}{\partial t}\right]$$

$$\mathbf{B} = \nabla \times \mathbf{A}$$

This dual nature of the electromagnetic fields has been investigated by various researchers, e.g. Berdichevskiy and Faynberg (1972). A rigorous development of the concept, applied to forward modeling, was presented by Vasseur and Weidelt (1977). When the dimensions of the anomalous region are sufficiently small, the primary electromagnetic fields are characterized by small spatial variations within this zone. As these variations decrease the electrodynamic solution approaches the static solution and the gradient of the scalar potential becomes the dominant term representing the secondary fields.

## [ II ] The Evaluation of a Distortion

### Removal Technique

Since the distortion in the frequency range below 1.0 hertz is dominantly galvanic in nature, one may assume with some confidence that the mutual coupling between various inhomogeneous structures, whether they are topographic features or buried bodies, would not be a significant factor. This would imply that the property of superposition commonly associated with the solution to Laplace's equation could be utilized to separate the effects of topography and buried anomalous zones. The problem of detecting and removing the effects of near surface inhomogeneities is not new; one approach was presented by Larson (1977). However, the removal of the field distortion due to topography has not been investigated. The idea of normalizing the estimated impedance elements to compensate for the topographically induced distortions was simplified since the only field component which suffered a significant degree of distortion was the electric field directed perpendicular to strike.

The procedure is based on the assumption that the measured electric field in the vicinity of a topographic feature may be linearly related to a reference electric field located where no topographic distortion is present.

$$\mathbf{E}_x^m(\omega) = d(\omega) \mathbf{E}_x^{Ref}(\omega)$$

The distorted impedance is defined as follows,

$$\mathbf{Z}_{xy}(\omega) = \frac{\mathbf{E}_x^m(\omega)}{\mathbf{H}_y(\omega)}$$

which is related to the undistorted impedance by the following relationship.

$$\mathbf{Z}'_{xy}(\omega) = \frac{1}{d(\omega)} \frac{\mathbf{E}_x^m(\omega)}{\mathbf{H}_y(\omega)} = \frac{1}{d(\omega)} \mathbf{Z}_{xy}(\omega)$$

As in the models presented in Figures 3.1 and 3.2, the frequency dependent distortion factor may be well approximated by its D.C. value when the maximum dimension of the feature is much less than the skin depth in the media.

In order to check the validity of the assumptions used in this stripping procedure, the first model with all dimensions increased by a factor of two and with the addition of a buried conductor was used to test the technique. Their relative geometry is indicated in Figure 3.4(b). The distortion factor calculated using a model of the topographic feature alone is provided in Figure 3.3. The corrected electric fields are calculated for various frequencies using both the frequency dependent and the D.C. distortion factors. The results are shown in Figure 3.4. The solid line indicates the electric fields on the surface due only to the buried conductor. The square symbol indicates the corrected field using the frequency dependent distortion factor and the triangular symbol depicts the corrected fields utilizing the D.C. distortion factor. The procedure worked well at all frequencies considered, when a frequency dependent complex distortion factor was used. However, the D.C. distortion factor only provided a reasonable correction for frequencies below 0.1 hertz. The poor results obtained using the D.C. factor at 1.0 hertz is probably related to the size of the scatterer. The skin depth being on the same scale as the dimension of the scatterer at this frequency.

A possible pitfall, in the use of this stripping technique may be associated with using a homogeneous topographic feature to calculate the distortion factor. Any anomalous conductivity within the topographic feature would have a degrading effect on the method. The model provided in Figure 3.5(b) is the same as the previous model with the addition of a 200 meter thick 30 Ohm-m layer, located in the base of the ridge. As one would expect the observations in the vicinity of the layer intersection with the surface are greatly distorted. However, the corrected fields near the crest of the ridge are only slightly distorted by using the distortion factor calculated from the homogeneous ridge model. The complex distortion factor provides a phase

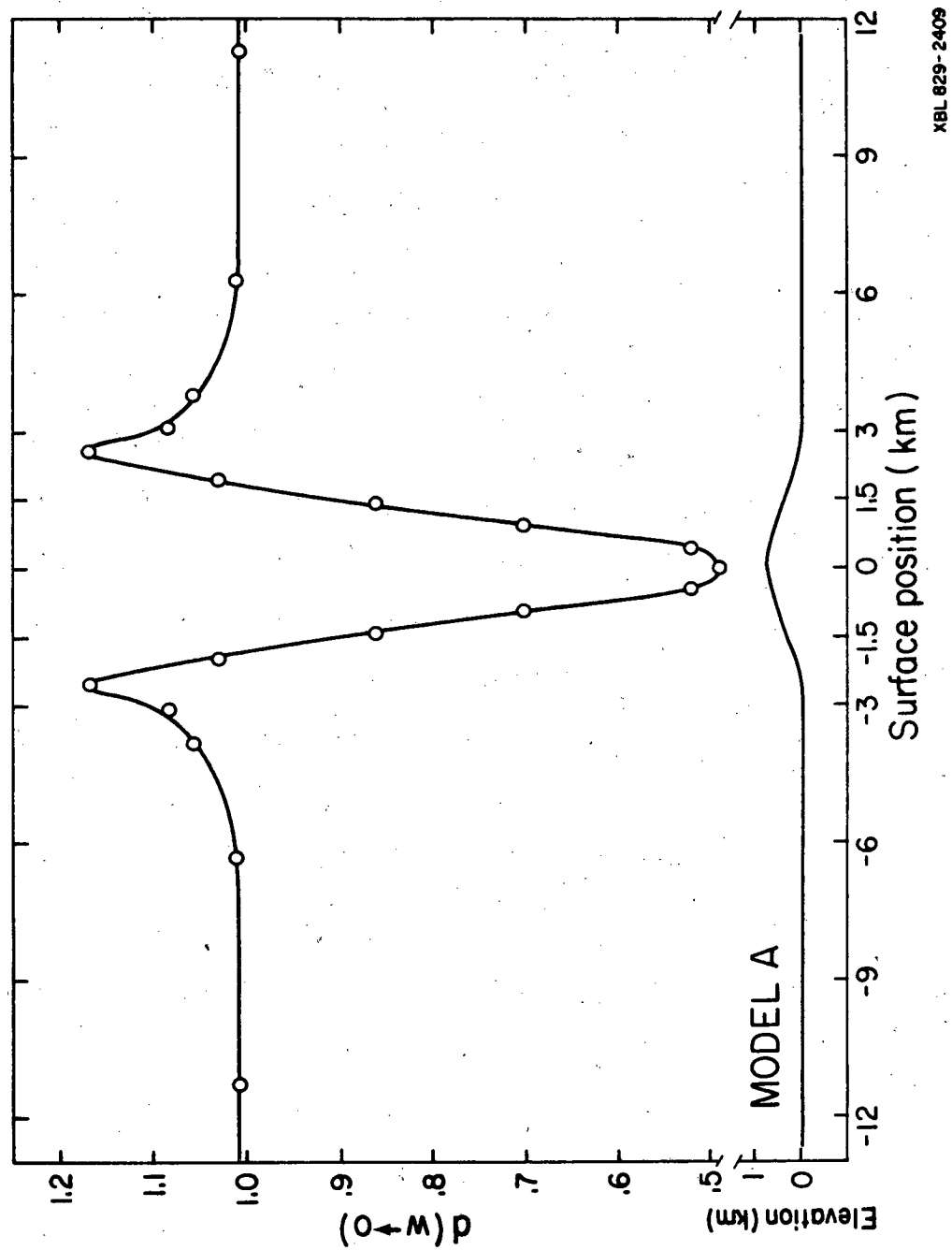
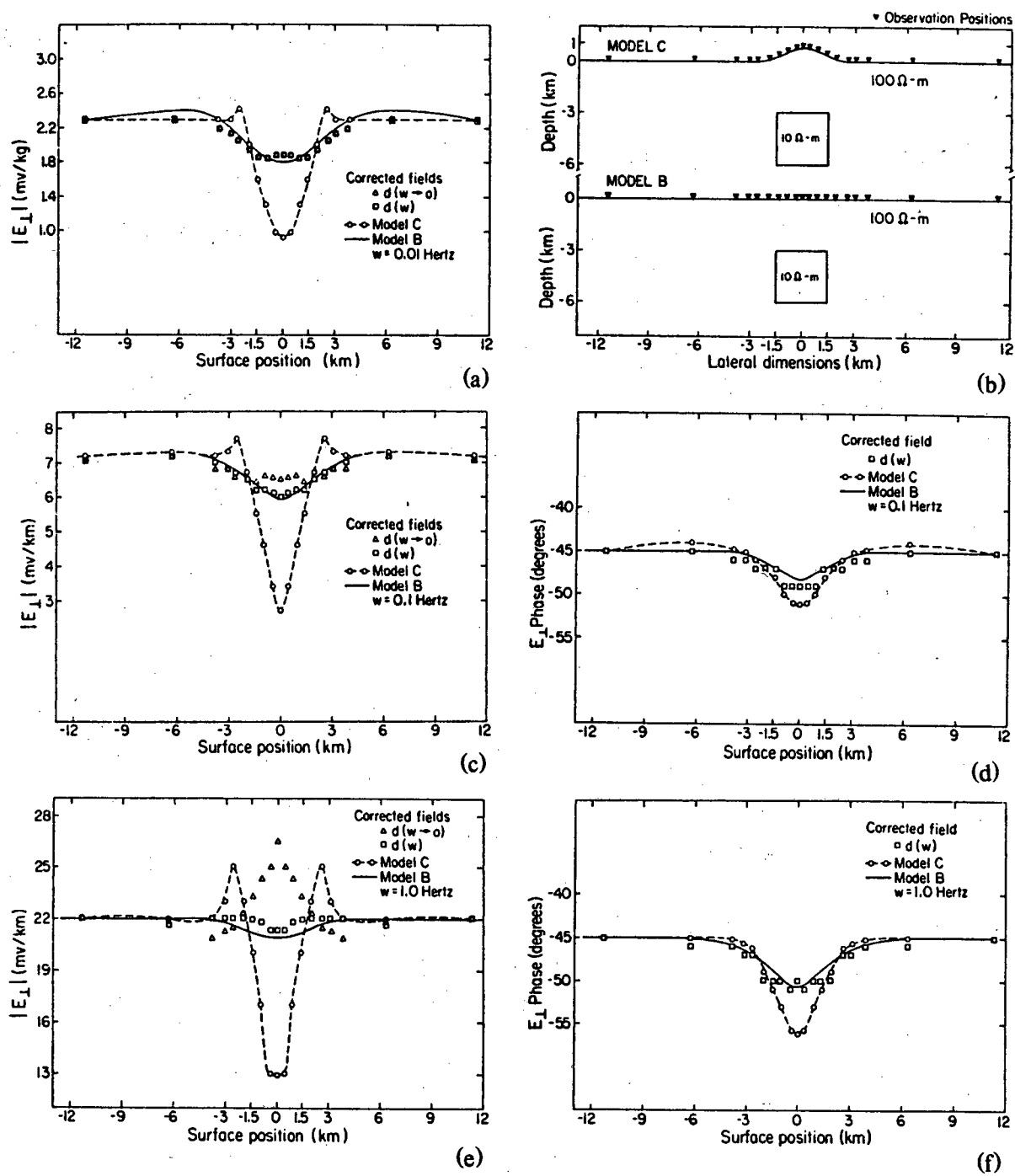


Figure 3.3 The D.C. distortion factor for the two dimensional model A.



**Figure 3.4** The stripping technique applied to model C using both the D.C. and frequency dependent distortion factors calculated from the response provided by model A.

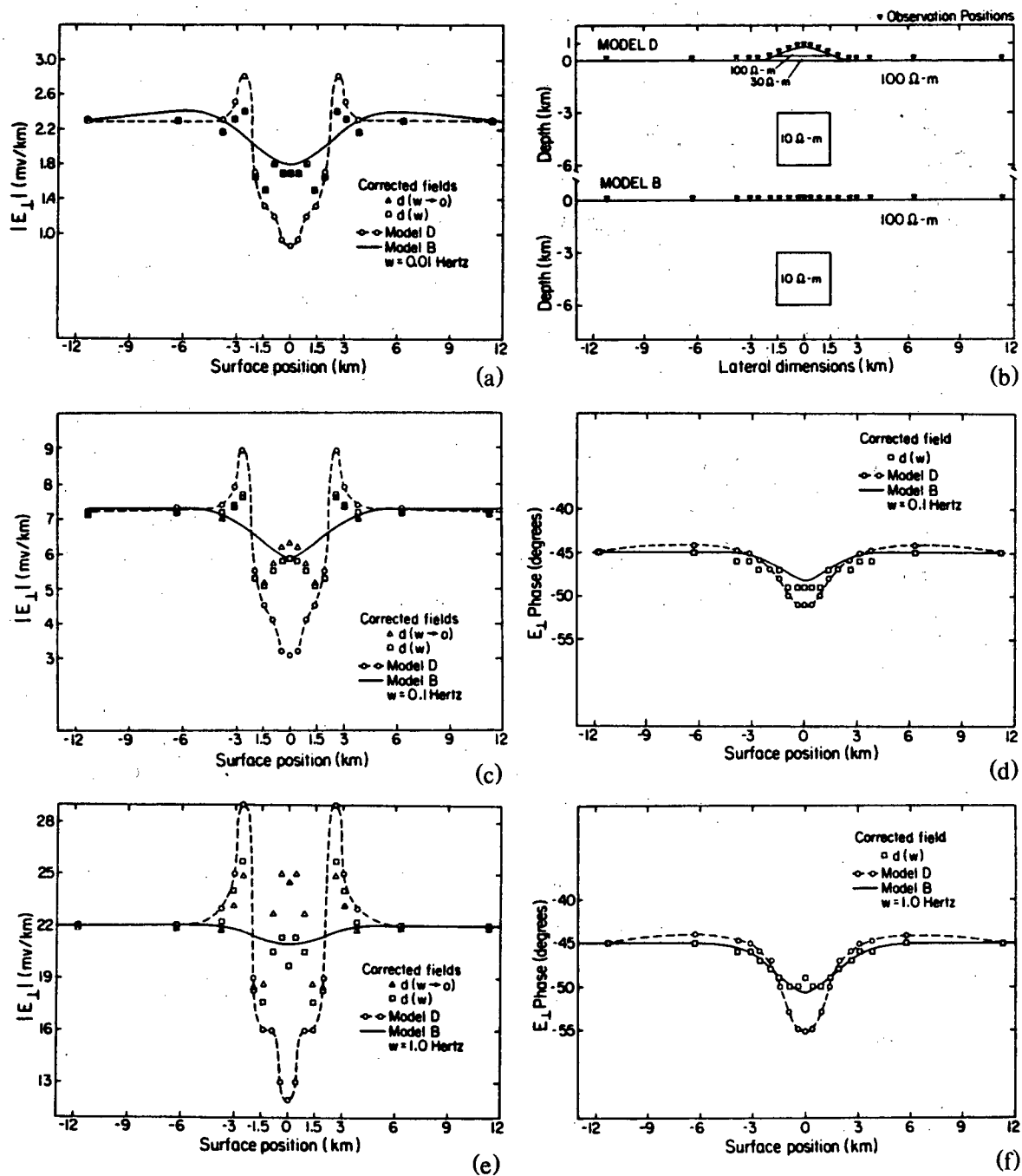


Figure 3.5 The stripping technique applied to model D using both the D.C. and frequency dependent distortion factors calculated from the response provided by model A.

correction which is virtually unaffected by the presence of the anomalous layer.

### [ III ] A Three Dimensional Extension and Application of the Stripping Technique

The use of the topographic distortion factor may be extended to three dimensions. The distorted electric fields are linearly related to the undistorted reference electric fields through the matrix relationship which is in general a two by two tensor with complex elements.

$$\begin{bmatrix} E_x^m \\ E_y^m \end{bmatrix} = \begin{bmatrix} D_{xx} & D_{xy} \\ D_{yx} & D_{yy} \end{bmatrix} \begin{bmatrix} E_x^{Ref} \\ E_y^{Ref} \end{bmatrix}$$

This may be indicated in vector notation as follows.

$$\mathbf{E}^m = [\mathbf{D}]\mathbf{E}^{Ref} \quad (3.1)$$

The distorted impedance tensor  $\mathbf{Z}$  is related to the measured field components in the following way.

$$\mathbf{E}^m = [\mathbf{Z}]\mathbf{H}^m \quad (3.2)$$

$$\mathbf{H}^m \approx \mathbf{H}^{Ref} \quad (3.3)$$

Substitute equations 3.1 and 3.3 into equation 3.2.

$$\mathbf{E}^{Ref} = [\mathbf{D}]^{-1} [\mathbf{Z}] \mathbf{H}^{Ref} = [\mathbf{Z}]' \mathbf{H}^{Ref} \quad (3.4)$$

where

$$[Z]' = [D]^{-1} [Z]$$

The distortion matrix  $D^{-1}$  is defined as follows.

$$[D]^{-1} = \begin{bmatrix} A(1) & A(3) \\ A(2) & A(4) \end{bmatrix}$$

The undistorted impedance tensor  $Z$  may be easily calculated once a forward simulation of the field response due to the topographic feature has been provided.

$$[Z]' = \begin{bmatrix} (A(1)Z_{xx} + A(3)Z_{yx}) & (A(1)Z_{xy} + A(3)Z_{yy}) \\ (A(2)Z_{xx} + A(4)Z_{yx}) & (A(2)Z_{xy} + A(4)Z_{yy}) \end{bmatrix} \quad (3.5)$$

In a similar manner, field distortions due to a known near surface inhomogeneity with dimensions on the order of or less than a skin depth, may be removed. This however, may require the use of a linear relationship relating the distorted horizontal magnetic fields to the undistorted reference magnetic fields.

$$H^m = [G] H^{Ref} \quad (3.6)$$

Substitute equations 3.6 and 3.1 into equations 3.2 which provides equation 3.7 after some simple algebraic manipulations.

$$E^{Ref} = [Z]'' H^{Ref} \quad (3.7)$$

where

$$[Z]'' = [D]^{-1} [Z] [G]$$

For the topographic cases where the dimensions of the features are much less than the skin depth, the field distortion is due to the surface charges which accumulate on the nonuniform air-earth interface. The resulting distortion has a major effect on the

normally incident electric field and minimal effect on the tangential electric and horizontal magnetic field components.

The models presented in Figures 3.1 and 3.2, provide extreme examples of local topographic variations observed in the vicinity of Mount Hood. These models indicate that the distortion factor was nearly independent of frequency and therefore could be approximated by the D.C. value. This approximation greatly simplifies the forward modeling requirements, since the D.C. solution is a scalar problem as compared to a vector solution for the frequency dependent case.

The topography data, covering a thirty five square kilometer area surrounding Mount Hood, was digitized and interpolated onto a forty by forty unit square grid, as depicted in Figure 3.6. The arrows indicate the field measurement sites and a vertical to horizontal scaling ratio of 2:1 was used to enhance the topographic relief. This figure represents the model with an exaggerated vertical scale which was used for the D.C. integral equation solution. These data are presented with the correct scales in the contour map provided in Figure 3.7.

The resulting forward models were used to calculate the distortion matrix. The diagonal components  $A(1)$  and  $A(4)$  of this matrix are shown in contour form on Figures 3.8(a) and 3.8(b) respectively, the contours representing positions of equal field distortion. The unit contour indicates regions where no distortion of the impedance tensor occurs. Contour values greater than unity indicate that observed impedance elements on these contours would be biased down. These contours usually coincide with positions of high topographic relief. The contours for values less than unity represent regions of abnormally high current density and are generally associated with topographic lows. Impedance measurements on these contours would be biased up.

The off-diagonal components of the distortion matrix represent that component of distortion due to a lateral deflection of the primary fields. The direction of this deflected current component is represented by the sign of the distortion element.

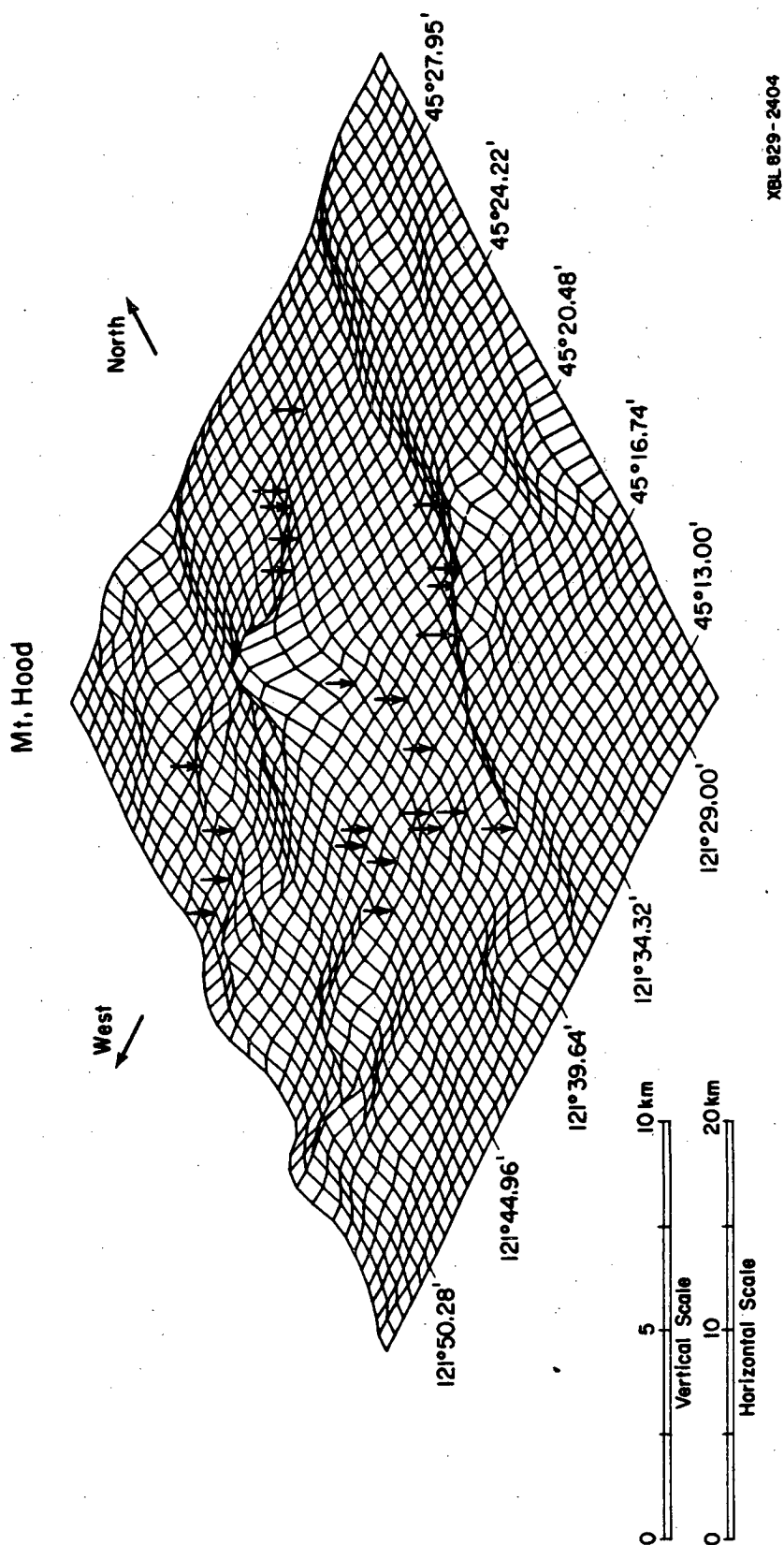


Figure 3.6 Three-dimensional topographic model used to simulate the D.C. response for the region around Mount Hood. The arrows indicate the field measurement locations and a vertical to horizontal scaling ratio of 2:1 was used to enhance the relief.

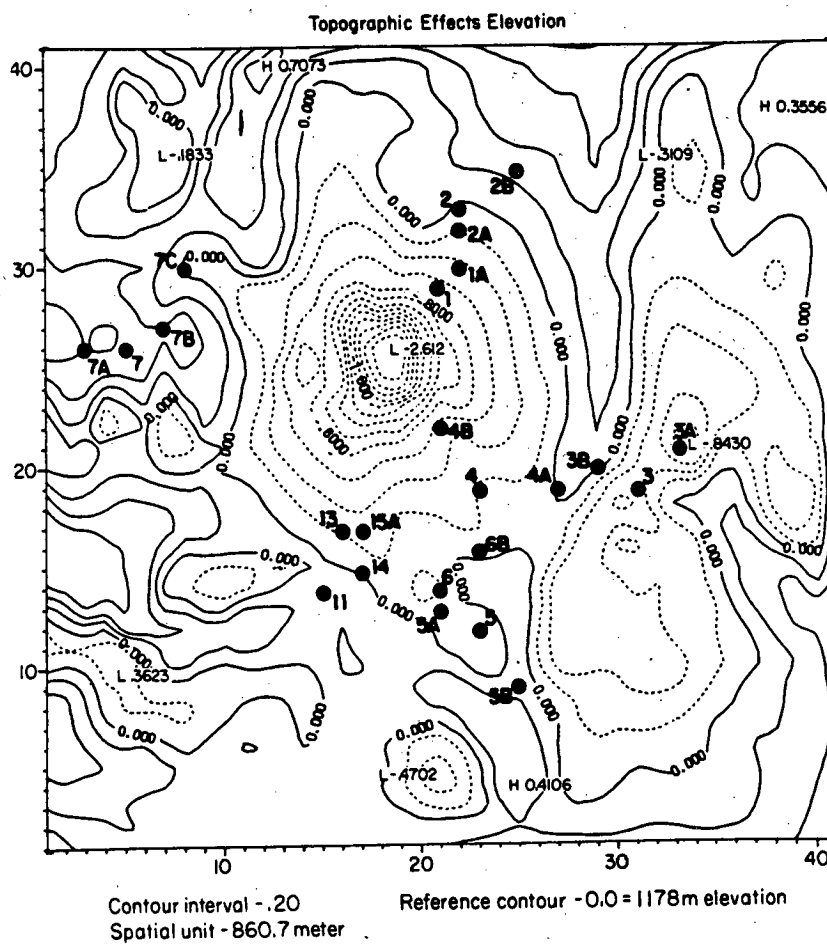
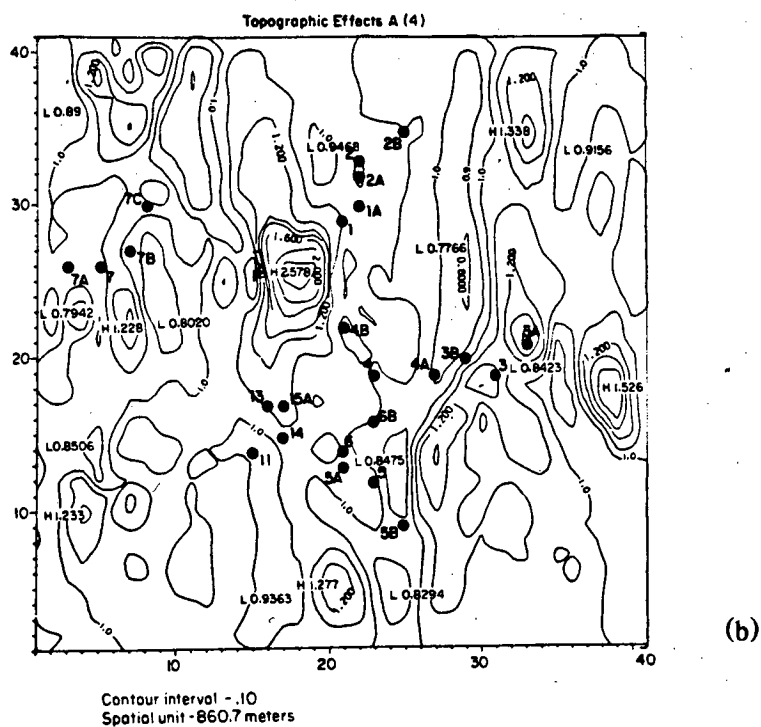
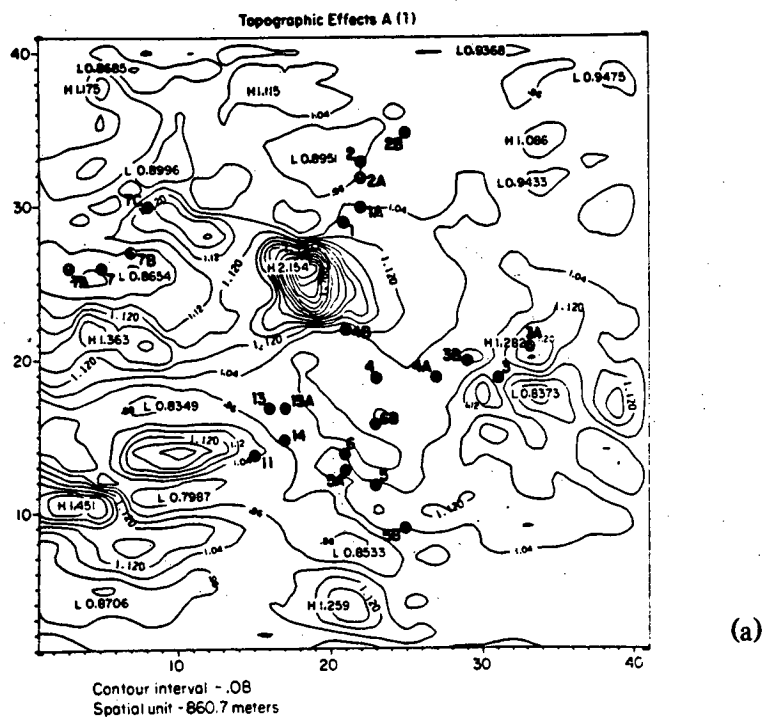
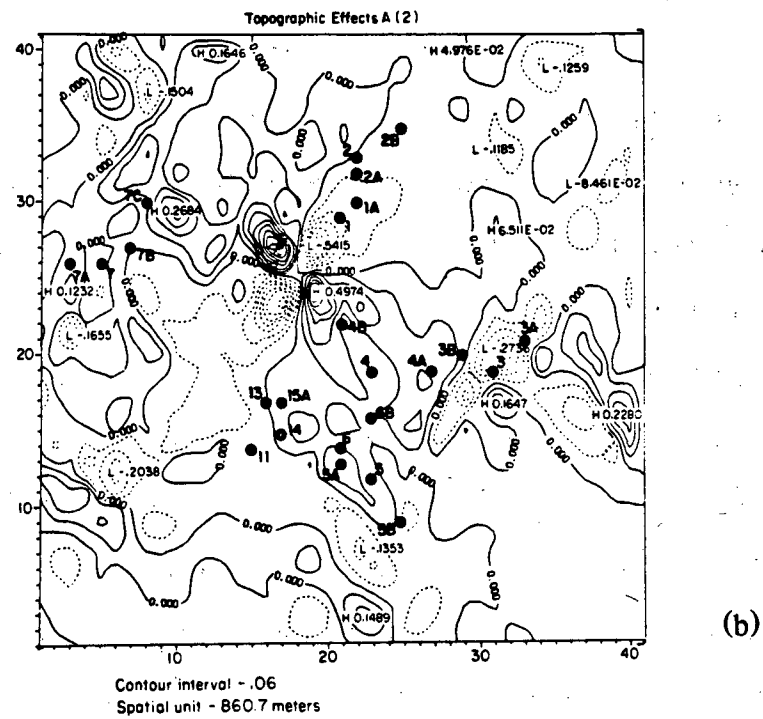
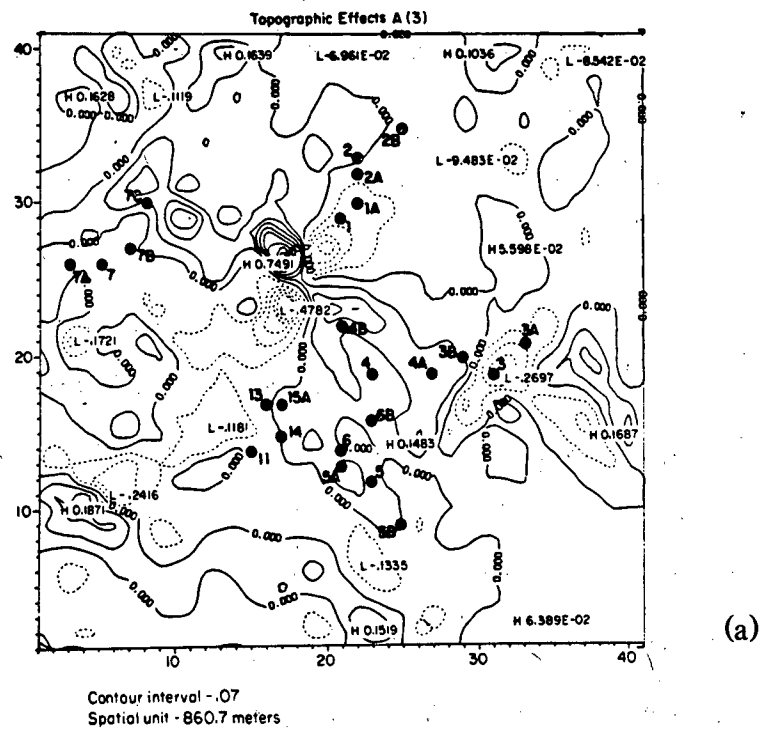


Figure 3.7 Topographic model used to simulate the topographic distortion at Mount Hood.



**Figure 3.8** The diagonal components of the distortion matrix for the Mount Hood model.



**Figure 3.9** The off-diagonal components of the distortion matrix for the Mount Hood model.

These components  $A(3)$  and  $A(2)$  are provided in Figures 3.9(a) and 3.9(b) respectively. For these components the zero contour indicates positions where no distortion of the electric field is observed. For measurements within areas where these elements deviate significantly from zero, one could expect a resulting bias in the impedance estimates.

A detailed examination of the distortion elements, presented in Figures 3.8 and 3.9, indicate that the field measurement locations most affected by the topographically induced field distortions are sites 3 and 3A. These sites are located on points of high elevation, approximately ten kilometers east of Mount Hood. The D. C. distortion matrix was applied to these data and the results are shown in Figures 3.10(a), (b), (c), (d).

The apparent resistivity at site 3 was characterized by a three decade separation between the diagonal impedance components. This measurement was acquired on a narrow ridge connecting two dominant topographic high points in the area. The ridge had steeply dipping slopes, with elevation changes of 450 meters over lateral dimensions of 1800 meters. The diagonal distortion elements presented in Figure 3.8 are both near unity at this location, providing no evidence of distortion. However, the off-diagonal components shown in Figure 3.9 deviate from zero by a significant amount, which indicates that current is laterally distorted in this vicinity. The effects of the resulting corrections on the apparent resistivities are shown on Figures 3.10(a) and 3.10(b). These corrections which are provided for the off-diagonal elements of the impedance tensor, resulted in a smaller separation between the resulting apparent resistivities calculated in the principal directions. This correction was insignificant in comparison to the distortion caused by subsurface inhomogeneities.

The second location which was appreciably affected by the terrain was site 3A. This measurement was acquired on a mountain peak east of Mount Hood. Both diagonal distortion elements in Figure 3.8 indicate that distortion occurs at this location.

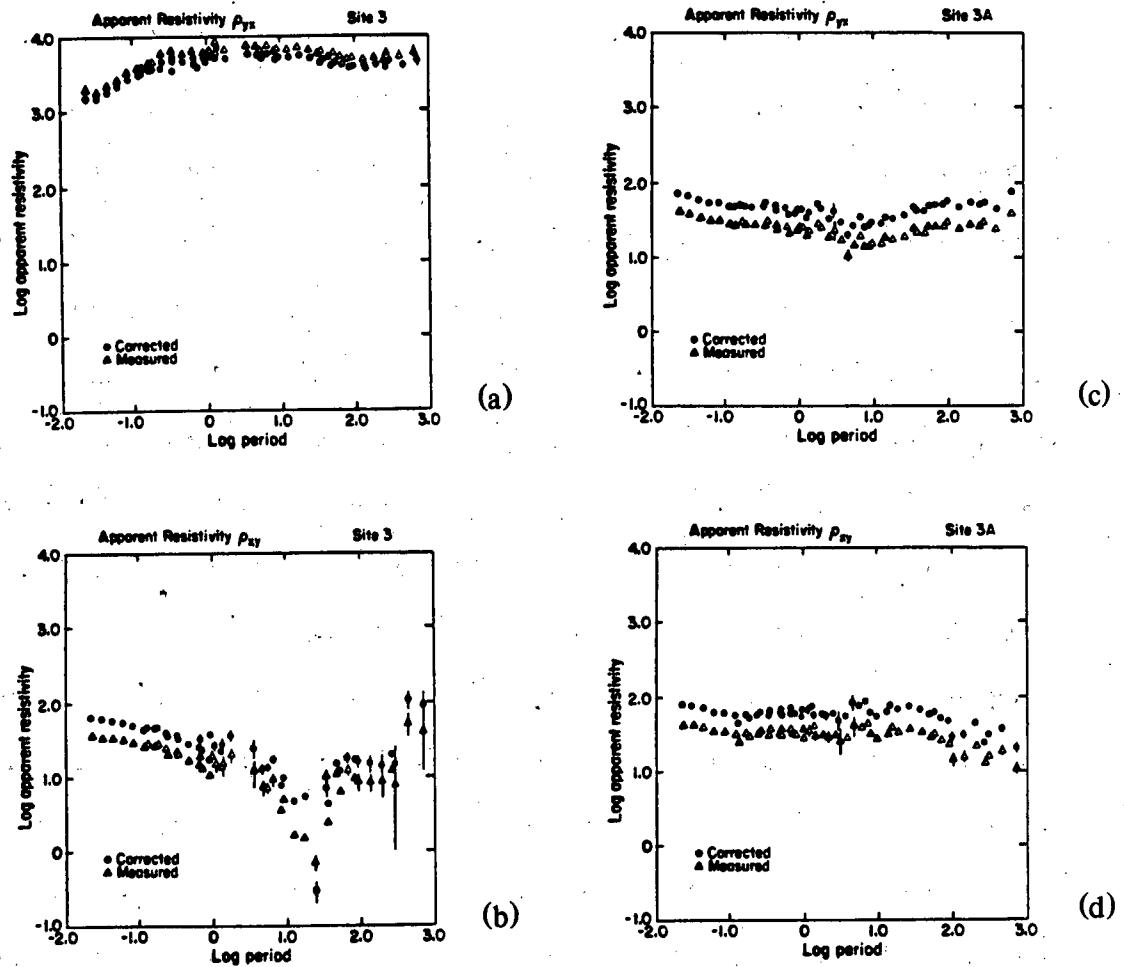


Figure 3.10 The corrected apparent resistivities calculated from the off-diagonal elements of the impedance tensor using the distortion matrix elements shown in Figures 3.8 and 3.9 for (a) site 3-Zyx (b) site 3-Zxy (c) site 3A-Zyx (d) site 3A-Zxy.

The off-diagonal elements shown in Figure 3.9 are non-zero, providing additional evidence indicating a significant amount of field distortion in this area. The results of the correction are shown in Figures 3.10(c) and 3.10(d). They are similar to the TM mode response of the two dimensional ridge model, indicating that the surface electric fields were reduced in amplitude on the crest of the ridge. However, both electric field components at site 3A were affected by the three dimensional terrain, resulting in a corrected impedance with larger apparent resistivities in both principal directions.

This analysis implies that the topographic features in mountainous regions may significantly affect local impedance measurements. These sources of field distortion may be effectively removed by the simple stripping technique presented. The major limitation on the method is related to the difficulties associated with obtaining the solution of the general three dimensional forward problem in electrodynamics. For cases where the topography is sufficiently resistive, such that the dimensions of the topographic features are small relative to the skin depth of the media, one may calculate the distortion factors from the solution of Laplace's equation. This scalar problem is much more amenable to accurate solutions representing realistic topographic features than the general electromagnetic problem. The utility of the technique was demonstrated by correcting the impedance estimates calculated from data acquired in the vicinity of extreme topographic relief.

## Chapter 4

### Numerical Preliminaries Required for the Three Dimensional Model Studies

#### [ I ] Introduction to a Hybrid Modeling Technique

The data acquired at Mount Hood, were characterized by three dimensional response functions. In order to interpret this data, it was necessary to study the response from a suite of simple three dimensional models which would reflect some of the observed characteristics. There have been several numerical techniques developed in the past few years which could have been implemented to obtain these simulations.

The finite element technique has been used to model arbitrary conductivity distributions by various researchers (Reddy, Rankin, and Phillips 1977; Pridmore 1978). The method is quite expensive and requires a large amount of computer storage since the entire earth must be discretized into an element mesh. The finite difference modeling scheme used by Jones and Vozoff (1978) for magnetotelluric studies has the same disadvantages as the finite element method. The third scheme which has found extensive use in three dimensional magnetotelluric problems has been the integral equation method developed by Weidelt (1975) and Hohmann (1975). This technique has the advantage of confining the discretization zone to that portion of the model occupied by the anomalous conductivity structure. This technique has been implemented using the assumption that the secondary current distributions induced by the zone of anomalous conductivity are constant over each cell. This assumption limits the accuracy of the method but provides a great deal of computational advantages.

The hybrid modeling technique was introduced by Scheen (1978). This scheme combines the versatility and accuracy of the finite element linear shape functions with economic parameterization of the integral equation method. The hybrid modeling technique was chosen for this study because of its availability and computational advantages. The details of the original version of the algorithm and the initial modeling results were presented by Lee, Pridmore and Morrison (1981). The general three dimensional electromagnetic scattering problem was solved in terms of the secondary electric fields. The electric field solution was preferred over the magnetic field formulation because the integral equation component of the algorithm required the electric field values within the anomalous finite element cells. The solution in terms of the magnetic fields would have required the calculation of the electric fields within the mesh via a numerical approximation of the curl operator. This approximation would have been difficult to accurately implement.

The hybrid method consists of discretizing the anomalous region of the earth and describing the field solutions within the resulting mesh by a mathematical functional defined by the minimization theorem, Pridmore (1978).

$$F(E_s) = E_s^T [K] E_s + 2 E_s^T [S] E_p \quad (4.1)$$

$E_s$  = secondary electric fields

$E_p$  = primary electric fields

$$E_s = \sum_{q=1}^8 N_q E_s^q$$

$N_q$  = linear shape function for hexahedral elements

$[K]$  = symmetric banded system matrix

$[S]$  = source matrix

The variation of the functional or the derivative of the functional with respect to the secondary electric fields equated to zero, provides a linear system of equations.

$$[K] E_s = -[S] E_p$$

The solution of this system of equations provides the secondary electric fields which numerically satisfy the vector wave equation. This solution does not however satisfy the correct internal boundary conditions. The finite element solution in this form assumes the continuity of all electric field components within the anomalous region. The physically defined boundary conditions at an interface between different conductivities results in the discontinuity of electric fields, which are required for the continuity of normal current. This omitted boundary condition in conjunction with some numerical problems which will be discussed later, resulted in a poor finite element solution. The algorithm initially assumed the secondary electric fields were zero on the mesh boundaries. The linear system was solved, providing the secondary fields within the mesh. These solutions within the internal region of the mesh containing anomalous conductivities were used by a set of integral equations to update these boundary values. The procedure was repeated until the boundary values converged to a solution. The poor finite element solutions caused by the above errors often resulted in the iterative procedure either diverging or converging to the wrong solution.

## [ II ] The Modified Hybrid Algorithm

The method used to incorporate the correct boundary conditions into the finite element formulation was based on earlier work by Kiha Lee. The scheme which is elegant in its simplicity, may be easily described using one anomalous cell as an

example. This cell with conductivity  $\sigma_a$  surrounded by regions with conductivities  $\sigma_1, \sigma_2, \sigma_3, \dots, \sigma_6$  is shown in Figure 4.1. The x directed electric field inside the cell  $E_{x_a}$  is related to the external field  $E_{x_e}$  at the cell boundary between nodes 5,6,7 and 8 by the following relation:

$$\sigma_a E_{x_a}^{total} = \sigma_2 E_{x_e}^{total}$$

which may be formulated in terms of secondary electric fields  $E^{s,q}$  and primary electric fields  $E^{p,q}$  at the  $q^{th}$  node,

$$\sigma_a (E_{x_a}^{s,q} + E_{x_a}^{p,q}) = \sigma_2 (E_{x_e}^{s,q} + E_{x_e}^{p,q})$$

where  $E_{x_a}^{p,q} = E_{x_e}^{p,q}$ . This relation is a statement of the continuity of normal current on this surface of the cell. When the continuity condition is extended to include the entire surface, one obtains the following set of equations.

$$E_{x_a}^{s,q} = \frac{\sigma_1}{\sigma_a} E_{x_e}^{s,q} + \left( \frac{\sigma_1}{\sigma_a} - 1 \right) E_{x_e}^{p,q} \quad q = 1, 2, 3, 4$$

$$E_{x_a}^{s,q} = \frac{\sigma_2}{\sigma_a} E_{x_e}^{s,q} + \left( \frac{\sigma_2}{\sigma_a} - 1 \right) E_{x_e}^{p,q} \quad q = 5, 6, 7, 8$$

$$E_{y_a}^{s,q} = \frac{\sigma_3}{\sigma_a} E_{y_e}^{s,q} + \left( \frac{\sigma_3}{\sigma_a} - 1 \right) E_{y_e}^{p,q} \quad q = 1, 3, 5, 7$$

$$E_{y_a}^{s,q} = \frac{\sigma_4}{\sigma_a} E_{y_e}^{s,q} + \left( \frac{\sigma_4}{\sigma_a} - 1 \right) E_{y_e}^{p,q} \quad q = 2, 4, 6, 8$$

$$E_{z_a}^{s,q} = \frac{\sigma_5}{\sigma_a} E_{z_e}^{s,q} + \left( \frac{\sigma_5}{\sigma_a} - 1 \right) E_{z_e}^{p,q} \quad q = 3, 4, 7, 8$$

$$E_{z_a}^{s,q} = \frac{\sigma_6}{\sigma_a} E_{z_e}^{s,q} + \left( \frac{\sigma_6}{\sigma_a} - 1 \right) E_{z_e}^{p,q} \quad q = 1, 2, 5, 6$$

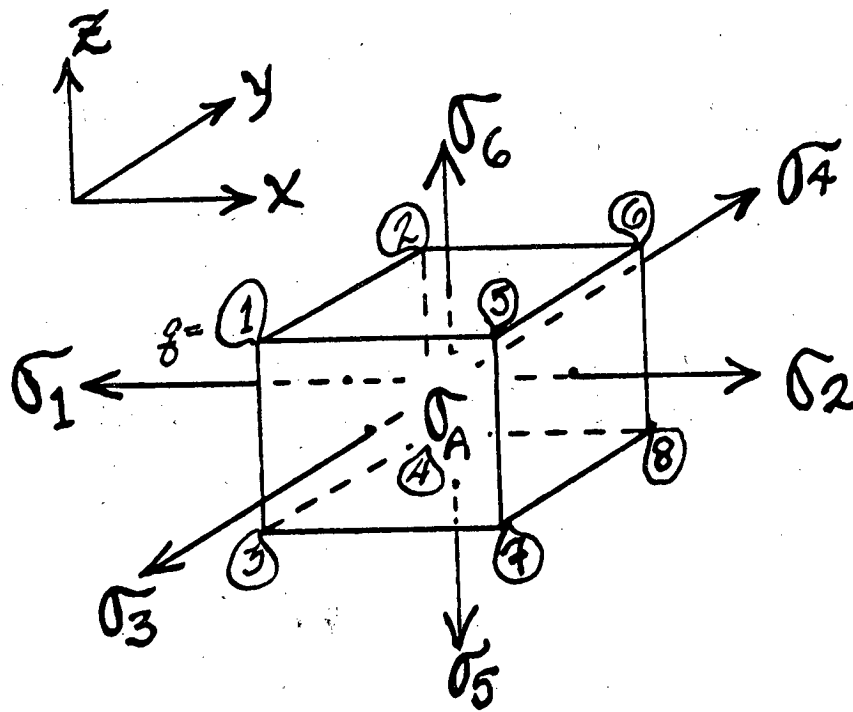


Figure 4.1 Finite element cell with an anomalous conductivity of  $\sigma_a$  surrounded by conductivities  $\sigma_1, \sigma_2, \sigma_3, \dots, \sigma_6$ .

This set of simple transformations are used in each anomalous cell in the mesh. These transformations may be combined into vector notation where  $\mathbf{E}^T$  defines the transpose of  $\mathbf{E}$  and the vectors have twenty-four terms defining the three field components at the eight nodes of the cell as indicated by the following form:

$$\begin{aligned}
 \mathbf{E}_a^{sT} &= \frac{1}{\sigma_a} \left[ \sigma_1 \mathbf{E}_{x_e}^{s,1}, \sigma_3 \mathbf{E}_{y_e}^{s,1}, \sigma_6 \mathbf{E}_{z_e}^{s,1}, \dots, \sigma_2 \mathbf{E}_{x_e}^{s,8}, \sigma_4 \mathbf{E}_{y_e}^{s,8}, \sigma_5 \mathbf{E}_{z_e}^{s,8} \right]^T \\
 &+ \left[ \left( \frac{\sigma_1}{\sigma_a} - 1 \right) \mathbf{E}_{x_e}^{p,1}, \left( \frac{\sigma_3}{\sigma_a} - 1 \right) \mathbf{E}_{y_e}^{p,1}, \left( \frac{\sigma_6}{\sigma_a} - 1 \right) \mathbf{E}_{z_e}^{p,1}, \dots, \right. \\
 &\quad \left. \left( \frac{\sigma_2}{\sigma_a} - 1 \right) \mathbf{E}_{x_e}^{p,8}, \left( \frac{\sigma_4}{\sigma_a} - 1 \right) \mathbf{E}_{y_e}^{p,8}, \left( \frac{\sigma_5}{\sigma_a} - 1 \right) \mathbf{E}_{z_e}^{p,8} \right]^T \\
 &= [\mathbf{A}] \hat{\mathbf{E}}_s + [\mathbf{B}] \mathbf{E}_p \quad (4.3)
 \end{aligned}$$

where matrix  $\mathbf{A}$  is defined as,

$$[\mathbf{A}] = \begin{bmatrix} \sigma_1/\sigma_a & & & & & & & \\ & \sigma_3/\sigma_a & & & & & & \\ & & \sigma_6/\sigma_a & & & & & \\ & & & \ddots & & & & \\ & & & & \ddots & & & \\ & & & & & \sigma_2/\sigma_a & & \\ & 0 & & & & & \sigma_4/\sigma_a & \\ & & & & & & & \sigma_5/\sigma_a \end{bmatrix}$$

and matrix **B** as the following.

$$[B] = \begin{bmatrix} (\sigma_1/\sigma_a - 1) & & & & & & \\ & (\sigma_3/\sigma_a - 1) & & & & & \\ & & (\sigma_6/\sigma_a - 1) & & & & \\ & & & \ddots & & & \\ & & & & (\sigma_2/\sigma_a - 1) & & \\ & 0 & & & & (\sigma_4/\sigma_a - 1) & \\ & & & & & & (\sigma_5/\sigma_a - 1) \end{bmatrix}$$

To enforce the above constraints on the finite element solution, substitute equation (4.3) into equation (4.1). The resulting modified functional is obtained.

$$\begin{aligned} F(\hat{E}_s) = & \hat{E}_s^T [A] [K] [A] \hat{E}_s + 2\hat{E}_s^T [A] [K] [B] E_p \\ & + E_p^T [B] [K] [B] E_p + 2\hat{E}_s^T [A] [S] E_p + 2E_p^T [B] [S] E_p \end{aligned} \quad (4.4)$$

Take the variation of the modified functional with respect to the secondary electric fields and equate the results to zero. This procedure provides the modified finite element linear system.

$$[A] [K] [A] \hat{E}_s = -[A] [S] E_p - [A] [K] [B] E_p$$

where

$$[A][K][B] = \begin{bmatrix} a_1 & & & & 0 \\ & a_2 & & & \\ & & a_3 & & \\ & & & \ddots & \\ 0 & & & & a_p \end{bmatrix} \begin{bmatrix} K_{11} & K_{12} & \dots & K_{1p} \\ K_{21} & K_{22} & \dots & K_{2p} \\ \vdots & \vdots & \ddots & \vdots \\ K_{p1} & K_{p2} & \dots & K_{pp} \end{bmatrix} \begin{bmatrix} b_1 & & & & 0 \\ & b_2 & & & \\ & & b_3 & & \\ & & & \ddots & \\ 0 & & & & b_p \end{bmatrix}$$

When this system of equations are solved, the resulting secondary electric fields will satisfy the necessary internal boundary conditions. The solutions in the anomalous cell for all normal electric field components are in terms of the external fields. These solutions must be rescaled in order to obtain the correct total field solution in the anomalous region by the following relationship.

$$\mathbf{E}^{total} = \left( \mathbf{E}_s + \mathbf{E}_p \right) = [\mathbf{A}] \left( \hat{\mathbf{E}}_s + \mathbf{E}_p \right)$$

The total rescaled fields in each anomalous cell, provided the source term in the volume integral component of the formulation.

$$\mathbf{E}(r) = \sum_{i=1}^n \int_{v_i} G^E(r, r') \Delta\sigma_i (\mathbf{E}_s(r') + \mathbf{E}_p(r')) dv$$

where

$$\Delta\sigma_i = \sigma_{ai} - \sigma_B$$

$\sigma_{ai}$  = anomalous conductivity in the  $i^{th}$  cell

$\sigma_B$  = background conductivity

$v_i$  = volume of the  $i^{th}$  cell

$G_{(r,r')}^E$  = Green's function

A numerical quadrature scheme was used to approximate the integration over each anomalous cell. This procedure was originally implemented using a fixed order quadrature for all integrations. This was where the second source of trouble with the algorithm was encountered. The order of the quadrature was a dominant factor in the over-all computation costs, since a major portion of the central processor time was devoted to the calculation of the Green's functions. A first order quadrature required

one Green's function compared to a third order quadrature which required the calculation of twenty-seven Green's functions. This cost dependence on the order of the quadrature required that a lower order be used for most models. This often resulted in large numerical errors which decreased the convergence rates and in some cases caused the iterative procedure to diverge.

To minimize both the error and the computation time, the quadrature integration scheme was modified such that the order was automatically adjusted to be inversely proportional to the distance between the mesh boundary or the observation position and the anomalous cell being integrated. After studying the results obtained from a small suite of models a second order quadrature was established as a minimum requirement for the integrations used to calculate the updated boundary conditions on each iteration. The calculation of the surface fields in the vicinity of the anomalous zone required third order quadrature when this zone was located near the surface of the half-space. However, first order quadrature could be safely used when the observation point was located several cell dimensions away from the scatterer. A clear criteria for the adjustment of the quadrature order was not established since the order required for a given accuracy was a strong function of the model parameters. The adjustment procedure used for the models considered in this study, was straight forward but expensive. For each general type of model at the highest frequency to be considered, the order criteria was adjusted until the solutions no longer varied as the order of quadrature increased. This criteria was then used with all similar models.

One of the most unexpected results encountered during the modification of the algorithm, was that the internal boundary conditions were not required for an accurate simulation of a resistive scatterer. In fact, the method used to enforce these conditions failed completely for the case of a resistive anomaly. This was probably related to the different secondary field distributions in the vicinity of a resistive body as compared to a conductive region. For a conductive body, a large component of the

secondary currents is directed into or normal to the boundaries of the body. Therefore the boundary condition enforcing the continuity of the normal component of current is a very important factor in accurately representing the electric fields for such models. For the resistive models however, the dominant components of the secondary currents are tangential to the boundaries of the anomalous zone. The smaller normal electric fields are probably dominated by numerical noise and hence when these fields are scaled up by an order of magnitude through the transformation required to enforce the internal boundary conditions, one obtains a poor solution. This problem was resolved by simply using the modified finite element equations to define the fields only in the anomalous cells where the cell conductivity was greater than the background conductivity. In anomalous cells where the conductivity is less than the background values, the normal linear equations were used.

### [ III ] Numerical Checks on the Modified Algorithm

A Most difficult phase in working with any three dimensional electromagnetic modeling technique is associated with the verification that the code provides an accurate solution. In this study, three basic checks were used to evaluate the accuracy of the program.

The first and most certain test, would be to extend a three dimensional body and see if the fields measured across the center of the body approached the two dimensional solution as the length of the scatterer increased. The results from this test are shown in Figure 4.2. The scatterer was characterized by a strike length of 2850 meters and a conductivity of 10 Ohm-m, buried in a 100 Ohm-m half-space. This figure shows the electric field oriented perpendicular to strike and measured on a surface

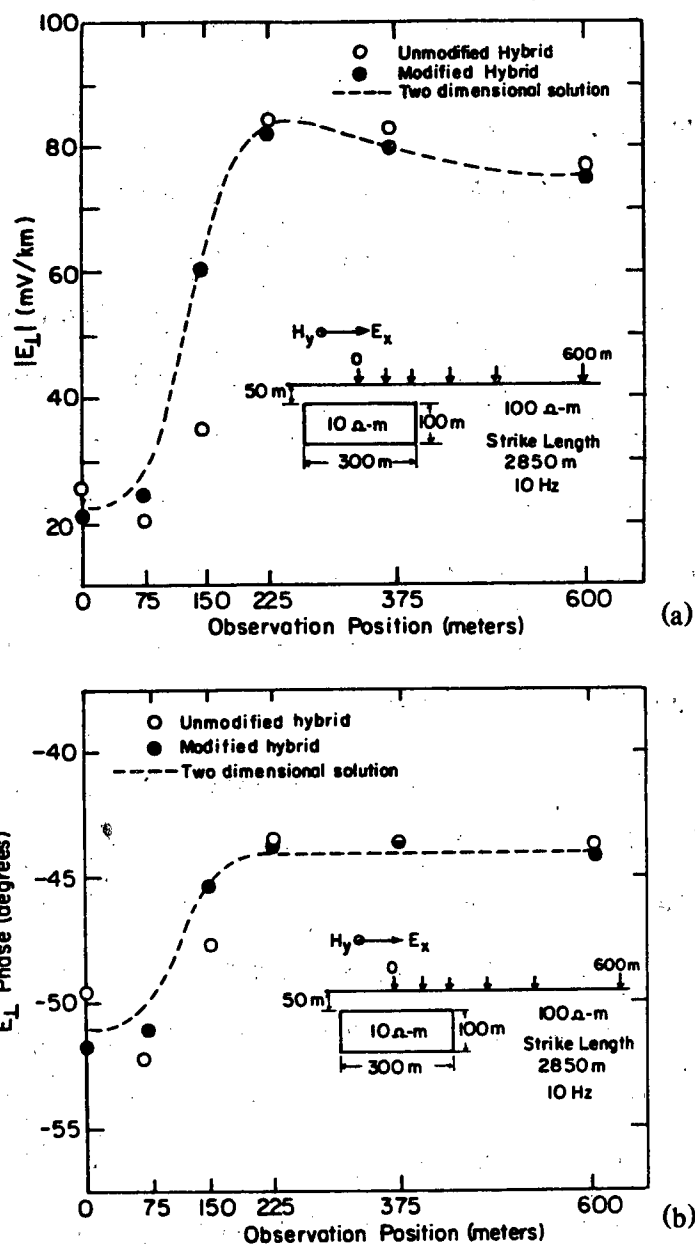


**Figure 4.2** The comparison of the (a) amplitude of the electric field perpendicular to strike and (b) the corresponding phase for the modified hybrid, original hybrid and the two dimensional response over an elongate three-dimensional conductor.

profile. The observation positions are denoted by the vertical arrows on the insert. The dashed curve indicates the two dimensional response of a body with the cross section shown. The frequency used for both models was 10. hertz. This solution was provided by a program developed by T. Madden which solves the two dimensional scattering problem by means of the transmission line and network analogies. The solid circles indicate the results obtained by the modified hybrid and the open circles show the results obtained with the original version. The same numerical accuracies on all spatial integrations were used to obtain these data. The differences between the solutions indicated in this figure are due only to the missing internal boundary condition in the original version of the program. The close fit between the modified hybrid and the two dimensional solution indicates that the hybrid algorithm is now providing an accurate solution for this elongate model. The phase response for the model at 10. hertz is provided in Figure 4.2(b). Again, good agreement between the two dimensional and modified hybrid results are evident.

The next example was for an elongate resistive body with the dimensions indicated on the insert in Figure 4.3. This figure shows the modified hybrid results indicated by the triangular symbols with the primary electric field oriented perpendicular to strike. This is compared to the two dimensional results indicated by the open circles connected by the curved line. Since this body is resistive with respect to the background media, the internal boundary conditions are not enforced and therefore the same finite element equations are solved on each iteration as used in the original hybrid version. As the figure indicates the apparent resistivities are very similar between the two and three dimensional cases. The impedance phase curves for the two cases are similar but differences of as much as four degrees are evident. The model used for this comparison was buried only 50 meters. This shallow depth of burial may have introduced some numerical problems which were responsible for the phase discrepancies observed in Figure 4.3. This model probably represents a "worst

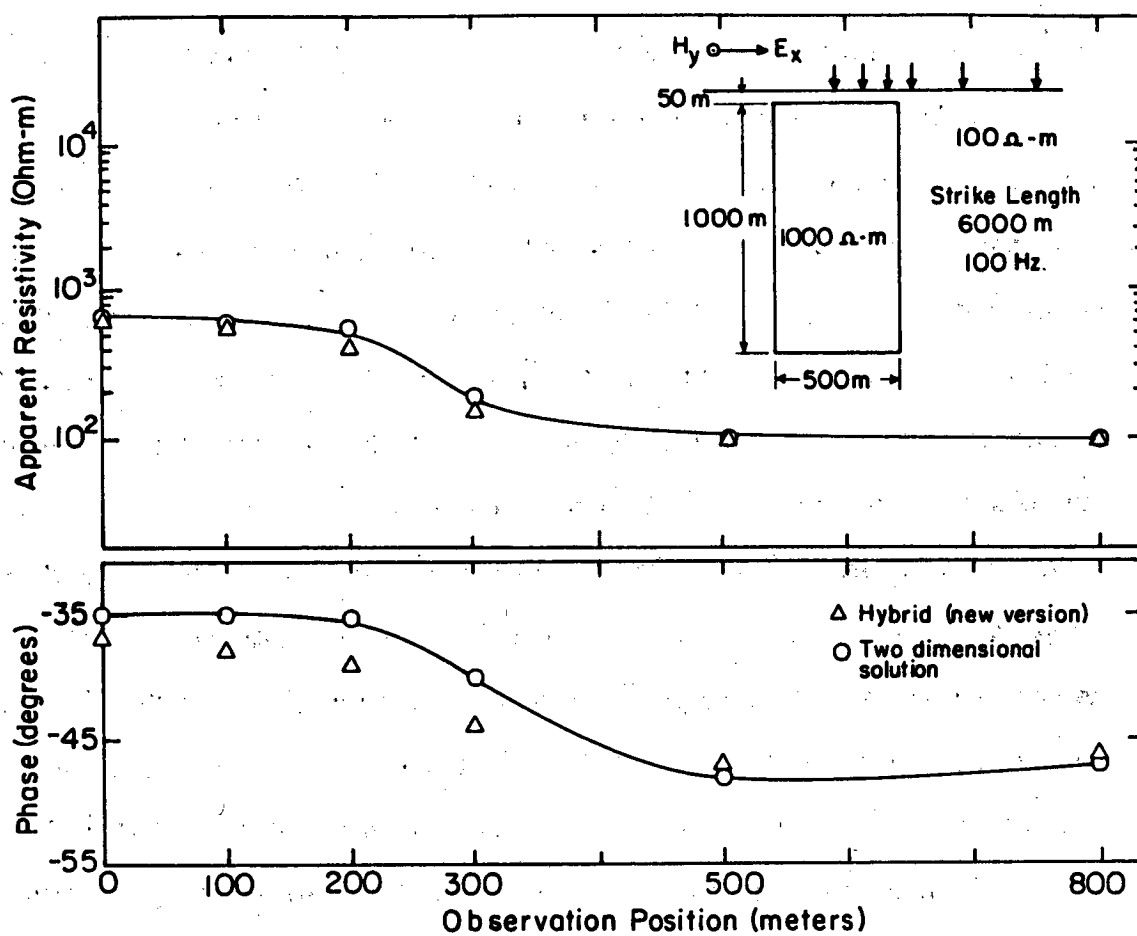


Figure 4.3 Comparison of the two dimensional apparent resistivity and impedance phase with the response of an elongate three-dimensional resistive body.

case" situation, for a resistive scatterer.

The second check available was to compare the results for the modified algorithm with an independent numerical technique. The next two figures show the comparison of the modified hybrid with the integral equation formulation developed by Hohmann (1975). The comparison of apparent resistivities is provided in Figure 4.4(a). The model simulates a shallow 5 Ohm-m conductor buried 250 meters in a 100 Ohm-m media. The solution is at 0.1 hertz with the observation position indicated by the vertical arrows. The results from the modified hybrid program are again indicated by the black circles. The results of the integral equation method published by Ting and Hohmann (1981), are indicated by the open triangles. The two programs provide similar responses with only one significantly different apparent resistivity occurring at the observation position  $x = 250$  meters. The modified hybrid results seems to provide a trend along the profile which is an enhanced version of the two dimensional response. This is reasonable since the body has a strike length of only 2000 meters which is equal to its depth extent. The fields along a profile over a conductor characterized by a short strike length should be affected by additional surface charges resulting from the lateral current distortion introduced by the ends of the three dimensional body. The impedance phase response for this model is shown in Figure 4.4(b). The phase responses for both three dimensional techniques are nearly coincident with the two dimensional response.

A second comparison with the integral equation method provided by Hohmann (1982) is shown in Figure 4.5. This model has the same geometry as the previous comparison with the conductor now buried 500 meters with a conductivity of 0.5 Ohm-m. The apparent resistivity response from the two programs are provided in Figures 4.5(a) and 4.5(b) with two source polarizations. The smooth curve provides the two dimensional apparent resistivities for the two source polarizations on a profile across the body. The results from the three dimensional programs vary by over a 100

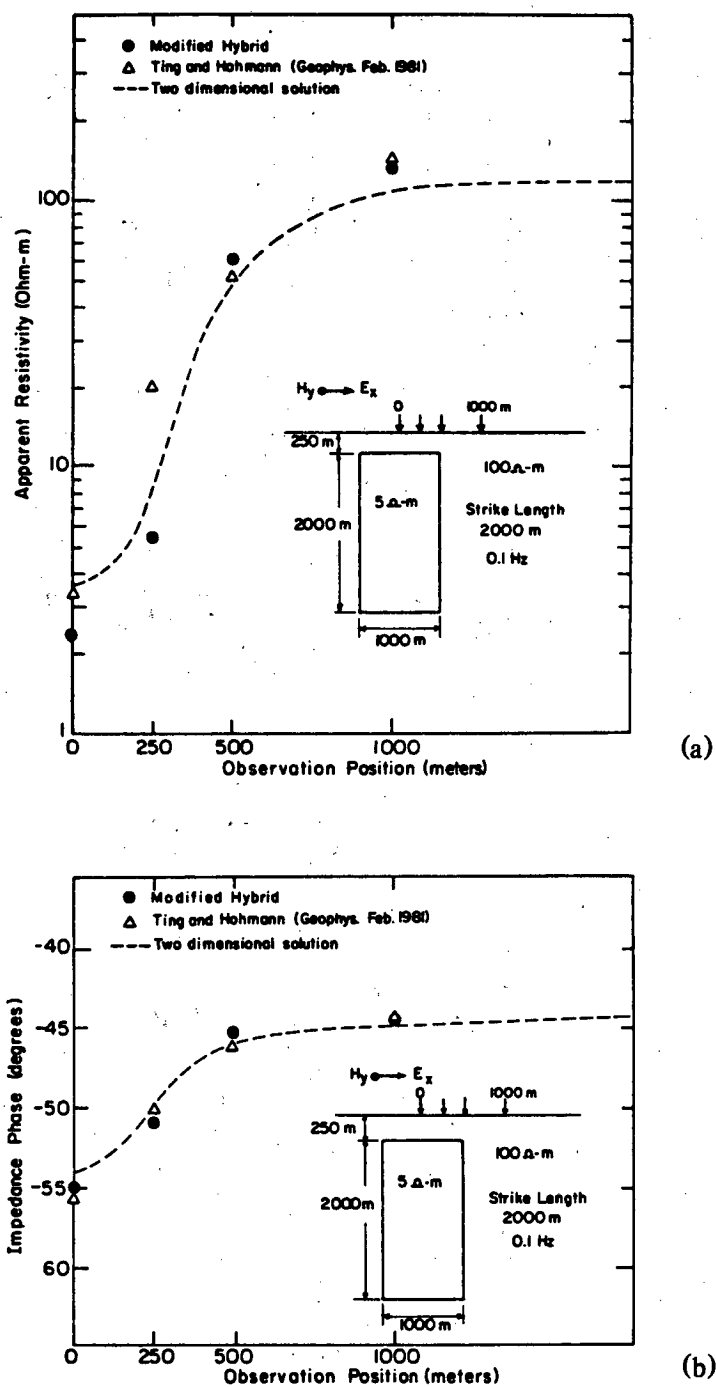


Figure 4.4 Comparison of the hybrid and integral equation solutions for (a) apparent resistivity and (b) impedance phase.

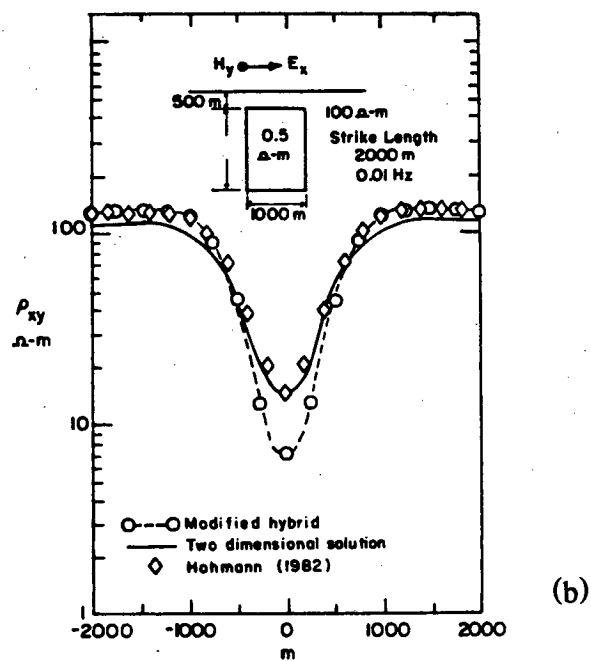
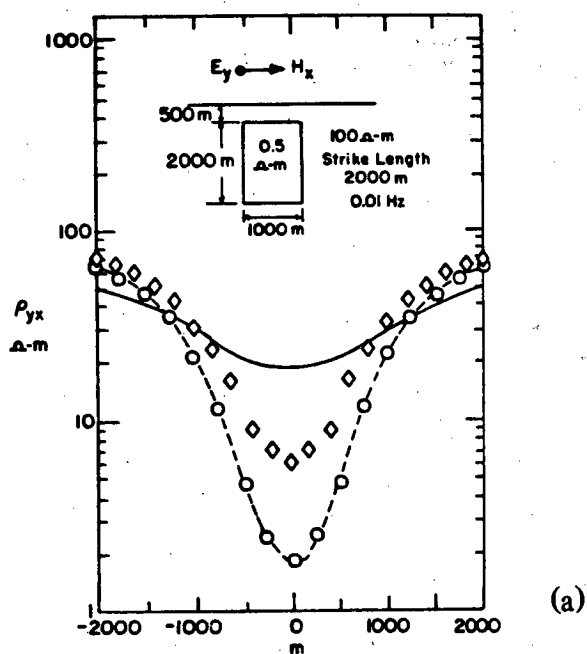
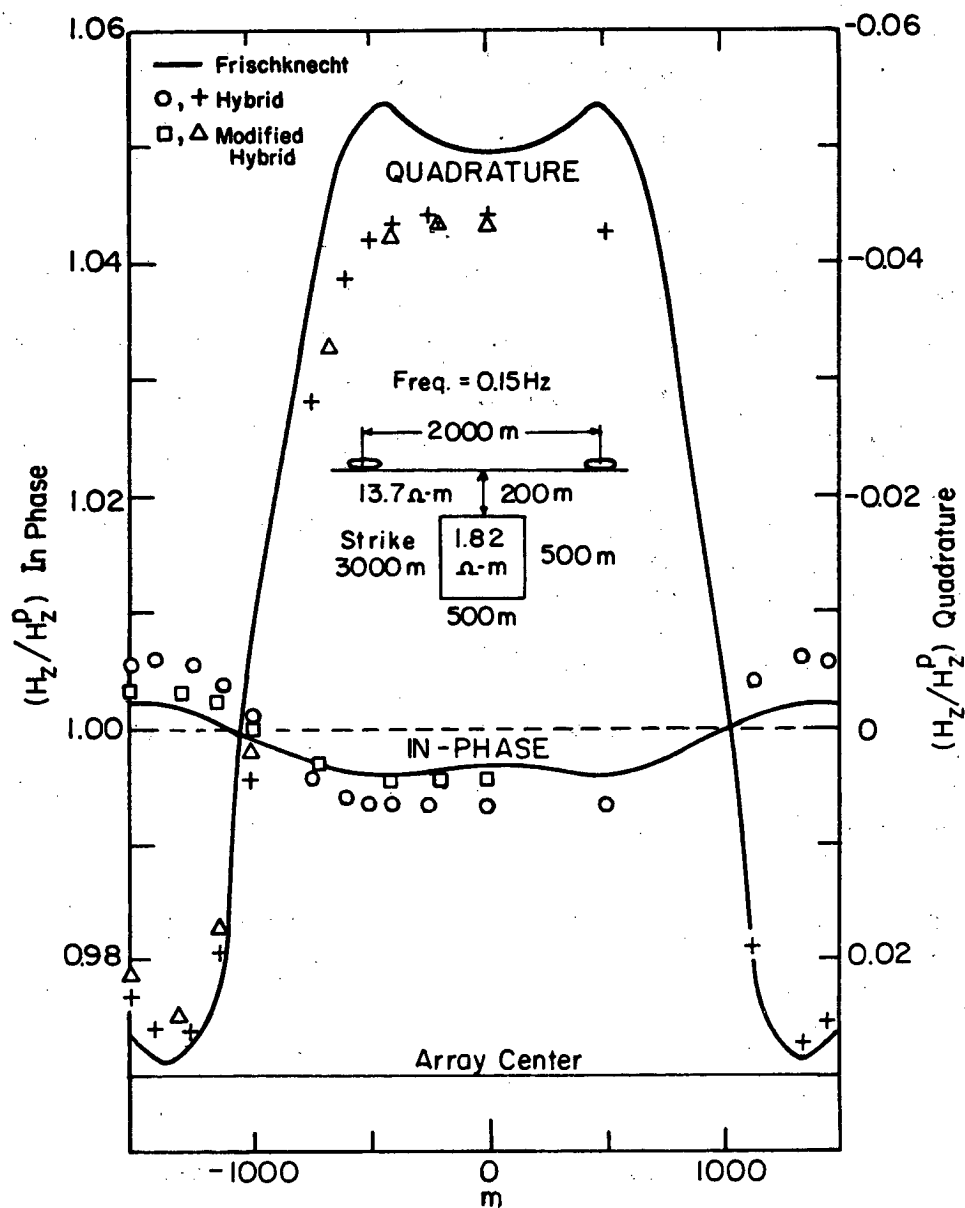


Figure 4.5 Comparison of the integral equation and hybrid solutions for (a) the primary electric field parallel to strike and (b) the primary electric field perpendicular to strike.

percent over the center of the body. This discrepancy indicates that the body is probably too large, too conductive and too near surface for either or both of the algorithms. The short strike of the body would indicate that the two dimensional response should be greatly different than the three dimensional results for an electric field source polarization parallel to strike, as shown in Figure 4.5(a). The source polarization with the primary electric field perpendicular to strike should have been less sensitive to the strike length. However, since the strike and depth of the scatterer are equal as in the previous model, there should be a significant lateral distortion of current due to the ends of the body. This lateral distortion would require an additional charge component in the anomalous region which would result in an enhanced response at the surface. The integral equation response which is enhanced on the external edges of the conductor but is less than or equal to the two dimensional response over the conductor as indicated by the diamond shaped symbols in Figure 4.5(b), is therefore physically unlikely.

The last check available was to compare the numerical results with those from an analog or tank model. This comparison for a vertical dipole source-receiver with a fixed separation is shown in Figure 4.6. The curved lines indicate the tank model results obtained with the tank modeling system described by Frischknecht (1971). The open circles and plus symbols indicate the results obtained by the original hybrid version; and the square and triangular symbols represent the results provided by the modified hybrid program. The major change in the results was on the inphase component. The original version provided a 100 percent mismatch for this component. The modified version however, provided similar results to those obtained from the analog model for both inphase and quadrature components.

The test results shown in Figures 4.2 and 4.3 indicate that the modified algorithm provides solutions which asymptote to a reasonable approximation of the two dimensional solutions for conductive and resistive scatterers. The similar results between



XBL 829-2466

Figure 4.6 Comparison of the original hybrid version and the modified hybrid with the analog (tank model) solution.

the integral equation and hybrid techniques presented in Figure 4.4 for a low contrast model, provides additional evidence that the solutions are reasonably accurate. The discrepancies between these modeling methods for the high contrast model shown in Figure 4.5, indicate care should be exercised when applying these schemes to such models. The simulations used in this study had conductivity contrasts of no more than twenty, thereby preventing numerical inaccuracies. The similar response between the numerical and tank modeling results shown in Figure 4.6, depicts the last bit of evidence supporting the accuracy of the modified algorithm. In summary, these checks indicate that the modified hybrid scheme presented in this section has provided accurate solutions for low contrast scatterers which are buried at reasonable depths.

## Chapter 5

### Data Interpretation

#### [ I ] Introduction

The interpretation of magnetotelluric data acquired in an environment where the electrical conductivity varies only as a function of depth  $\sigma(z)$ , has been considered by many investigators over the past thirty years. Most of these interpretation schemes utilized the frequency response of the scalar surface impedance ( $Z = E_x/H_y = -E_y/H_x$ ) and may be separated into two categories. The first and most easily implemented approach consists of fitting the frequency response of a parameterized model to the measured data. This may be done by using either a trial and error approach or an automated scheme to "minimize" the difference between the observations and the calculated fields using a systematic search in parameter space. These iterative techniques using various minimization criteria have been implemented by a number of researchers, e.g. Oldenburg (1979); Jupp and Vozoff (1975). The main advantage to this type of inversion scheme is that it requires only a forward solution and a minimization procedure both of which are easily calculated for the one-dimensional case. Its disadvantage is that an initial model or parameterization is required to begin the procedure. The alternative approach is to use a direct inversion method. These direct techniques require only the surface conductivity with no prior assumptions made concerning the conductivity variations with depth. The methods in this category are based on the application of a sequence of non-linear transformations on the measured data. After the solution of a set of integral equations and the necessary transforms are implemented, the conductivity as a function of depth is obtained

without solving the forward problem. The disadvantage associated with these schemes is that the numerical implementation of the required transforms is difficult and requires sophisticated techniques, e.g. Becher and Sharpe (1969); Weidelt (1972). Recent innovations by Coen and Chang (1982) have to a large degree overcome this disadvantage through the development of simplified numerical techniques which provide a direct inverse solution.

When the conductivity varies as a function of two spatial dimensions  $\sigma(y, z)$ , the scalar surface impedance or simple field ratios will no longer be time invariant. This problem was identified by Cantwell (1960). He resolved the problem by introducing the tensor impedance which is independent of source polarization. The tensor impedance is the transfer function which linearly relates the two component horizontal magnetic fields to the horizontal electric field components ( $E_x = Z_{xx} H_x + Z_{xy} H_y$ ,  $E_y = Z_{yx} H_x + Z_{yy} H_y$ ). The two resulting equations may be solved for the four unknowns by using two independent sets of field measurements (i.e. electric and magnetic fields with two different source polarizations). The two sets of field measurements provide four independent equations, the solution of which yields the four complex impedance elements. The tensor impedances resulting from this type of conductivity distribution vary as a function of both frequency and observation position.

The differential equations defining the two-dimensional scattering problem may be decomposed into two independent components, each requiring a scalar solution. These solutions are designated as the transverse electric mode ( $E_x, H_y, H_z$ ) and the transverse magnetic mode ( $E_y, E_z, H_x$ ). The four element impedance tensor for the two-dimensional case, reduces to two non-zero off-diagonal elements when the measurement coordinates are rotated parallel to strike. These off-diagonal elements are equal and of opposite sign in a one-dimensional environment. In an interpretation scheme based on an incomplete data set both modes should be used to understand the

conductivity variations. The impedance element ( $Z_{yx} = E_y/H_x$ ) associated with the transverse magnetic (TM) mode is very sensitive to near surface lateral changes in conductivity and relatively insensitive to conductivity variations occurring at great depth. In contrast, the impedance element ( $Z_{xy} = E_x/H_y$ ) corresponding to the transverse electric (TE) mode is less responsive to lateral surface contrasts than the TM mode and is characterized by a strong response to deep conductors. The vertical magnetic field is an additional surface measurement parameter associated with the TE mode which has only a secondary component within the frequency range considered in this study. The vertical and horizontal fields are assumed to satisfy a linear relationship ( $H_z = T_x H_x + T_y H_y$ ). These geomagnetic transfer functions or "tippers" provide a measure of the field response which is independent of the source field polarization and reduces to one complex component ( $T_y = H_z/H_y$ ) for the two-dimensional case. This component which varies as a function of frequency and observation position is non-zero only in the vicinity of a lateral contrast in conductivity.

These various time invariant measures of the surface fields ( $Z_{yx}$ ,  $Z_{xy}$ ,  $T_y$ ) are related to the anomalous current distributions caused by conductivity inhomogeneities through five different Greens functions. Therefore the various transfer functions calculated from the surface measurements may be characterized by differing sensitivities to an anomalous conductivity distribution. The relative resolution and sensitivity of these parameters will be considered later.

As in the one-dimensional inversion methods, one may calculate the electromagnetic response of a parameterized earth model. The resulting simulations may be used to fit the observed data as a function of both frequency and position in an iterative manner. Automated techniques for minimizing the difference between the measured and computed fields have been implemented by Jupp and Vozoff (1977), and Weidelt (1975). These techniques are difficult to use because the forward solutions require a great deal of computer storage and are expensive. The rate of convergence and the

final model obtained by these schemes depend on the initial parameterization used to begin the iterative procedure. Two-dimensional direct inversion schemes have not yet been successfully implemented for electromagnetic scattering problems. However, as indicated by Newton (1982) the generalization of direct techniques used for the solution of the one-dimensional inverse problems of quantum mechanics are under investigation. Perhaps these techniques may be adapted in the future for the two-dimensional magnetotelluric problem as similar schemes were in the past for the one-dimensional case.

Matching the simulations to the observations by trial and error is currently the most widely used technique for the interpretation of two-dimensional magnetotelluric data. A suite of simple forward models are generated. These models are implicitly and on rare occasions explicitly constrained by any geological or other geophysical data available. The characteristics of the model responses for the various components are then compared to the field observations and model refinements are made in a subjective manner.

The earth unfortunately is usually characterized by a three-dimensional conductivity distribution. This complication provides four non-zero impedance elements and two non-zero geomagnetic transfer functions. The simulation of these frequency responses require the vector solution of Maxwell's equations. The computational complexity of the forward problem is more than an order of magnitude more difficult than the two-dimensional problem. This, in conjunction with the absence of any direct three-dimensional inverse method has so far prevented the quantitative interpretation of data acquired in a complex environment.

## [ II ] Constraints, Objectives and Presentation Techniques

The data acquired at Mount Hood were distinguished by complex frequency characteristics in conjunction with rapid spatial variations of the impedance tensors and geomagnetic transfer functions. These characteristics indicated that the conductivity distribution under this Cascade volcano was extremely complex in nature. The complex environment coupled with the sparse data set provided an impenetrable barrier to a quantitative interpretation. There were four major constraints associated with this data set.

The first of these constraints was the finite band width of the data. The lower end at approximately 0.001 hertz was limited by the acquisition time which in turn was dictated by cost factors. The high frequency end was set by transducer and acquisition system limitations to approximately 50 hertz. The upper limit was too low to define the surface conductivities and the low frequency limits hindered attempts to estimate upper mantle conductivity variations. The interpretation was affected by these poorly constrained extremes in the vertical conductivity structure since both deep and shallow conductors may distort significantly the various transfer functions within the frequency band acquired.

Another factor which greatly impeded the interpretation was the small spatial window over which these data were acquired. The data were limited in spatial extent to a thirty square kilometer area centered on the volcanic peak. This narrow window is an important consideration in any interpretation scheme since lateral conductivity variations occurring beyond the limits of the survey area may distort the frequency response of the magnetotelluric and geomagnetic transfer functions in the lower portion of the frequency band. A second problem created by this small spatial sample is associated with defining the geometry of deep conductors underlying the survey area.

These conductors may provide distinctive characteristics in the lower frequency range. However, the spatial variations of these frequency responses which indicate the lateral extent of the conductors are truncated and thereby limit the interpretation.

An additional constraint was caused by the spatial aliasing created by the availability of only twenty four irregularly spaced observations spread over the thirty square kilometer area. A qualitative interpretation of these data indicated that three-dimensional near surface conductivity variations in this region were characterized by a wide range of dimensions and the limited sampling prevented a detailed delineation of these features. Thus, a quantitative evaluation of the resulting field distortions caused by these scatterers was not feasible.

The last factor which significantly restricted the interpretation was associated with the low signal to noise ratio at many locations. Some examples of impedance tensor and tipper estimates which were characterized by large statistical errors based on data acquired at sites 11,13,14 and 15A are provided in appendix A. The error bars on these examples indicate the 50 percent confidence interval based on a normal distribution as described by Gamble, Goubau and Clarke (1979). A significant noise component in the measurements provided poorly defined transfer functions at some frequencies throughout the data set. The remote reference processing technique described in chapter 2 greatly minimized this problem.

The objective of the research presented here was the development of a procedure utilizing the crude interpretational tools currently available which would provide a conductivity distribution based on a sparse data set and which would be consistent with geological and other geophysical information. The procedure which evolved was composed of two basic components. First, one dimensional interpretation schemes were used to estimate the parameters of some near surface inhomogeneities. This was followed by fitting various data subsets with two-dimensional simulations. The resulting models were then combined into a composite three-dimensional representation of the

spatial conductivity variations. In parallel with the parameterized data fitting procedure, a sensitivity analysis was performed on the various measurement parameters through the use of simple two- and three-dimensional models. These models provided information regarding the relative reliability of the various parameters in the composite model.

The pitfalls in such an approach are many. The effects on the transfer functions caused by inductive coupling in a multiconductor environment are difficult to quantify. In addition, near surface lateral changes in conductivity may cause broad-band distortions in the various transfer functions, a problem well described in an excellent review paper by Berdichevskiy and Dmitriev (1976). The effects of these surface inhomogeneities are difficult to evaluate since the sparse data set does not provide the necessary spatial resolution to delineate these structures. This, coupled with the narrow frequency and spatial windows which characterized the data, obscured the definition of the subsurface parameters. To reduce the ambiguities caused by this "ill-posed" problem, constraints provided by other geophysical methods were utilized to provide the simplest consistent model.

The general character of the data was quite complex. As noted earlier, apparent resistivities varied by orders of magnitude over distances as small as two kilometers. The principal direction of the impedance tensor based on the minimization of the diagonal elements as described in Vozoff (1972), changed as a function of both frequency and observation position. The geomagnetic transfer function (tipper) was bimodal, that is both components  $T_x$  and  $T_y$  were characterized by amplitude peaks within two decades in the frequency domain. The strike directions indicated by these tipper responses were extremely variable as a function of both position and frequency. These strike directions seldom corresponded to the principal directions indicated by the tensor impedances. The phase of the tipper at some locations swept through 300 degrees over the frequency band of five decades.

To obtain a coherent view of these spatial variations as a function of frequency, band averaged tensor impedances and geomagnetic transfer functions were used to generate smoothed polar diagrams. The polar diagram is a simple graphical procedure, which provides a convenient vehicle by which one can study the dependence of the transfer functions at each frequency or band of frequencies on the orientation of the measurement coordinates. This useful interpretation aid was popularized by Berdichevskiy (1968) and by Berdichevskiy and Smirnov (1971). This scheme has been used extensively to portray field results in Eastern European electrical studies and has recently gained some popularity in the West as indicated by Thayer (1975).

The generation of the polar diagram is quite simple. The impedance tensor or geomagnetic transfer function at each frequency is rotated through a 360 degree coordinate system rotation. The apparent resistivity is then calculated and averaged over a number of harmonics at each angle of rotation if smoothed diagrams are desired. This procedure provides a graphical representation of the apparent resistivity which varies as a function of coordinate rotation angle and frequency band at each measurement location. These data are then scaled by a convenient amount and plotted in map form with the diagram centered on the geographical coordinates of the observation position. An example of this procedure for one field observation is provided in Figure 5.1(a). This figure describes the calculation of the apparent resistivity in a polar form which is consistent with common usage in literature.

Figure 5.1(b) defines the notation for describing the geomagnetic or tipper diagrams which will be used in this study. The evolutionary root of these diagrams is related to an interesting observation made by Parkinson (1959). He found that the geomagnetic transfer function estimated from data acquired near the Pacific Ocean in Australia was characterized by the curious property that it was consistently oriented perpendicular to coast line. This observation initiated an era of inquiry which resulted in the complex induction arrow. The variable notation associated with these induction

# IMPEDANCE ELEMENTS AND APPARENT RESISTIVITY

$$E_X = Z_{XX}H_X + Z_{XY}H_Y$$

$$E_Y = Z_{YX}H_X + Z_{YY}H_Y$$

$$Z_{XY}[\theta] = Z_{XY} \cos^2[\theta] + [Z_{YY} - Z_{XX}] \sin[\theta] \cos[\theta] - Z_{YX} \sin^2[\theta]$$

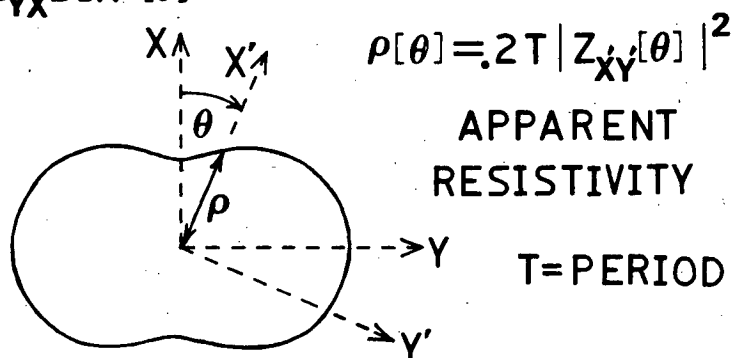


Figure 5.1(a) Notation defining the apparent resistivity polar diagram.

## COMPLEX TIPPER & INDUCTION

ARROWS:  $R_\epsilon[IA]$ ,  $Im[IA]$

$$H_Z = T_X H_X + T_Y H_Y$$

$$T_X[\theta] = T_X \cos[\theta] + T_Y \sin[\theta] = \text{TIPPER}[X]$$

$$R_\epsilon[IA] = R_\epsilon[T_X] + R_\epsilon[T_Y]$$

$$Im[IA] = Im[T_X] + Im[T_Y]$$

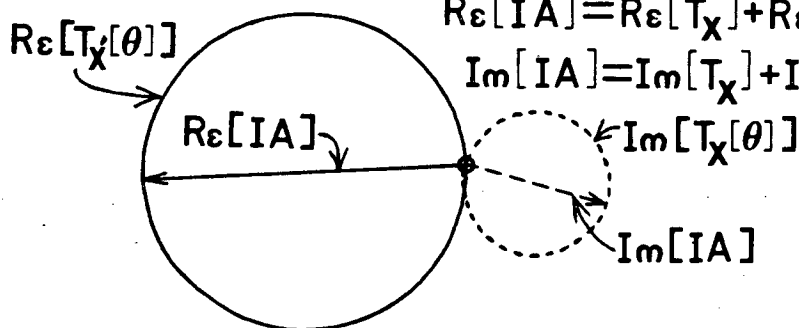


Figure 5.1(b) Notation defining the complex geomagnetic transfer function (tipper) polar diagrams and the real and imaginary induction arrows.

arrows reflects this evolution in the literature as indicated by Gregori and Lanzerotti (1980); Jones (1981). These arrows simply portray the geometrical relationship, which was first empirically derived from field observations and later verified by model studies, between the tipper phase at an observation position and the relative lateral positions of induced current concentrations in the earth. The real and imaginary components of the tipper are shown in Figure 5.1(b). These real and imaginary functions are plotted in polar form or as functions of the coordinate system rotation angle and are indicated by the solid and dashed circles respectively. The rotation invariant measures which bisect the solid and dashed circles are the real and imaginary induction arrows. The observation position is located at the point of intersection of these real and imaginary induction arrows. The utility of these arrows are easily seen in the simple rule which holds for all two-dimensional confined single-body conductors investigated in this study. These models indicate that for frequencies below the peak amplitude response of the tipper function, the imaginary induction arrows are oriented toward, and the real arrows are oriented away from, regions characterized by high current concentrations.

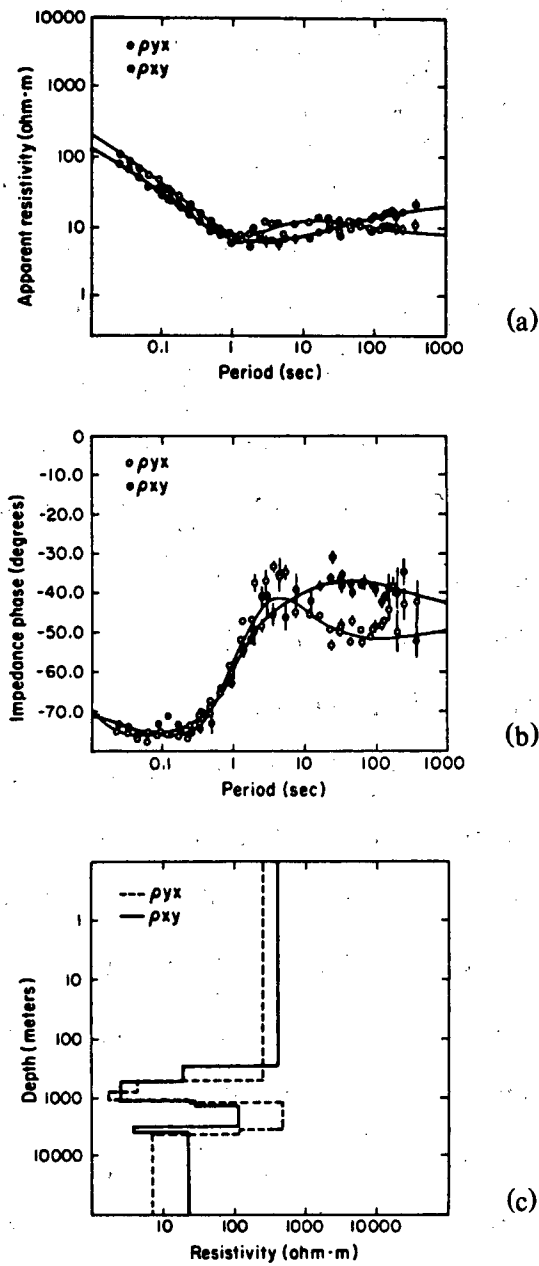
To minimize the confusion, all simulations and field data provided by a variety of programs were changed into a form using common conventions. A right-handed coordinate system was used with x directed north, y east and z into the earth. A negative time dependency ( $e^{-i\omega t}$ ) provided impedance phase responses in the second and fourth quadrants. The phases in the second quadrant were shifted into the fourth quadrant for display purposes.

### [ III ] A Qualitative Interpretation of the Near Surface Conductivity Distribution

The initial step in the interpretation scheme was to unravel the near surface conductivity distribution using the magnetotelluric and tipper data supplemented by three electromagnetic loop soundings. The one-dimensional interpretation of these data are presented by Goldstein, Mozley and Wilt (1982). The results are only qualitative since this region is characterized by a complex near surface conductivity distribution which could introduce large errors in such a simplistic analysis. However, the similarity of the results from both methods did suggest that at least two near surface conductors were located in this area.

The one-dimensional analysis was first used on the north-eastern flank of Mount Hood. This measurement array consisted of magnetotelluric sites 1 and 2 (Figure 2.3) and the associated remote telluric measurements. The data in this array were characterized by similar principal directions and a small separation in the apparent resistivities calculated from the off-diagonal elements of the impedance tensor. These characteristics implied that these data were only moderately distorted by near surface inhomogeneities. The impedance data in this cluster of sites were rotated into the same principal direction, based on the average value at all frequencies of all sites in the array. This direction for the impedance ( $Z_{xy}$ ) which is associated with the x directed electric field was north 80 degrees east.

An example of a one-dimensional inversion of the off-diagonal impedance elements measured at site 1 are shown in Figure 5.2. The parameterized inversion technique developed by Jupp and Vozoff (1975) was used to obtain these results. Both apparent resistivities corresponding to the off-diagonal impedance elements provided similar conductivity variations with depth. Since the data at periods greater than 1.0



XBL816-3217

**Figure 5.2** An example of the one-dimensional Inversion of the off-diagonal impedance elements at site 1. The smooth curves indicate the forward model based on the inferred conductivity variation with depth presented in (c). The field data are represented by the symbols with the apparent resistivities in (a) and the impedance phases in (b).

second indicate that the one-dimensional model is not valid, the conductivity variation below 3 kilometers was disregarded.

A selection of one-dimensional parametric inversions for all sites in this array are shown in Figure 5.3. The results are projected onto a profile directed north 35 degrees east. These results imply that there exists a very conductive zone at a depth of approximately 500 meters under site 1. The one-dimensional interpretation of the loop sounding data acquired in this vicinity indicate a conductor at approximately 700 meters depth. The profile inversions presented in this figure indicate that the conductive zone thins and becomes more resistive on the north eastern end of the profile.

The next region where the simple one-dimension inversions were attempted was on the southern flank of the volcanic peak. The magnetotelluric data in this area provided poor quality impedance estimates which were characterized by large statistical error bars. The impedance estimates were available only at periods greater than 0.1 second. The two loop soundings in this area however provided some control on the near surface conductivities. These results indicate that a conductive zone of 5-20 Ohm-m exists at a depth of 300-700 meters. These interpretations are subject to a great deal of error since the data characteristics in this vicinity imply the existence of a two or three-dimensional conductivity distribution.

The shallow conductor indicated by the loop soundings and which was consistent with the magnetotelluric data on the southern flank of Mount Hood correlated with the water level in a drill-hole located near Timberline Lodge. This implied that the conductor was associated with a saturated zone in the massive pyroclastic debris which has accumulated on the southern flank of the volcano over the past few thousand years. The high degree of north-south polarization which characterized the electric fields measured in this area indicated that this shallow conductive zone was elongated in the same direction as the pyroclastic flows.

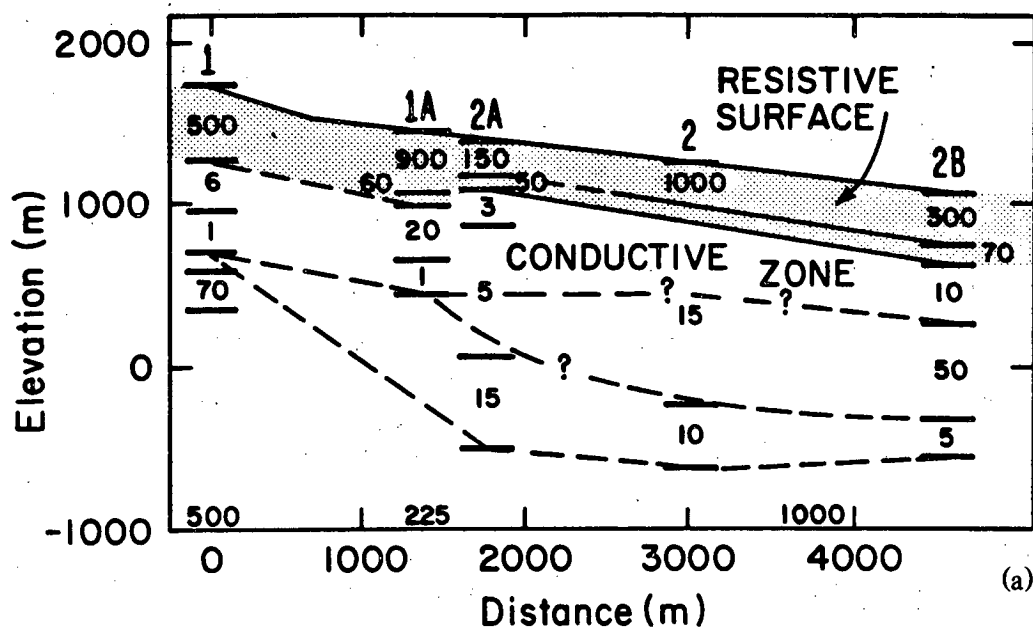
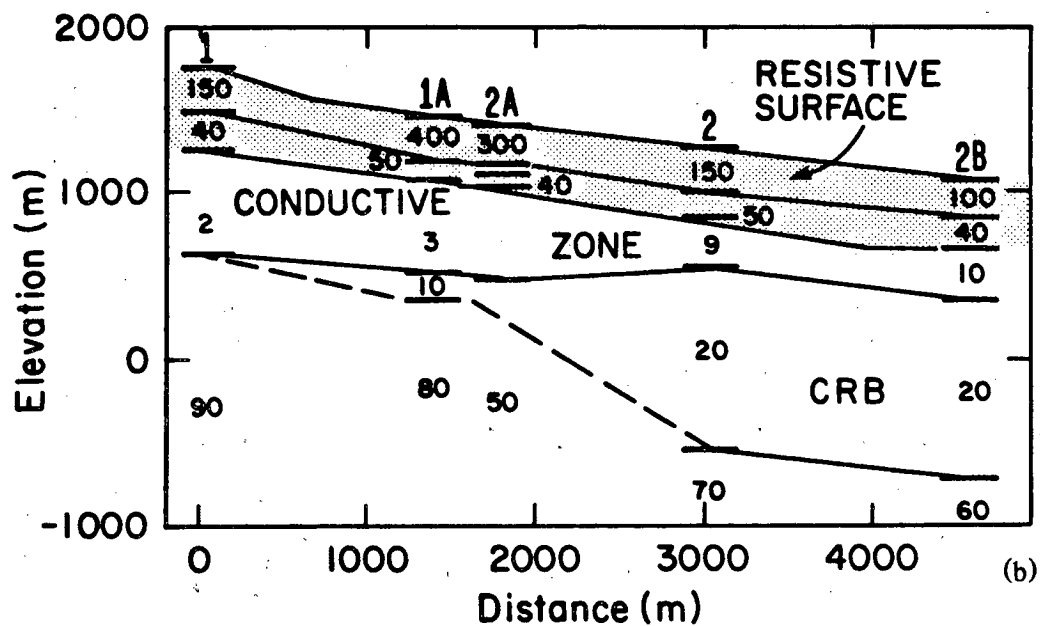


Figure 5.3 Conductivity distribution based on a one-dimensional inversion of (a) The impedance element  $Z_{xy}$  associated with the electric field oriented north 80. degrees east, (b) impedance element  $Z_{yx}$  associated with the electric field oriented south 10. degrees east.



To verify that the distortions observed in the apparent resistivities were due to these saturated pyroclastics, some simple three-dimensional simulations were implemented using the modified hybrid modeling scheme described in Chapter 4. The stippled region on Figure 5.4(a) indicates the area characterized by a north-south polarization of the electric fields as indicated by the figure-eight shaped polar diagrams of apparent resistivity. These polar diagrams are presented using the logarithmic scale shown at the bottom of the figure. This was necessary because of the large range in apparent resistivities observed. Figure 5.4(b) shows the results in plan-view of the near surface conductor indicated in the insert. This 10 Ohm-m conductor has a length to width ratio of two and is buried 500 meters in a 100 Ohm-m media. The data are provided at 0.01 hertz over only one quadrant of the model since there are two planes of symmetry. The dashed line indicates the lateral extent of the conductor. The observation positions are located at the center of each polar diagram. The diagrams are linearly scaled with the apparent resistivity as indicated in the upper left corner of the figure. These diagrams indicate that the apparent resistivities associated with the electric field parallel to strike are only a factor of two greater than the apparent resistivities related to the electric field perpendicular to strike. This model was calculated at 0.1 hertz and 0.001 hertz. The resulting apparent resistivities for both frequencies were similar to those at 0.01 hertz shown in Figure 5.4(b).

A second simulation at 0.022 hertz is shown in Figure 5.5 in the same form as the previous model. The conductor in this simulation is a 10 Ohm-m body with a length to width ratio of three buried 1500 meters in a 100 Ohm-m material. The difference in apparent resistivities oriented parallel and perpendicular to strike, again vary only by a factor of two. The change in geometry and depth of burial for these simple low contrast models provided similar results indicating that the variation of these parameters may not provide the desired characteristics. Due to time and cost factors, further parametric variations were not attempted. However, the 1500 meter

AVERAGED FREQS. IN THE RANGE OF .01- .001 HERTZ

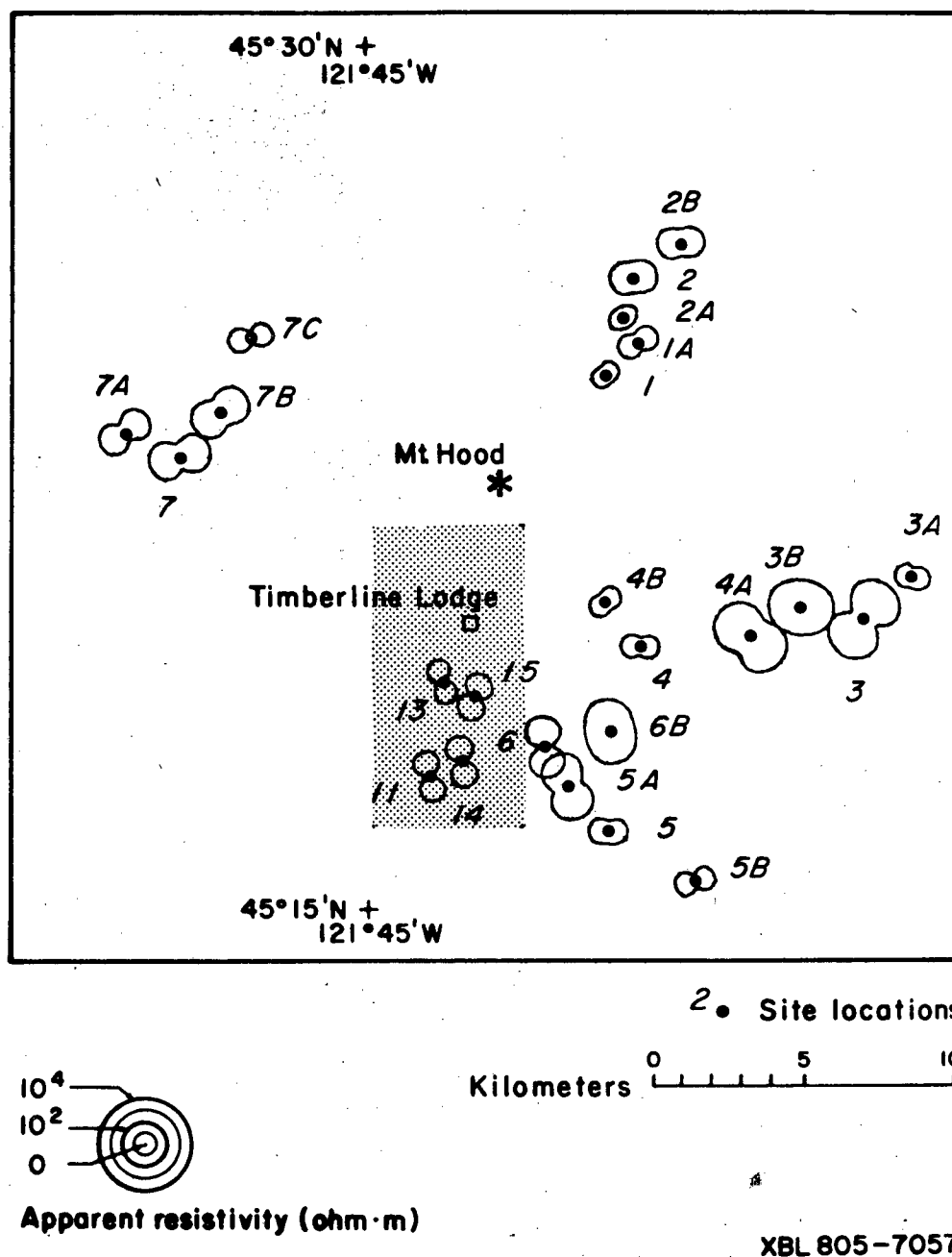


Figure 5.4(a) Apparent resistivity polar diagrams for the field data averaged over the frequency band of .01-.001 hertz. The stippled region indicates the probable location of a near surface conductor.

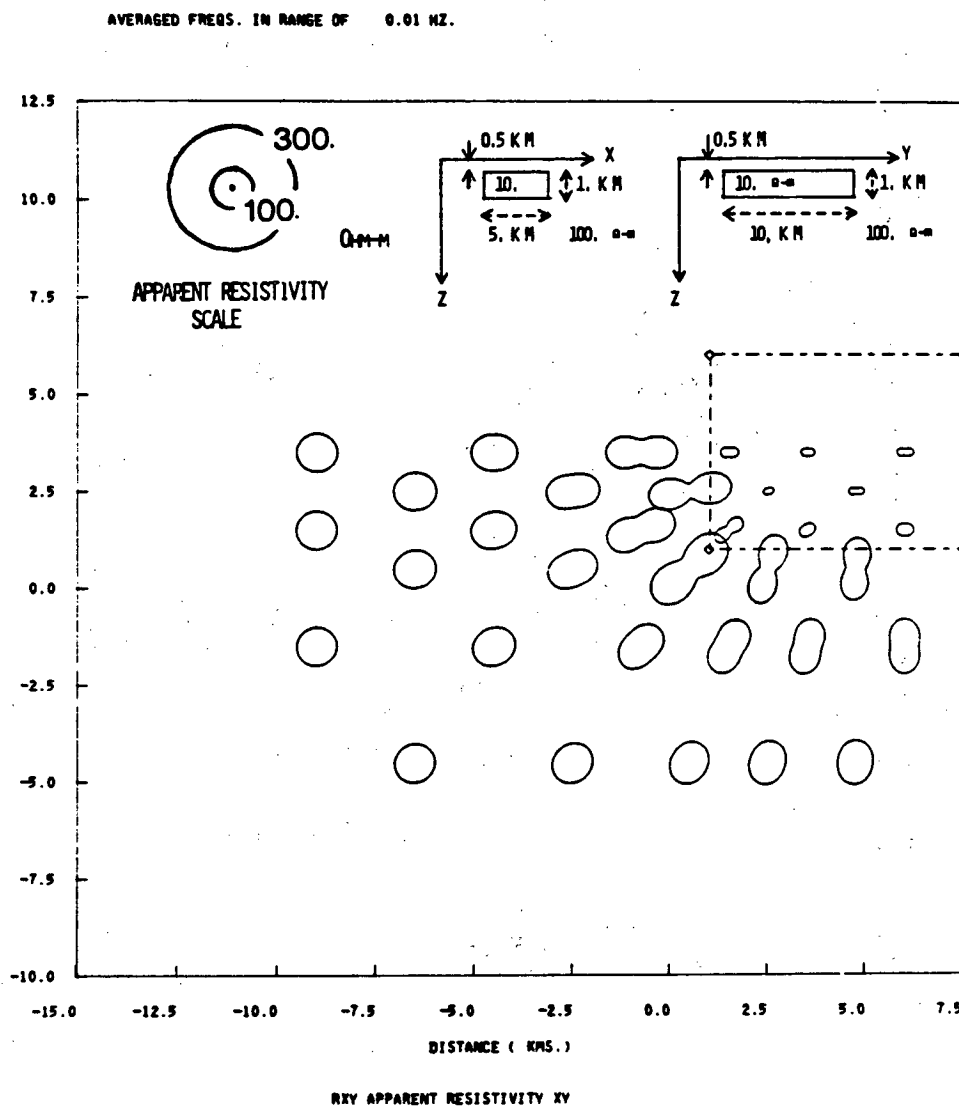
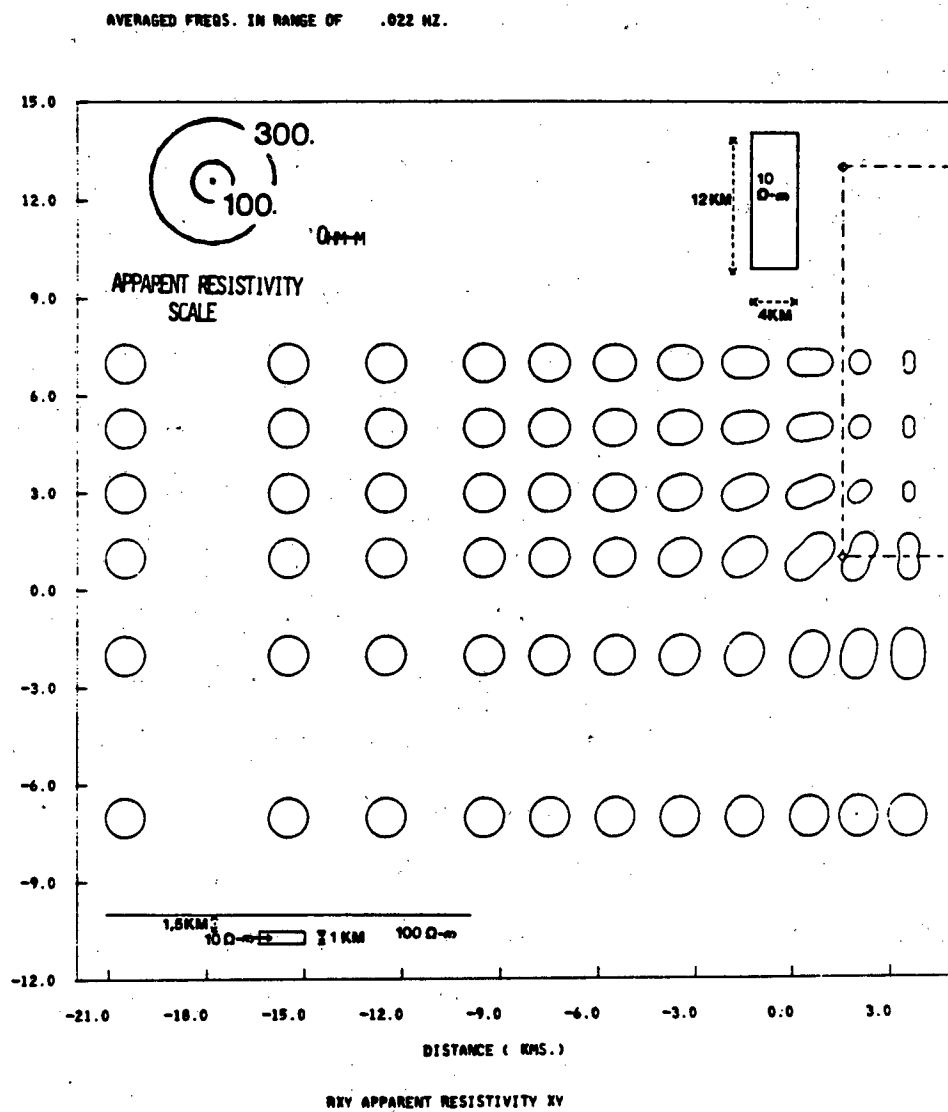


Figure 5.4(b) Apparent resistivity diagrams for a three-dimensional model with horizontal dimensions similar to the stippled region in Figure 5.4(a). The parameters of the model are specified on the insert.



**Figure 5.5** Apparent resistivity polar diagrams for the elongate near surface conductor indicated in the insert.

depth of burial of this model which was necessary to insure numerical accuracy on a related two body model, which will be considered next, was probably a significant factor in decreasing the difference between the orthogonal apparent resistivities.

The next approach used to simulate the field characteristics at sites 11,13,14 and 15A, shown in Figure 5.4(a), was based on a two body model. This simulation is shown in Figure 5.6. The shallow elongate conductor in this simulation has the same parameters as the model previously considered in Figure 5.5. This new simulation has a second deep resistive body with a strike perpendicular to that of the shallow body. The full plan-view and a cross-section are shown as inserts in this figure. As in the previous models the dashed lines delineate the lateral dimensions of the conductors under the observation positions. These observation positions are again confined to one quadrant of the model since two planes of symmetry were used. For observation points over the conductor, one can see that the ratio of the apparent resistivities associated with the electric fields parallel to the strike of the conductor relative to those using the electric field perpendicular to strike are approximately three to one. This indicates that the existence of a resistive structure under a three-dimensional surface conductor can enhance the field polarization measured over this conductor. This result mimics the observed field responses in a general way. However, the degree of distortion of the model results shown by a linear scale are less by an order of magnitude than the field data presented on a logarithmic scale. One factor which may contribute to this large difference between the magnitude of the simulations and the field observations may be associated with the difference between the conductivity contrasts used in the models and those that actually occur in the earth. The model contrasts used were small to insure numerical accuracy. The contrasts in conductivity which may occur in this area may be greater than those used in the simulation by an order of magnitude or more.

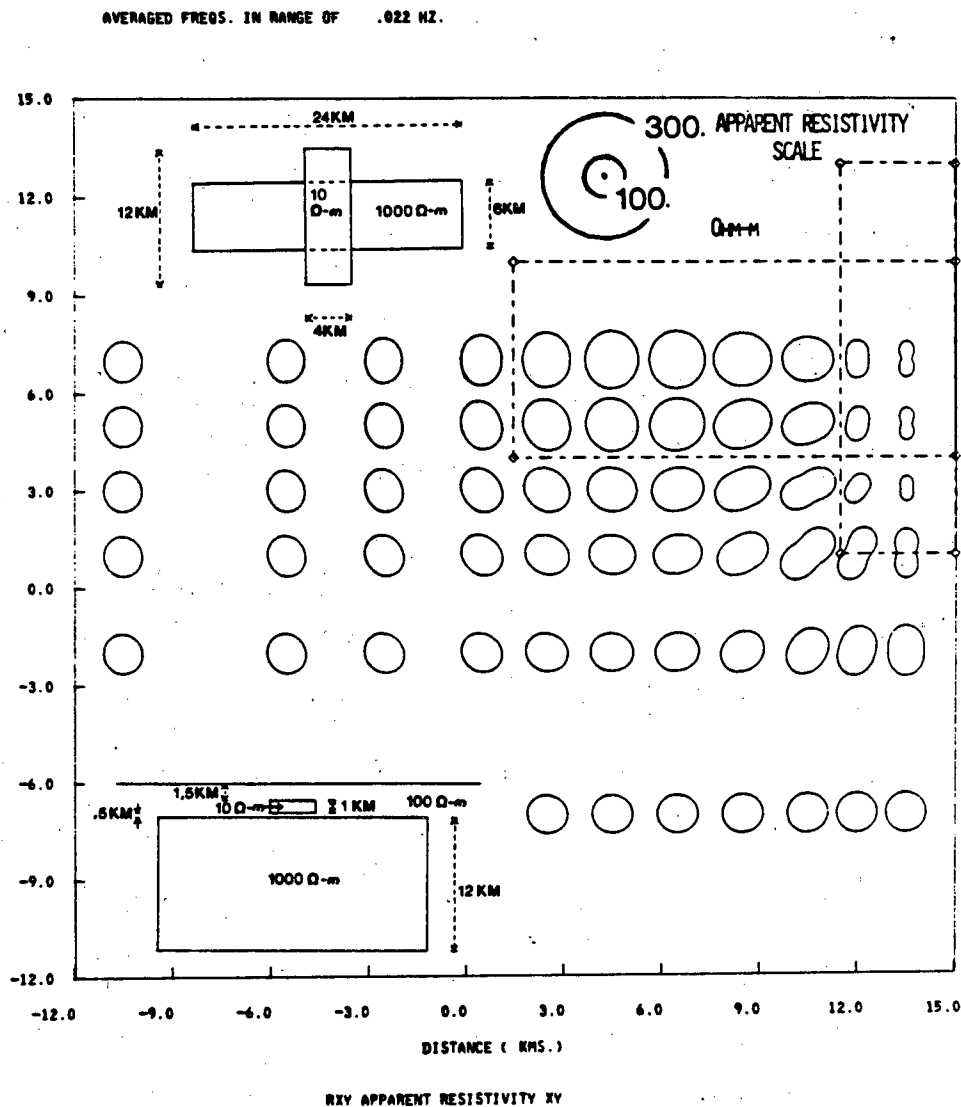


**Figure 5.6** Apparent resistivity polar diagrams for a two body three-dimensional model which consists of a shallow conductive body characterized by the same parameters as the model presented in Figure 5.5.

The third area which was characterized by similar polar diagrams is indicated in Figure 5.7(a) by the stippled region. The large apparent resistivities in this area indicate the presence of a near surface resistive body. To verify this conjecture, the simulation shown in Figure 5.7(b) was calculated. The same conventions are used in this figure as was used with previous models. The polar diagrams of apparent resistivities provided by this simulation indicate that the region is probably underlain by a resistive structure which may extend to relatively great depths.

The last two areas were evaluated using only the distortion characteristics of the apparent resistivity diagrams. The sensitivity of the apparent resistivity to near surface conductivity structures is quite evident in these models. By considering these models over two decades in frequency, one can see that this distortion is a broad-band phenomenon. Therefore it may be used quite effectively to interpret near surface conductivity variations, but may present problems when deep conductors buried under complex surface conductivity distributions are the desired targets. This problem will be considered in more detail in Section [IV].

The second set of measurement parameters which may be used to analyze the surface conductivity are the induction arrows. The distribution of the complex transfer functions and the associated induction arrows for the simple near surface conductor considered earlier are shown in Figure 5.8. The frequency used in this example is 0.1 hertz. This frequency is below the peak in the amplitude of the complex transfer function. The phase at this frequency has shifted into the second quadrant which results in the orientation of the real and imaginary induction arrows away and toward the region of high current density respectively. This property of the induction arrows and the relative reliability of the real and imaginary components will be considered in Section [V]. The ability of the geomagnetic data to indicate the relative lateral position of current concentrations as indicated in this figure is a valuable tool in any interpretation scheme.

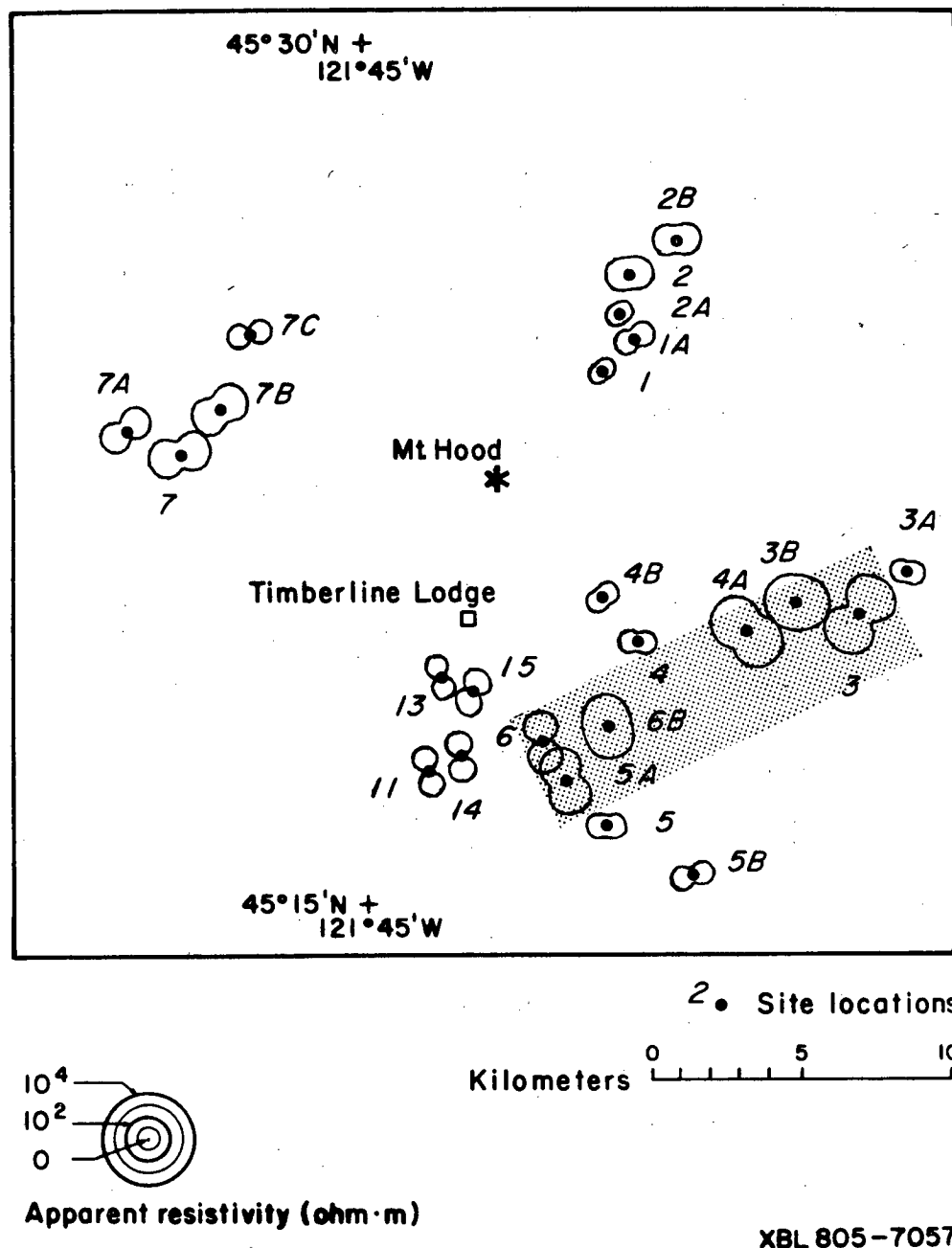


Figure 5.7(a) Apparent resistivity polar diagrams for the field data averaged over the frequency band of .01-.001 hertz. The stippled region indicates the probable location of a near surface resistive body.

0.01 HZ.

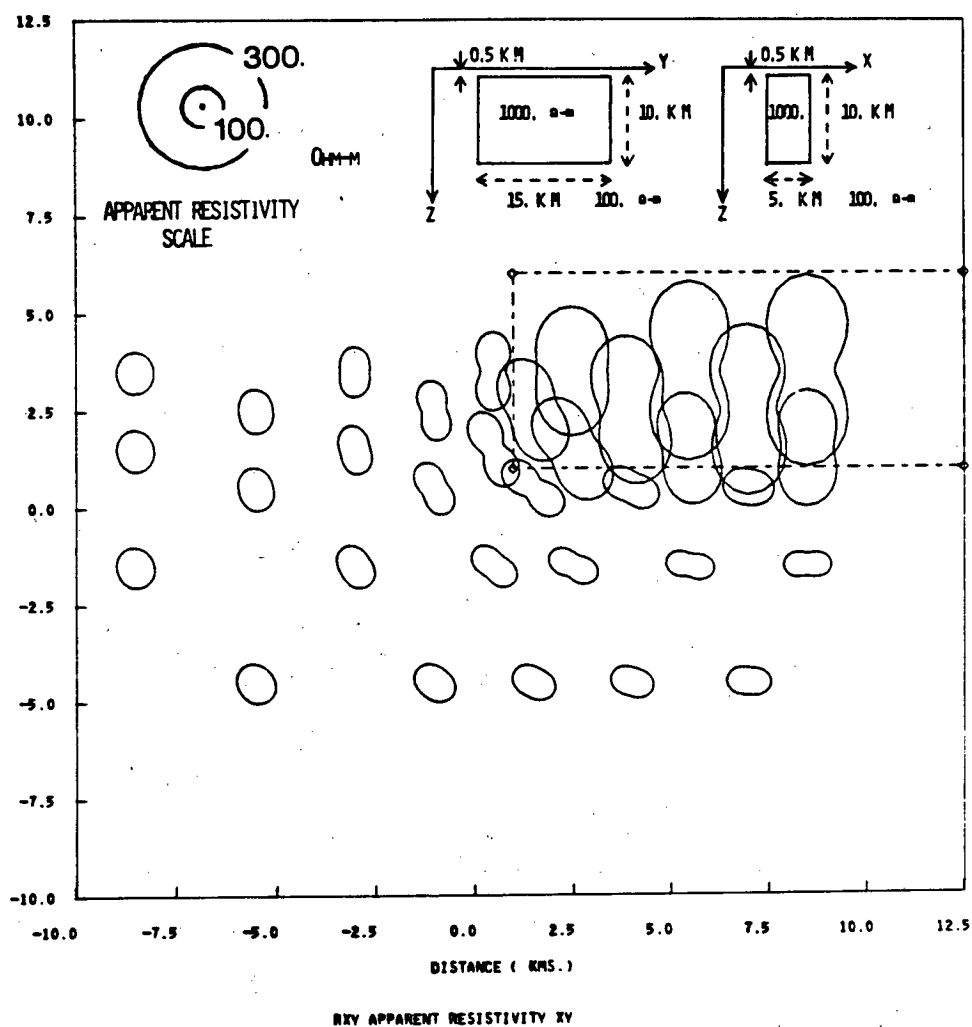
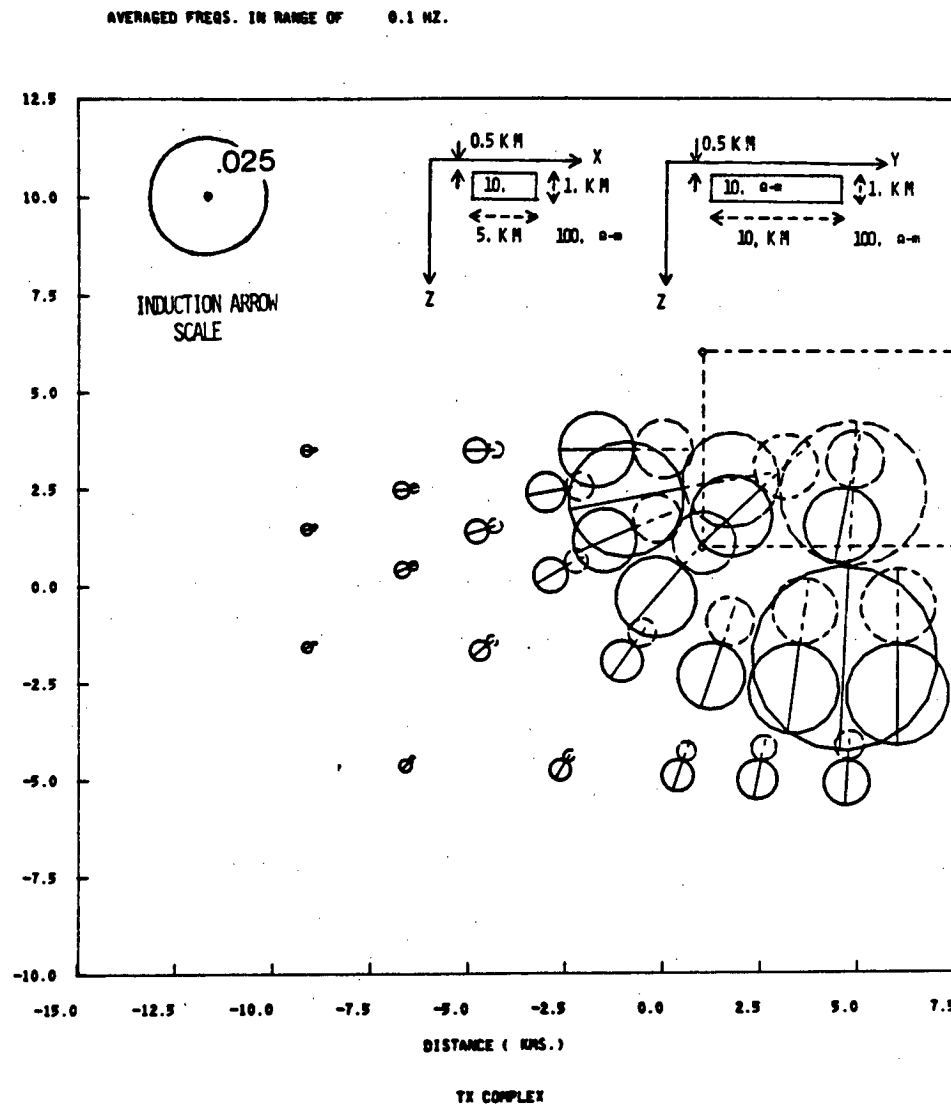


Figure 5.7(b) Apparent resistivity polar diagrams for a three-dimensional model with horizontal dimensions similar to the stippled region in Figure 5.7(a). The parameters of the model are specified on the insert.



**Figure 5.8** Complex tipper and induction arrow diagrams for a three-dimensional shallow conductor at 0.1 hertz. The dashed circles with bisects indicate the imaginary components and the solid circles with bisects represent the real components.

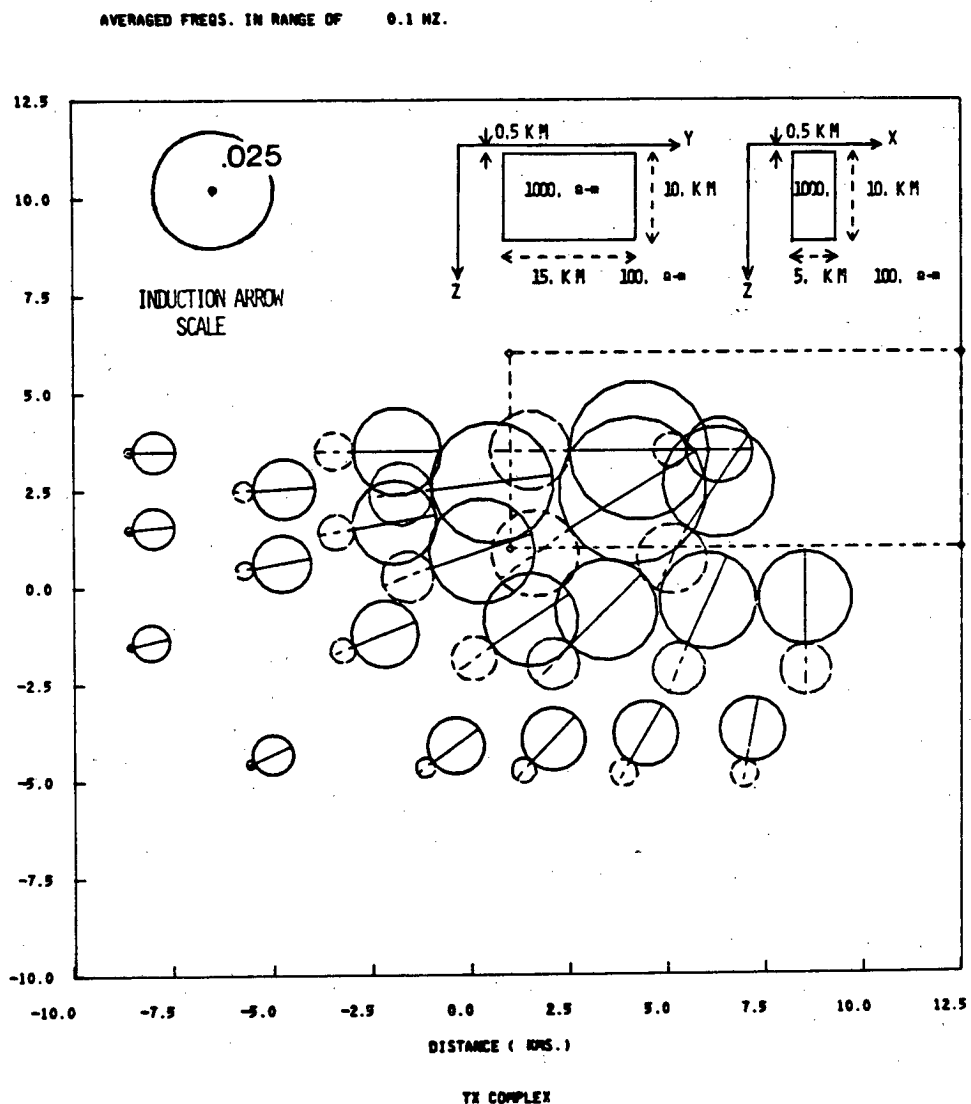


Figure 5.9 Complex tipper and induction arrow diagrams for a three-dimensional shallow resistive body at 0.1 hertz. The dashed circles with bisects indicate the imaginary components and the solid circles with bisects represent the real components.

The complementary case of a buried resistive body is the next example considered. The complex tipper and induction arrows for the resistive model presented earlier are shown in Figure 5.9. Again the frequency used is 0.1 hertz which is sufficiently low that the phase response has shifted into the fourth quadrant and the real and imaginary induction arrows are oppositely directed. The real arrows are directed away from the high current density and the imaginary arrows are oriented toward the current concentrations. An important observation provided by these models is that the amplitude of the induction arrows decay rapidly as the observation position moves away from the conductive body. However, this decay is relatively slow as one moves away from the resistive body. Therefore, one would expect to observe a much broader induction arrow anomaly for large buried resistive bodies than for surface conductors.

The complex tippers and associated induction arrows for the field data averaged over the frequency band of 5.0-1.0 hertz are presented in Figure 5.10. This frequency band was chosen to coincide with a high frequency peak in the amplitude of the geomagnetic transfer function at several locations. The small imaginary induction arrows indicate that the phase of the transfer function is near 0 or  $\pm 180$  degrees. The three previous areas interpreted through the use of the apparent resistivities are indicated by regions A, B, and C. From two-dimensional model studies, it can be shown that conductivity contrasts located in the first kilometer below the earth's surface will result in a tipper maximum occurring in this frequency band. These surface conductivity changes are delineated by the real induction arrows in this figure. The real induction arrow at this frequency will be oriented perpendicular the conductivity contrasts and be directed away from concentrations of induced currents. The earlier interpretations are therefore supported by these results. In addition, there is some indication that a resistive body resides in region D.

Figure 5.10 The complex tipper and induction arrows for the frequency band of 5.0-1.0 hertz. The dashed circles with bisects indicate the imaginary components and the solid circles with bisects represent the real components. The stippled regions indicate the locations of near surface resistive bodies and the banded zones are locations of near surface conductors.

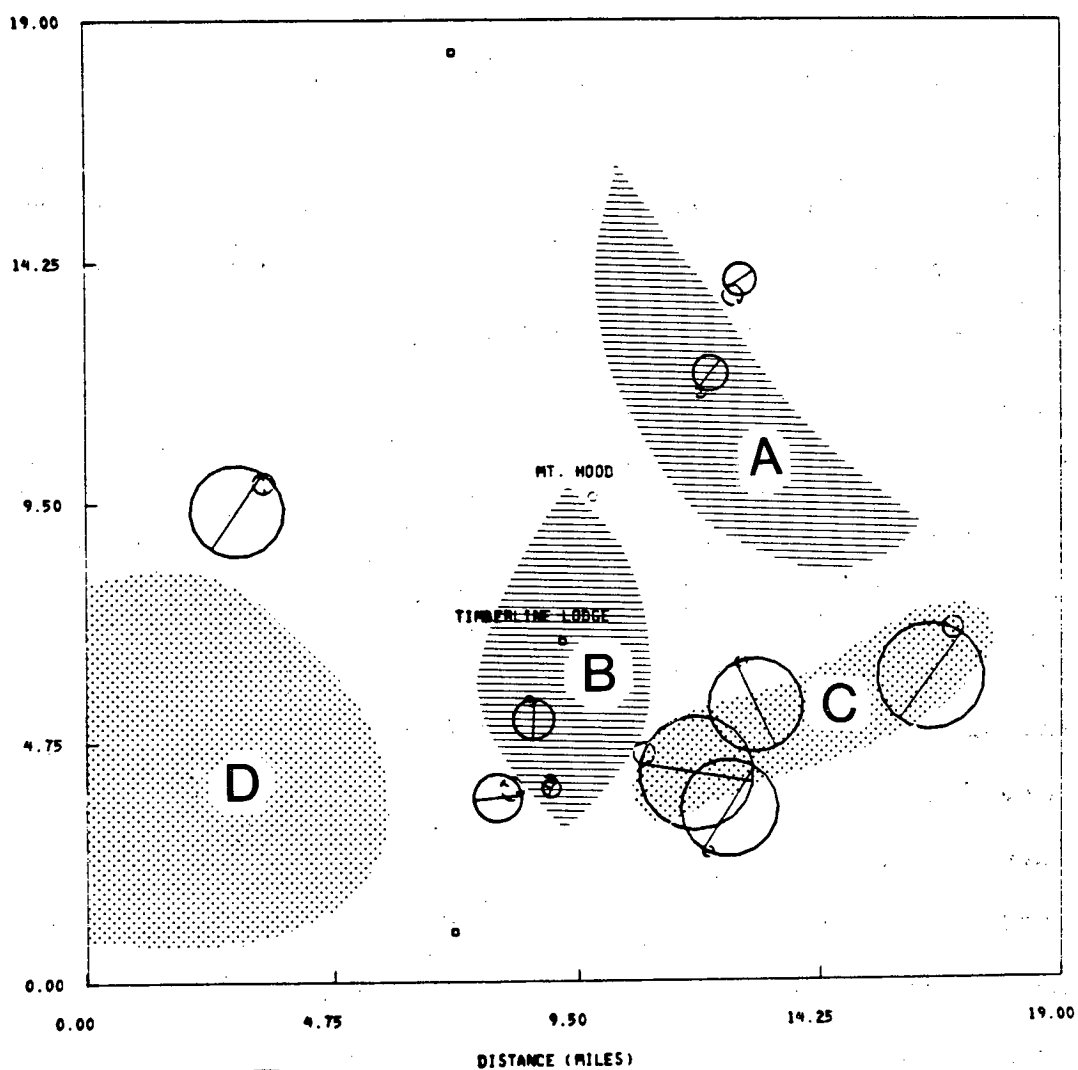
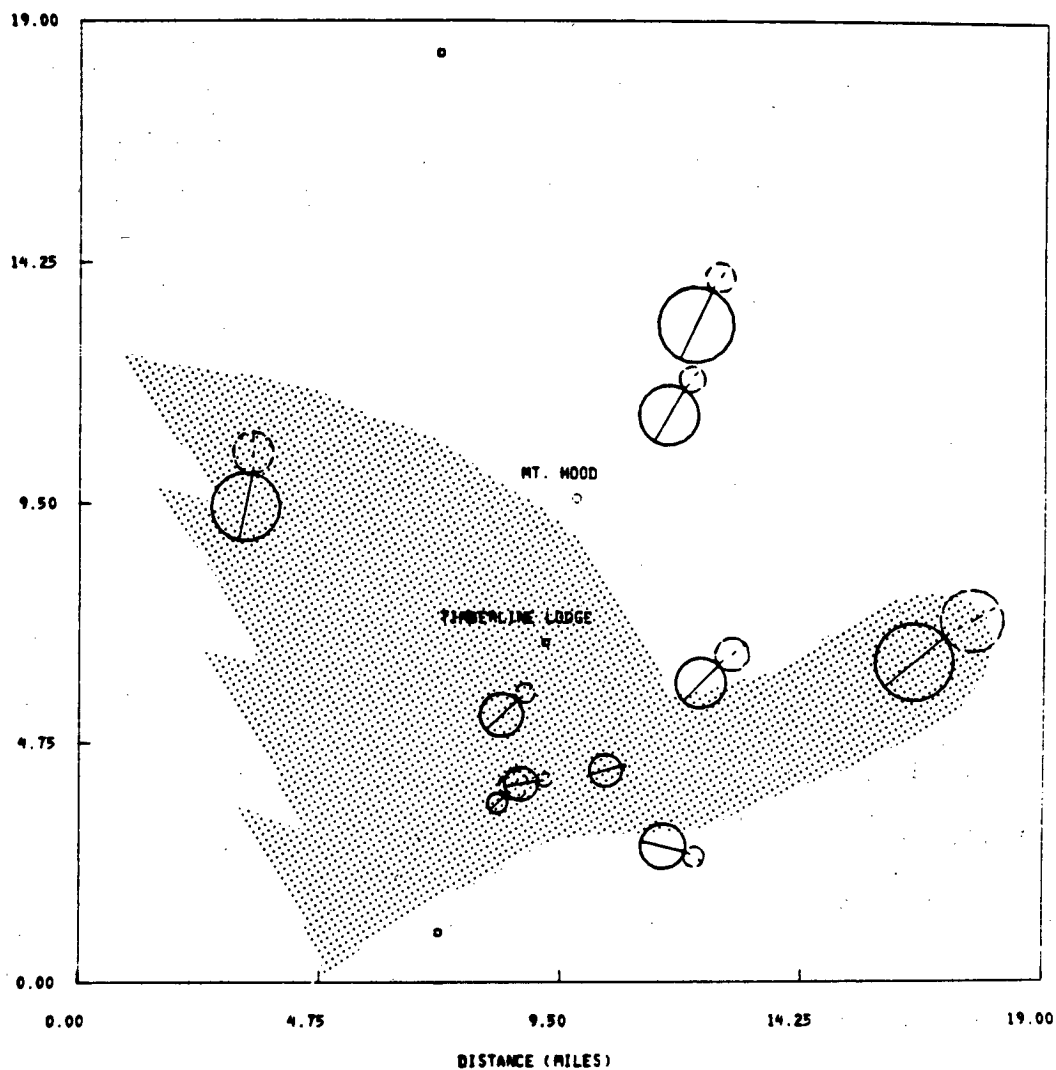


Figure 5.11 The complex tipper and induction arrows for the frequency band of .03-.006 hertz. The dashed circles with bisects indicate the imaginary components and the solid circles with bisects represent the real components. The stippled region represents a resistive body.



A second frequency band 0.03-0.006 hertz was chosen such that it would be located below the 0.02 hertz low frequency tipper maximum observed at several measurement locations. Again, two-dimensional models indicate probable depths for the lateral changes in conductivity responsible for this tipper maximum to be on the order of 4 to 6 kilometers. The induction arrows for the field data in this band are shown in Figure 5.11. All survey sites indicate a region of abnormally low current density in the south-western portion of the area. The stippled region presented with some artistic flare indicates this resistive region which has sufficient depth extent to dominate the tippers over the entire area in this low frequency band.

#### [ IV ] Principal Directions Defined

##### by the Residual Phase

The simulations of near surface inhomogeneities considered in the last section indicated that the presence of scatterers above a deep conductive target would create problems for an interpreter. The resulting distortion of the surface measurements would be broad-band in character. Their removal would depend on the availability of a dense high quality data set which would in-turn provide detailed information as to the parameters of the near surface conductivity distributions. This information could then be used to simulate the response of these features and then a removal technique such as the one introduced in Chapter 3 could be utilized to remove or at least reduce the effects caused by this "geologic noise". The sparse nature of the data set at Mount Hood prevented a detailed delineation of any of the surface inhomogeneities whose effects are quite evident in the data, thereby preventing the quantitative removal of these distortions. This situation initiated an investigation of the various measurement parameters, in order to find which components of the various transfer functions would

least be affected by these near surface contrasts. A few details of this search follows in condensed form.

A second significant question, concerns the effect of a finite strike on a "cheap" two-dimensional interpretation. The data at Mount Hood provided an interesting problem which is not unique to this area. The impedance data in the lower frequency bands had certain frequency characteristics which were suggestive of a two-dimensional response caused by a conductor buried at depth. The structure which may represent the object of the quest was not expected to be two-dimensional, due to the geological and geophysical constraints suggested in Chapter 1. This led into a small scale investigation of the various measurement parameters which are indicative of deep conductors in two- and three-dimensions. Differences and similarities were noted as the strike length shrank from infinite to finite dimensions.

The third and final problem which will be touched upon in this section is the relative sensitivity of the impedance parameters to perturbations in the geometry of subsurface conductors. An understanding of this sensitivity is important since it provides a measure of the resolution provided by the impedance parameter. This will have important ramifications on the joint application of impedance tensor and tipper estimates in the interpretation of data acquired in a three-dimensional environment, as will be seen in the next section.

The three problems will be considered in light of the response provided by three simple three-dimensional models. The results will be used to justify the use of a two-dimensional model to represent the deep conductivity variations under Mount Hood.

The investigation begins with a comparison of the two and three-dimensional response of a conductor buried 15 kilometers with a 15 kilometer square cross-section. The strike length of the three-dimensional body was 60 kilometers. The frequency response for the two cases are shown in Figure 5.12 for the observation position over the center of this elongate conductor. The two and three-dimensional responses are

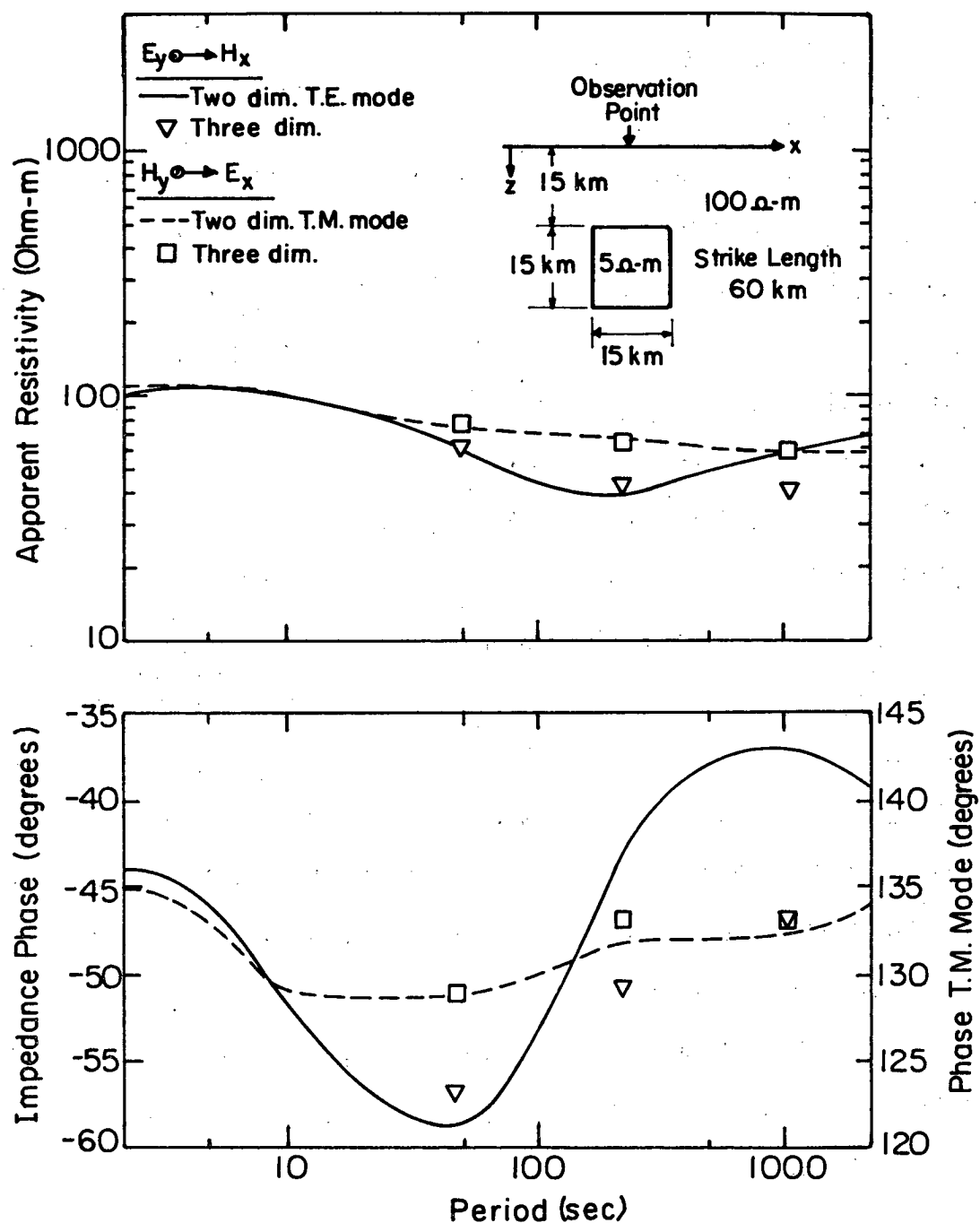


Figure 5.12 The frequency response of the apparent resistivity and impedance phase calculated directly over the buried elongate conductor. The symbols indicate the response from this three-dimensional conductor. The smooth curves indicate the associated two-dimensional responses.

nearly the same for the source polarization with the primary electric field perpendicular to strike. Both the apparent resistivity and the phase for this polarization provide only a weak frequency response for the model. From the earlier models considered in Section III, one can see that the response for this source polarization is greatly affected by near surface scatterers. These observations indicate that the TM mode in two dimensions or the corresponding source polarization in three-dimensions provide apparent resistivities and impedance phases which are not of great use in prospecting for deep conductors. This is especially the case when near surface inhomogeneities are present.

Next consider the model responses for the primary electric field parallel to strike. The two-dimensional frequency response provides a significant indication of the conductor in the apparent resistivity and impedance phase. The absolute phase maximum occurring in the vicinity of 50 seconds provides a major response characteristic. Extensive two-dimensional sensitivity studies indicated that the frequency of this peak response may be shifted by many factors; conductivity of the conductor, depth of burial of the conductor, the dimensions of the conductor and conductivities of the over burden and back ground media to mention a few. This phase peak however, does represent an important diagnostic feature in the frequency response. The three-dimensional response for this source polarization indicated in Figure 5.12 by the triangular symbols, shows a significant departure from the two-dimensional response. The apparent resistivity at the shorter periods are quite similar for both cases. The phase in the vicinity of the absolute maximum is also similar for both cases. The main difference in the frequency response is that the long period "over-shoot" in the impedance phase which is a standard two-dimensional characteristic is missing in the three-dimensional frequency response.

This model shows two important features of the phase. First, the three-dimensional frequency response is characterized by a maximum in the same frequency range and of similar amplitude as the two-dimensional TE mode phase, which as

explained above, is an important interpretation aid. The second important feature to note is that the two-dimensional over-shoot in the long period phase response is missing in the three-dimensional response. This provides a three-dimensional impedance phase characterized by variations which are confined to a smaller frequency band than the two-dimensional response.

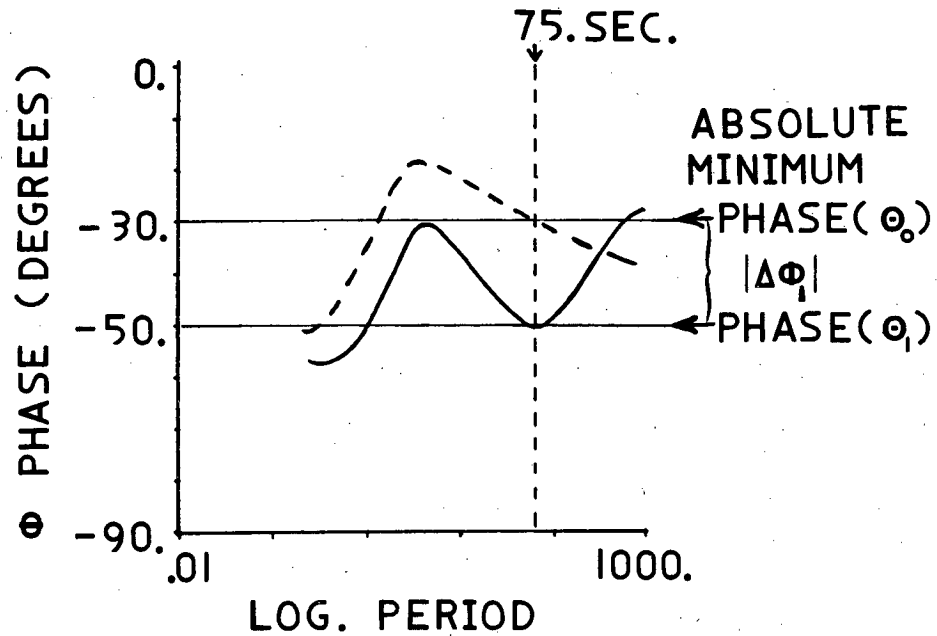
The frequency range over which the conductor affects the various measurement parameters is very important when interpreting data acquired in a media characterized by multiconductors. The models considered in Section III indicated that near surface conductivity variations may distort apparent resistivities over very wide frequency ranges. The phase responses from these models as well as the model presented above are characterized by relatively narrow frequency responses. This small model study indicates that the three-dimensional impedance phases are generally characterized by narrower range of frequency variations than the corresponding two-dimensional model. This phase characteristic may be utilized to minimize the affects of near surface inhomogeneities on an investigation of the underlying structures.

The useful impedance phase properties summarized above may be easily utilized through an impedance normalization procedure. This impedance normalization results in a simple phase differencing scheme which is described in Figure 5.13. The phase of the impedance defined in the first equation is calculated as a function of rotation angle  $\theta$ . All phases are then shifted into the fourth quadrant.

An example of the phase as a function of period for some typical field data is shown in the top sketch of Figure 5.13. The absolute minimum phase response as a function rotation angle is found at the angle  $\theta_0$ . This phase minimum equals 30 degrees for the period of 75 seconds. The frequency response in the fourth quadrant of the impedance phase at the angle of rotation  $\theta_0$  is indicated by the dashed curve. Next consider the phase response for another angle of rotation  $\theta_1$ , represented by the solid curve. The absolute value of the phase at this rotation angle for the period of 75

$$\Phi = \text{ARCTAN} \{ \text{IM}[Z_{XY}(\Theta)] / \text{RE}[Z_{XY}(\Theta)] \}$$

$$= \text{PHASE}(\Theta)$$



RESIDUAL PHASE  $\equiv |\Delta\Phi(\Theta)| = 20.$   
FOR PERIOD = 75. SEC.

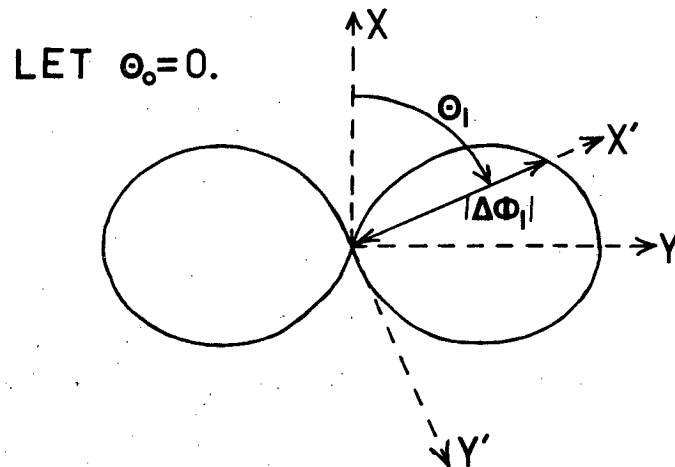


Figure 5.13 Description of the residual phase and the associated polar diagram.

seconds is 50 degrees. The difference between the absolute phases  $|\Delta\Phi_1| = 20$  degrees is defined as the residual phase at the angle of rotation  $\theta_1$ .

The residual phase may be calculated at various angles of rotation over a range of 360 degrees. These values may then be plotted in a polar diagram as indicated by the bottom sketch in this figure. The length of the arrow in this diagram represents the residual phase at the coordinate rotation angle of  $\theta = \theta_1$ . The arc circumscribed by the tip of this arrow, as all angles of rotation from 0 to 360 degrees are plotted, represents the polar diagram of the residual phase.

The residual phase for the model shown in Figure 5.12 may be easily found at the frequency of 0.02 hertz. First shift the phase response for the primary electric field perpendicular to strike (TM mode) into the fourth quadrant. For this observation position the impedance phase associated with the impedance tensor element  $Z_{xy}$  will provide the absolute minimum phase at  $\theta_o = 0$  degrees. This phase component coincides with the absolute value of the TM phase response which equals approximately 51 degrees. As this impedance tensor is rotated to  $\theta = 90$  degrees, the absolute value of its phase becomes approximately 57 degrees. The frequency response for the phase of this impedance element at  $\theta = 90$  degrees is equivalent to the model response for the primary electric field parallel to strike (TE mode). The residual phase for this model has a minimum of 0 degrees for the rotation angle  $\theta = \theta_o = 0$  since this was the angle at which the absolute minimum value occurred (i.e.  $51-51=0$ ). The maximum residual phase occurs when the rotation angle  $\theta = 90$  degrees (i.e.  $57-51=6$ ), which is when the electric field is oriented parallel to strike.

The residual phase polar diagrams for this three dimension conductor are provided in Figure 5.14. The polar diagram described in the previous paragraph is located over the center of the conductor (i.e. the upper right diagram in Figure 5.14). The distance from the center of the polar diagram to its maximum dimension represents the 6 degree residual phase oriented parallel to strike. These simple diagrams clearly

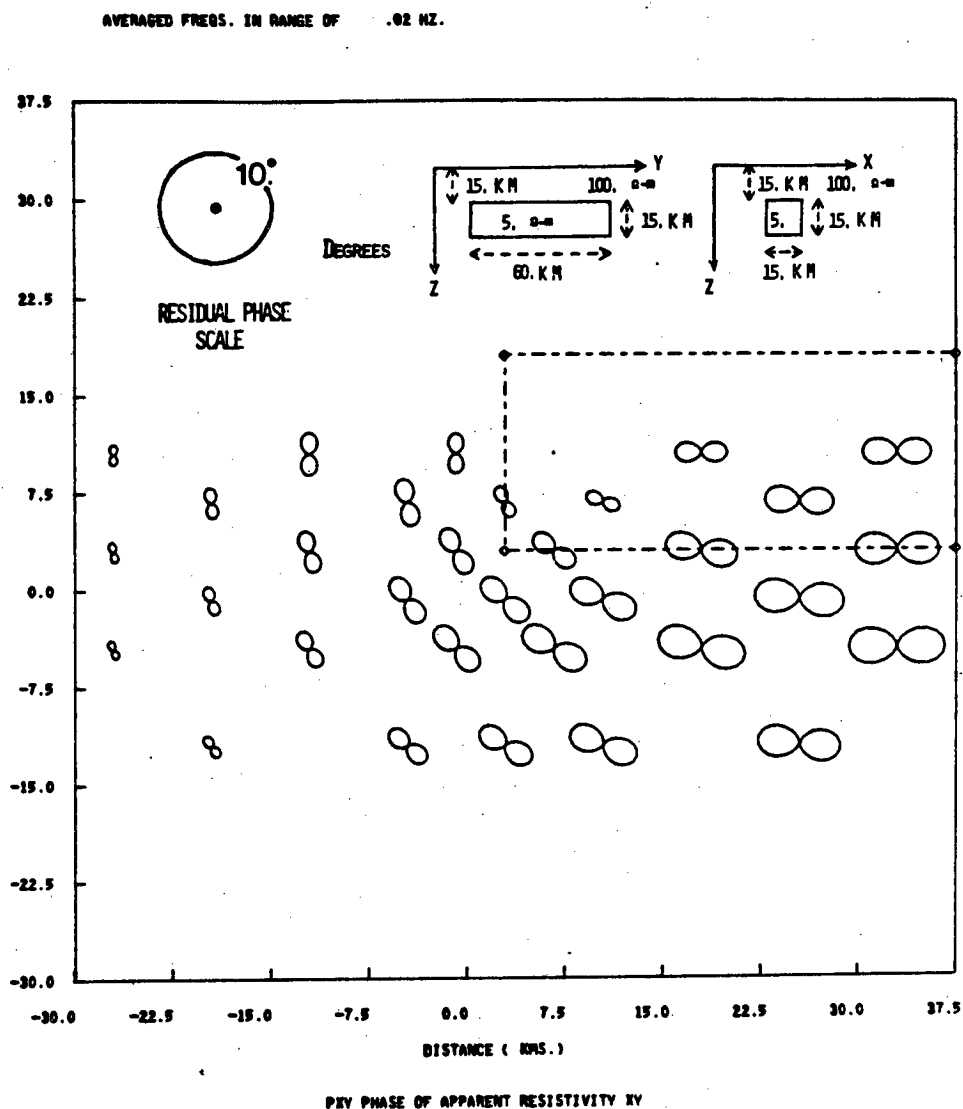


Figure 5.14 Residual phase polar diagrams for the three-dimensional elongate conductor described in Figure 5.12 at the frequency of 0.02 hertz. The observation positions are confined to one quadrant since the model has two planes of symmetry.

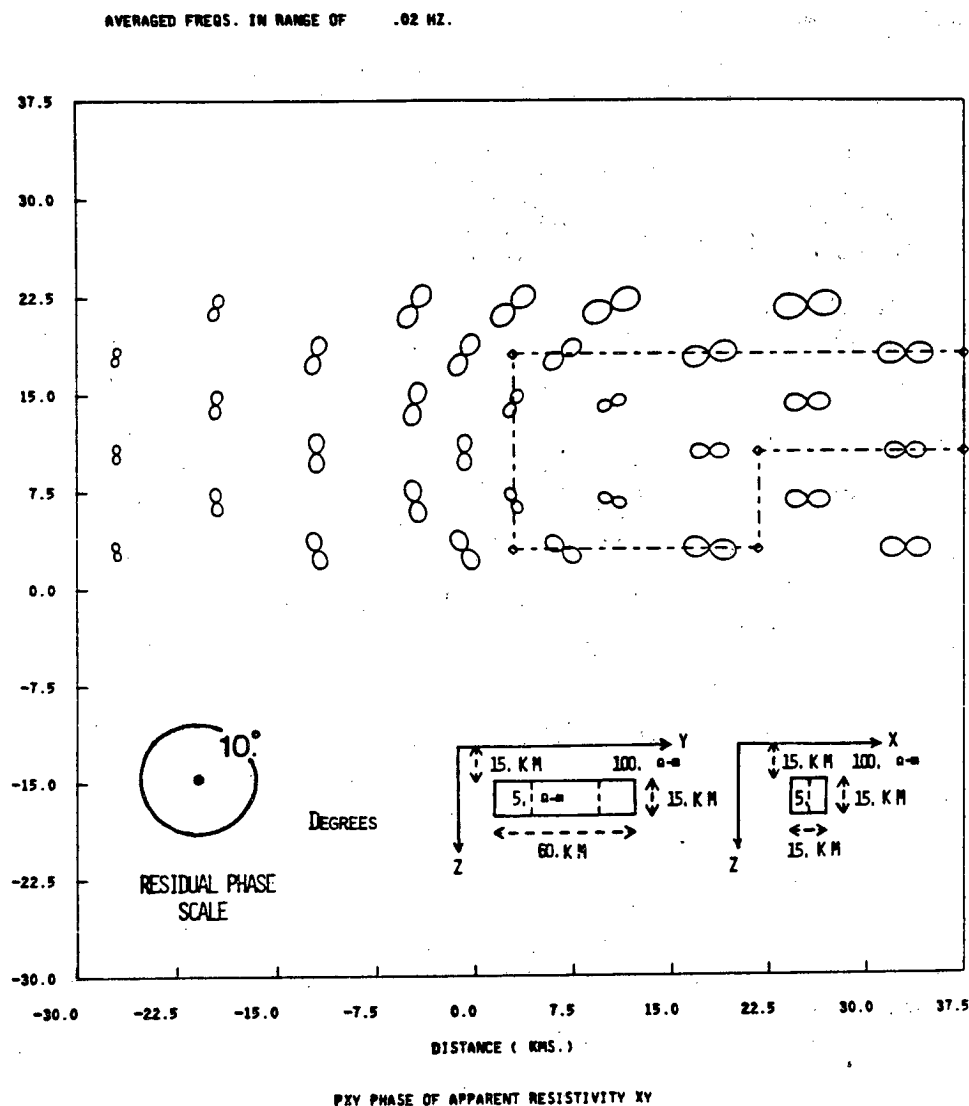
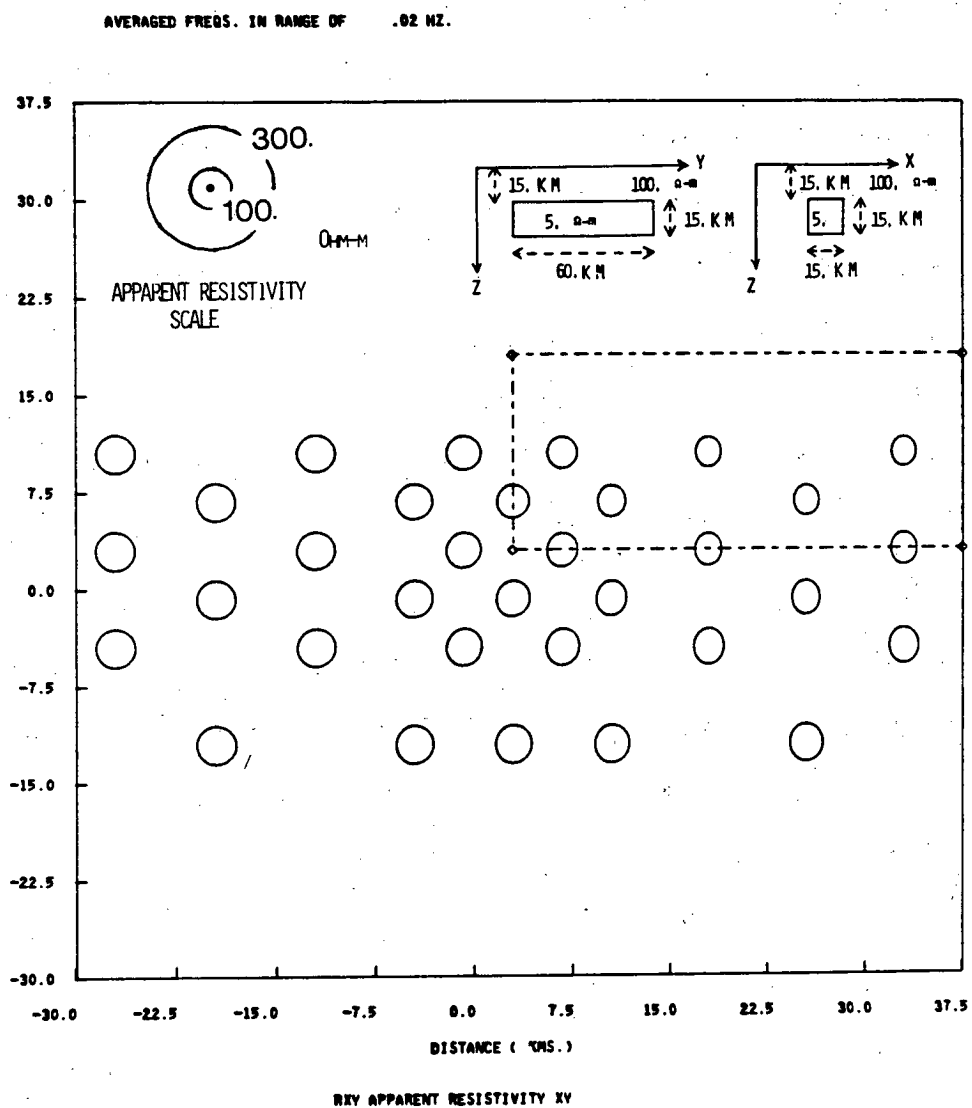


Figure 5.15. Residual phase polar diagrams for a modified version of the model shown in Figure 5.12. This new model has a section of the conductor removed as indicated by the dashed lines on the cross-sections provided in the inserts and by that portion of the plan-view shown. Since the model has one plane of symmetry, the observation positions are confined to the left half of the model.

provide an accurate estimation of the local strike for this model. To evaluate the sensitivity of the impedance parameters on structural changes in the scatterer a perturbation of the above model was created by removing a section from the center of the conductor as indicated in Figure 5.15. The polar diagrams shown in this figure indicate that the impedance phase in the form of the residual phase is fairly insensitive to significant changes in the geometry of the conductor. The strikes indicated by these diagrams are undisturbed by the structural changes even when the observation positions are directly over those portions of the altered model characterized by rapid changes in geometry. The only noticeable change in the diagrams is the decrease in the absolute value of the residual phases measured over the conductor. This is reasonable since the effective cross-section of the modified conductor has only half the area of the original model.

The relative sensitivity of the apparent resistivity to the strike direction of the elongate conductor is indicated in Figure 5.16. The only characteristic which is observed is a slight decrease in the apparent resistivity over the conductor at all rotation angles. This was expected since both source polarizations provide similar apparent resistivities as indicated in Figure 5.12.

Next consider the sensitivity of the apparent resistivity to changes in the geometry of the conductor. Figure 5.17 shows the apparent resistivity polar diagrams for the same model perturbation as considered earlier with the residual phase diagrams. The apparent resistivities at this frequency are not significantly affected by the change in the model cross-section. This indicates that the residual phase is more sensitive than the apparent resistivity to variations in the effective cross-section of the model at 0.02 hertz. However, neither apparent resistivity nor residual phase were sufficiently sensitive to detect local changes in strike caused by the change in shape of the conductor.



**Figure 5.16** Apparent resistivity polar diagrams for the three-dimensional elongate conductor described in Figure 5.12 at the frequency of 0.02 hertz. The observation positions are confined to one quadrant since the model has two planes of symmetry.

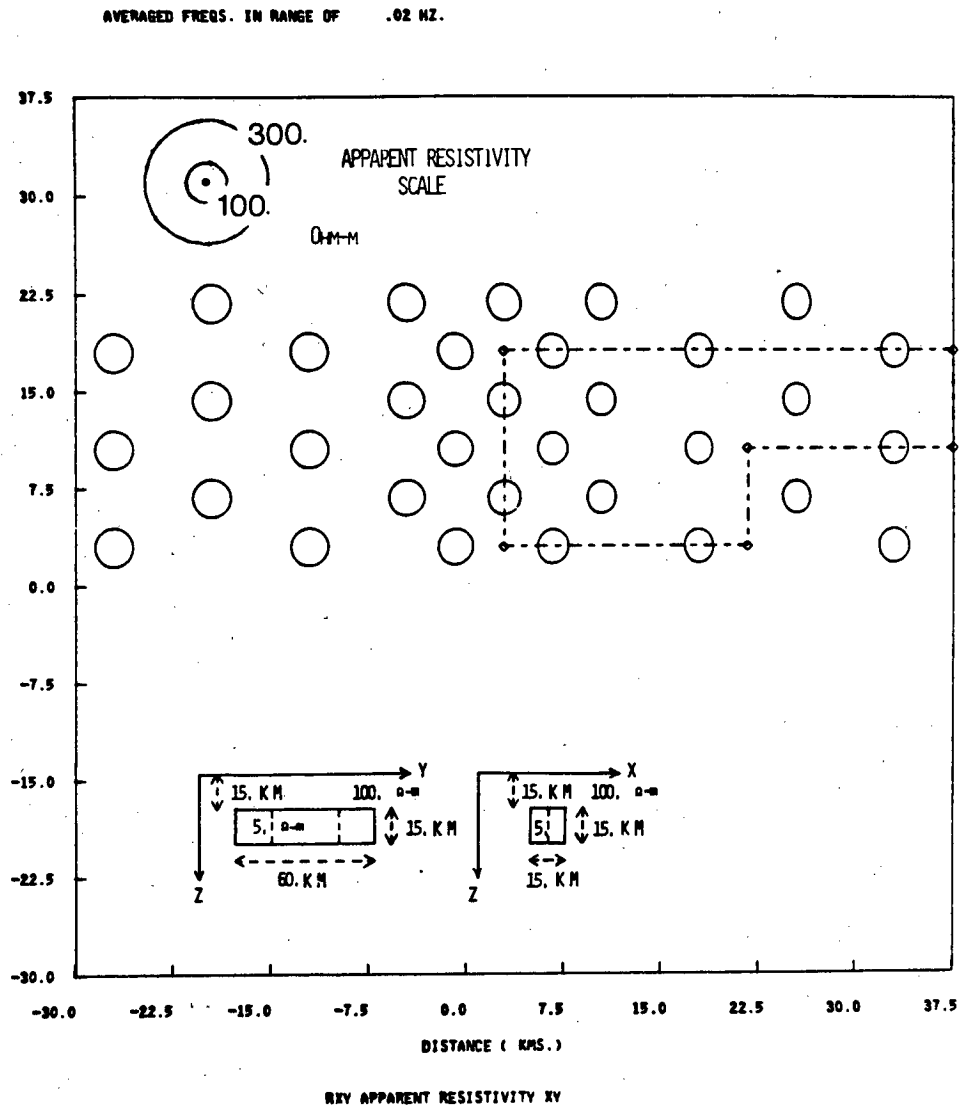


**Figure 5.17** Apparent resistivity polar diagrams for a modified version of the model presented in Figure 5.12. This new model has a section of the conductor removed as indicated by the dashed lines on the cross-sections provided in the inserts and by that portion of the plan-view shown. Since the model has one plane of symmetry, the observation positions are confined to the left half of the model.

The relationship of the above models to the field data may be seen in the following example. Two acquisition arrays, Old Maid Flat with magnetotelluric site 7 and Cloud Cap with magnetotelluric sites 1 and 2 provided similar transfer functions with characteristics which indicated that these data were relatively undistorted by near surface inhomogeneities. Based on the frequency variations of the tipper and impedance phase responses, the transfer functions were separated into five bands. A set of smoothed polar diagrams for all the field data were generated for each frequency band. The five bands are indicated by the vertical sections numbered one through five in Figure 5.18. The impedance parameters provided in this figure are rotated into the principal direction defined at each frequency by the maximization of the off-diagonal elements of the impedance tensor as described by Vozoff (1972).

The impedance phase characteristics of the field data which were interpreted as an indication of an elongate conductor buried at 10-15 kilometers, are clearly evident in this example. The phase maximum which occurs in band 4 on only one phase component associated with the impedance element  $Z_{xy}$  is analogous to the absolute phase maximum observed in the model response shown in Figure 5.12. At this location, the absolute minimum phase in band 4 is approximately equal to the impedance phase associated with the impedance element  $Z_{yx}$  which has an average absolute value of 38 degrees. This is then the normalization value which will be subtracted from phases calculated at all other rotation angles. The maximum phase response as a function of rotation angle in band 4 coincides with the phase associated with  $Z_{xy}$  in this figure. The absolute value of this maximum phase is approximately 50 degrees which provides a residual phase of 12 degrees. In this example the principal directions based on a maximization of the off-diagonal impedance tensor elements coincides with the principal direction indicated by the direction of the maximum residual phase in band 4. This occurred at this measurement site because the impedance tensor was relatively undistorted by near surface inhomogeneities. When a significant degree of distortion

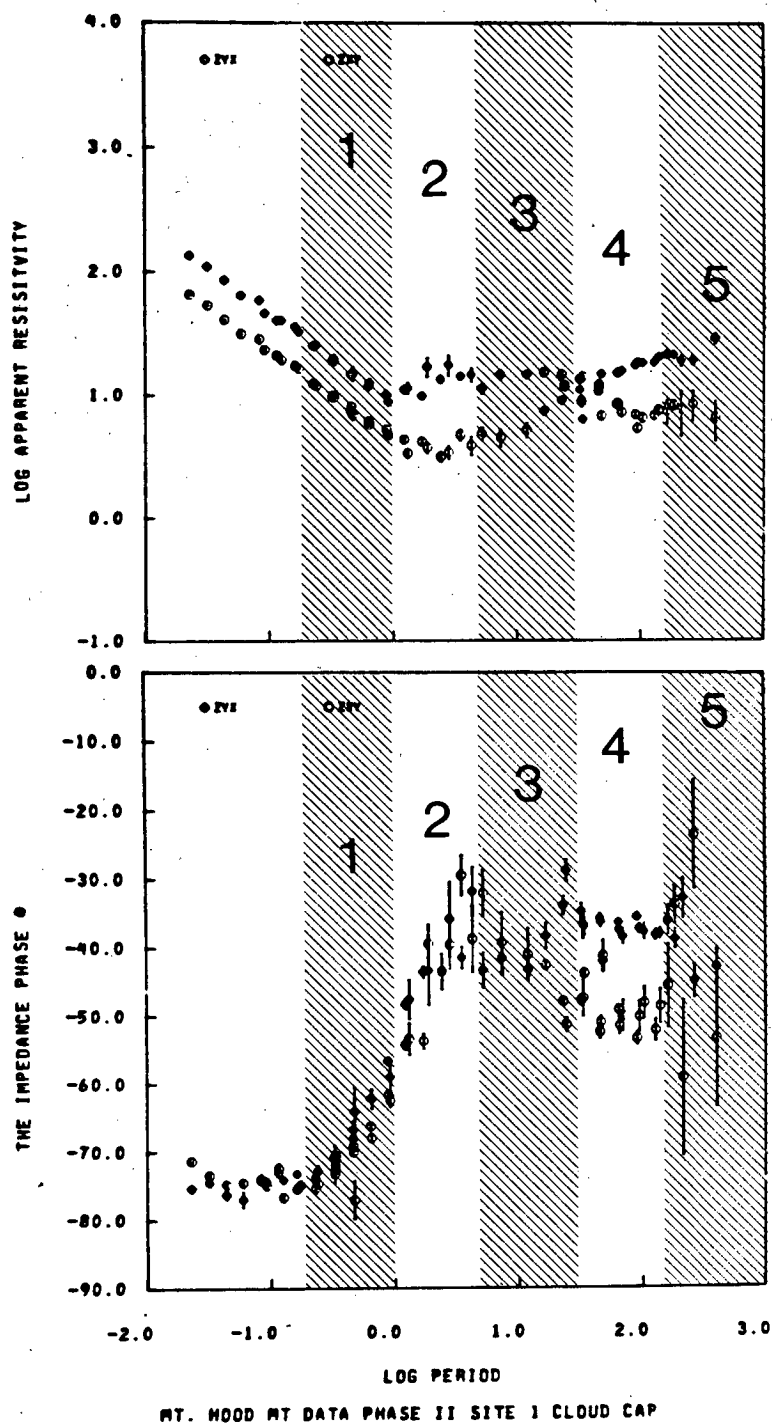


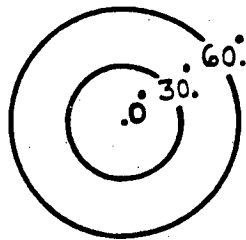
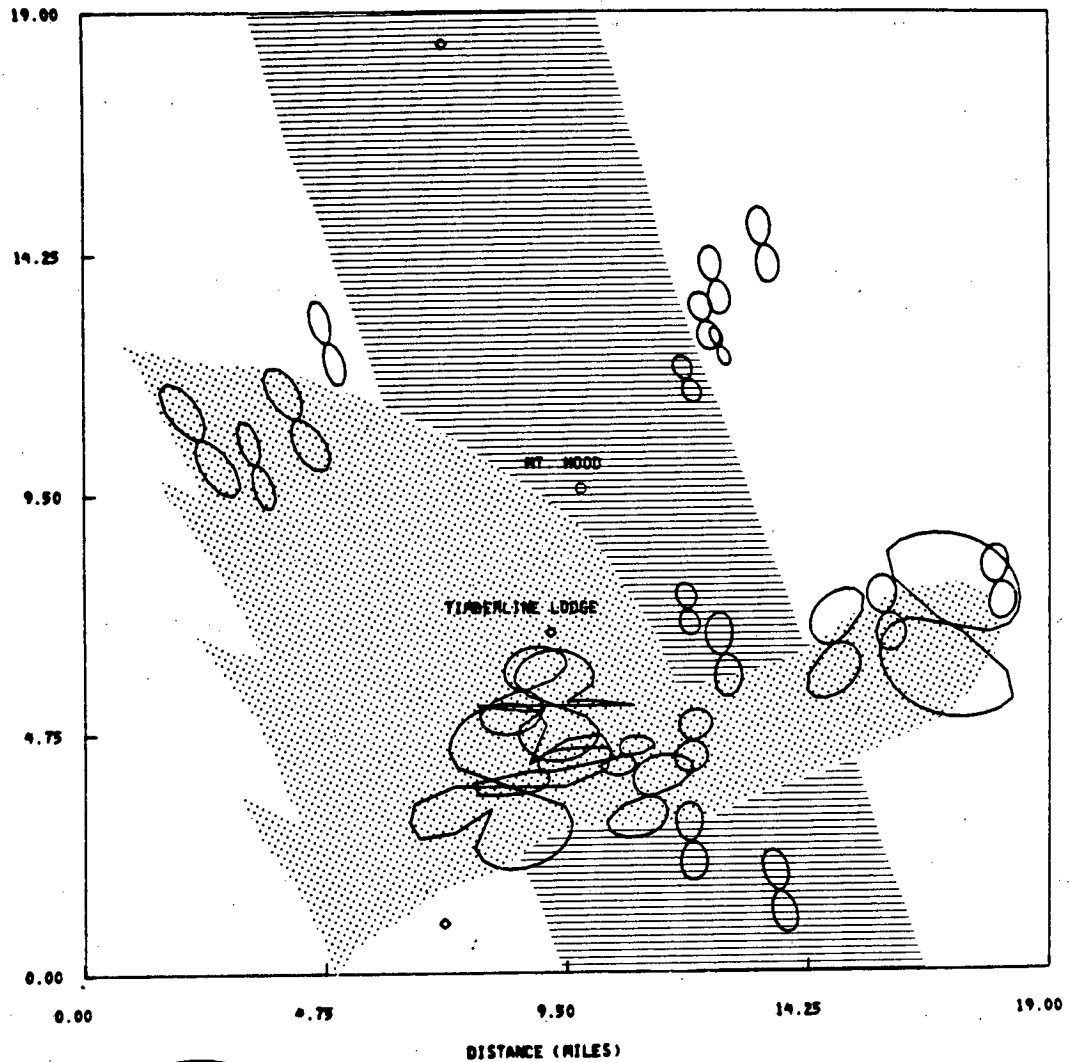
Figure 5.18 An example of the apparent resistivities and impedance phases estimated from field data characterized by only moderate distortions associated with near surface inhomogeneities. The bands over which the field data were averaged to generate the five sets of polar diagrams are designated by the vertical sections numbered one through five.

does occur these estimates of the principal direction are no longer coincident. Some examples of field data where this phenomenon is observed will be shown later in this section.

If the impedance phase response in band 4 for site 1 is caused by a deep conductor similar to the model presented in Figure 5.12, then the resulting phase diagrams throughout the survey area should be characterized by a reasonably high degree of spatial coherency and provide an estimate of the average strike of the conductor. The residual phase diagrams for all the field data in band 4 are provided in Figure 5.19. These diagrams show a surprising degree of spatial coherency throughout the area. If one assumes that the anomalous conductivity structure is centered under the volcano, one has a situation similar to that indicated in Figure 5.14. For this case, the maximum dimension of the residual phase diagram is oriented parallel to strike. Under the above assumption, this analysis indicates that the regional strike of the conductor under Mount Hood is approximately north 20 degrees west. This conductor is indicated in the figure by the banded region. Also included in this figure as the stippled area is the resistive structure inferred from the apparent resistivities and induction arrows in Section III. The residual phase diagrams in the vicinity of this resistive body south-east of the volcanic peak are characterized by a significant amount of distortion. These diagrams, distorted as they are, still provide a strong indication of the regional strike.

Due to modeling limitations, it was not feasible to model the phase distortions observed in the field data south-east of Mount Hood. In order to simulate these responses, two body three-dimensional models were required with a sufficient depth separation such that the phase variations caused by these bodies occur in significantly different frequency ranges. Due to this limitation the broad band problem of amplitude distortion was considered. To understand the magnitude of the distortion due to complex surface conductivity distributions, the simulation shown in Figure 5.20 was

Figure 5.19 Residual phase diagrams of the field data in frequency band 4 (.03-.006 hertz) with inferred conductor at depth indicated by the banded zone and a resistive region which extends from near surface to depths near the conductor is indicated by the stippling.



Residual Phase  
(degrees)

PHY PHASE OF APPARENT RESISTIVITY XY

implemented. The conductor is a laminar shaped 10 Ohm-m body 1 kilometer thick buried 1 kilometer below the surface. The plan-view of the structure is shown as an insert. The observation positions are confined to the left half of the model since it has one plane of symmetry. The apparent resistivity is shown in this figure at 0.001 hertz. The impedance phase response which is included in appendix D has nearly returned to the half space value of 45 degrees at this frequency. In contrast, the impedance amplitudes are distorted in a broad-band fashion. The apparent resistivities and the associated principal direction calculated by maximizing the off-diagonal elements of the impedance tensor are dominated by this surface distribution even at near D.C. frequencies.

It is not difficult to visualize the superposition of this complex surface conductor positioned over the elongate conductor buried at a depth of 15 kilometers. The observation positions located in the vicinity the two ninety degree bends in the conductor would be characterized by distorted apparent resistivities and associated principal directions of about 45 degrees at frequencies below 0.1 hertz. These distortions would slowly increase to those indicated in this figure at 0.001 hertz. The impedance phase will also be affected by this surface structure. However, this phase distortion will probably have a maximum effect above 0.1 hertz and will decrease to near zero at 0.001 hertz. The elongate conductor on the other hand was characterized by a small change in apparent resistivity and a large impedance phase response at 0.02 hertz. It is therefore very likely that the superposition of these models would result in an apparent resistivity and associated principal directions which are completely dominated by the surface conductor in this region. However, this would probably not be the case for the impedance phase. Since a significant component in the range of 0.02 hertz would be caused by the underlying conductor. This phase signature would provide an indication of the deep conductor if the impedance estimates are not rotated to the 45 degree angle dictated by the maximization of the off-diagonal elements of the

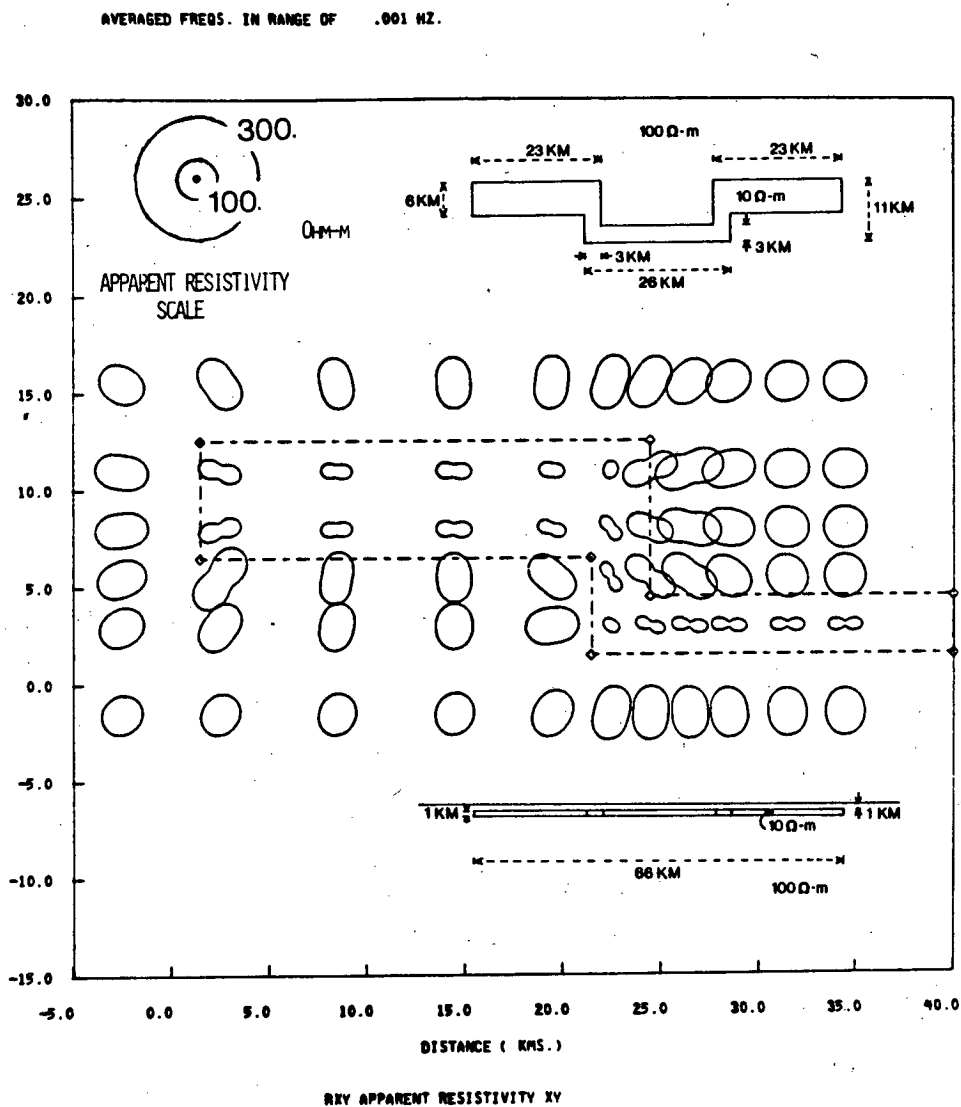


Figure 5.20 Apparent resistivity polar diagrams in the vicinity of a thin near surface conductor with a complex lateral geometry characterized by one plane of symmetry.

impedance tensor. At this rotation angle the phase response would be half-way between the two principal phase responses and no indication of the conductor would be evident.

There are some examples in the field data acquired in the south-eastern region of the survey area that provide characteristics which are similar to those expected from the above composite model. Figure 5.21 depicts the first example of this masking effect caused by surface inhomogeneities. These data were acquired at site 3A. The impedance phase calculated from off-diagonal impedance tensor elements rotated into the principal directions provided by the maximization of these elements for each frequency are presented in Figure 5.21(a). The frequency response of these impedance phases provide no variations below 1.0 hertz which would indicate the presence of a conductor at depth.

The same phase responses rotated into the principal direction of -20 degrees (north 20 degrees west) at all frequencies is shown in figure 5.21(b). This principal direction is based on the average direction of the maximum residual phase in band 4 as indicated in figure 5.19. The separation of the principal phases is obvious at this coordinate rotation angle and is consistent with the phase response provided by a deep conductor with the strike indicated by the principal direction.

A second example of this phenomenon is shown in Figure 5.22 which provides the impedance phase responses at site 3. The apparent resistivities at this location, calculated from the off-diagonal impedance elements, were separated by four orders of magnitude. The data processing techniques described in Chapter 2 indicated that the horizontal magnetic fields were significantly distorted at frequencies above 0.1 hertz at this site. These observations indicate that there exists a near surface inhomogeneity under this location which provides the distorted phase functions shown in Figure 5.22(a). These phases vary as a function of the rotation angles calculated by maximizing the off-diagonal impedance elements. The electric fields were highly polarized and

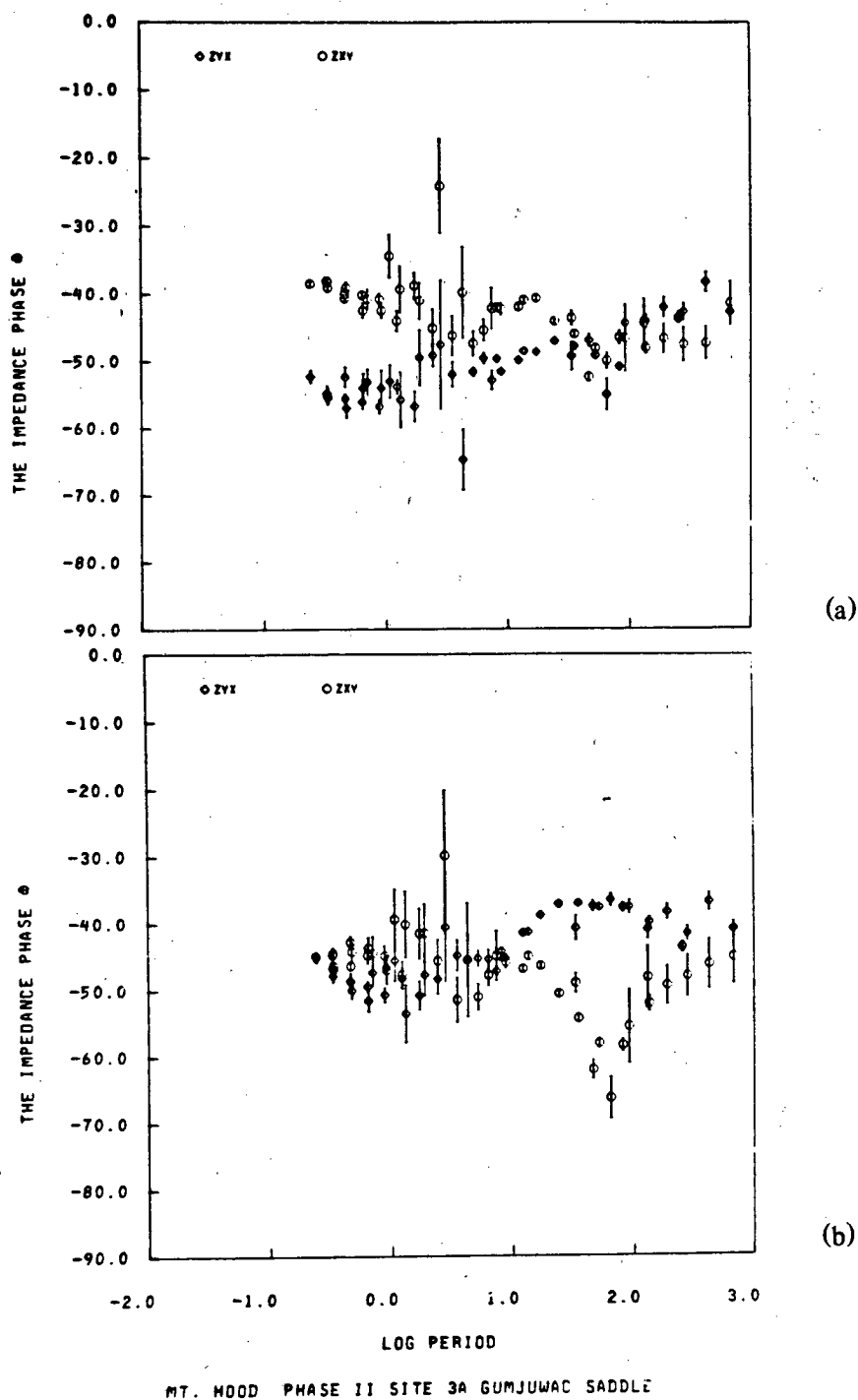


**Figure 5.21** An example of the impedance phase for the field data acquired at site 3A calculated from the off-diagonal impedance elements (a) in the principal direction defined by the maximization of the off-diagonal impedance tensor elements at each frequency (b) in the principal direction defined by the average maximum of the residual phase in band 4 using all sites in the survey area.

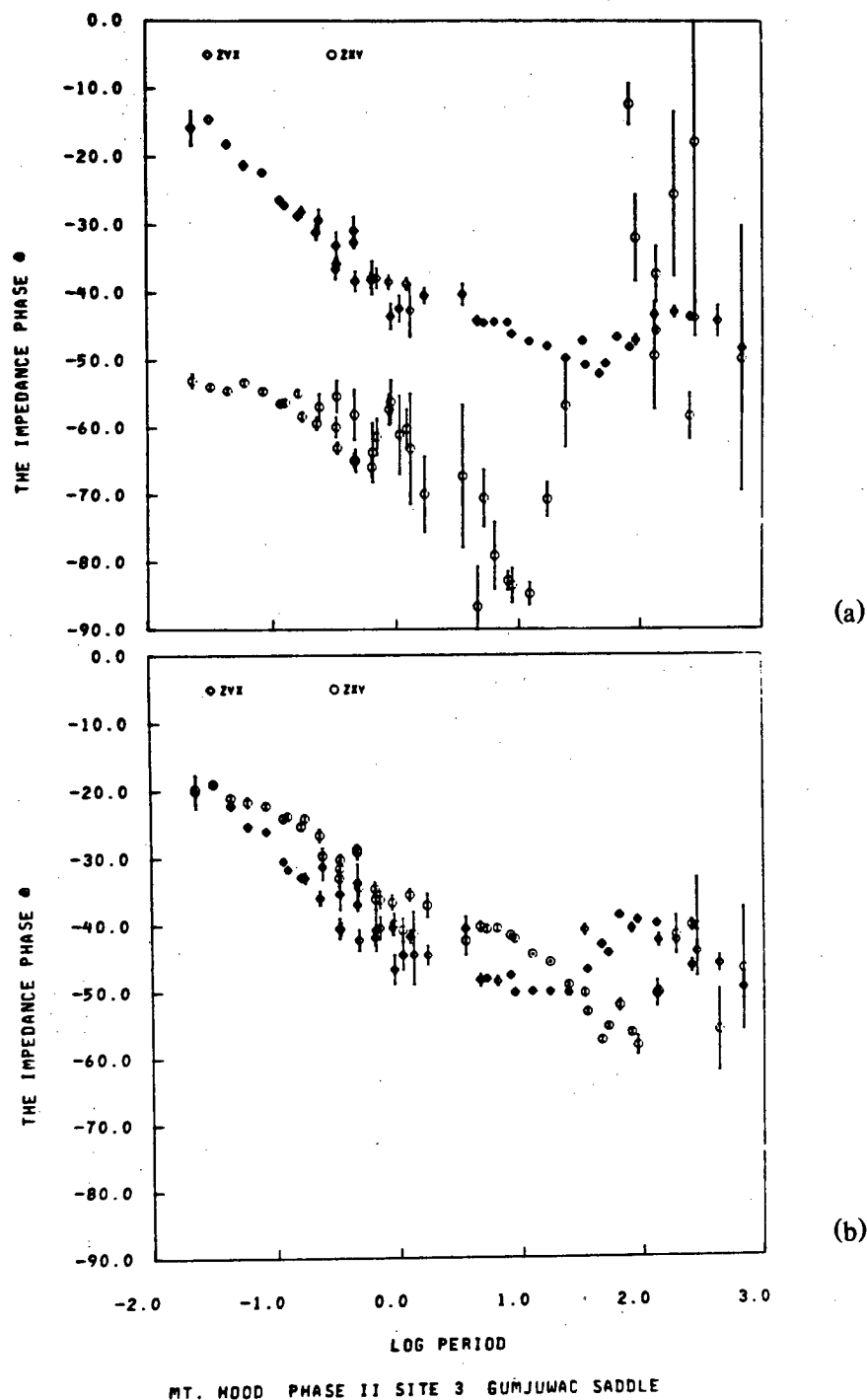


**Figure 5.22** An example of the impedance phase for the field data acquired at site 3 calculated from the off-diagonal impedance elements (a) in the principal direction defined by the maximization of the off-diagonal impedance elements at each frequency (b) in the principal direction defined by the average maximum of the residual phase in band 4 using all sites in the survey area.

the principal direction was controlled by this polarization throughout the measurement band. The resulting phase values shown in this figure are scattered and appear to drift out of the fourth quadrant. This type of phase response would not be amendable to any kind of interpretation.

Figure 5.22(b) provides the same impedance phases rotated into the principal direction defined by the average maximum of the residual phase in band 4. The phase functions in the vicinity of 0.01 hertz are significantly distorted. However, the separation of the principal phases at this frequency is still evident and an indication of the deep conductor is again provided by using the correct rotation angle.

The model studies coupled with the high spatial coherency observed in the field data in band 4 indicated that the residual phase would be a useful method to estimate the average strike of the dominant conductors at depth. This strike was used to establish a perpendicular profile indicated by the straight line in Figure 5.23(a). The observations in this vicinity were relatively undistorted by surface inhomogeneities and indicated principal directions similar to the rotation angle obtained by the residual phase throughout the frequency band acquired. These factors indicated that a reasonable estimate of the conductivity variations in the area could be obtained by projecting these data onto the profile and then applying a two-dimensional parameterization to simulate the observations. The results of this parametric inversion is provided in Figure 5.23(b).

The most important parameters in this model were associated with the 1 Ohm-m conductor with a 10 kilometer cross-section buried 12 kilometers. The second most important portion of the model was the large resistive body on the south-western end of the profile which extended from a depth of 2.5 kilometers to 14 kilometers. The near surface 3 Ohm-m conductor near the center of the model simulated the conductor detected under Cloud Cap (Site 1) by the high frequency magnetotelluric data and the single electromagnetic loop sounding. The 3 Ohm-m conductor buried directly

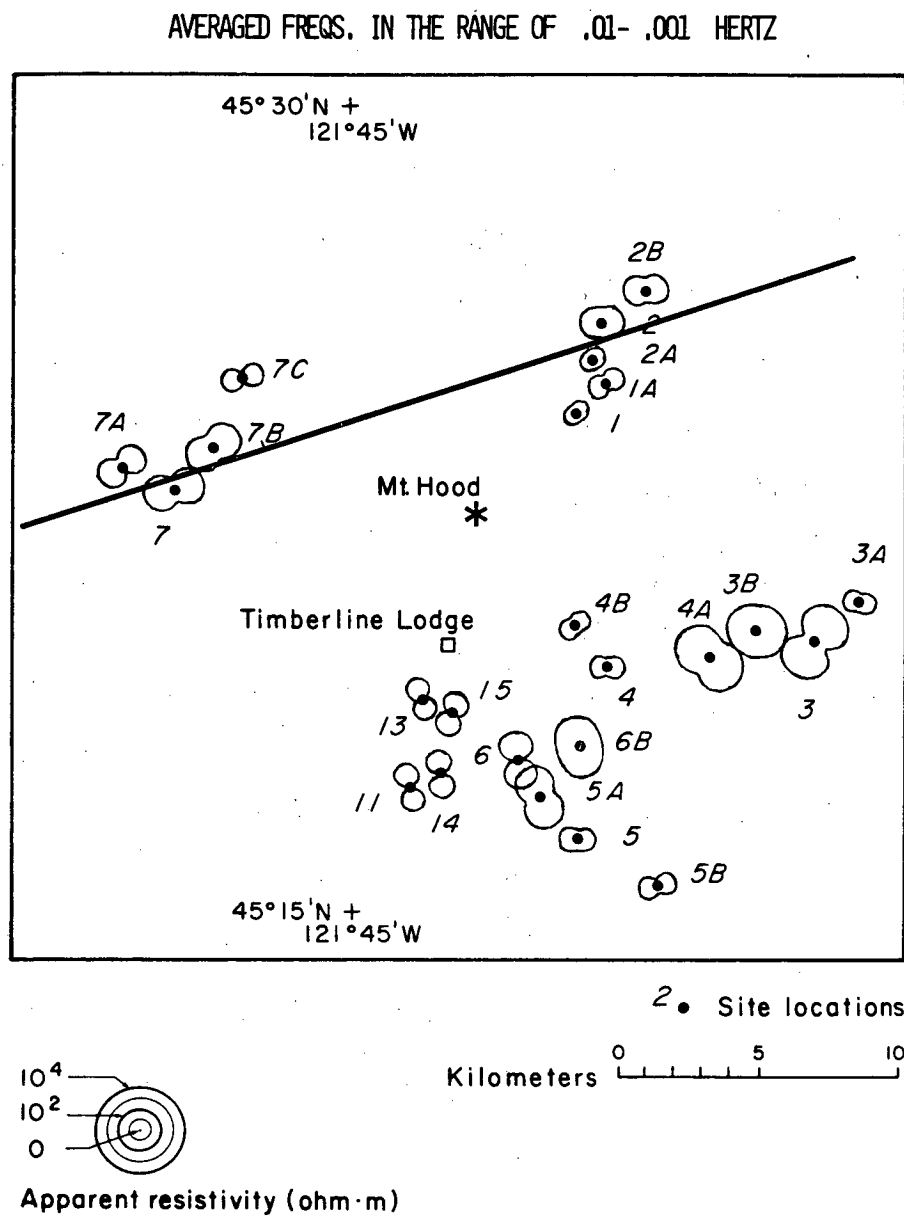
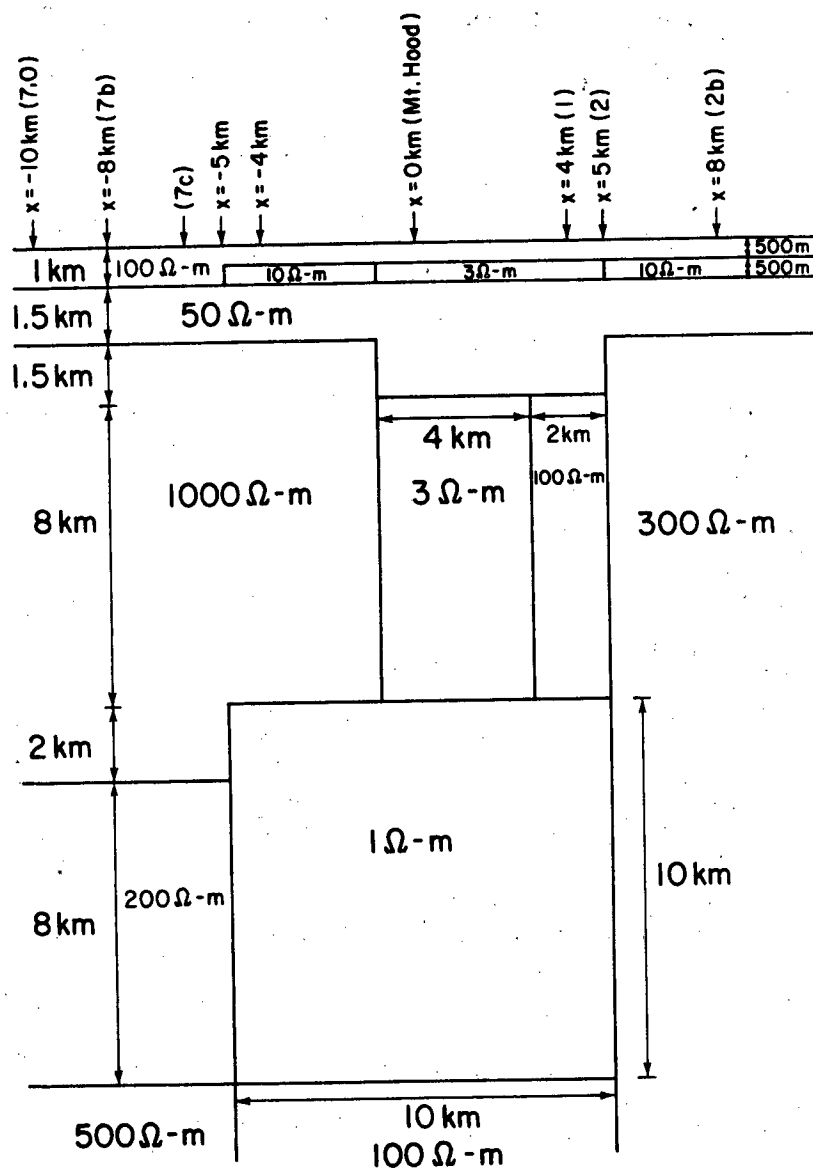


**Figure 5.23(a)** Polar diagrams of the field data with a profile perpendicular to the inferred strike based on the residual phase in band 4 indicated by the straight line.



XBL 819-11651

Figure 5.23(b) The conductivity cross-section along the profile indicated in Figure 5.23(a) based on a two-dimensional analysis.

under the projected position of Mount Hood at a depth of 4 kilometers was not a sensitive parameter for the impedance response functions. However, the induction arrows which will be considered in the next section provided a strong response from a conductor in this vicinity at approximately this depth.

There were two implicit constraints utilized in this model. The first was associated with the near surface conductivity distribution under the Old Maid Flat array near site 7B. A 1.2 kilometer bore-hole in this vicinity provided information which indicated that the near surface material in this area was composed of impermeable rocks characterized by high seismic velocities at shallow depths. The electrical logs from this bore-hole match fairly well with the results obtained from a magnetotelluric one-dimensional inversion of the impedance parameters at site 7B associated with the electric field oriented north 70 degrees east. These results indicate a relatively resistive near surface zone with higher resistivities at depth.

The next constraint and the most important single factor in the interpretation was associated with initial parameterization which resulted in the large conductor at a depth of 12. kilometers. There are at least two basic families of models which could have been adapted to provide low frequency response characteristics similar to those observed in the impedance parameters measured at Mount Hood. The spatially confined data proved to be insufficient to distinguish between these two major categories of possible models. The first possibility was a model based on the existence of a large near surface lateral conductivity contrast existing outside of the survey area. The parameters of various models investigated in this family which would provide the necessary frequency characteristics were not considered to be reasonable for this geological environment. The second suite of candidates considered were associated with a deep conductive anomaly under the survey area. This general model was chosen as the appropriate starting point for the two-dimensional parameterized inversion, based on the heat flow measurements acquired by Blackwell and Steele (1979) in the

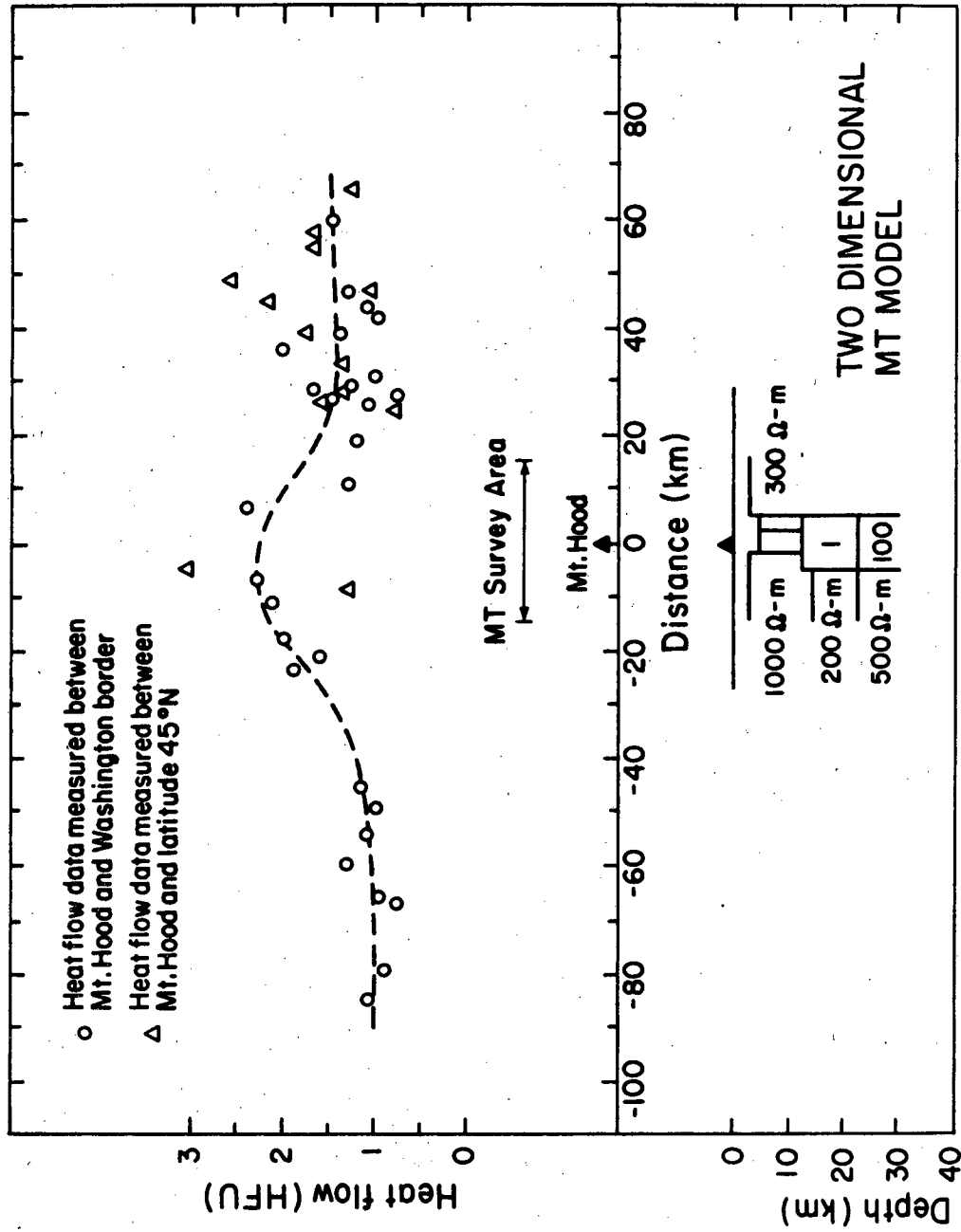


Figure 5.24 The cross-section of the two-dimensional model with respect to the heat flow measurements projected onto an east-west profile across Mount Hood (Heat flow profile by Blackwell and Steele, 1979).

Cascades near Mount Hood. These data shown in Figure 5.24 indicate an anomalous zone of heat flow confined to an area in the immediate vicinity of Mount Hood. The strong thermal dependency of electrical conductivity in conjunction with the localized heat flow high, indicated that the most reasonable source of the low frequency impedance variations exhibited by the data would be associated with this thermal anomaly centered on the volcano.

The model response is compared to the field data at two positions along the profile to indicate the quality of the fit. Since the field data were grouped on each end of the profile a representative site from each is shown. Figure 5.25(a) indicates the match between the simulated and the observed data at  $x=5$  kilometers which corresponds to site 2. The solid and dashed curves indicate the TE and TM model responses respectively. The symbols indicate the field data. The data at site 7B observed at  $x=-8$  kilometers is shown in Figure 5.25(b). This figure indicates the quality of the fit between the field measurements and the simulations on the southwest end of the profile. In this figure, the solid curve provides the TM response and the dashed curve indicates the TE solution. The degree of fit for the other sites were similar to the two examples shown in these figures, since the frequency responses between locations in each of the two arrays shared similar characteristics.

The degree of fit between the observed and the calculated impedance parameters are similar in both examples. The match is good at frequencies below 1 hertz with one important exception. The phase for the TE mode simulations and the observations below 0.02 hertz provide different frequency responses. The differences between these phase responses are similar to the departures observed between the two- and three-dimensional model results provided in Figure 5.12. This would indicate that the observed mismatch in the TE mode phase response may be related to the finite strike length of the 1 Ohm-m conductor buried at a depth of approximately 12 kilometers.

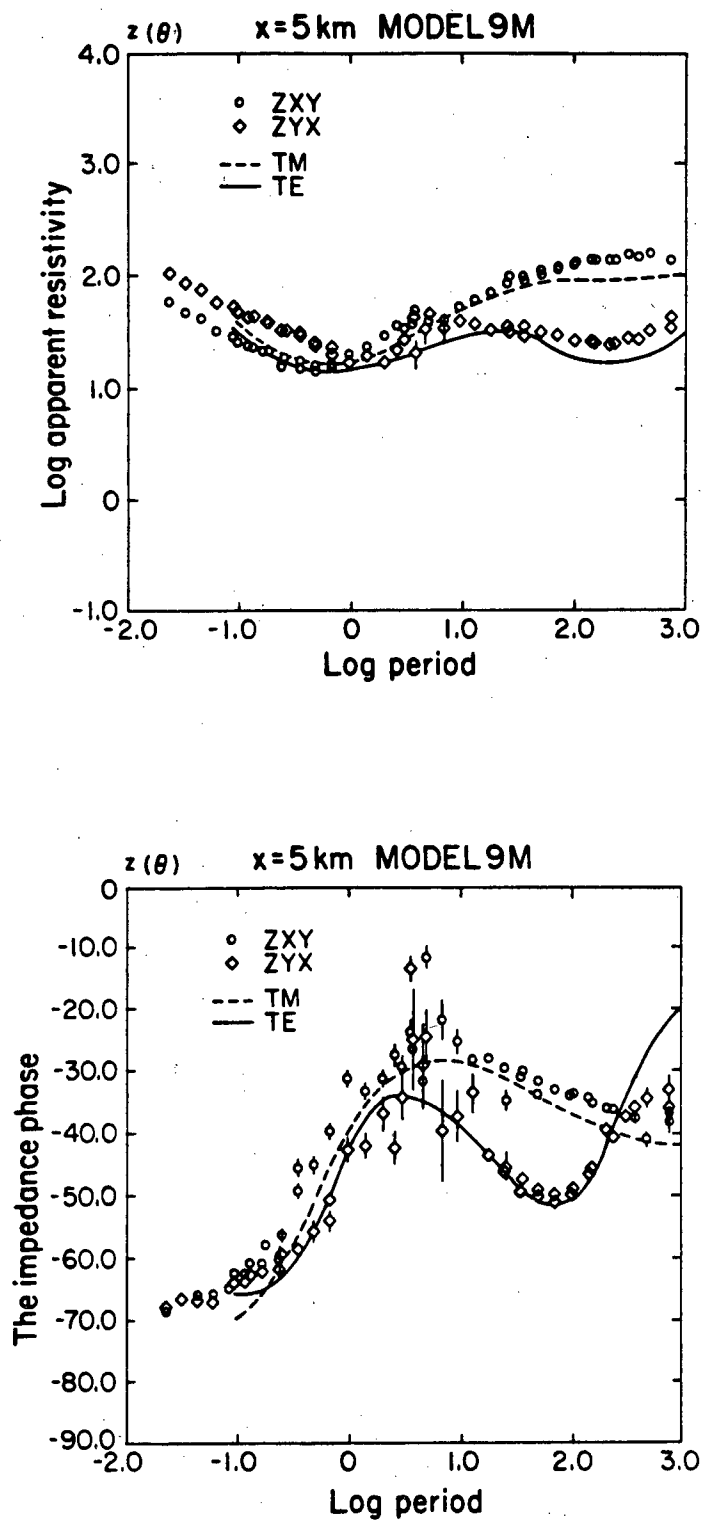


Figure 5.25(a) An example of the comparison between the two-dimensional model provided in Figure 5.23(b) which are indicated by the solid and dashed curves and the field observations at site 2 designated by the symbols. This site is located on the north-eastern end of the profile provided in figure 5.23(a).

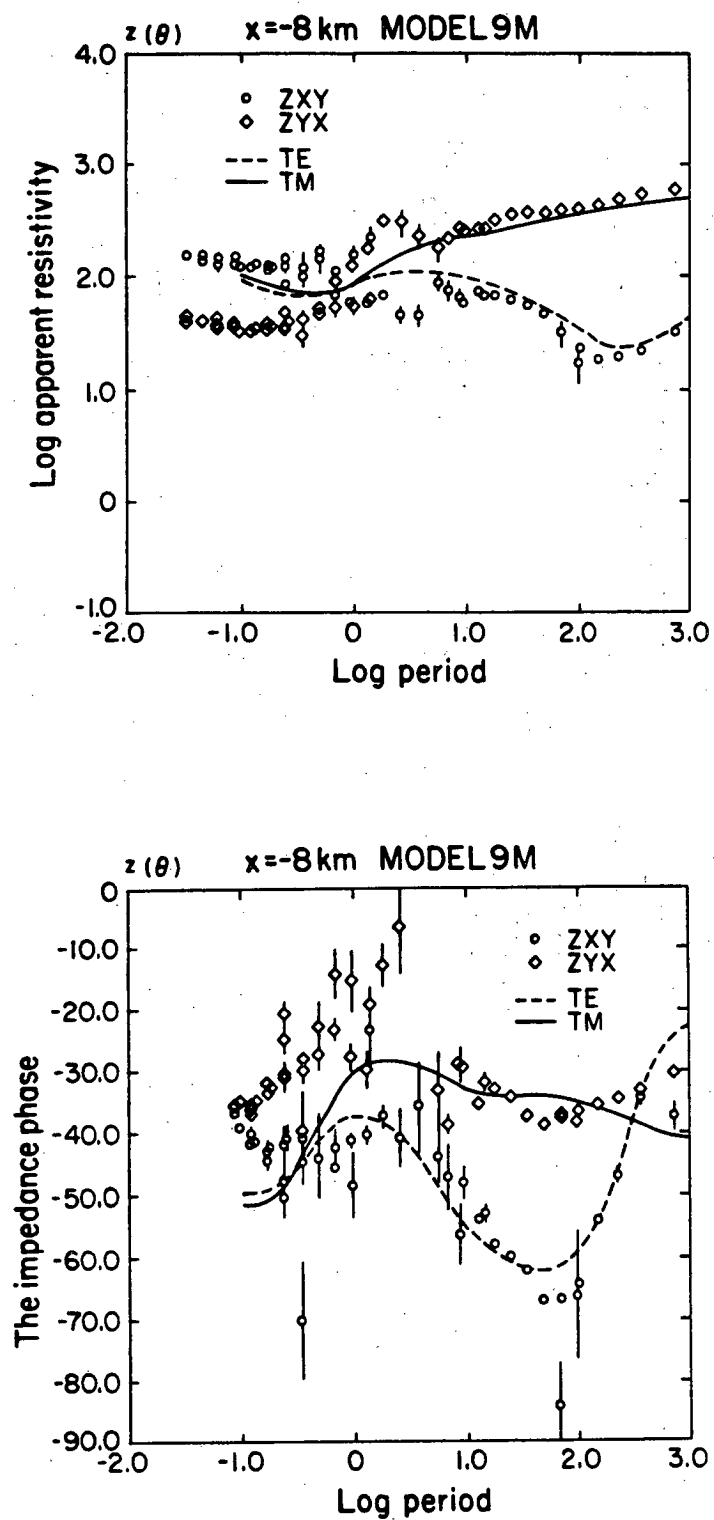


Figure 5.25(b) An example of the comparison between the two-dimensional model provided in Figure 5.23(b) which are indicated by the solid and dashed curves and the field observations at site 7B designated by the symbols. This site is located on the south-western end of the profile provided in Figure 5.23(a).

### [ V ] Induction Arrows: A Sensitivity Study

The impedance data over the entire survey area provided a dominant low frequency phase characteristic which displayed a high degree of spatial coherency. The electrical conductivity models, which satisfied this regional phase response and which were consistent with a local heat flow high, indicated that there was an elongated conductor under Mount Hood at a depth of 10-15 kilometers. A conductor at this depth with the dimensions indicated in Section IV should provide a significant secondary vertical magnetic field. The resulting tipper should have a phase response of 0 or  $\pm 180$  degrees at a frequency of approximately 0.0023 hertz. Such a response was not seen in the data. The problem posed by this apparent inconsistency between the tipper and the impedance estimates required a solution before the credibility of this model could be established.

The resolution of this paradox was attempted through the use of a suite of simple to complex two- and three-dimensional models. These models were designed such that their responses would provide an indication of the relative sensitivity of the various tipper parameters, an indication of the effects of strike length on these parameters, and an estimate of their sensitivity with respect to the impedance tensor estimates.

To initiate this investigation, the simplest case was considered which would provide the tipper parameters which would be observed in the vicinity of the deep 1 Ohm-m conductor obtained by the parameterized inversion of the profile data presented at the end of Section IV. This two-dimensional model is presented in Figure 5.26(a). The TE mode impedance phase response for this model in pseudo-section is provided in Figure 5.26(b). This figure shows the dominant absolute maximum in the impedance phase at approximately 0.022 hertz. The phase characteristic is similar to that observed in the impedance phase estimates when with the electric field is oriented north 20 degrees west. This maximum phase response is centered

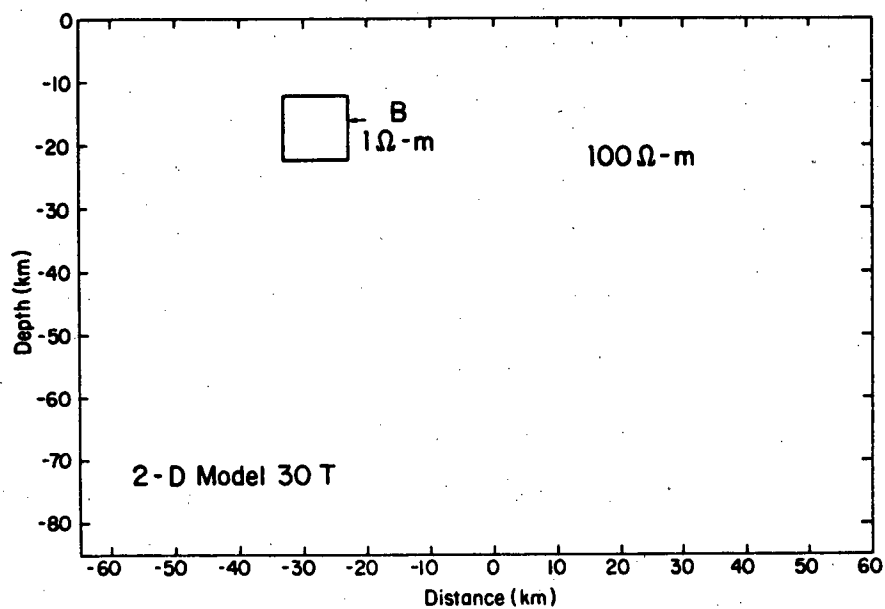


Figure 5.26(a) A single body two-dimensional model.

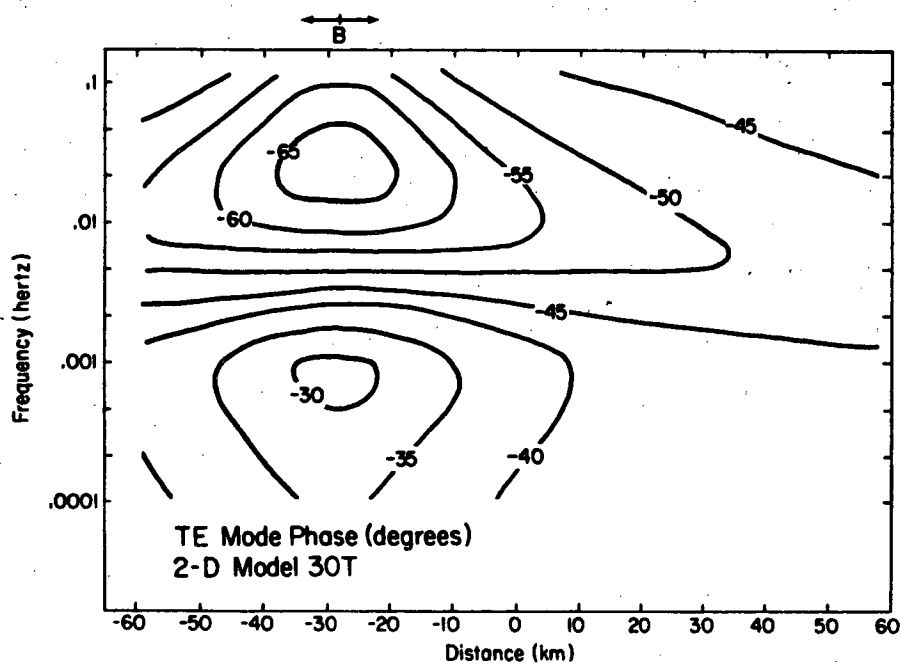


Figure 5.26(b) The TE mode impedance phase response.

over the conductor and decreases slowly as the observation positions are moved away from the conductor. A strong response would be expected over a 30 to 40 kilometer range centered on the conductor.

The tipper amplitudes associated with this structure are presented in Figure 5.26(c). The first interesting observation is that the amplitude response along the profile seems to complement the TE impedance phase response. The amplitude of the tipper is zero on the symmetry plane through the center of the conductor and doesn't reach a maximum until the observation position is nearly 20 kilometers from the center of the conductor. The next point of interest is that the maximum tipper amplitude on each side of the conductor occurs at about 0.0022 hertz. This maximum in the tipper response is a decade below the absolute impedance phase maximum which occurred at approximately 0.022 hertz over the center of the conductor. This figure indicates that the tipper amplitude maximum is spread over a very broad frequency range in the vicinity of the conductor. For data acquired only over the conductor, the frequency response of the tipper amplitude would be a very insensitive parameter to use in the estimation of the depths to the anomalous zone.

The tipper phase response is shown in Figure 5.26(d). The phase information is indicated by quadrant with the orientation of the associated real and imaginary induction arrows indicated by the solid and dashed arrows respectively. The presentation clearly indicates that the tipper phase response would provide a stable frequency characteristic as a function of position along the profile. The tipper phase has a value of 0 or  $\pm 180$  degrees at approximately 0.0025 hertz. This phase value provides a zero imaginary induction arrow and occurs at approximately the same frequency as the peak in the tipper amplitude. These 0 or  $\pm 180$  degree phase points however should provide a much more reliable estimation of the depth to the conductor for observation points near the body. This would be the case since the zero imaginary induction arrow is confined to a much narrower range of frequencies than the broad tipper amplitude

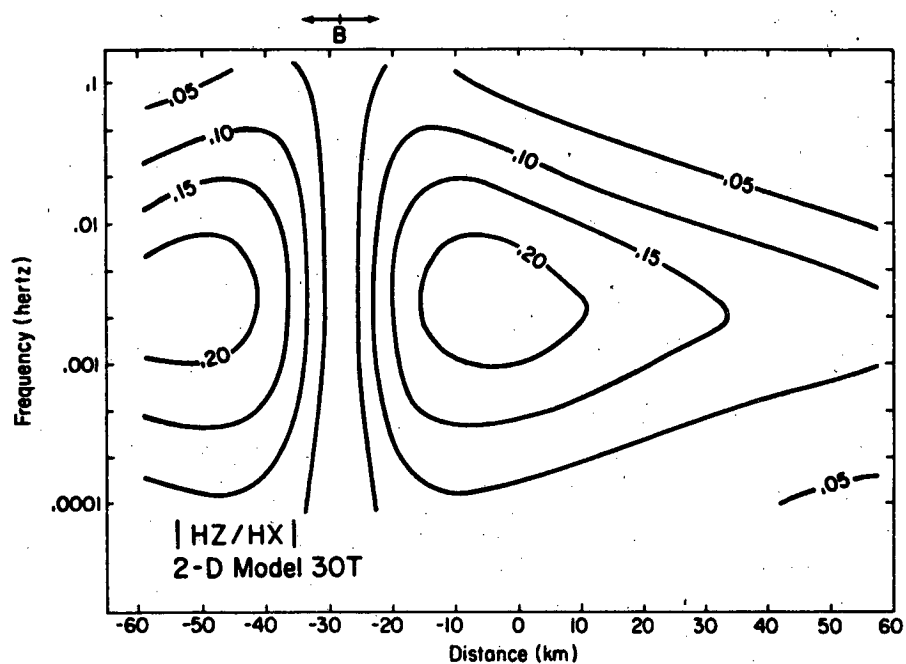


Figure 5.26(c) Tipper amplitude response.

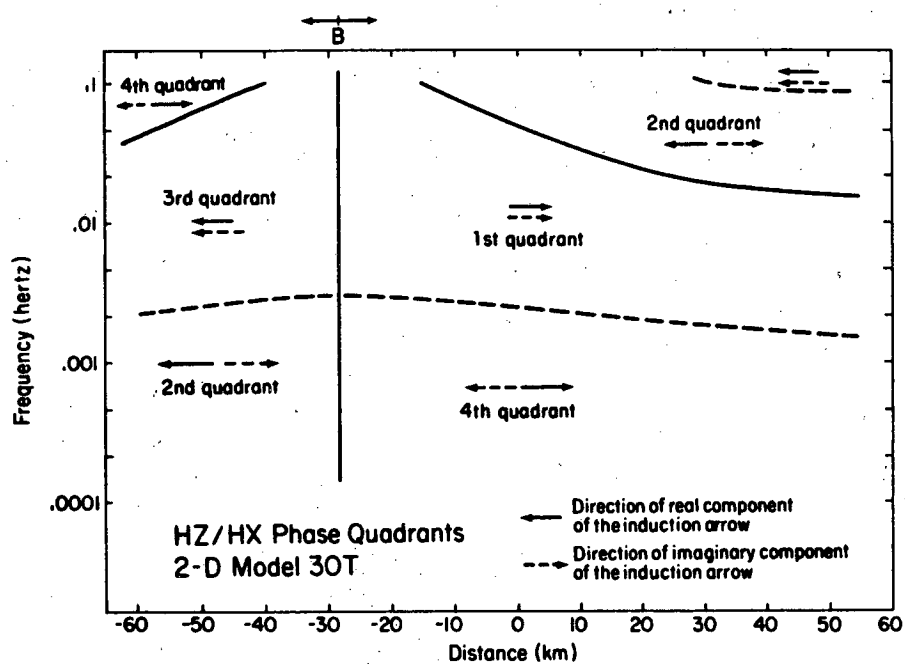


Figure 5.26(d) Induction arrow orientation diagram.

in this area. A limiting factor on the use of this parameter is that its reliability when applied to field data would be subject to the degrading effects of noise in the region near the conductor caused by the attenuation of the amplitude response.

The next step is to evaluate the effects of a finite strike length on the two-dimensional characteristics indicated in the last model. The model used for this comparison is shown in Figure 5.27. This model consists of a 5 Ohm-m body with a 15 square kilometer cross-section buried 15 kilometers in a 100 Ohm-m half space. This model was initially introduced in Figure 5.12 where the impedance frequency responses were presented. The smooth curves in Figure 5.27 indicate the two-dimensional amplitude and phase response calculated at the position indicated by the arrow on the insert. The corresponding responses for the three-dimensional model with the same cross-section and a strike length of 60 kilometers is indicated by the symbols. The conductivity of this model is less than the previous model considered (Figure 5.26). This was necessary to insure an accurate numerical solution for the three-dimensional model. Despite this difference in conductivity, the tipper amplitude and phase characteristics of these two-dimensional models are similar.

The comparison of the two- and three-dimensional results in Figure 5.27 indicate two important features. First, the tipper phase in the lower diagram appears to be relatively insensitive to the finite strike length of this model. The difference between the two- and three-dimensional case is only ten degrees. This small difference may indicate a slight upward shift in the frequency at which the phase value equals -180 degrees. However, these differences in the two phases are so small that they may be numerical in nature.

The second point of interest is the attenuation of the tipper amplitude response at the two lower frequencies in the three-dimensional case. This attenuation results in a frequency shift of the peak amplitude response of the tipper to higher frequencies. This sensitivity of the amplitude frequency response to strike length would lead to

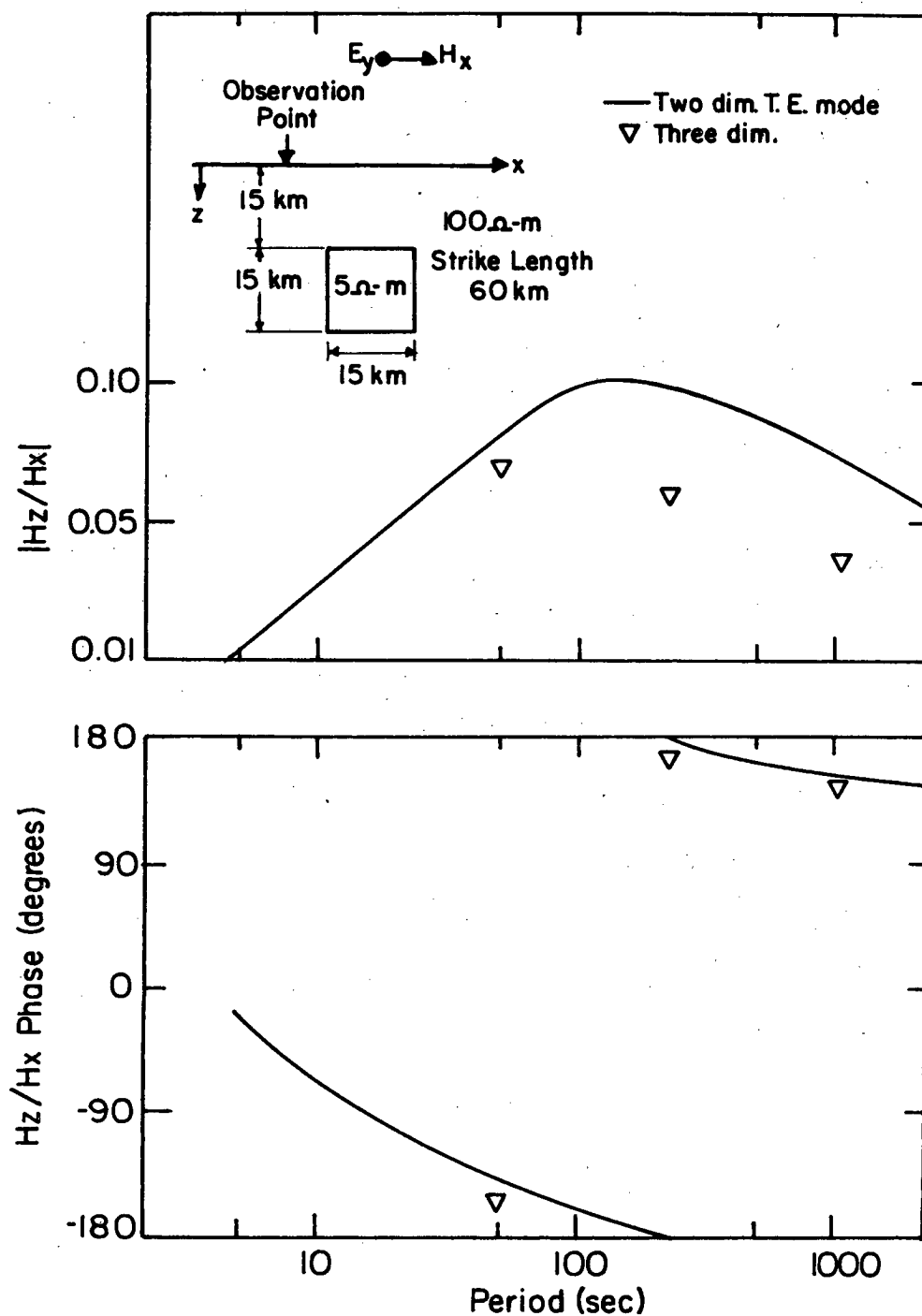
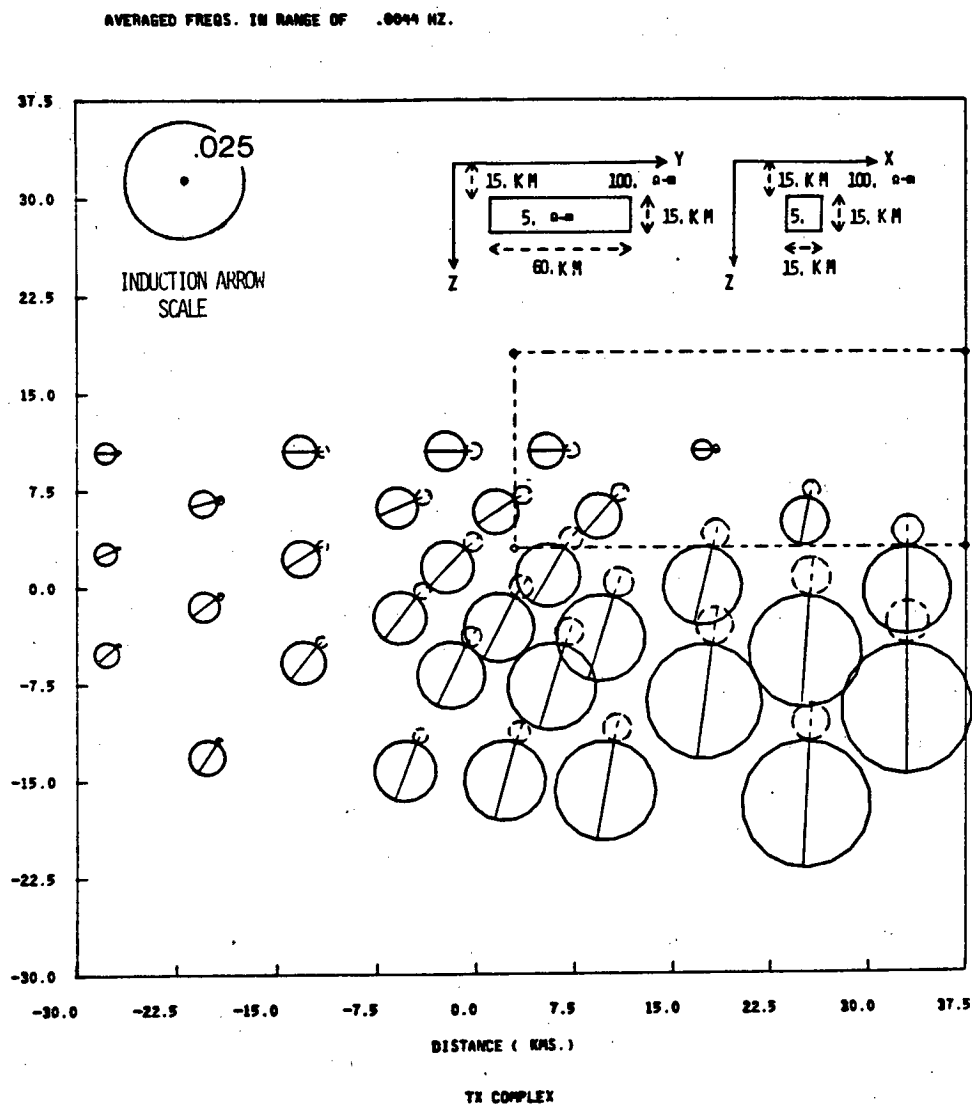


Figure 5.27 The frequency response of the complex geomagnetic transfer function (tipper) calculated on a central profile at the position indicated on the insert. The symbols indicate the three-dimensional responses and the smooth curves indicate the corresponding two-dimensional responses.

erroneous depth estimates when used for a two dimensional analysis. These results indicate that if a frequency domain match is used for a two-dimensional analysis the tipper phase would be the "best" parameter to use.

The spatial variations of the tipper parameters for the above three-dimensional model are considered at 0.0044 hertz in Figure 5.28. This frequency provided the tipper phase of approximately 170 degrees in Figure 5.27. This phase response results in a small imaginary induction arrow and since it is in the second quadrant the real and imaginary induction arrows have opposite orientations with the real component directed away from the region of current concentration. The complex tipper diagrams in Figure 5.28 indicate that the real and imaginary responses over most observation positions share similar ratios and orientations with respect to the region of high current density. This implies that the tipper phase is not a strong function of position. This characteristic is similar to that displayed by the phase at 0 or  $\pm 180$  degrees for a similar two-dimensional model in Figure 5.26(d). The tipper amplitude for this three-dimensional model as indicated by the magnitude of the induction arrows is characterized by a high degree of spatial variability with the attenuation most pronounced over the conductor.

The spatial variations of the complex tipper response for the same model at the frequency of 0.02 hertz is presented in Figure 5.29. For this frequency, the tipper phase was shifted into the third quadrant at the observation position indicated in Figure 5.27. The resulting induction arrows have a common orientation for both real and imaginary components away from the region of high current density. This portion of the frequency response of the two-dimensional phase is characterized by an increased dependency on frequency. The spatial distribution at 0.02 hertz of the complex tipper components provided in Figure 5.29 indicate that the tipper phase or the ratio of real and imaginary components is characterized by a greater degree of spatial variability than was observed at 0.0044 hertz. The phase variations however are not significant



**Figure 5.28** The complex tipper and induction arrows for the three-dimensional elongate conductor at 0.0044 hertz. The observation positions are confined to one quadrant since the model has two planes of symmetry.

enough to change quadrants as indicated by the uniformity of the induction arrow orientations for both components away from the region of current concentration.

The sensitivity of the induction arrows to changes in the geometry of a conductor are considered using the same model perturbation as utilized in Section IV for the impedance parameters. This model with the complex tipper responses at 0.02 hertz is shown in Figure 5.30. The model considered is a modified version of the model indicated in Figure 5.29. This model was altered by removing a center section of the conductor. This change is indicated by the dashed lines on the cross-section in the inserts and by the outline of the conductor in plan-view in Figure 5.30. The orientation of the induction arrows in this figure indicate that the phase remained in the third quadrant. The direction of the induction arrows at observation points remotely located with respect to the altered portion of the conductor are generally the same as those provided by the original model. Those observations in the vicinity of the altered portion of the model generally provided slightly different orientations than the original model. For one observation position over the conductor designated by the letter A in Figures 5.29 and 5.30 the two models provide significantly different results. The direction of the induction arrows over the perturbed model at this point differ from the direction given at the same point over the original model by nearly 90 degrees. A comparison of these results with the results presented in Section IV on Figures 5.14-5.17 indicates that the induction arrows are more sensitive to local changes in the model geometry than the impedance estimates.

The sensitivity to structural changes in a conductor at depth indicated by the last model, suggest that the tipper may also be very sensitive to near surface variations in conductivity. To obtain a measure of understanding for this sensitivity and the relative depth-frequency resolution, a two body three-dimensional model was designed. Results from this model were obtained using the modified hybrid method at two frequencies.

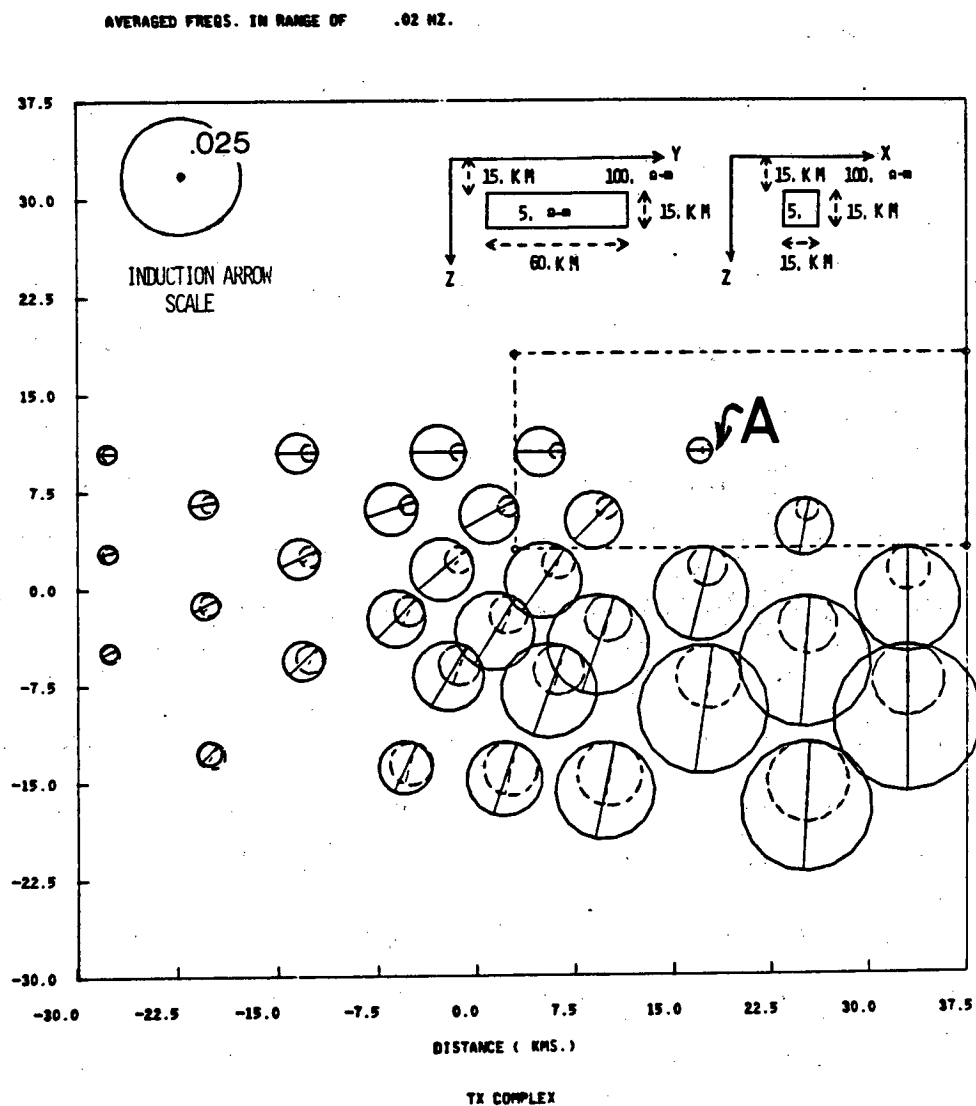
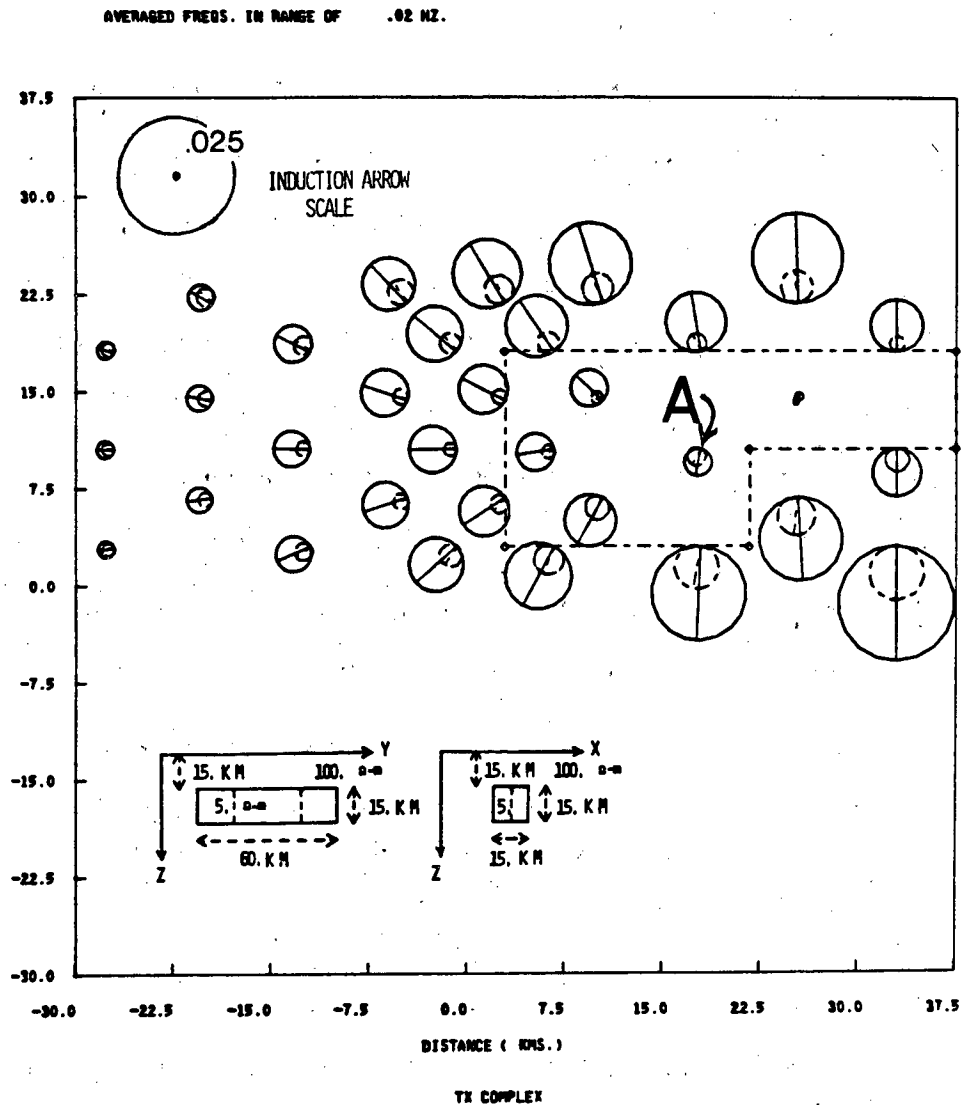


Figure 5.29 The complex tipper and induction arrows for the three-dimensional elongate conductor at 0.02 hertz. The observation positions are confined to one quadrant since the model has two planes of symmetry.



**Figure 5.30** The complex tipper and induction arrows for a modified version of the model presented in Figure 5.27. This new model has a central section of the conductor removed as indicated by the dashed lines on the cross-sections provided on the inserts on this figure and by that portion of the plan-view shown. Since the model has one plane of symmetry the observation positions are confined to the left half of the model.

The initial model used as the reference for this study is indicated in Figure 5.31. This simulation consists of a single 10 Ohm-m elongate body buried 6 kilometers in a 100 Ohm-m media. The conductor dimensions are indicated in the cross-section and plan-view on the inserts. The results are provided in the form of the complex tipper components and associated induction arrows at 0.22 hertz. As in earlier models the solid and dashed circles indicate the real and imaginary components respectively. The results in this figure indicate that the tipper phase at this frequency is well into the third quadrant and varies to a fair degree as a function of position. This is indicated by the uniform orientation of both the real and imaginary components away from the current concentration and by the large imaginary component. The spatial variability in the phase is indicated by the variable ratio of real to imaginary components. The tipper amplitude response which is related to the size of the induction arrows as shown in the figure reaches a maximum on a profile perpendicular to strike at a distance from the center of the body approximately equal to its width.

The next model will be similar to the above simulation with the addition of a surface conductor. This two body model is shown on the inserts in Figure 5.32. The complex tipper responses at 0.22 hertz are provided at fewer locations than the previous model to simplify the diagram. The observation positions provided here correspond to some of the same observation points given in Figure 5.31. The affects of the shallow 10 Ohm-m body are very evident in the complex components presented. Those observation points which are distant from the shallow body provide a phase response in the third quadrant consistent with the results from only the deep conductor. However the orientation of the real and imaginary components are no longer in the same direction. As the observation positions are moved near the conductor the phase shifts quadrants and the real and imaginary components provide radically different directions. The real component however consistently is oriented away from the region of high current density and would provide a reasonably accurate

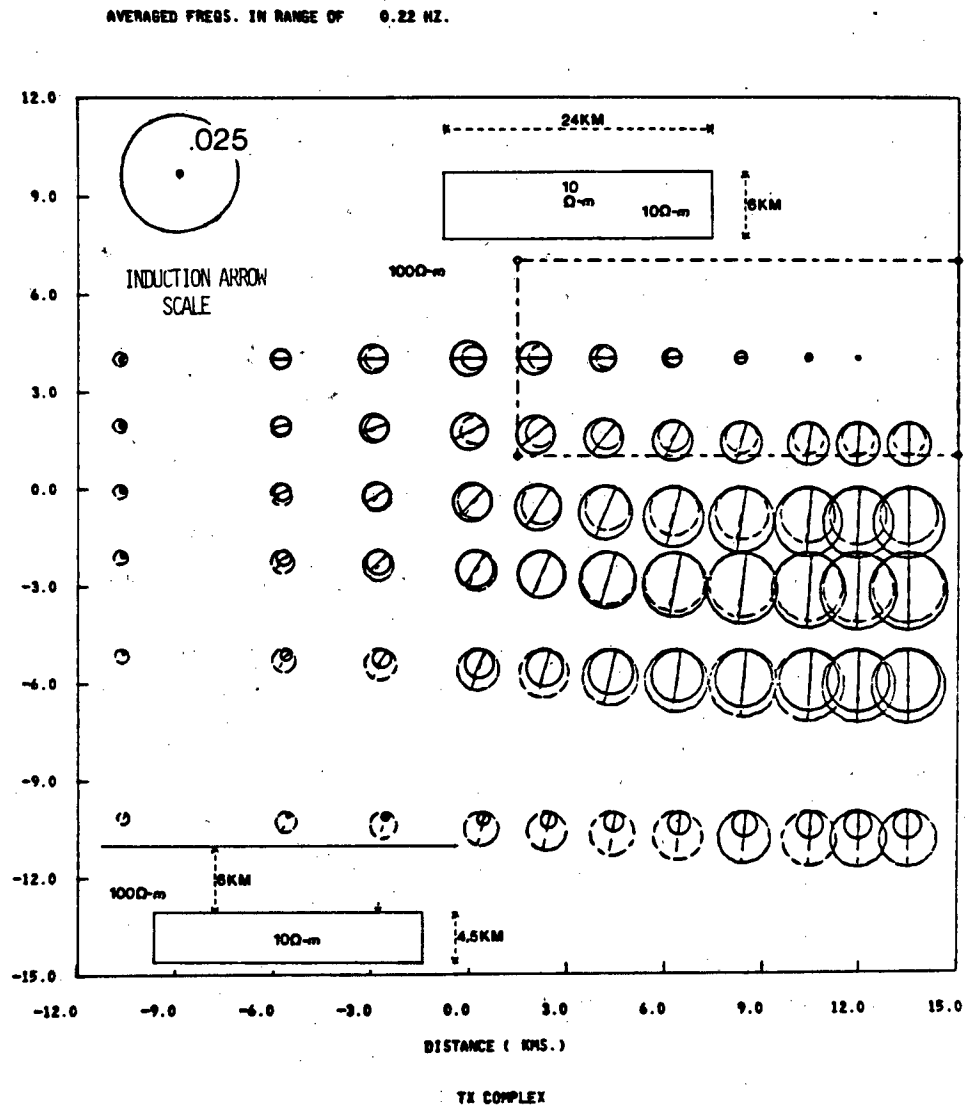


Figure 5.31 The complex tipper and induction arrows for a three-dimensional single conductor model at 0.22 hertz. The conductor in this model has the same dimensions and conductivity as the deep conductor of the model presented in Figure 5.32.

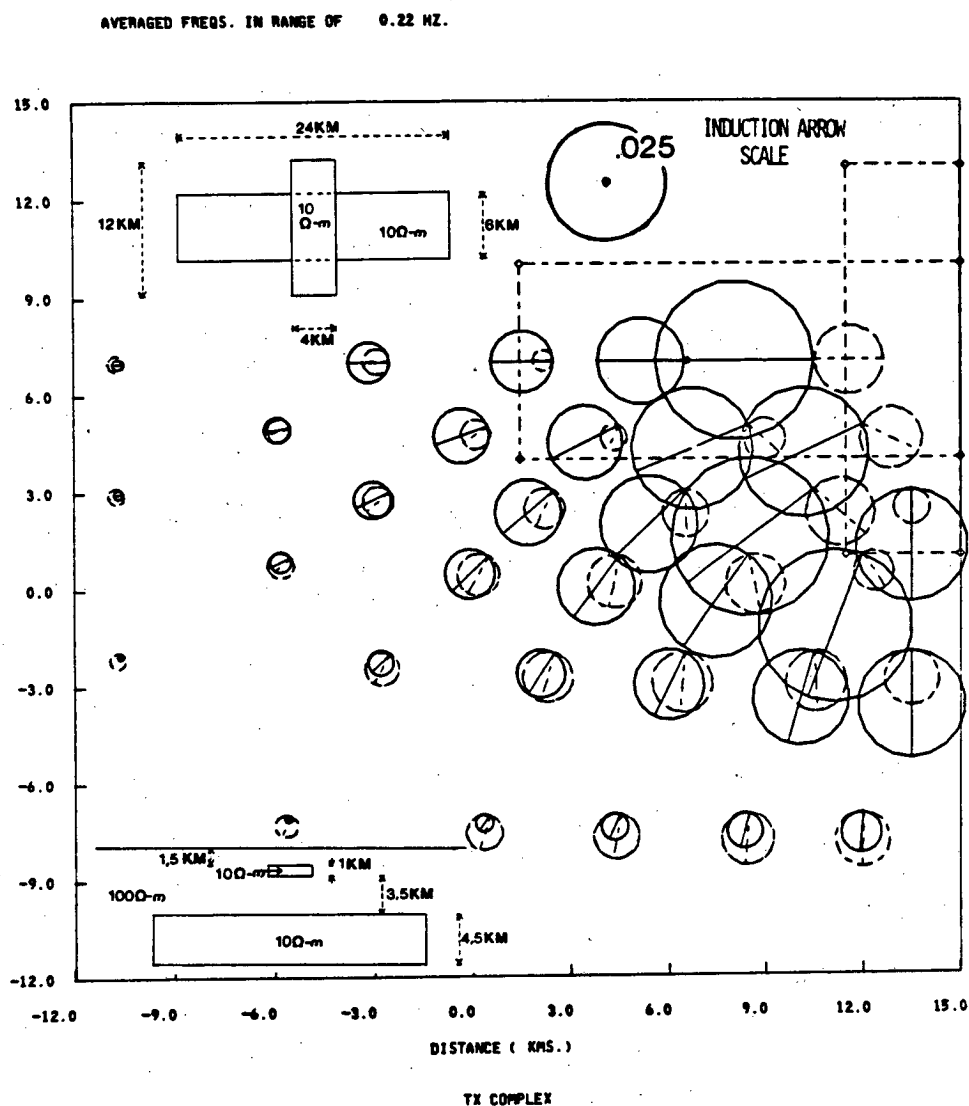


Figure 5.32 The complex tipper and induction arrows for a three-dimensional two conductor model at 0.22 hertz. A cross-section and plan-view are provided as inserts. The deep conductor has the same dimensions as the model presented in Figure 5.31.

position for the center of the conductive zone. The imaginary component in the vicinity of the shallow conductor provides an orientation that is a strong function of the measurement position. At some locations the imaginary induction arrows are oriented toward the regions of current concentration and at other positions are oriented away or tangential to the high current density. This model indicates that when two conductive bodies are present the real induction arrow will provide a more reliable estimate of the relative position of the conductor than the imaginary component.

To investigate the dependence on frequency of the complex tipper over this multibody model, the surface fields were calculated at an additional frequency of 0.022 hertz. The results at this frequency for the single conductor buried 6 kilometers (reference model) is provided in Figure 5.33. These results show that the phase has shifted into the second quadrant and provides a uniform value near 180 degrees. This is indicated by the uniform and opposite orientation of the real and imaginary induction arrows with real component oriented away from the current concentration. The small imaginary component indicates that the phase is near the 180 degree value and the spatial uniformity of the ratio of the real and imaginary components indicate that the phase at this frequency has a weak spatial dependency. These characteristics are the same as those previously provided by two-dimensional and other three-dimensional models.

As in the previous set of models, a new model is formed by combining the conductor buried at a depth of 6 kilometers with a shallow conductor. The results from this model at 0.022 hertz are shown on Figure 5.34. The model response for this frequency provides a much simpler spatial distribution of induction arrows than observed at the higher frequency. The tipper phase remains in the second quadrant for all observation positions which is consistent with the results from the single deep body model. The amplitude and orientation of both real and imaginary components for this model are very similar to the response of the reference model when the observation

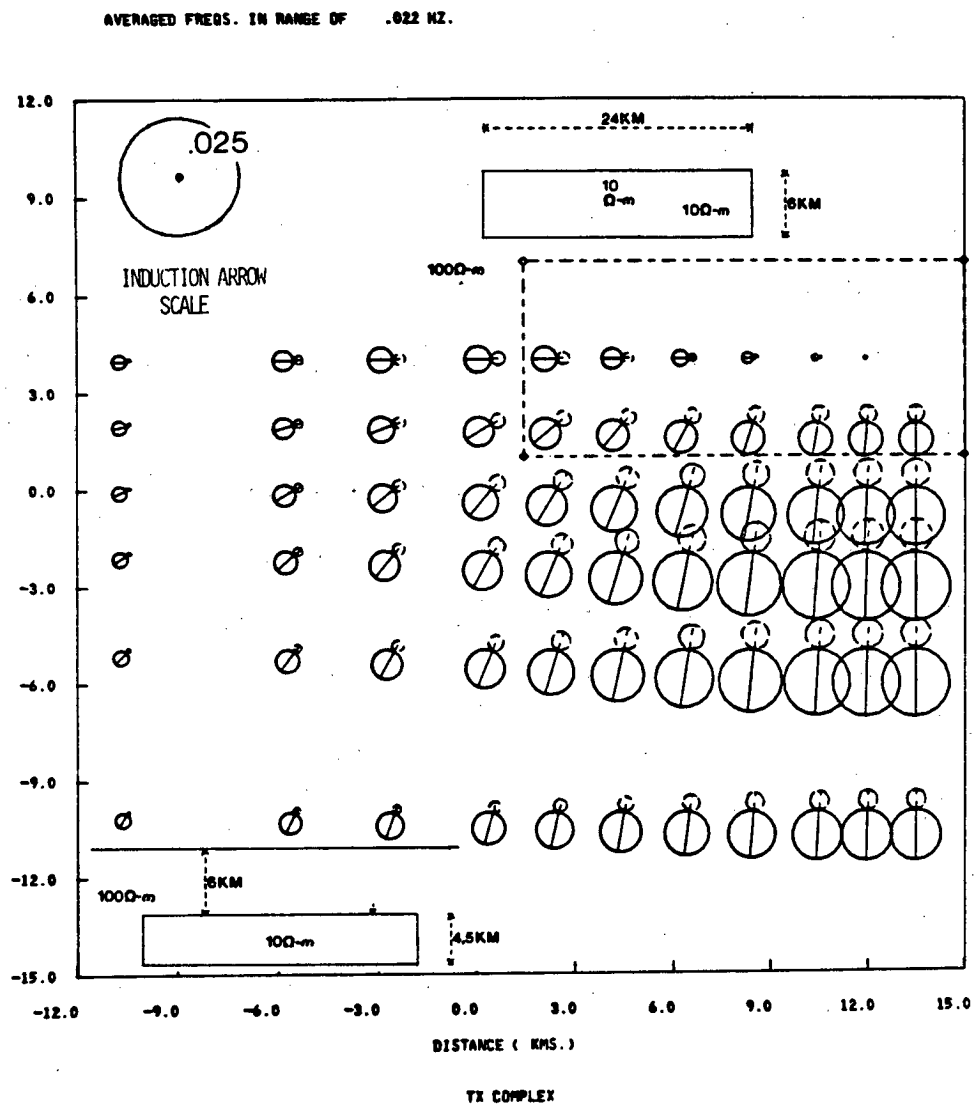


Figure 5.33 The complex tipper and induction arrows for a three-dimensional single conductor model at 0.022 hertz. The conductor in this model has the same dimensions and conductivity as the deep conductor of the model presented in Figure 5.34.

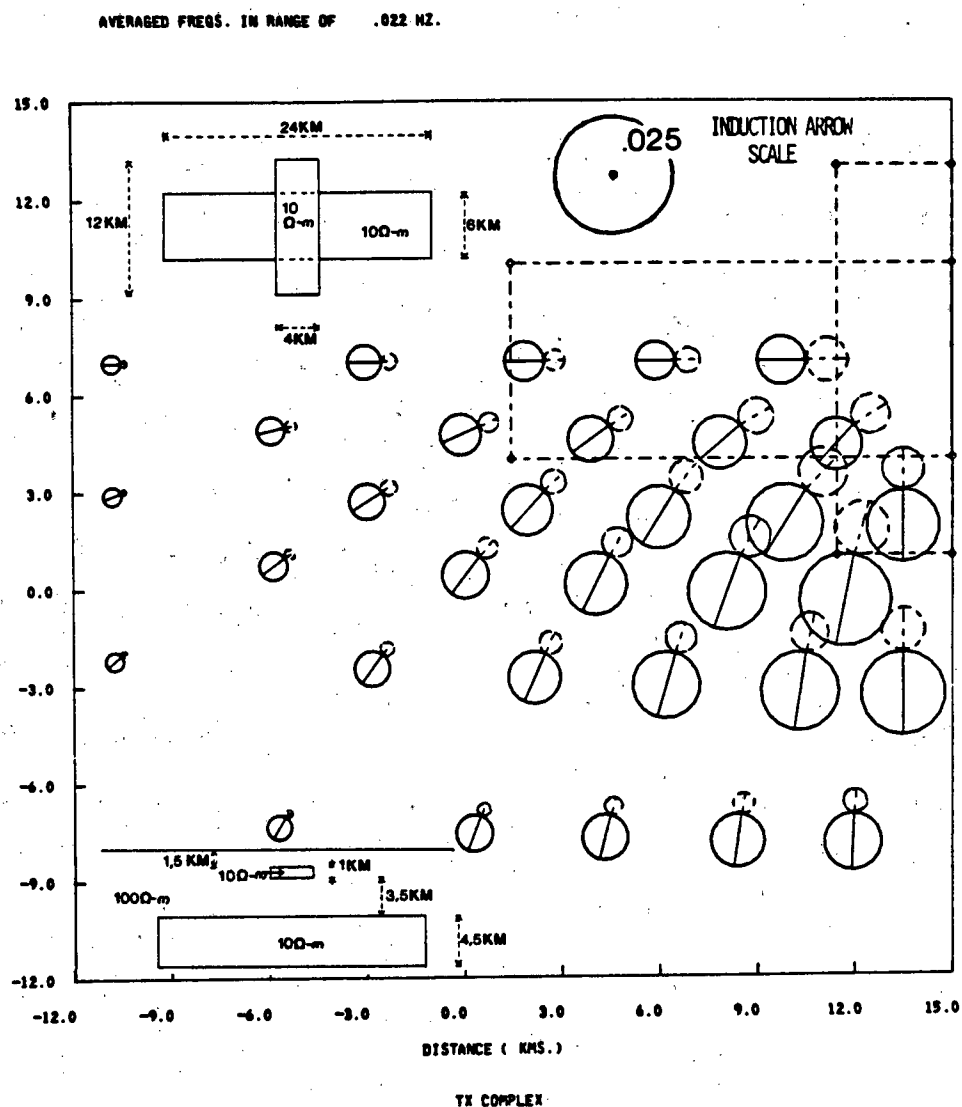


Figure 5.34 The complex tipper and induction arrows for a three-dimensional two conductor model at 0.022 hertz. A cross-section and plan-view are provided as inserts. The deep conductor has the same dimensions as the model presented in Figure 5.33.

positions are remote with respect to the shallow conductor. When the observations are made in the vicinity of the shallow body, both real and imaginary components increase in amplitude and change orientation. Both real and imaginary induction arrows provide a coherent picture of an average current concentration in the vicinity of the two conductors.

Two important points are indicated by these results. The first is that when frequency responses from multibody scatterers are evaluated, one should look for the lowest frequency which provides a phase value of 0 or  $\pm 180$  degrees. This frequency should be a slowly varying function of position if it is indeed the lowest 0 or  $\pm 180$  degrees phase point. If this weak spatial dependence is observed, then one should obtain a spatially coherent tipper phase in the second or fourth quadrant which would provide a real and imaginary induction arrows which are oppositely oriented with the real component directed away from the region of high current density. This lowest 0 or  $\pm 180$  degree phase point corresponds to the lowest frequency maximum in the tipper amplitude response for two-dimensional models. This however may not be true for the three-dimensional case since the tipper amplitude is a sensitive function of strike length as indicated in Figure 5.27.

The second note of interest is that care must be exercised in the multiconductor case at frequencies above the lowest 0 or  $\pm 180$  degree phase point, when using the spatial distribution of imaginary induction arrows in an interpretation scheme. The ability of real induction arrows to provide a more reliable estimate of the location of an anomalous region in this frequency range is clearly indicated in Figure 5.32.

The last multibody three-dimensional model considered in this section is devoted to the case of a buried resistive body overlain by a shallow conductor. This model is of interest in this study since the induction arrows were used in Section III to supply supporting evidence for the existence and location of resistive bodies indicated by a two-dimensional inversion and the spatial distribution of characteristic distortions of

the apparent resistivities. The complex tipper response for a single buried resistor provided in Figure 5.9 was used to justify this interpretation. However, the conductivity environment south of Mount Hood was interpreted as being a near surface conductor overlying a buried resistor (see Figures 5.4(a) and 5.6). The effects of these near surface conductors on the complex tipper components were not considered at that time. In light of the results from the previous models which indicated that a surface conductor overlying a deep conductor could cause a significant amount of distortion in the complex tipper components, the case of a buried resistor overlain by a shallow conductor should be considered.

The complex tipper components for this conductor over a resistive body are shown in Figure 5.35. This model was initially used in Section III to provide the apparent resistivity diagrams provided in Figure 5.6. The tipper results considered here are at a frequency of 0.022 hertz. This frequency is sufficiently low that the tipper phase is in the second quadrant below the 180 degree phase value provided by the large underlying resistive body. Since the large resistor provides the lowest frequency response in the model, this 180 degree phase represents the last (lowest frequency) 0 or  $\pm 180$  degree point over the entire frequency response. As in the previous models the complex components in Figure 5.35 provide very uniform variations which clearly indicate the resistive region characterized by an abnormally low current density. The real and imaginary induction arrows are oriented in opposite directions with the real component directed toward the resistive body. The distortion caused by the small near surface conductor would provide an induction arrow distribution which would indicate two resistive zones, one on each side of the north-south plane of symmetry. The induction arrows at observation points remotely located with respect to the shallow conductor provide a small imaginary component indicating that these data are near the 180 degree phase value provided by the deep resistor.

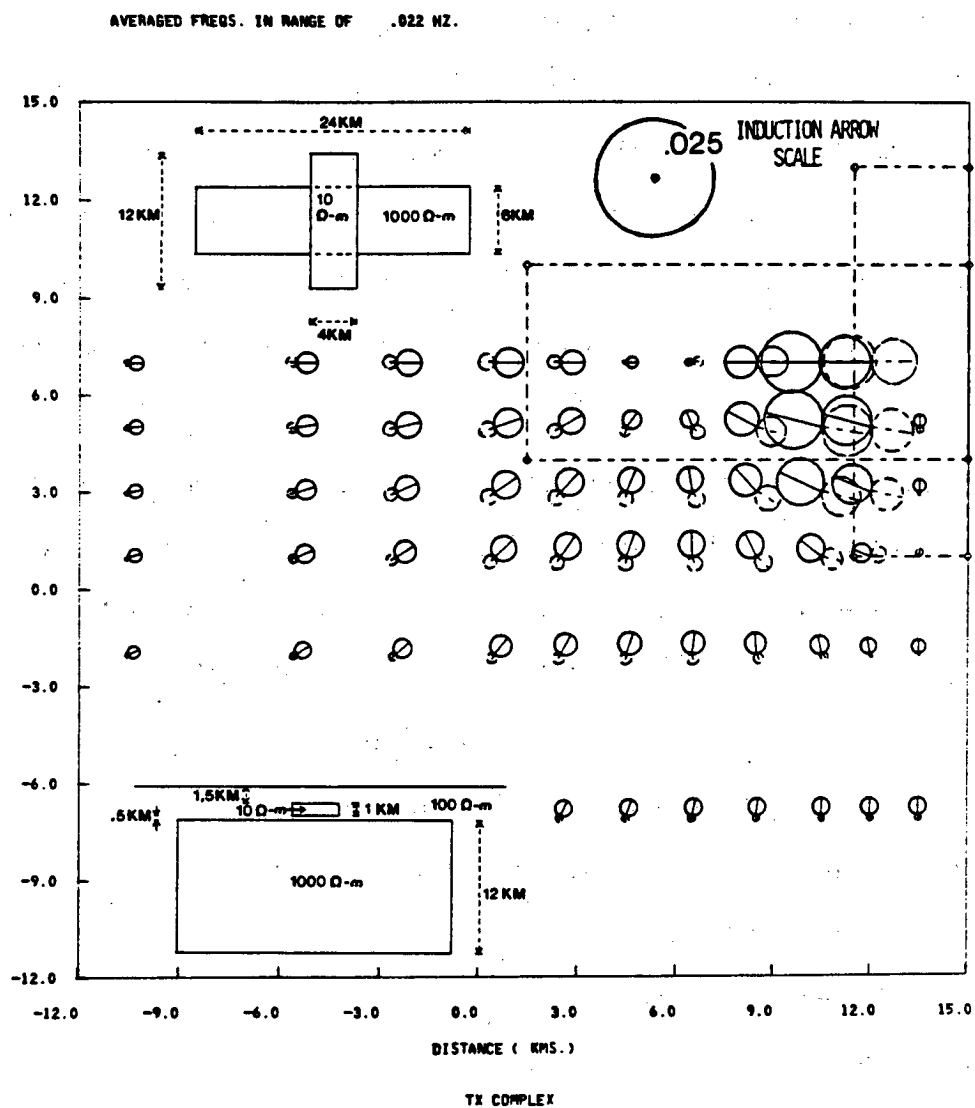


Figure 5.35 The complex tipper and induction arrows for a three-dimensional two body model at 0.022 hertz. A cross-section and plan-view are provided as inserts. The shallow conductor has the same parameters as the model presented in Figure 5.5.

These simple two body models provide some assurance that if one chooses the frequency window such that it is below the low frequency 0 or  $\pm 180$  degree phase value, then the real and imaginary induction arrows may be relied upon to provide the relative lateral locations of both anomalously resistive and conductive regions underlying small near surface conductors. At higher frequencies the real component provided a reasonably accurate location of the anomalous current distribution but the imaginary component proved to be unreliable.

The models considered here were seriously limited in their scope. One important consideration in a multiconductor environment is the resolution of the complex tipper components. The above models did not provide sufficient separations in depth between bodies to provide a separation of their responses in the frequency domain. Therefore an evaluation of the depth resolution in these frequency domain functions could not be implemented. Perhaps numerical improvements in the future will provide a sufficiently versatile three-dimensional modeling scheme such that a comprehensive study of the frequency resolution of both tipper and impedance functions may be carried out.

This digression into the details of simple three-dimensional responses indicated that the induction arrows provided the expected diagnostic features with or without the presence of a near surface conductor when the frequencies were in the asymptotic limit (i.e. below the lowest 0 or  $\pm 180$  degree phase value). This was consistent with simple two-dimensional model studies. These results imply that if the elongated conductor buried at 10-15 kilometers were the dominant conductor at depth then a diagnostic phase value of 0 or  $\pm 180$  degrees should exist at approximately the frequency indicated by a two-dimensional simulation. The simple one body response in Figure 5.26 indicated that this transition into the asymptotic range for the expected conductor would occur in the frequency band of 0.0022-0.0033 hertz (300.-450. seconds).

The example of the tipper parameters in Figure 5.36 provides no indication of a 0 or  $\pm 180$  degree phase value in the entire decade between 100 and 1000 seconds. These response functions are representative of all the data at Mount Hood for periods greater than 10 seconds. The top two diagrams provide the tipper amplitude and phase responses at site 1. These parameters are provided at the rotation angles indicated in the bottom diagram on this figure. The rotation angle is obtained by finding that angle at each frequency which provides a maximum complex response of the component shown in this figure in the form of amplitude and phase. The frequency bands over which these data were averaged to provide the smoothed complex diagrams presented in Figures 5.10 and 5.11 are indicated by the banded zones numbered 1 and 4 respectively.

The data at site 1 were chosen for this example since the rotation angle which maximized the tipper component corresponding to the horizontal magnetic field perpendicular to strike was nearly independent of frequency. This "approximate" two-dimensional response at this location, provided a situation where the simplified presentation provided in Figure 5.36 would be easily related to model results. This lack of dependence on rotation angle was not usually found at Mount Hood. At some locations in this area the rotation angle designated by the direction of the maximum tipper component varied by 90 degrees over one or two decades in frequency. These rotation angle variations are clearly indicated by comparing the complex tipper diagrams for data in band 1 and 4 shown in Figures 5.10 and 5.11.

Another reason this site was used as an example is because the 0 or  $\pm 180$  phase values are clearly evident in two of the bands. The first is located in the high frequency portion of band 1 indicated by a 0 degree phase. The second is located between band 3 and 4 and is designated by a -180 degree phase. These phase values imply that there are two conductors at varying depths. A two dimensional analysis based on the frequency where these 0 or  $\pm 180$  degree phase values occur indicate

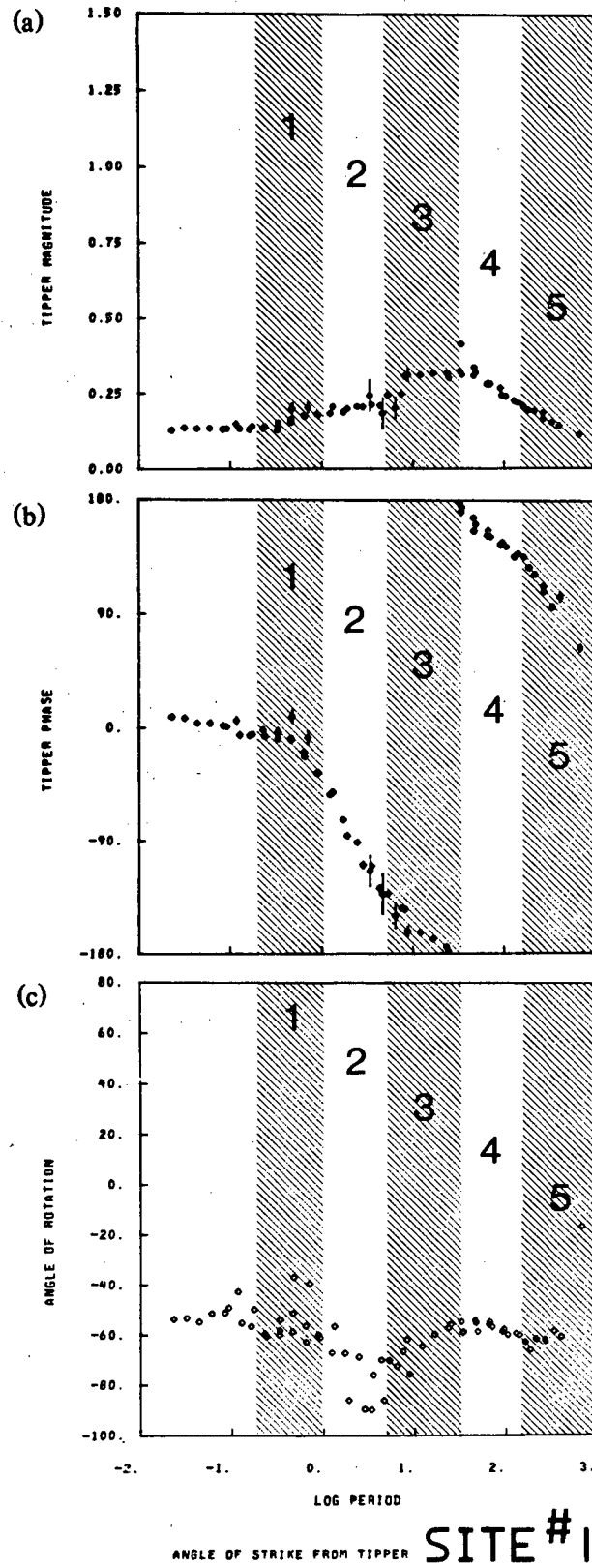


Figure 5.36 An example of the (a) tipper amplitude (b) tipper phase and (c) angle of rotation required to minimize one component. The bands over which the field data are averaged to generate the five sets of polar diagrams are designated by the vertical sections numbered one through five.

approximate depths of 0.5 kilometers and 5 kilometers for the lateral current variations responsible for these phase characteristics.

The phase response indicated in bands 4 and 5 provides a very interesting frequency variation. Instead of observing the 0 or  $\pm 180$  degree phase value expected from the interpretation based on the impedance functions, one sees a rapid frequency response which results in a phase of approximately 90 degrees. This type of response requires the presence of yet another conductor. Based on a projection of this frequency trend one would expect the 0 degree phase to occur at approximately 10,000 seconds period. Again a simplistic two-dimensional analysis implies a depth of approximately 50 kilometers for the lateral conductivity variation responsible for this predicted frequency response.

The complex nature of this phase response may be observed in a more realistic three-dimensional frame of reference by considering the data in these bands in the form of the complex tipper and phase polar diagrams. These diagrams are presented in Figure 5.37. The observation position (site 1) is located at the center of each small diagram. The left column of the figure displays the complex tipper responses with the associated induction arrows for each of the five bands of Figure 5.36. The right hand column provides the tipper phase polar diagrams. Model results in this form were not covered in this chapter for the sake of brevity, however some examples may be found in appendix D. The interesting characteristic of this form of presentation for the phase is that the fan shaped diagram, seen in a relatively undistorted form in band 4 of this example, opens toward the region of high current density.

The sequence of polar diagrams shows the rapid changes in the direction of the induction arrows which are a manifestation of the rapid variations of the tipper phase observed in the last figure. The data were averaged over the band indicated above each row of diagrams. The data in band 1 corresponds to the inferred source at a depth of 0.5 kilometers. The polar diagrams indicate a relative position for a resistive

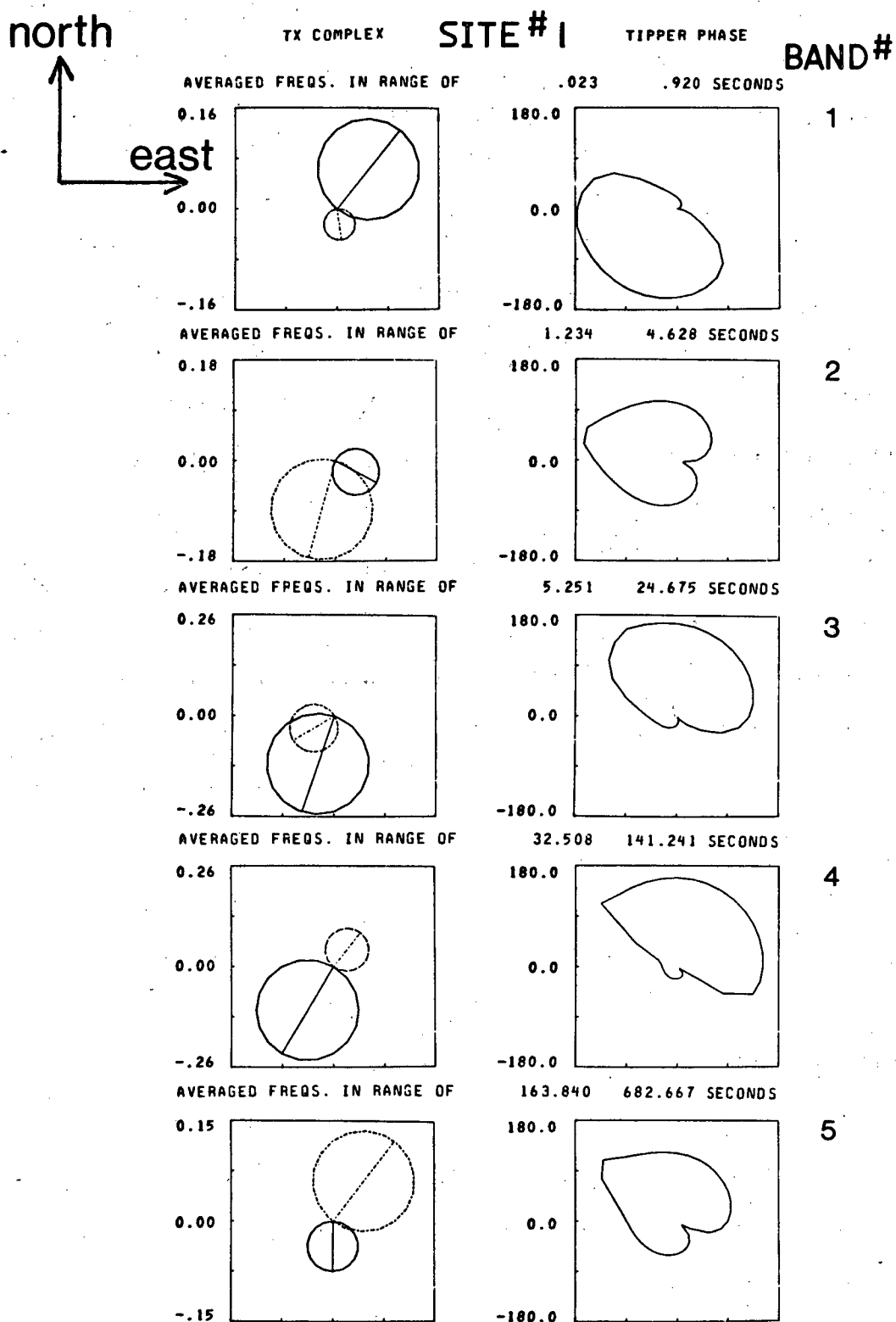


Figure 5.37 An example of the complex tipper diagrams with induction arrows and the tipper phase diagrams are presented for the data at site 1 over the five frequency bands indicated in Figure 5.36.

region to the north-east of Site 1. This coincides with the results indicated by the one-dimensional interpretation of the profile at Cloud Cap (Figure 5.3) and with the two-dimensional inversion based on the profile through the arrays at Old Maid Flat and Cloud Cap drawn in Figure 5.23(b).

Band 2 provides a small real induction arrow component indicating the -90 degree phase response which is interpreted as being the transition zone from that portion of the spectra dominated by the near surface conductivity distribution to that portion controlled by a conductor located at greater depths. This transition continues into band 3 where the real induction arrow has changed direction with respect to the band 1 resulting from a phase shift of 180 degrees. By band 4 the peak amplitude response for the conductivity variation at 5 kilometers has been passed. This corresponds to the phase response at periods greater than the  $\pm 180$  degree phase point for this conductivity variation. For this band the real and imaginary induction arrows are oriented such that a resistive zone is indicated to the south-west of the Cloud Cap array. This 5 kilometer transition from conductive to resistive structures coincides with the inferred 3 Ohm-m /1000 Ohm-m contact in the two-dimensional results indicated in Figure 5.23(b).

Band 5 provides a similar picture of a transition zone as observed in band 2. The data at this frequency seem to be moving out of the frequency range dominated by the 5 kilometer conductivity variations and are entering a portion of the spectra controlled by the lateral variations at a depth in excess of 50 kilometers. The form and orientation of this diagram may indicate a more conductive region to the south or southwest. This is very speculative since the data at periods greater than a 1000 seconds are required to see where this trend will lead.

These data indicate that the resolution properties are such that the tipper can resolve anomalous regions with depth separations of a decade or more (i.e. 0.5, 5 and 50 kilometers). The effects of structures which lie between these resolvable features

in the frequency domain is of great importance in this data set since the inferred conductor at 10-15 kilometers would be sandwiched between the 5 and 50 kilometer anomalous zones.

To understand the response from the complex conductivity structure proposed above, a three-dimensional simulation of three conductors with a significant depth separation is required. The three-dimensional requirement is important since the conductor at a depth exceeding 50 kilometers may have a local east-west strike as compared to the approximate north-south strike of the impedance anomaly at 10-15 kilometers depth. The effects caused by two conductors with different strikes was observed in Figures 5.32 and 5.34. These simulations provided a distorted view of the deeper conductor when the bodies were separated by small vertical distances.

The requirements for the above three body model exceeded the limitations of the three-dimensional modeling method available. To circumvent this difficulty a three body two-dimensional simulation was implemented. This model presented in Figure 5.38(a) is not directly appropriate for an interpretation of the field data. However, it does provide some indication of the problems created by the existence of three bodies confined to a total depth separation of only a decade. The three bodies designated as A, B and C correspond to the conductors expected at depths of 5, 12 and 50 kilometers respectively. The response of conductor B was considered earlier in Figure 5.26.

The TE phase response is provided in Figure 5.38(b) to show that the distinctive absolute phase maximum at 0.025 hertz which was the main feature in Figure 5.26(b) is still a dominant phase characteristic in the region above body B. The shape of the absolute maximum is somewhat distorted but still would provide an indication of the location of body B. An interesting difference between the single body and this three body response is that the phase minimum located at frequencies below the absolute maximum for the one body case is no longer evident in the multibody response. The removal of the one body "over-shoot" was caused by the presence of body C. An

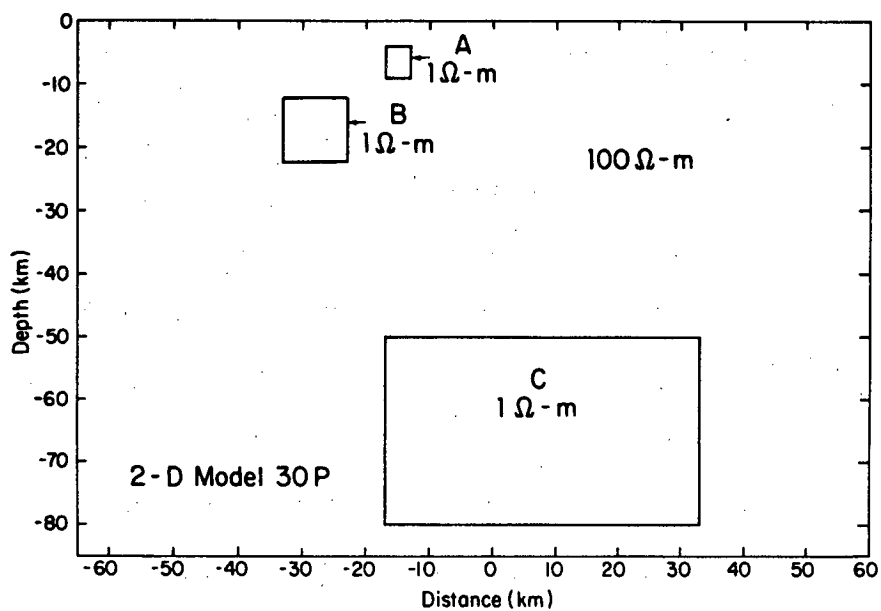


Figure 5.38(a) A three body two-dimensional model.

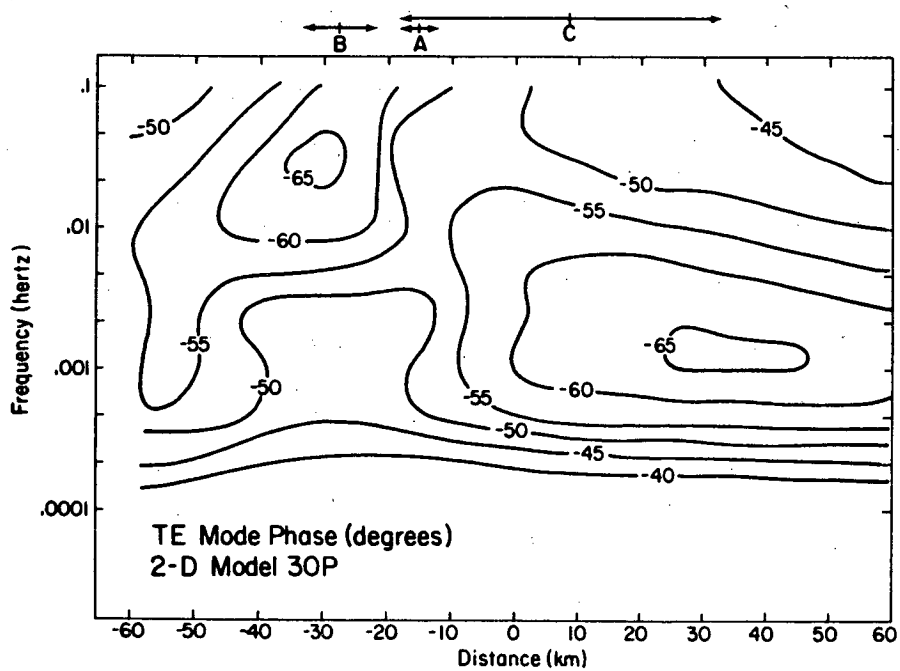


Figure 5.38(b) The TE mode impedance phase response.

interpretation of the structure at the depth indicated by body C was not attempted on the two-dimensional profile inversion discussed in Section IV since the conductivities at these depths were poorly defined due to the low frequency limits of the data. A simpler way to remove this low frequency "over-shoot" is by incorporating a finite strike of the elongate conductor into the interpretation as was done in the earlier section.

The tipper amplitude of this multiconductor model is presented in Figure 5.38(c). This amplitude response as compared to the one body case is appreciably distorted. However, the region over body B is still characterized by a very low amplitude response between 0.01-0.001 hertz. The effect of body C would not be detectable in the tipper amplitude for measurements above 0.001 hertz.

Figure 5.38(d) provides the phase quadrant diagram for this multiconductor model. This diagram is so altered by the presence of bodies A and C that the phase values of -180 degrees (designated as the dashed line separating the second and third quadrants) is completely missing in the region to the left of the -35 kilometer observation position for frequencies greater than 0.001 hertz. For the remaining observation points in the vicinity of body B, the boundaries of the phase quadrants vary so rapidly with frequency that the 0 or  $\pm 180$  degree phase point would be of very little help to interpret a sparse data set confined to frequencies greater than 0.001 hertz.

When this rapidly varying phase combines with the greatly attenuated amplitude in the vicinity of body B, it is not surprising that it results in very little evidence for the existence of body B. If in addition the three-dimensionality and varying strikes are considered, it seems quite reasonable that the combination of shallow and deep conductivity distributions have effectively masked the response from the elongate conductor buried at 10-15 kilometers when the observation positions are confined to the region near this body.

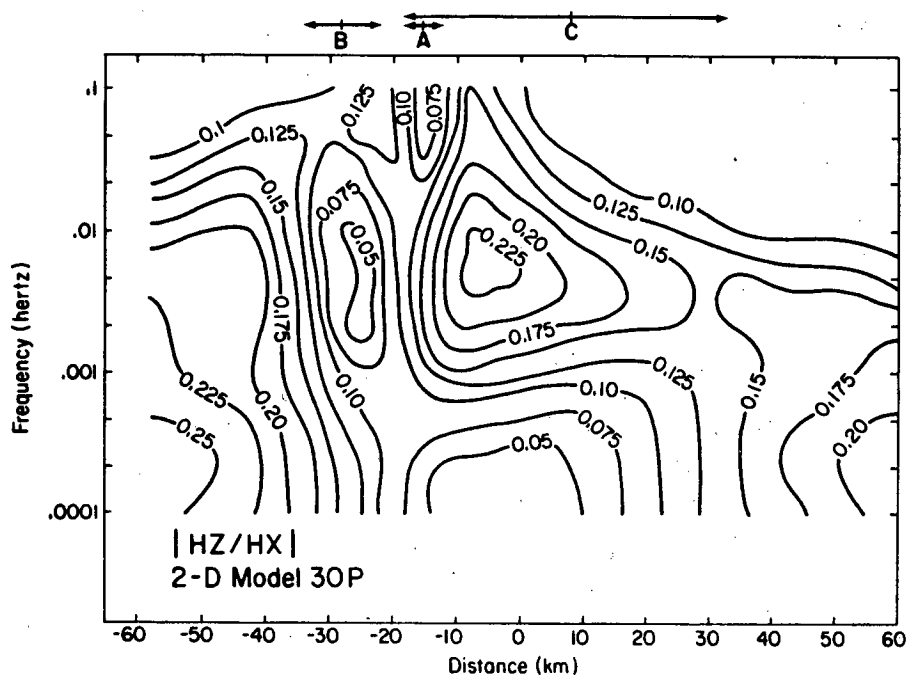


Figure 5.38(c) Tipper Amplitude Response.

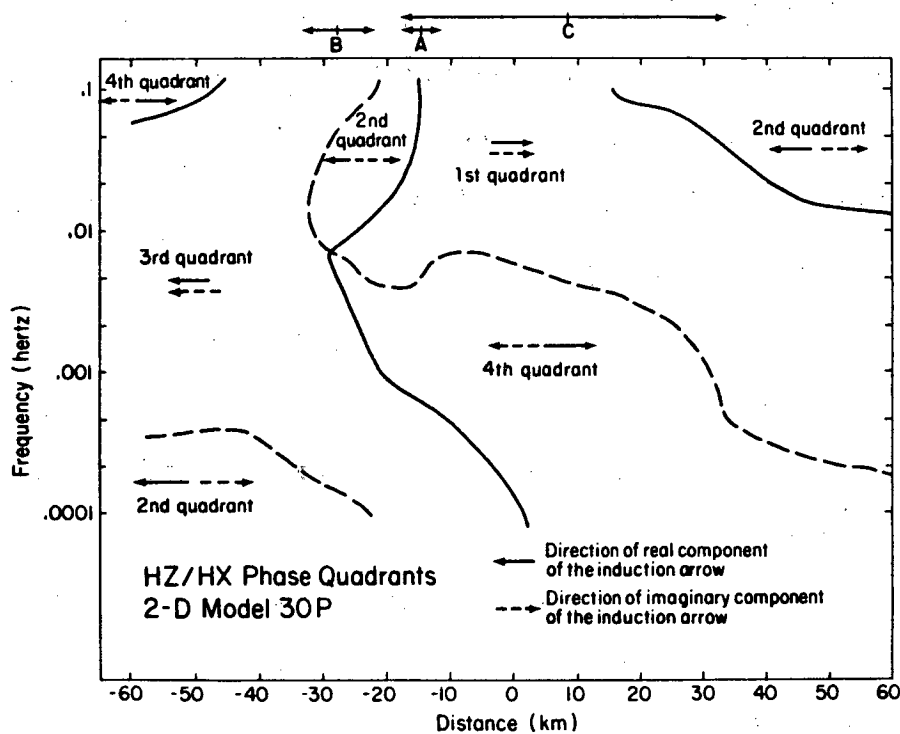


Figure 5.38(d) Induction arrow orientation diagram.

## [ VI ] The Composite Model

In the last three sections various one-, two- and three-dimensional models have been proposed to satisfy various components of the data. Some matches have been made, similarities obtained and differences justified. The entire procedure was not satisfying since there existed no means by which to quantitatively evaluate the overall interactions between various pieces of the story. However for lack of a better way, these various isolated anomalous regions were combined in a subjective manner and resulted in the model presented in Figure 5.39. A short summary of this composite model follows with appropriate references provided to the preceding maze of models.

The interpretation summary will begin at the surface, where the interpreted structure is as complex as the measurement density will allow. The first anomalous region and possibly the most conductive near surface zone in the area is located north-east of Mount Hood and is designated by the stippled zone labeled 3 Ohm-m. This zone was detected by the magnetotelluric one-dimensional inversions which indicated a conductive zone at a depth of 500 meters which became more resistive to the north-east. A 10 Ohm-m contact with this conductor which was consistent with the above interpretation was provided by the two-dimensional profile inversion presented in Figure 5.23(b). The relative position of these anomalous zones was also indicated by the induction arrows for band 1 in Figure 5.10.

The next near surface conductor detected was probably associated with the saturated pyroclastic flows which have accumulated on the south flank of Mount Hood. This zone is indicated by the stippled area near Timberline Lodge labeled as 10 Ohm-m. The conductor was detected by electromagnetic loop soundings and has estimated depths of 300-700 meters. These results were supported by one-dimensional magnetotelluric inversions. The distortion characteristics of the apparent resistivities in this area indicated that this shallow conductor covered a more resistive

# INFERRED CONDUCTIVITY DISTRIBUTION

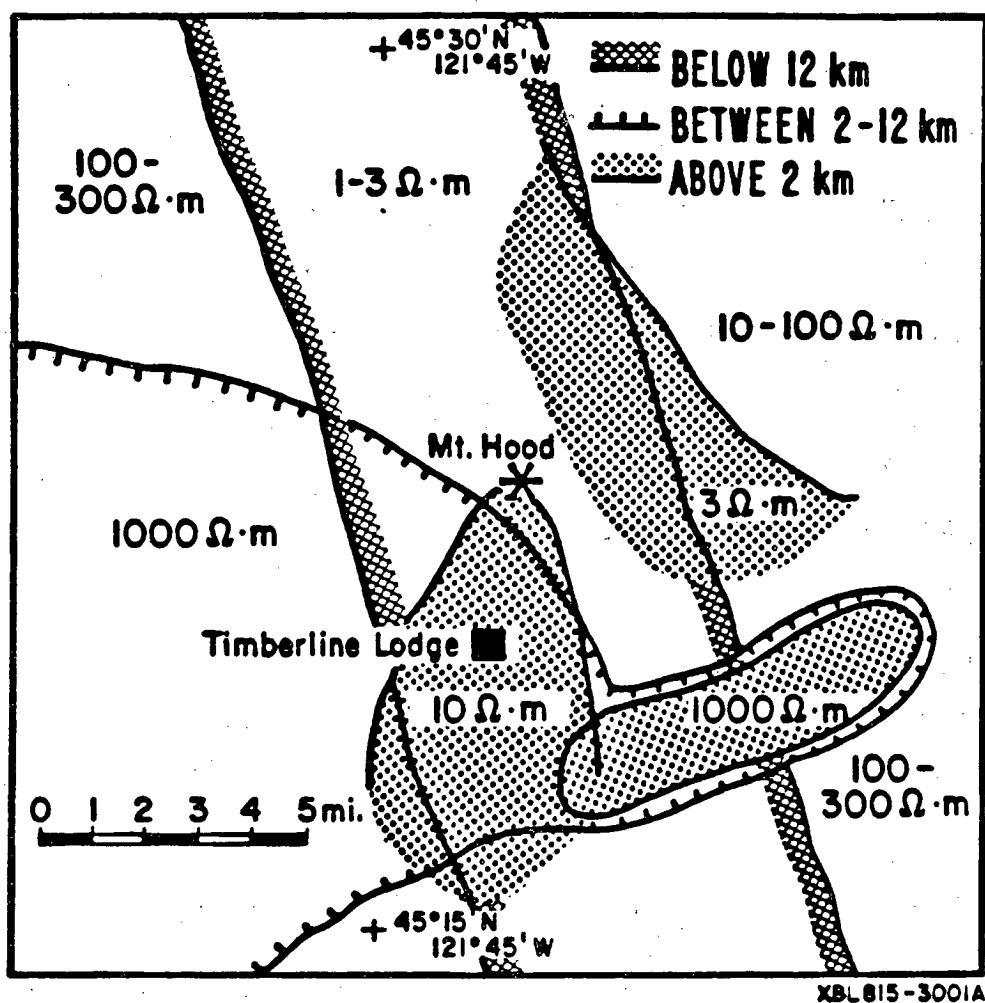


Figure 5.39 The composite conductivity model for Mount Hood.

zone. The model which mimicked the field observations "best" is shown in figure 5.6.

The next zone localized was the near surface resistive body indicated by the stippled zone south-east of Mount Hood labeled 1000 Ohm-m. This body was indicated by the distortion of the apparent resistivities and by the induction arrows in band 1. These results are provided in Figures 5.7 and 5.10.

The area west of Mount Hood enclosed in the region labeled 1000 Ohm-m was indicated as a resistive zone by the induction arrows in band 1 calculated from data in the Old Maid Flat array. The one-dimensional inversions of the impedance element associated with an electric field orientation of north 70 degrees east, supplemented by well logs from a 1.2 kilometer drill-hole, indicated a resistive region near surface. The two-dimensional inversion along the profile between Old Maid Flat and Cloud Cap, Figure 5.23(b), also indicated a resistor in this area which extended to a depth of 14 kilometers. The induction arrows in band 4 shown in figure 5.11 and the impedance parameter distortions in Figures 5.7(a) and 5.19 all indicate that the resistive zone probably covers an area indicated by the tick marks.

This resistive structure, which may be associated with a Pliocene intrusive, dominates much of the near surface and intermediate depth conductivity distribution. The two-dimensional profile inversion indicated that a conductive zone at a depth of 4 or 5 kilometers was adjacent to the north eastern edge of the large zone of low conductivity. The depth to this conductor coincides with the estimated depth of the lateral conductivity variations which provide the induction arrows in band 4. The arrows outline the north and eastern boundary of the resistor. This large resistive structure characterized by low porosity would control the local hydrology. The conductor at a depth of 4-5 kilometers may represent meteoric water confined to the north-east side of this structure and which may be circulating around the warm conduit of Mount Hood.

The last feature indicated on Figure 5.39 is the conductor buried at a depth of 10-15 kilometers and indicated by the cross hatched area labeled 1-3 Ohm-m. The strike of this structure was established using the impedance phase as shown in Figure 5.19. The two-dimensional profile inversion provided the dimensions and conductivity. The mismatch between the model TE phase and the field data in the low frequency range was considered to be an artifact of the finite strike of the body. However the results of the multibody two-dimensional simulation provided in the last section indicated that the mismatch could be resolved by providing the appropriate conductivity distribution at depths below 50 kilometers. The parameters of this deep north-south striking conductor are not well defined since the data set were confined to a small spatial window over the conductor.

Finally, the induction arrow and tipper phase responses observed between 0.01-0.001 hertz indicate the existence of a conductor at a depth in excess of 50 kilometers with a local east-west strike. The existence of this structure is based on a prediction of the phase response at 0.0001 hertz from a projection of the data in the frequency band of 0.01-0.001 hertz.

The validity of this highly speculative model will be known when additional data are acquired in this region of the Cascades. The most important constraints which must be relaxed are the limits on the spatial and frequency windows. More data must be acquired in the region surrounding Mount Hood and some of these data must be acquired to at least 0.0001 hertz.

## Chapter 6

### The End of the Quest

#### [ I ] The Conductivity Model in Relation to Other Geophysical Information

The conductivity model developed in the last chapter was based on the interpretation of magnetotelluric-remote telluric data supplemented by three electromagnetic loop soundings with model constraints provided by shallow bore-hole information and regional heat flow measurements. This model resulted from only one aspect of a multidisciplinary exploration effort at Mount Hood. Geochemical studies by White (1980) and a detailed geologic investigation by Crandell provided additional information associated with the recent volcanism, extending the earlier detailed examination of the geology and petrology of this Cascade volcano by Wise (1969). Regional geological studies supplemented by Landsat, side-looking radar and infrared measurements were used to understand the surface structural features and the thermal manifestations at Mount Hood by Williams, Hull, Ackermann and Beeson (1982); and Friedman, Williams and Frank (1982). Aeromagnetic data by Flanagan and Williams (1982) and gravity measurements by Couch and Gemperle (1979) provided detailed potential field information in the immediate vicinity of Mount Hood. The regional gravity has been presented by Couch, Pitts, Braman and Gemperle (1981), and the regional aeromagnetics are currently being acquired and processed. A 16-station seismic network was established in the vicinity of Mount Hood to study local earthquake activity and to provide a means of understanding the seismic velocity structure under the volcano.

The results of this study were presented by Weaver, Green and Iyer (1982). Additional information about the near surface properties were obtained by means of a refraction survey by Kohler, Healy and Wegener (1982). These various geophysical techniques provided a great deal of indirect information pertaining to the physical properties which characterized the region in the vicinity of the composite conductivity model. The data from some of the above techniques were compared to this model and a correlation was observed between the inferred electrical conductivities, the seismic velocities and the regional Bouguer gravity anomalies.

The aeromagnetic data were acquired in the vicinity of Mount Hood by Flanagan and Williams (1982). These data were reduced to the pole and upward continued to 4,267 meters. The smoothed response provided a dominant low of -257 nano-tesla located south-west of Mount Hood in the vicinity of some silicic intrusives. This magnetic low was attributed to the porphyritic quartz diorite to quartz monzonite intrusives which have relatively low magnetization as compared to basalts and andesites, the dominant rock types in the area. The low coincided with the location of the large resistive body extending from near surface to 10-15 kilometers depth. This represented the only correlation observed between the model components and these data. On a larger scale, the aeromagnetic data should provide an indication of a shallow Curie depth corresponding to the elongate conductor buried a depth of 10-15 kilometers since this conductor probably represents a partial melt zone in the lower crust. However, this regional data is only now being acquired and this most important comparison cannot be made.

The local gravity measurements were acquired and processed to provide a complete Bouguer gravity anomaly map of Mount Hood. A summary of the work by Couch and Gemperle (1979) related to the acquisition, processing and interpretation of these data follows. The data were initially reduced using a 2.67 gm/cc density. This provided an anomaly distribution characterized by a north-south low which was closed

to the north and broadened into an east-west feature south of Mount Hood. The above density provided little topographic correlation east of Mount Hood indicating that this was an appropriate density for the near surface rock in this area. However, a detailed study indicated that a density of 2.27 gm/cc was required to minimize the correlation between the anomalies and the topography throughout most of the survey area. The minimum was broad indicating the presence of a wide range of near surface densities. An interpretation of the anomalies obtained by using the 2.27 gm/cc reduction density indicated that Mount Hood may be located in a north-south graben structure bounded by prominent faults on the east side. Lineations were observed with orientations of north 85 degree east and north 23 degrees west. These data were spatial filtered at 8.1 and 13. km/cycle and the anomaly maps for the data above and below these spatial frequencies were presented. The resulting smoothed anomaly maps indicated no direct correlation with any of the conductivity model parameters.

The regional gravity data (state of Oregon) were presented by Couch, Pitts and Braman (1981) as a complete Bouguer anomaly map using a reduction density of 2.67 gm/cc. A portion of this anomaly map in the vicinity of Mount Hood is shown in Figure 6.1. The electrical conductivity model represented by the elongate conductor buried at a depth of 10-15 kilometers and the overlying large resistive zone are indicated by the stippled region on this figure. The correlation between the buried conductor striking north 20 degrees west and the broad low in the anomaly map is clearly evident. The characteristics of this gravity anomaly are similar to those observed in the small scale study by Couch and Gemperle (1979) using the same reduction density. The anomalous low closes to the north and is open to the south of Mount Hood. This would indicate that if the buried conductor is related to the north-south low in the anomalous gravity data then a finite strike would be expected. The east-west trend in the anomalous gravitational field south of the volcano may be related to the local east-west conductivity variations below a depth of 50 kilometers implied by the low

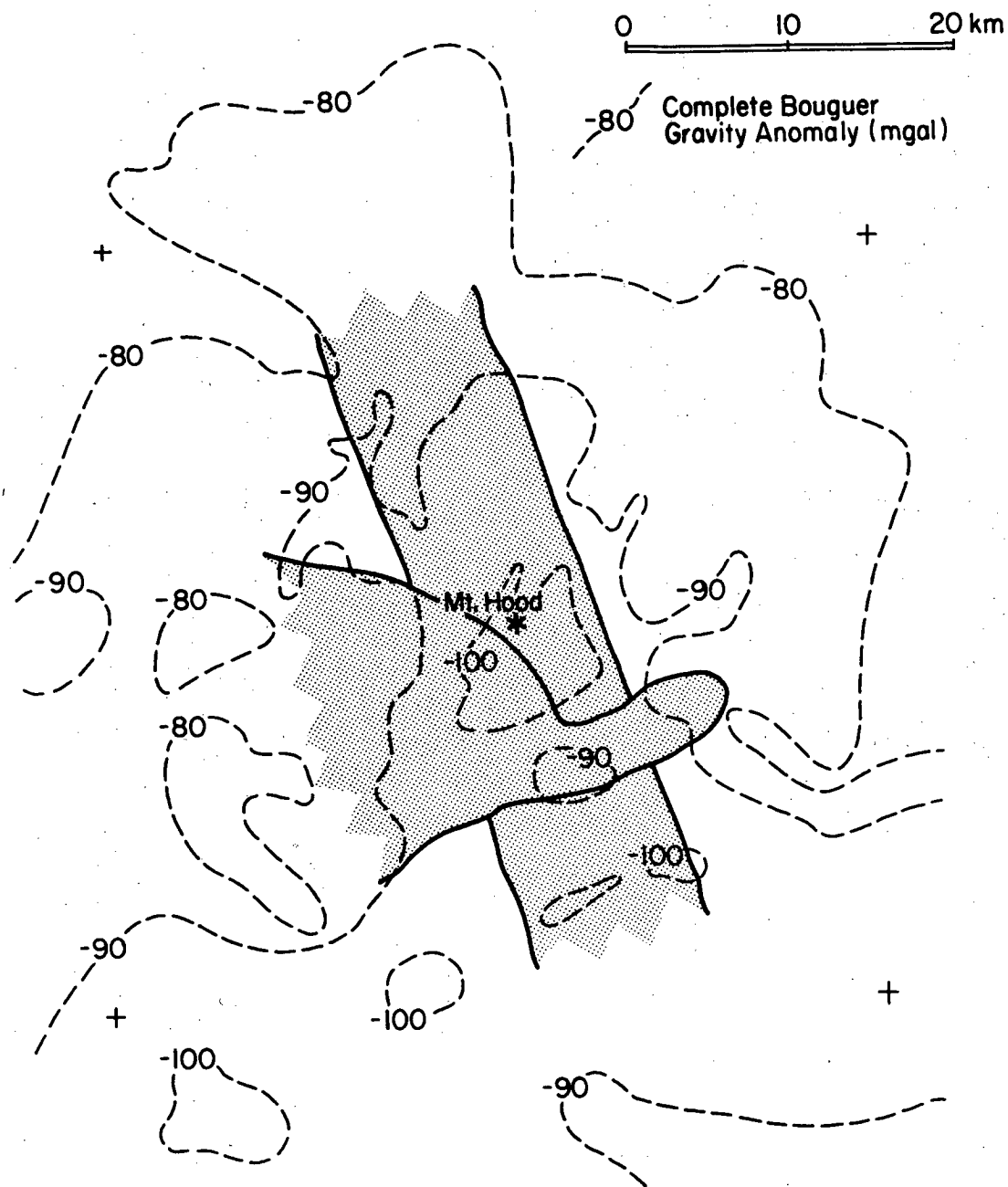


**Figure 6.1** The model components consisting of the elongate conductor buried at 10.-15. kilometers with the large resistive body which extends from near surface to intermediate depths of 10.-15. kilometers indicated by the stippled region are superimposed on the complete Bouguer gravity anomaly map by Couch, Pitts, Braman and Gemperle (1981) with a 2.67 gm/cc reduction density used.

frequency tipper phase variations.

A teleseismic P wave delay study was undertaken in 1977 at Mount Hood by the U.S. Geological Survey. A 16 site seismic array spread over a 40 by 50 kilometer region around the volcanic peak was in operation for 13 months. The results of this investigation were presented by Weaver, Green and Iyer (1982).

Throughout this period of operation, only 10 local earthquakes were recorded. All of these were located at shallow depths of less than 15 kilometers under the slopes of Mount Hood. The fault plane solutions for 8 of the earthquakes indicated strike-slip faulting and one event implied a normal fault mechanism. All strike-slip fault plane solutions indicated a north-northwest strike direction. This direction corresponds roughly to the principal direction of the impedance tensor based on the maximum residual phase in band 4 of the magnetotelluric data.

The teleseismic data consisted of 55 events with three dominant azimuths of approach. These seismic data were reduced to relative residuals by subtracting the network average from the calculated residual at each measurement location. These relative residuals were calculated for each of the three ranges of source azimuths. The resulting spatial distribution indicated that most of the residuals were independent of the azimuth of approach. The residuals were then averaged over all azimuths and some correlation was observed with station elevation. These topographic effects were removed through the use of a simple linear regression analysis.

The average residuals corrected for topography are shown in Figure 6.2. The large negative residuals indicate regions of relatively high velocity material and the positive residuals are associated with low velocity zones. This velocity distribution was interpreted as being caused by variations in the near surface rock properties.

The irregular black areas in this figure indicate the locations of Pliocene intrusives and andesitic plugs as mapped by Wise (1969). The large black region south-west of Mount Hood near the -0.2 second P wave residual contour represents the silicic

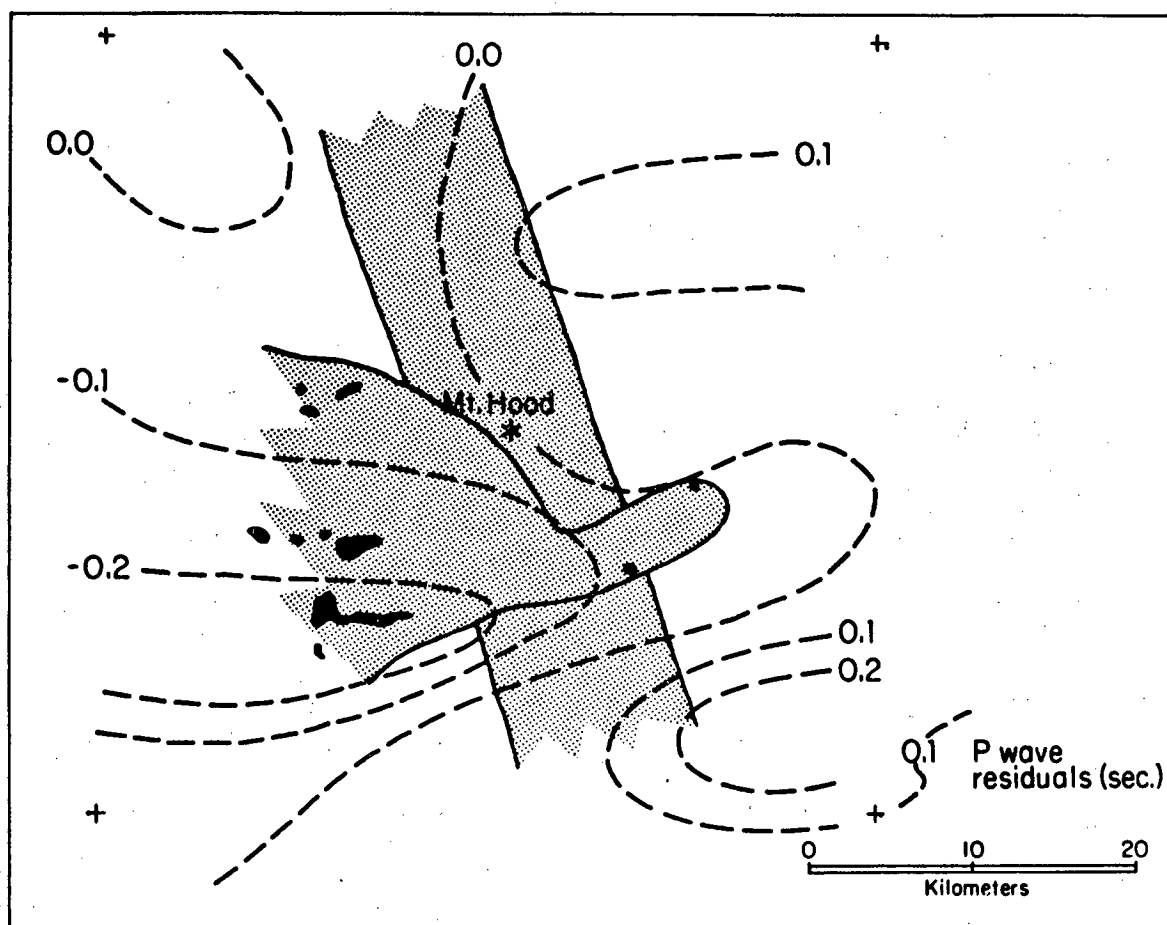


Figure 6.2 The model components consisting of the elongate conductor buried at 10.-15. kilometers with the large resistive body which extends from near surface to intermediate depths of 10.-15.kilometers indicated by the stippled region are superimposed on the P wave residual data by Weaver, Green and Iyer (1982) averaged over three source polarizations and corrected for topographic effects. The irregularly shaped black areas represent Pliocene intrusives and andesitic plugs indicated by Wise (1969).

intrusives which correlated with the large magnetic low. This zone of high velocity indicated by the negative residuals coincides with the large shallow resistive component of the electrical conductivity model. This component of the model is shown as part of the stippled area in Figure 6.2. The second component of the model also signified by the stippling is the elongate conductor buried beneath the resistive body. The residual data exhibits no correlation with this deep conductor. This indicates that the inferred Pliocene intrusive which greatly affects the apparent resistivities and the complex tipper components in the vicinity of the volcanic peak may also dominate the velocity structure in this area as indicated by the teleseismic residuals.

If the high seismic velocities are associated with the same media characterized by high resistivities, then based on the model presented in the last chapter, the high velocities may extend to depths of 10-15 kilometers and have complex lateral variations. With this kind of upper crustal velocity distribution, it would be difficult to distinguish those components of the velocity variations due to a confined partial melt zone represented by the deep elongate conductor in the conductivity model. This type of complex near surface velocity environment may explain why P wave residual studies have not been successful in locating low velocity zones beneath Cascade volcanos associated with high heat flow and recent volcanic activity.

The absence of any indication of a low velocity zone under the Cascade volcanos has been considered by Iyer, Rite and Green (1982). These investigators moved from the local studies such as at Mount Hood and Newberry Crater to a regional scale covering the entire Cascade range in Oregon to resolve the enigma presented by the presence of local geothermal resources but the absence of an associated low velocity zone. The results obtained by a three-dimensional parameterized inversion of the regional teleseismic data indicated a complex velocity structure in the northern Oregon Cascades within the upper 20 kilometers of the crust. The velocity structure in central and southern Oregon indicated an inclined boundary dipping to the east between high

and low velocities which may indicate a subduction zone. The inversion model was characterized by relatively low velocity material under the entire high Cascade region. This was interpreted as an indication of the existence of low-density high-temperature rock at depth. Perhaps this low velocity zone at depth is related to the conductivity variations indicated by the long period variations of the tipper phase response.

In addition to the teleseismic data, a large scale refraction study was undertaken at Mount Hood by Kohler, Healy and Wegener (1982). The refraction survey was carried out using 6 shot-points and two sets of 100 receiver locations over an area of 60 to 70 square kilometers. The data were interpreted by dividing the travel time data into three sections for source receiver separations of 4.-19.7, 19.7-40. and distances greater than 40. kilometers. In order to obtain a relative velocity distribution, a time term analysis was applied to each section of the travel time data.

The time term analysis is basically a least square fit of the entire data set to a simple model for each source receiver pair which provides one unknown for the travel time from the source to the refractor, a second unknown is the velocity of the refractor and the third unknown is the travel time from the refractor to the receiver. The time term value at any receiver will be related to the time required for the seismic signal to travel from the refractor to the surface for all six shot-points and will therefore be averaged over several different azimuths.

The time term solution for a source receiver separation range of 19.7-40. kilometers is shown in Figure 6.3. The lower time term values indicate regions characterized by relatively high velocities. The two components of the conductivity model, indicated by the stippled areas as before are superimposed on these data in this figure. The Pliocene intrusives are again depicted by the black regions. The near surface media is clearly characterized high velocities and high resistivities in the vicinity of these silicic intrusives. The detailed distribution of these near surface velocities as indicated by

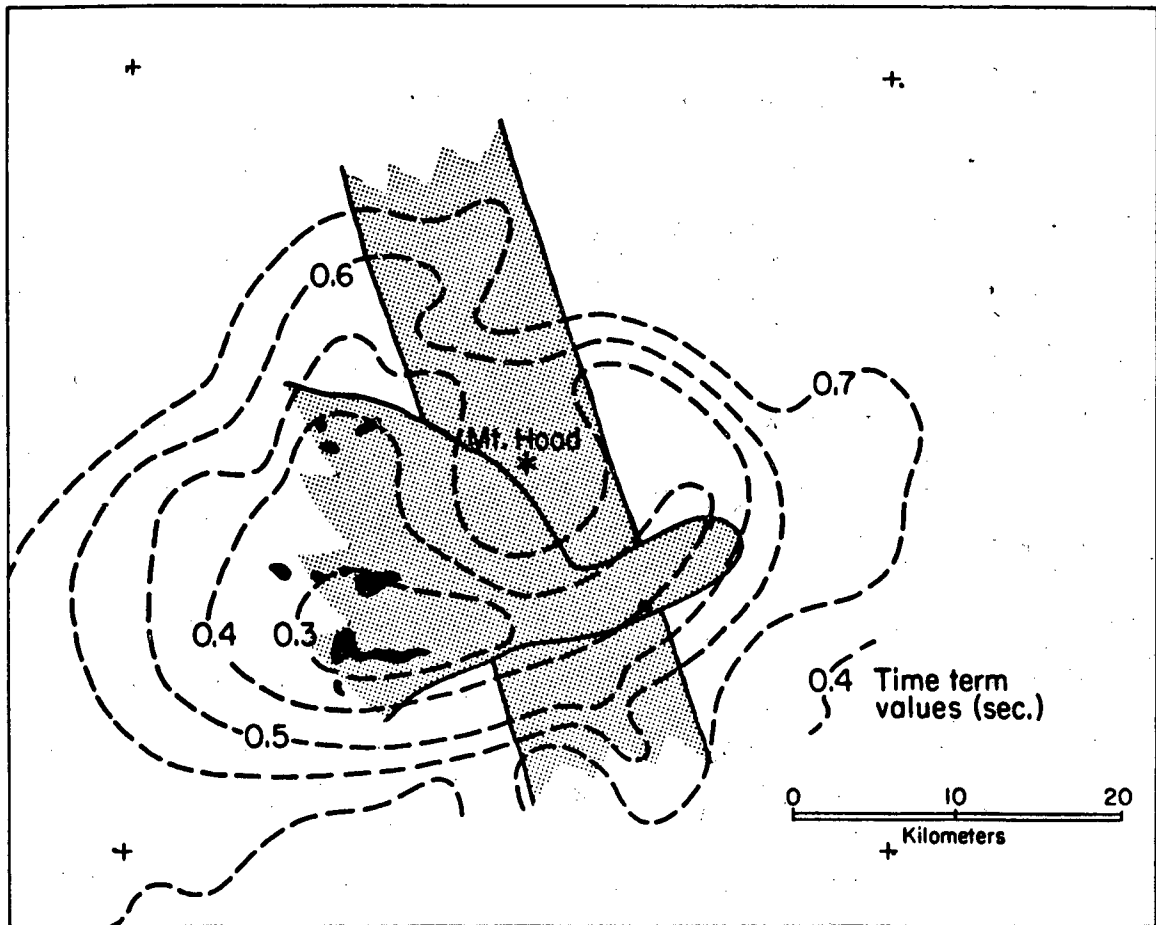


**Figure 6.3** The model components consisting of the elongate conductor buried at 10.-15. kilometers with the large resistive body which extends from near surface to intermediate depths of 10.-15. kilometers indicated by the stippled region are superimposed on the time term data by Kohler, Healy and Wagner (1982) for source receiver separations of 19.7-40. kilometers. The irregularly shaped black areas represent Pliocene intrusives and andesitic plugs indicated by Wise (1969).

both the teleseismic residuals and the time term analysis indicate an extraordinary degree of correlation with the large resistive body indicated by the magnetotelluric and geomagnetic data.

The fumaroles in the vicinity of Crater Rock on the summit of Mount Hood represent the major thermal manifestation in the region. A shallow temperature probe traverse across this fumarole field and a regional aerial infrared survey were used by Friedman; Williams and Frank (1982) to estimate the heat discharge from the thermal sources in the area. The volume and frequency of recent volcanic eruptions as estimated by Crandell (1980) and others have provided a means to gauge the available residual heat from past volcanic activity. These estimates indicated that the cooling dacitic plug on the summit would not have been able to provide the present heat flux observed. This suggested to these investigators that the fumarole activity is primary and is due to a deep heat source. The heat transfer mechanism was postulated to be convective in nature with hydrothermal fluids transporting the heat through fractures around the margin of the plug dome.

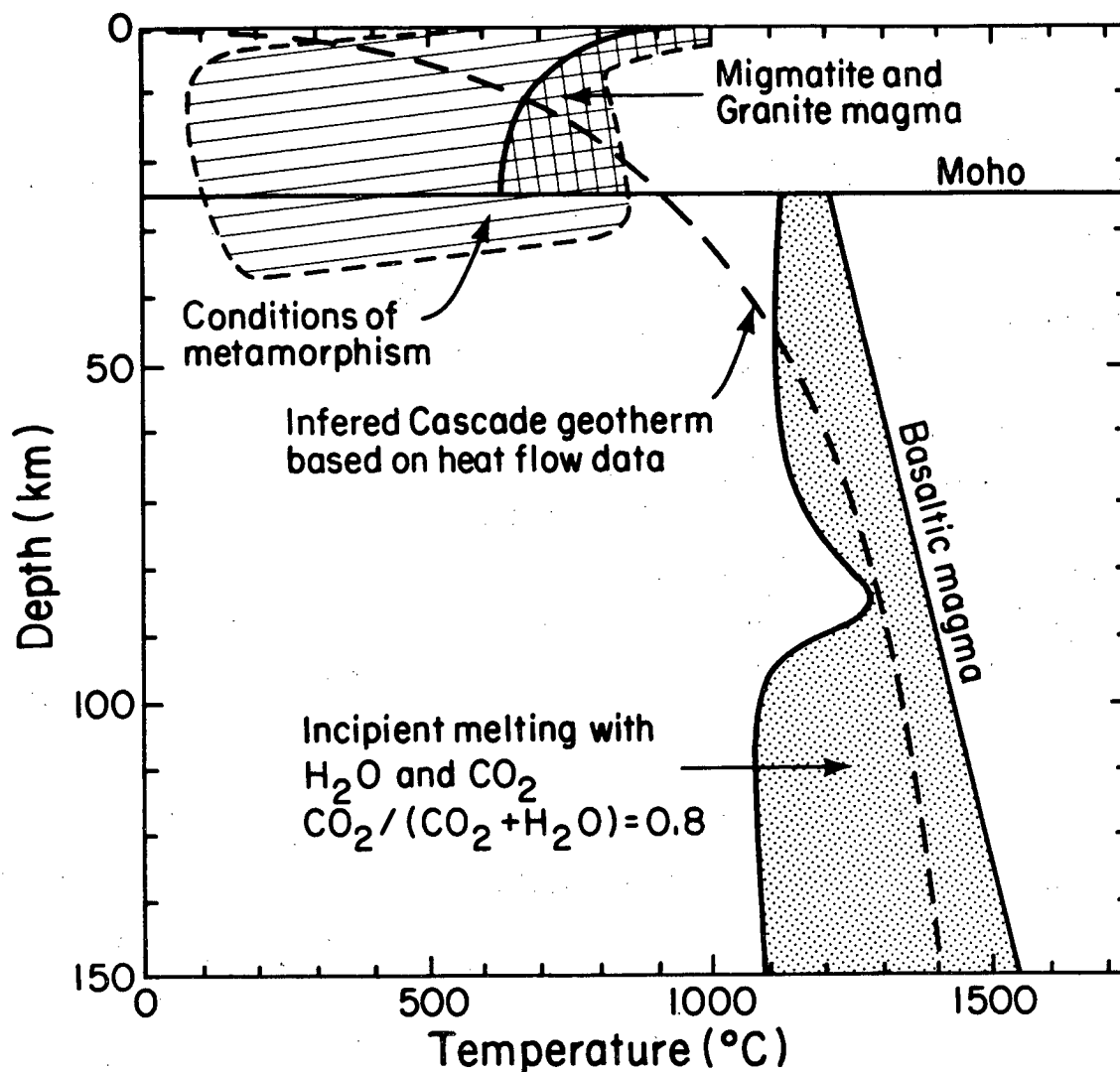
The existence of a deep seated convective system associated with the conduit under Mount Hood provides a convenient source for the anomalous conductivities at depths of 4-5 kilometers indicated in this vicinity by both the magnetotelluric and tipper frequency responses. The induction arrows in band 4 and the two-dimensional model which provided a reasonable fit to the magnetotelluric data along the profile presented in Chapter 5 both indicated a high lateral contrast in conductivity located in the vicinity of the north-east and eastern boundary of the large near surface resistive region. This body delineated by both the electrical and seismic data probably represents an impermeable zone which controls the local hydrology and thus limits the lateral extent of any hydrothermal system existing under Mount Hood. This would create an environment around the edges of the Pliocene intrusive characterized by hot saturated rock which would be expected to exhibit elevated conductivities.

The last but not least consideration is the feasibility of the conductivity model in relation to an appropriate petrogenetic model for this tectonic setting. The tectonic model chosen by Iyer, Rite and Green (1982) to satisfy their seismic interpretation was a marginal basin behind an island arc. This type of setting although not completely appropriate of the Cascades is associated with calc-alkaline volcanism which characterizes the north-western United States.

The petrogenetic models may be quite complex as indicated by Hildreth (1981). The fractionation of magma occurs over large ranges of both depth and time. This may result in magma residing at multilevels within a subsurface volcanic column at the same time. A simplified form of this complex depth-temperature environment expected in the vicinity of a subduction zone is shown in Figure 6.4. This figure is from Wyllie (1981) with the Moho depth adjusted to 25 kilometers.

The thickness of the crust was chosen to be 25 kilometers based on seismic evidence on the east and west sides of the Cascades. A long refraction profile by Hill (1972) provided a estimate for the crustal thickness of 25 kilometers under the Columbia River Plateau of south-eastern Washington and north-eastern Oregon. The P wave conversion studies by Langston (1981) provided a depth of 20 kilometers to the Moho in northwestern Oregon. This evidence coupled with the change in volcanism discussed in Chapter 1 indicated a relatively thin crust may be expected in the vicinity of Mount Hood.

The depth-temperature ranges indicated in this figure for metamorphism and magma generation in the crust is based on the availability of aqueous pore fluids. The inferred Cascade geotherm shown in this figure for shallow depths is based on an extrapolation of the surface heat flow measurements at Mount Hood by Blackwell and Steele (1979). The asymptotic limit of the geotherm at depth was taken from Oxburgh (1980).



XBL 829-2478

Figure 6.4 Depth-temperature ranges for metamorphism and magma generation in the continental crust and mantle by Wyllie (1981) with an adjusted Moho depth. The inferred Cascade geotherm with estimates at shallow depths based on an extrapolation of surface thermal gradients of 60 C/km from Blackwell and Steele (1979). The asymptotic limit of the geotherm at depth was from Oxburgh (1980).

An examination of the geotherm in this figure indicates that the depth at which partial melt could occur would be approximately 12 kilometers and that a significant portion of melt would be expected before a solid phase is entered at the mantle boundary. This large percentage of melt would indicate the existence of high conductivities in the depth range of 12-25 kilometers. The solid phase on entering the mantle would provide a resistive media at depth. The geotherm would again at approximately 45 kilometers enter a region where partial melting could occur with the availability of water and carbon dioxide. This would provide a conductive zone at a depth in excess of 45 kilometers.

This simple model indicates that at least the existence of a partial melt zone between 12 and 25 kilometers and again at 50 kilometers is feasible with a simple petrogenetic model. Therefore the high model conductivities in these depth ranges are reasonable for a tectonic environment characterized by surface heat flow measurements such as those observed at Mount Hood.

In summary the conductivity model appears to be feasible with respect to the petrogenetic models appropriate for this setting. The other geophysical data available however provides very little support of any of the model components with exception of the large resistive body located south and southwest of Mount Hood. The high degree of correlation evident between the seismic data and the details of the resistive component of the conductivity model indicated that these high resistivities and high velocities delineate the same geologic structure which is probably a large Pliocene intrusive.

## [ II ] Conclusions

The results obtained from the magnetotelluric data at Mount Hood were mixed. The impedance and the complex tipper transfer functions calculated from these data provided beautifully intricate spectral characteristics which both confounded and inspired the interpretation attempts. The elusive magma chamber, the object of our search is probably associated with the elongate conductor buried 12 kilometers with a depth extent of approximately 10 kilometers. This conductor however is not alone. It is located below two conductive zones buried at depths of 0.5 and 5. kilometers and above a conductive region located at depths below 50 kilometers. The relationship between this model and the true conductivity of the earth is certainly open to question. The small spatial and frequency window through which one may peer into the depths provides many ambiguities.

The validity of this model may only be tested by the acquisition of additional data throughout north-central Oregon and south-central Washington with some data acquired to .0001 hertz. Care should be exercised when acquiring this data, since magnetotelluric data acquired at large site separations will be affected by different near surface environments and would not provide sufficient information to evaluate these affects. The data acquisition scheme used here, with four to five measurement locations distributed as an array with 2-5 kilometer separations between sites is recommended to provide sufficient local control to obtain a qualitative understanding of the near surface conductivity distribution.

These data with their rich spectral content provided a number of hints in regard to the relationship between the various measurement parameters. There are two points indicated by these data which may prove to be quite useful in other complex environments. The first is associated with the advantages of relying on the impedance phase response characteristics as a function of coordinate rotation to provide a means

of obtaining an accurate indication of deep conductors when the impedance amplitudes are greatly distorted by near surface conductivity distributions. A second useful but well disguised hint suggested that the relative sensitivities between the impedance and tipper parameters were quite different with tipper components providing the highest resolution.

The important property associated with the impedance phase is that its frequency response associated with near surface inhomogeneities is band limited. That is, the high frequency portion of the phase spectra responds to a near surface conductor but the phase returns to the half space response at low frequencies. The impedance amplitude or the apparent resistivities on the other hand are distorted in a broad-band sense. They respond at higher frequencies to surface conductors but instead of asymptoting to the half space value they remain distorted into the D.C. limit. This broad-band distortion will dominate the principal direction calculated by maximizing the off-diagonal impedance tensor elements at each frequency. This provides a principal direction which is nearly independent of frequency when the near surface conductors create a highly polarized electric field.

If a target happens to be buried beneath this surface conductor the impedance amplitude distortions caused by the deep conductor would be only a minor component of the total low frequency response. The surface distribution would therefore dominate the choice of the principal direction. A deep target characterized by a significant strike length would provide a narrow band impedance phase response in the lower frequency range associated with primary electric field oriented parallel to strike. This phase response may dominate the low frequency band since the effects from the surface body should be approaching the half space value when there exists a sufficient depth separation between the near surface conductor and buried target.

An indication of the location and strike direction of this target may then be obtained when the impedance estimates are rotated into the principal direction based

on a maximum phase response in the appropriate low frequency band. If the principal direction were chosen in the standard manner by simply maximizing the off-diagonal elements of the impedance tensor when the near surface conductivity distribution is such that the surface fields are polarized at approximately 45 degrees with respect to the strike of the underlying target then the diagnostic frequency characteristics would not be evident and the target would be missed. The residual phase defined in Chapter 5 provides a simple vehicle to search for these diagnostic phase characteristics and provide an estimate of the strike direction for targets buried at depth.

The utility of this method is strongly dependent on the depth separations required to obtain a reasonable separation of the responses in the frequency domain caused by the two conductors. This important relationship could not be investigated here since the near surface bodies are generally three-dimensional in nature and the three-dimensional modeling technique available was unable to simulate the appropriate conductivity distributions. This however would be a very interesting area for future research.

The second interesting feature in this data was related to the observed sensitivity differences between the various impedance and complex tipper parameters. This study did not provide a comprehensive comparison of the relative resolution of these time independent field measures. However, the field data and models considered did indicate that the tipper frequency response was more sensitive to the effects of complex geometries and multiconductors than the impedance parameters.

The slower frequency response of the impedance functions will probably provide parameters which may be simulated adequately with simpler models than those required to match the rapidly varying frequency characteristics of the tipper functions. This high sensitivity endows the tipper parameters with the ability to detect many details in a conductivity distribution which would remain undetected by the slower response of the impedance parameters. This enhanced sensitivity may create

confusion in a complex environment as indicated by the rapid spatial variations observed in the imaginary tipper component over the multiconductor three-dimensional model presented in Chapter 5.

The importance of considering these relative sensitivities is paramount for a successful interpretation of magnetotelluric and tipper data in a complex geological setting. When these data appear to indicate different conductivity distributions, this may simply indicate the differing sensitivities of these various measurement parameters to different conductivity components. Improved modeling techniques are required to adequately understand the complex relationship between these parameters. This study however indicates that the impedance and tipper parameters may provide complementary measures of the subsurface properties in a multiconductor environment.

## Bibliography

- Ando, M. and E.I. Balazs, 1979. Geodetic Evidence for Aseismic Subduction of the Juan de Fuca Plate, *J. Geophys. Res.*, 84 (B6), 3023-3028.
- Bacon, C.R., 1981. Geology and Geophysics of the Cascade Range, paper presented at the 51st Annual International Meeting, Soc. Expl. Geophys. Los Angeles, Calif.
- Becher, W.D., and C.B. Sharp, 1969. A Synthesis Approach to Magnetotelluric Exploration, *Radio Science*, 4 (11), 1089-1094.
- Berdichevsky, M. N., 1968. *Electrical Prospecting by Magnetotelluric Profiling Method*, Moscow: Nedra.
- Berdichevskiy, M.N. and V.S. Smirnor, 1971. Methods of Analyzing Observations During Magnetic Variation Profiling, *Geomagn. i Aeronomiya*, 11 (2), 310-312.
- Berdichevskiy, M.N. and E.B. Faynberg, 1972. Possibility of Experimental Separation of the Variable Geomagnetic Field into a Poloidal and Toroidal Part, *Geomagn. i Aeronomiya*, 12 (5), 826-830.
- Berdichevskiy, M.N. and V.I. Dmitriev, 1976. Distortion of Magnetic and Electrical Fields by Near Surface Lateral Inhomogeneities, *Acta Geodaet., Geophys. et Montanist. Acad. Sci. Hung.*, 11 (3-4), 447-483.
- Blackwell, D.D., 1978. Heat Flow and Energy Loss in the Western United States, published in *Geol. Soc. Am. Memoir 152*, 175-208.
- Blackwell, D.D., D.A. Hull, R.G. Bowen and J.L. Steele, 1978. Heat Flow of Oregon, *Spec. Pap. 4*, 42 pp., Oreg. Dep. of Geol. and Miner. Ind., Portland.
- Blackwell, D.D. and J.L. Steele, 1979. Heat Flow Modeling of the Mount Hood Volcano, Oregon, in *Geothermal Resource Assessment of Mount Hood, Open File Report 0-79-8*, 190-264, Oreg. Dep. of Geol. and Miner. Ind., Portland.
- Cantwell, T., 1960. Detection and Analysis of Low Frequency Electromagnetic Signals, *Ph.D. Dissertation, Dept. of Geol. and Geophys., M.I.T.*
- Cantwell T. and A. Orange, 1965. Further Deep Resistivity Measurements in the Pacific Northwest, *J. Geophys. Res.*, 70 (16), 4068-4072.
- Coen, S. and G. Cheng, 1982. Towards a Direct Inversion of Magnetotelluric Data: Part I, One-Dimensional Data, *Geophysics*, in press.
- Couch, R.W. and M. Gemperle, 1979. Gravity Measurements in the Area of Mount Hood, Oregon, in *Geothermal Resource Assessment of Mount Hood, Open File Report 0-79-8*, 137-189, Oreg. Dep. of Geol. and Miner. Ind., Portland.

- Couch, R.W., G.S. Pitts, D.E. Braman and M. Gemperle, 1981. Free-Air Gravity Anomaly Map and Complete Bouguer Gravity Anomaly Map, Cascade Mountain Range, Northern Oregon, *Geol. Map Ser., GMS-15*, Ore. Dep. of Geol. and Miner. Ind., Portland.
- Crandell, D.R., 1980. Recent Eruptive History of Mount Hood, Oregon, and Potential Hazards from Future Eruptions, *Geological Survey Bulletin 1492*, 81 pp.
- Flanagan, G.F. and D.L. Williams, 1982. A Magnetic Investigation of Mount Hood, Oregon, *J. Geophys. Res.*, 87 (B4), 2804-2814.
- Friedman, J.D., P.L. Williams, and D. Frank, 1982. Structural and Heat Flow Implications of Infrared Anomalies at Mt. Hood, Oregon, 1972-1977, *J. Geophys. Res.*, 87 (B4), 2793-2803.
- Frischknecht, F.C. 1971. Electromagnetic Scale Modeling, in *Electromagnetic Probing in Geophysics*, Editor: J.R. Wait, Publ. Golem Press.
- Gamble, T.D., 1978. Remote Reference Magnetotellurics with SQUIDS, *Ph.D. Dissertation Dept. of Physics Univ. of California, Berkeley*.
- Gamble, T.D., W.M. Goubau and J. Clarke, 1979. Magnetotellurics with a Remote Magnetic Reference, *Geophysics*, 44 (1), 53-68.
- Gamble, T.D., W.M. Goubau and J. Clarke, 1979. Error Analysis for Remote Reference Magnetotellurics, *Geophysics*, 44 (5), 959-968.
- Goldstein, N.E., E. Mozley and M. Wilt, 1982. Interpretation of Shallow Electrical Features from Electromagnetic and Magnetotelluric Surveys at Mount Hood, Oregon, *J. Geophys. Res.*, 87 (B4), 2815-2828.
- Goubau, W.M., T.D. Gamble and John Clarke, 1978. Magnetotelluric Data Analysis : Removal of Bias, *Geophysics*, 43 (6), 1157-1166.
- Gregori, G.P. and L.J. Lanzerotti, 1980. Geomagnetic Depth Sounding by Induction Arrow Representation: A Review, *Rev. Geophys. Space Phys.*, 18 (1), 203-209.
- Hildreth, W., 1981. Gradients in Silicic Magma Chambers: Implications for Lithospheric Magmatism, *J. Geophys. Res.*, 86 (B11), 10153-10192.
- Hill, D.P., 1972. Crustal and Upper Mantle Structure of the Columbia Plateau from Long Range Seismic-Refracton Measurements, *Geol. Soc. Am. Bull.*, 83, 1639-1647.
- Hohmann, G.W., 1975. Three-dimensional Induced Polarization and Electromagnetic Modeling, *Geophysics*, 40 (2), 309-324.
- Hohmann, G.W., 1982. Numerical Modeling for Electrical Methods, paper presented at the 52nd Annual International Meeting, Soc. Expl. Geophys. Dallas, Texas.

- Hollister, V.F., 1979. Porphyry Copper-Type Deposits of the Cascade Volcanic Arc, Washington, *Minerals Sci. Engng.*, 11 (1), 22-35.
- Iyer, H.M., A. Rite and S.M. Green, 1982. Search for Geothermal Heat Sources in the Oregon Cascades by Means of Teleseismic P-Residual Technique, paper presented at the 52nd Annual International Meeting, Soc. Expl. Geophys. Dallas, Texas.
- Jones, A.G., 1981. Comment on "Geomagnetic Depth Sounding by Induction Arrow Representation: A Review" by G.P. Gregori and L.J. Lanzerotti, *Rev. Geophys. Space Phys.*, 19 (4), 687-688.
- Jones, F.W. and K. Vozoff, 1978. The Calculation of Magnetotelluric Quantities for Three-dimensional Conductivity Inhomogeneities, *Geophysics*, 43 (6), 1167-1175.
- Jupp, D.L.B., 1978. Estimation of the Magnetotelluric Impedance Functions, *Phys. Earth Planet. Inter.*, 17, 75-82.
- Jupp, D.L.B., and K. Vozoff, 1975. Stable Iterative Methods for the Inversion of Geophysical Data, *Geophys. J. R. astro. Soc.*, 42, 957-976.
- Jupp D.L.B. and K. Vozoff, 1977. Two-dimensional Magnetotelluric Inversion, *Geophys. J. R. astr. Soc.*, 50, 333-352.
- Kao, D.W. and D. Rankin, 1977. Enhancement of Signal to Noise Ratio in Magnetotellurics Data, *Geophysics*, 42 (1), 103-110.
- Kohler, W.M., J.H. Healy, and S.S. Wegener, 1982. Upper Crustal Structure of the Mount Hood, Oregon, Region as Revealed by Time Term Analysis, *J. Geophys. Res.*, 87 (B1), 339-355.
- Langston, C.A., 1981. Evidence for the Subducting Lithosphere Under Southern Vancouver Island and Western Oregon from Teleseismic P Wave Conversions, *J. Geophys. Res.*, 86 (B5), 3857-3866.
- Larson, J.C., 1977. Removal of Local Surface conductivity Effects from Low Frequency Mantle Response Curves, *Acta Geodaet., Geophys. et Montanist. Acad. Sci. Hung.*, 12 (1-3), 183-186.
- Lee, K.H., D.F. Pridmore and H.F. Morrison, 1981. A Hybrid Three-dimensional Electromagnetic Modeling Scheme, *Geophysics*, 46 (5), 796-805.
- Lienert, B.R., J.H. Whitcomb, R.J. Phillips, I.K. Reddy and R.A. Taylor, 1980. Long Term Variations in Magnetotelluric Apparent Resistivities Observed near the San Andreas Fault in Southern California, *J. Geomag. Geoelectr.*, 32, 757-775.
- Newton, R.G., 1982. Inverse Scattering. IV. Three Dimensions: Generalized Marchenko Construction with Bound States, and Generalized Gel'fand-Levitan Equations, *J. Math. Phys.*, 23 (4), 594-604.

- Oldenburg, D.W., 1979. One-dimensional Inversion of Natural Source Magnetotelluric Observations, *Geophysics*, 44 (7), 1218-1244.
- Oppliger, G.L., 1982. Three-Dimensional Terrain Effects in Electrical and Magnetometric Resistivity surveys, *Ph.D. Dissertation Dept. of Mat. Sci. and Miner. Enging. Univ. of Calif., Berkeley*.
- Oxburgh, E.R., 1980. Heat Flow and Magma Genesis, in *Physics of Magmatic Processes*, 161-199, editor: R.B. Hargraves, Princeton Univ. Press.
- Parkinson, W.D., 1959. Directions of the Rapid Geomagnetic Fluctuations, *Geophys. J. R. astr. Soc.*, 2 (1), 1-14.
- Pridmore, D.F., 1978. Three-Dimensional Modeling of Electric and Electromagnetic Data Using The Finite Element Method, *Ph.D. Dissertation, University of Utah*.
- Reddy, I.K., D. Rankin and R.J. Phillips, 1977. Three-dimensional Modeling in Magnetotelluric and Magnetic Variational Sounding, *Geophys. J. R. astr. Soc.* 51 (51), 313-325.
- Scheen, W.L., 1978. EMMMA, A Computer Program for Three-dimensional Modeling of Airborne Electromagnetic Surveys, in the proceedings of *A Workshop on Modeling of Electrical and Electromagnetic Methods* Lawrence Berkeley Laboratory Report LBL-7053.
- Sims, W.E., F.X. Bostick, Jr. and H.W. Smith, 1971. The Estimation of Magnetotelluric Impedance Tensor Elements from Measured Data, *Geophysics*, 36 (5), 938-942.
- Stodt, J.A., G.W. Hohmann, and S.C. Ting, 1981. The Telluric-magnetotelluric Method in Two- and Three-dimensional Environments, *Geophysics*, 46 (8), 1137-1147.
- Thayer, R.E., 1975. Telluric-Magnetotelluric Investigations of Regional Geothermal Processes in Iceland, *Ph.D. Dissertation Brown University*.
- Ting, S.C. and G.W. Hohmann, 1981. Integral Equation Modeling of Three-dimensional Magnetotelluric Response, *Geophysics*, 46 (2), 182-197.
- Vasseur, G. and P. Weidelt, 1977. Bimodal Electromagnetic Induction in Non-uniform Thin Sheets with an Application to the Northern Pyrenean Induction Anomaly, *Geophys. J. R. astr. Soc.*, 51, 669-690.
- Vozoff, K., 1972. The Magnetotelluric Method in the Exploration of Sedimentary Basins, *Geophysics*, 37 (1), 98-141.
- Waff, H.S., 1974. Theoretical Considerations of Electrical Conductivity in a Partially Molten Mantle and Implications for Geothermometry, *J. Geophys. Res.*, 79 (26), 4003-4010.

Waff, H.S. and D.F. Weill, 1975. Electrical Conductivity of Magmatic Liquids: Effects of Temperature, Oxygen Fugacity and Composition, *Earth Planet. Sci. Lett.*, 28, 254-260.

Watanabe, H., 1970. Measurements of Electrical Conductivity of Basalt at Temperatures Up to 1500 C and Pressures to About 20 Kilobars, *Spec. Contrib. Geophys. Inst. Kyoto Univ.*, 10, 159-170.

Watanabe, H., 1972. Measurements of Electrical Conductivity of Granite Under High Pressures, *Spec. Contrib. Geophys. Inst. Kyoto Univ.*, 12, 177-186.

Weaver, C.S., S.M. Green, H.M. Iyer, 1982. Seismicity of Mount Hood and Structure as Determined from Teleseismic P Wave Delay Studies, *J. Geophys. Res.*, 87 (B4), 2782-2792.

Weidelt, P., 1972. The Inverse Problem of Geomagnetic Induction, *Z. Geophys.*, 38, 257-289. Weidelt, P., 1975. Inversion of Two-Dimensional Conductivity Structures, *Phys. Earth Planet. Inter.*, 10, 282-291.

Weidelt, P., 1975. Electromagnetic Induction in Three-Dimensional Structures, *J. Geophys.*, 41, 85-109.

White, C., 1980. Geology and Geochemistry of Mt. Hood Volcano, *Spec. Pap.* 8, 26 pp., Oreg. Dep. of Geol. and Miner. Ind., Portland.

Williams, D.L., D.A. Hull, H.D. Ackermann, and M.H. Beeson, 1982. The Mt. Hood Region: Volcanic History, Structure, and Geothermal Energy Potential, *J. Geophys. Res.*, 87 (B4), 2767-2781.

Wise, W.S., 1969. Geology and Petrology of the Mt. Hood Area: A Study of High Cascade Volcanism, *Geol. Soc. Am. Bull.*, 80, 969-1006.

Wyllie, P.J., 1981. Magma Sources in Cordilleran Settings, in *Relations of Tectonics to Ore Deposits in the Southern Cordillera*, 39-48, editors: W.R. Dickinson and W.D. Payne.

Wyllie, P.J., 1981. Plate Tectonics and Magma Genesis, *Geol. Rundschau*, 70 (1), 128-153.

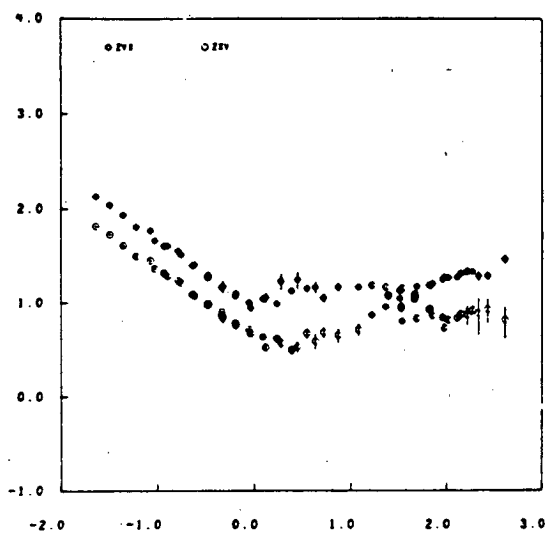
## Appendix A

### Field Data as a Function of Frequency and Rotation Angle

The impedance and geomagnetic parameters for the field data are provided for each measurement location. The impedance phases and apparent resistivities which correspond to the off-diagonal tensor elements are rotated into the principal direction defined by the maximization of these off-diagonal elements at each frequency. The principal direction associated with the  $Z_{xy}$  element which corresponds to the  $x'$  directed electric field is provided by the angle of rotation from the reference coordinate system with  $x$  directed north (positive angles of rotation are clockwise with respect to north). The geomagnetic transfer function or tipper components are rotated into that direction which maximizes the  $T_y$  component. This complex component is provided in this appendix in the form of amplitude and phase. The strike direction, indicated by the tipper coordinate rotation angle with respect to the reference coordinate system with  $x$  directed north, is provided.

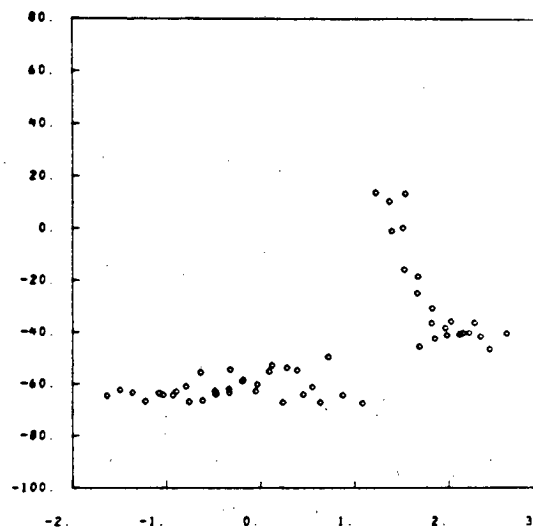
## SITE # 1

Log Apparent Resistivity

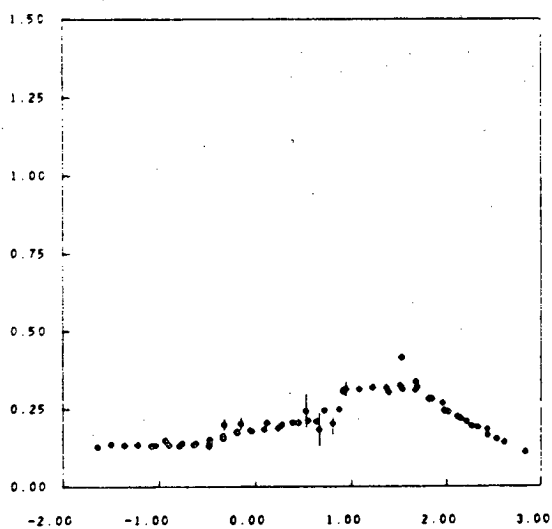


Log Period

Angle of Impedance Rotation

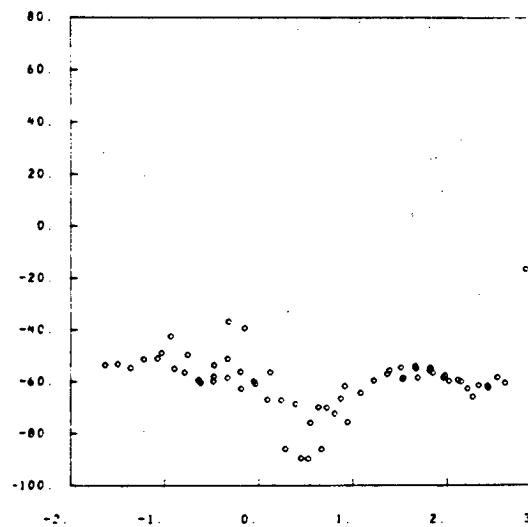


Log Period

Tipper Magnitude ( $T_y$ )

Log Period

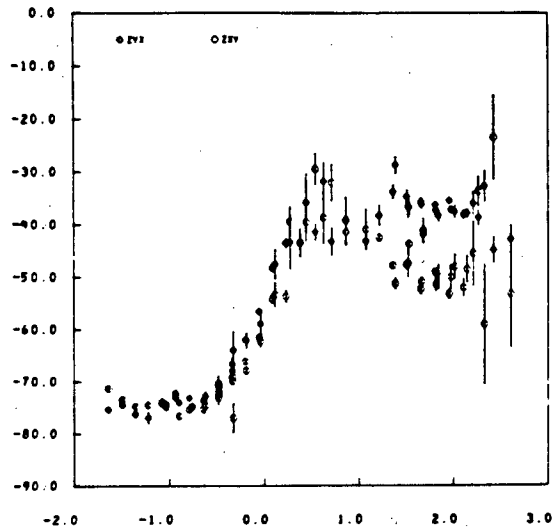
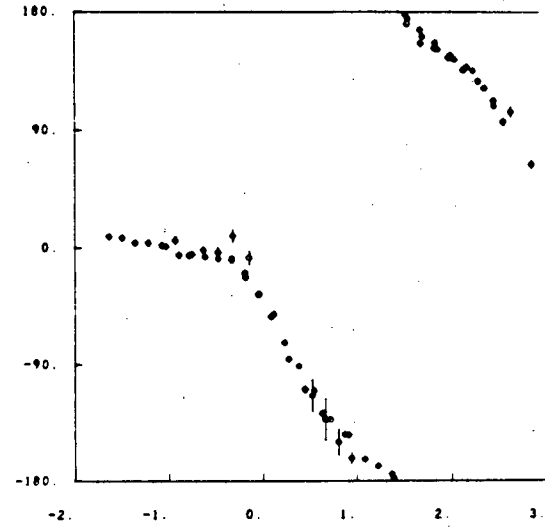
Strike Direction Indicated by Tipper



Log Period

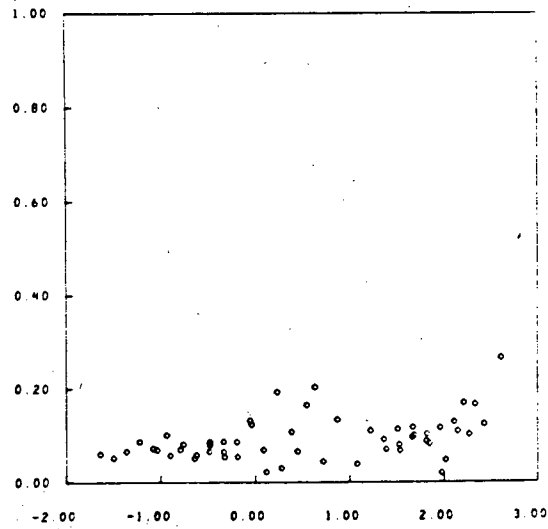
## SITE # 1

Impedance Phase

Tipper Phase ( $T_y$ )

Log Period

Log Period

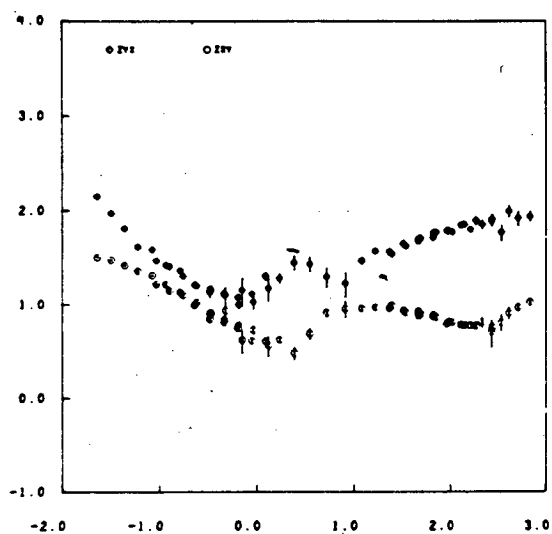


Log Period

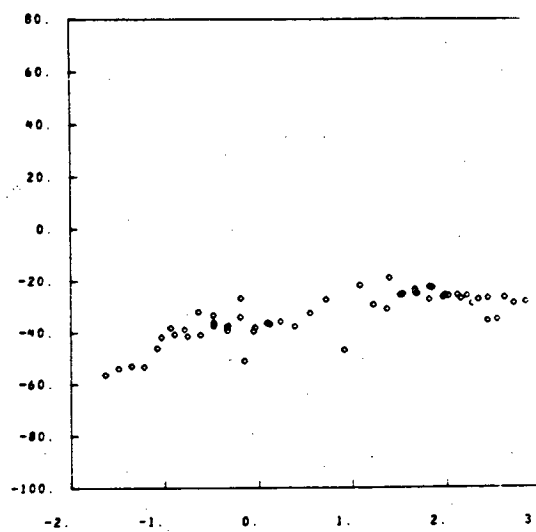
$$Skew = \left| \frac{(Z_{xx} + Z_{yy})}{(Z_{xy} - Z_{yx})} \right|$$

## SITE # 1A

Log Apparent Resistivity



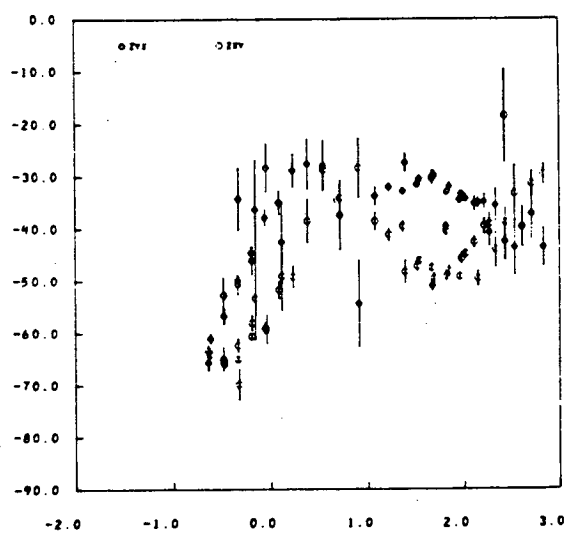
Angle of Impedance Rotation



Log Period

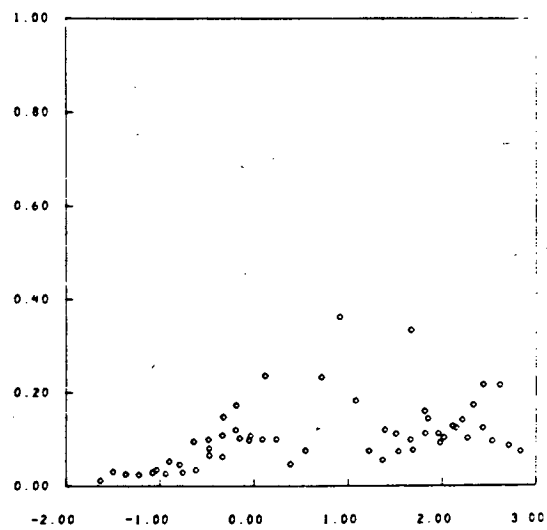
Log Period

Impedance Phase



Log Period

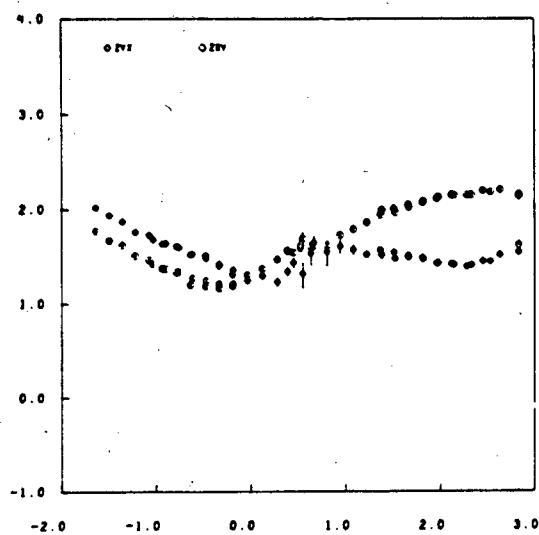
$$\text{Skew} = \frac{\left| \frac{Z_{xx} + Z_{yy}}{Z_{xy} - Z_{yx}} \right|}{\left| \frac{Z_{xy} - Z_{yx}}{Z_{xx} + Z_{yy}} \right|}$$



Log Period

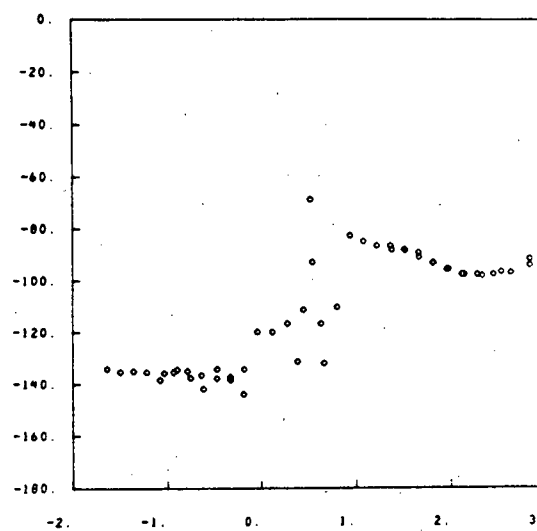
## SITE # 2

Log Apparent Resistivity

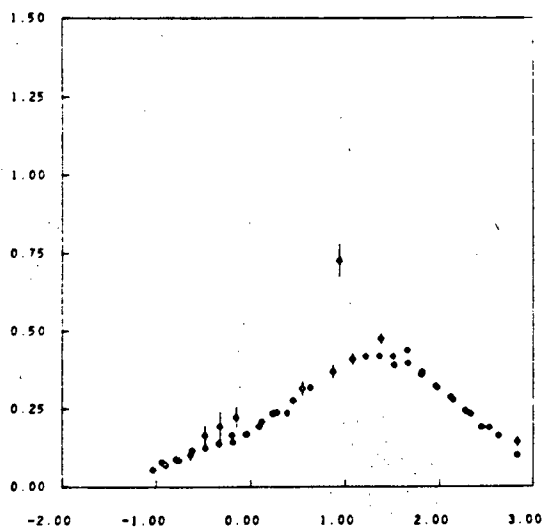


Log Period

Angle of Impedance Rotation

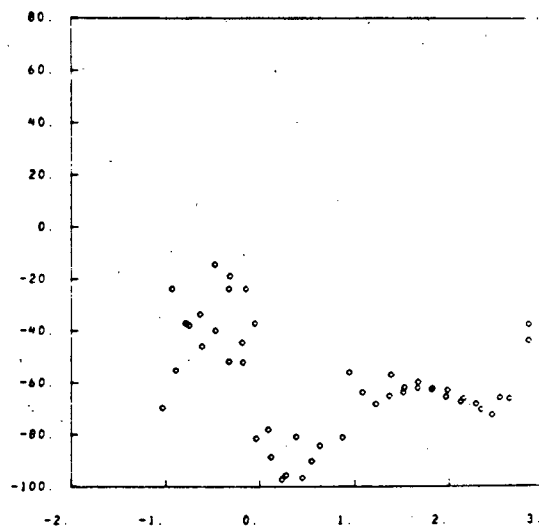


Log Period

Tipper Magnitude ( $T_y$ )

Log Period

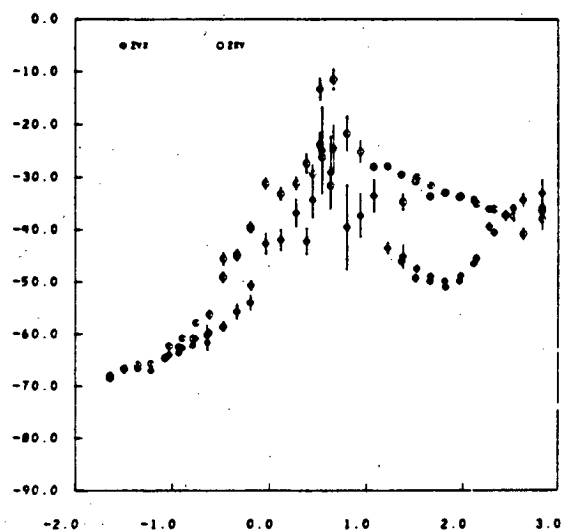
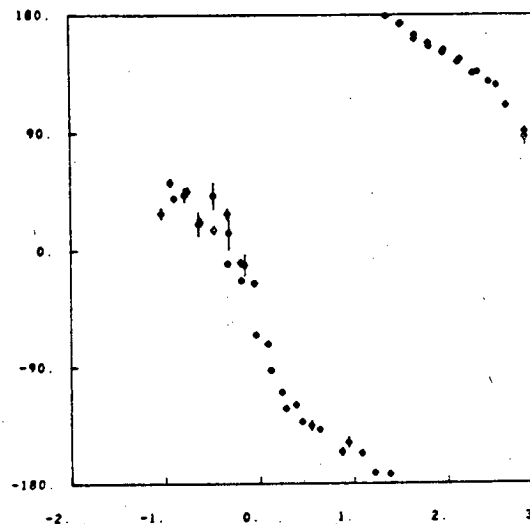
Strike Direction Indicated by Tipper



Log Period

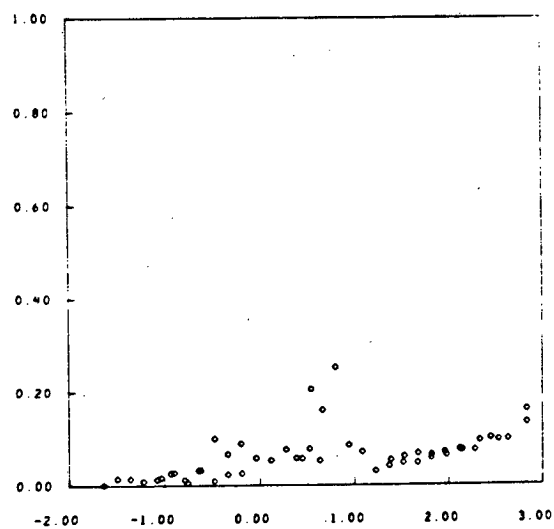
## SITE # 2

Impedance Phase

Tipper Phase ( $T_y$ )

Log Period

Log Period

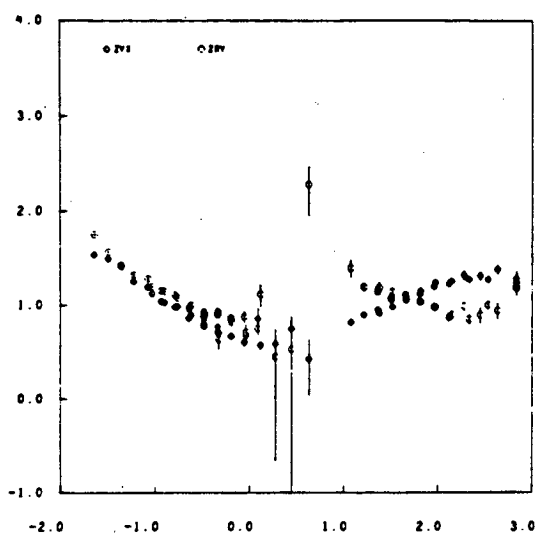


Log Period

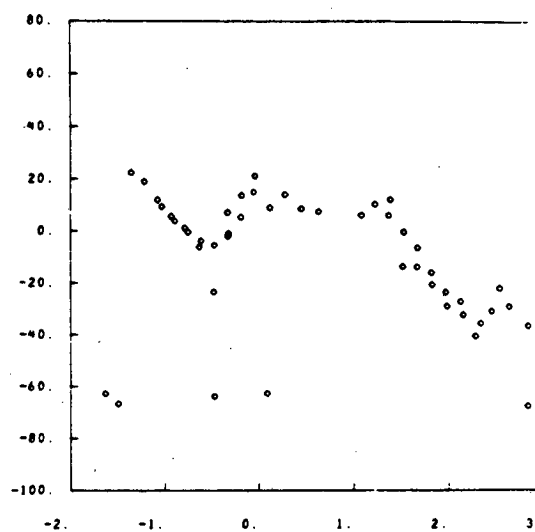
$$Skew = \left| \frac{(Z_{xx} + Z_{yy})}{(Z_{xy} - Z_{yx})} \right|$$

## SITE # 2A

Log Apparent Resistivity



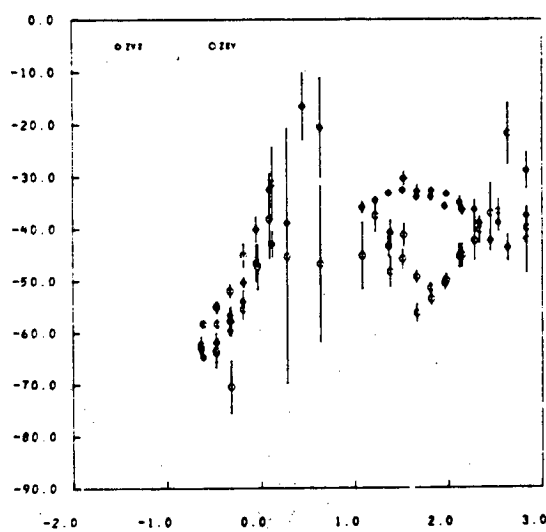
Angle of Impedance Rotation



Log Period

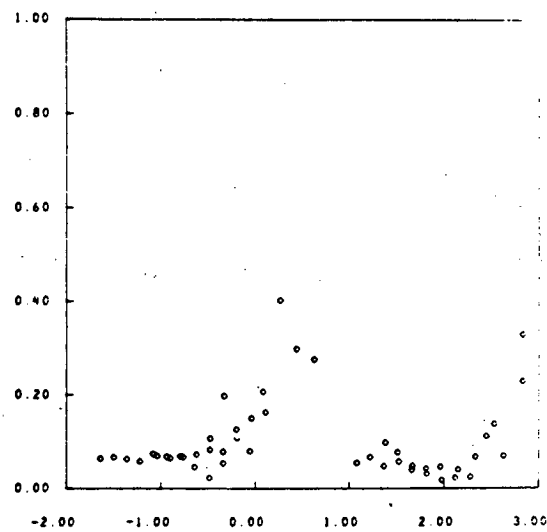
Log Period

Impedance Phase



Log Period

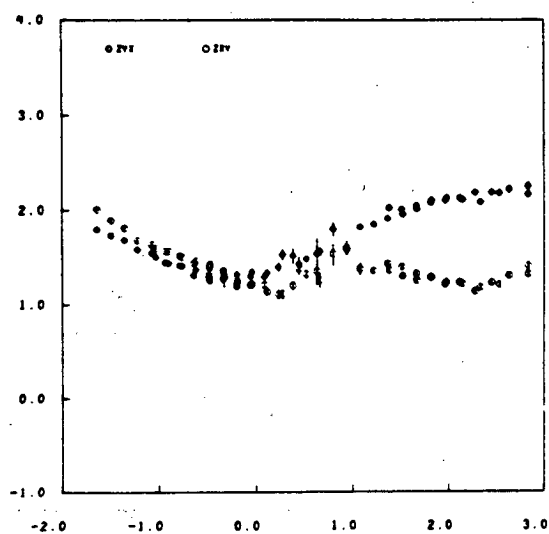
$$Skew = \frac{\left| \frac{Z_{xx} + Z_{yy}}{Z_{xy} - Z_{yx}} \right|}{\left| \frac{Z_{xx} + Z_{yy}}{Z_{xy} - Z_{yx}} \right|}$$



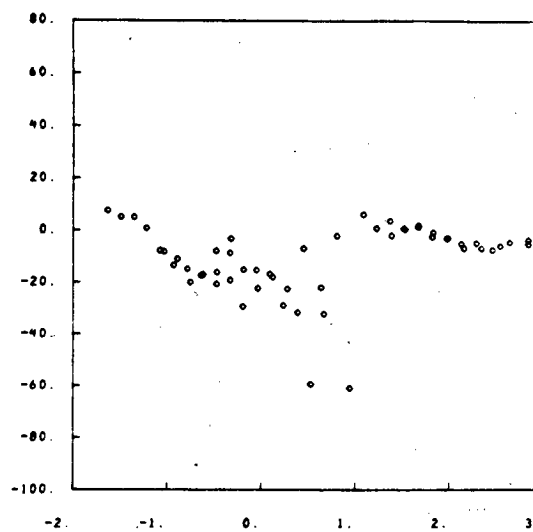
Log Period

## SITE # 2B

Log Apparent Resistivity



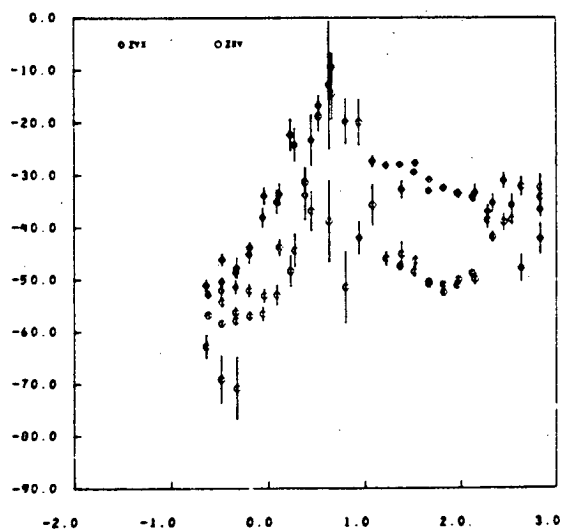
Angle of Impedance Rotation



Log Period

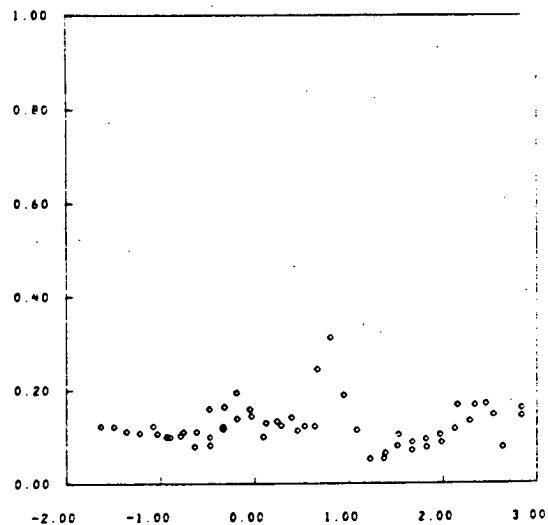
Log Period

Impedance Phase



Log Period

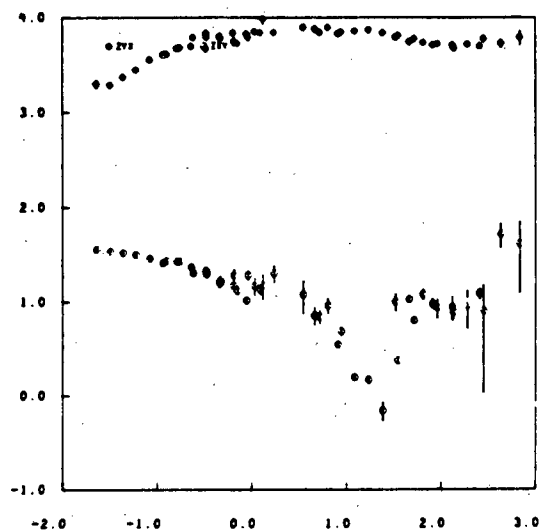
$$Skew = \frac{|(Z_{xx} + Z_{yy})|}{|(Z_{xy} - Z_{yx})|}$$



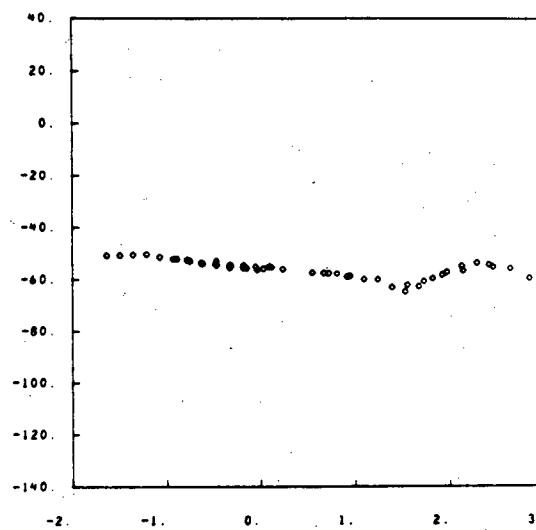
Log Period

## SITE # 3

Log Apparent Resistivity

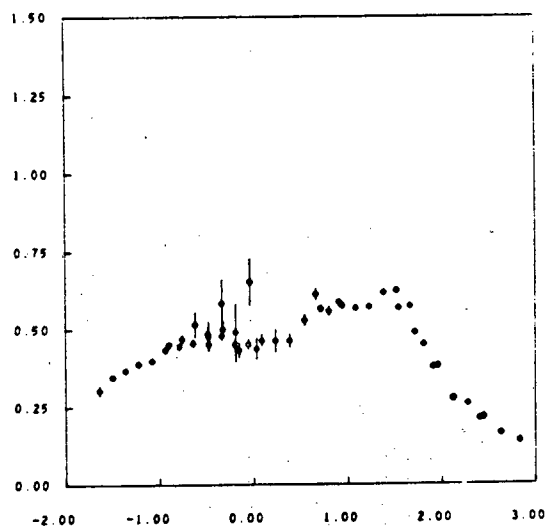


Angle of Impedance Rotation



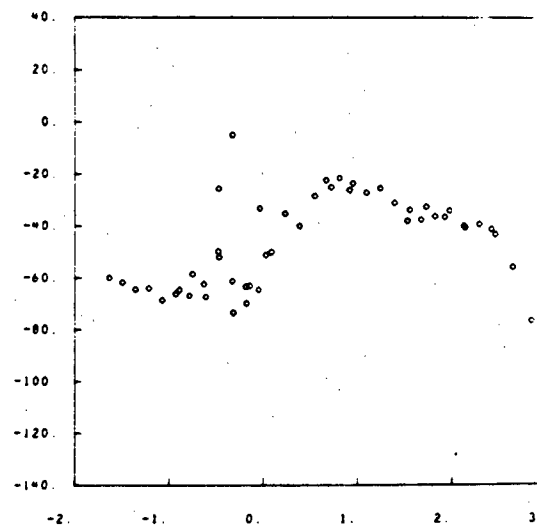
Log Period

Log Period

Tipper Magnitude ( $T_p$ )

Log Period

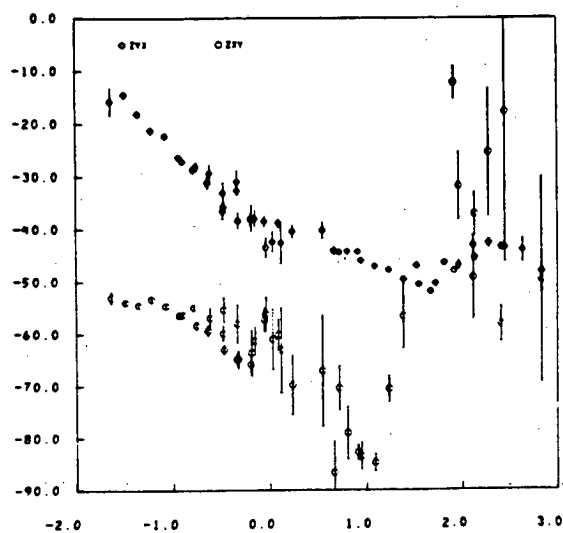
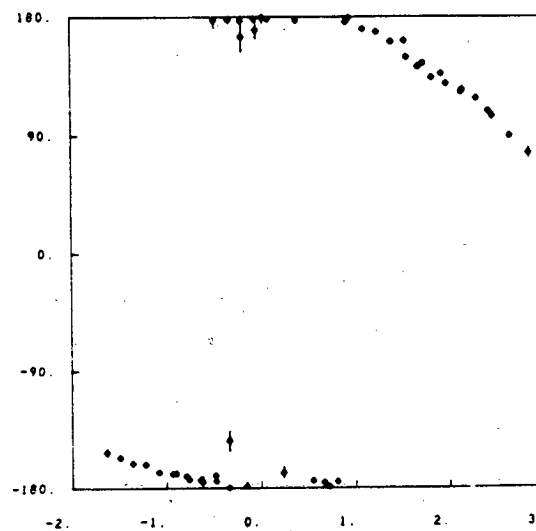
Strike Direction Indicated by Tipper



Log Period

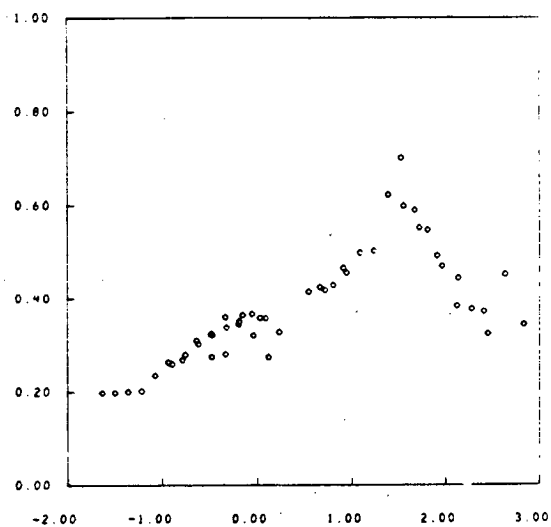
## SITE # 3

Impedance Phase

Tipper Phase ( $T_y$ )

Log Period

Log Period

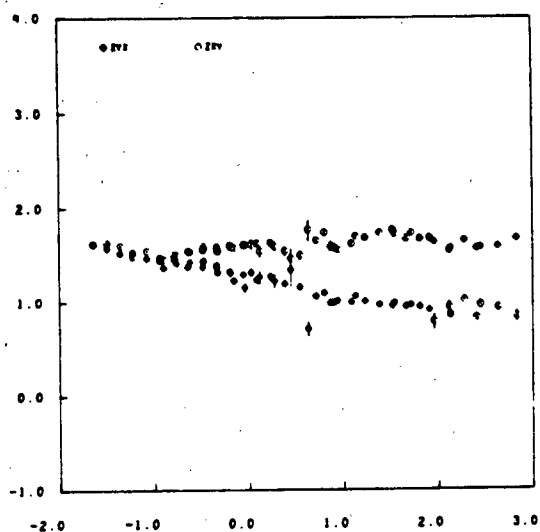


Log Period

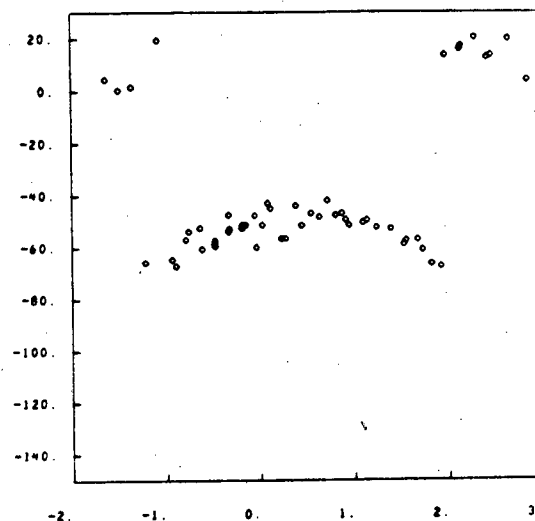
$$Skew = \left| \frac{Z_{xx} + Z_{yy}}{Z_{xy} - Z_{yx}} \right|$$

## SITE # 3A

Log Apparent Resistivity



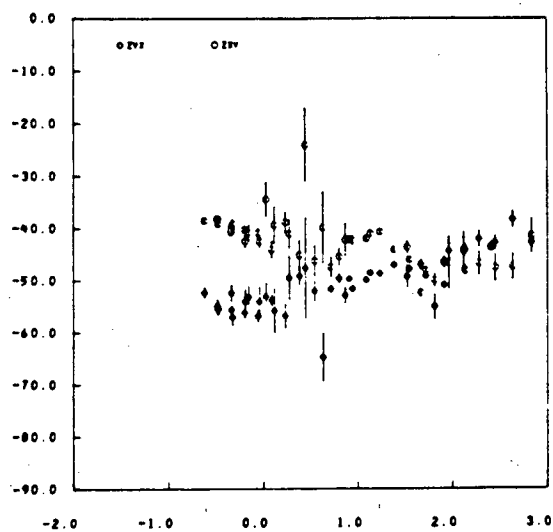
Angle of Impedance Rotation



Log Period

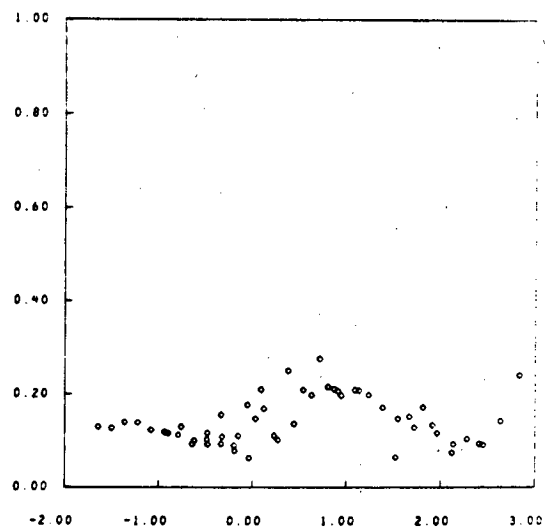
Log Period

Impedance Phase



Log Period

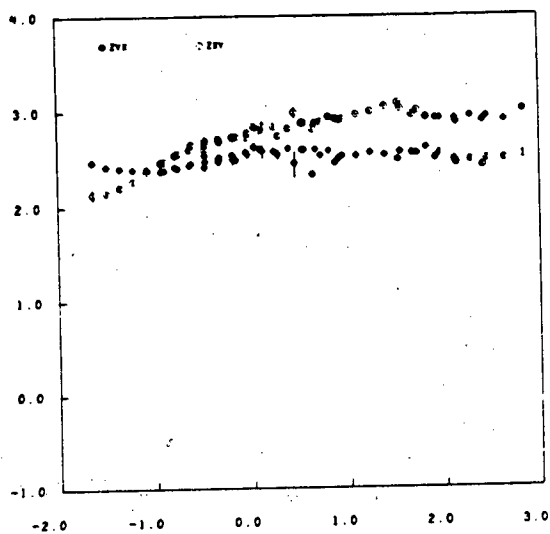
$$Skew = \frac{\left| \frac{Z_{xx} + Z_{yy}}{Z_{xy} - Z_{yx}} \right|}{\left| \frac{Z_{xx} + Z_{yy}}{Z_{xy} - Z_{yx}} \right|}$$



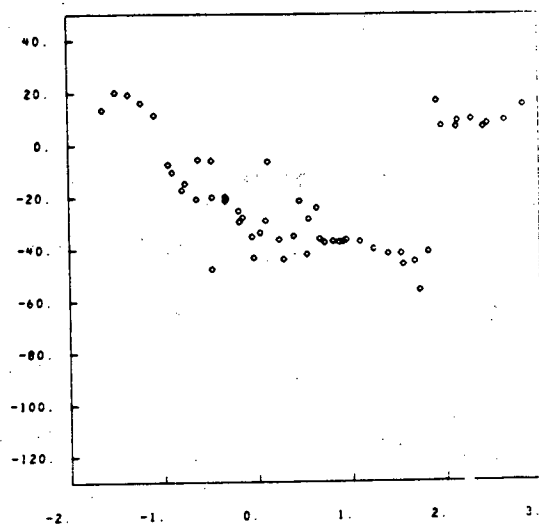
Log Period

## SITE # 3B

Log Apparent Resistivity



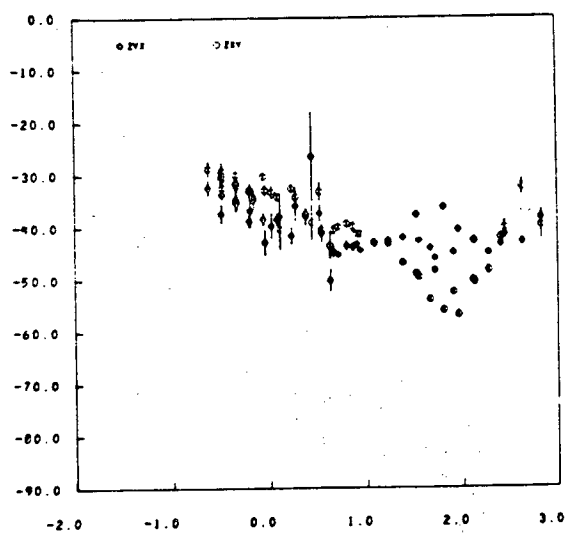
Angle of Impedance Rotation



Log Period

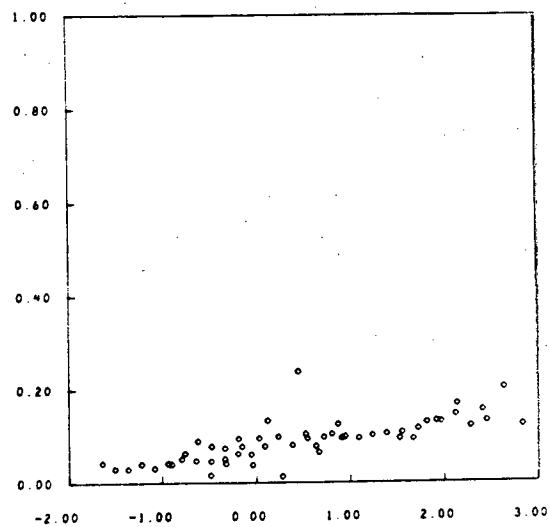
Log Period

Impedance Phase



Log Period

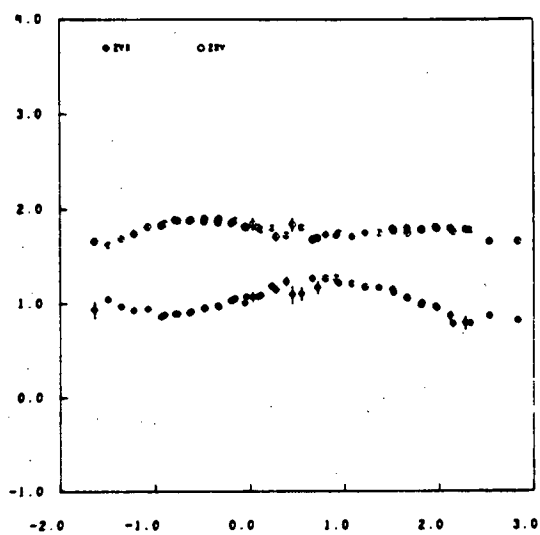
$$Skew = \frac{\left| \frac{Z_{xx} + Z_{yy}}{Z_{xy} - Z_{yx}} \right|}{\left| \frac{Z_{xx} + Z_{yy}}{Z_{xy} - Z_{yx}} \right|}$$



Log Period

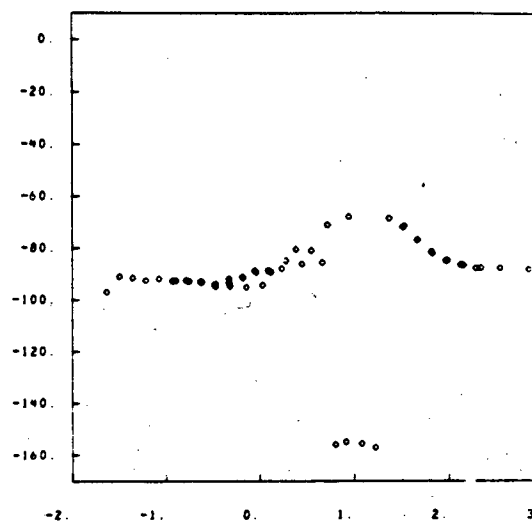
## SITE # 4

Log Apparent Resistivity

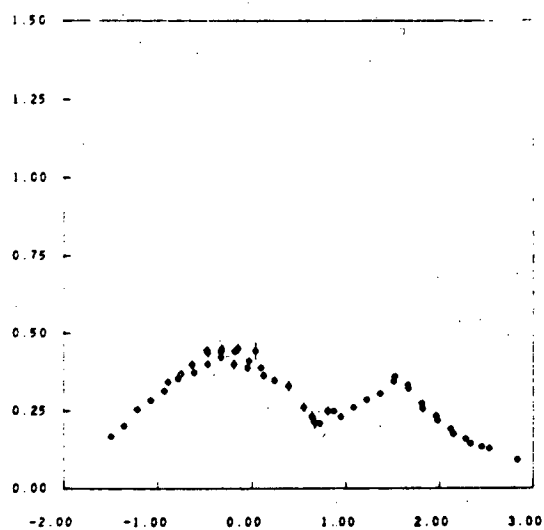


Log Period

Angle of Impedance Rotation

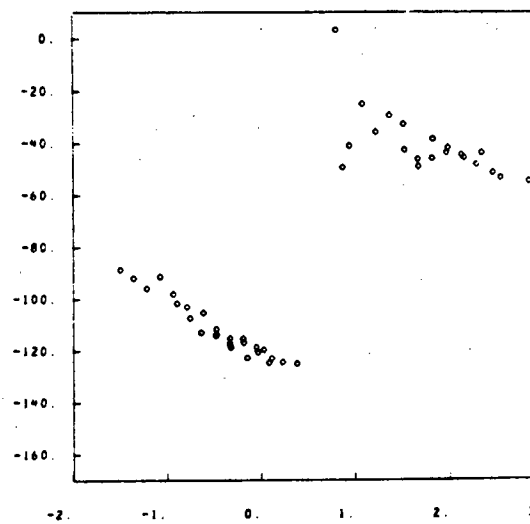


Log Period

Tipper Magnitude ( $T_y$ )

Log Period

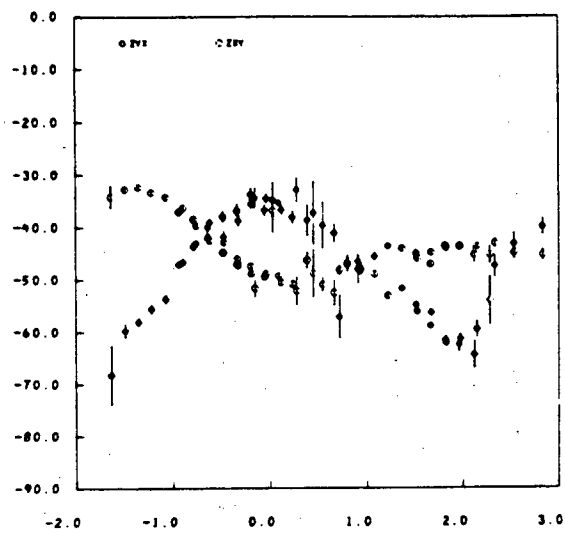
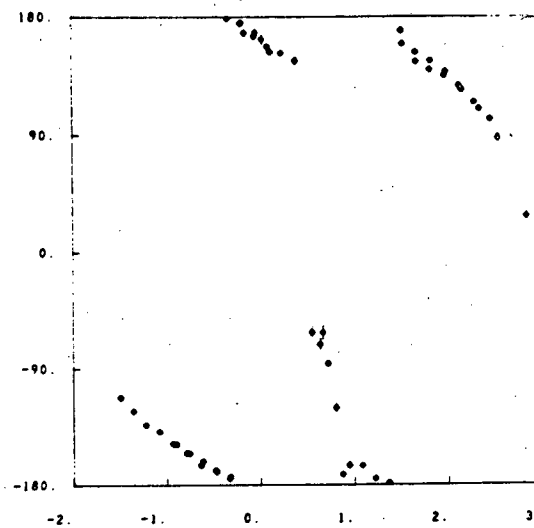
Strike Direction Indicated by Tipper



Log Period

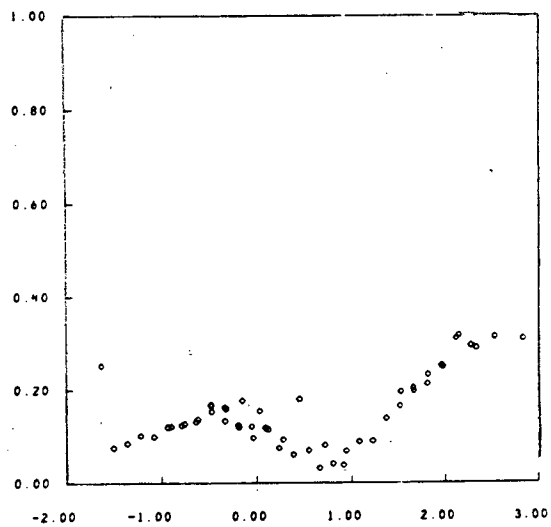
## SITE # 4

Impedance Phase

Tipper Phase ( $T_y$ )

Log Period

Log Period

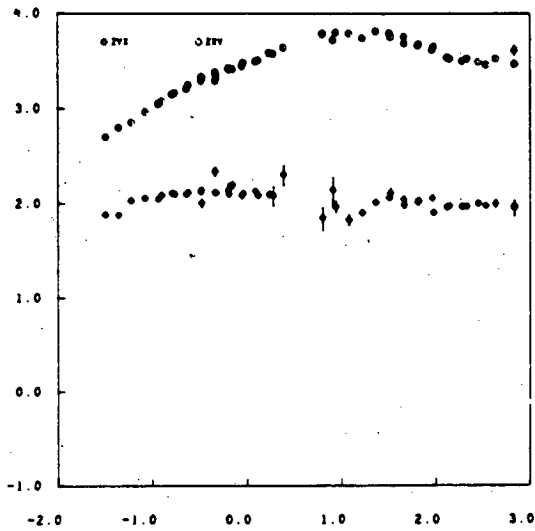


Log Period

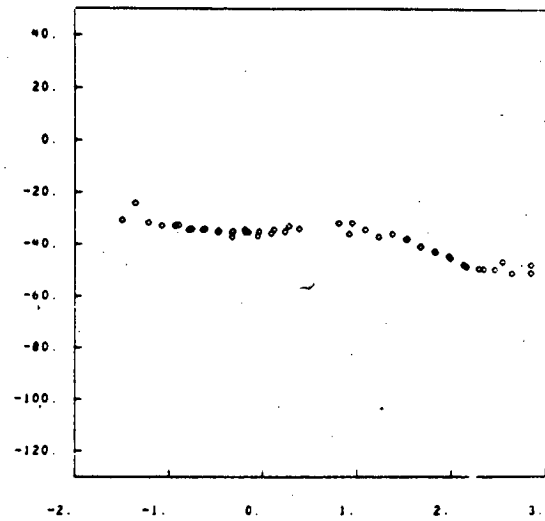
$$Skew = \left| \frac{(Z_{xx} + Z_{yy})}{(Z_{xy} - Z_{yx})} \right|$$

## SITE # 4A

Log Apparent Resistivity



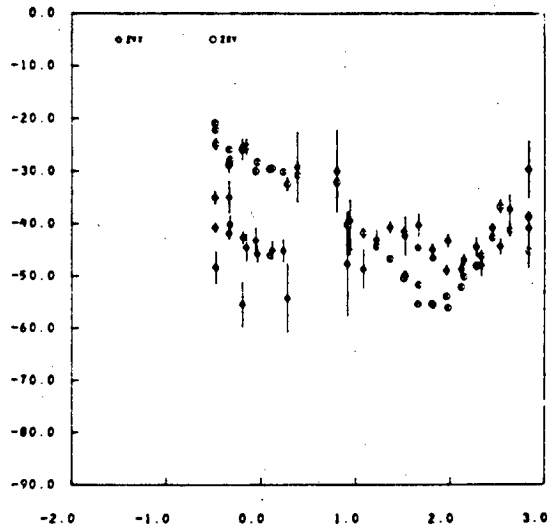
Angle of Impedance Rotation



Log Period

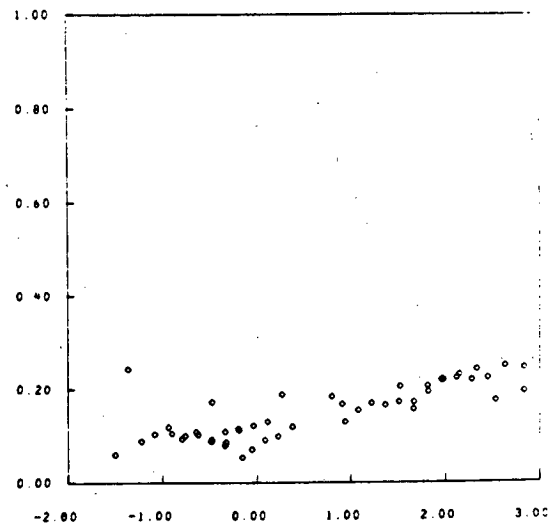
Log Period

Impedance Phase



Log Period

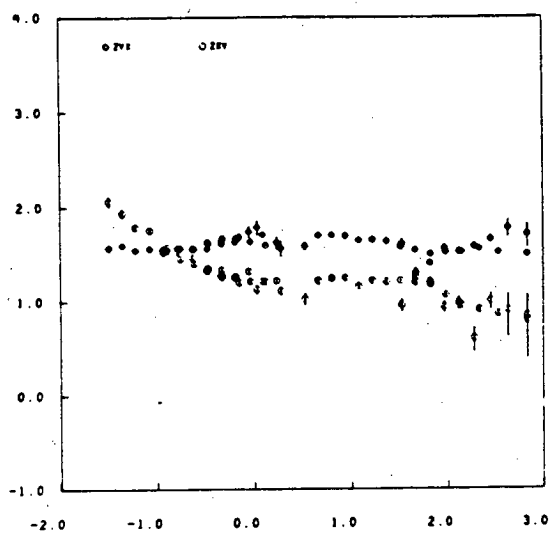
$$Skew = \frac{\left| \frac{Z_{xx} + Z_{yy}}{Z_{xy} - Z_{yx}} \right|}{\left| \frac{Z_{xx} + Z_{yy}}{Z_{xy} - Z_{yx}} \right|}$$



Log Period

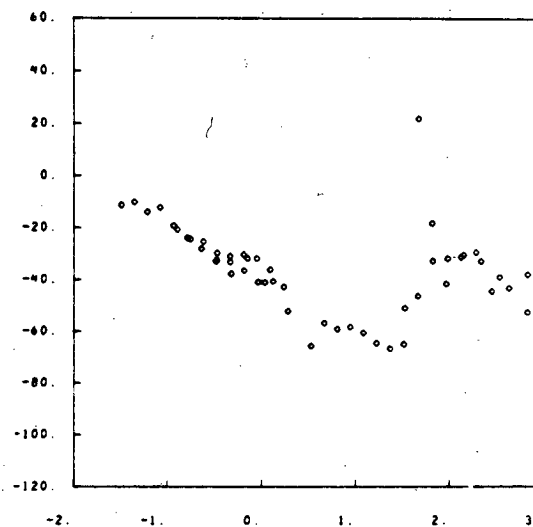
## SITE # 4B

Log Apparent Resistivity



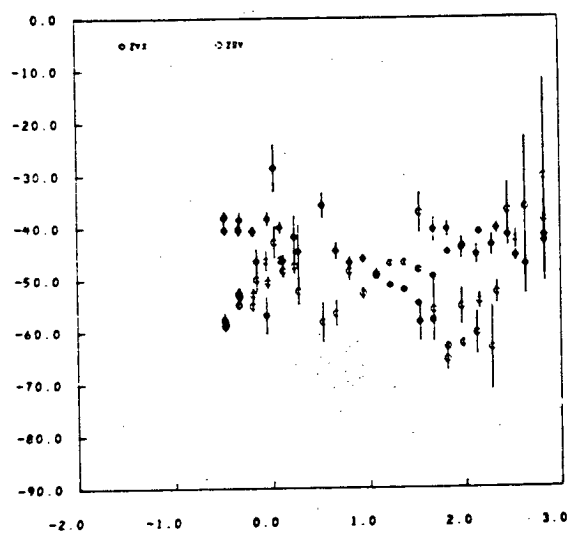
Log Period

Angle of Impedance Rotation



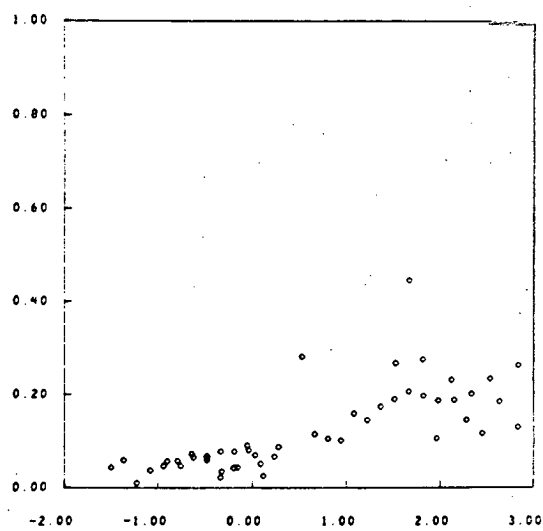
Log Period

Impedance Phase



Log Period

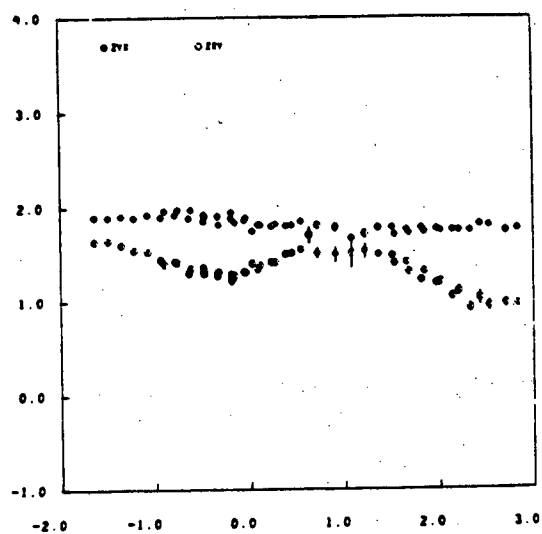
$$Skew = \frac{\left| \frac{Z_{xx} + Z_{yy}}{Z_{xy} - Z_{yx}} \right|}{\left| \frac{Z_{xy} - Z_{yx}}{Z_{xy} - Z_{yx}} \right|}$$



Log Period

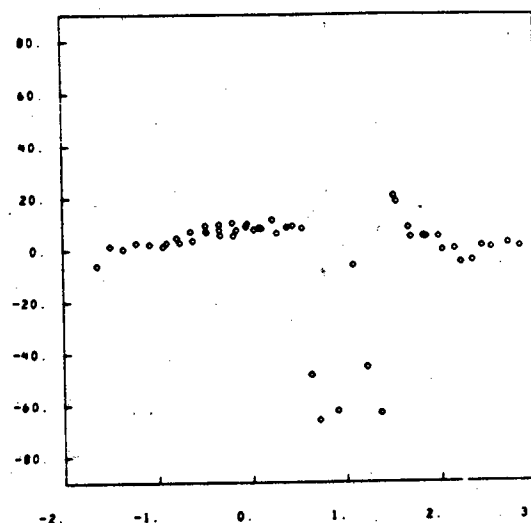
## SITE # 5

Log Apparent Resistivity

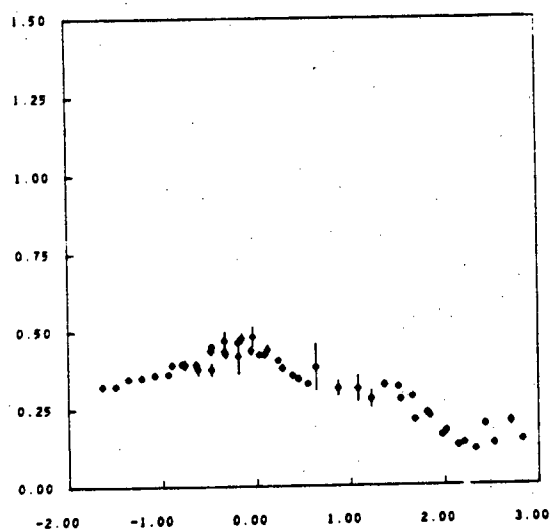


Log Period

Angle of Impedance Rotation

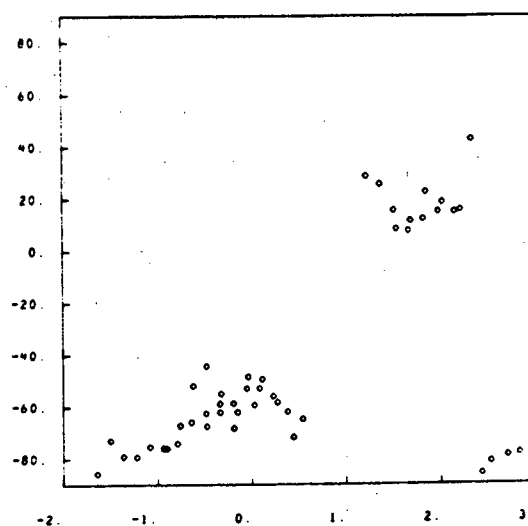


Log Period

Tipper Magnitude ( $T_y$ )

Log Period

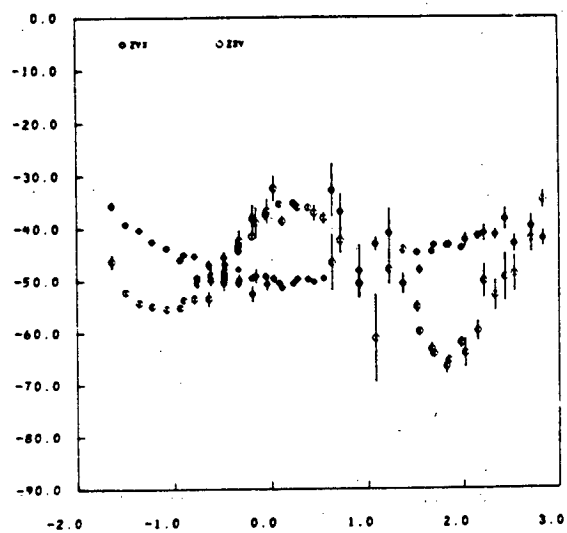
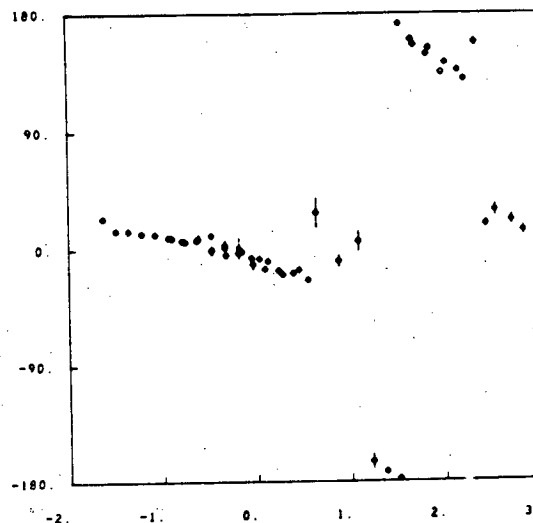
Strike Direction Indicated by Tipper



Log Period

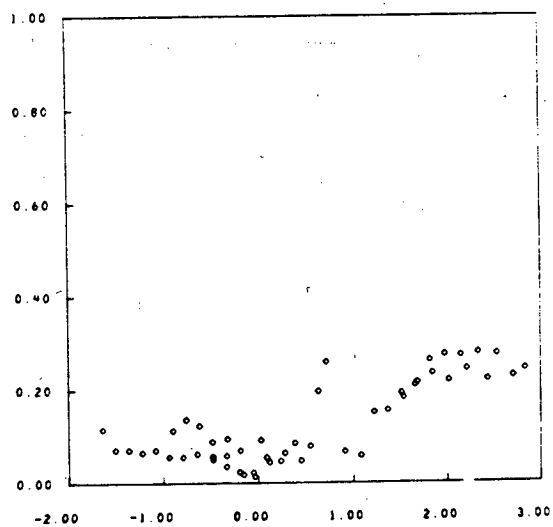
## SITE # 5

Impedance Phase

Tipper Phase ( $T_y$ )

Log Period

Log Period

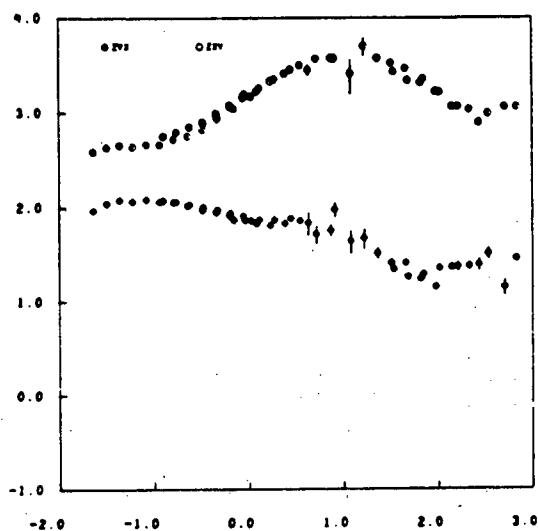


Log Period

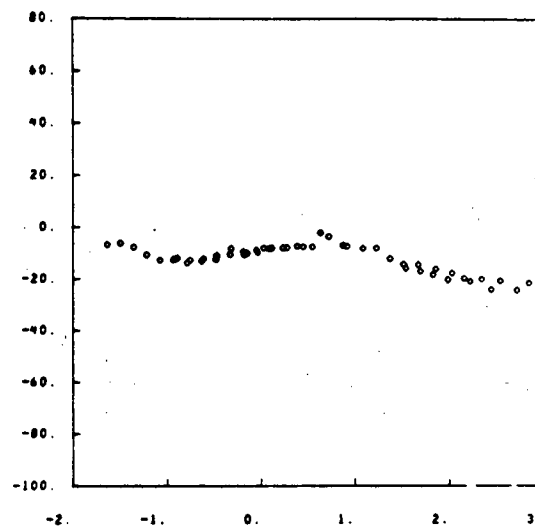
$$Skew = \left| \frac{(Z_{xx} + Z_{yy})}{(Z_{xy} - Z_{yx})} \right|$$

## SITE # 5A

Log Apparent Resistivity



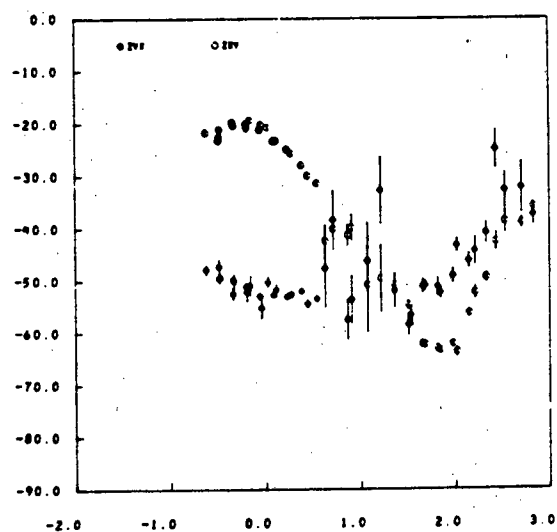
Angle of Impedance Rotation



Log Period

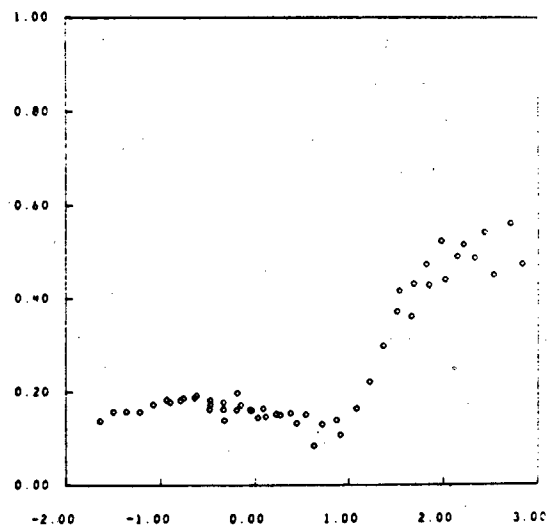
Log Period

Impedance Phase



Log Period

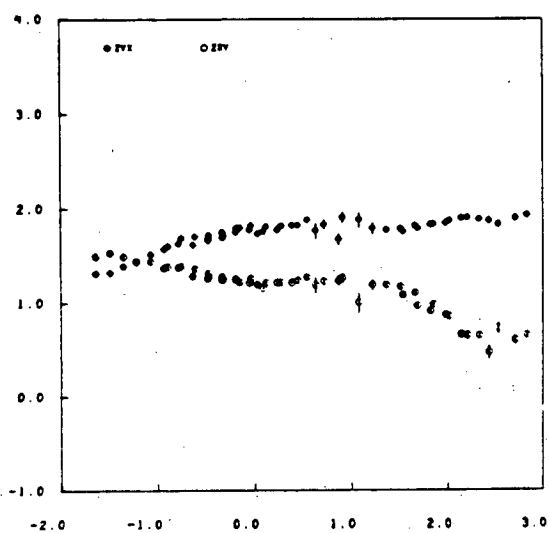
$$Skew = \frac{\left| \frac{Z_{xx} + Z_{yy}}{Z_{xy} - Z_{yx}} \right|}{\left| \frac{Z_{xx} + Z_{yy}}{Z_{xy} - Z_{yx}} \right|}$$



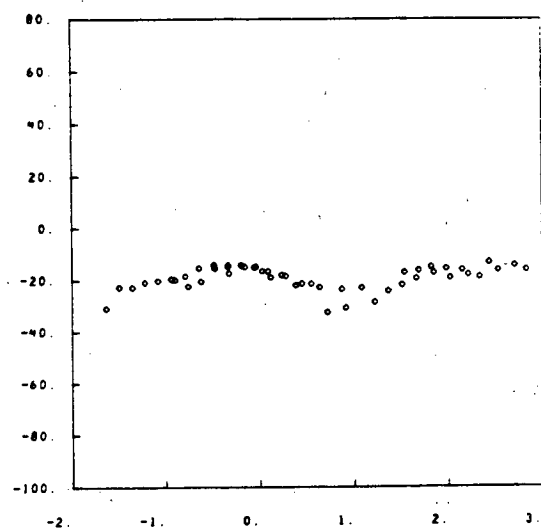
Log Period

## SITE # 5B

Log Apparent Resistivity



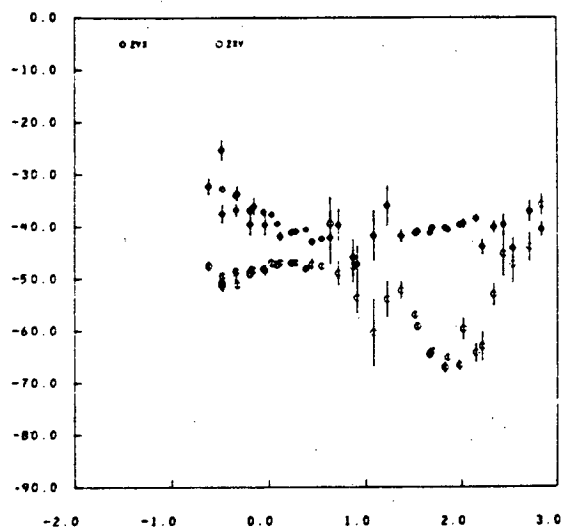
Angle of Impedance Rotation



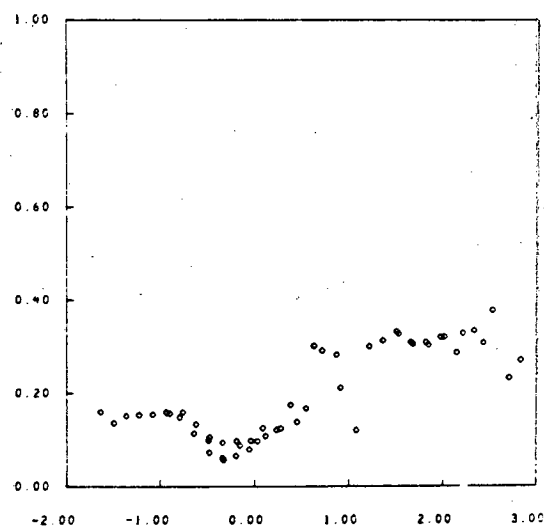
Log Period

Log Period

Impedance Phase



$$Skew = \frac{\left| \frac{Z_{xx} + Z_{yy}}{Z_{xy} - Z_{yx}} \right|}{\left| \frac{Z_{xx} + Z_{yy}}{Z_{xy} - Z_{yx}} \right|}$$

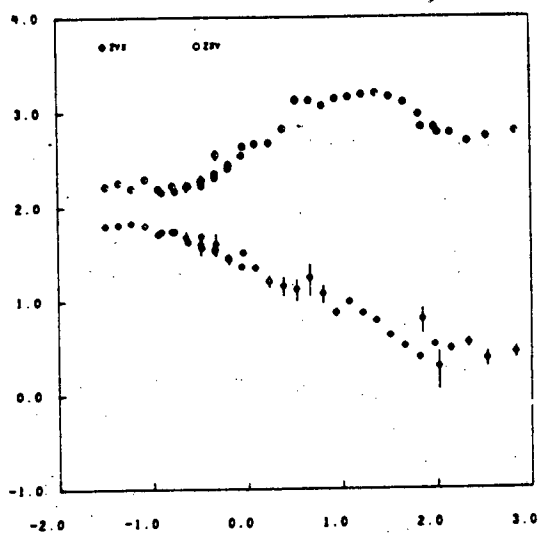


Log Period

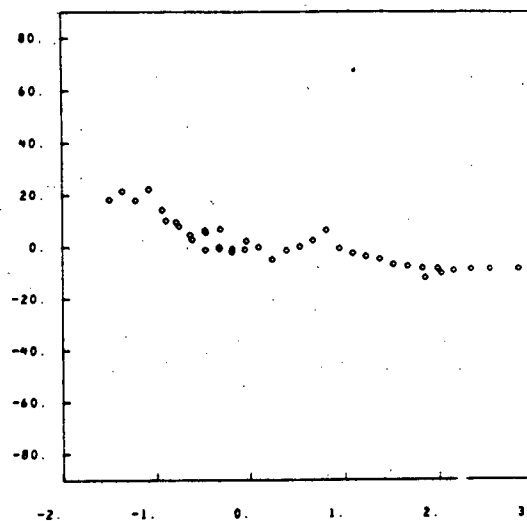
Log Period

## SITE # 6

Log Apparent Resistivity

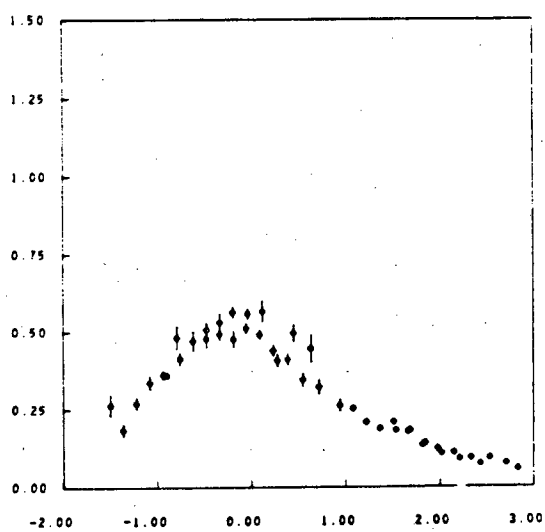


Angle of Impedance Rotation



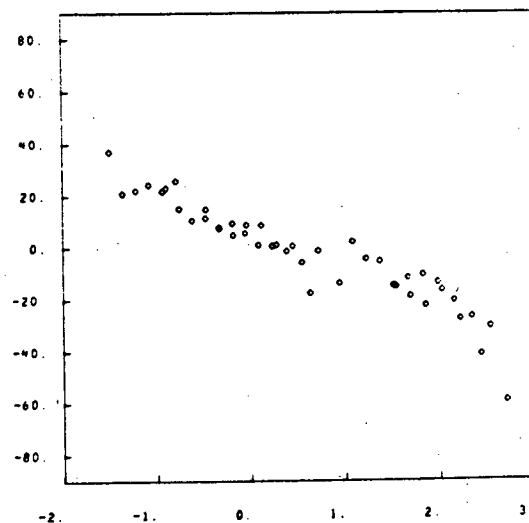
Log Period

Log Period

Tipper Magnitude ( $T_y$ )

Log Period

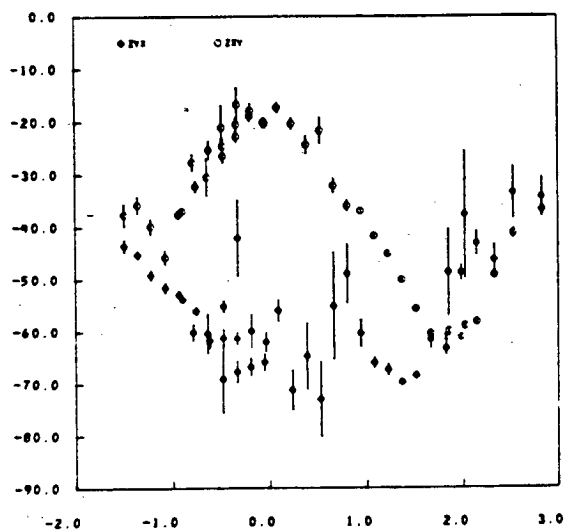
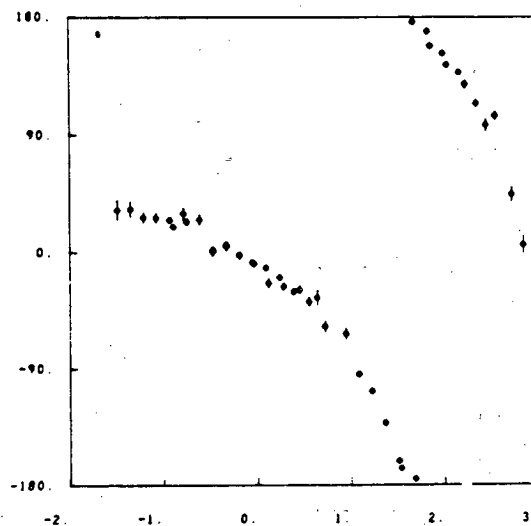
Strike Direction Indicated by Tipper



Log Period

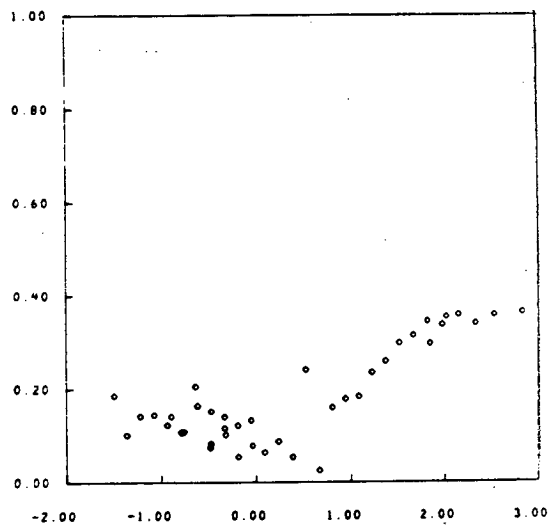
## SITE # 6

Impedance Phase

Tipper Phase ( $T_y$ )

Log Period

Log Period

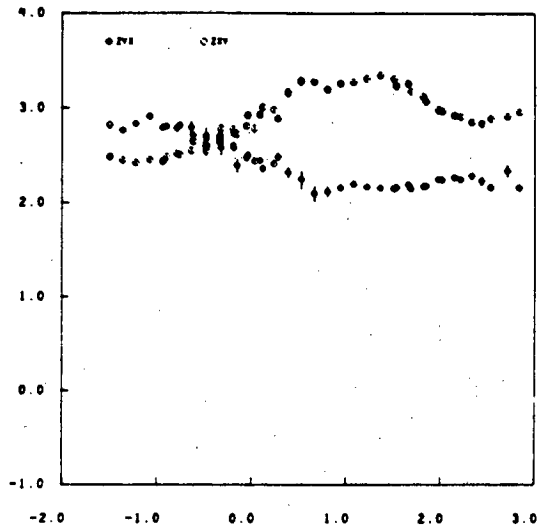


Log Period

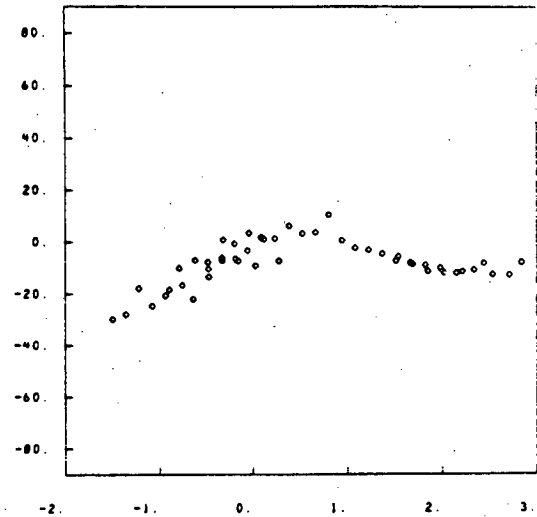
$$Skew = \left| \frac{(Z_{xx} + Z_{yy})}{(Z_{xy} - Z_{yx})} \right|$$

## SITE # 6B

Log Apparent Resistivity



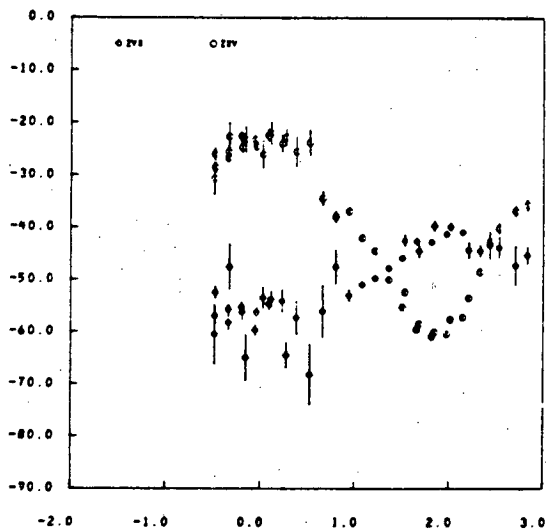
Angle of Impedance Rotation



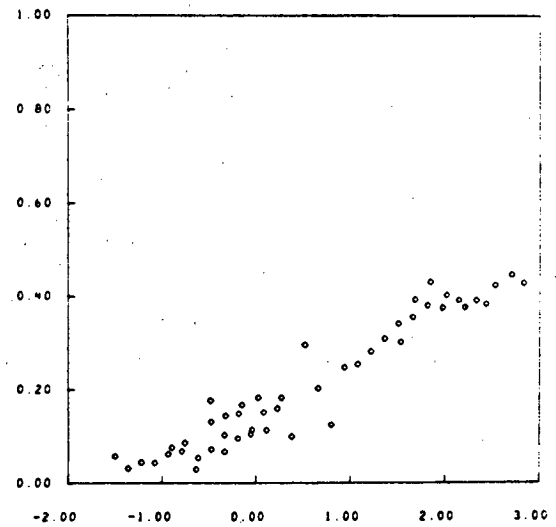
Log Period

Log Period

Impedance Phase



$$Skew = \frac{\left| \frac{Z_{xx} + Z_{yy}}{Z_{xy} - Z_{yx}} \right|}{\left| \frac{Z_{xx} + Z_{yy}}{Z_{xy} - Z_{yx}} \right|}$$

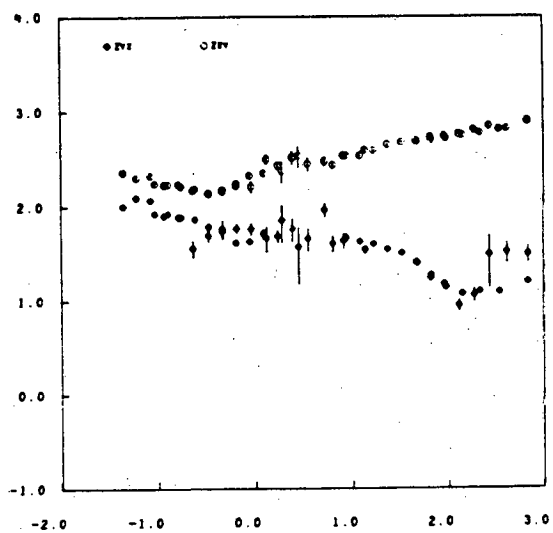


Log Period

Log Period

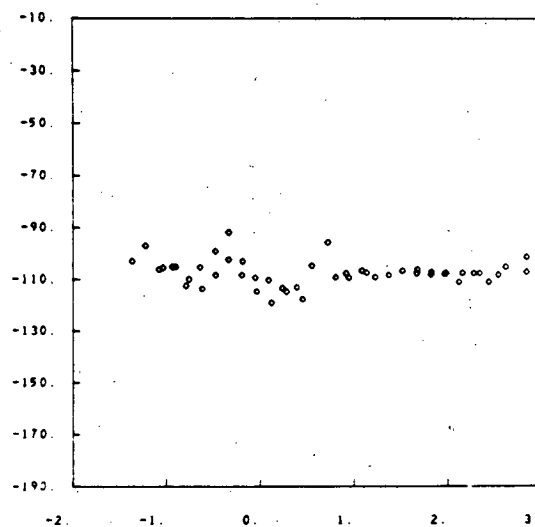
## SITE # 7

Log Apparent Resistivity

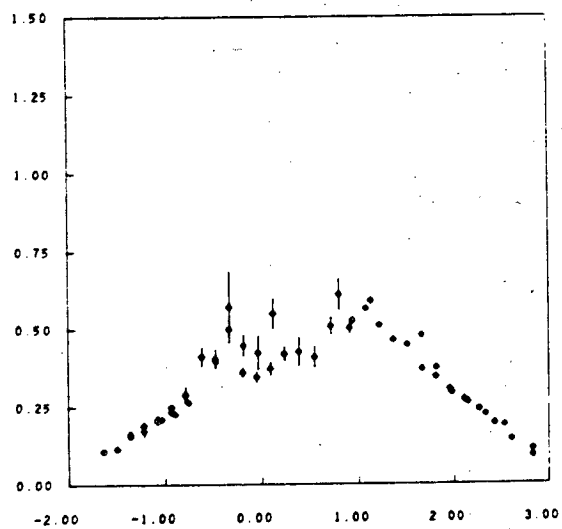


Log Period

Angle of Impedance Rotation

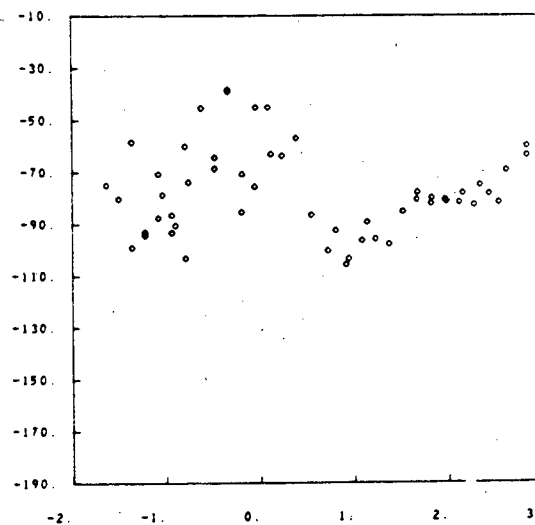


Log Period

Tipper Magnitude ( $T_y$ )

Log Period

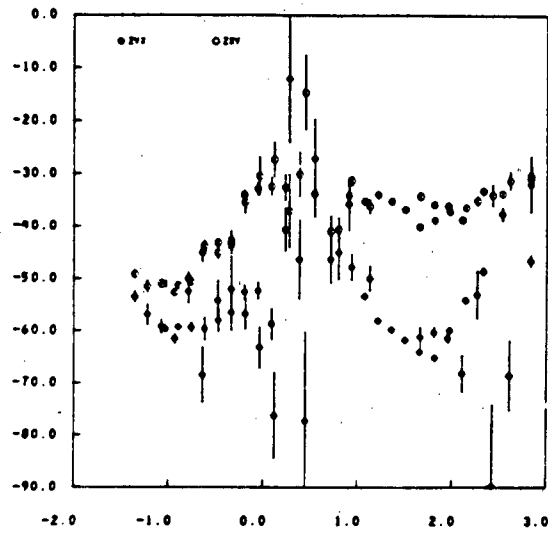
Strike Direction Indicated by Tipper



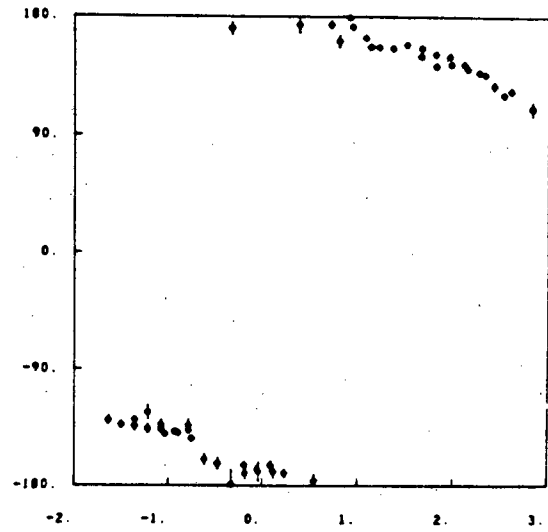
Log Period

## SITE # 7

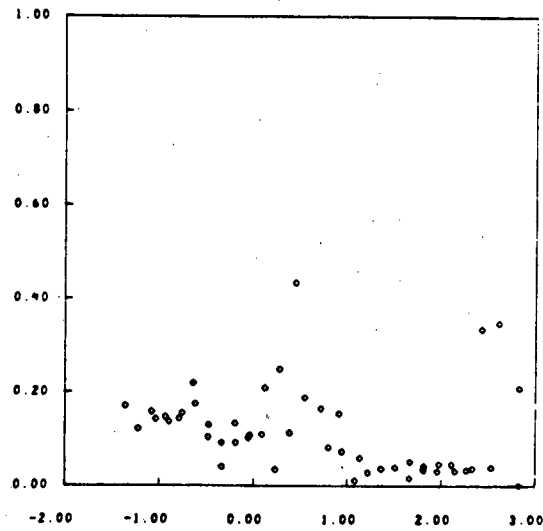
Impedance Phase



Log Period

Tipper Phase ( $T_y$ )

Log Period

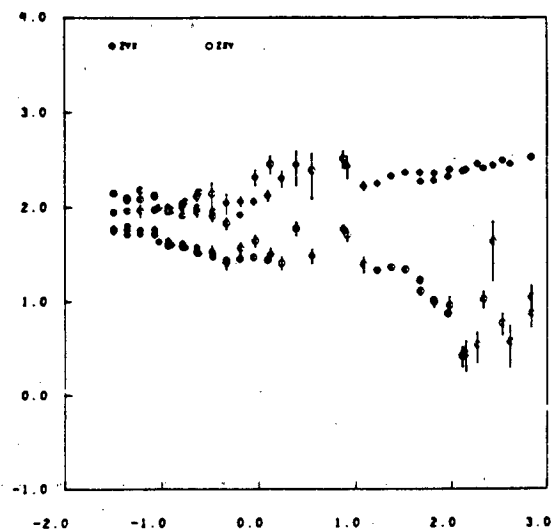


Log Period

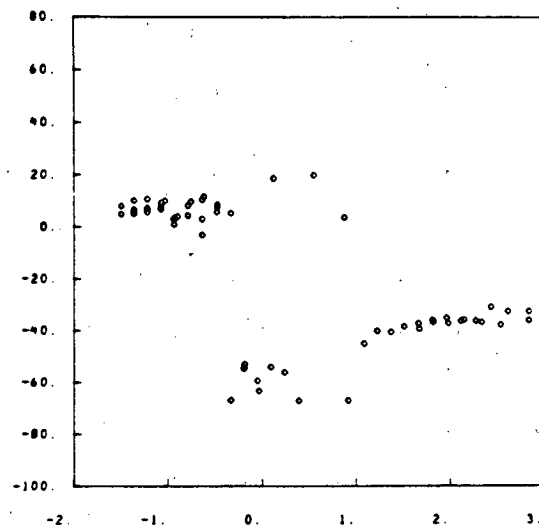
$$Skew = \left| \frac{(Z_{xx} + Z_{yy})}{(Z_{xy} - Z_{yx})} \right|$$

## SITE # 7A

Log Apparent Resistivity



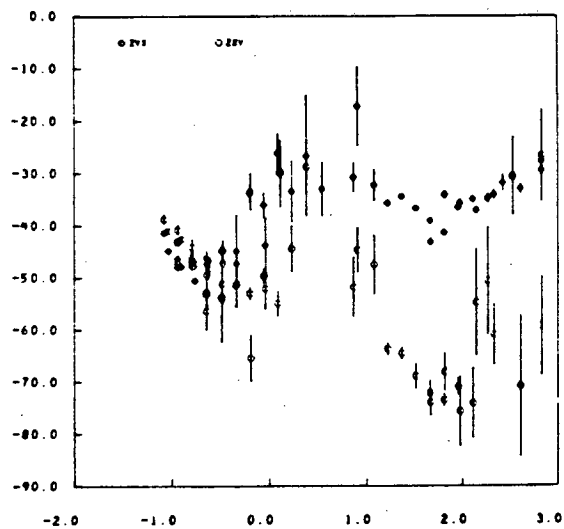
Angle of Impedance Rotation



Log Period

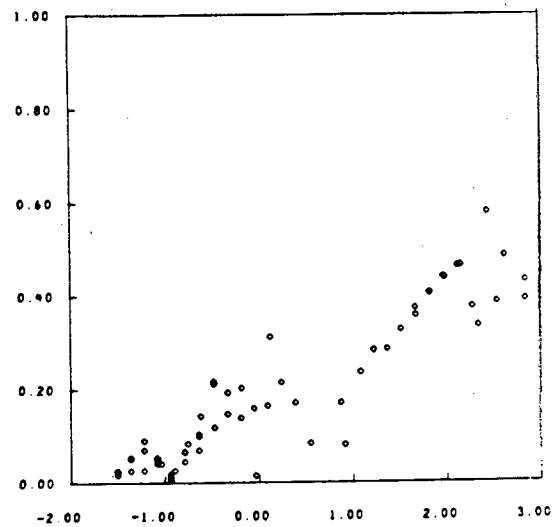
Log Period

Impedance Phase



Log Period

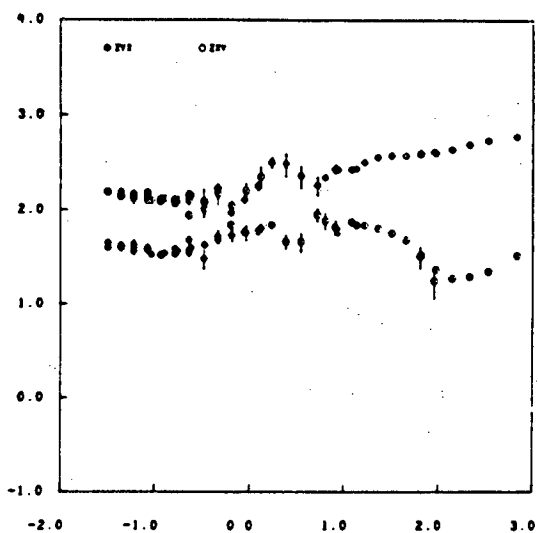
$$Skew = \frac{\left| \frac{Z_{xx} + Z_{yy}}{Z_{xy} - Z_{yx}} \right|}{\left| \frac{Z_{xx} + Z_{yy}}{Z_{xy} - Z_{yx}} \right|}$$



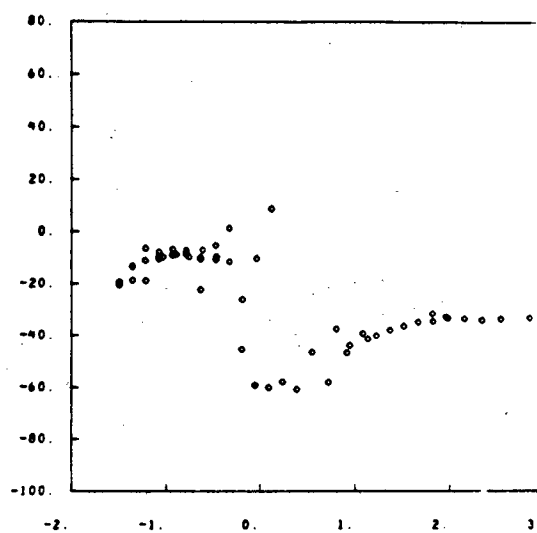
Log Period

## SITE # 7B

Log Apparent Resistivity



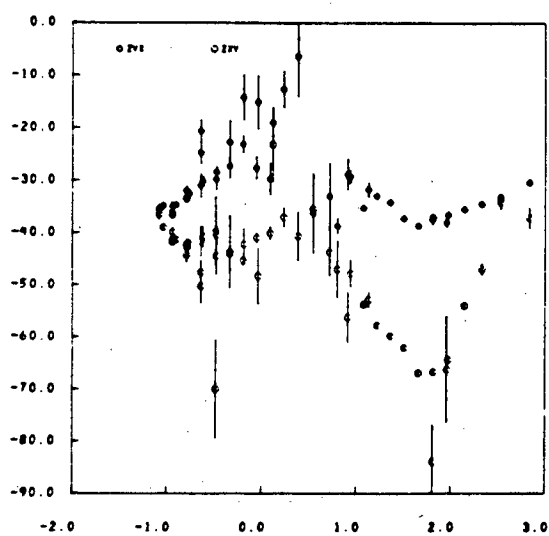
Angle of Impedance Rotation



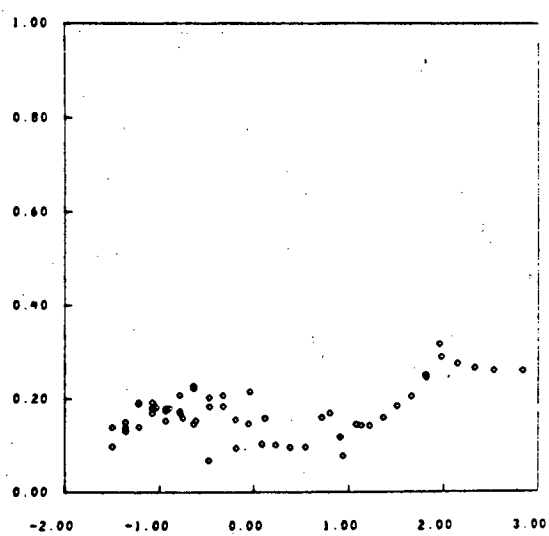
Log Period

Log Period

Impedance Phase



$$\text{Skew} = \frac{\left| \frac{Z_{xx} + Z_{yy}}{Z_{xy} - Z_{yx}} \right|}{\left| \frac{Z_{xx} + Z_{yy}}{Z_{xy} - Z_{yx}} \right|}$$

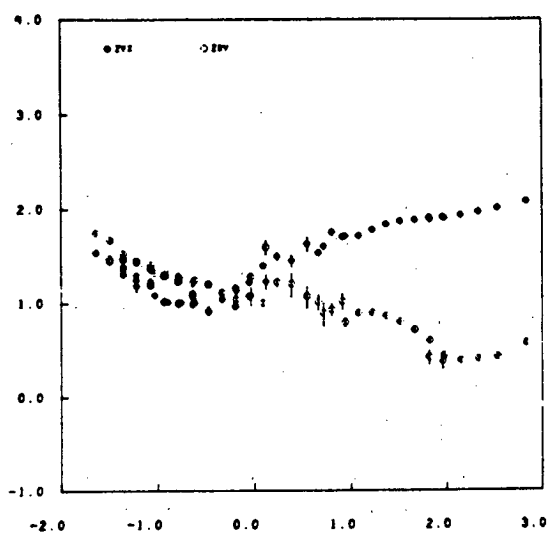


Log Period

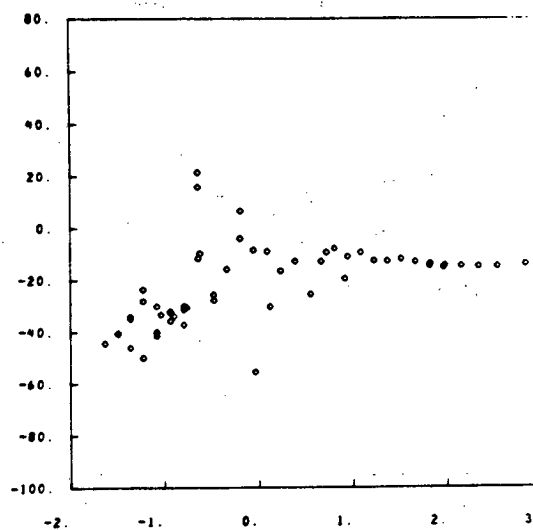
Log Period

## SITE # 7C

Log Apparent Resistivity



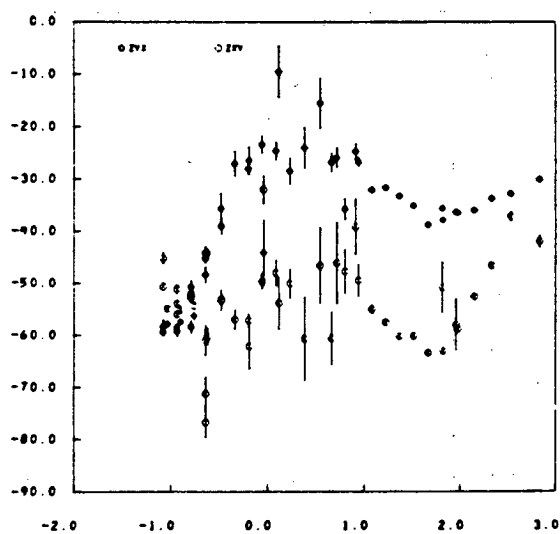
Angle of Impedance Rotation



Log Period

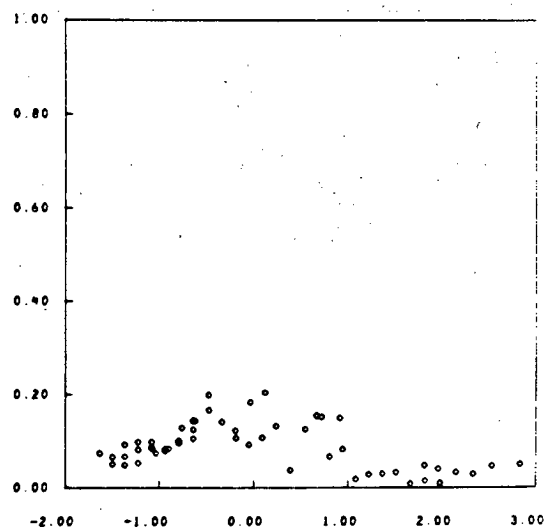
Log Period

Impedance Phase



Log Period

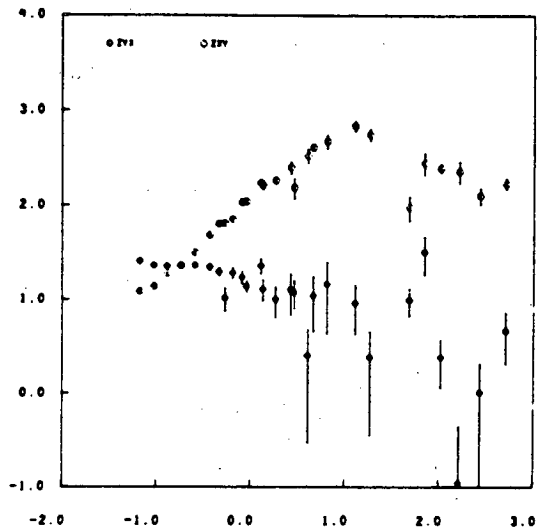
$$Skew = \frac{\left| \begin{matrix} Z_{xx} + Z_{yy} \\ Z_{xy} - Z_{yx} \end{matrix} \right|}{\left| \begin{matrix} Z_{xx} + Z_{yy} \\ Z_{xy} - Z_{yx} \end{matrix} \right|}$$



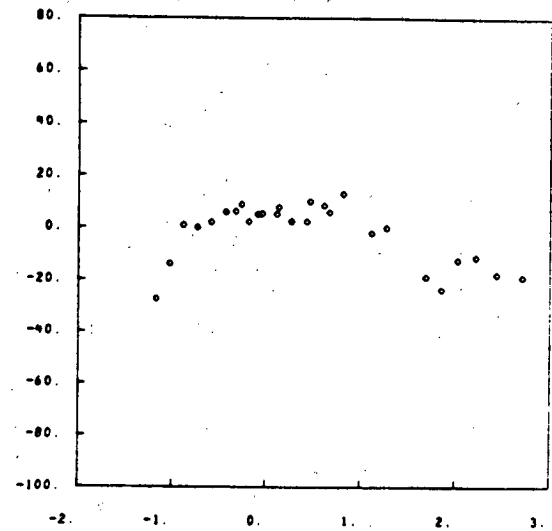
Log Period

## SITE # 11

Log Apparent Resistivity

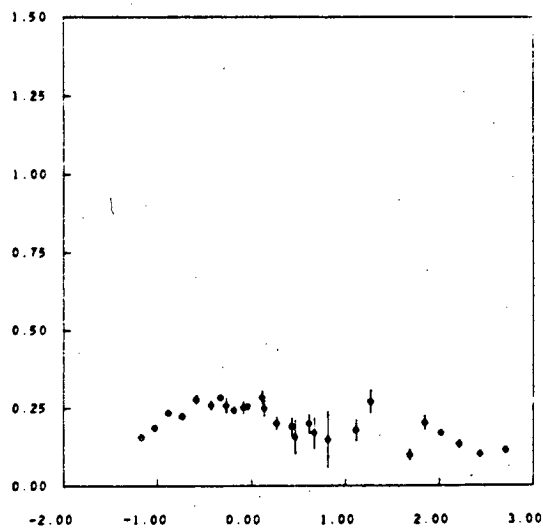


Angle of Impedance Rotation

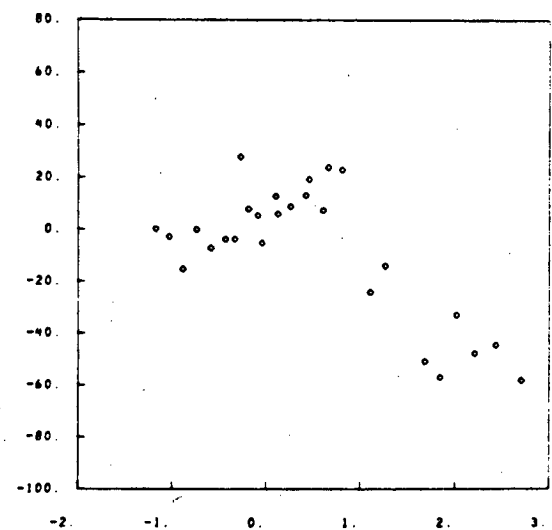


Log Period

Log Period

Tipper Magnitude ( $T_y$ )

Strike Direction Indicated by Tipper

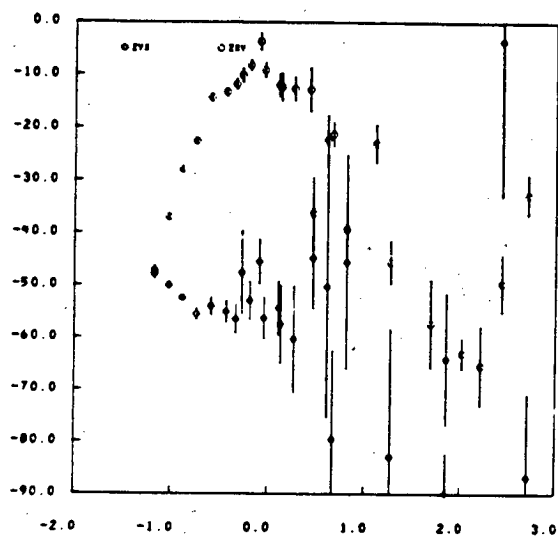
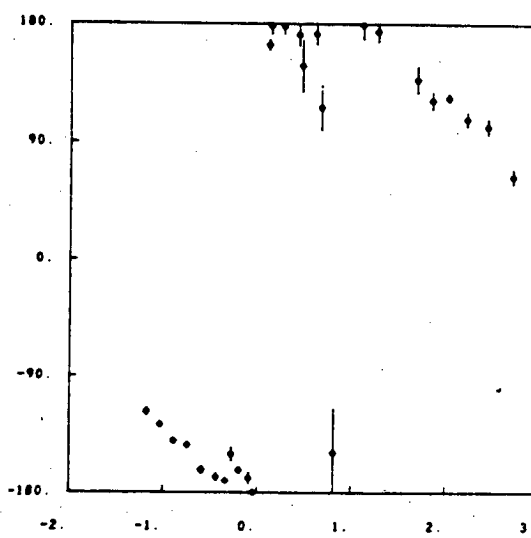


Log Period

Log Period

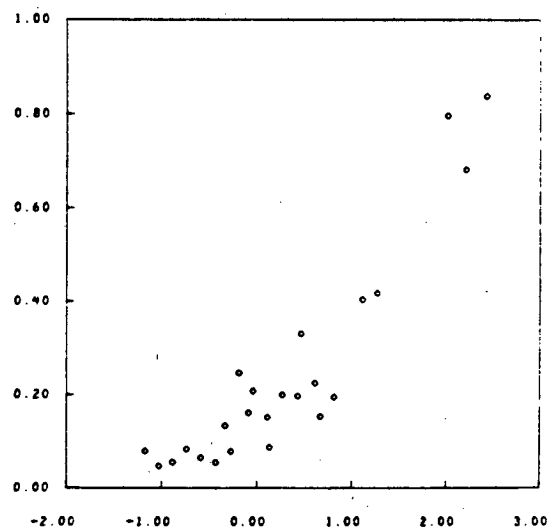
## SITE # 11

Impedance Phase

Tipper Phase ( $T_y$ )

Log Period

Log Period

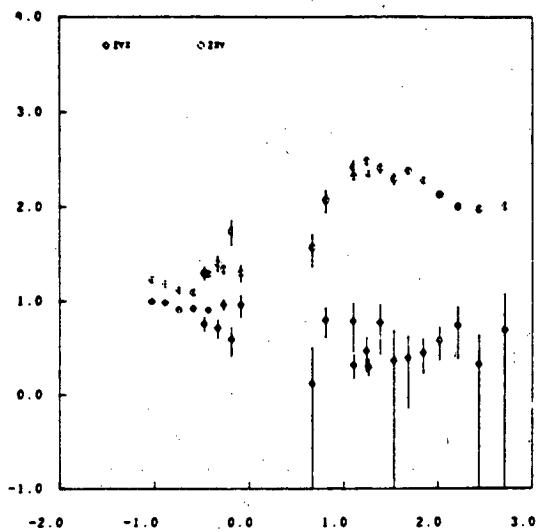


Log Period

$$Skew = \left| \frac{(Z_{xx} + Z_{yy})}{(Z_{xy} - Z_{yx})} \right|$$

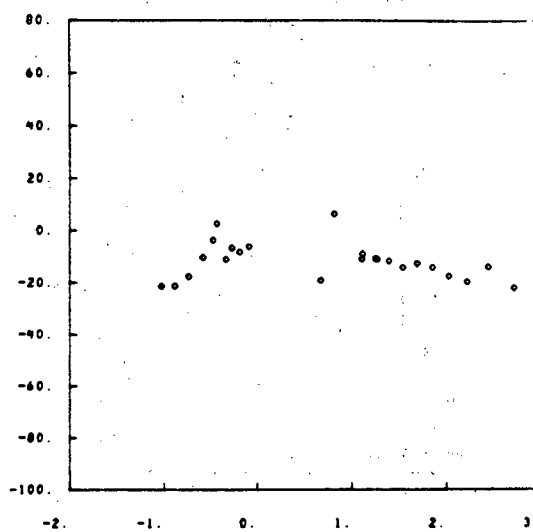
## SITE # 13

Log Apparent Resistivity

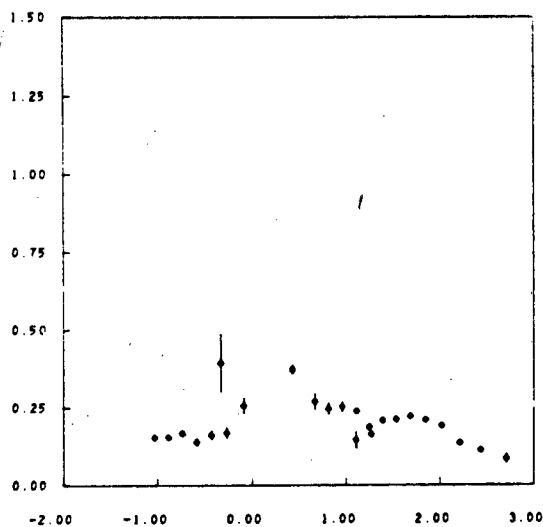


Log Period

Angle of Impedance Rotation

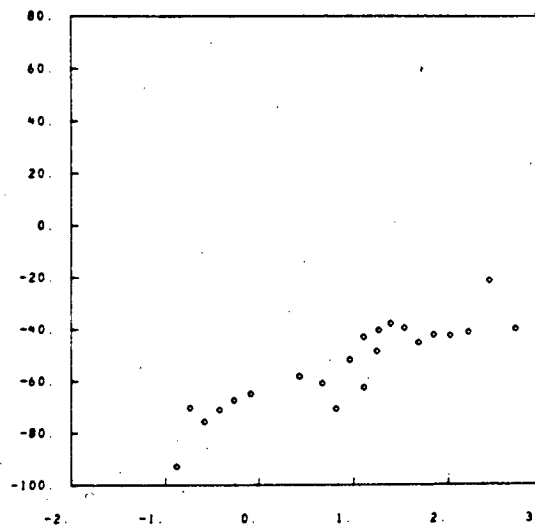


Log Period

Tipper Magnitude ( $T_y$ )

Log Period

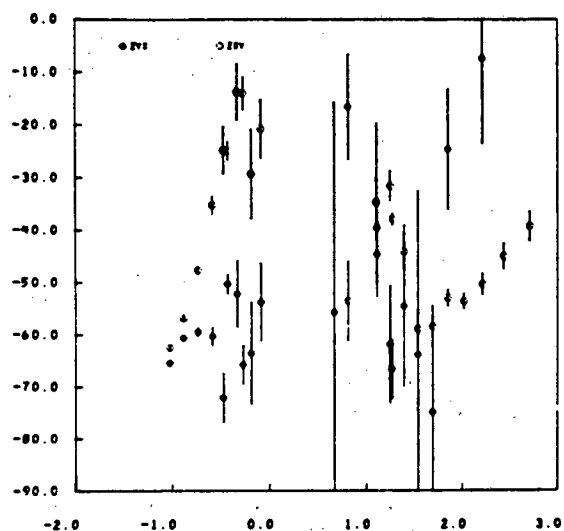
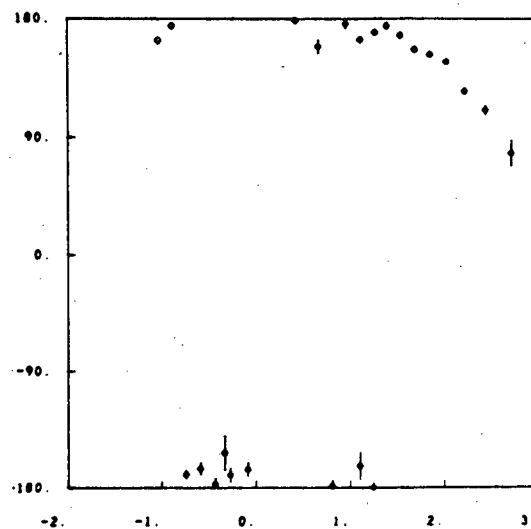
Strike Direction Indicated by Tipper



Log Period

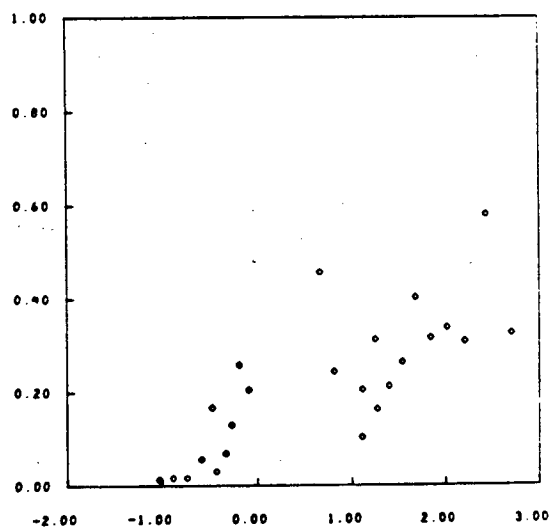
## SITE # 13

Impedance Phase

Tipper Phase ( $T_y$ )

Log Period

Log Period

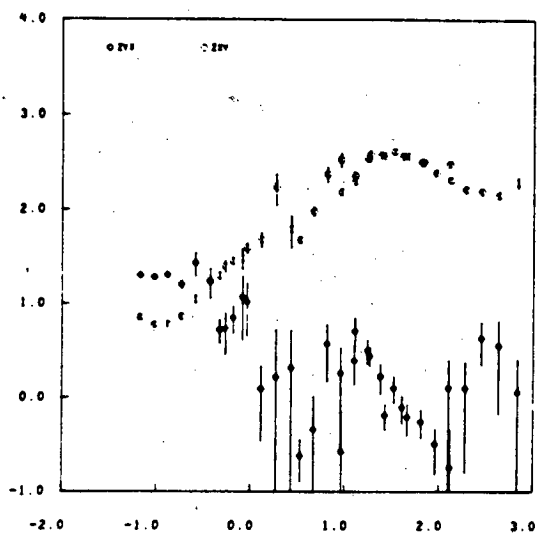


Log Period

$$Skew = \frac{\left| \begin{matrix} Z_{xx} + Z_{yy} \end{matrix} \right|}{\left| \begin{matrix} Z_{xy} - Z_{yx} \end{matrix} \right|}$$

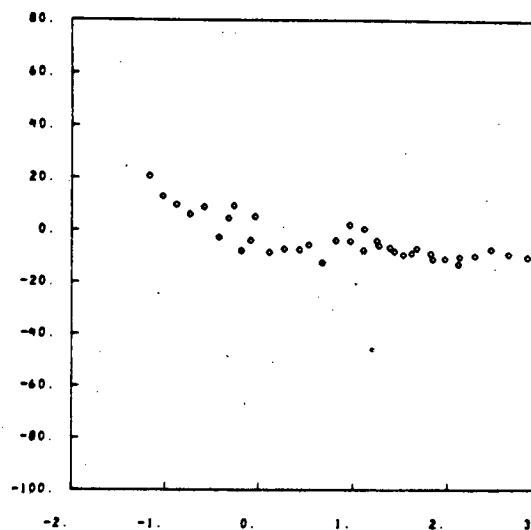
## SITE # 14

Log Apparent Resistivity

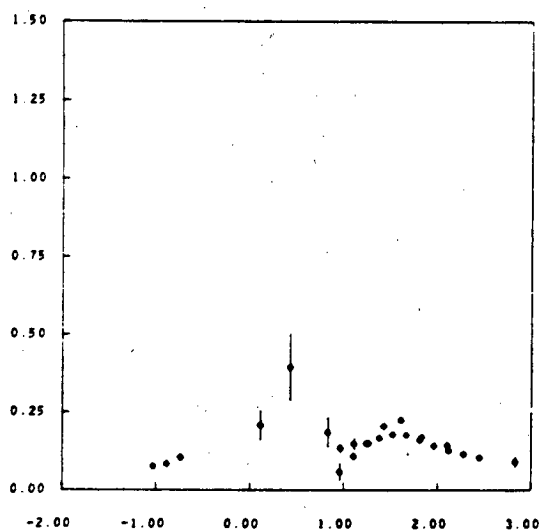


Log Period

Angle of Impedance Rotation

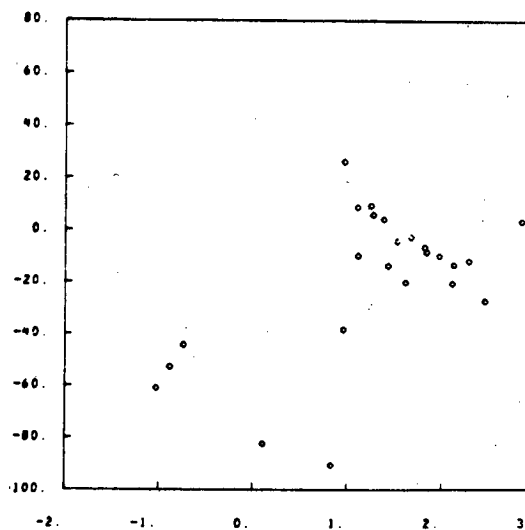


Log Period

Tipper Magnitude ( $T_y$ )

Log Period

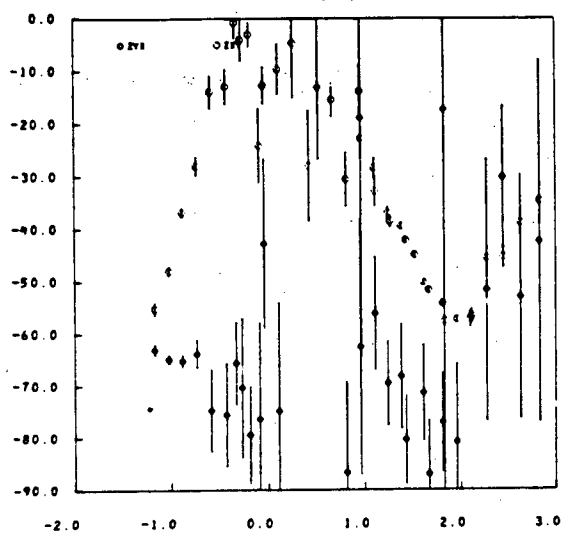
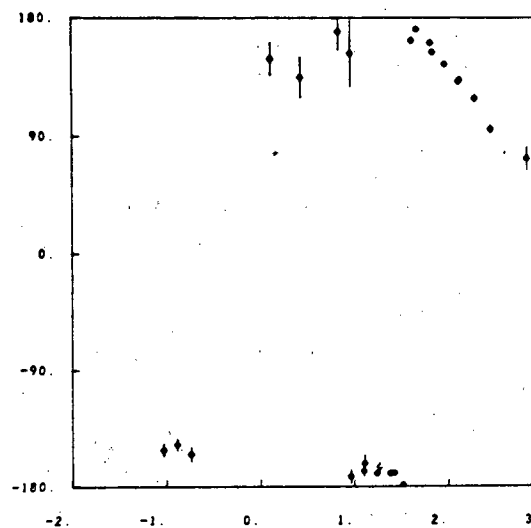
Strike Direction Indicated by Tipper



Log Period

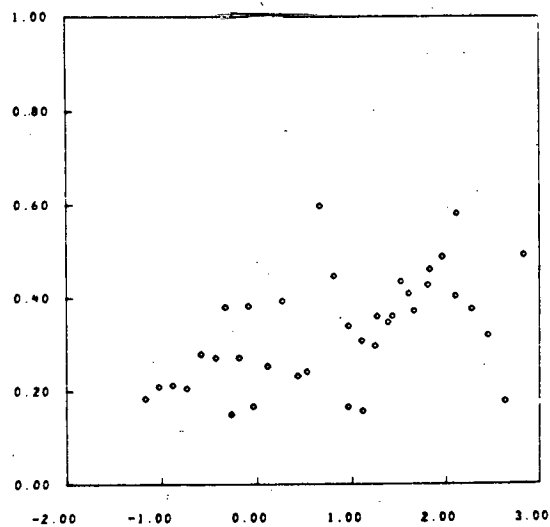
## SITE # 14

Impedance Phase

Tipper Phase ( $T_y$ )

Log Period

Log Period

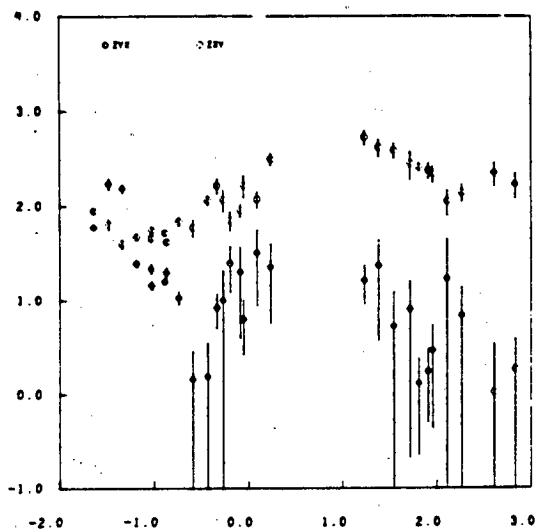


Log Period

$$Skew = \left| \frac{(Z_{xx} + Z_{yy})}{(Z_{xy} - Z_{yx})} \right|$$

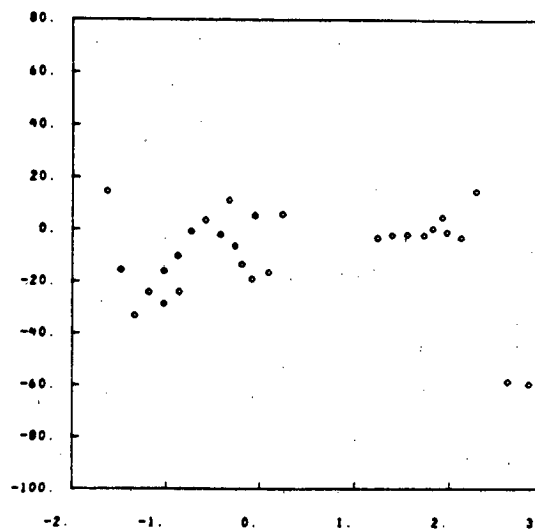
## SITE # 15A

Log Apparent Resistivity



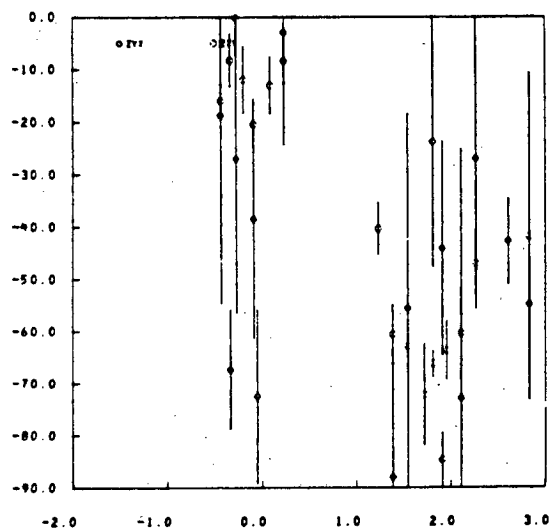
Log Period

Angle of Impedance Rotation



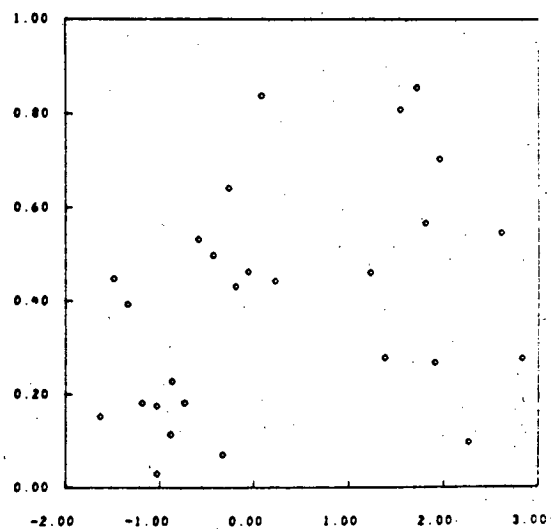
Log Period

Impedance Phase



Log Period

$$Skew = \frac{\left| \begin{matrix} Z_{xx} + Z_{yy} \\ Z_{xy} - Z_{yx} \end{matrix} \right|}{\left| \begin{matrix} Z_{xx} + Z_{yy} \\ Z_{xy} - Z_{yx} \end{matrix} \right|}$$



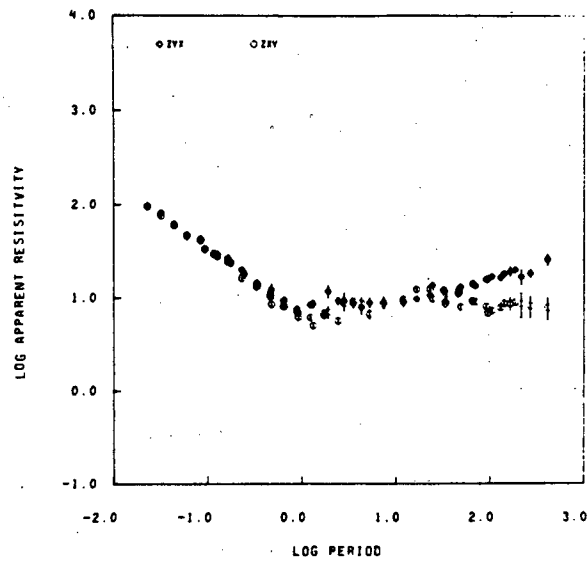
Log Period

## Appendix B

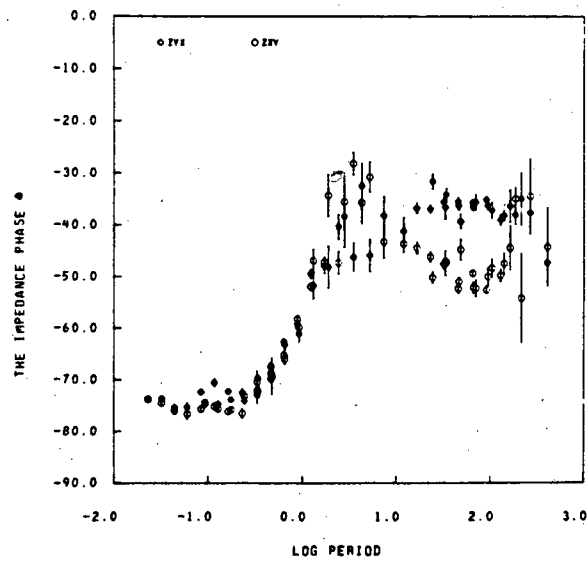
### Field Data as a Function of Frequency at a Constant Rotation Angle of -20 Degrees

The impedance parameters for the field data are provided for each measurement location. The impedance phases and apparent resistivities which correspond to the off-diagonal tensor elements are rotated into the principal direction at all frequencies defined by the maximum residual phase in band 4. This residual phase maximum averaged over all measurement locations provided a coordinate rotation angle of -20 degrees (north 20 degrees west).

## SITE # 1

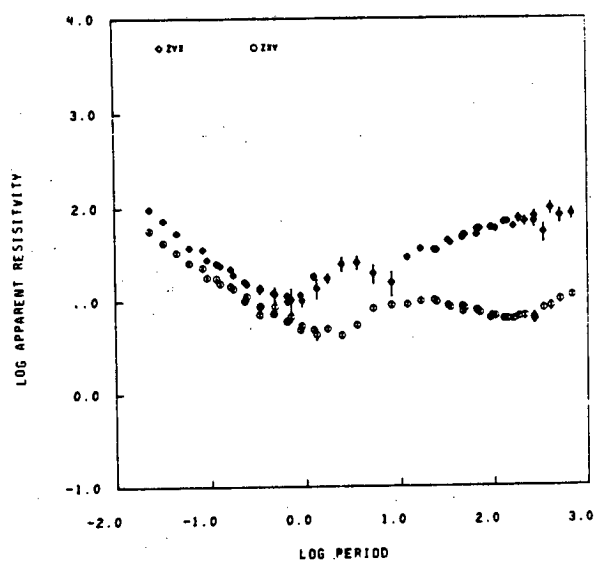


MT. HOOD MT DATA PHASE II SITE 1 CLOUD CAP

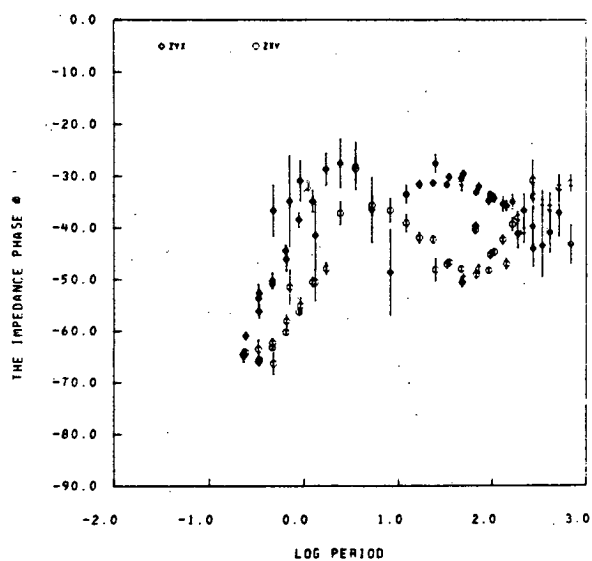


MT. HOOD MT DATA PHASE II SITE 1 CLOUD CAP

## SITE # 1A

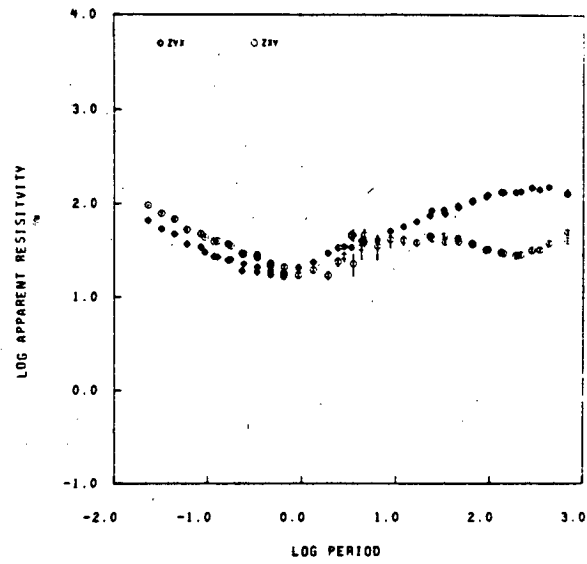


MT. HOOD MT DATA PHASE II SITE 1A CLOUD CAP

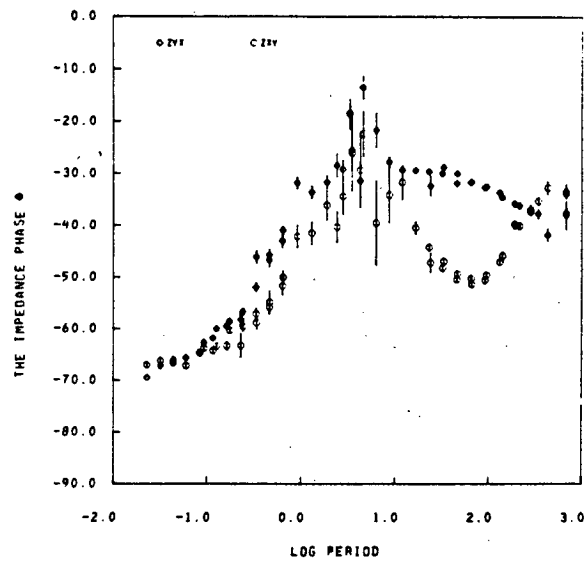


MT. HOOD MT DATA PHASE II SITE 1A CLOUD CAP

## SITE # 2

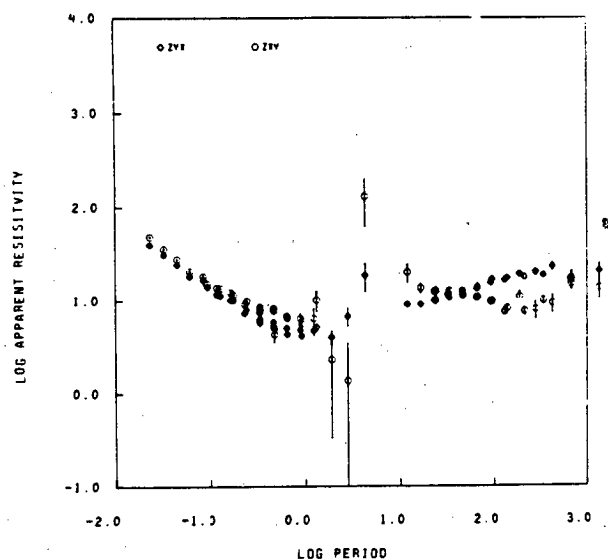


MT. HOOD MT DATA PHASE II SITE 2 CLOUD CAP

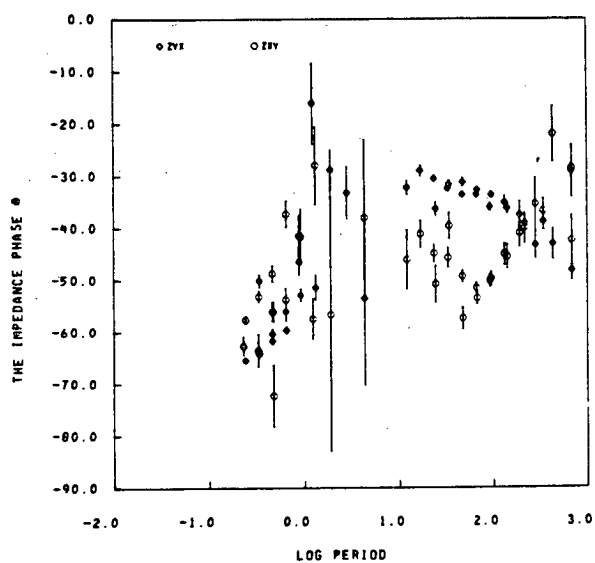


MT. HOOD MT DATA PHASE II SITE 2 CLOUD CAP

## SITE # 2A

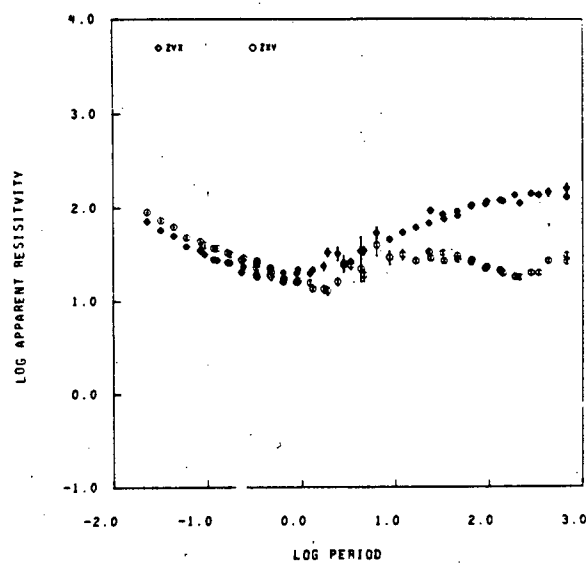


MT. HOOD MT DATA PHASE II SITE 2A CLOUD CAP

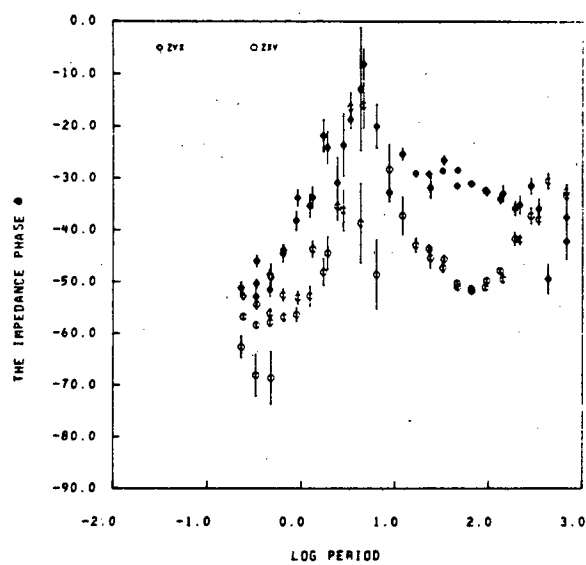


MT. HOOD MT DATA PHASE II SITE 2A CLOUD CAP

## SITE # 2B

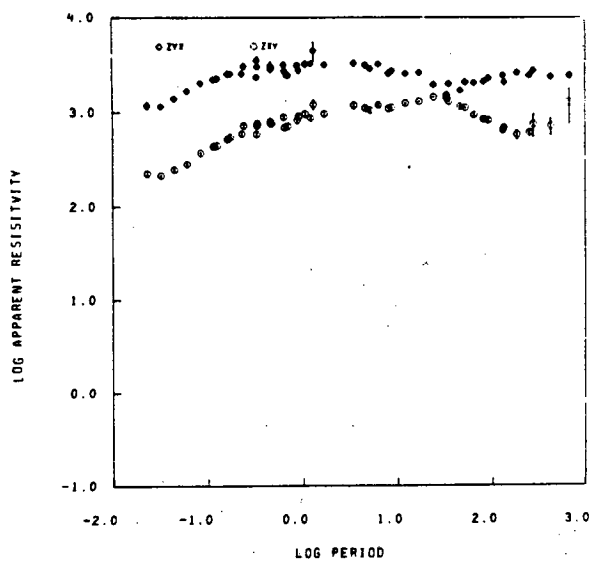


MT. HOOD MT DATA PHASE II SITE 2B CLOUD CAP

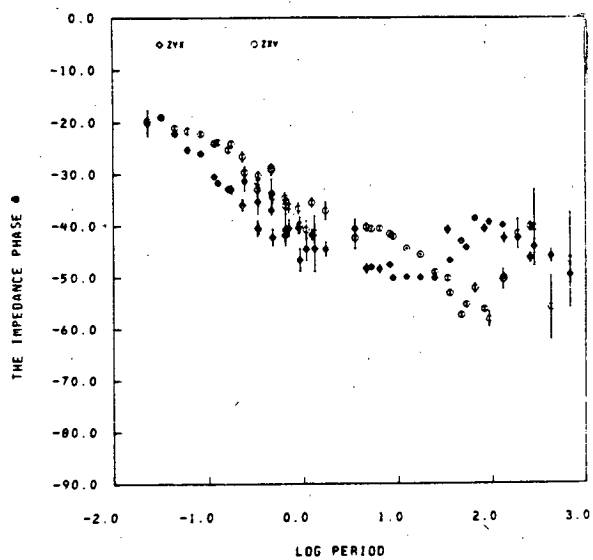


MT. HOOD MT DATA PHASE II SITE 2B CLOUD CAP

## SITE # 3

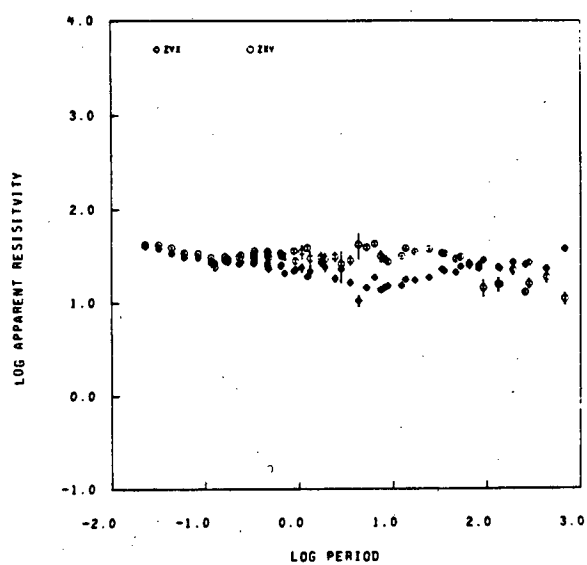


MT. MOOD PHASE II SITE 3 GUMJUWAC SADDLE

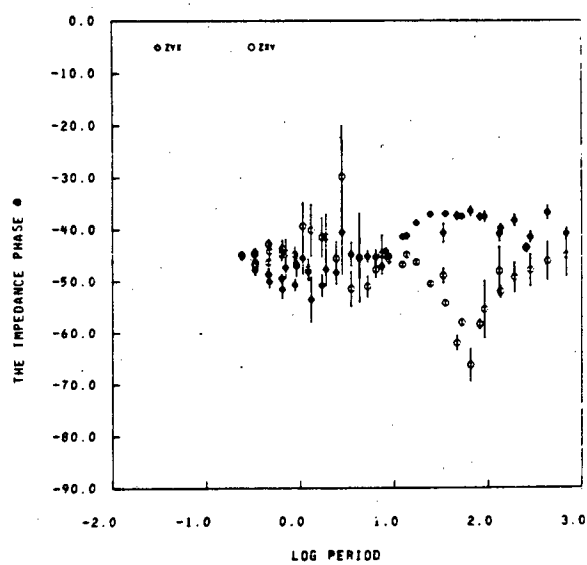


MT. MOOD PHASE II SITE 3 GUMJUWAC SADDLE

## SITE # 3A

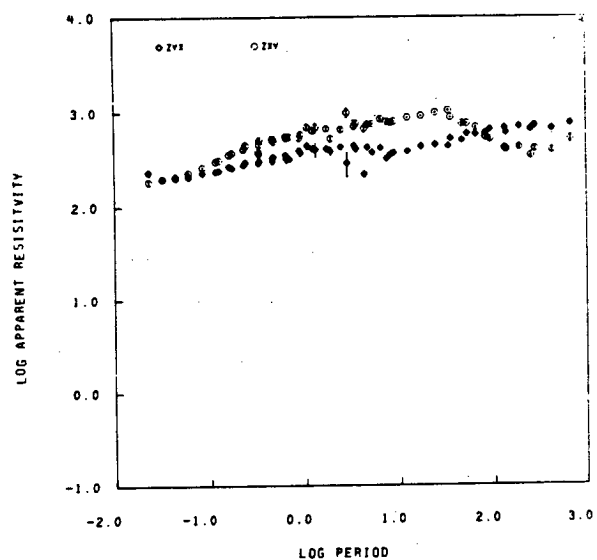


MT. HOOD PHASE II SITE 3A GUMJWAC SADDLE

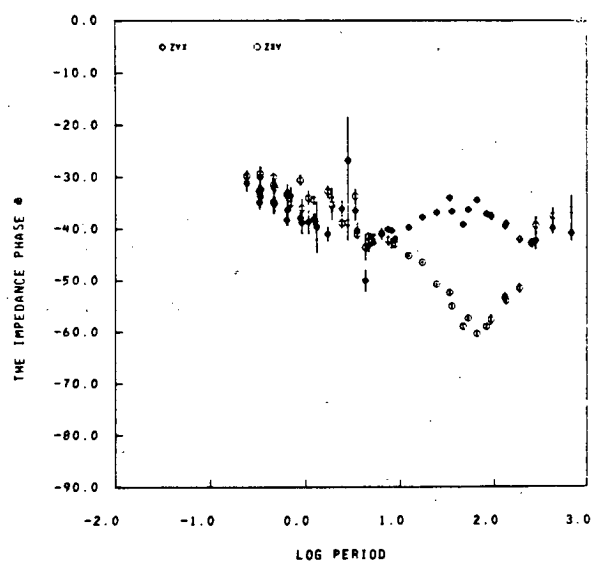


MT. HOOD PHASE II SITE 3A GUMJWAC SADDLE

## SITE # 3B

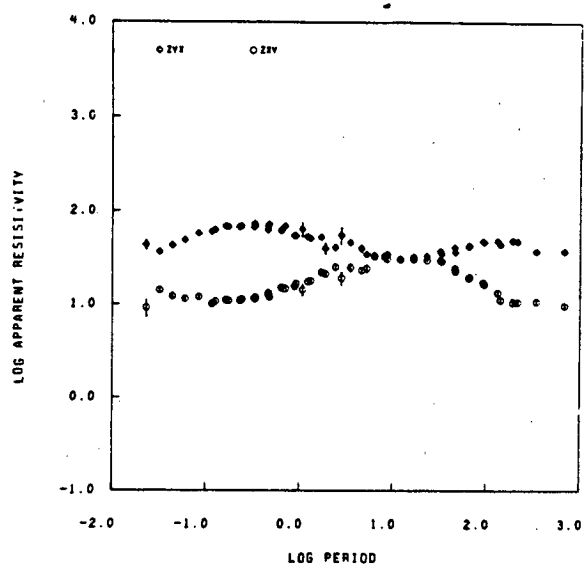


MT. HOOD PHASE II SITE 3B GUNJUNAC SADDLE

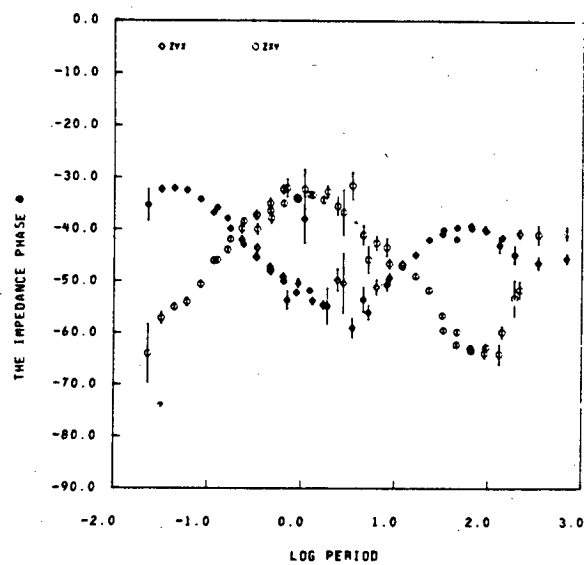


MT. HOOD PHASE II SITE 3B GUNJUNAC SADDLE

## SITE # 4

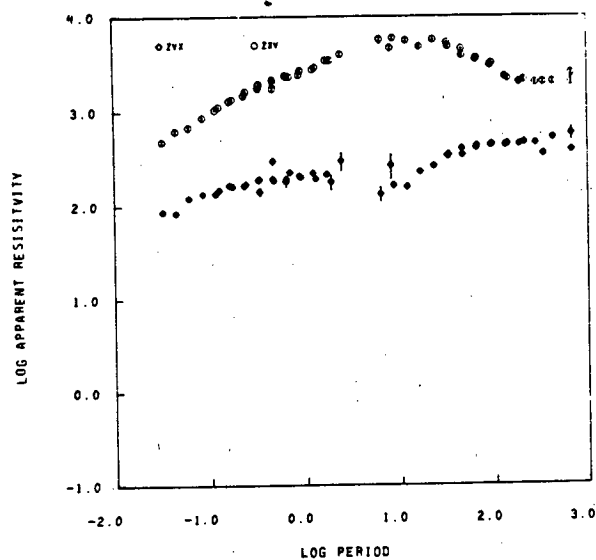


MT. HOOD PHASE II SITE 4 HOOD RIVER MEADOWS

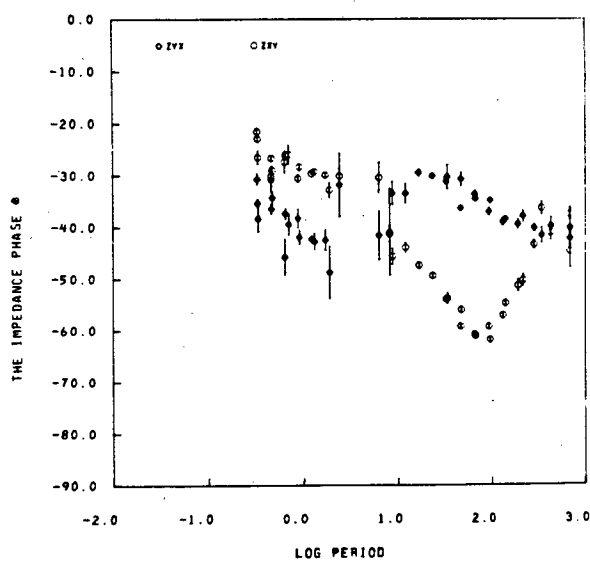


MT. HOOD PHASE II SITE 4 HOOD RIVER MEADOWS

## SITE # 4A

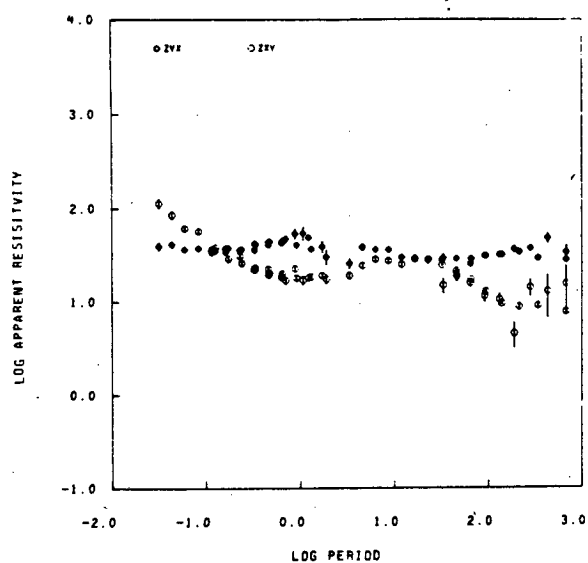


MT. HOOD PHASE II SITE 4A HOOD RIVER MEADOWS

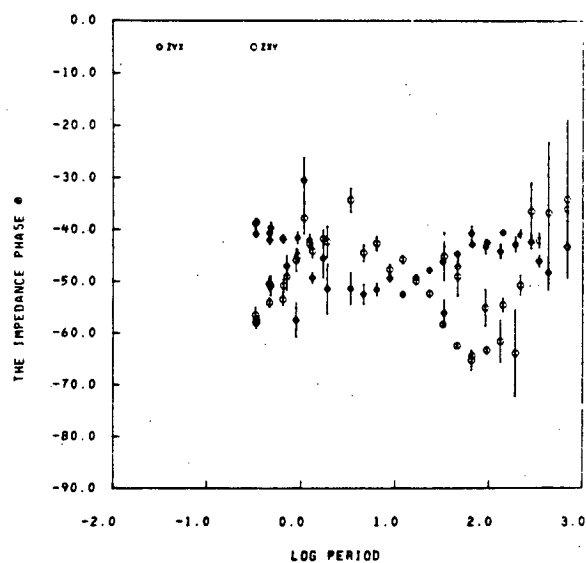


MT. HOOD PHASE II SITE 4A HOOD RIVER MEADOWS

## SITE # 4B

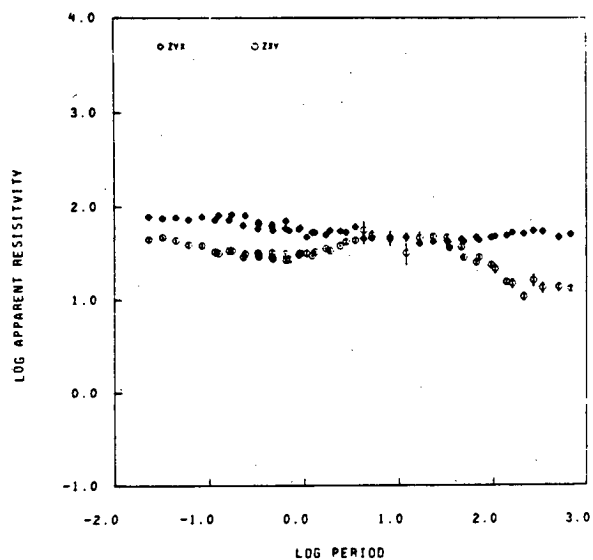


MT. HOOD PHASE II SITE 4B HOOD RIVER MEADOWS

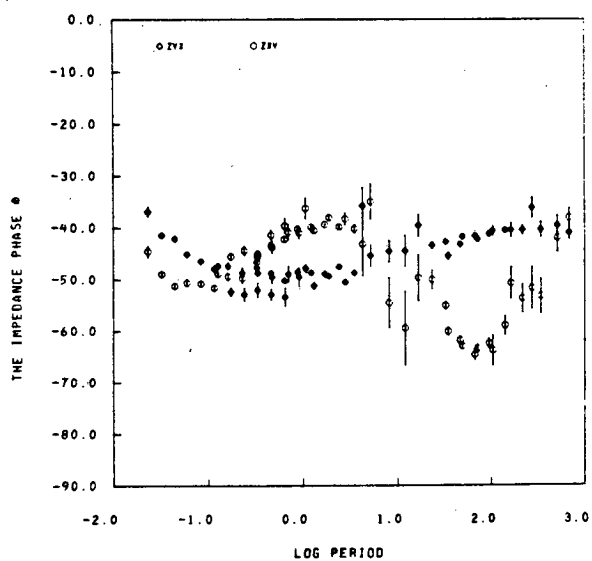


MT. HOOD PHASE II SITE 4B HOOD RIVER MEADOWS

## SITE # 5

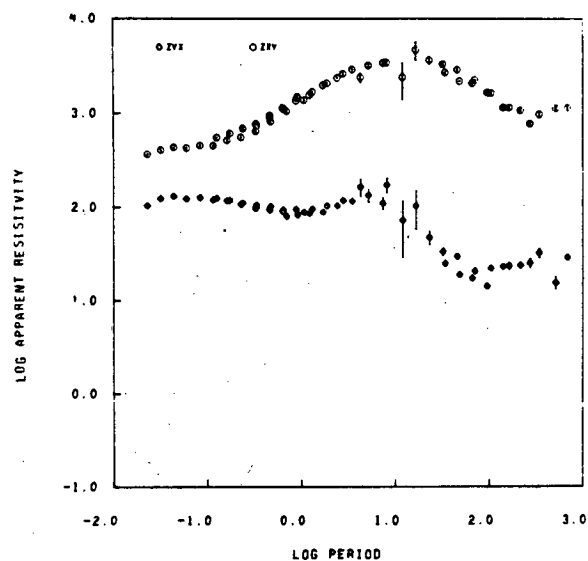


MT. HOOD MT DATA PHASE II SITE 5 BARLOW RIDGE

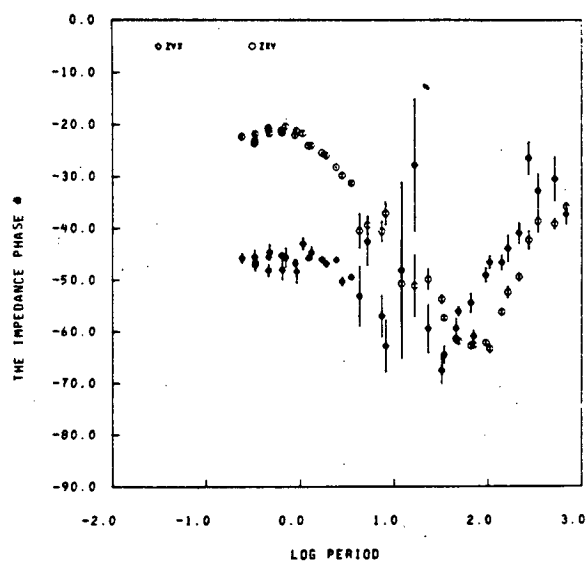


MT. HOOD MT DATA PHASE II SITE 5 BARLOW RIDGE

## SITE # 5A

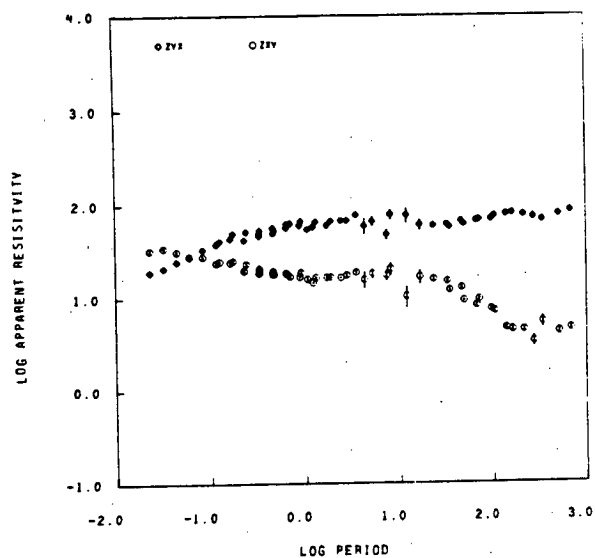


MT. MOOD MT DATA PHASE II SITE 5A BARLOW RIDGE

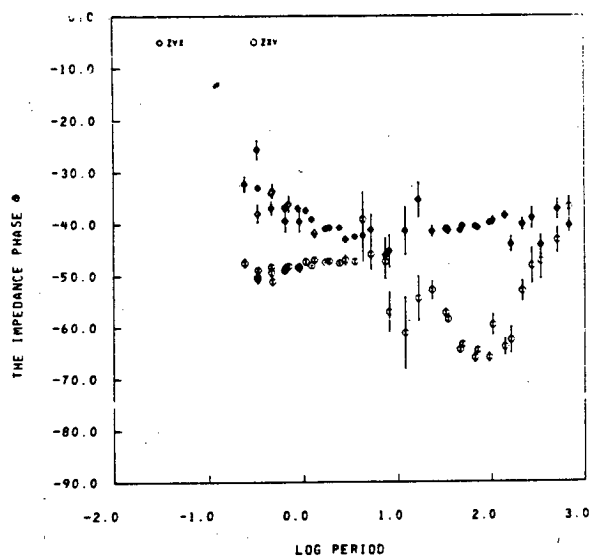


MT. MOOD MT DATA PHASE II SITE 5A BARLOW RIDGE

## SITE # 5B

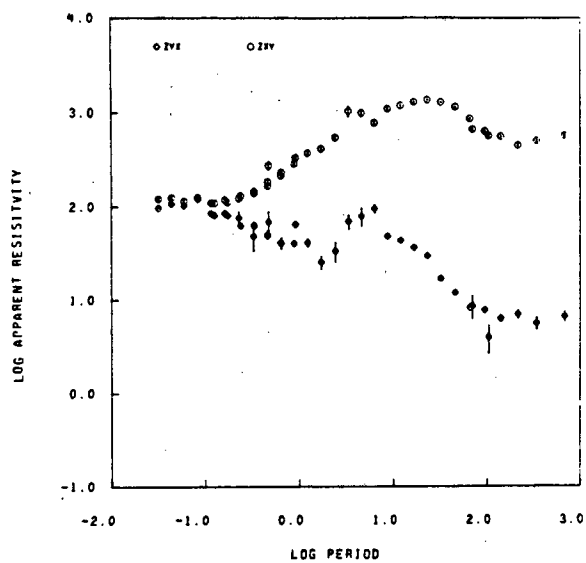


MT. HOOD MT DATA PHASE II SITE 5B BARLOW RIDGE

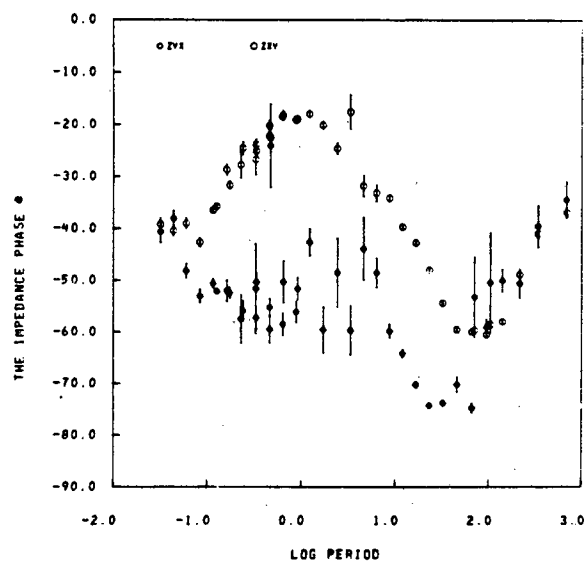


MT. HOOD MT DATA PHASE II SITE 5B BARLOW RIDGE

## SITE # 6

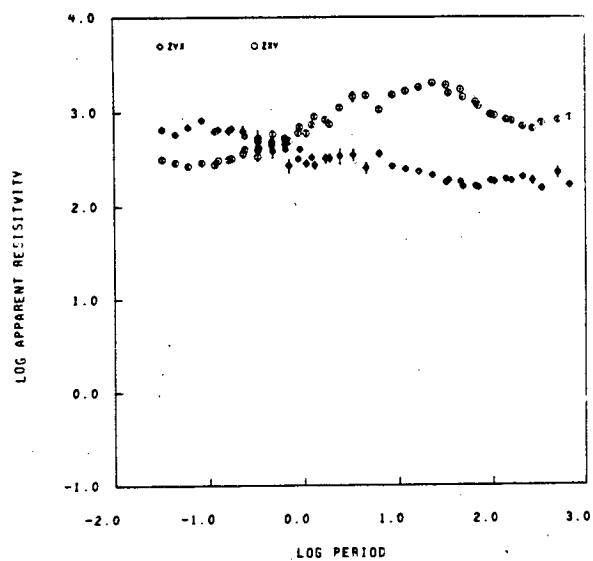


MT. MOOD MT DATA PHASE II SITE 6 LOG ROAD

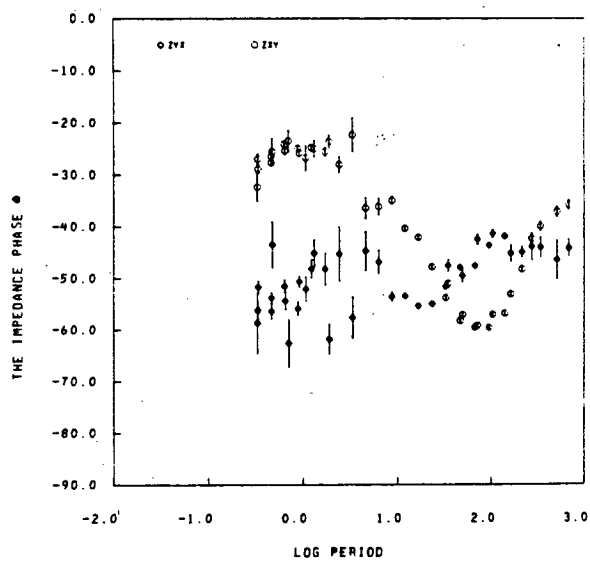


MT. MOOD MT DATA PHASE II SITE 6 LOG ROAD

## SITE # 6B

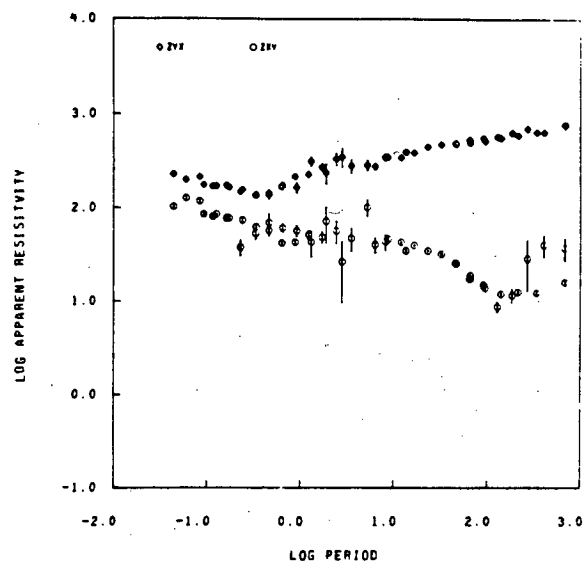


MT. HOOD MT DATA PHASE II SITE 6B LOG ROAD

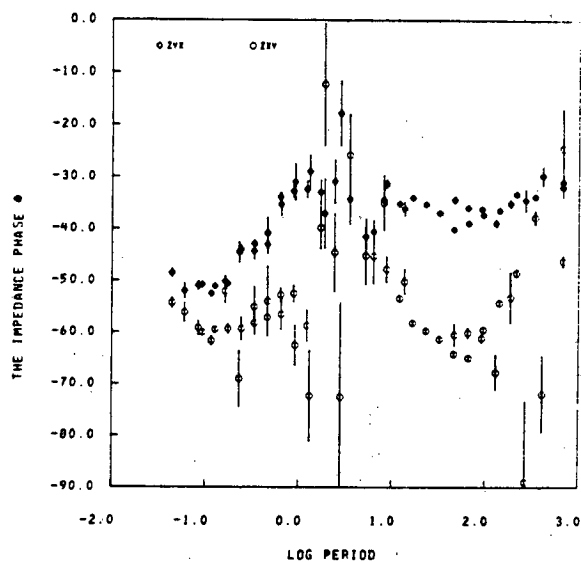


MT. HOOD MT DATA PHASE II SITE 6B LOG ROAD

## SITE # 7

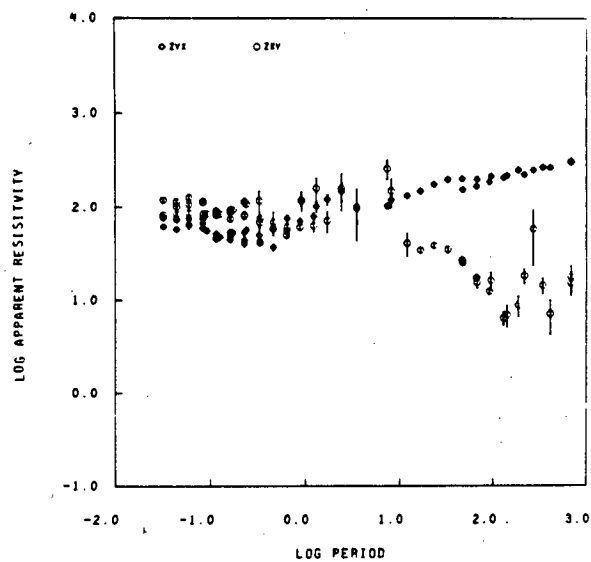


MT. MOOD PHASE II SITE 7 OLD MAID FLAT

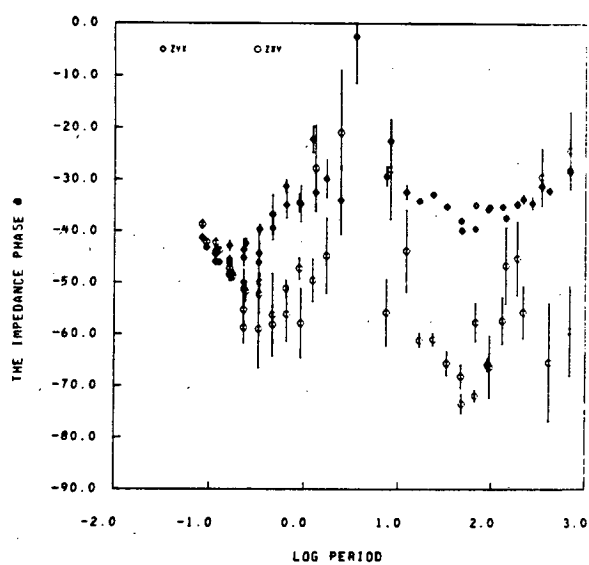


MT. MOOD PHASE II SITE 7 OLD MAID FLAT

## SITE # 7A

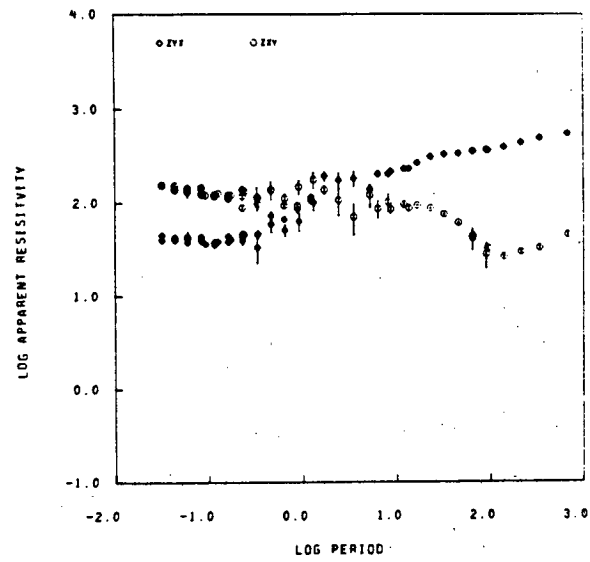


MT. HOOD PHASE II SITE 7A OLD MAID FLAT

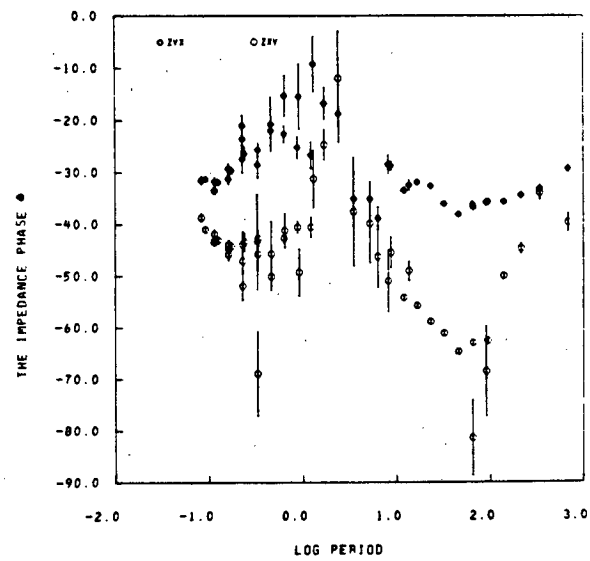


MT. HOOD PHASE II SITE 7A OLD MAID FLAT

## SITE # 7E

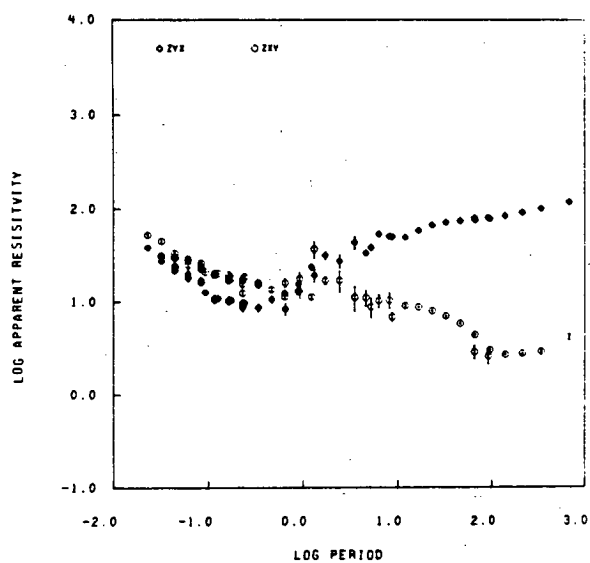


MT. WOOD PHASE II SITE 7B OLD MAID FLAT

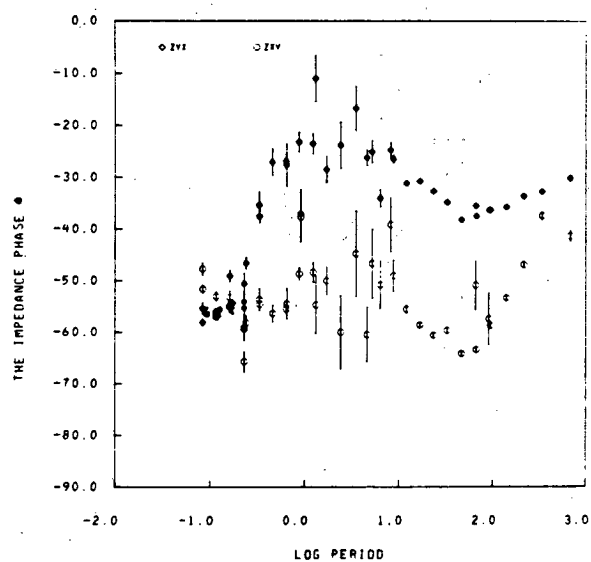


MT. WOOD PHASE II SITE 7B OLD MAID FLAT

## SITE # 7C

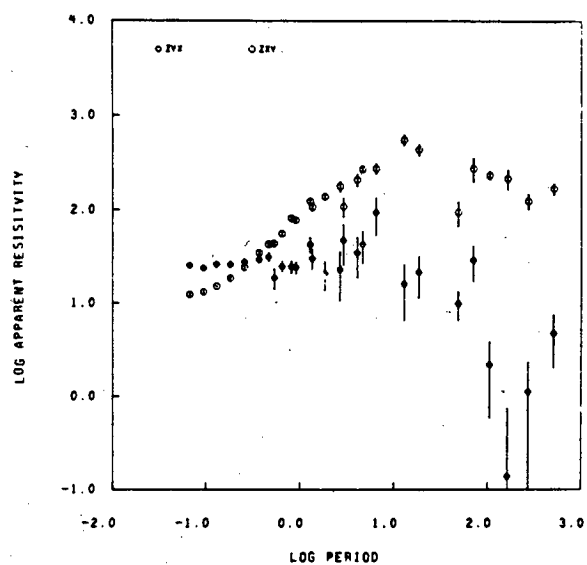


MT. MOOD PHASE II SITE 7C OLD MAID FLAT

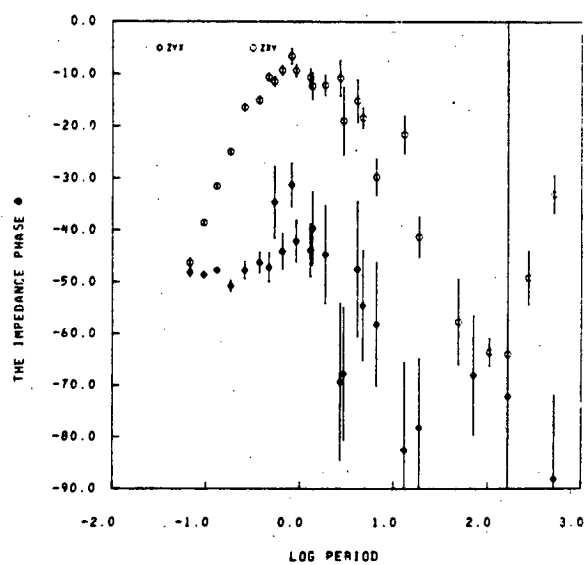


MT. MOOD PHASE II SITE 7C OLD MAID FLAT

## SITE # 11

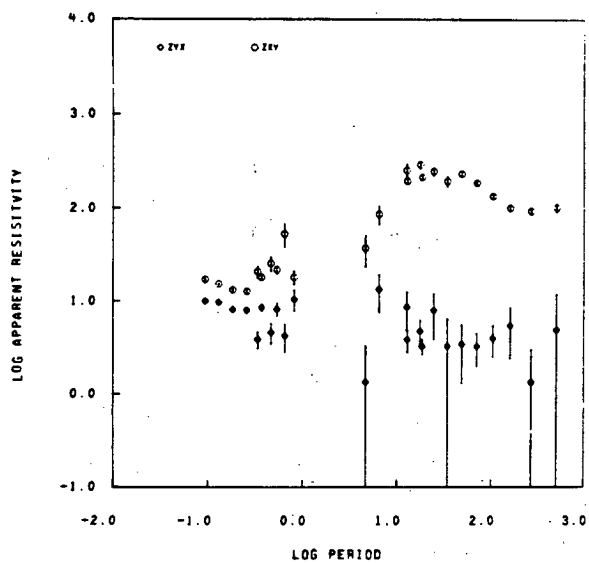


MT. HOOD MT DATA PHASE I SITE 4 TIMBERLINE

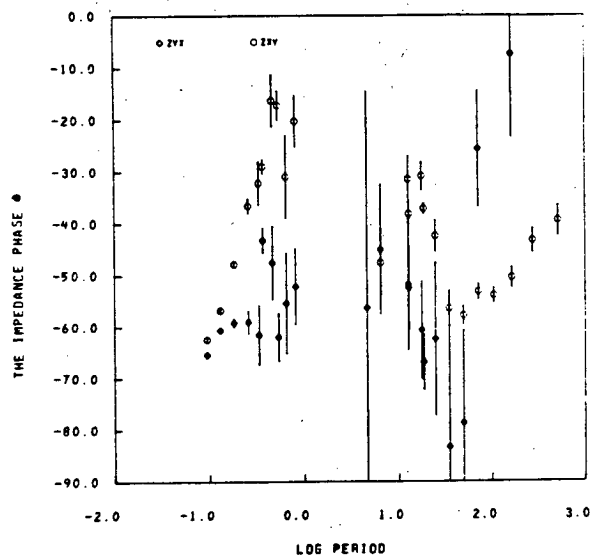


MT. HOOD MT DATA PHASE I SITE 4 TIMBERLINE

## SITE # 13

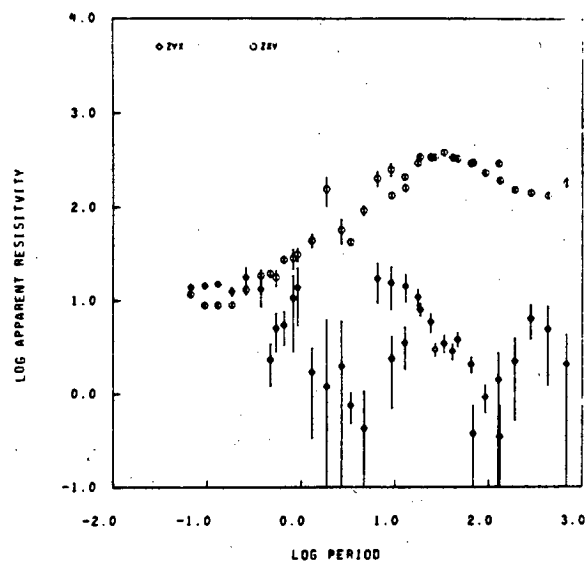


MT. HOOD MT DATA PHASE I SITE 6 TIMBERLINE

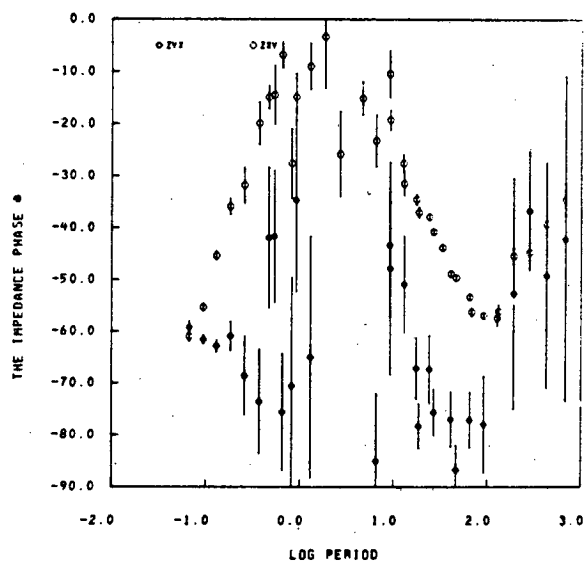


MT. HOOD MT DATA PHASE I SITE 6 TIMBERLINE

## SITE # 14

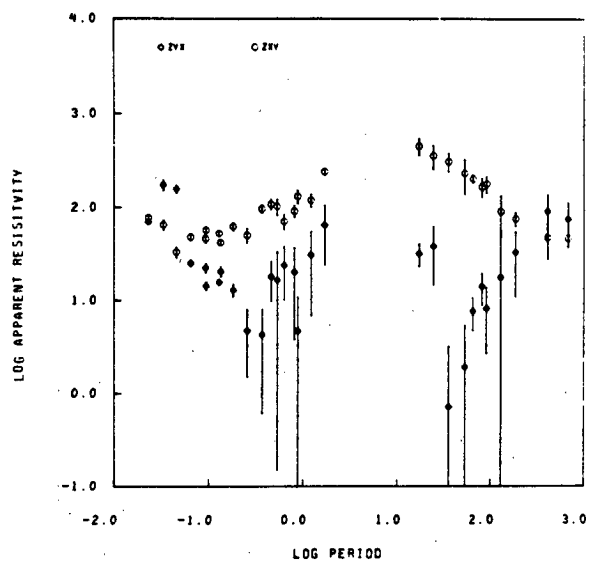


MT. HOOD MT DATA PHASE I SITE 7 TIMBERLINE

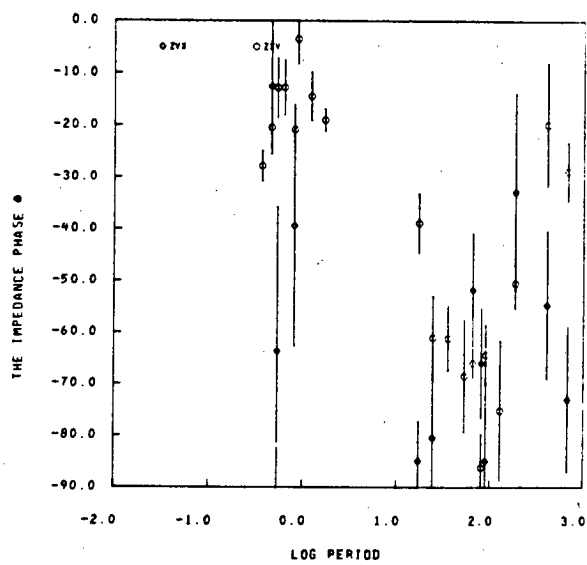


MT. HOOD MT DATA PHASE I SITE 7 TIMBERLINE

## SITE # 15A



MT. HOOD MT DATA PHASE I SITE 8A TIMBERLINE

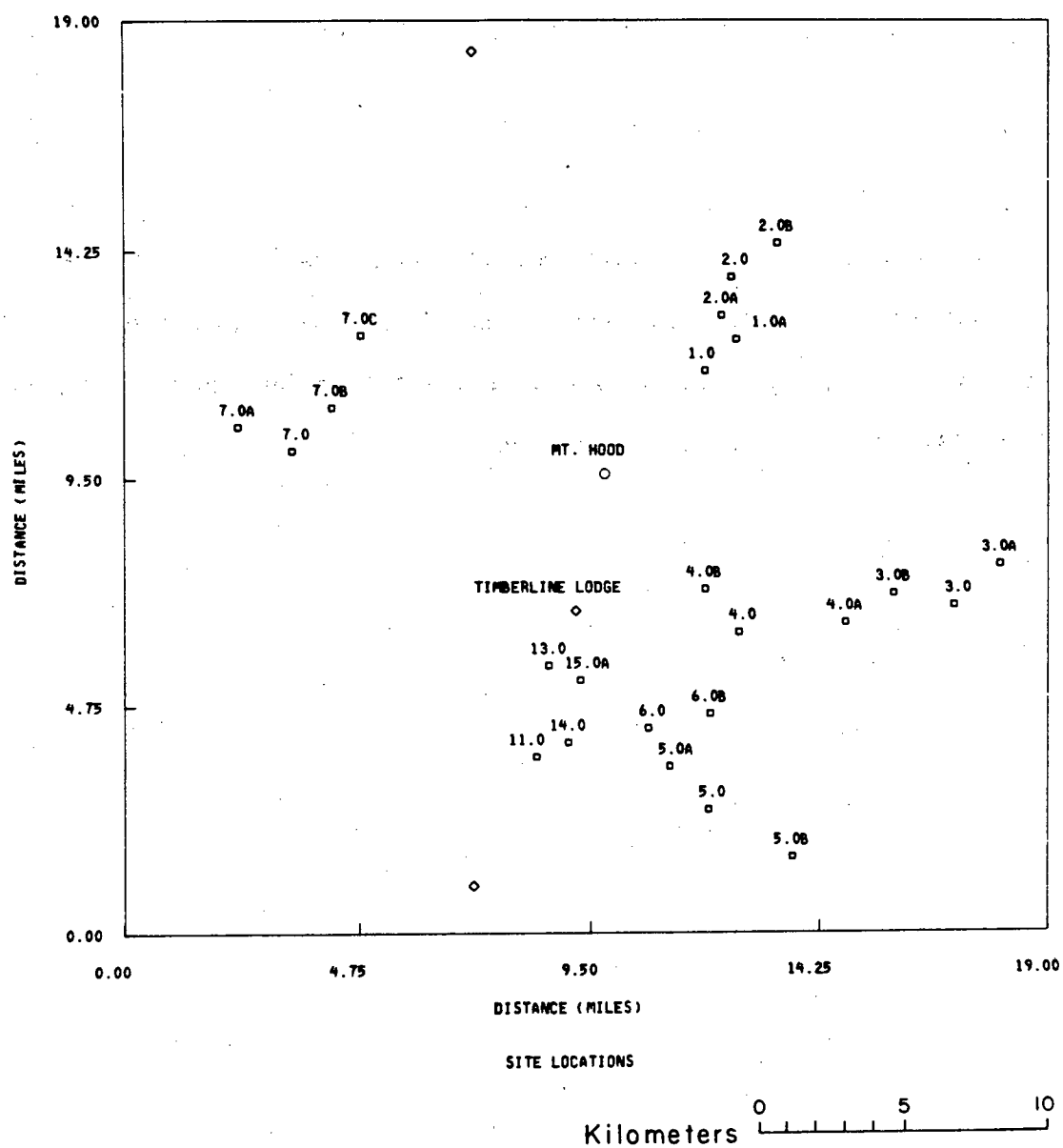


MT. HOOD MT DATA PHASE I SITE 8A TIMBERLINE

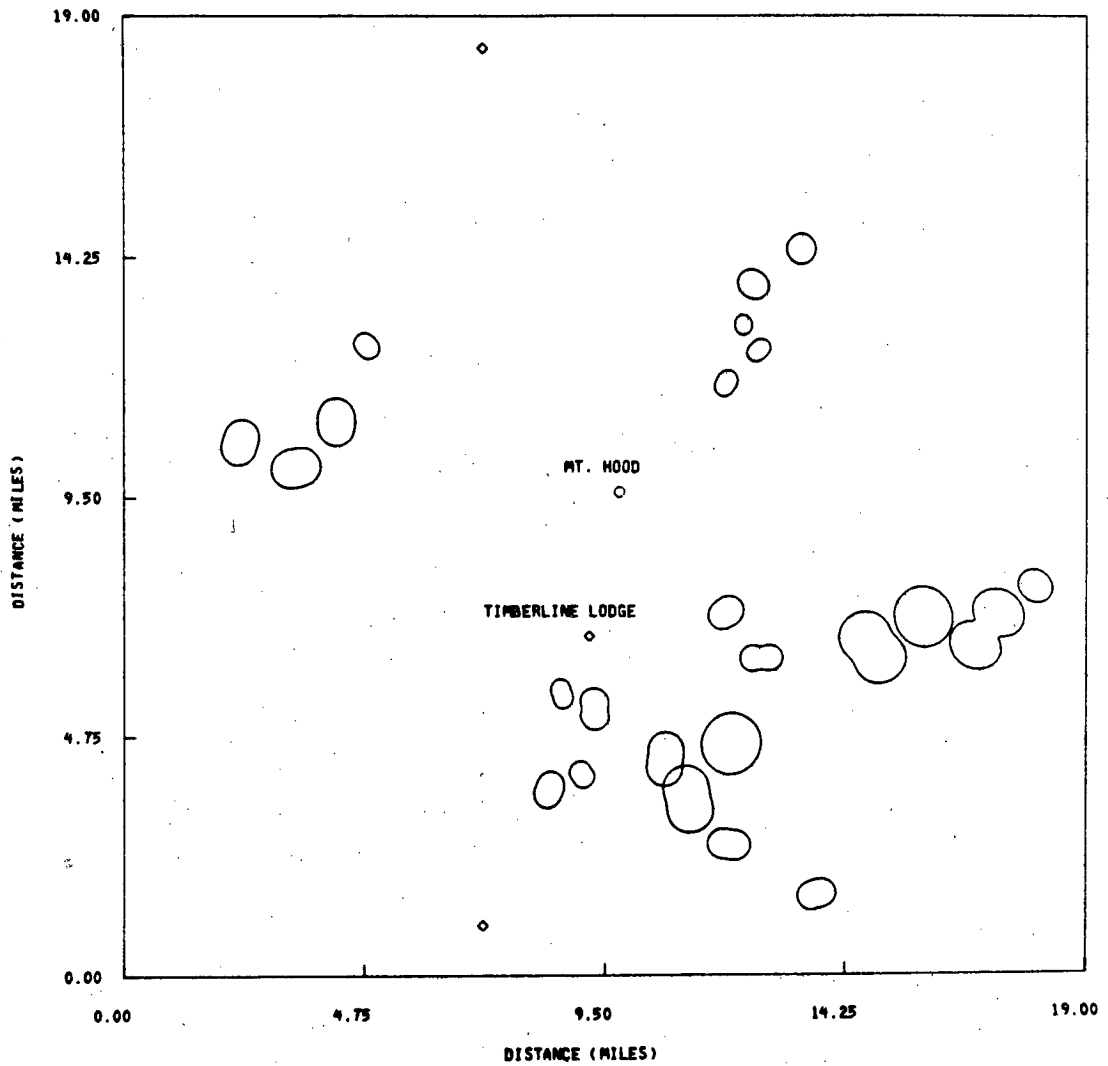
## Appendix C

### Polar Diagrams of the Field Data

A complete set of polar diagrams of the field data for the  $Z_{xx}$ ,  $Z_{xy}$  and  $T_X$  parameters averaged over each of the five frequency bands defined in Chapter 5 are presented. The phase diagrams for  $Z_{xy}$  are for the residual phase, all other phase diagrams are for un-normalized phase values.

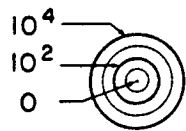


AVERAGED FREQS. IN RANGE OF 9.0-1.0 MZ



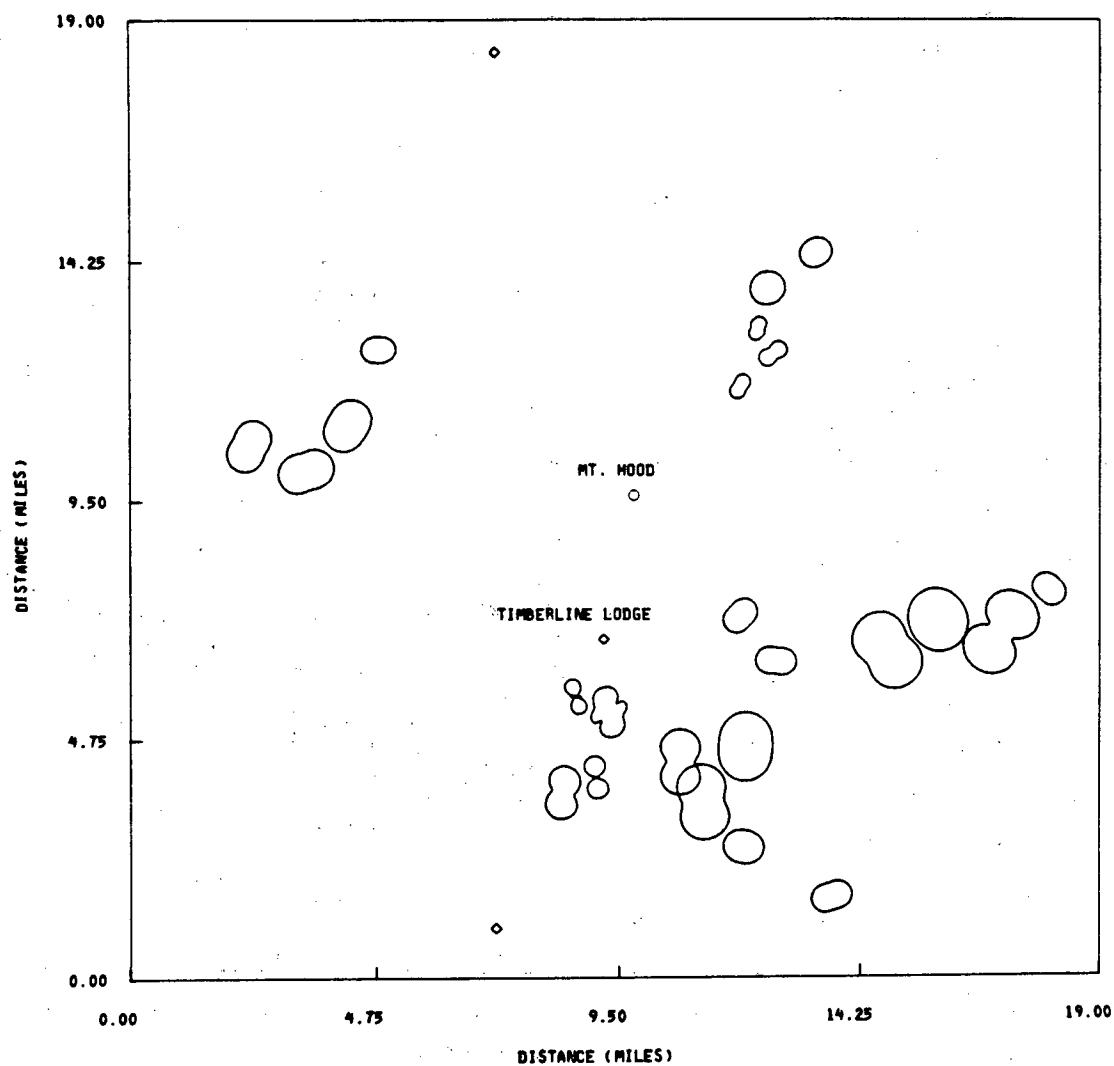
RXY APPARENT RESISTIVITY XY

Kilometers 0 5 10

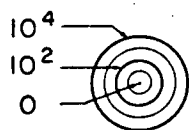


Apparent resistivity (ohm·m)

AVERAGED FREQS. IN RANGE OF 1.0-0.2 HZ



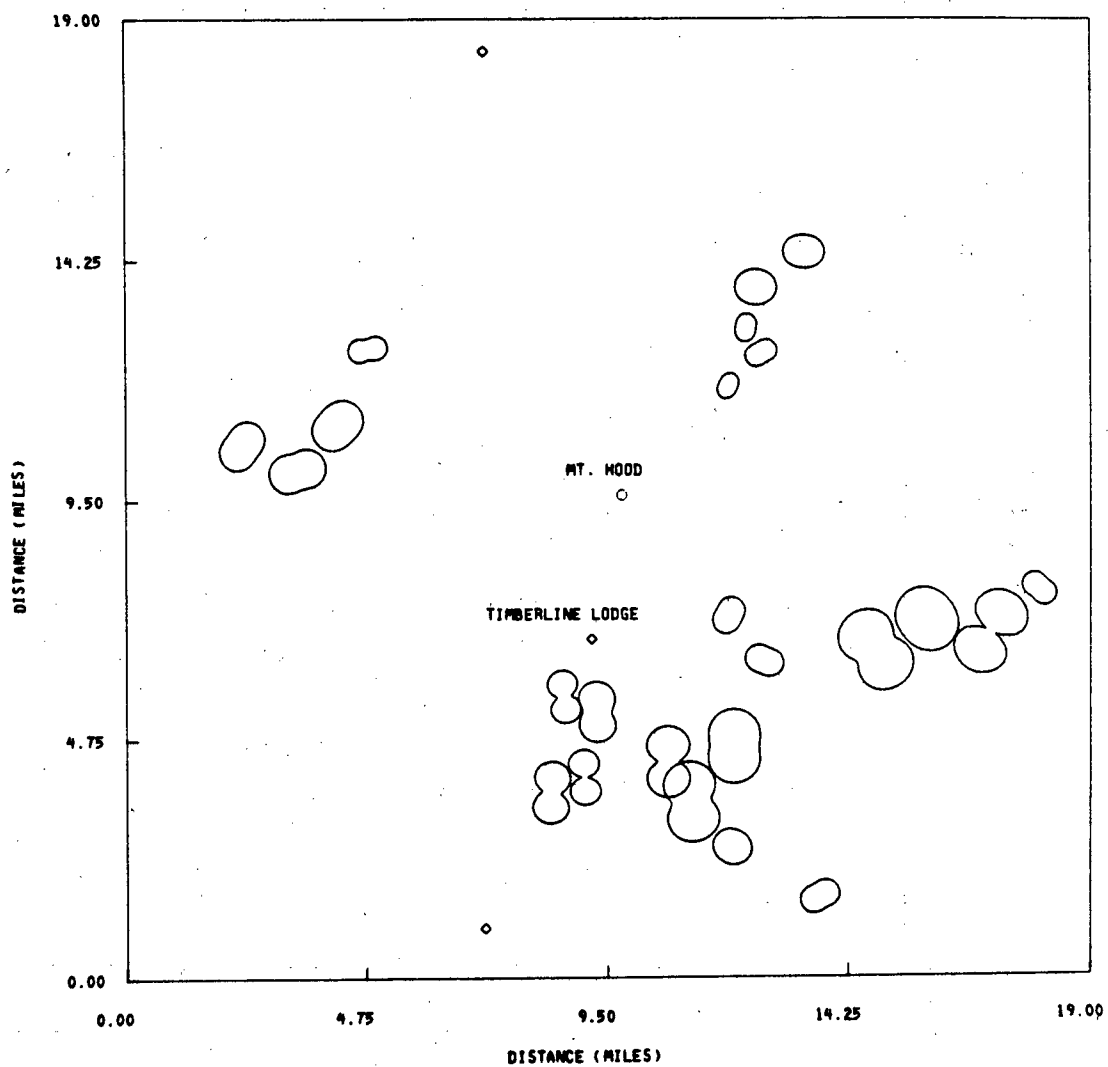
RXV APPARENT RESISTIVITY XY



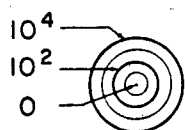
Apparent resistivity (ohm·m)

Kilometers 0 5 10

AVERAGED FREQS. IN RANGE OF .2-.03 HZ



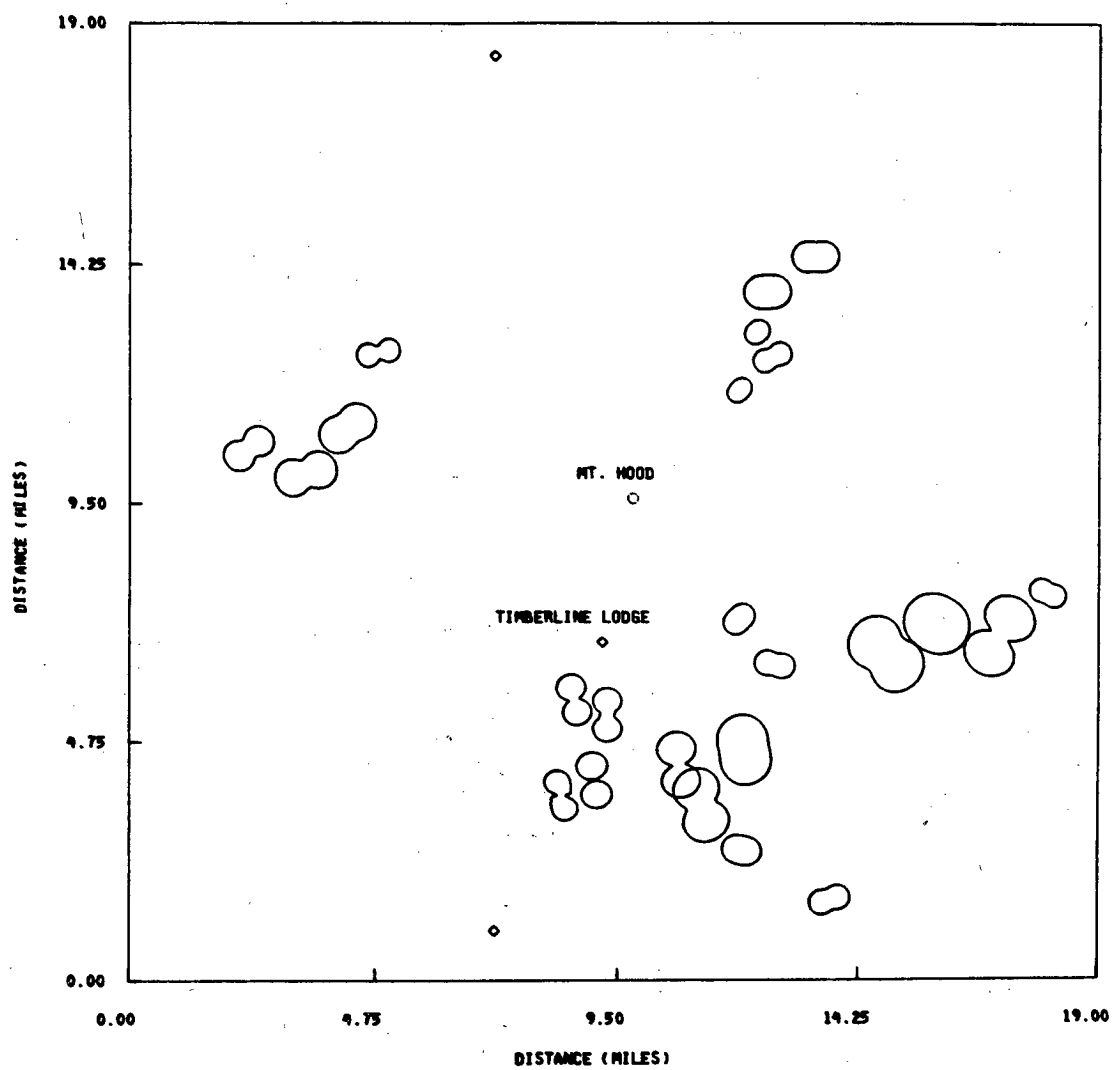
RXY APPARENT RESISTIVITY XY



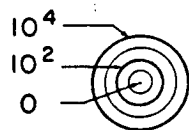
Apparent resistivity (ohm·m)

Kilometers 0 5 10

AVERAGED FREQS. IN RANGE OF .03-.004HZ



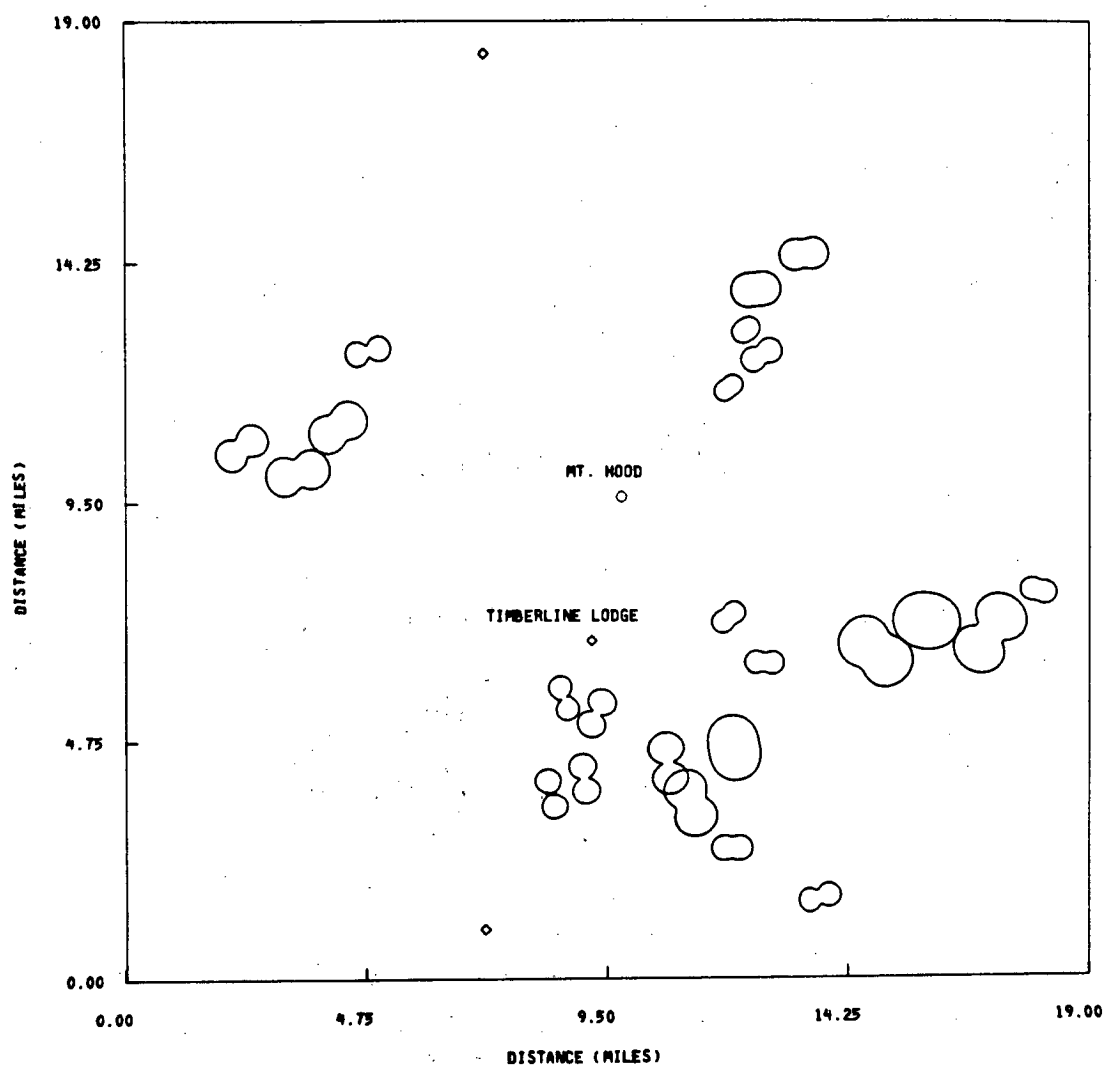
RXY APPARENT RESISTIVITY XY



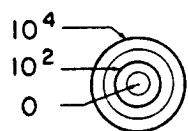
Apparent resistivity (ohm·m)

Kilometers 0 5 10

AVERAGED FREQS. IN RANGE OF .006-LOMHz



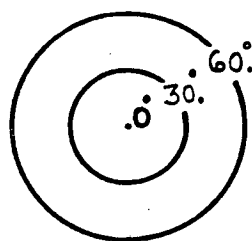
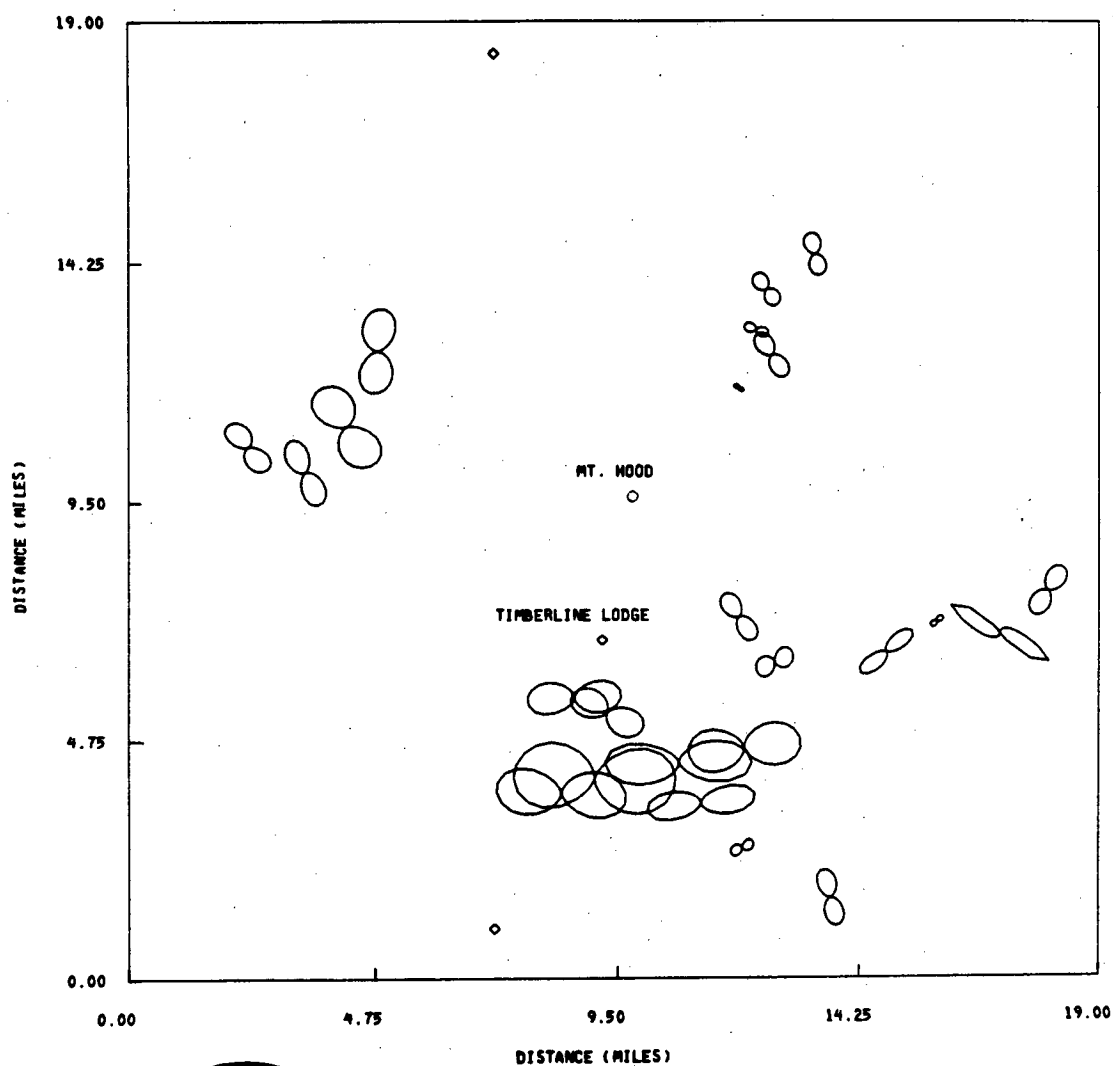
RXY APPARENT RESISTIVITY XY



Apparent resistivity (ohm-m)

Kilometers 0 5 10

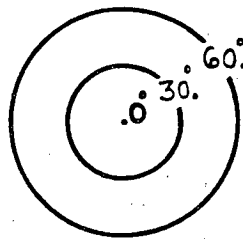
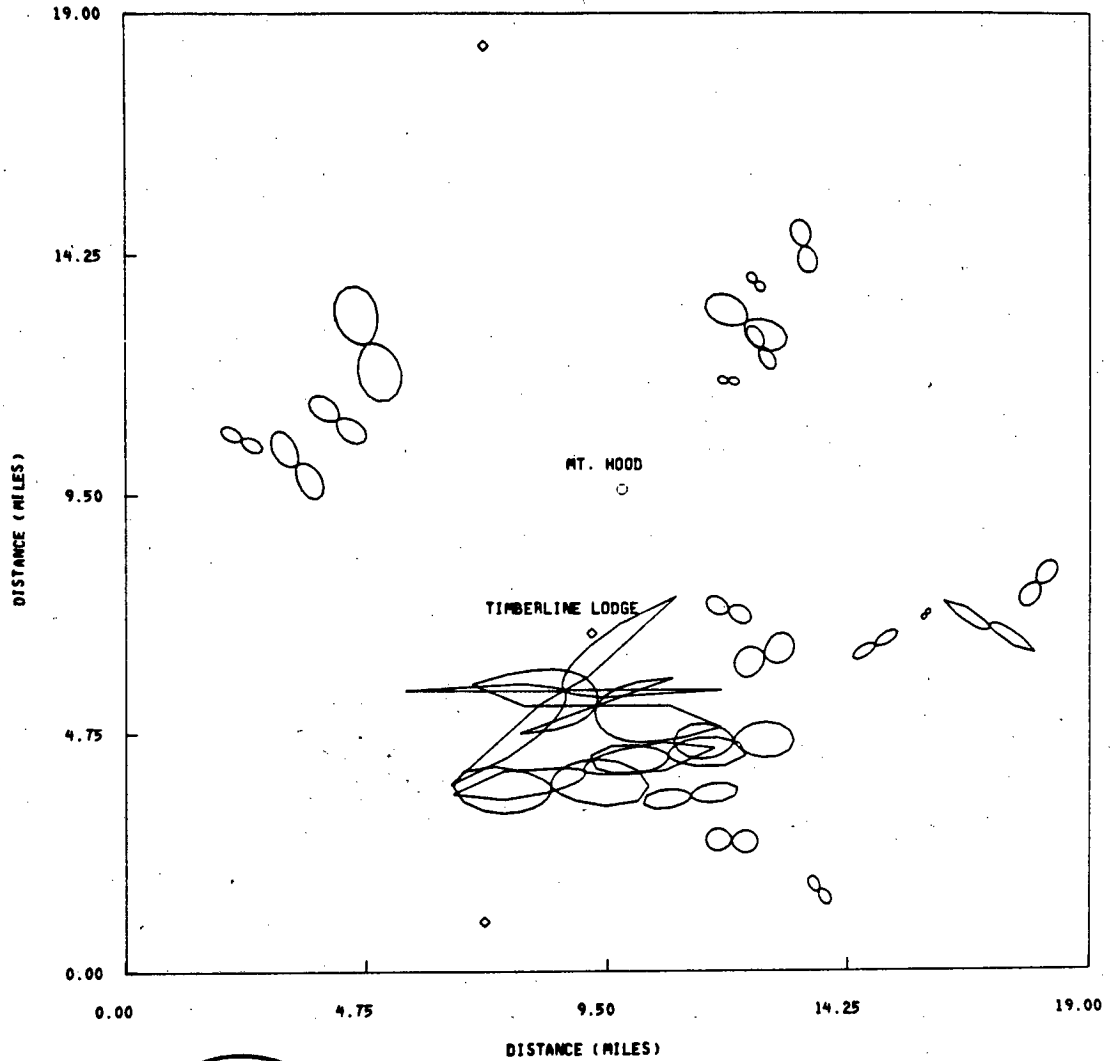
AVERAGED FREQS. IN RANGE OF 5.0-1.0 HZ



PXV PHASE OF APPARENT RESISTIVITY XV

Residual Phase  
(degrees)

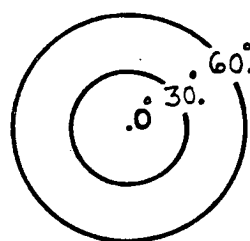
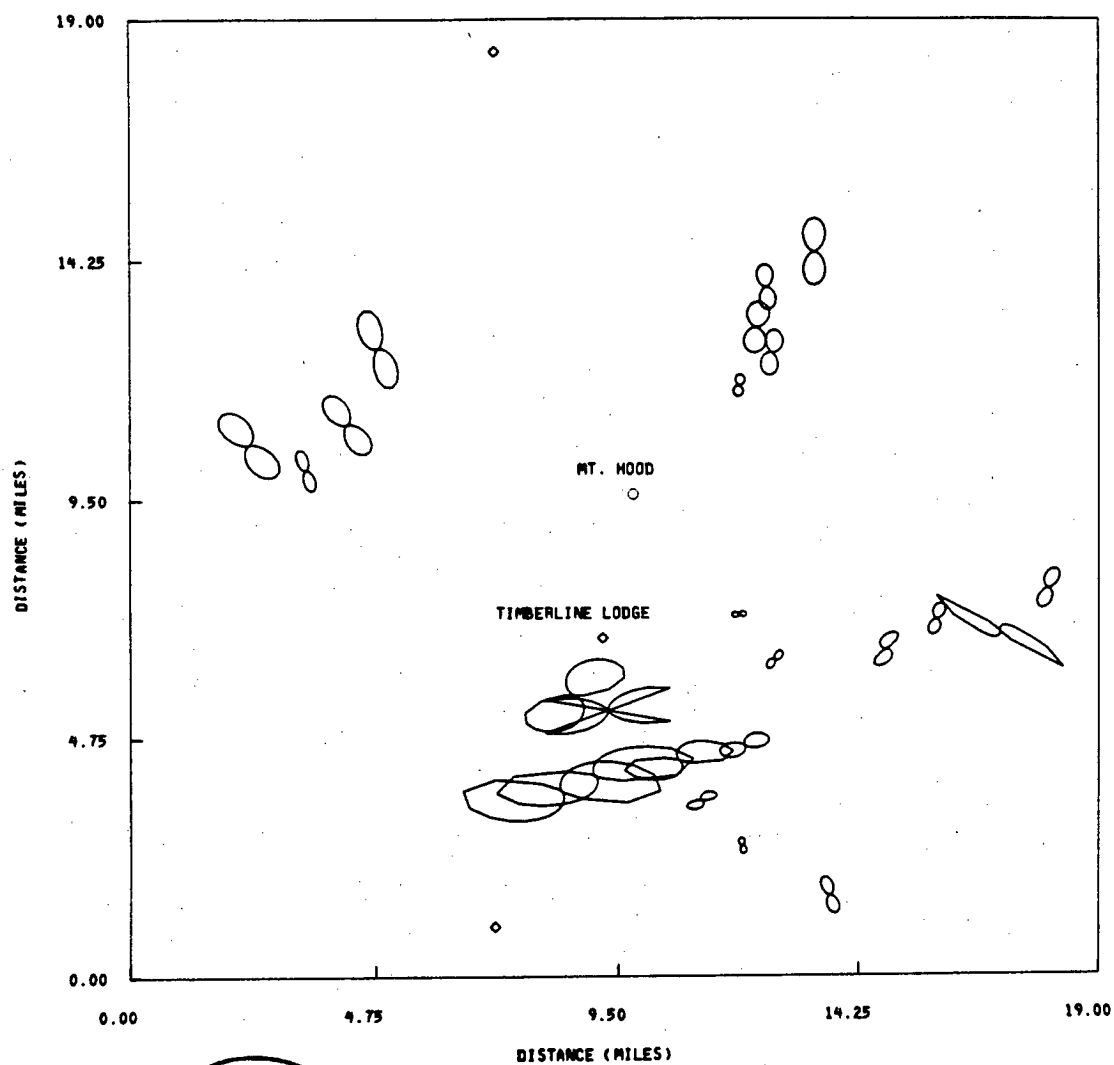
AVERAGED FREQS. IN RANGE OF 1.0-0.2 HZ



PXY PHASE OF APPARENT RESISTIVITY XY

Residual Phase  
(degrees)

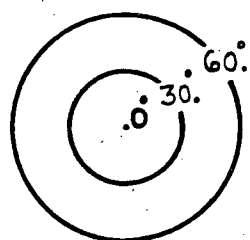
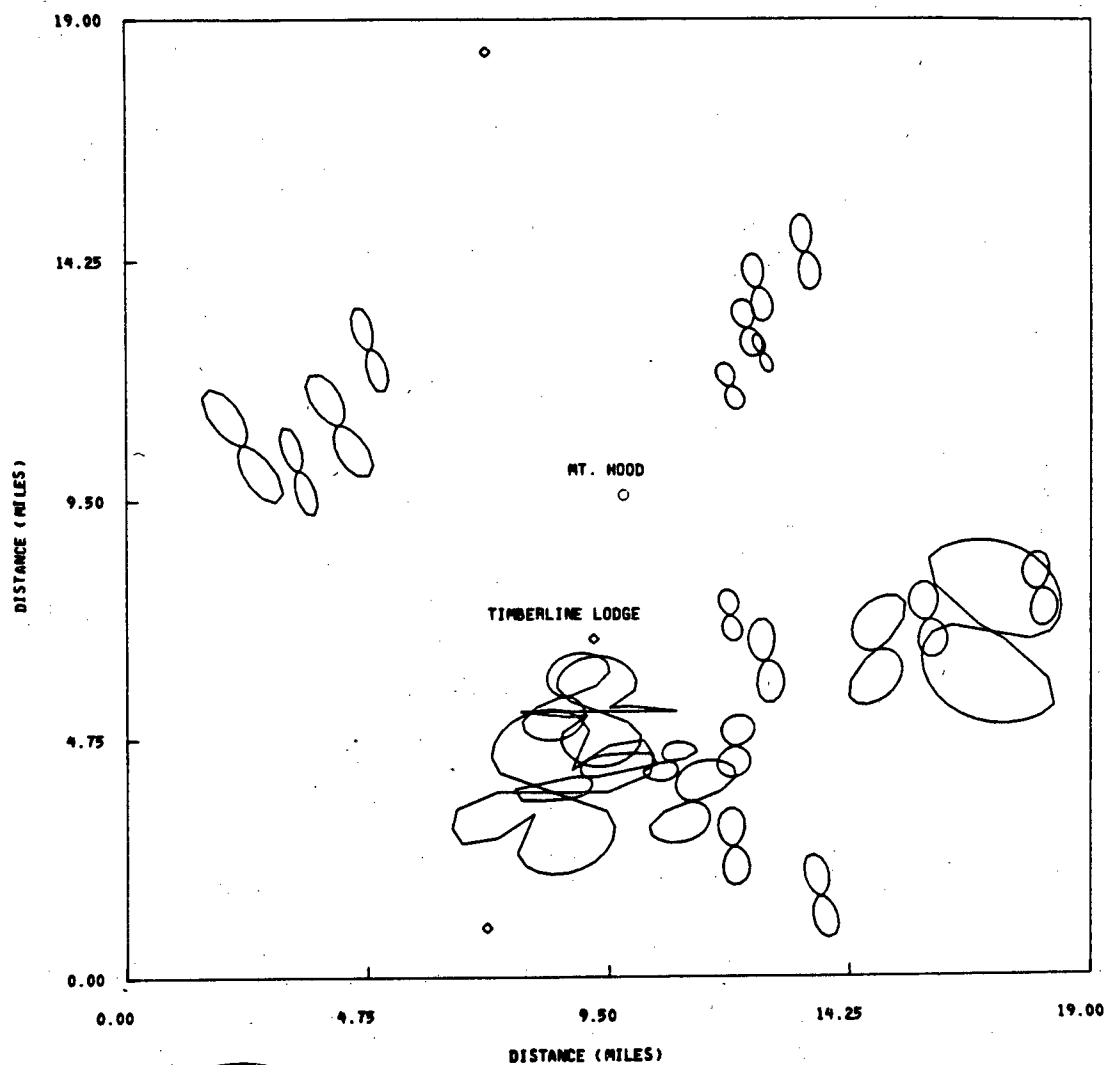
AVERAGED FREQS. IN RANGE OF .2-.03 HZ



Residual Phase  
(degrees)

PXY PHASE OF APPARENT RESISTIVITY XY

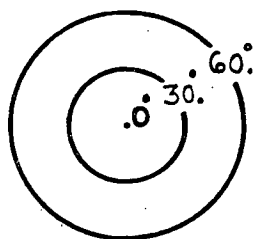
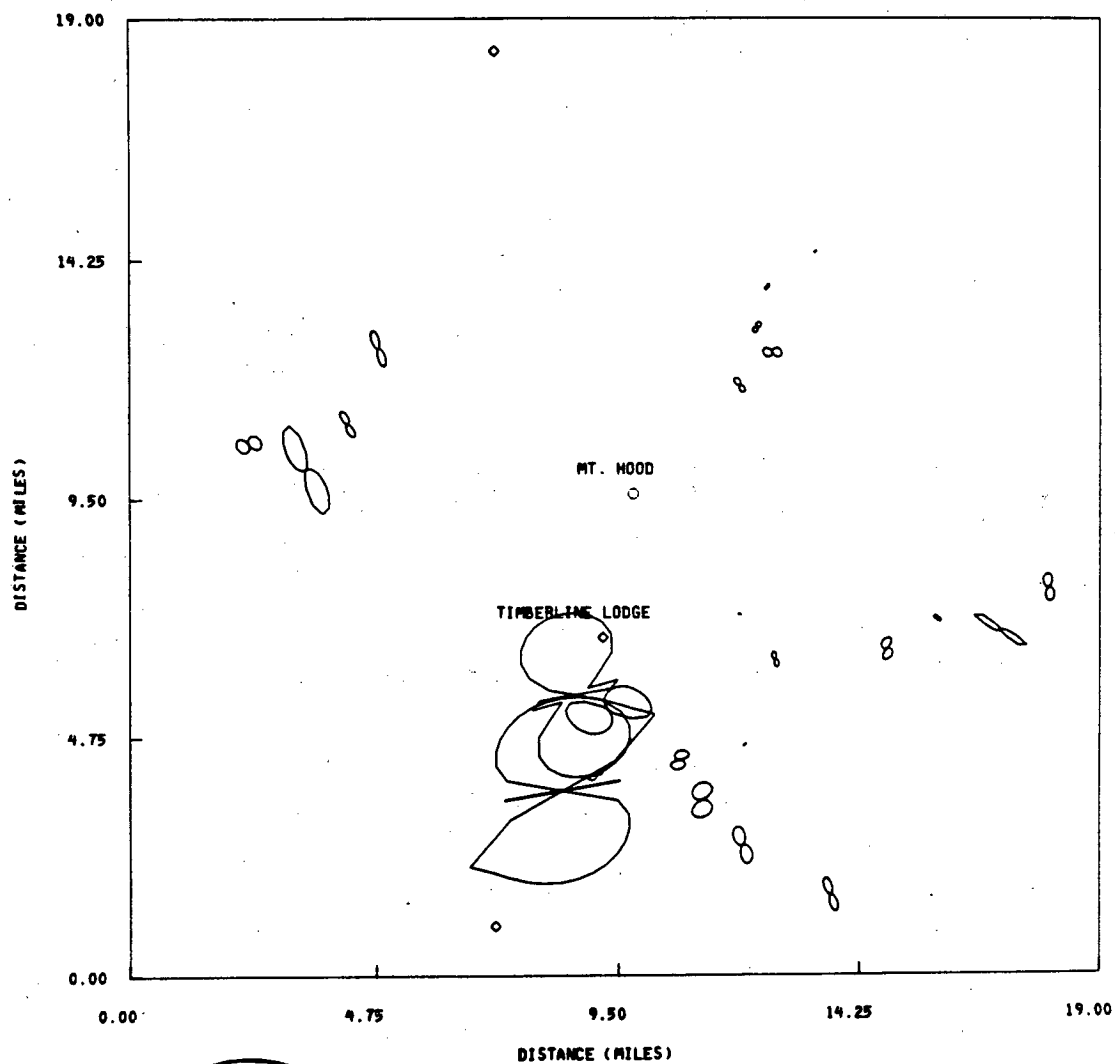
AVERAGED FREQS. IN RANGE OF .03-.006HZ



Residual Phase  
(degrees)

PXV PHASE OF APPARENT RESISTIVITY XV

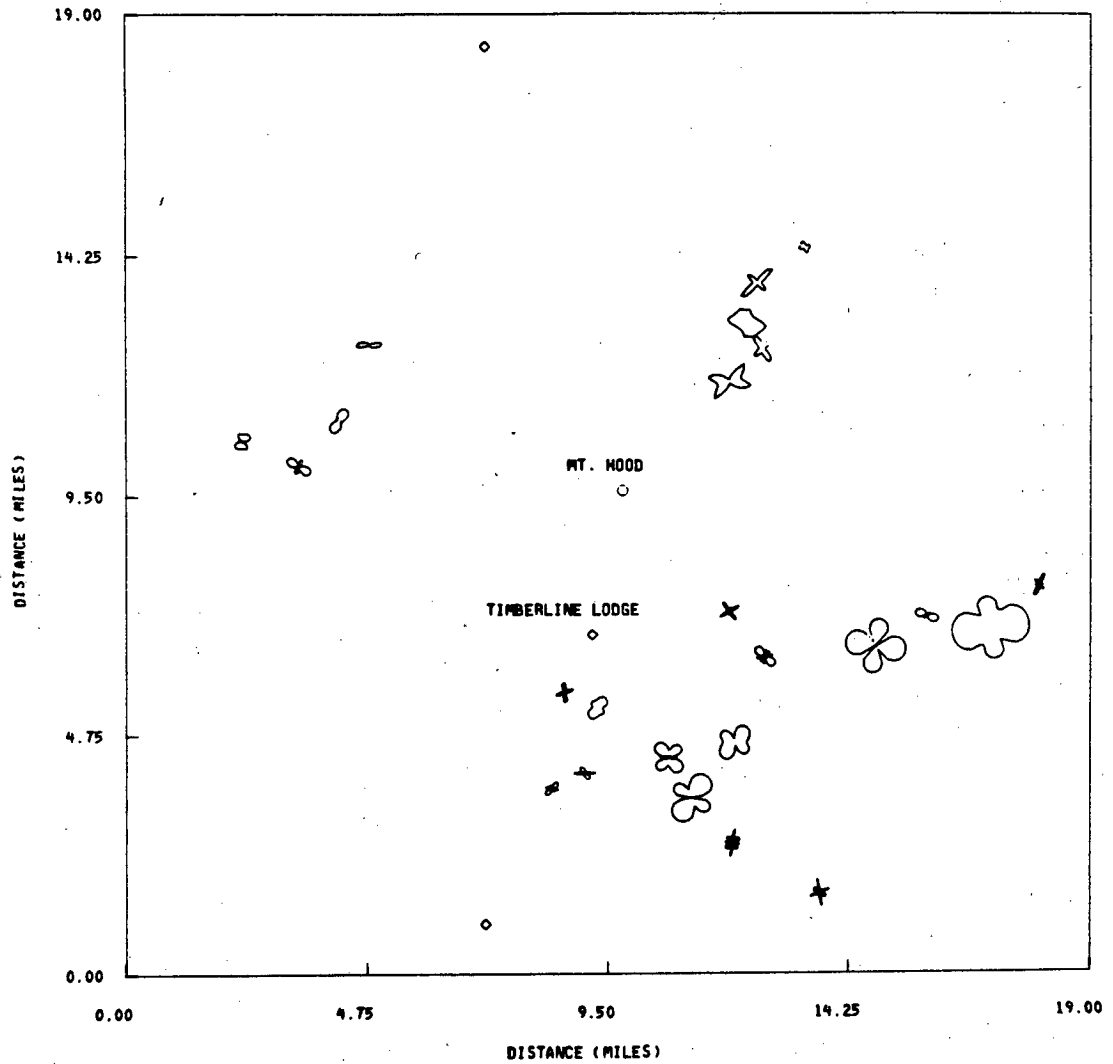
AVERAGED FREQS. IN RANGE OF .006-LOWHZ



PXY PHASE OF APPARENT RESISTIVITY XY

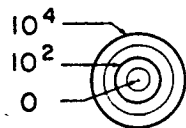
Residual Phase  
(degrees)

AVERAGED FREQS. IN RANGE OF 5.0-1.0 HZ



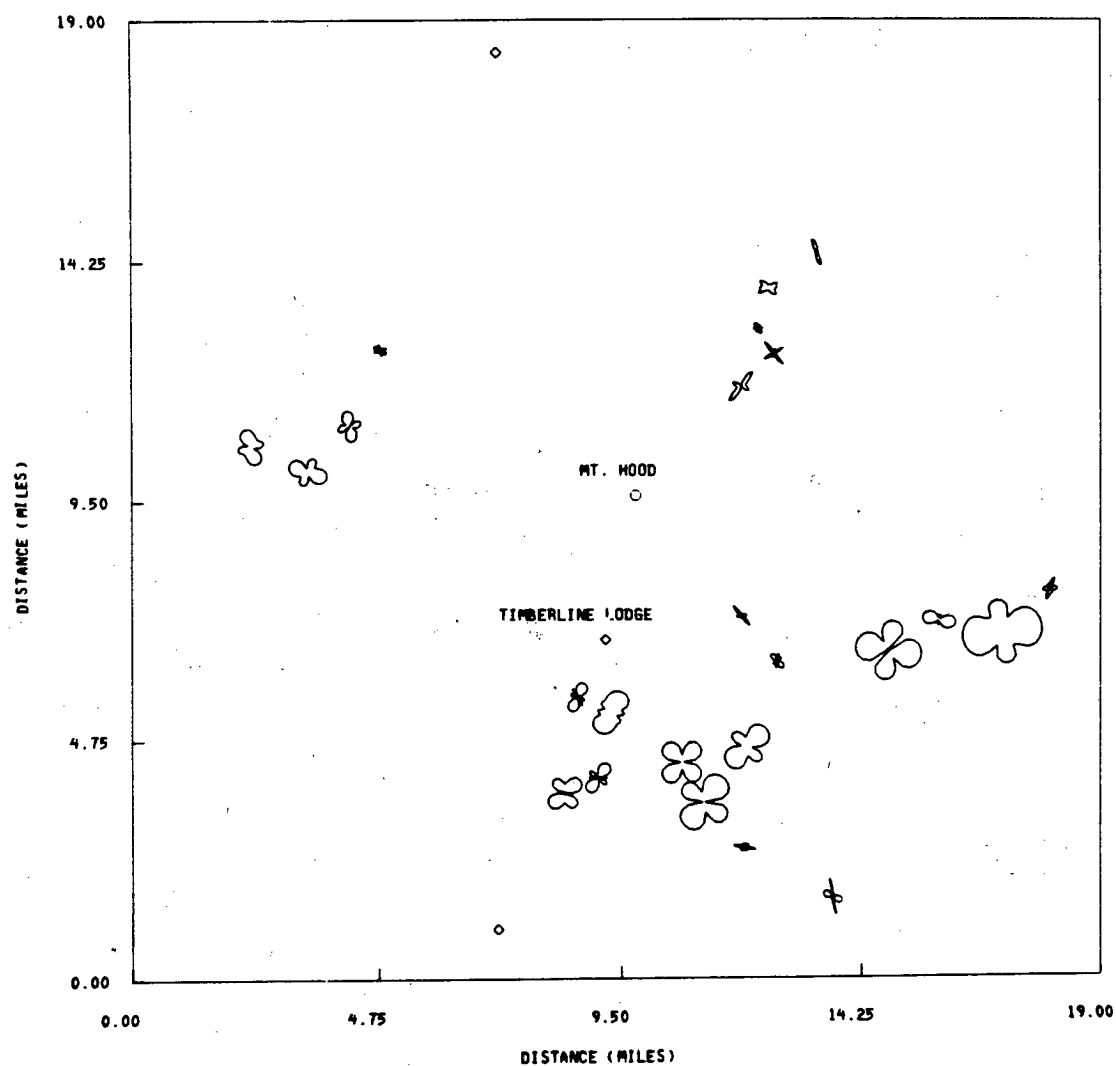
RXX APPARENT RESISTIVITY XX

Kilometers 0 5 10

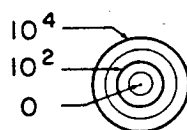


Apparent resistivity (ohm·m)

AVERAGED FREQS. IN RANGE OF 1.0-0.2 HZ



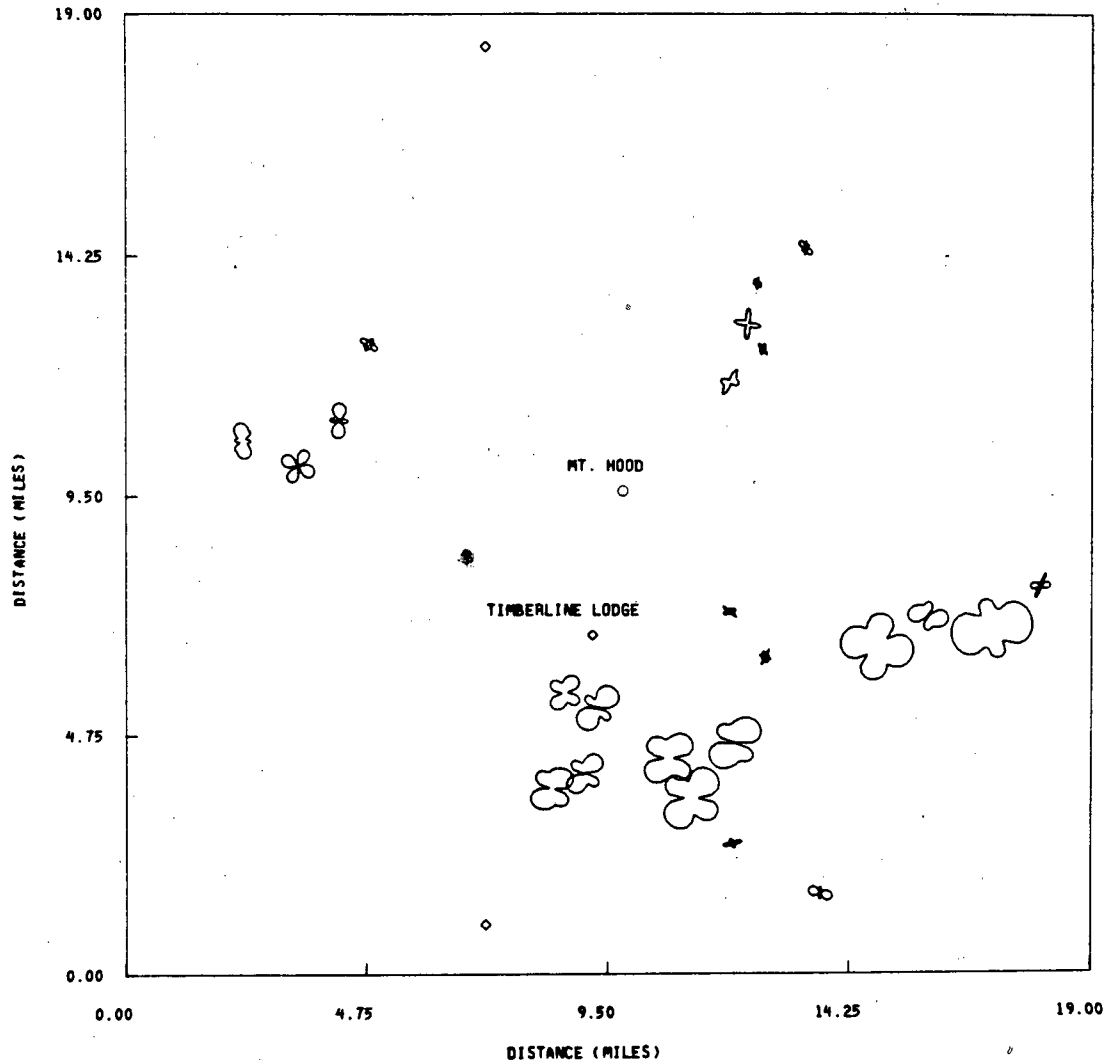
RXX APPARENT RESISTIVITY XX



Apparent resistivity (ohm·m)

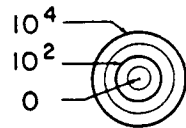
Kilometers 0 5 10

AVERAGED FREQS. IN RANGE OF .2-.03 HZ



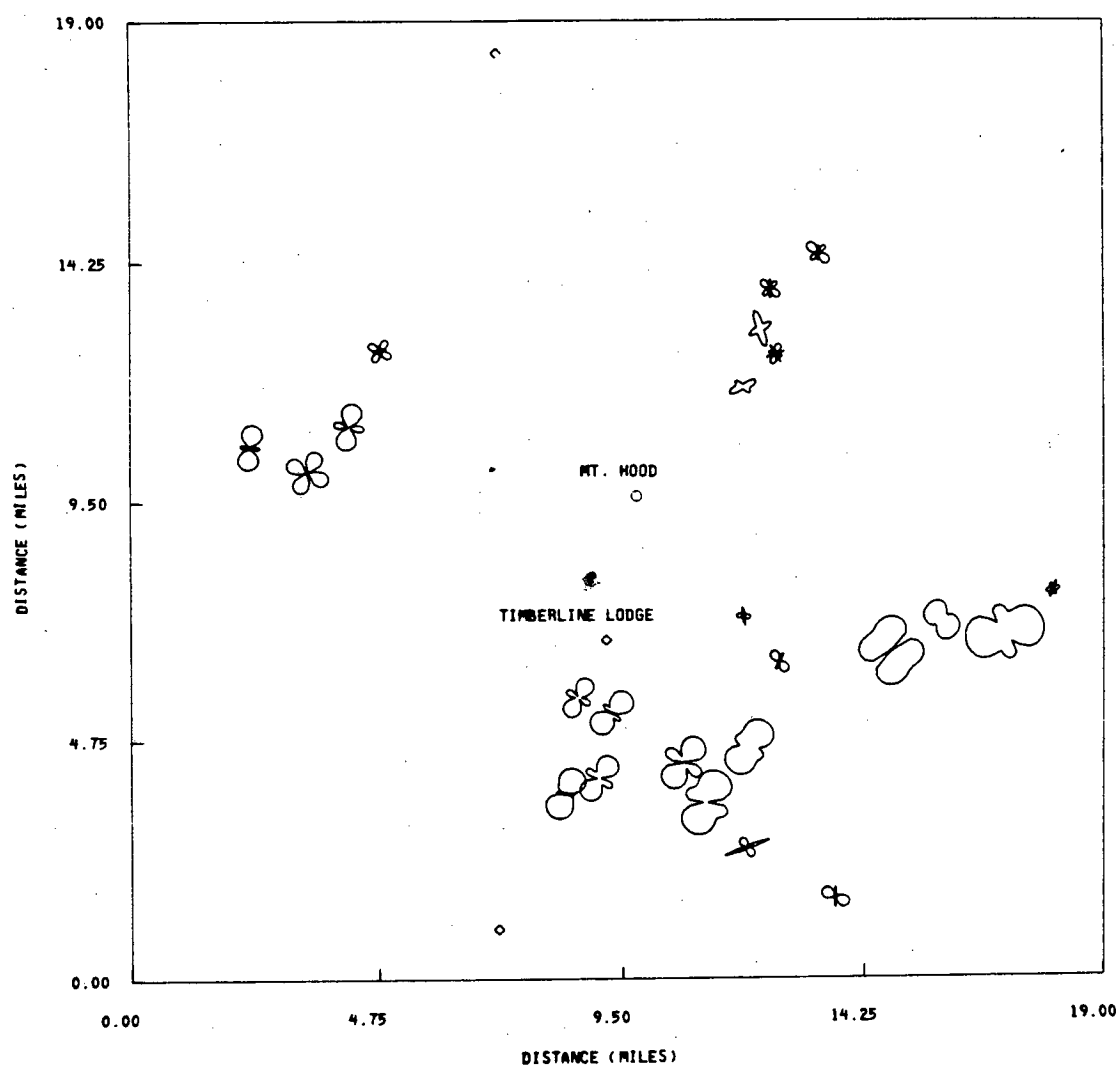
RXX APPARENT RESISTIVITY XX

Kilometers 0 5 10

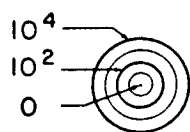


Apparent resistivity (ohm·m)

AVERAGED FREQS. IN RANGE OF .03-.006HZ



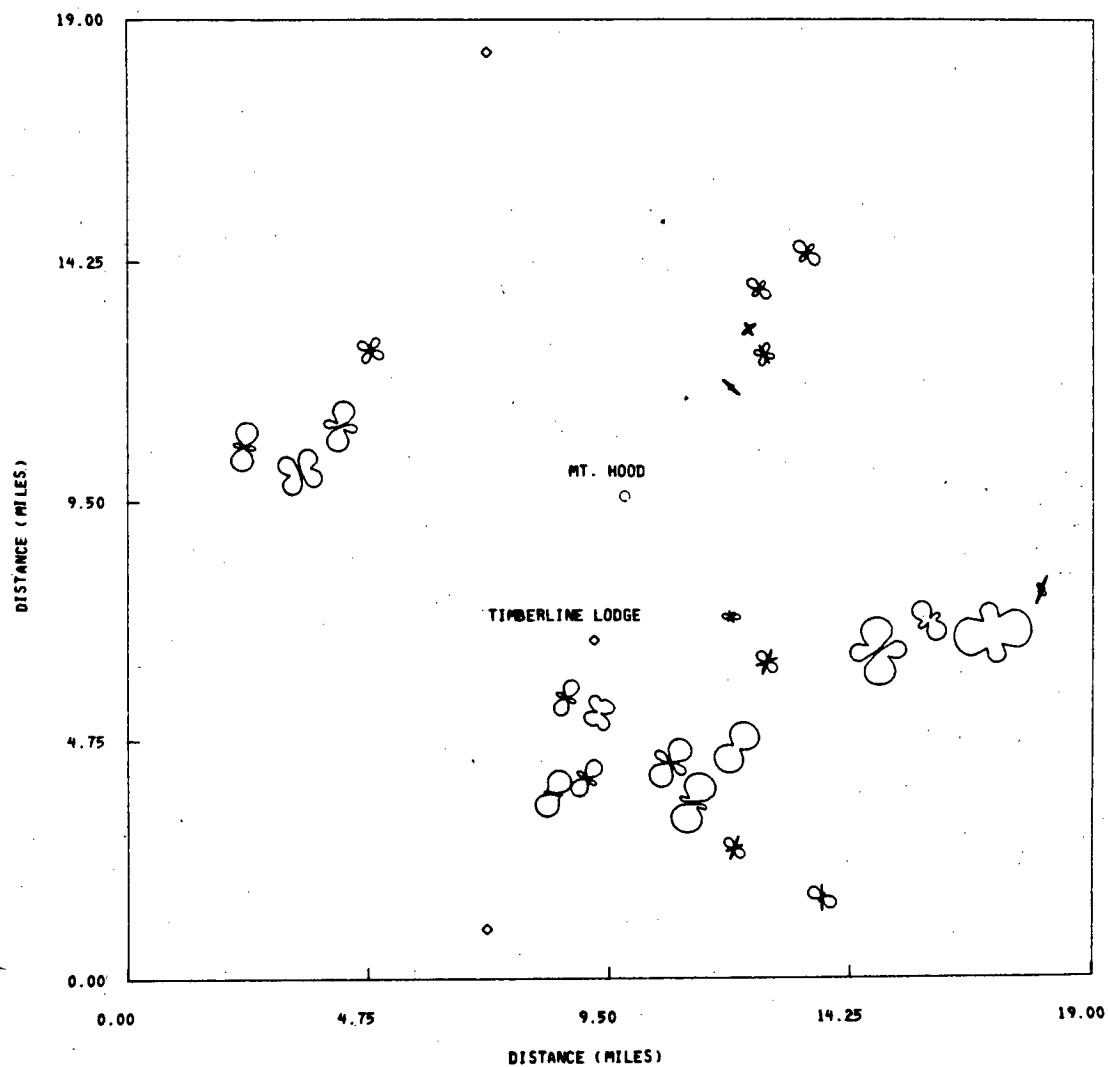
RXX APPARENT RESISTIVITY XX



Apparent resistivity (ohm·m)

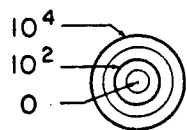
Kilometers 0 5 10

AVERAGED FREQS. IN RANGE OF .006-LOWHZ



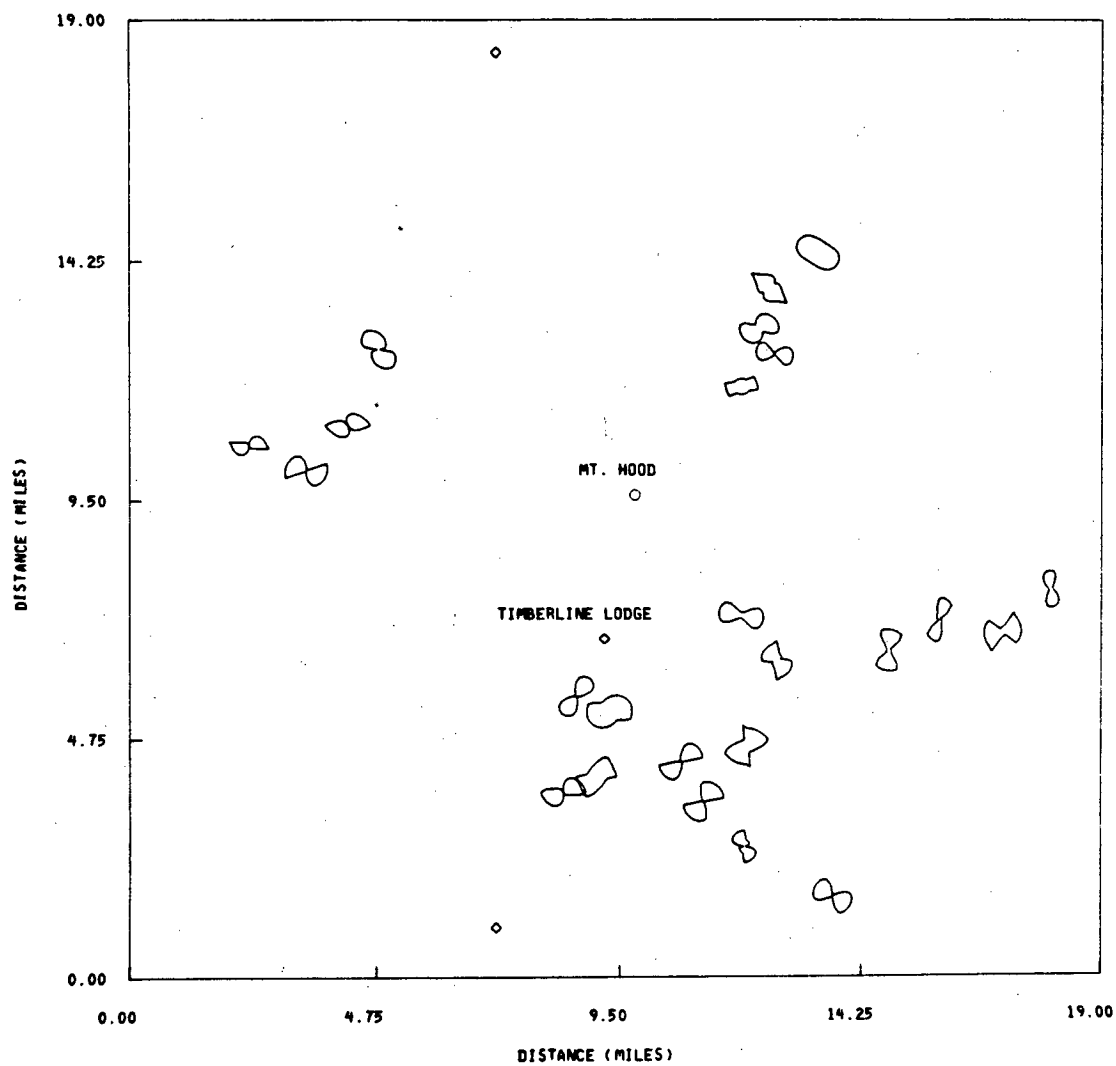
RXX APPARENT RESISTIVITY XX

Kilometers 0 5 10



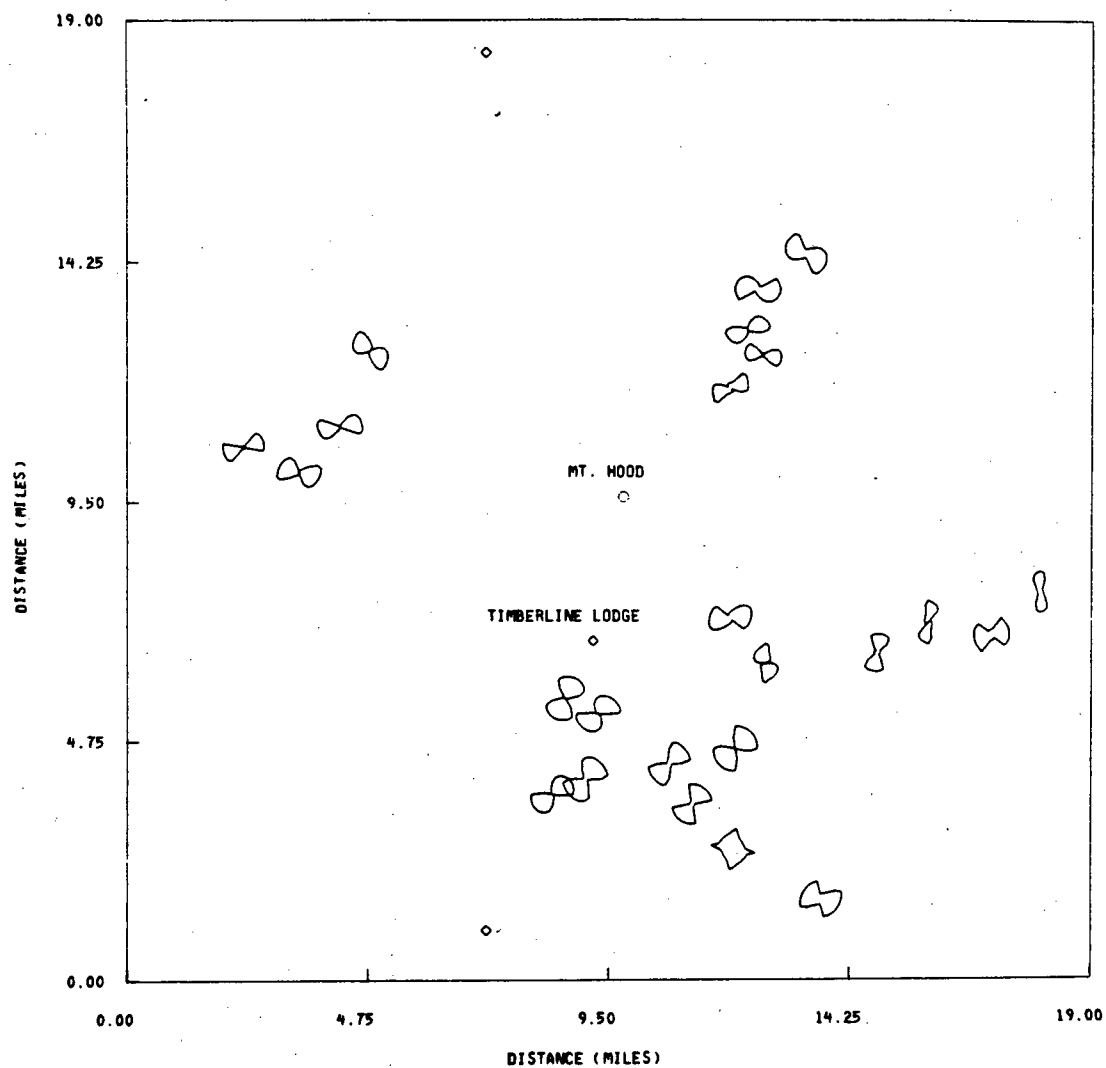
Apparent resistivity (ohm·m)

AVERAGED FREQS. IN RANGE OF 5.0-1.0 HZ

Phase Scale  
(degrees)

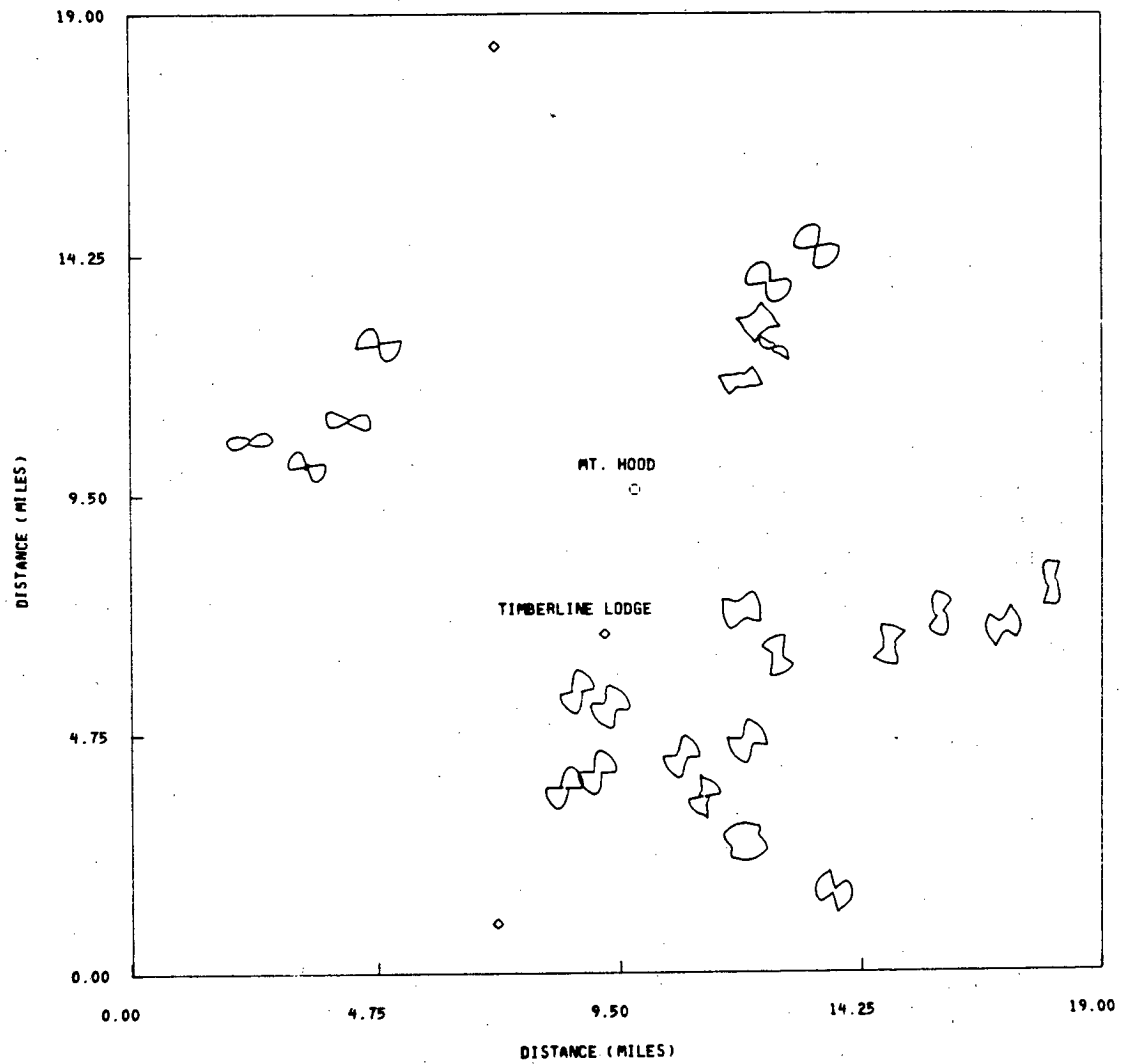
PXX PHASE OF APPARENT RESISTIVITY XX

AVERAGED FREQS. IN RANGE OF 1.0-0.2 HZ

Phase Scale  
(degrees)

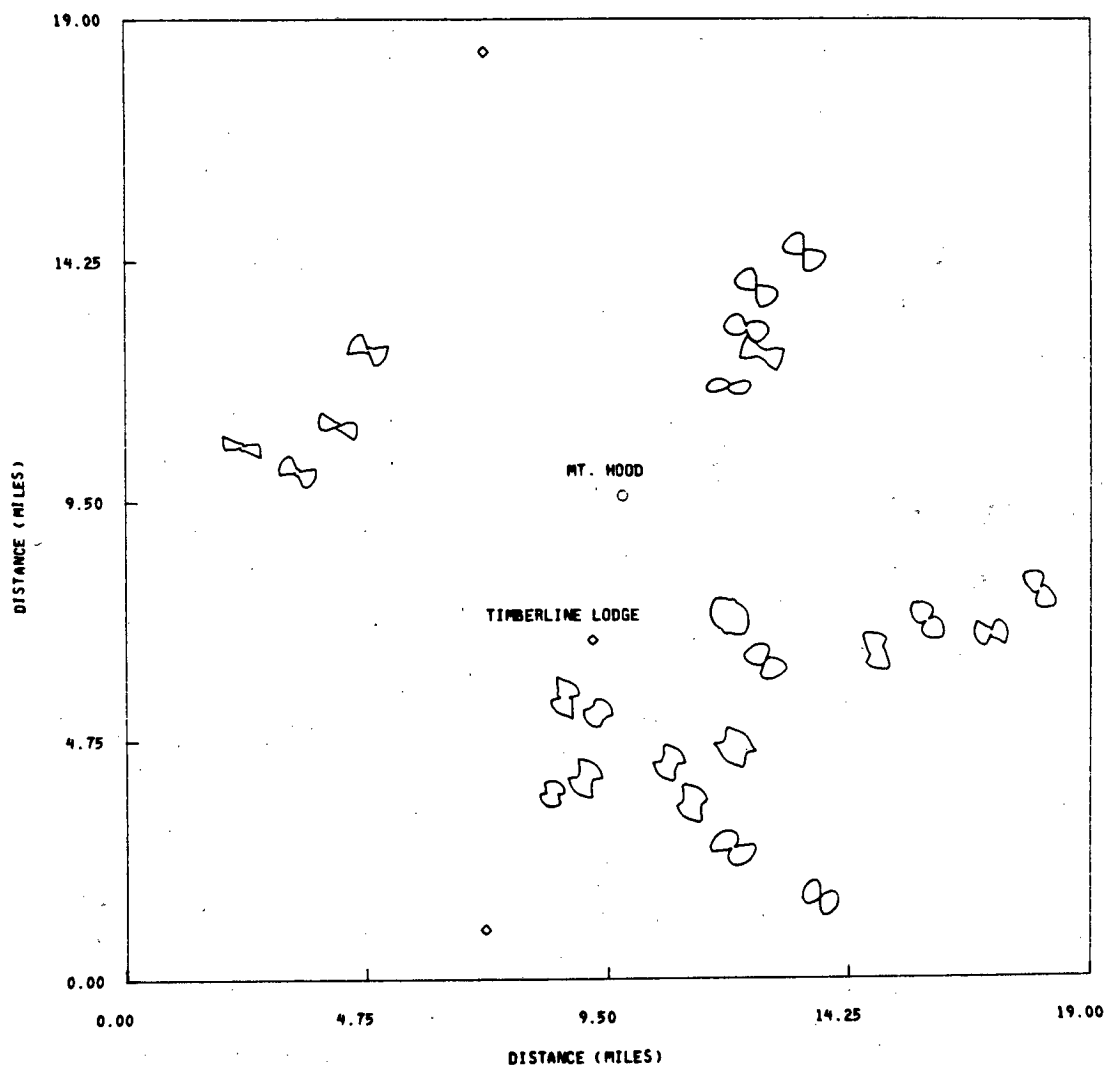
PXX PHASE OF APPARENT RESISTIVITY XX

AVERAGED FREQS. IN RANGE OF .2-.03 HZ

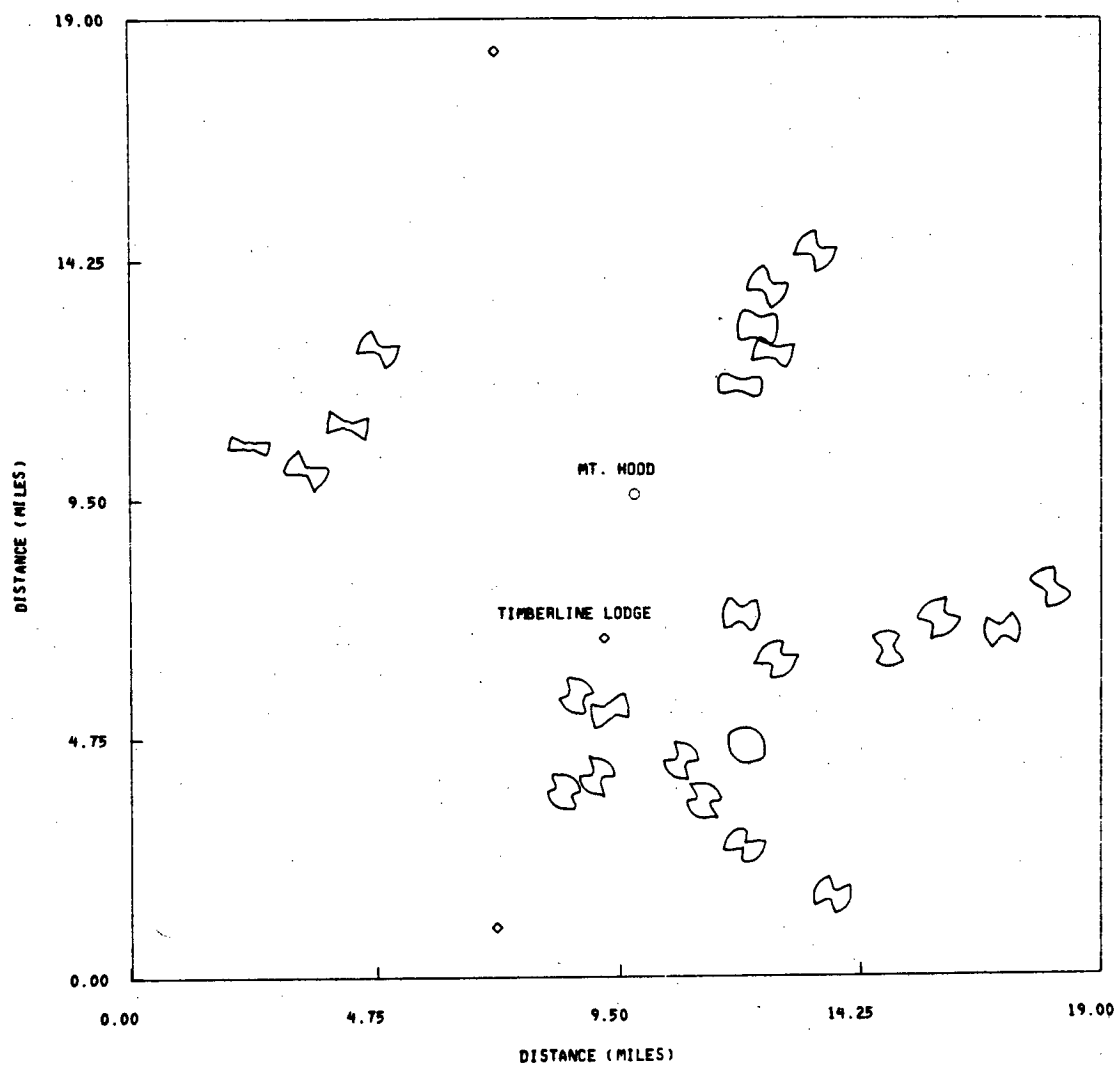


180°  
Phase Scale  
(degrees)

AVERAGED FREQS. IN RANGE OF .03-.006HZ



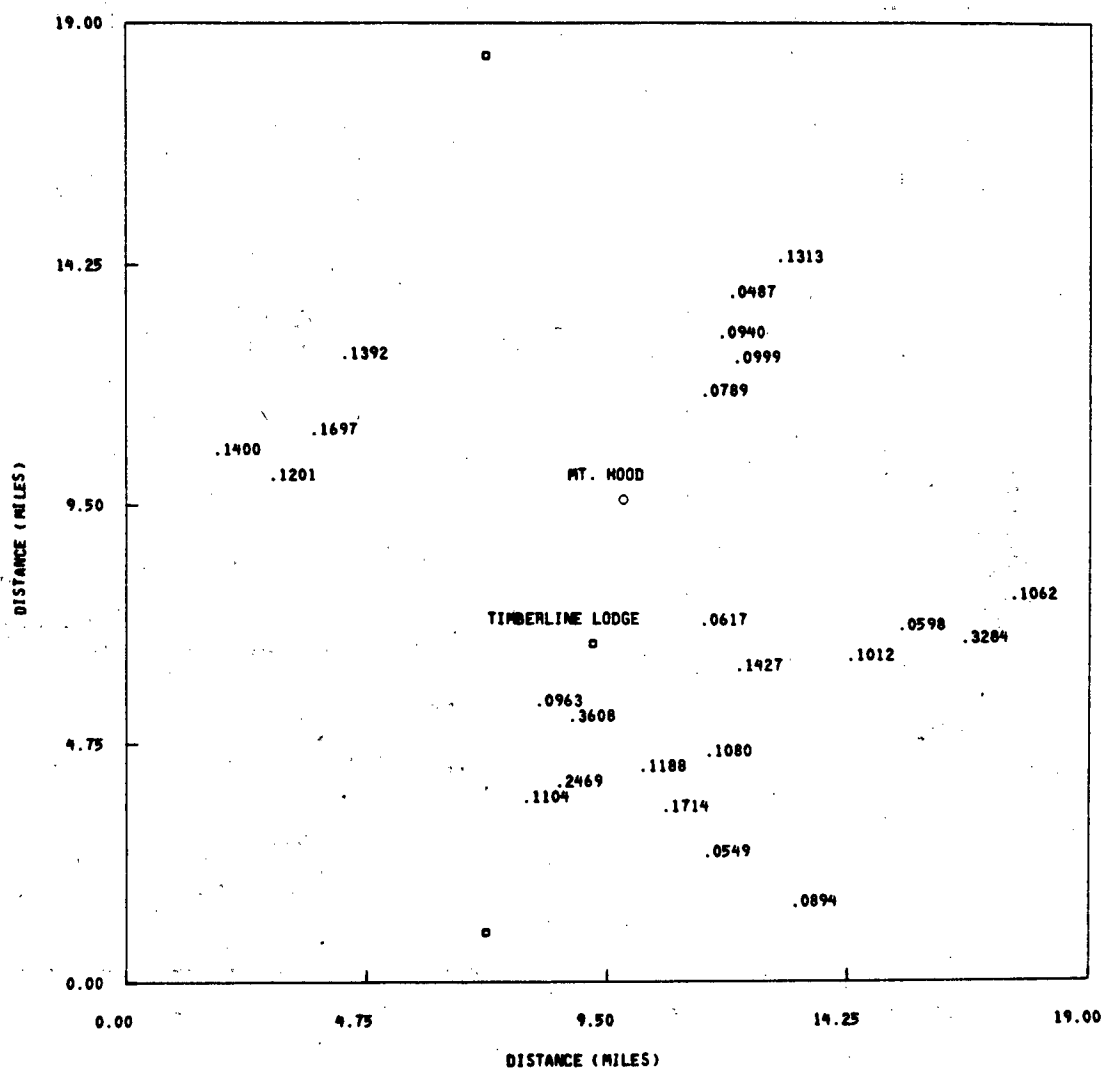
AVERAGED FREQS. IN RANGE OF .006-LOWHZ



180°  
Phase Scale  
(degrees)

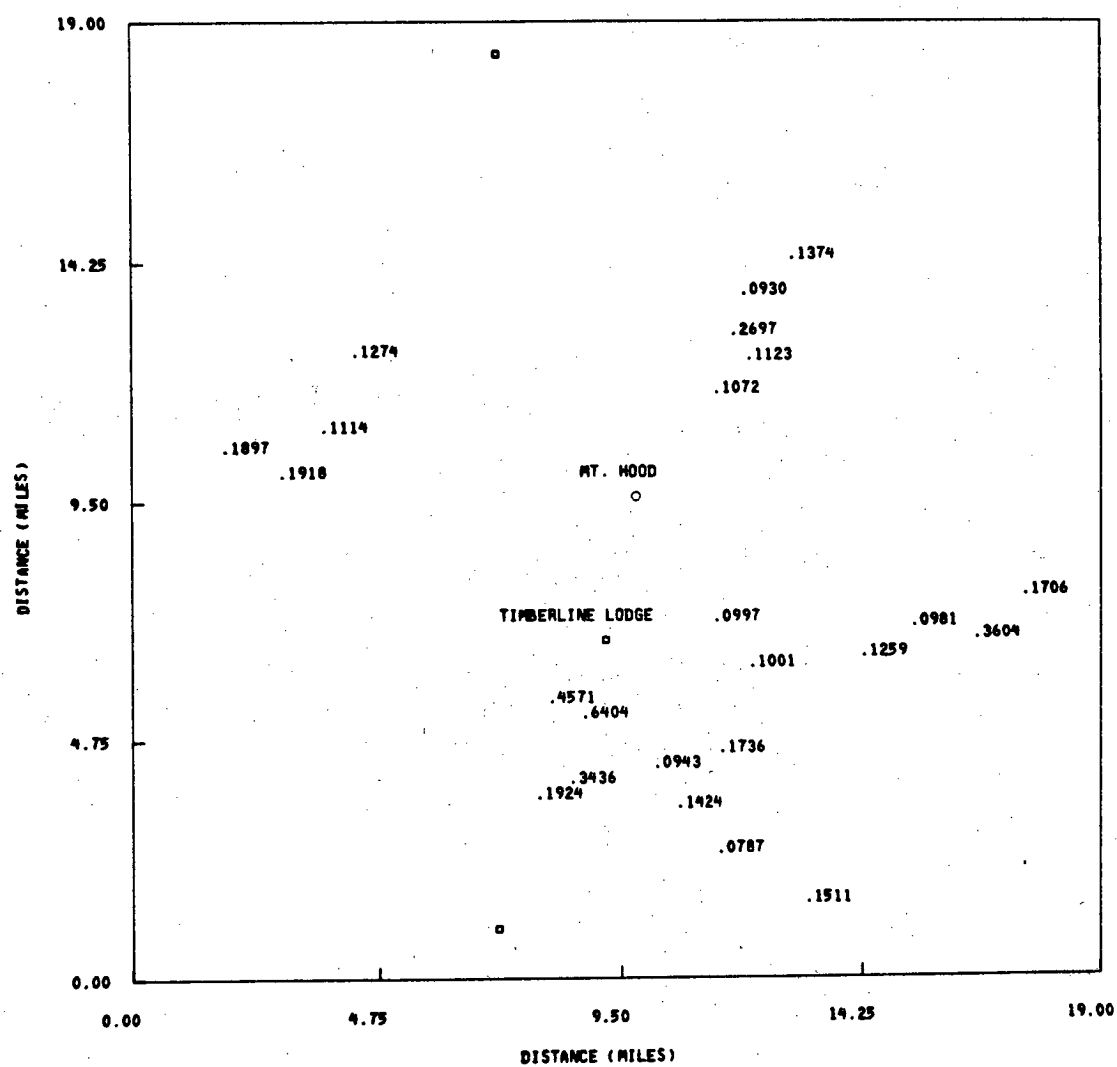
PXX PHASE OF APPARENT RESISTIVITY XX

AVERAGED FREQS. IN RANGE OF 5.0-1.0 HZ

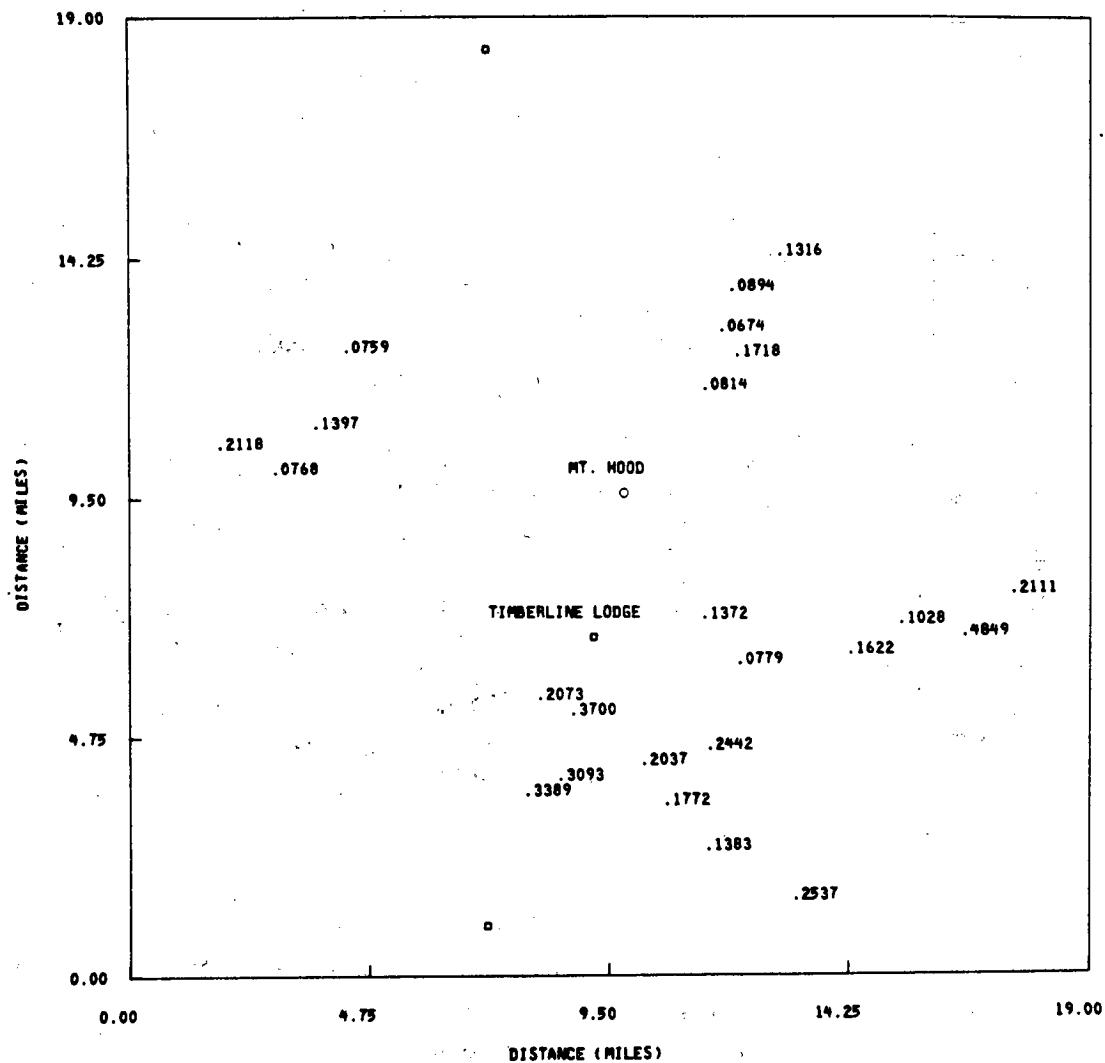


$$\text{SKEW} = \text{ABS}((ZXX + ZYY) / (ZXY - ZYX))$$

AVERAGED FREQS. IN RANGE OF 1.0-0.2 HZ

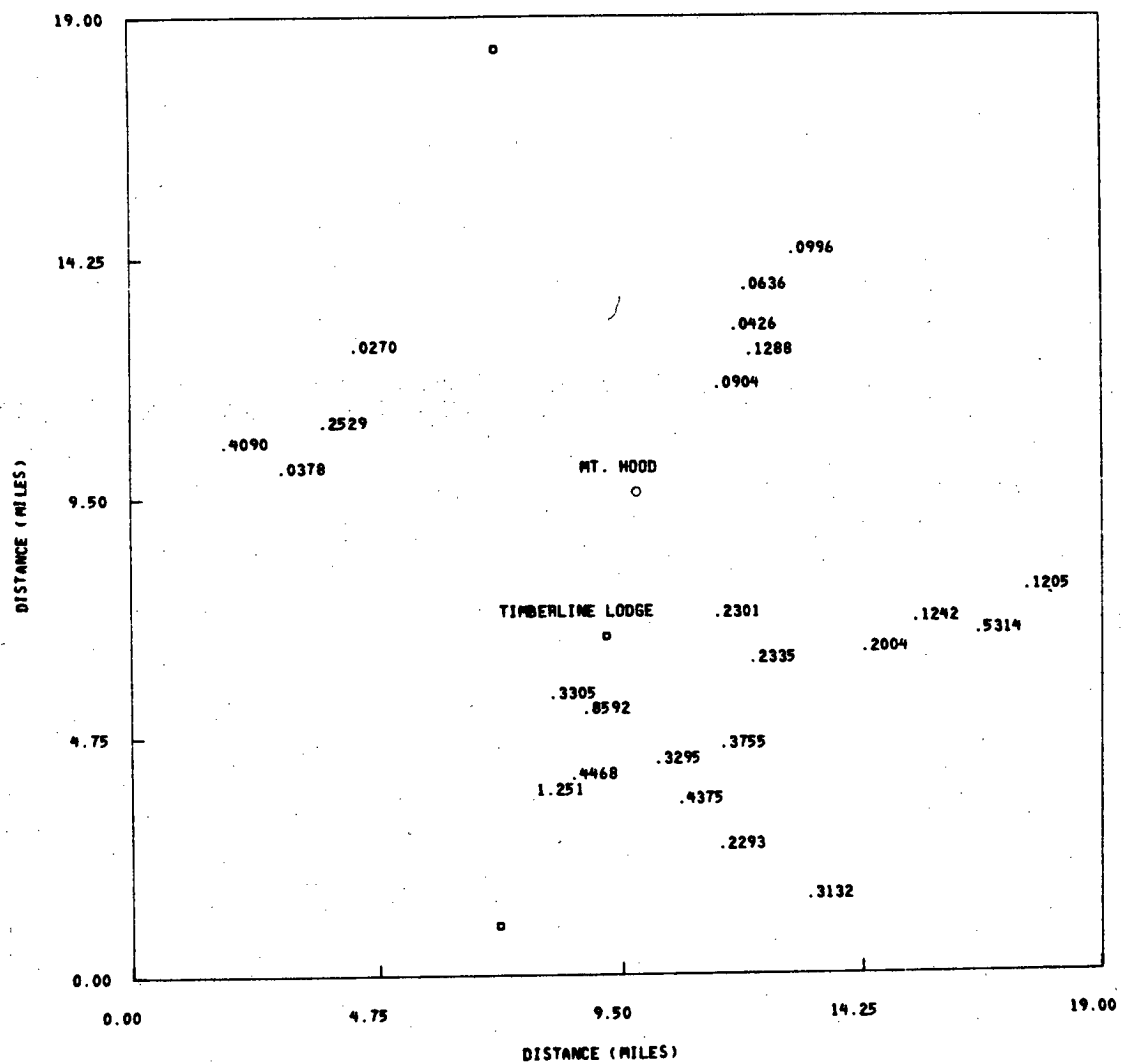

$$\text{SKEW} = \text{ABS}((ZXX + ZYY) / (ZXY - ZYX))$$

AVERAGED FREQS. IN RANGE OF .2-.03 HZ



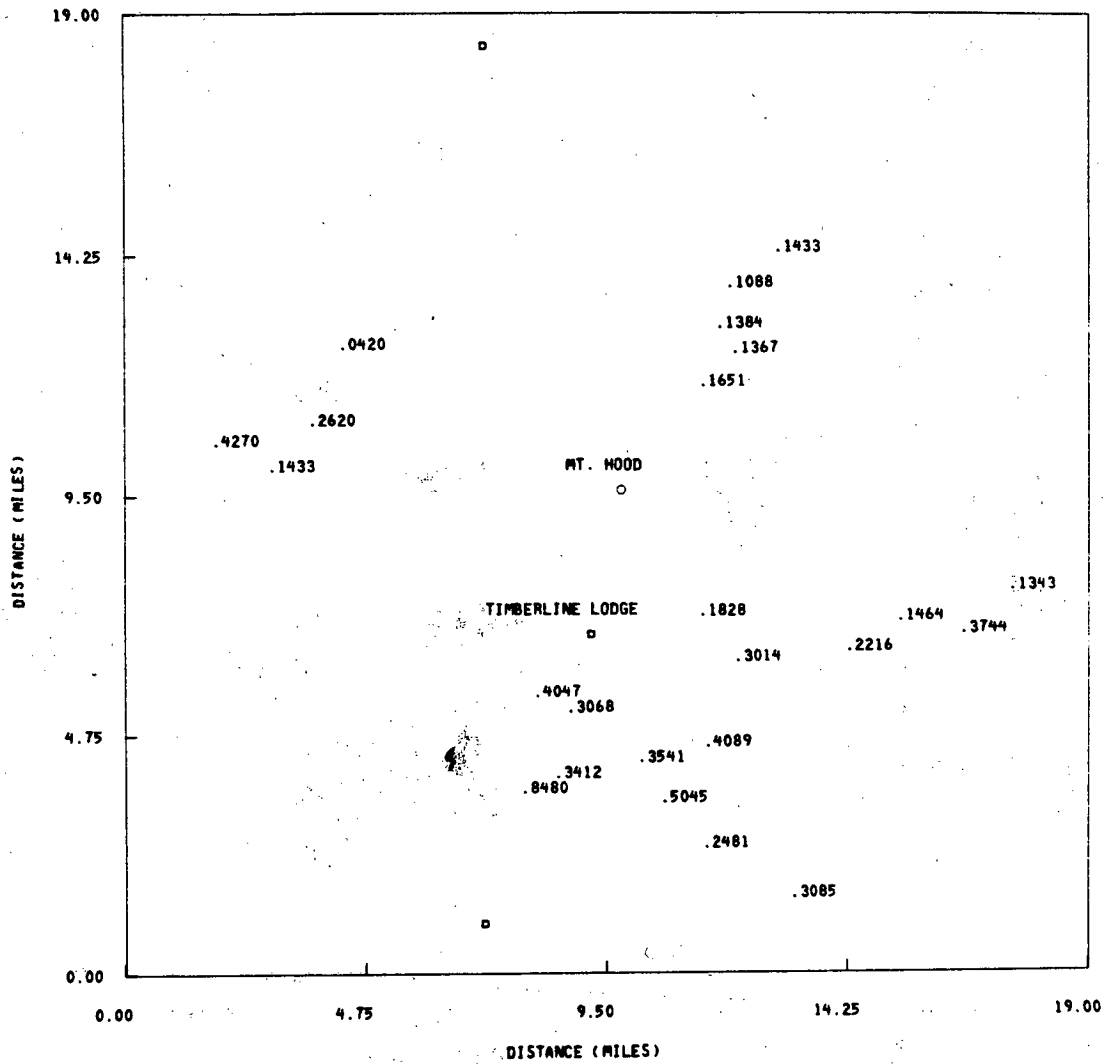
$$\text{SKEW} = \text{ABS}((ZXX + ZYY) / (-ZXY - ZYX))$$

AVERAGED FREQS. IN RANGE OF .03-.006HZ



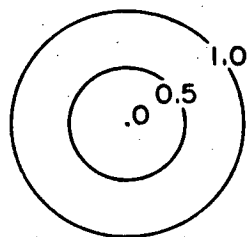
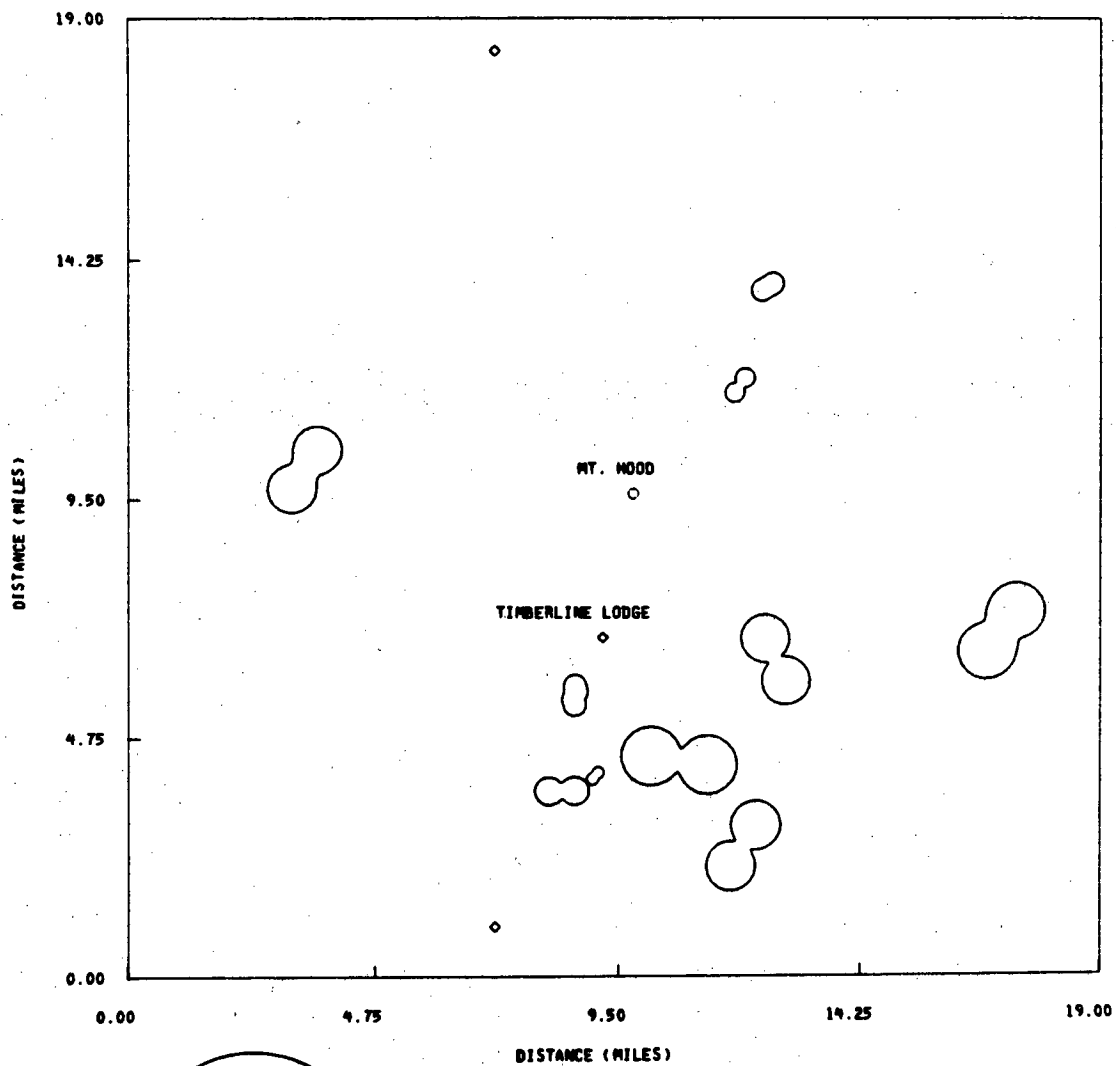
$$SKEW=ABS((ZXX+ZYY)/(ZXY-ZYX))$$

AVERAGED FREQS. IN RANGE OF .006-LOWHZ



$$\text{SKEW} = \text{ABS}((ZXX + ZYY) / (ZXY - ZYX))$$

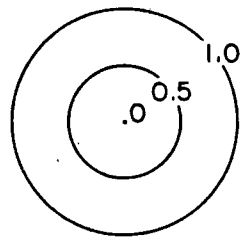
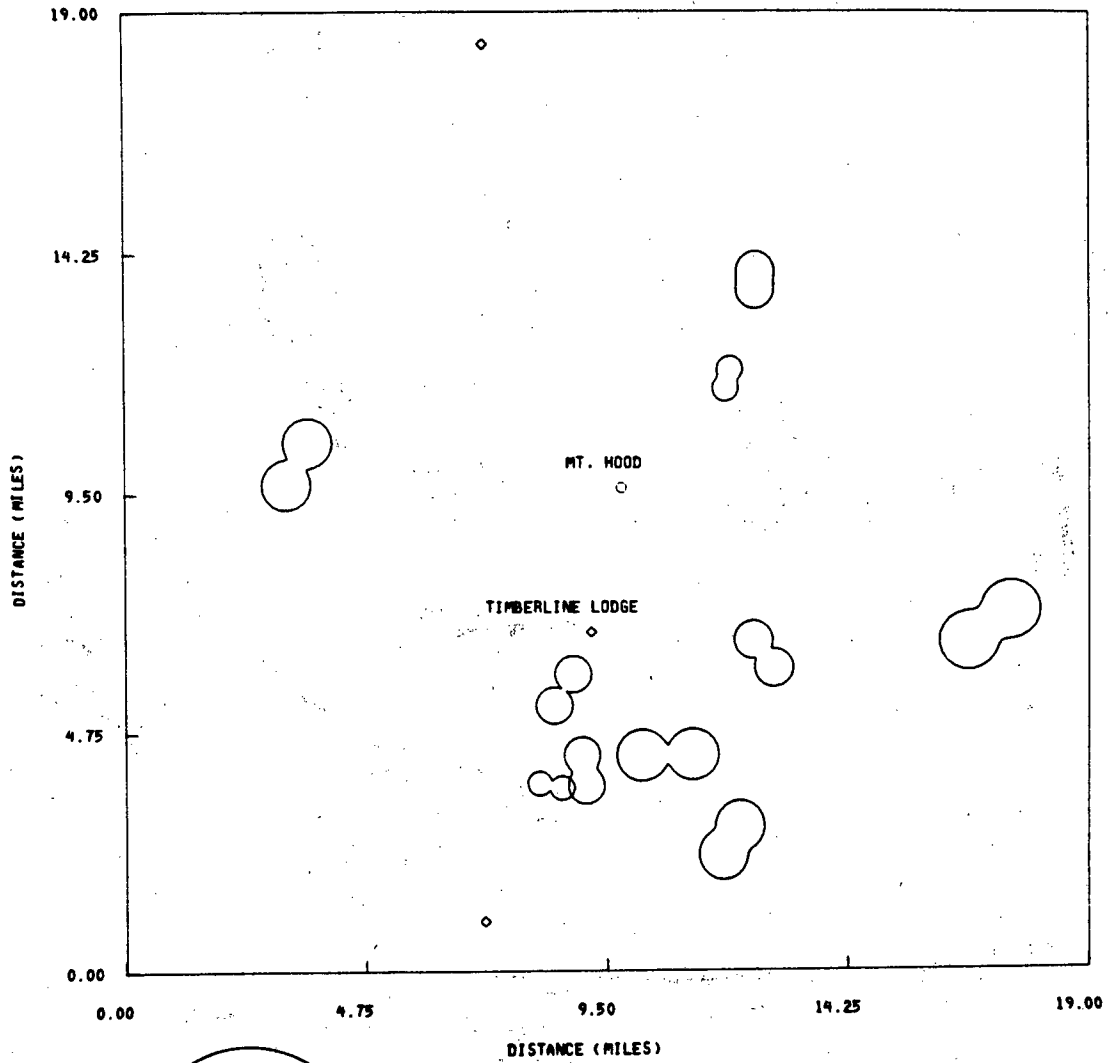
AVERAGED FREQS. IN RANGE OF 5.0-1.0 HZ



TMX TIPPER AMPLITUDE X

Tipper scale

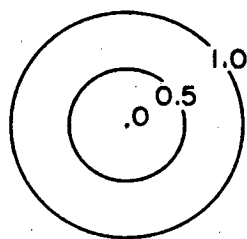
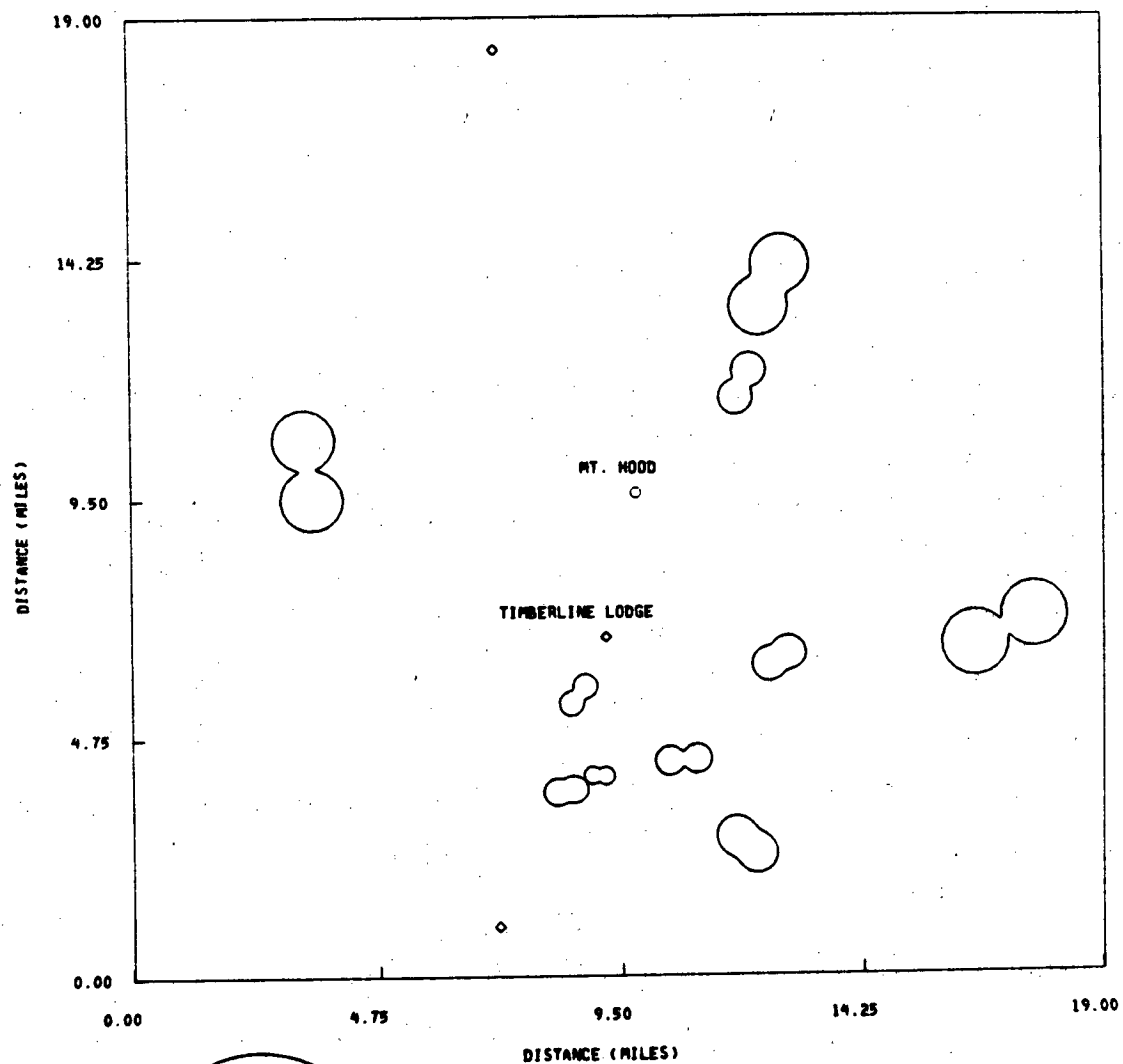
AVERAGED FREQS. IN RANGE OF 1.0-0.2 HZ



TRX TIPPER AMPLITUDE X

Tipper scale

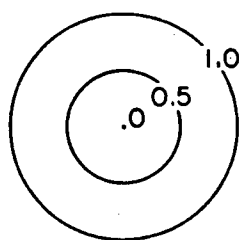
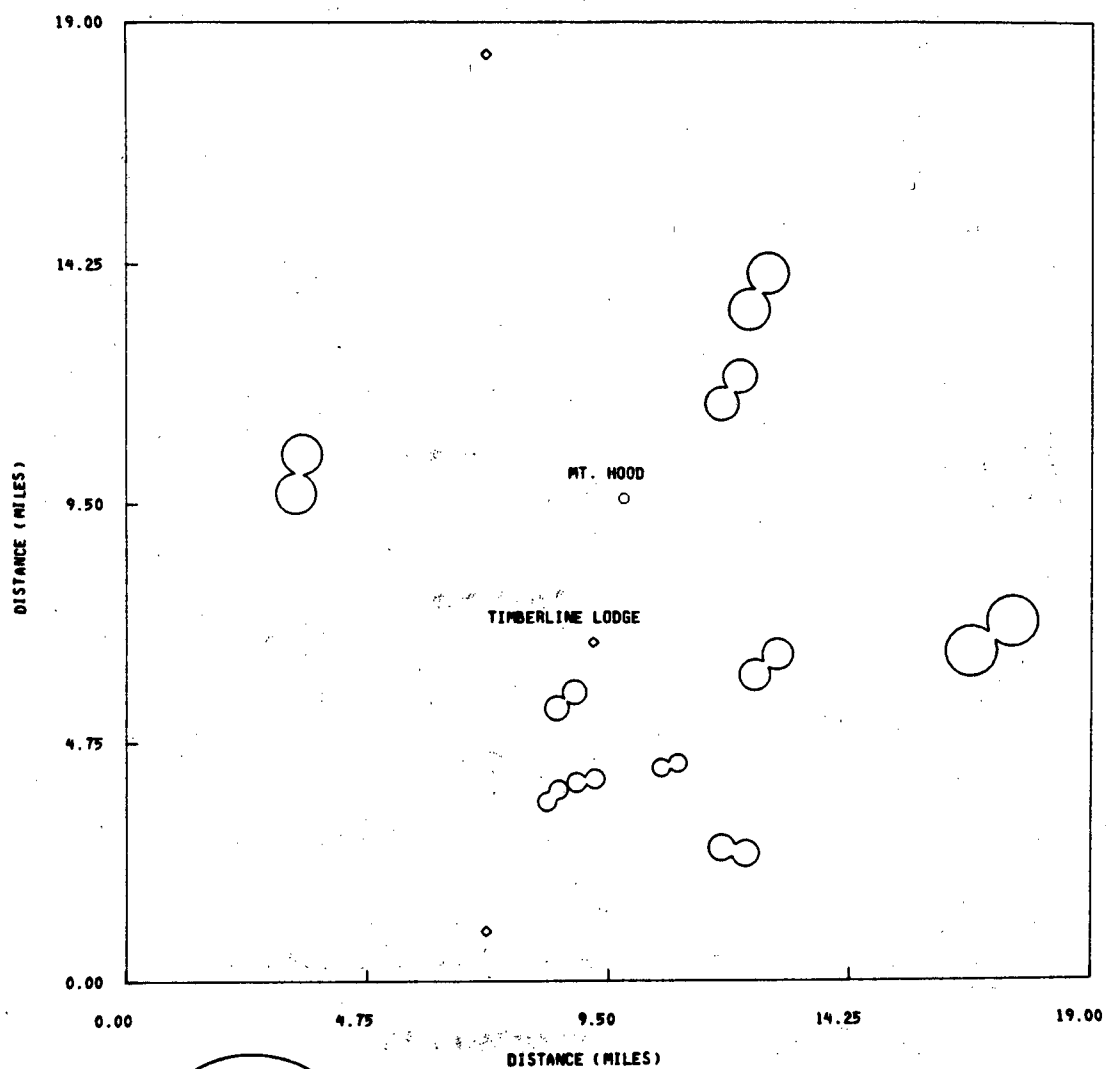
AVERAGED FREQS. IN RANGE OF .2-.03 HZ



TAX TIPPER AMPLITUDE X

Tipper scale

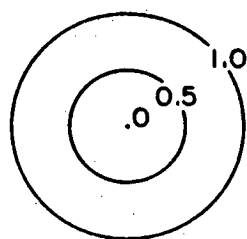
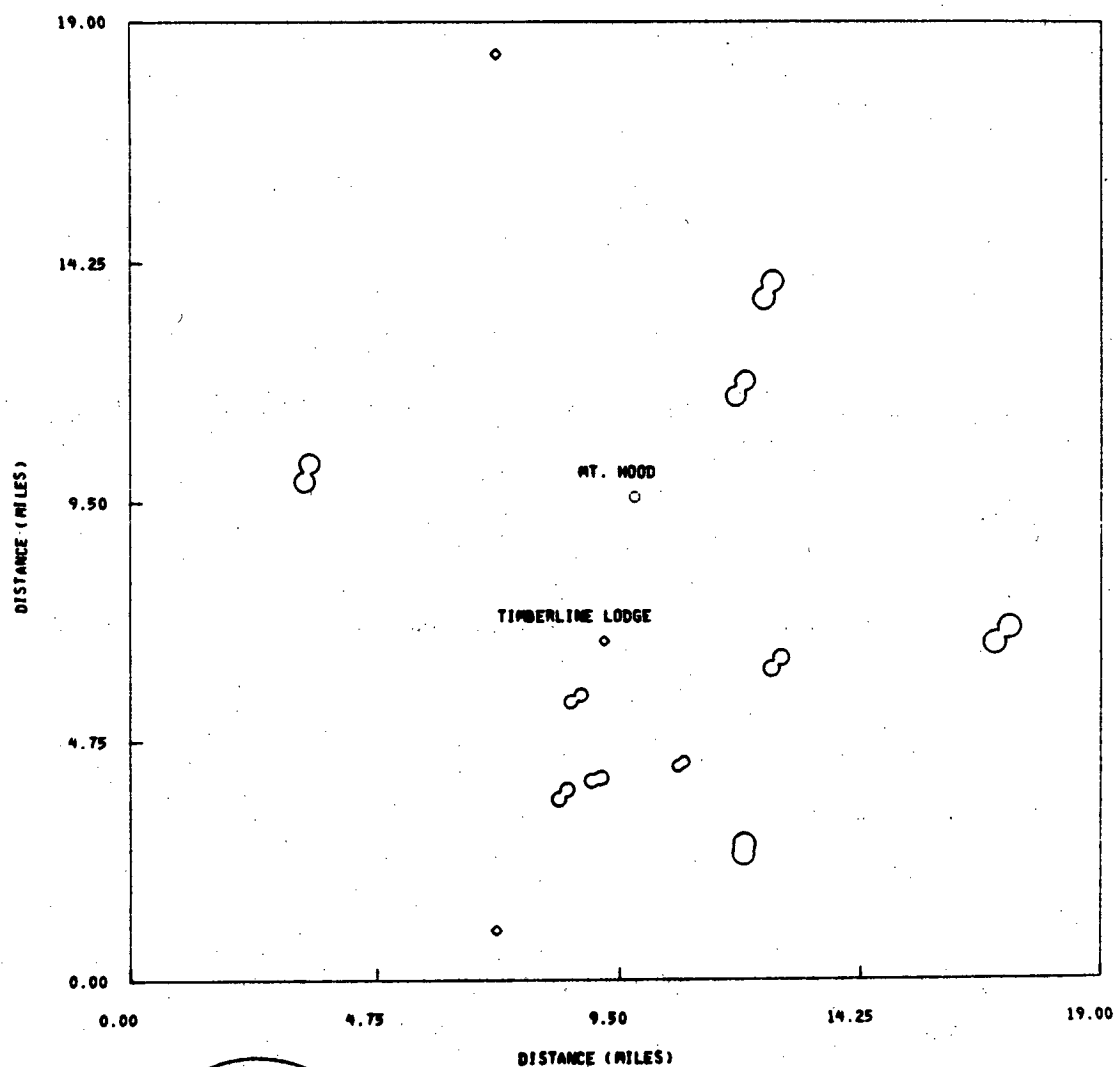
AVERAGED FREQS. IN RANGE OF .03-.006HZ



TMX TIPPER AMPLITUDE X

Tipper scale

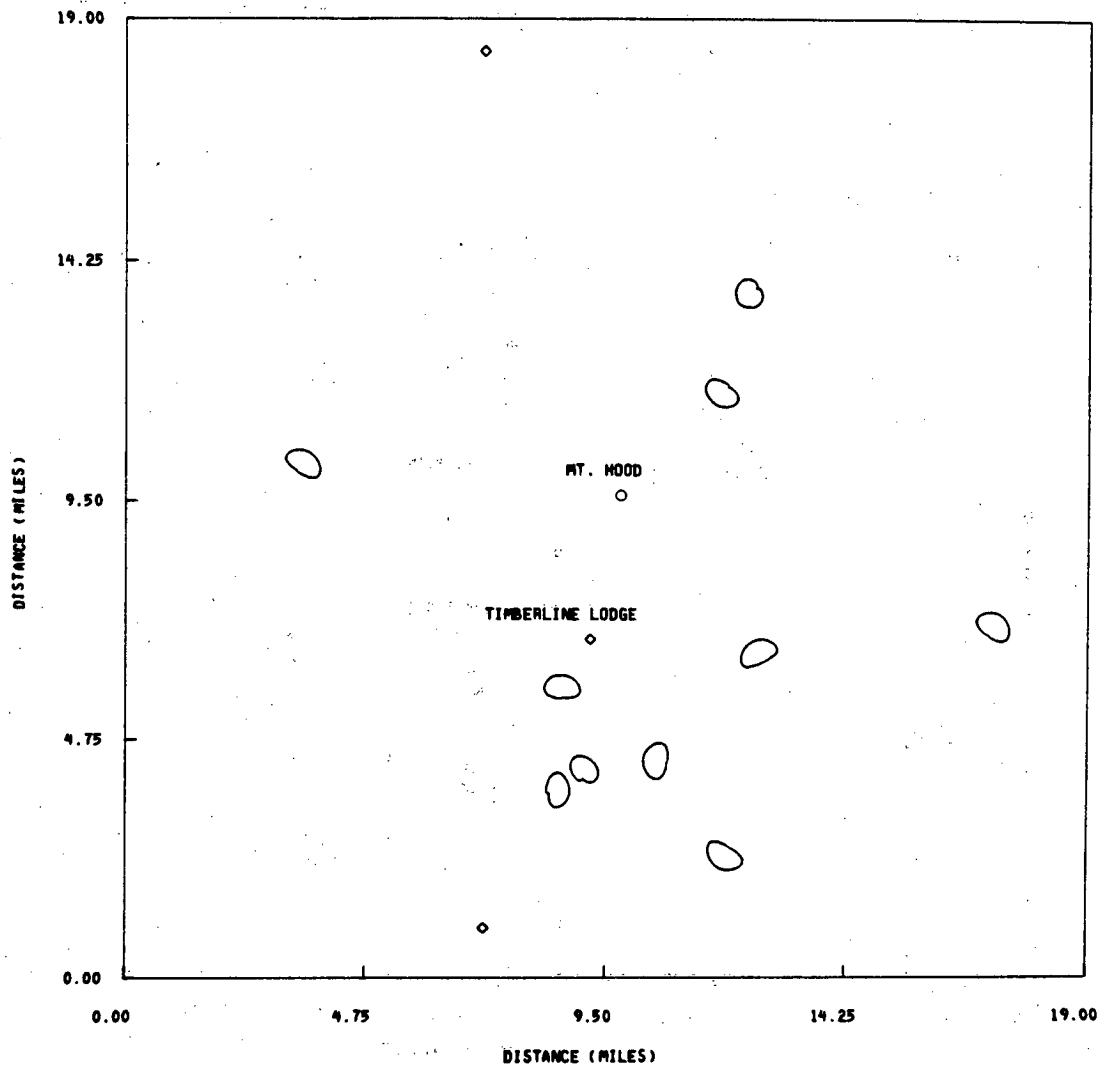
AVERAGED FREQS. IN RANGE OF .004-.006HZ



Tipper scale

THE TIPPER AMPLITUDE X

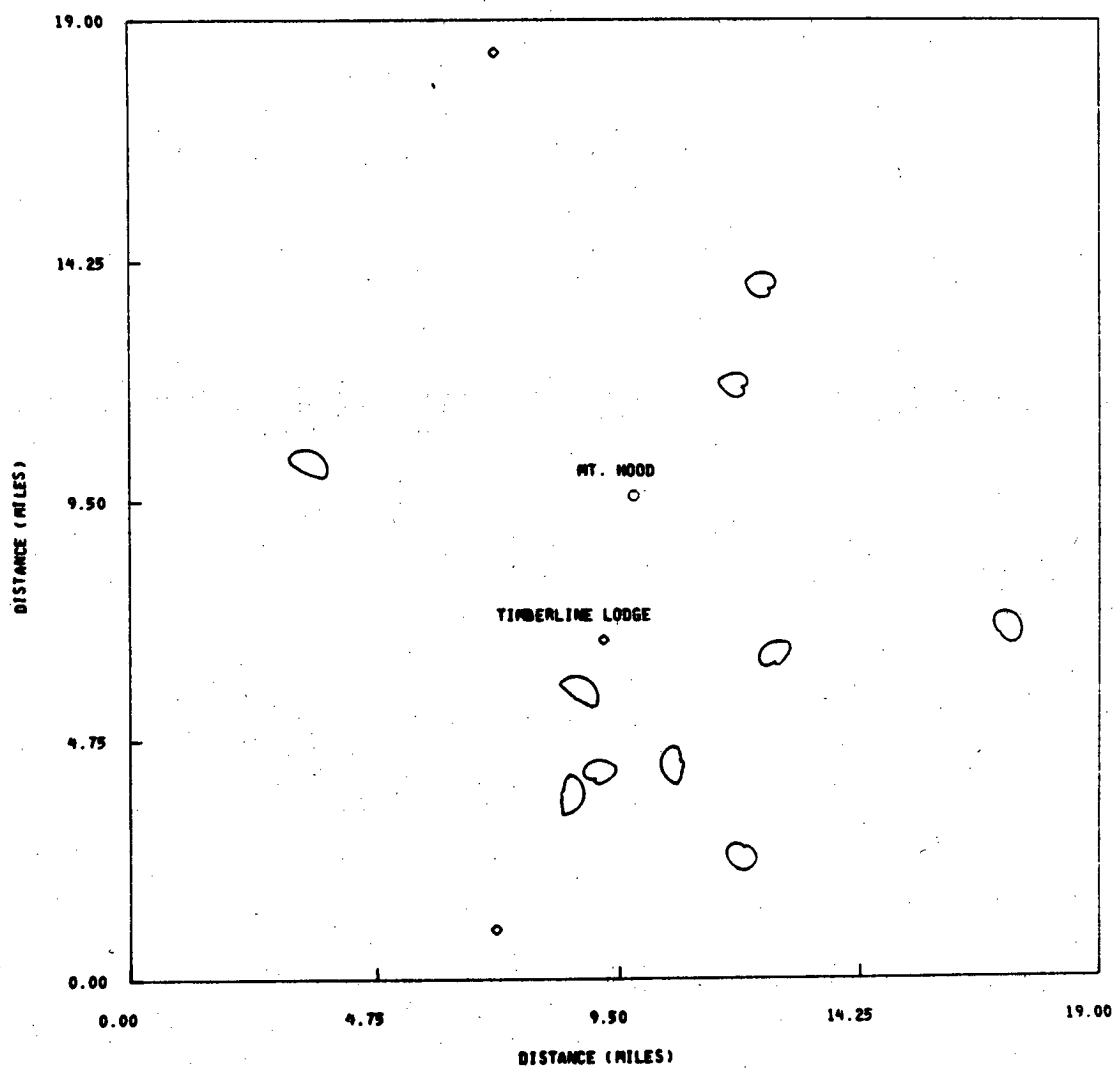
AVERAGED FREQS. IN RANGE OF 5.0-1.0 HZ



180°  
Phase Scale  
(degrees)

TPX TIPPER PHASE X

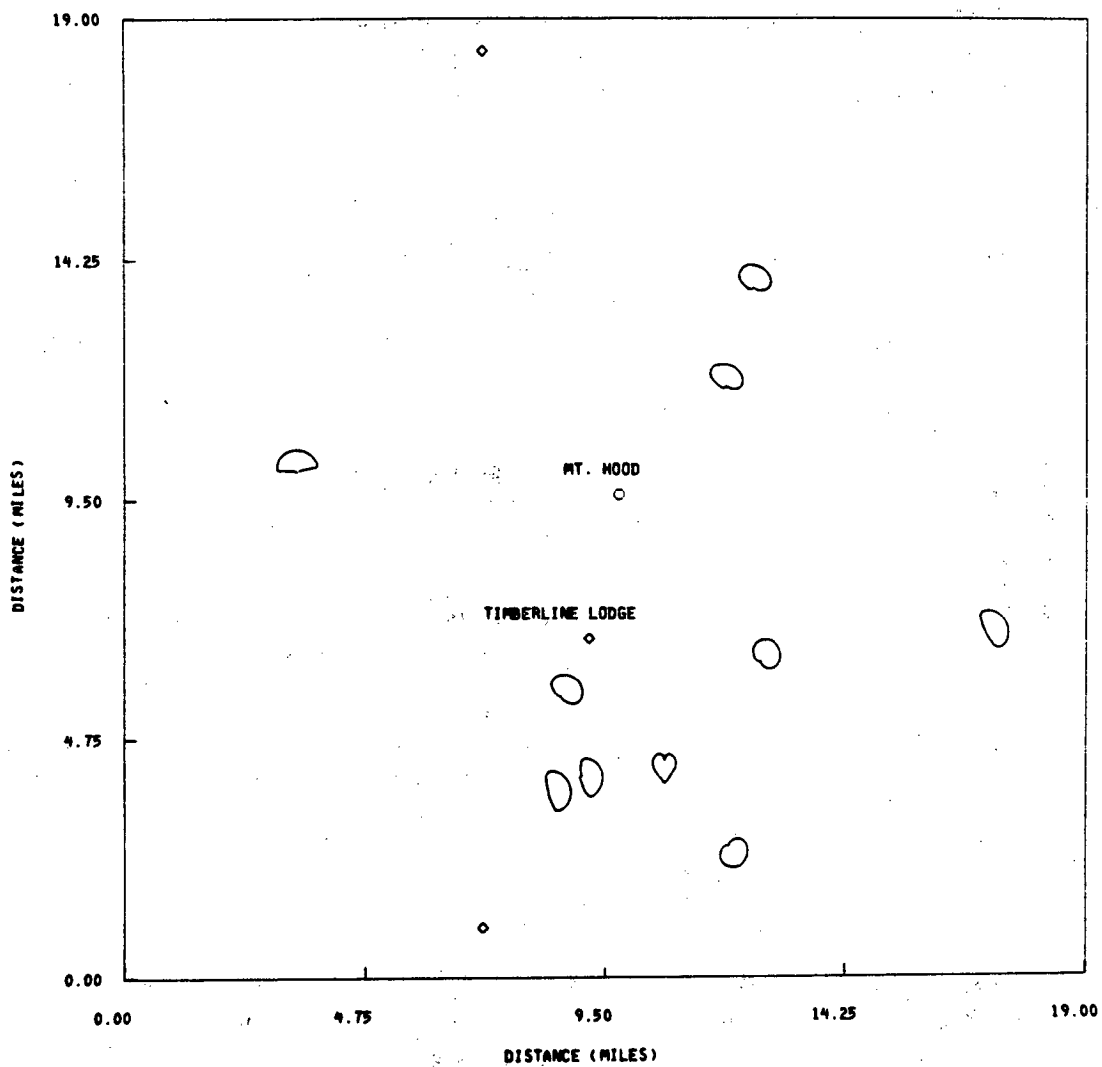
AVERAGED FREQS. IN RANGE OF 1.0-0.2 HZ



180°  
Phase Scale  
(degrees)

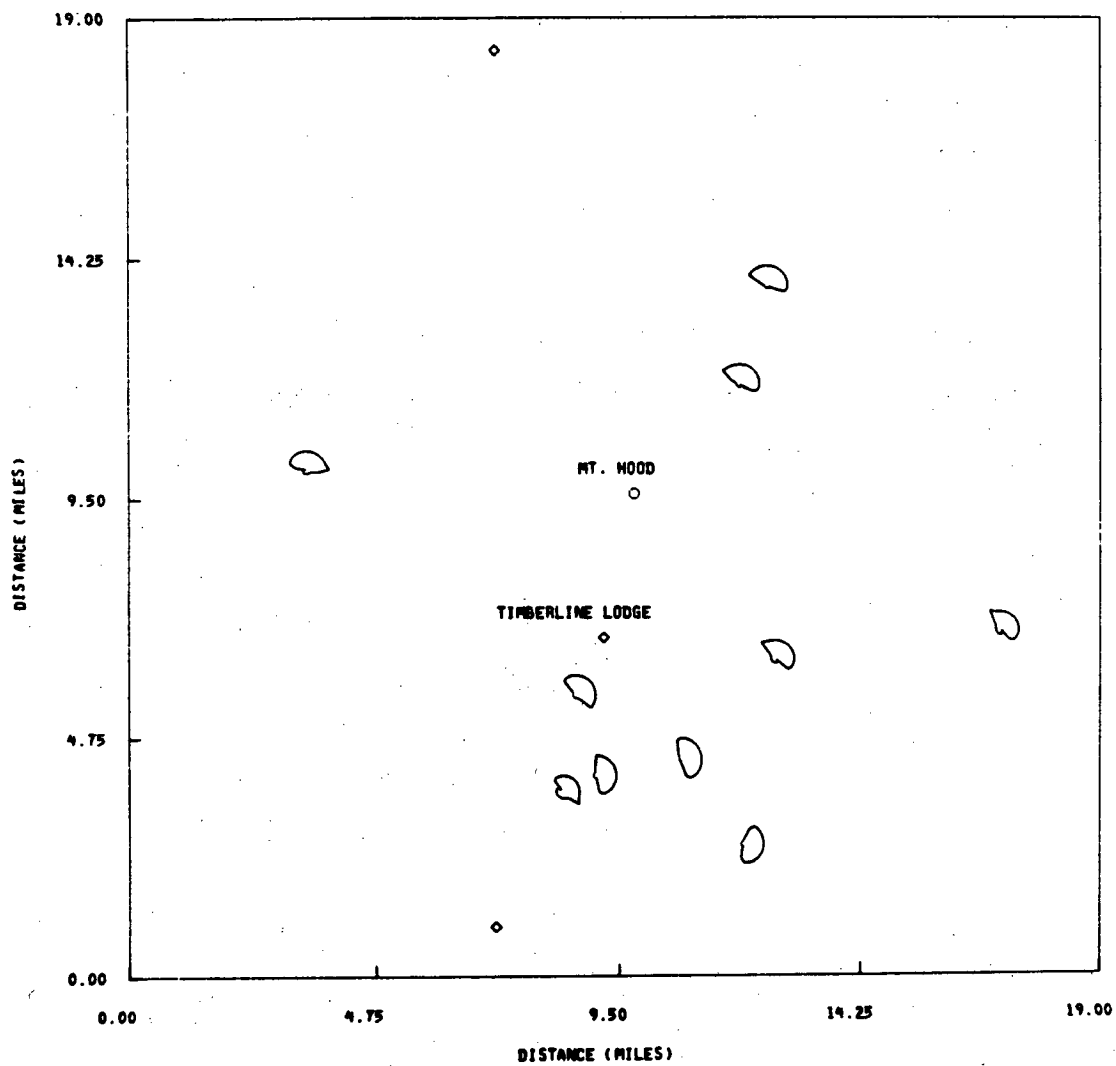
TPX TIPPER PHASE X

AVERAGED FREQS. IN RANGE OF .2-.03 MZ

Phase Scale  
(degrees)

TPX TIPPER PHASE X

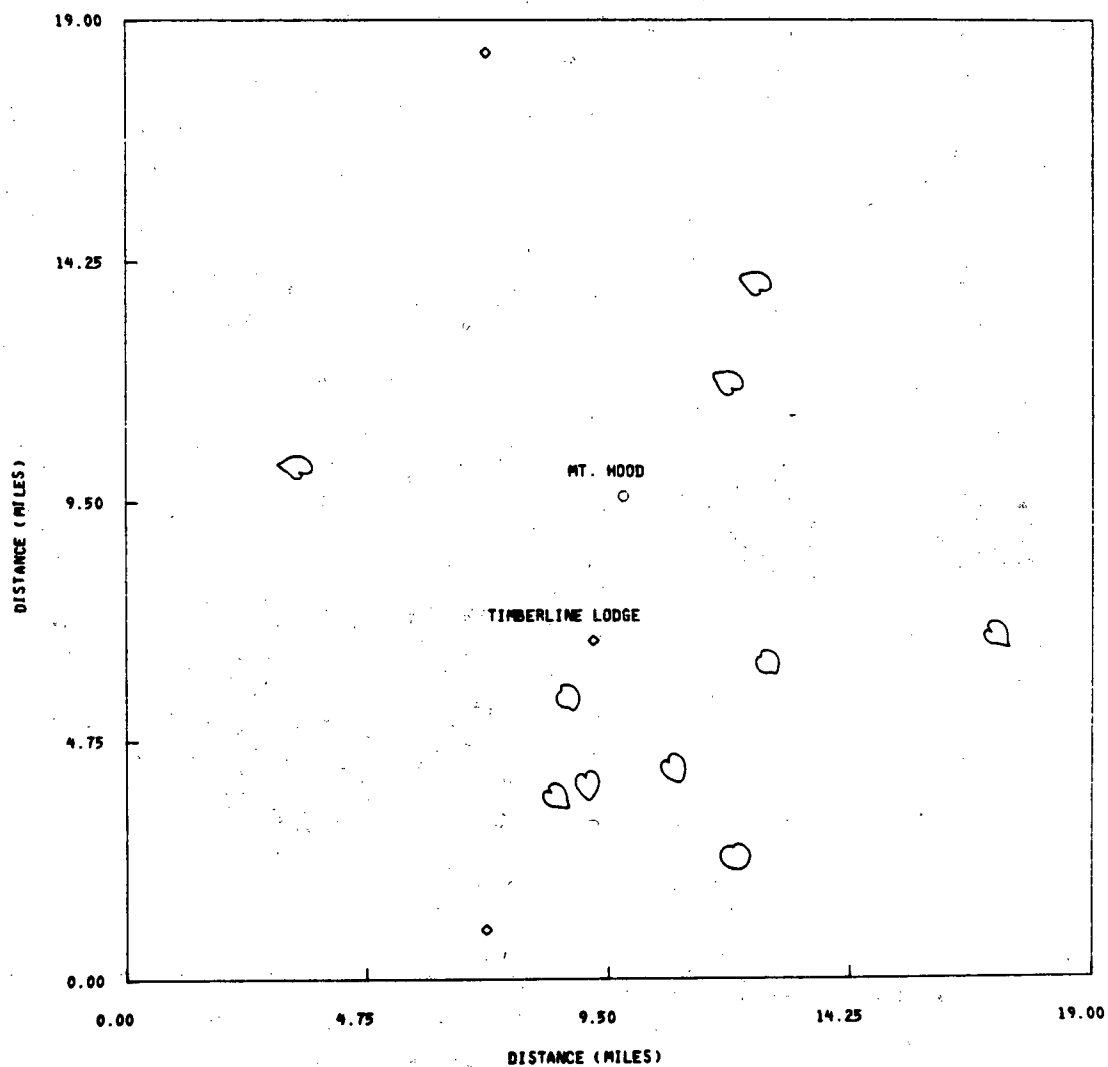
AVERAGED FREQS. IN RANGE OF .03-.006HZ



180°  
Phase Scale  
(degrees)

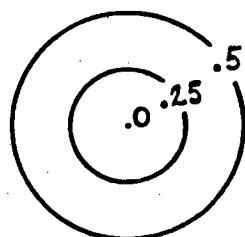
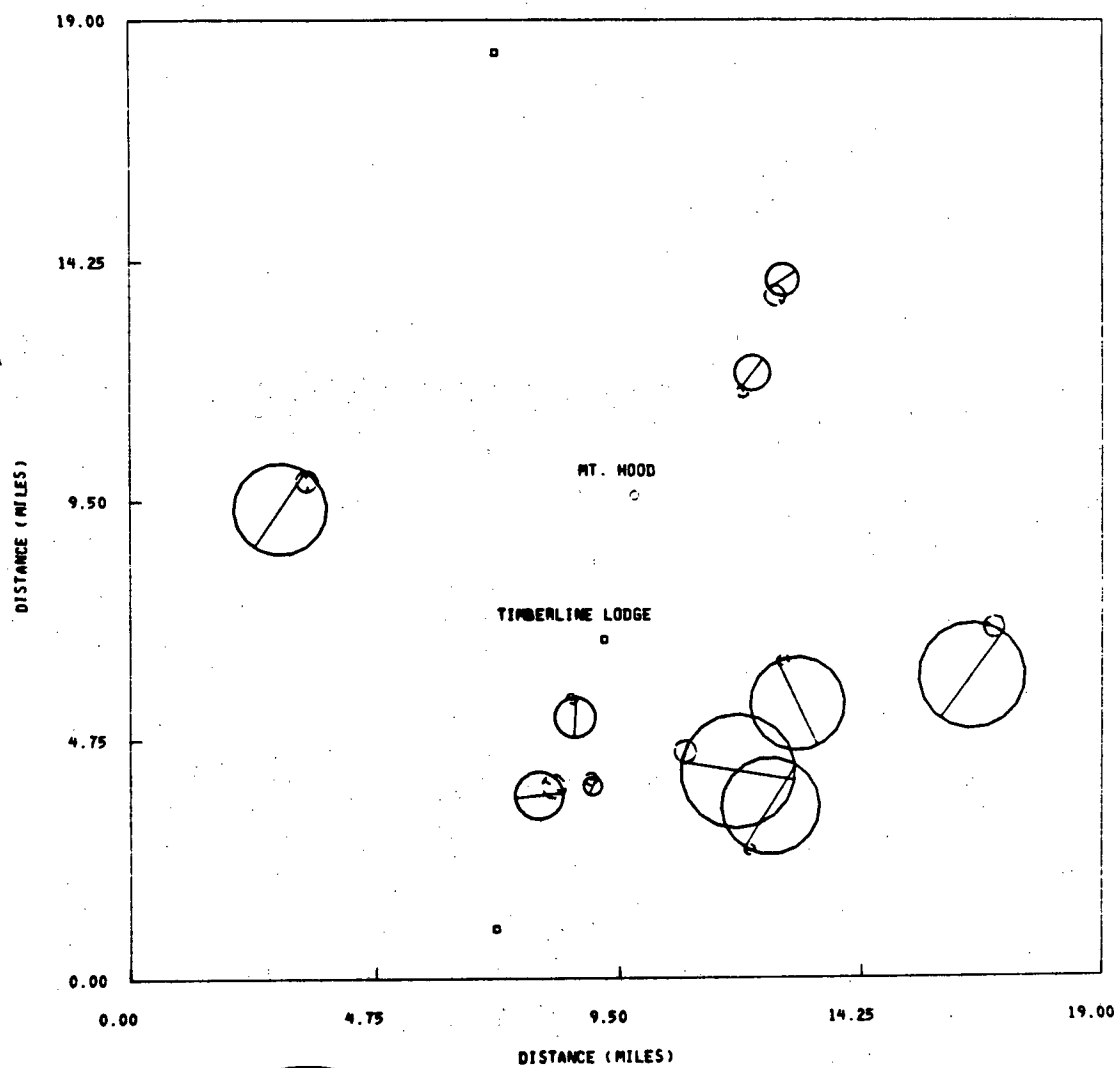
TPX TIPPER PHASE X

AVERAGED FREQS. IN RANGE OF .006-LOWHZ

Phase Scale  
(degrees)

TPX TIPPER PHASE X

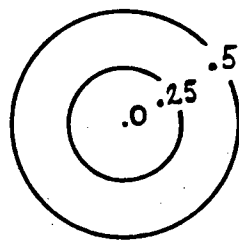
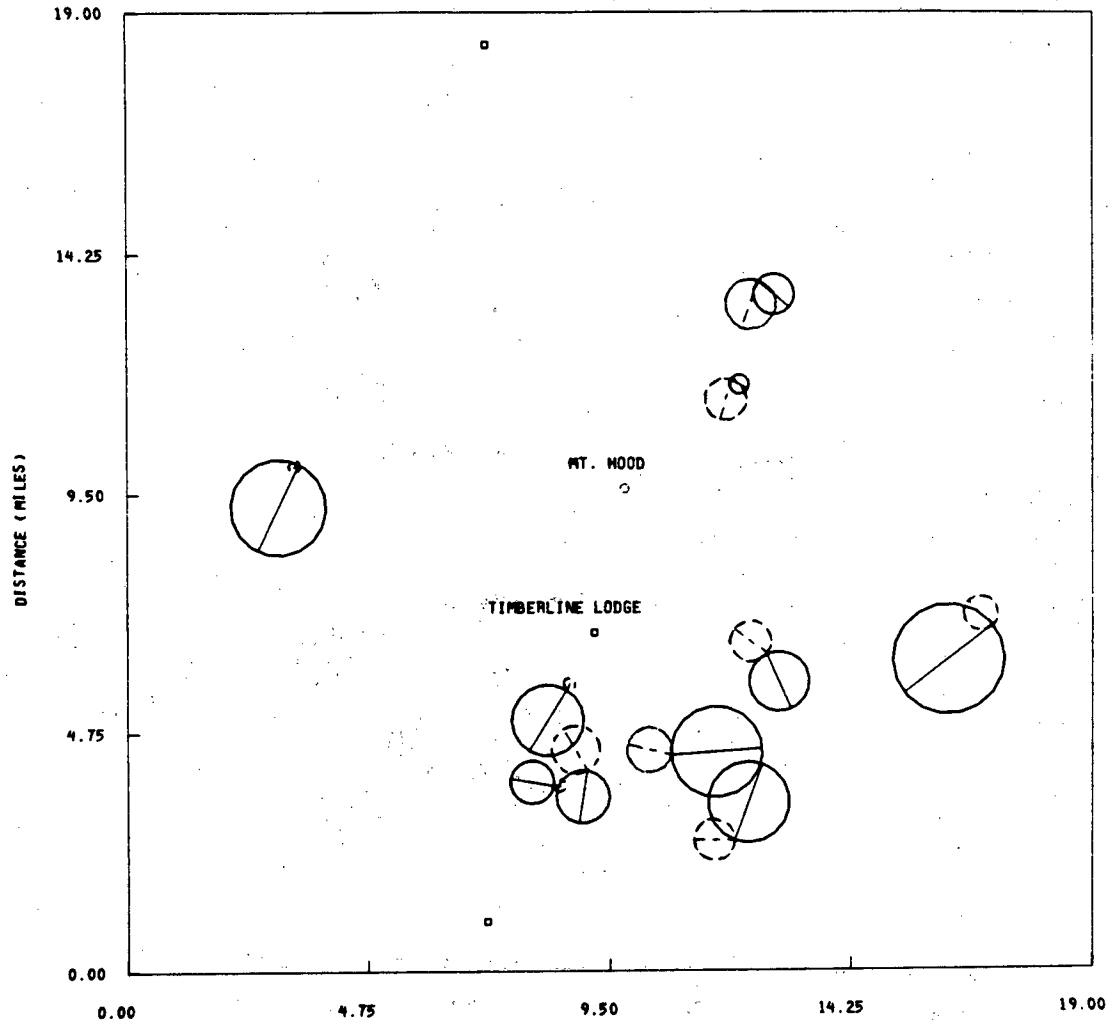
AVERAGED FREQS. IN RANGE OF 5.0-1.0 HZ



Induction Arrow  
Scale

TX COMPLEX

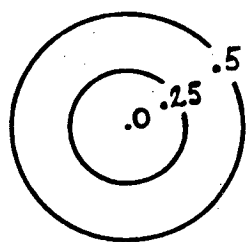
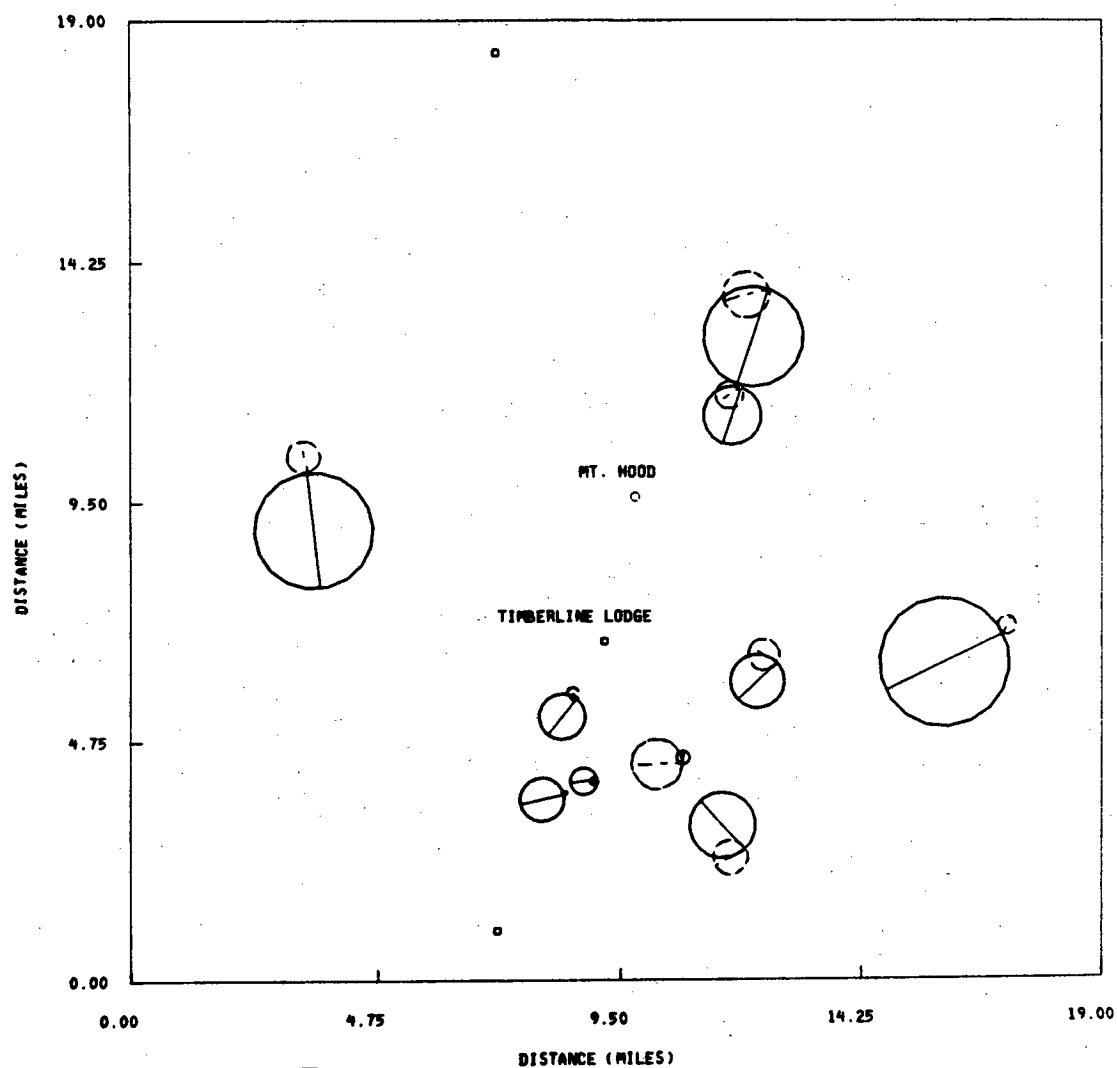
AVERAGED FREQS. IN RANGE OF 1.0-0.2 HZ



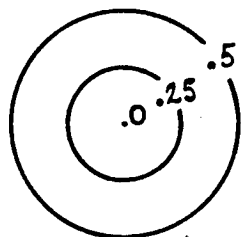
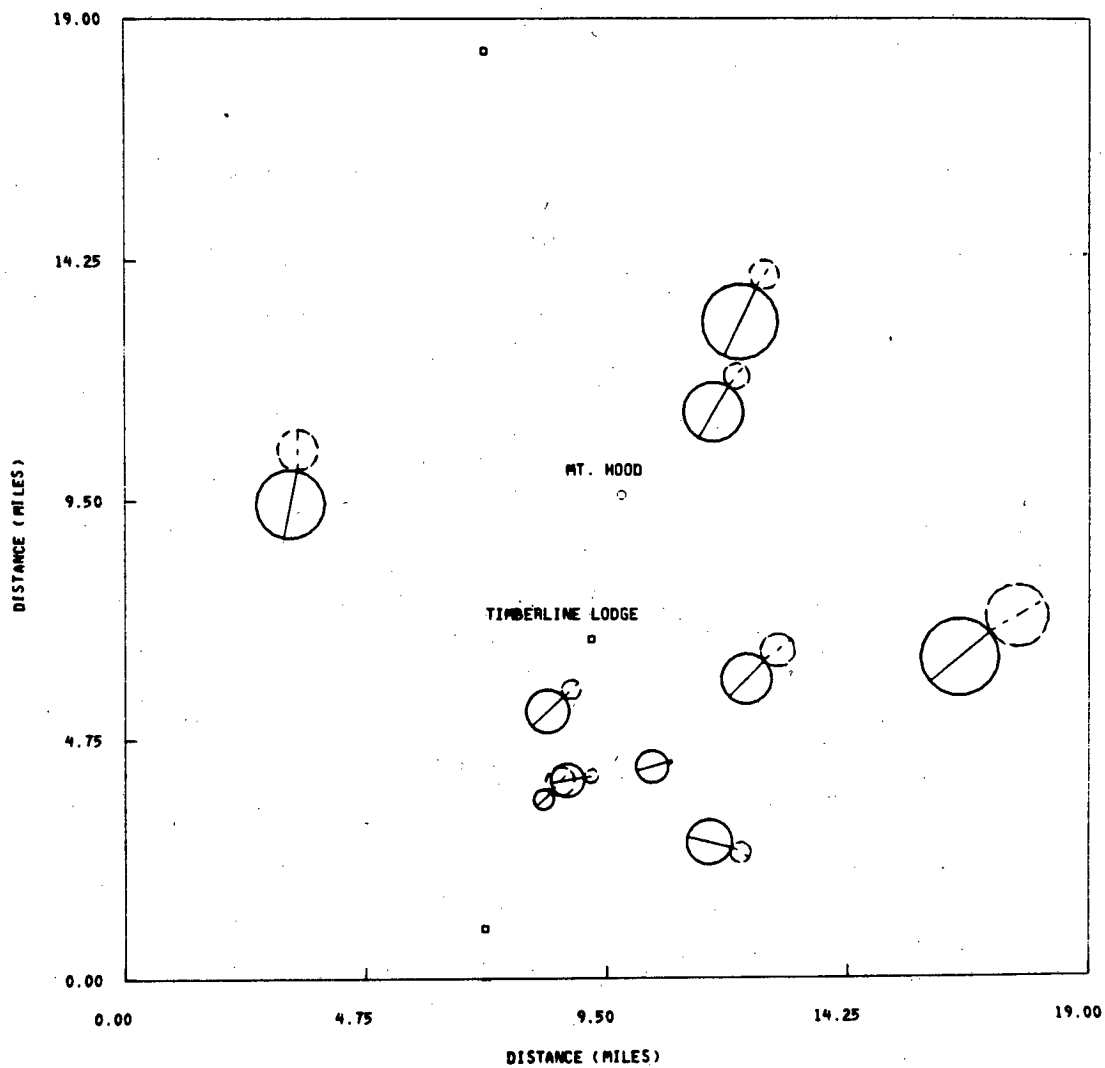
Induction Arrow  
Scale

TX COMPLEX

AVERAGED FREQS. IN RANGE OF .2-.03 HZ

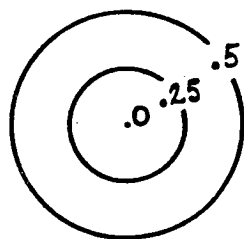
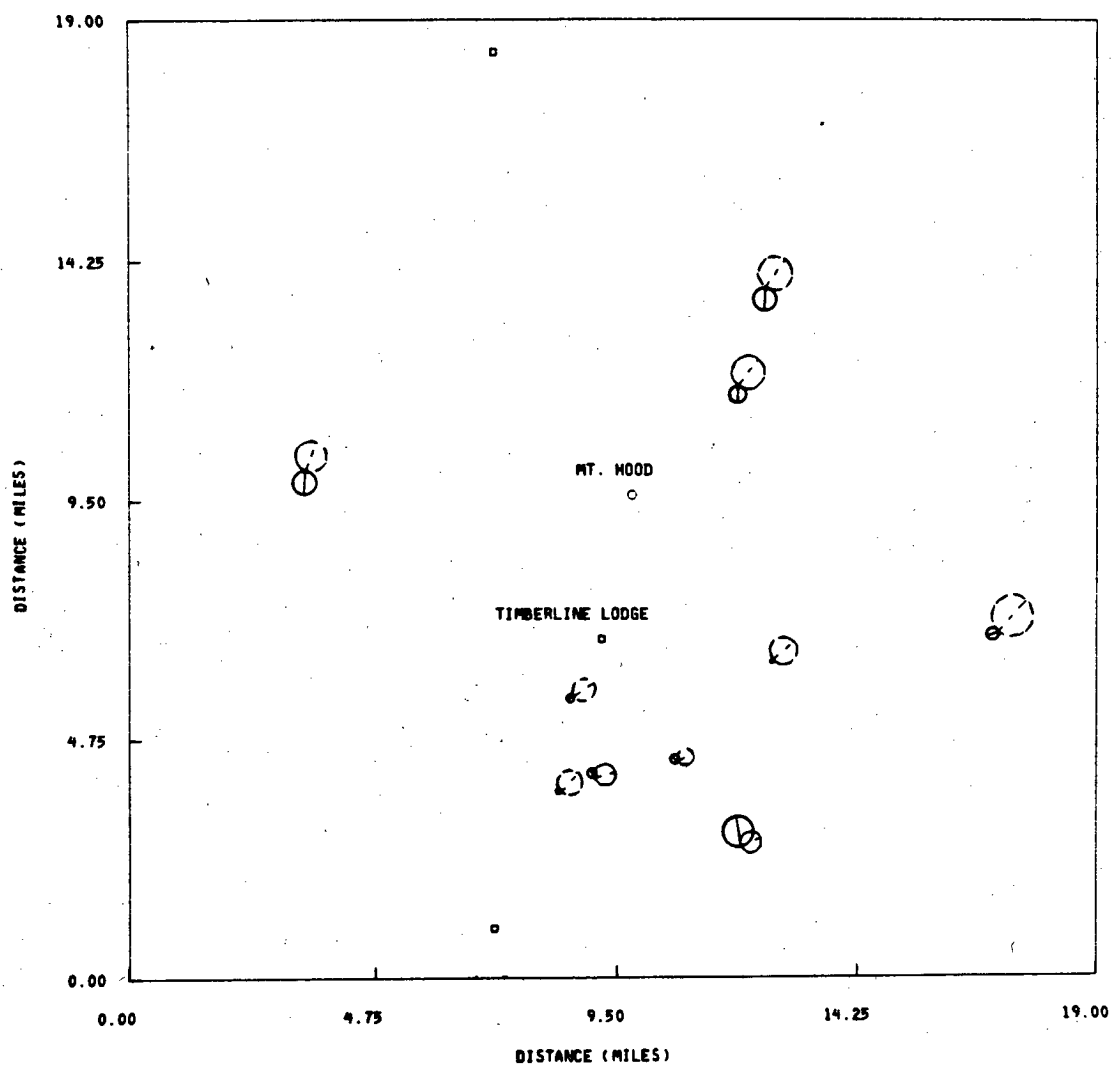
Induction Arrow  
Scale

AVERAGED FREDS. IN RANGE OF .03-.006HZ

Induction Arrow  
Scale

TX COMPLEX

AVERAGED FREQS. IN RANGE OF .006-LOWHZ

Induction Arrow  
Scale

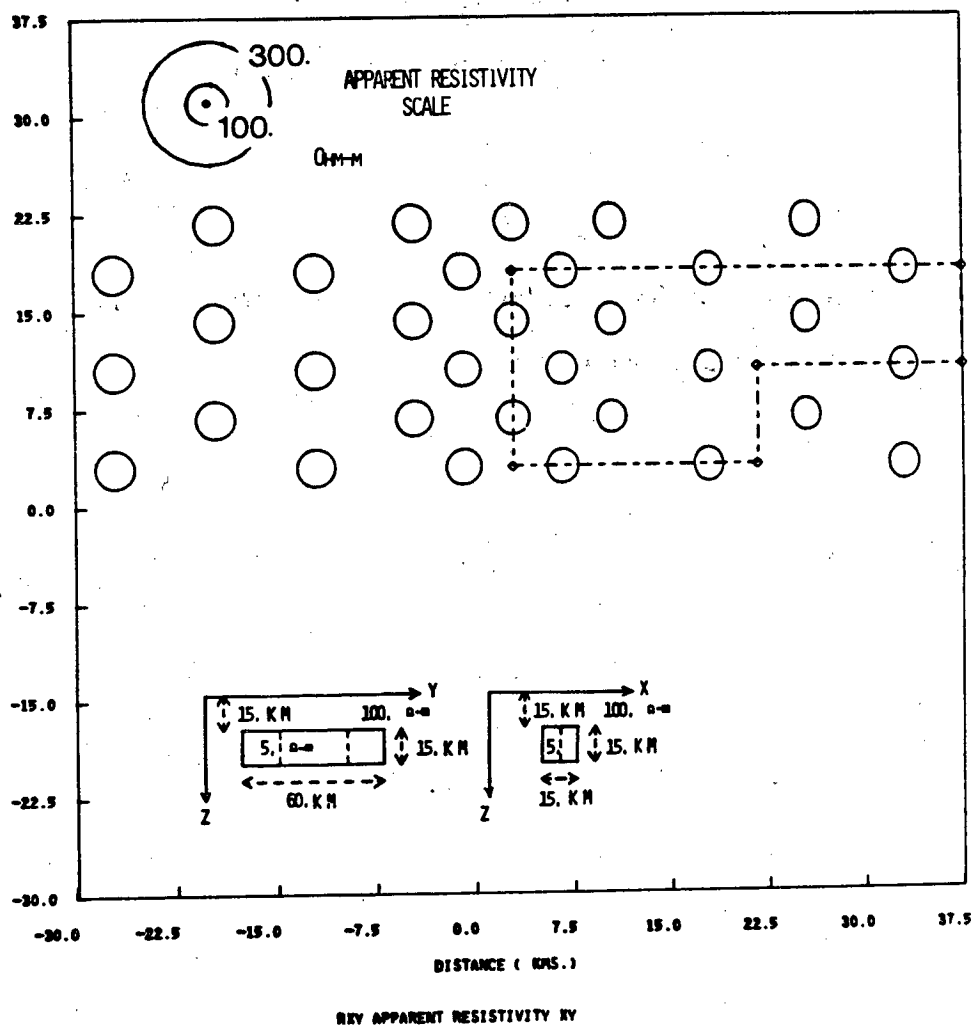
TX COMPLEX

## **Appendix D**

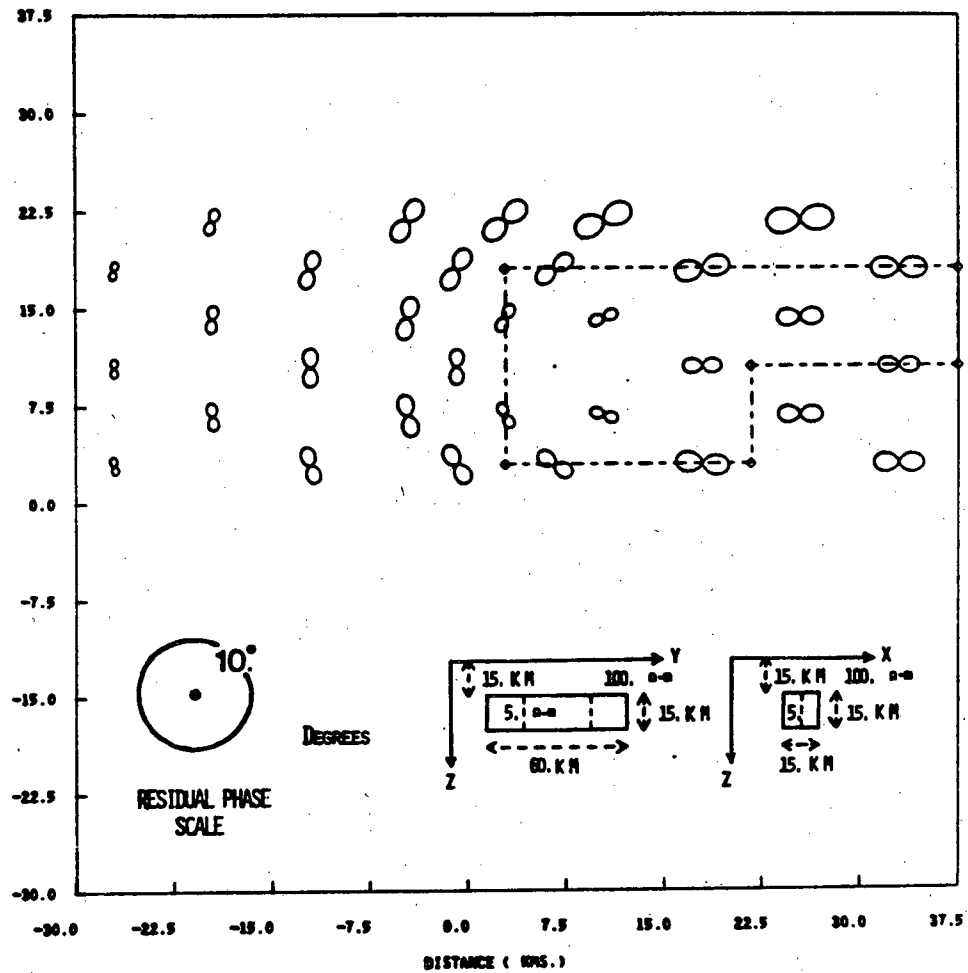
### **Polar Diagrams of the Three-Dimensional Model Results**

**This appendix provides a catalogue of polar diagrams for some of the three-dimensional model results used in this study.**

**AVERAGED FREQS. IN RANGE OF .02 HZ.**

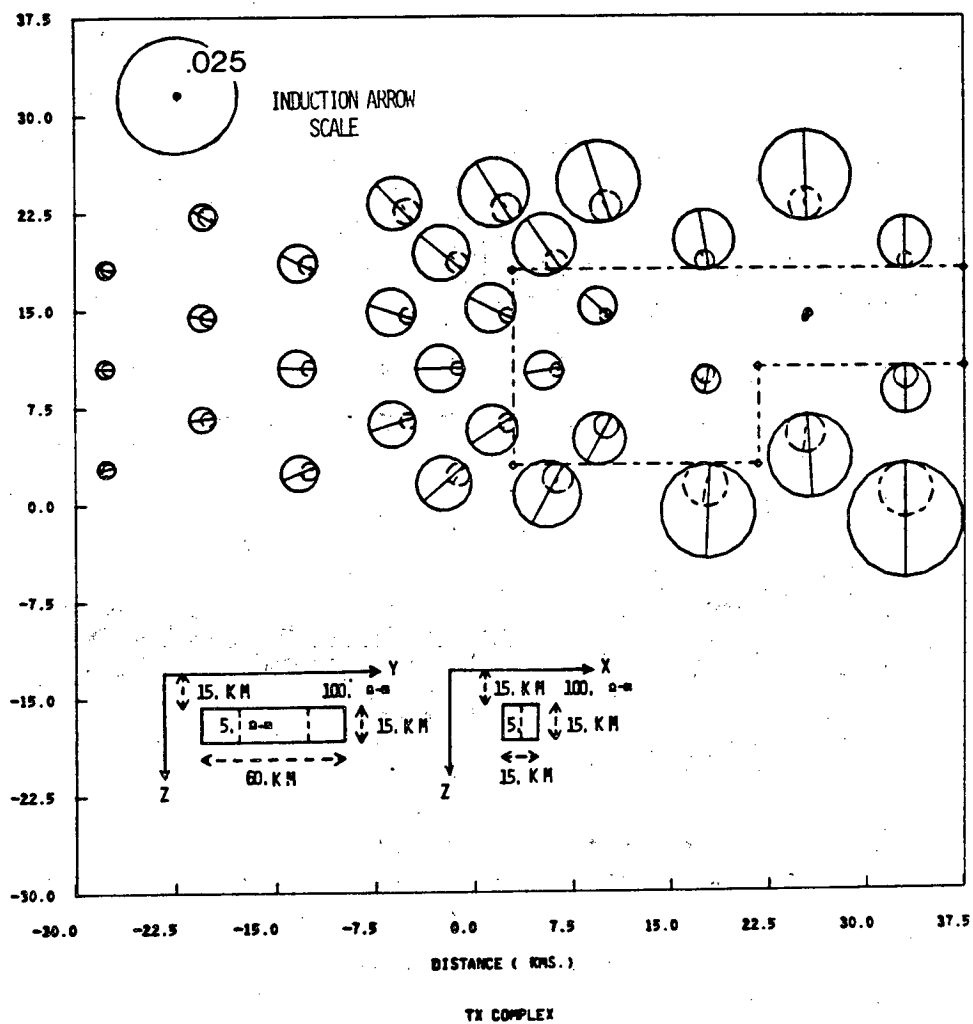


AVERAGED PRESS. IN RANGE OF .02 HZ.

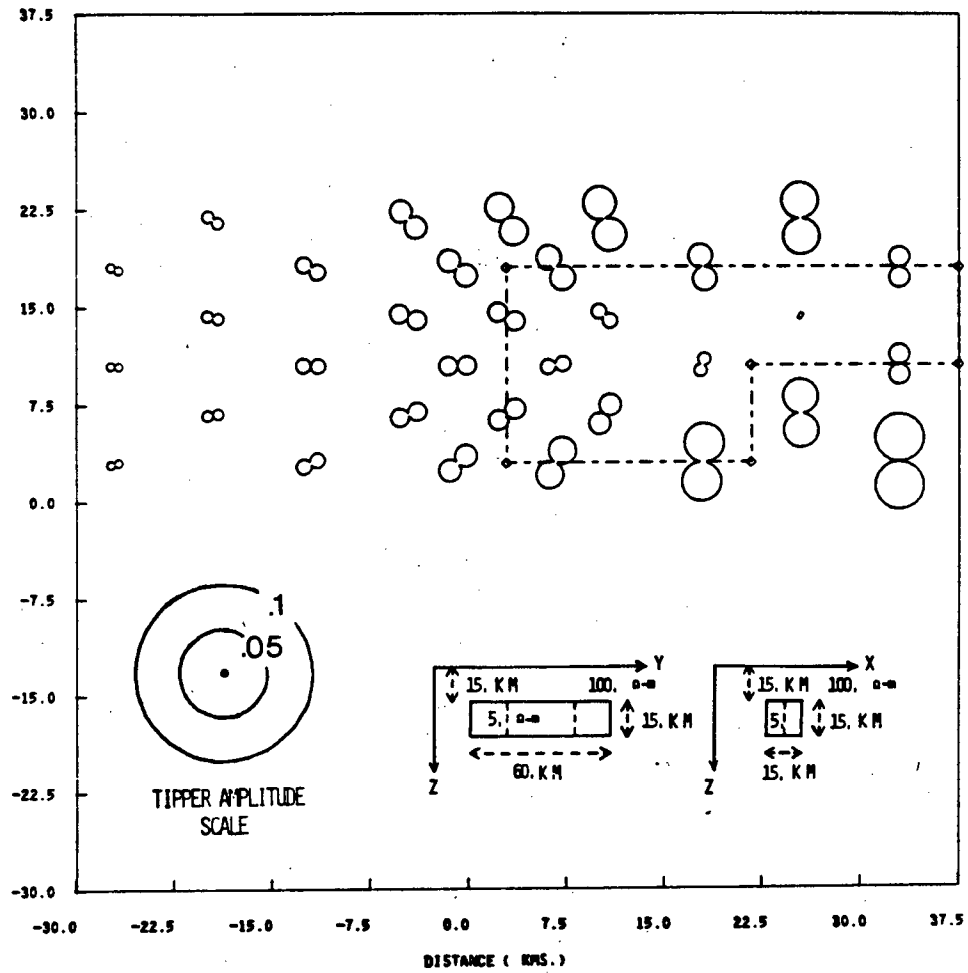


PRV PHASE OF APPARENT RESISTIVITY IN

AVERAGED FREES. IN RANGE OF .02 HZ.

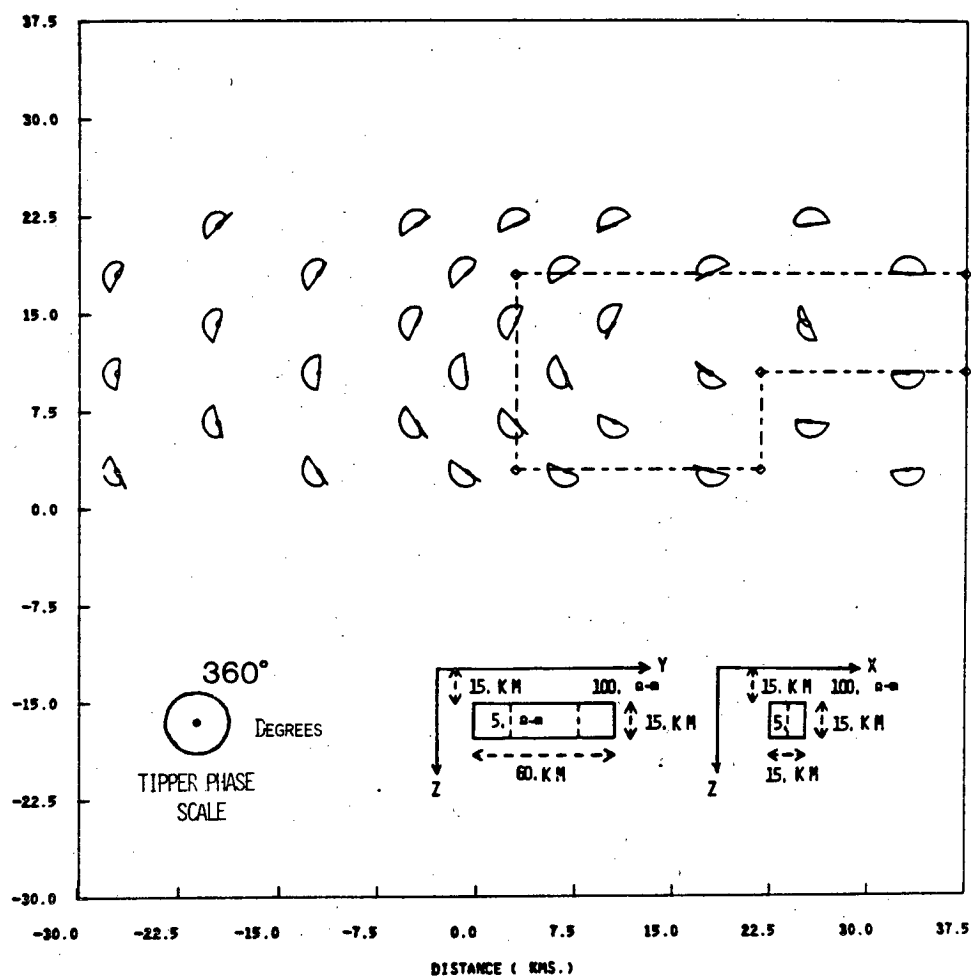


AVERAGED FREQS. IN RANGE OF .02 HZ.

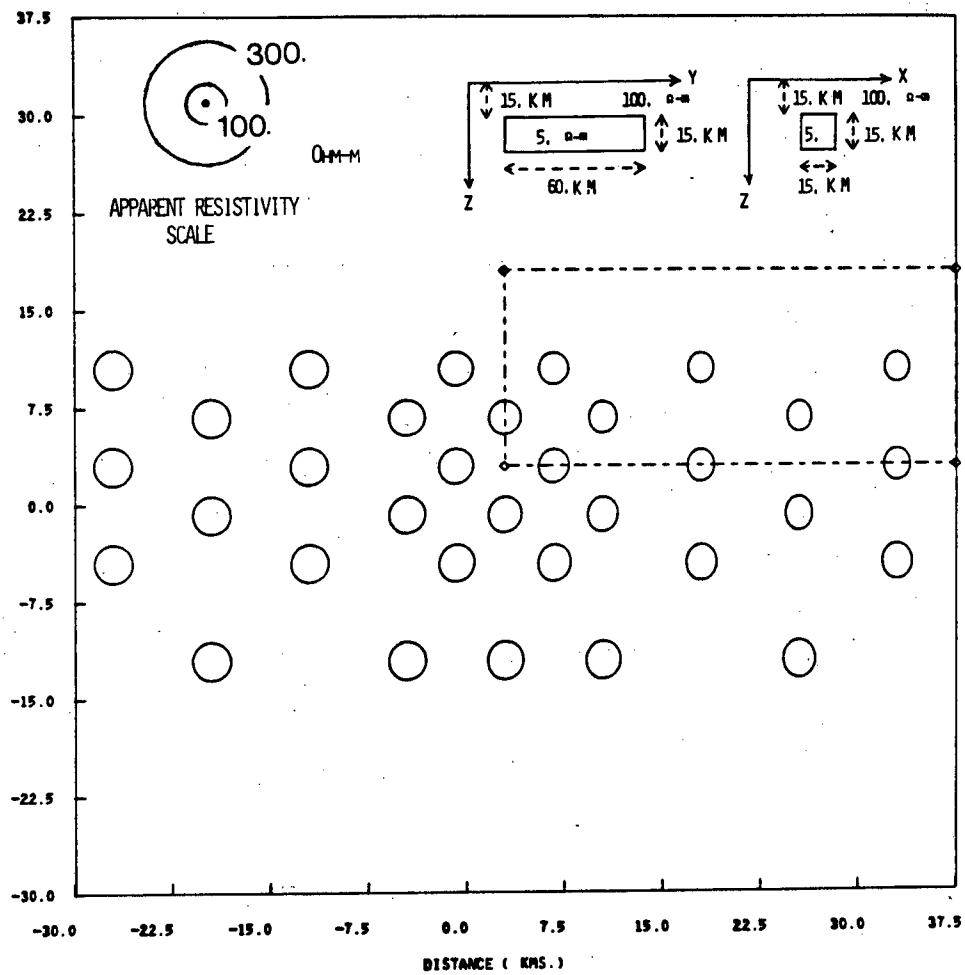


THE TIPPER AMPLITUDE X

AVERAGED FREQS. IN RANGE OF .02 HZ.

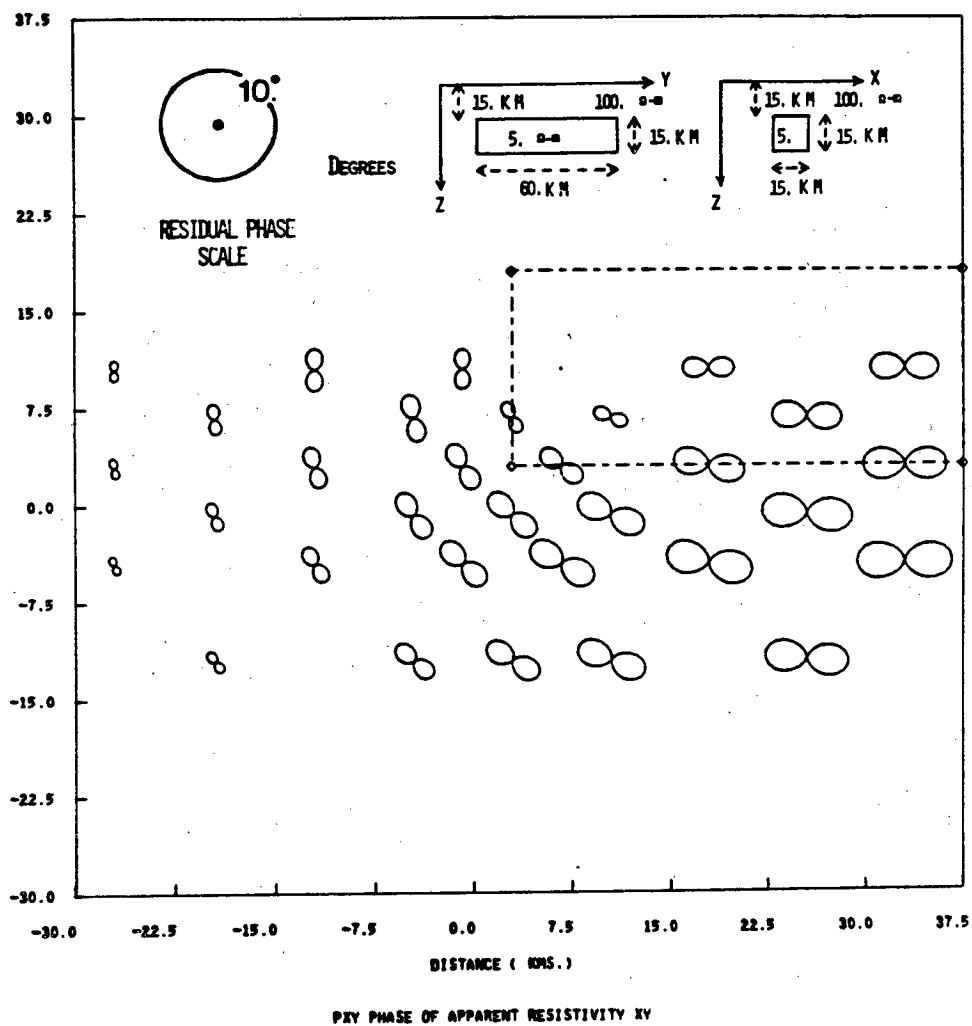


AVERAGED FREQS. IN RANGE OF .02 HZ.

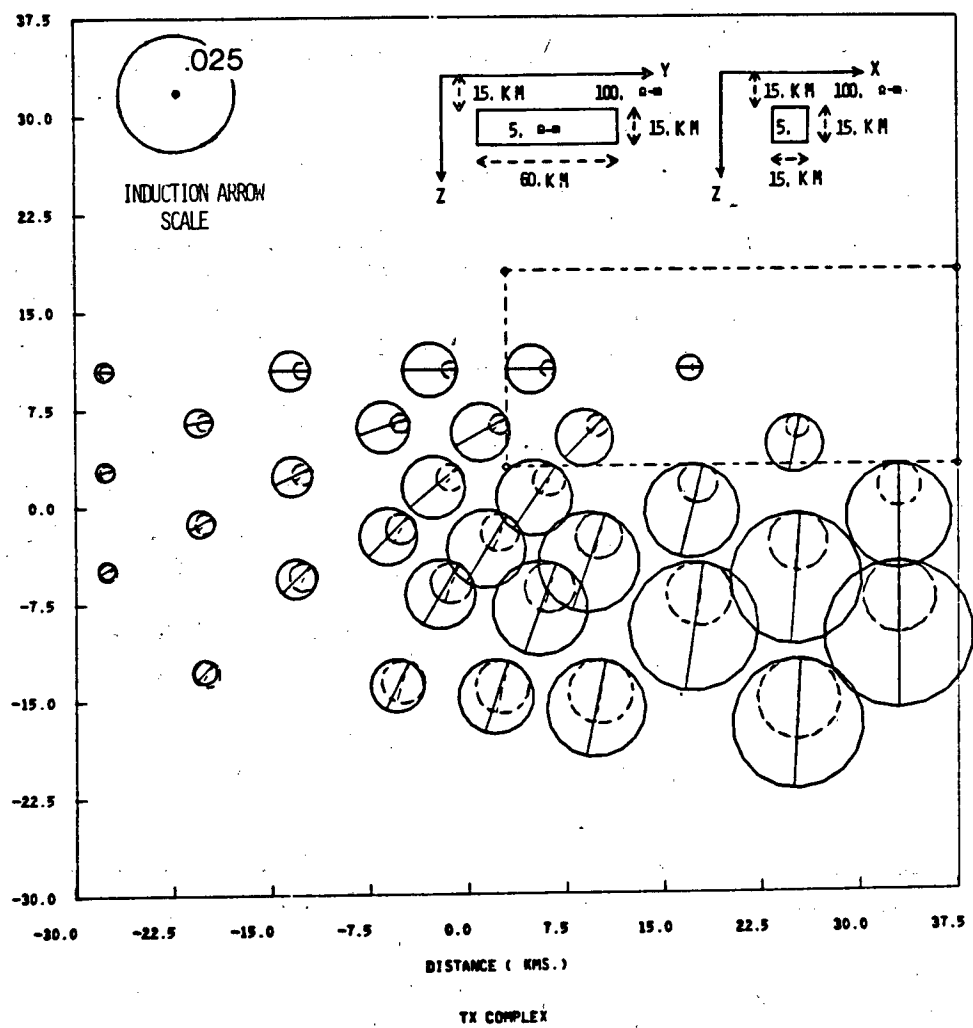


XY APPARENT RESISTIVITY XY

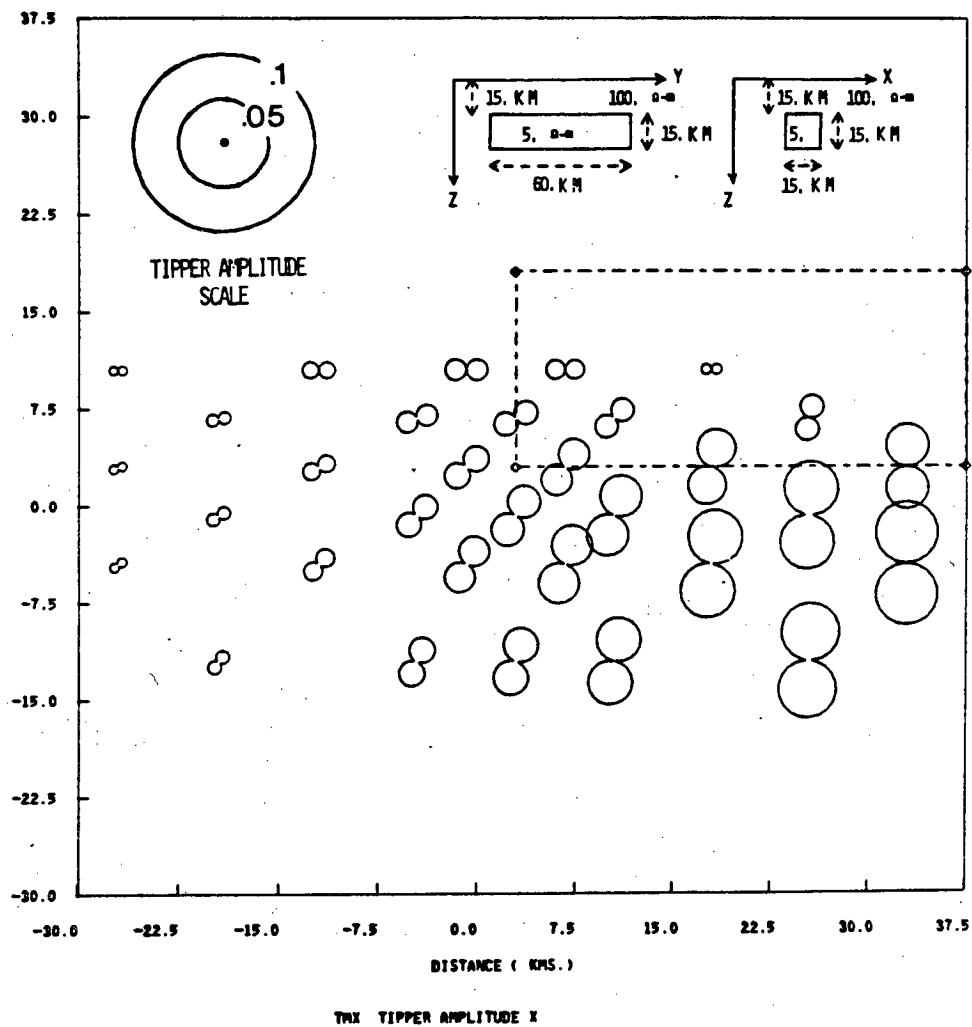
AVERAGED FREQS. IN RANGE OF .02 HZ.



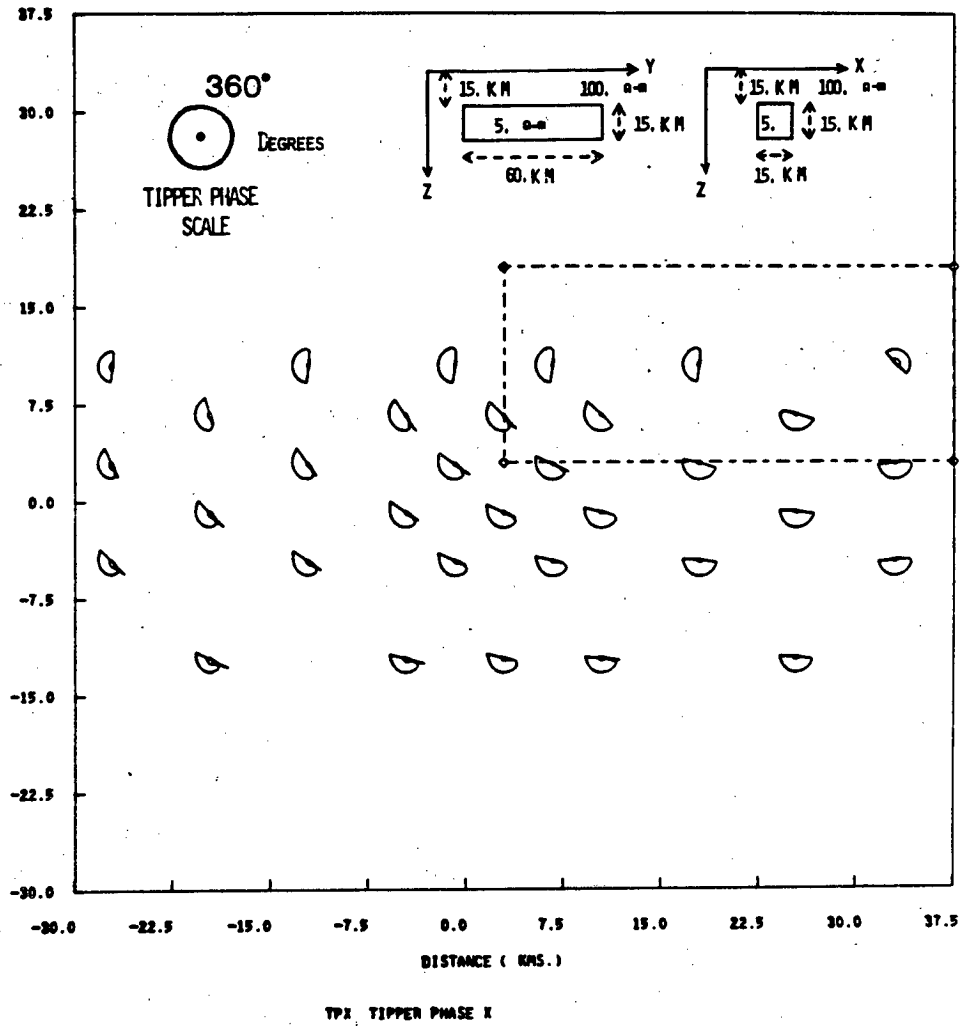
AVERAGED FREDS. IN RANGE OF .62 HZ.



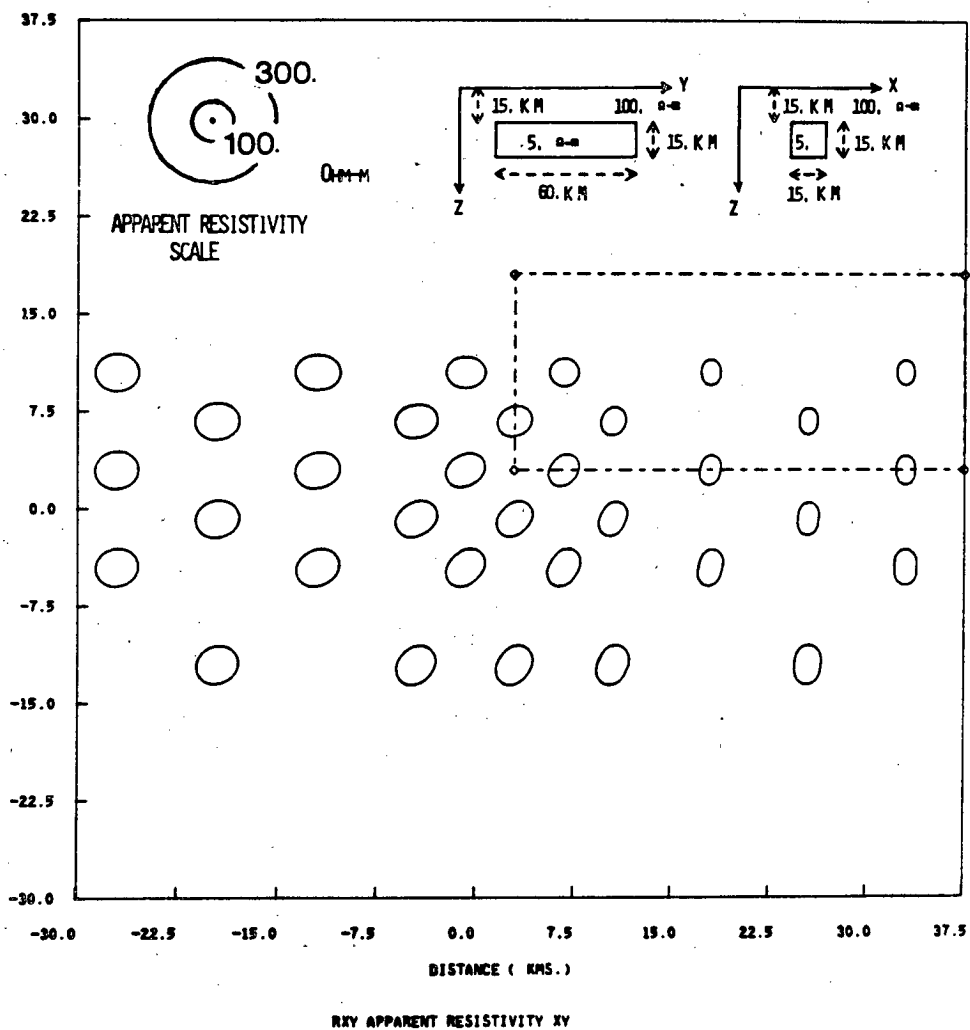
AVERAGED PRESS. IN RANGE OF .02 HZ.



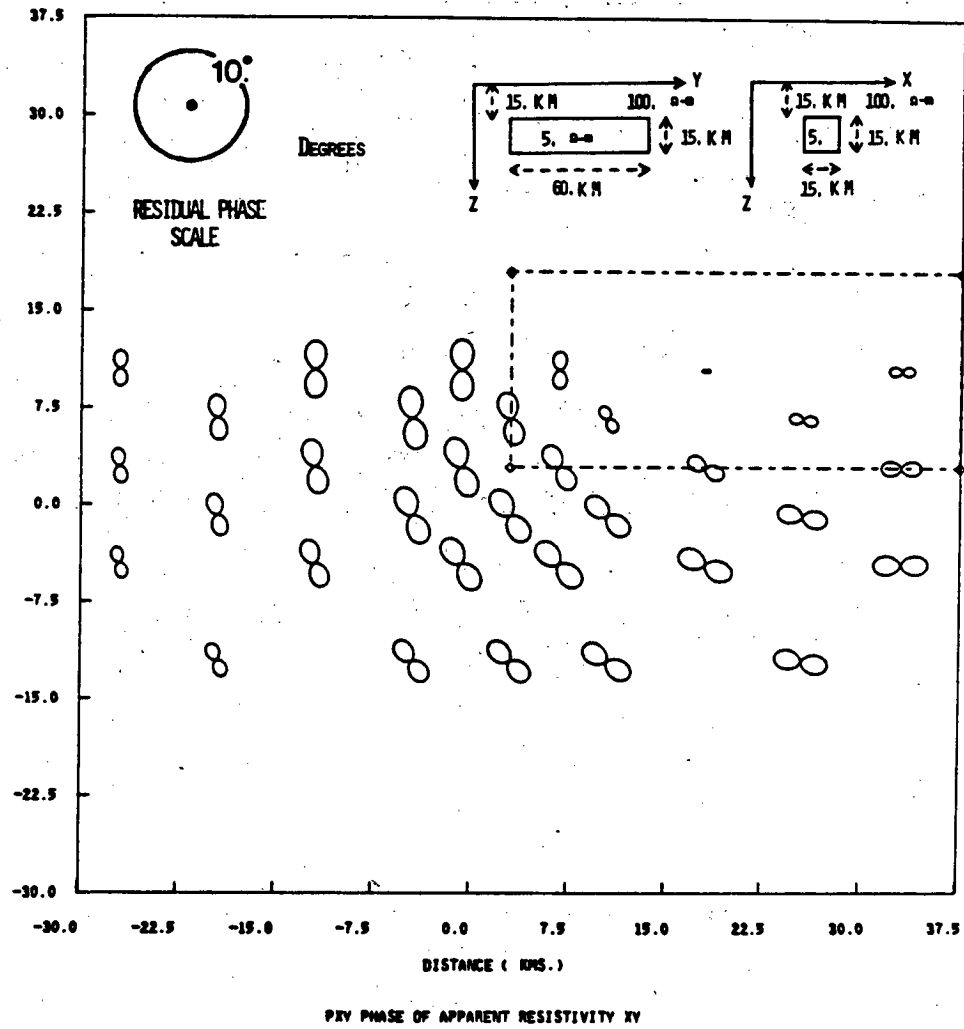
AVERAGED FREQS. IN RANGE OF .02 HZ.



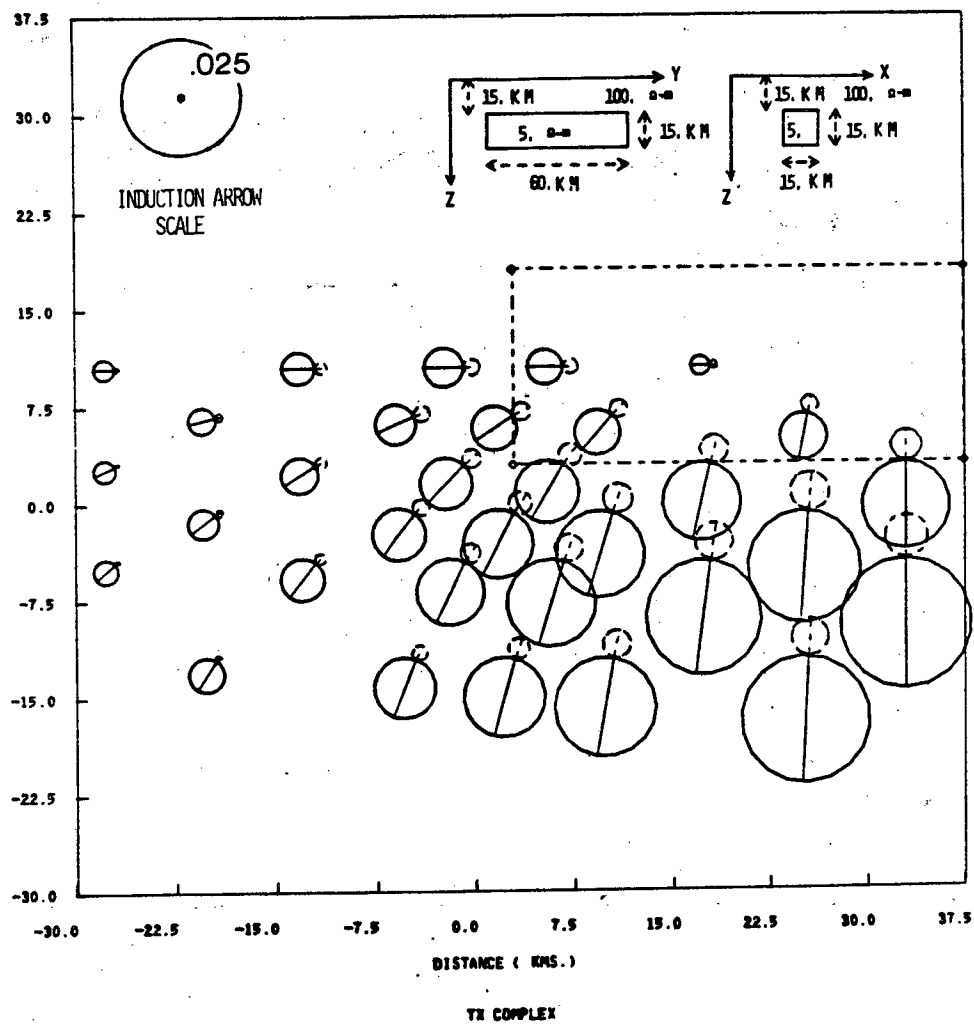
AVERAGED FREQS. IN RANGE OF .60-1.0 KZ.



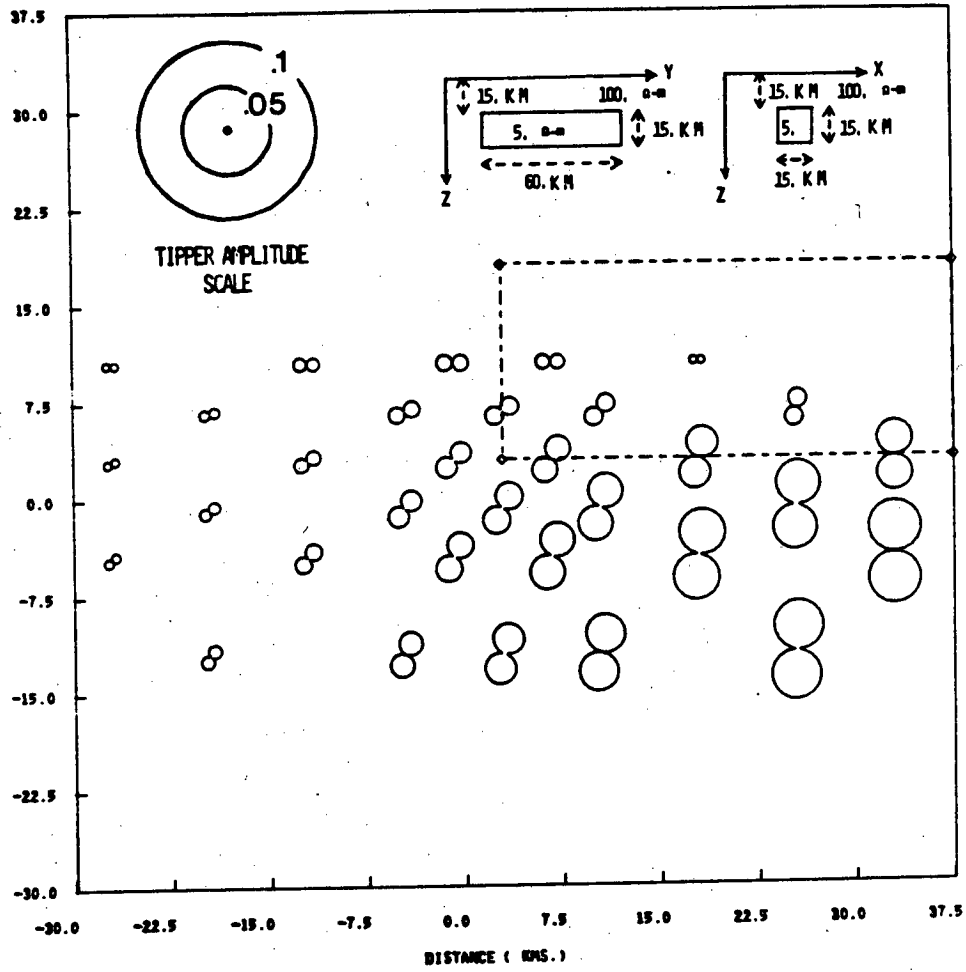
AVERAGED FREDS. IN RANGE OF .0044 HZ.



AVERAGED FREQS. IN RANGE OF .0044 HZ.

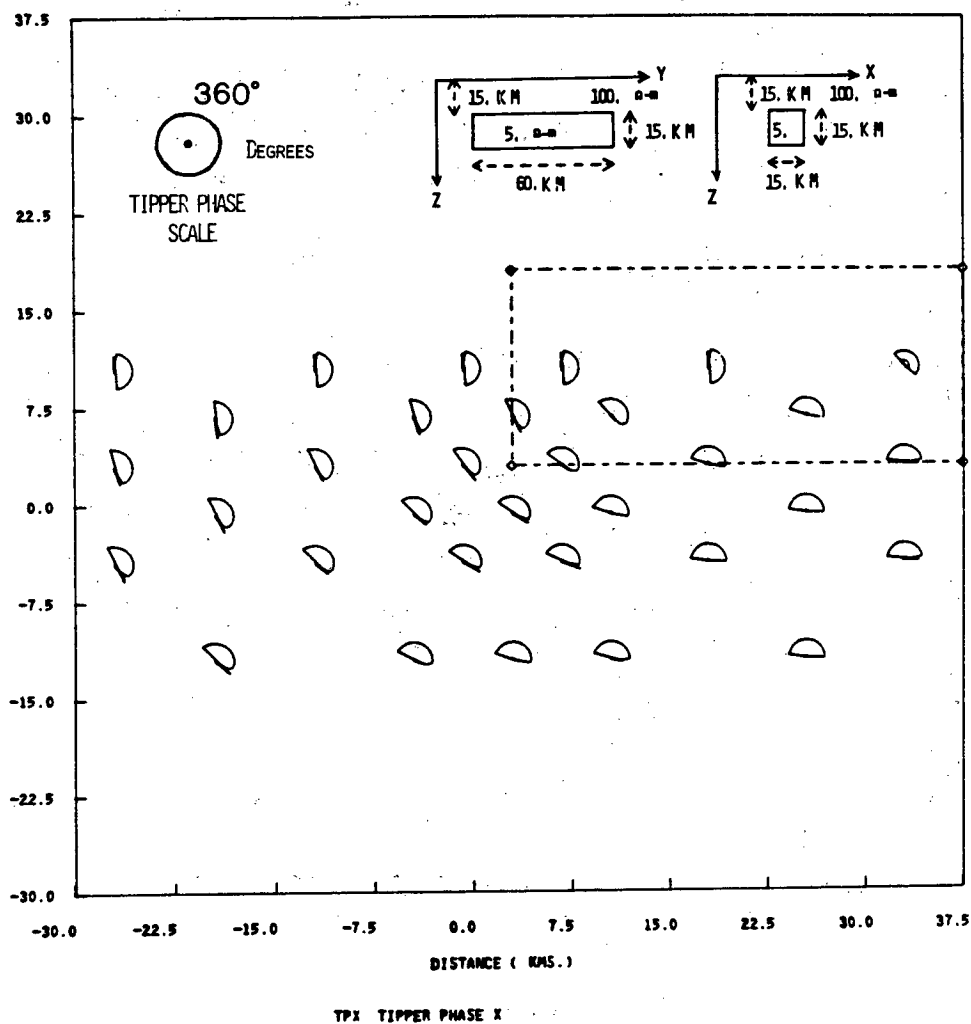


AVERAGED FREQS. IN RANGE OF .0044 HZ.

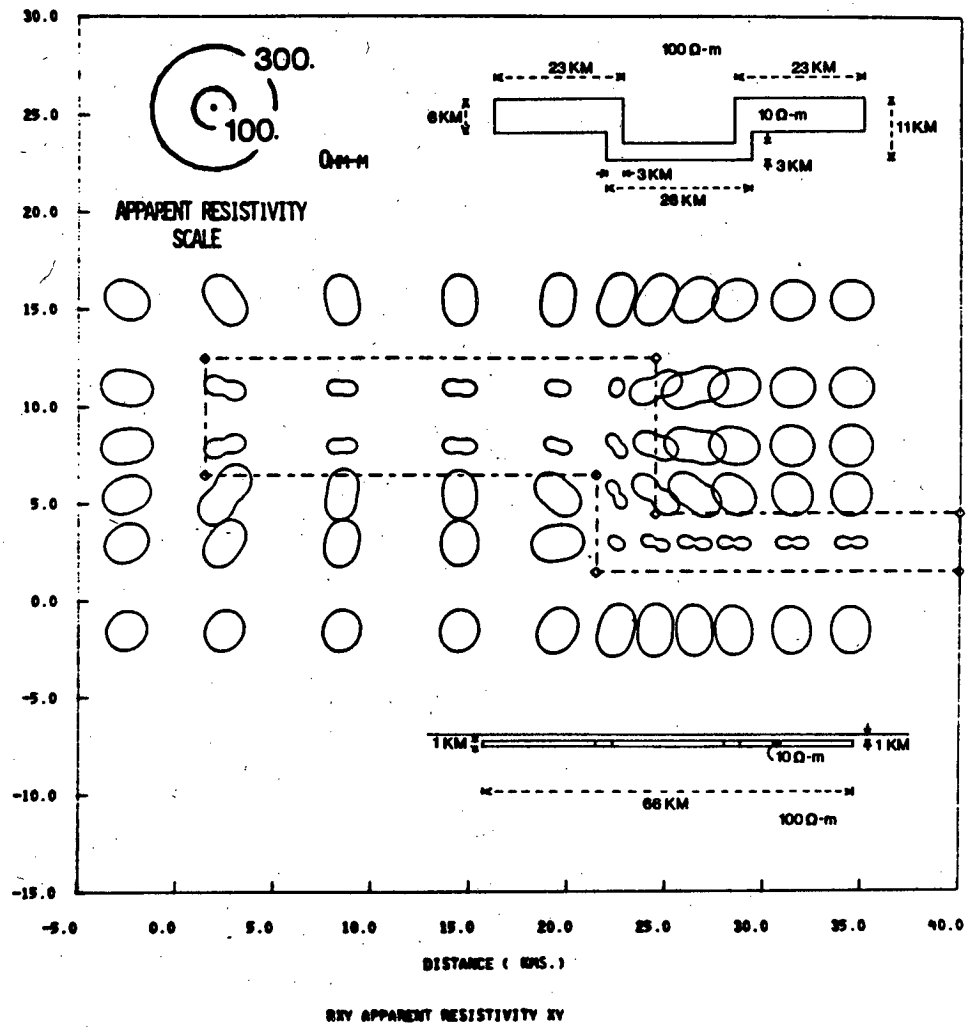


TAX TIPPER AMPLITUDE X

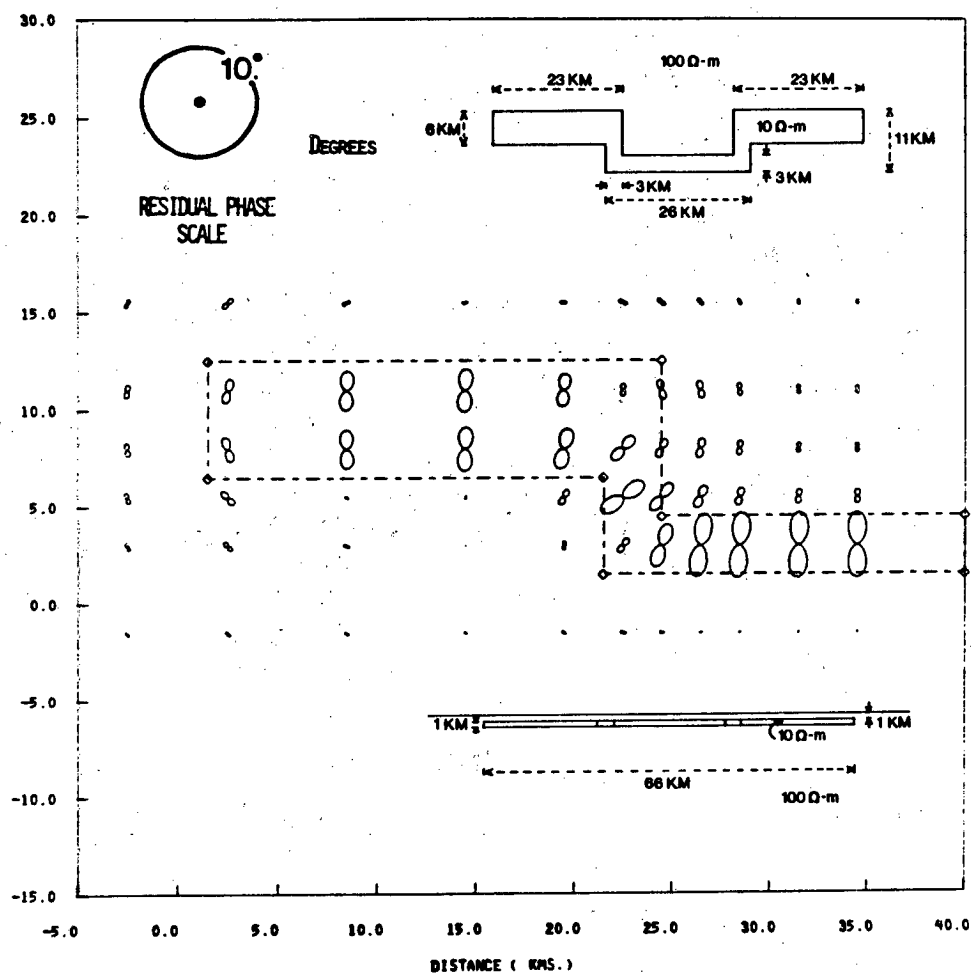
AVERAGED FREQS. IN RANGE OF .0044 HZ.



AVERAGED FREQS. IN RANGE OF .01 HZ.

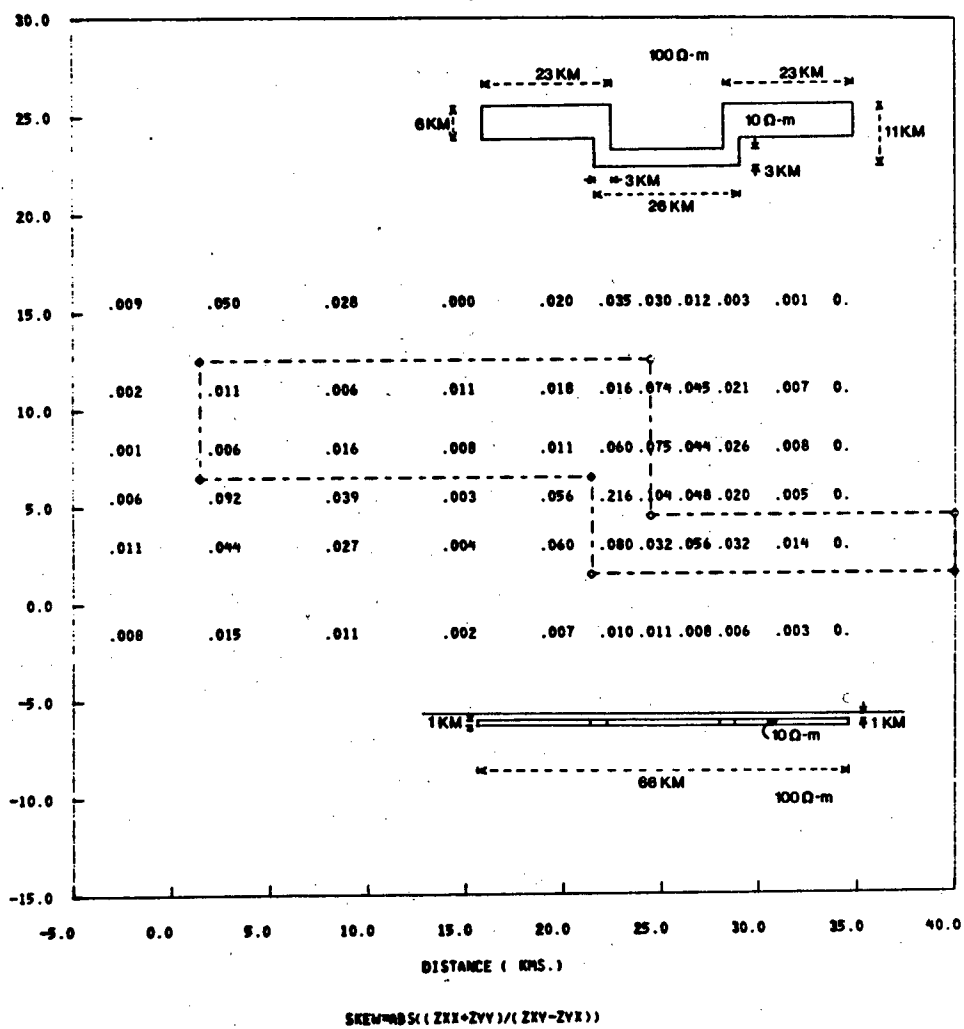


AVERAGED FREQS. IN RANGE OF .01 HZ.

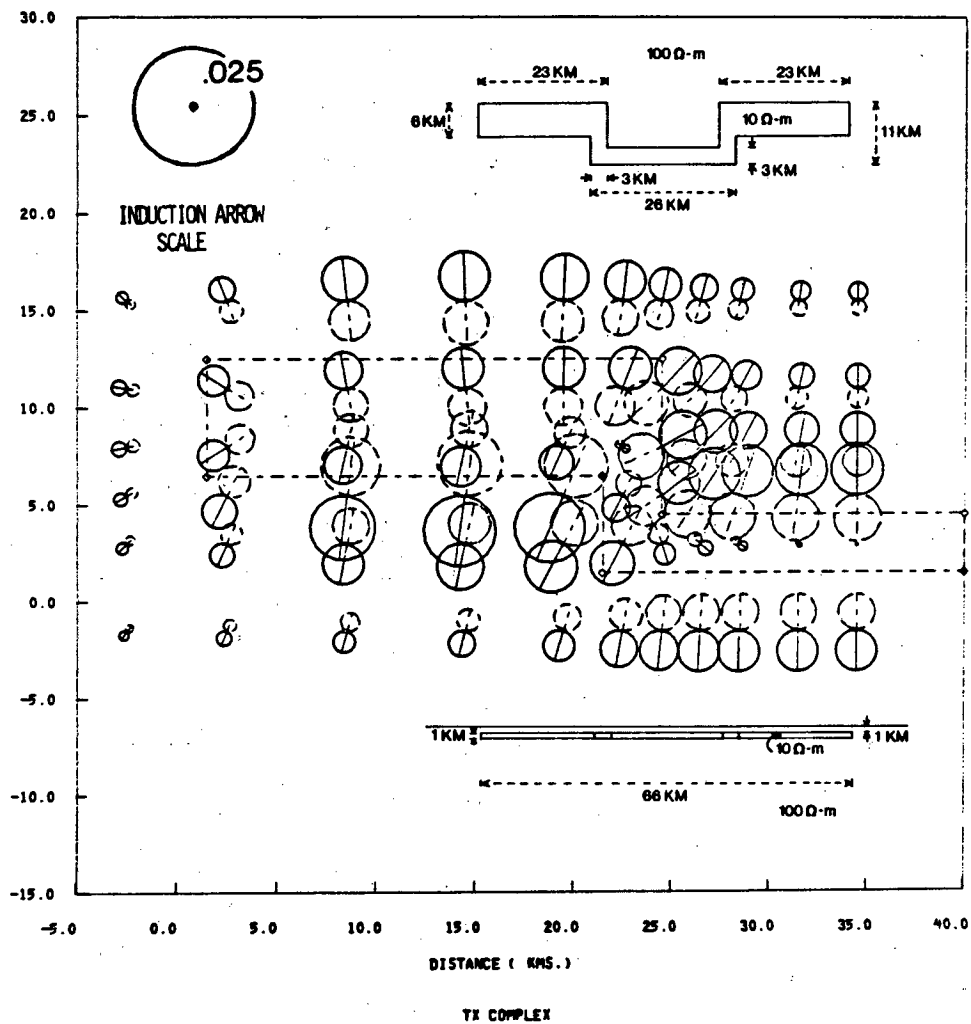


PRV PHASE OF APPARENT RESISTIVITY IN

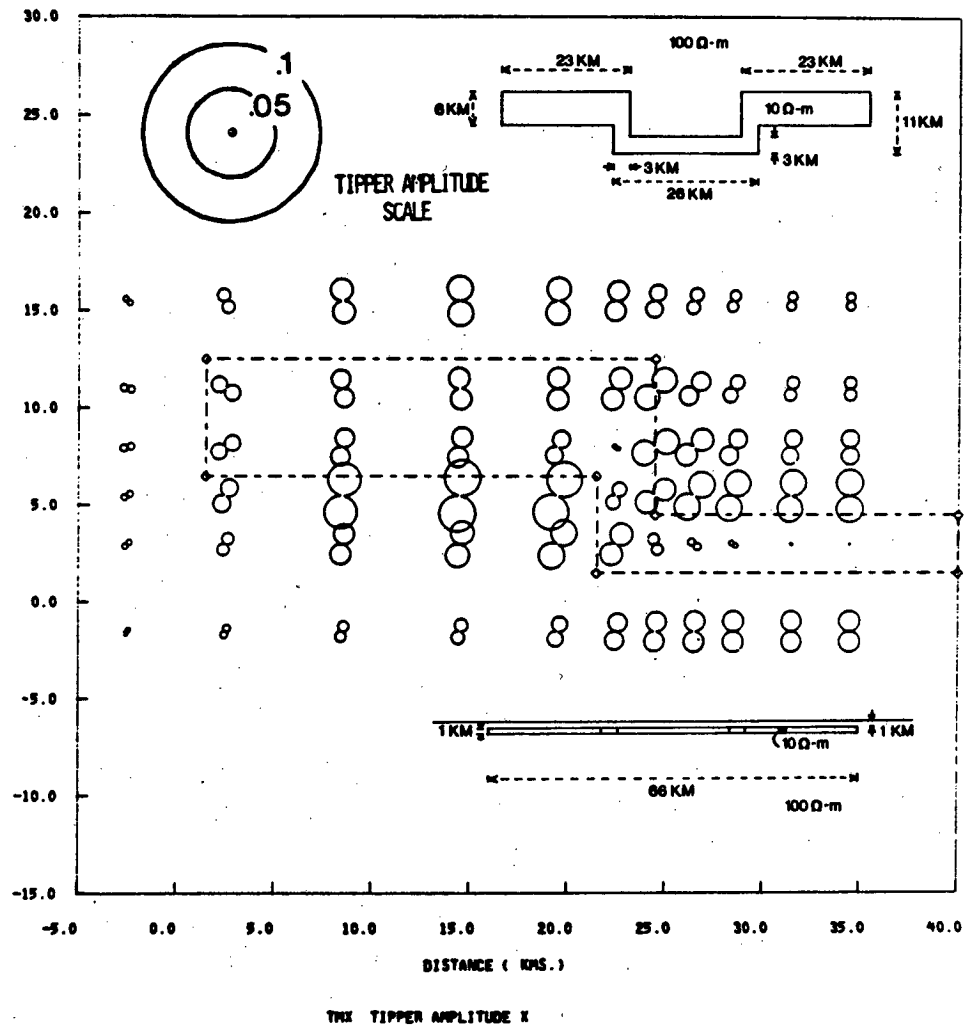
AVERAGED FREQS. IN RANGE OF .01 HZ.



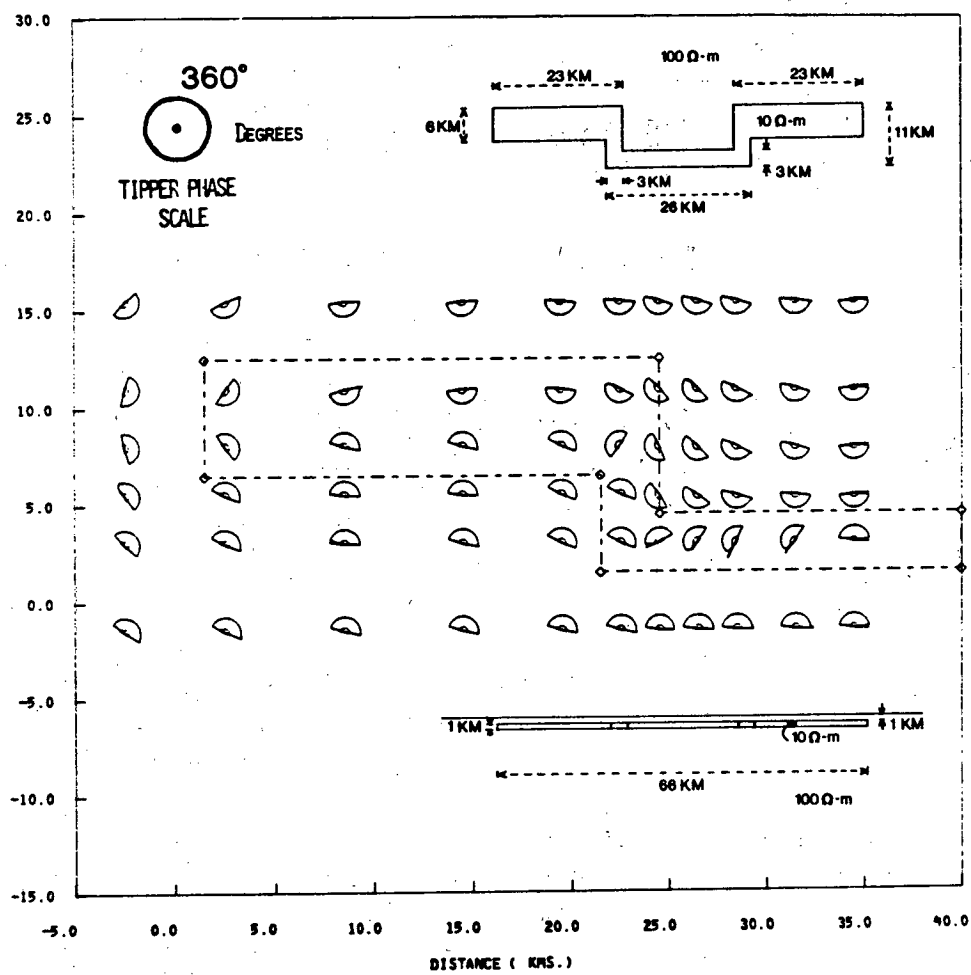
AVERAGED FREDS. IN RANGE OF .01 HZ.



AVERAGED FREQS. IN RANGE OF .01 HZ.

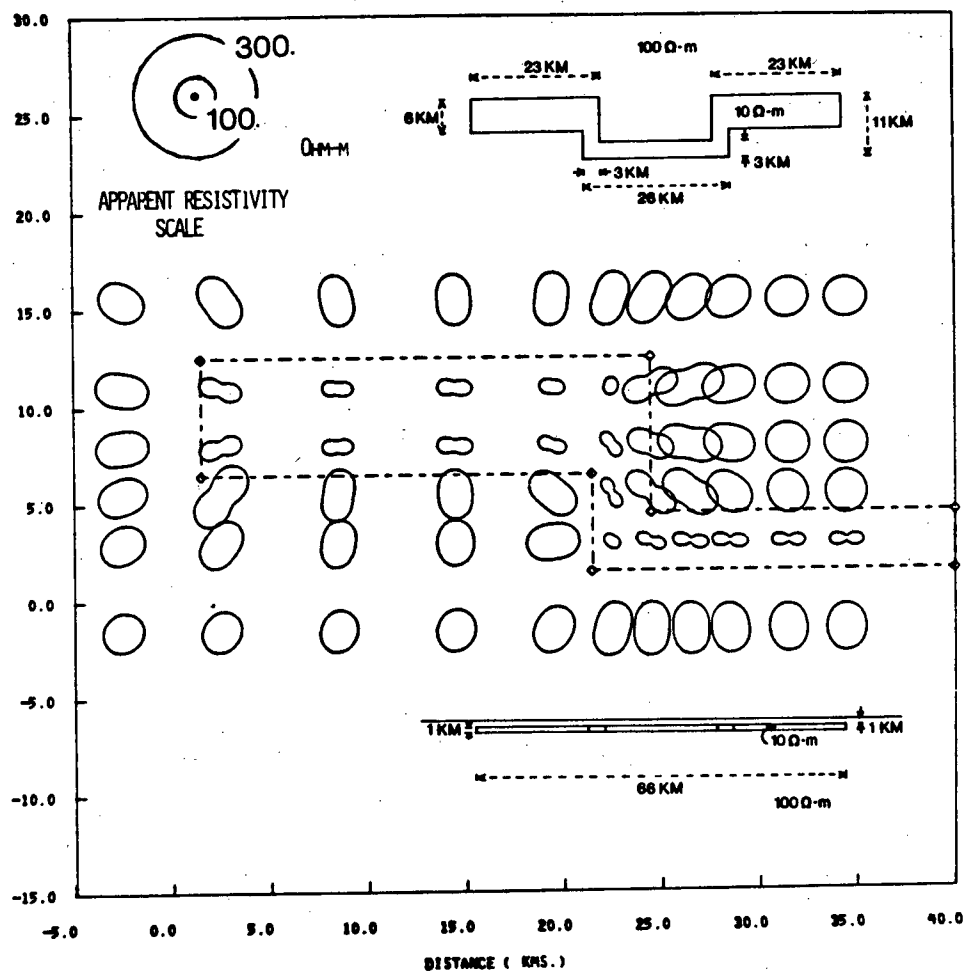


AVERAGED FREQS. IN RANGE OF .01 HZ.



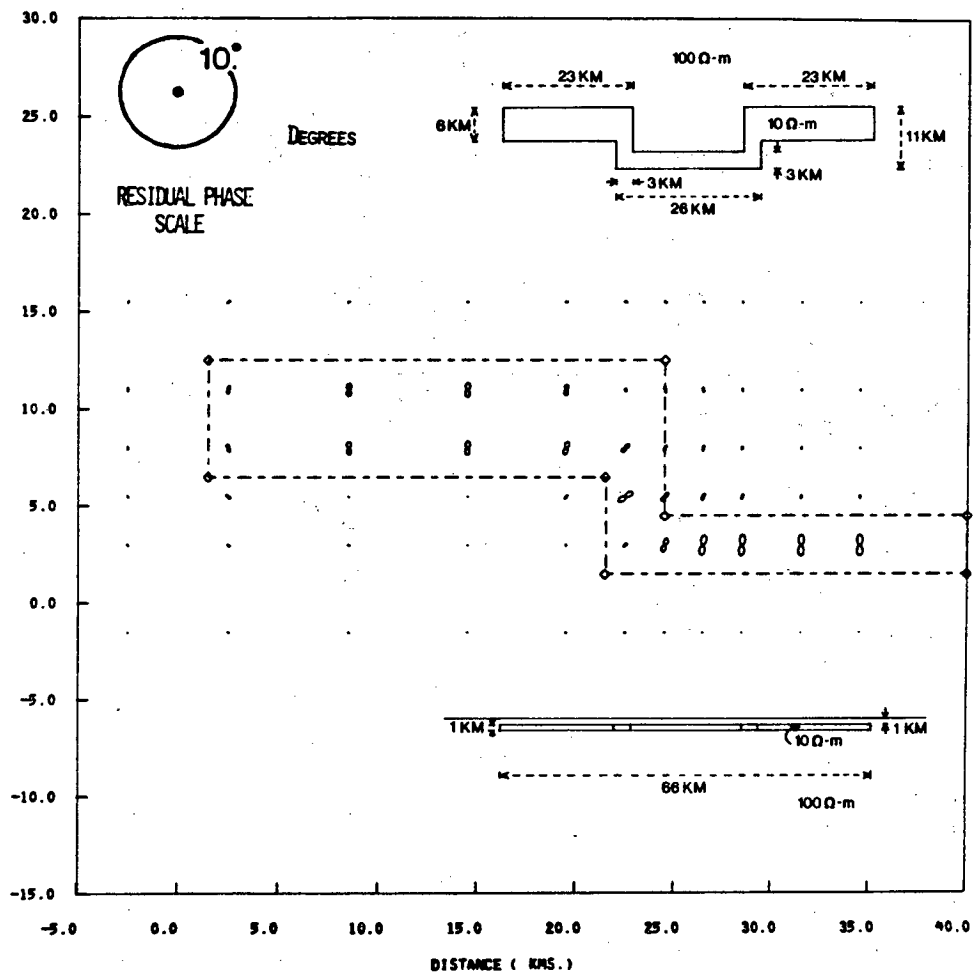
TPX TIPPER PHASE X

AVERAGED FREQS. IN RANGE OF .001 HZ.

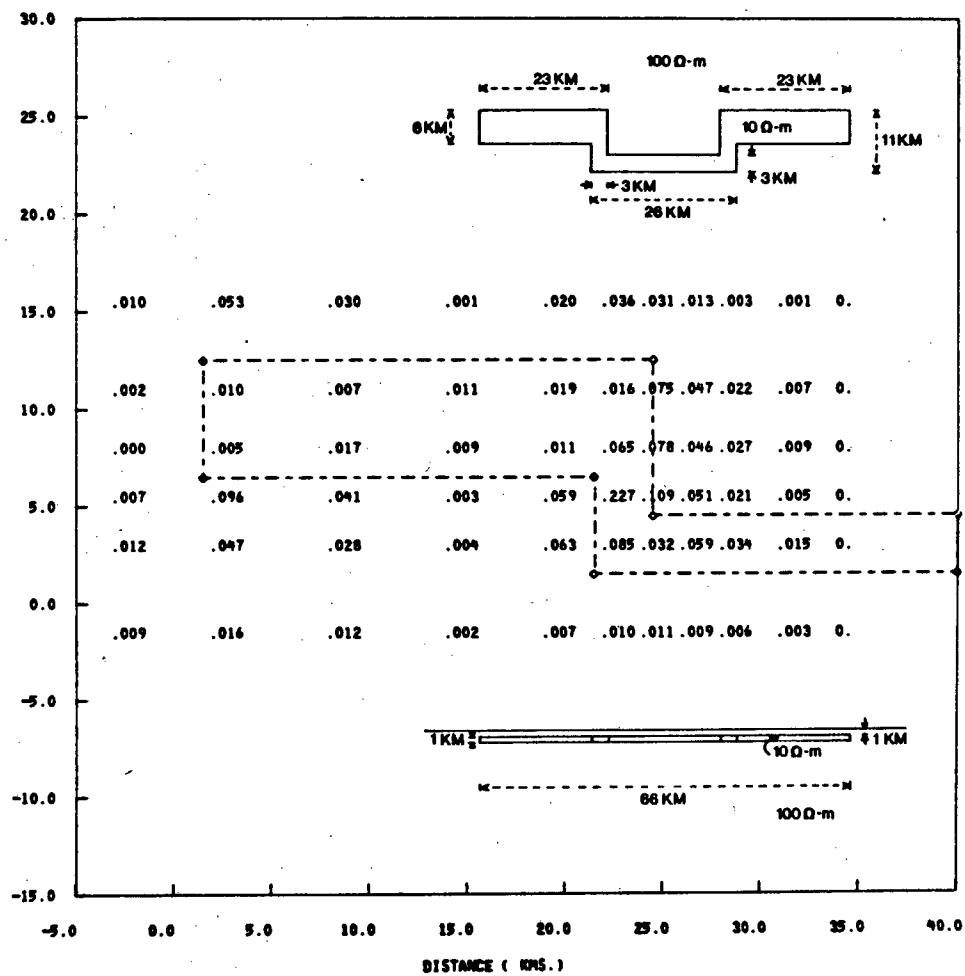


APPARENT RESISTIVITY XV

AVERAGED FREQS. IN RANGE OF .001 HZ.

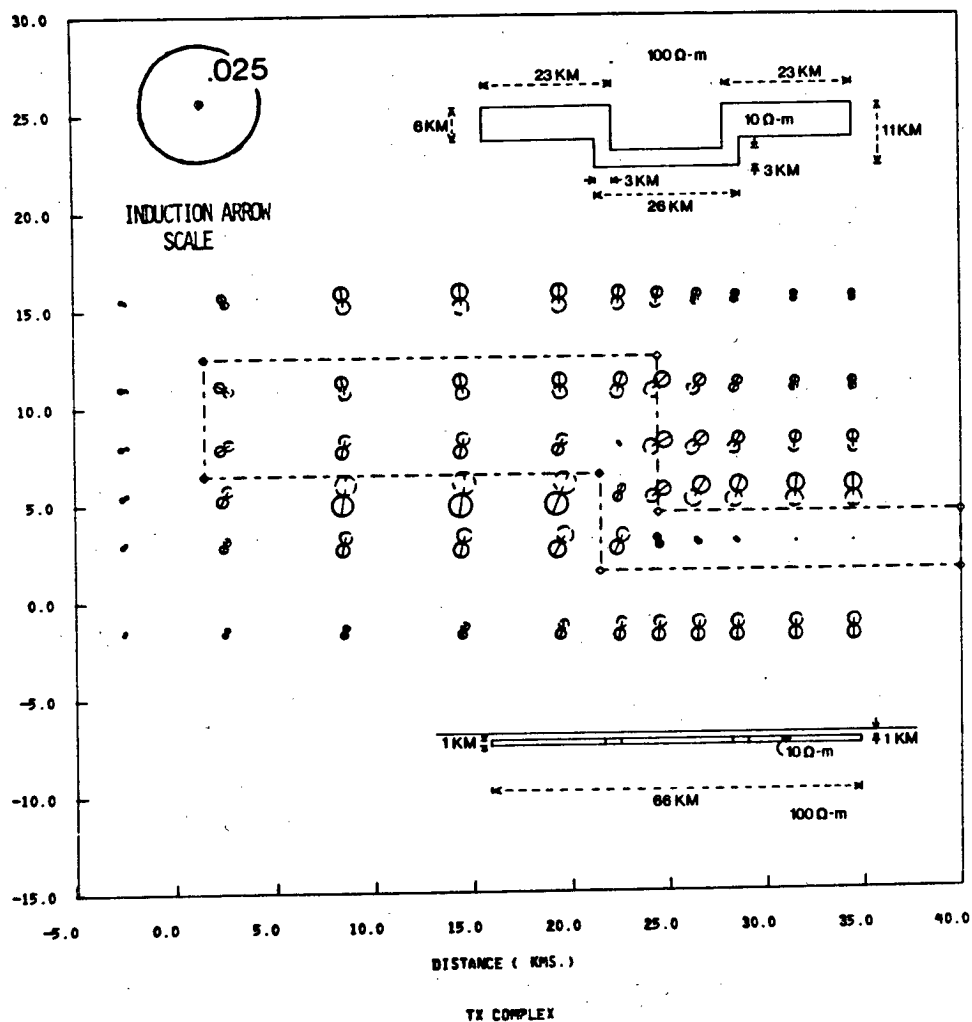


AVERAGED FREQS. IN RANGE OF .001 HZ.

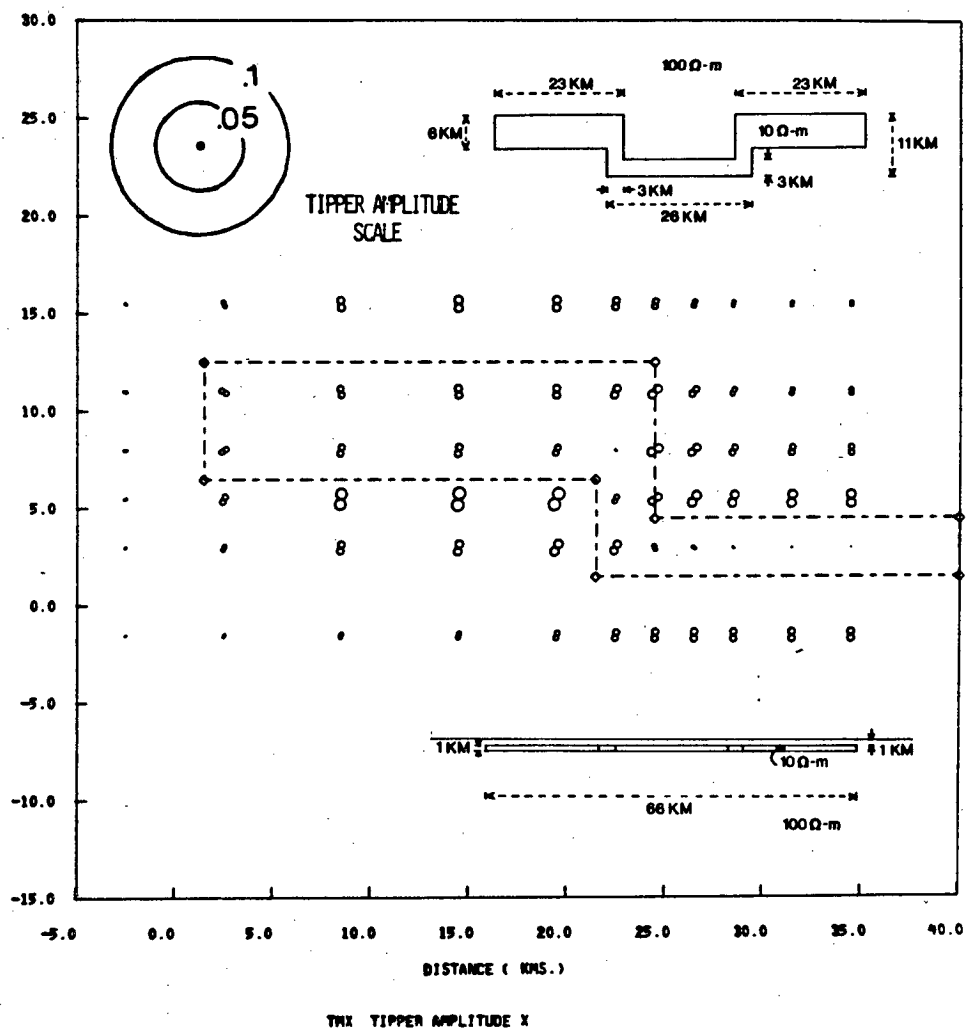


$$SKEW = \frac{ABS((ZXI + ZYV))}{(ZIV - ZYX)}$$

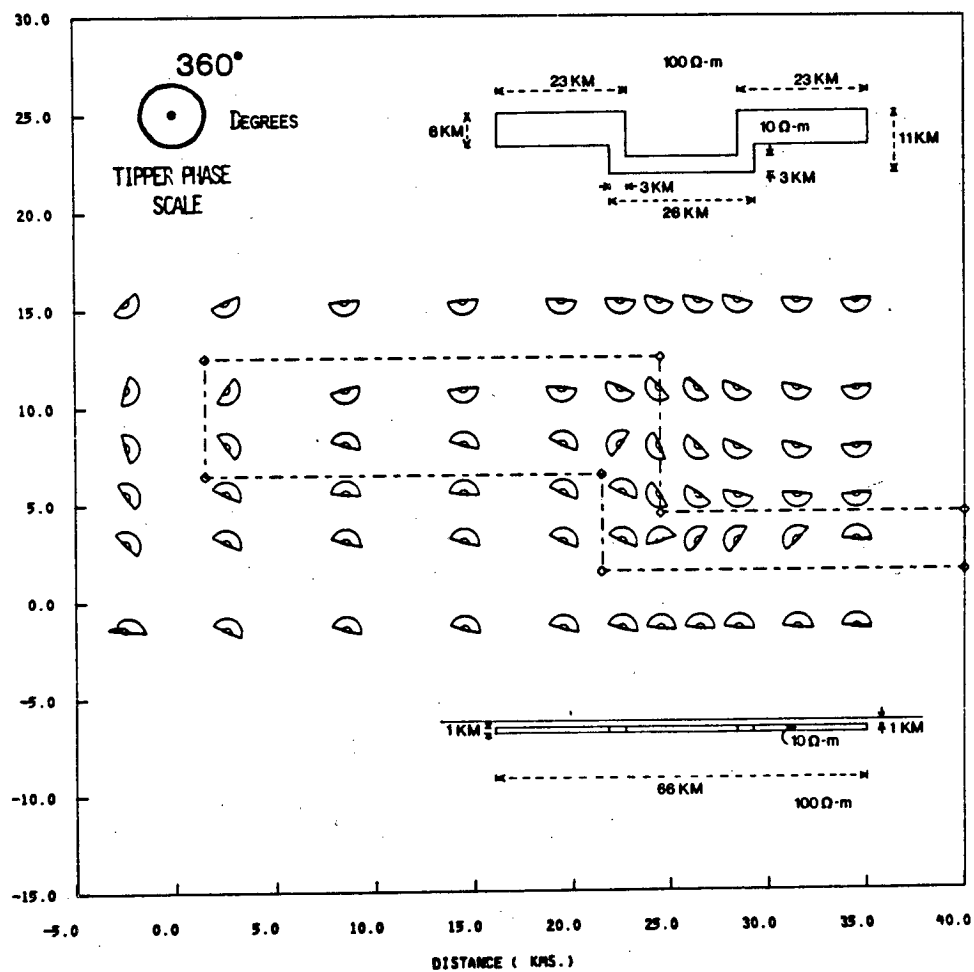
AVERAGED FREQS. IN RANGE OF .001 HZ.



AVERAGED FREQS. IN RANGE OF .001 HZ.

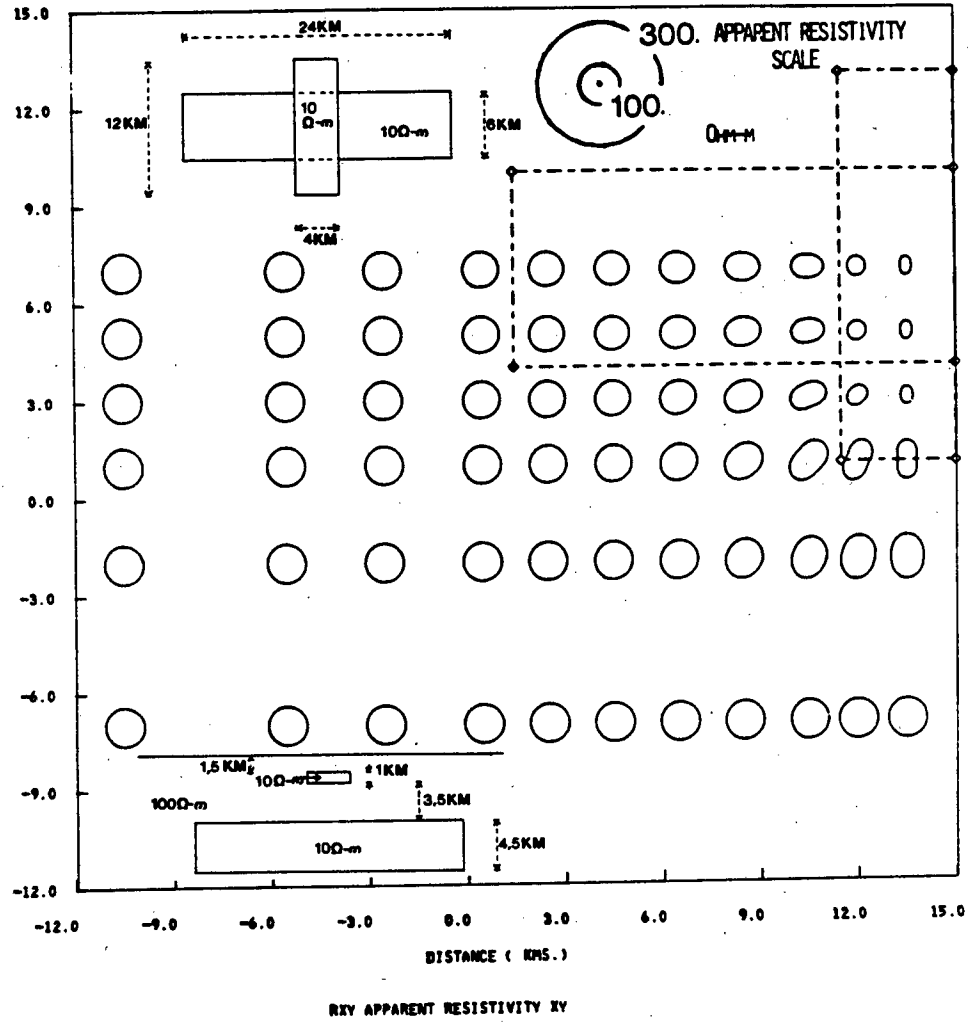


AVERAGED FREQS. IN RANGE OF .001 HZ.

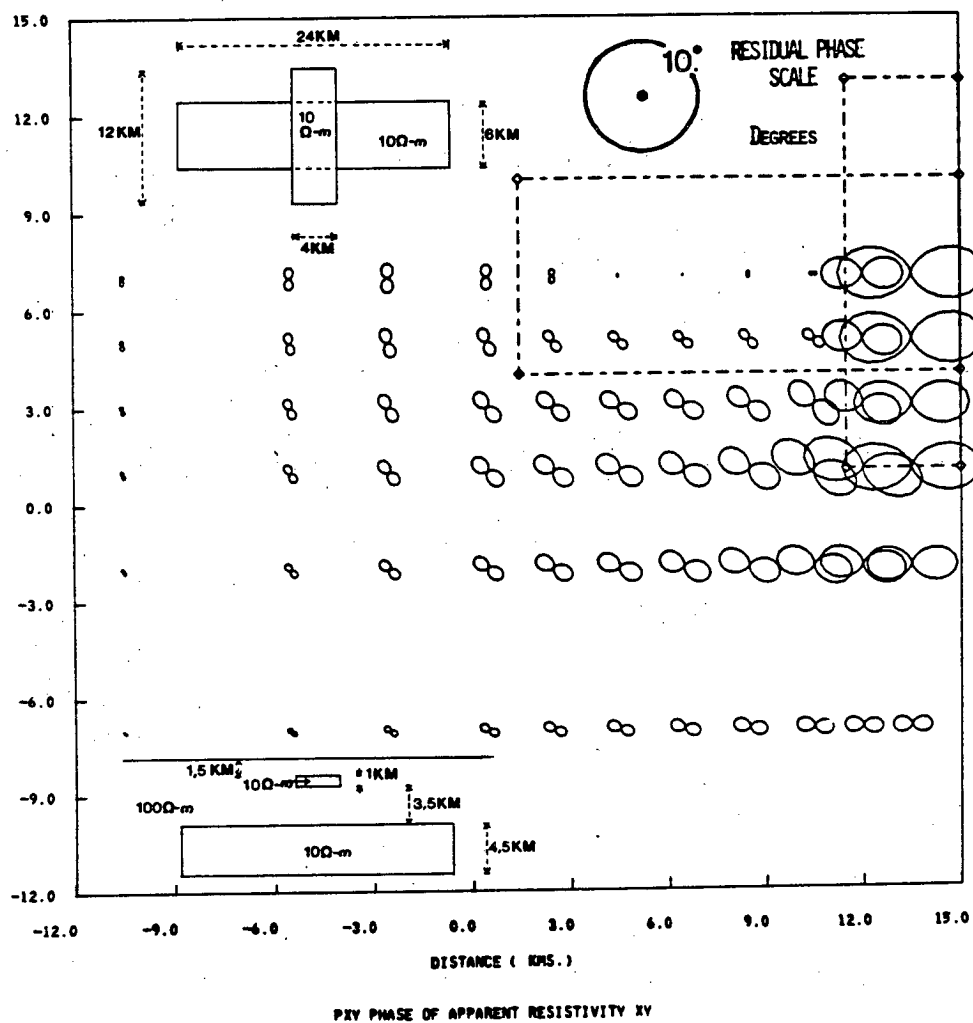


TPX TIPPER PHASE X

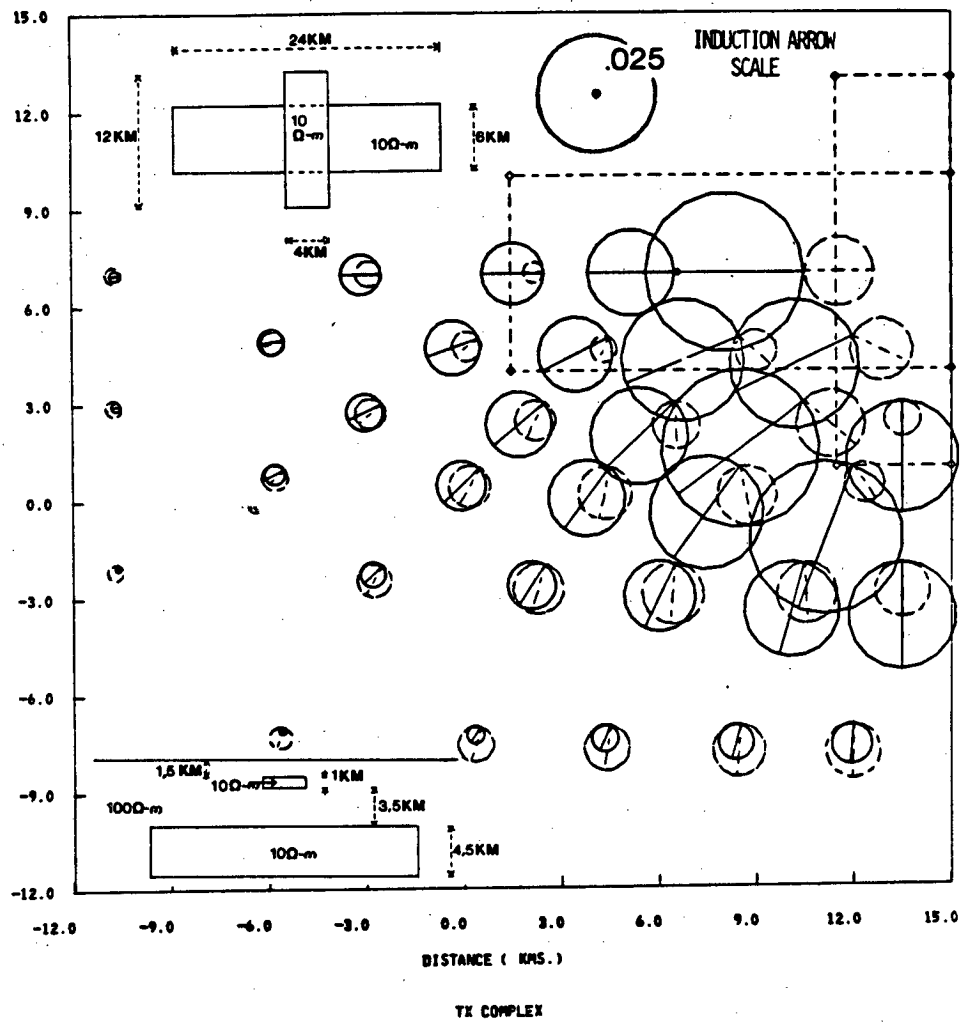
AVERAGED FREQS. IN RANGE OF 0.22 HZ.



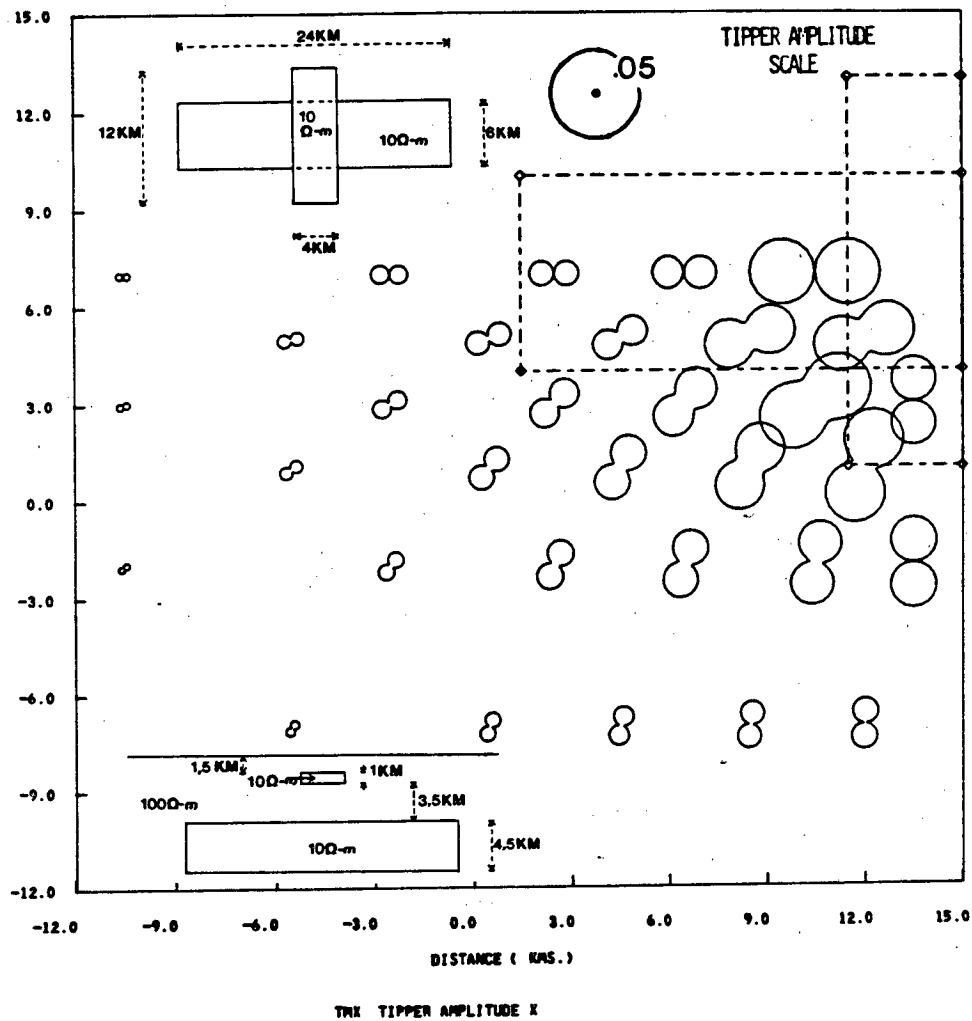
AVERAGED FREQS. IN RANGE OF 0.22 HZ.



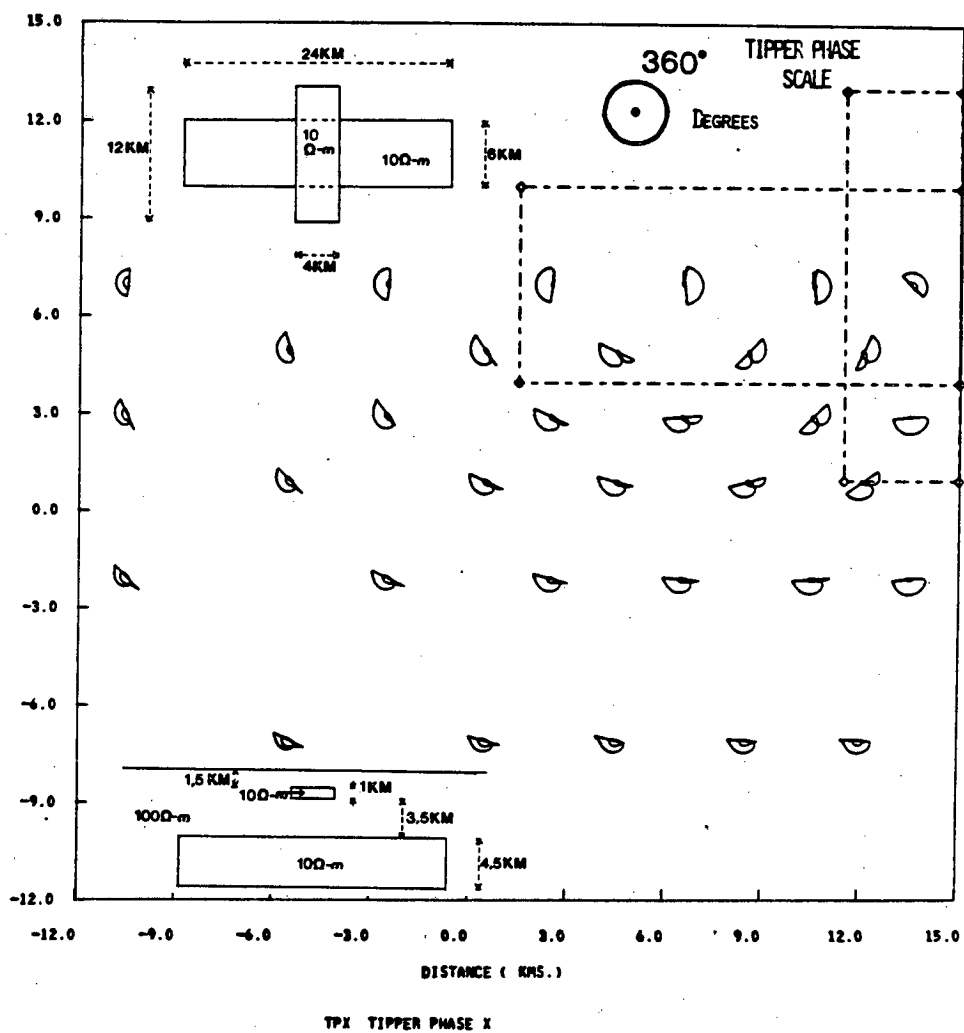
**AVERAGED FREQS. IN RANGE OF 0.22 HZ.**



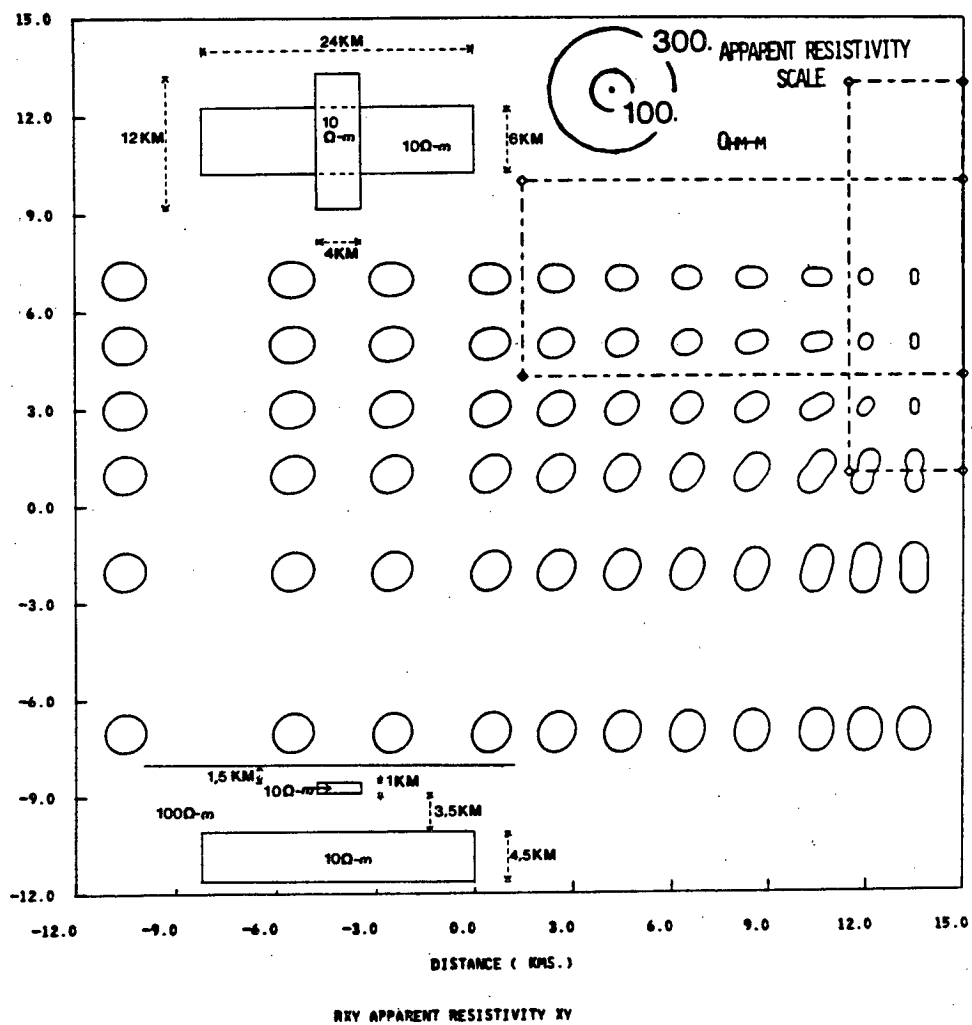
AVERAGED FREQS. IN RANGE OF 0.22 HZ.



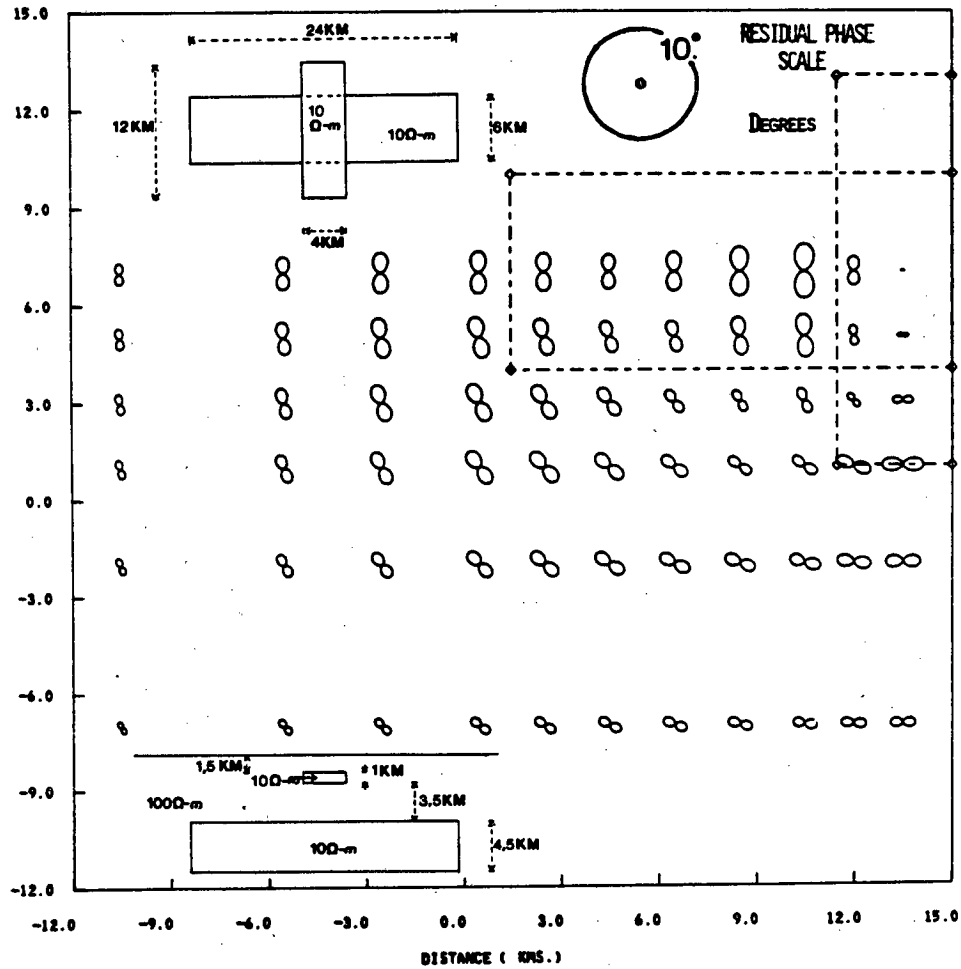
AVERAGED FREQS. IN RANGE OF 0.22 HZ.



AVERAGED FREQS. IN RANGE OF .022 HZ.

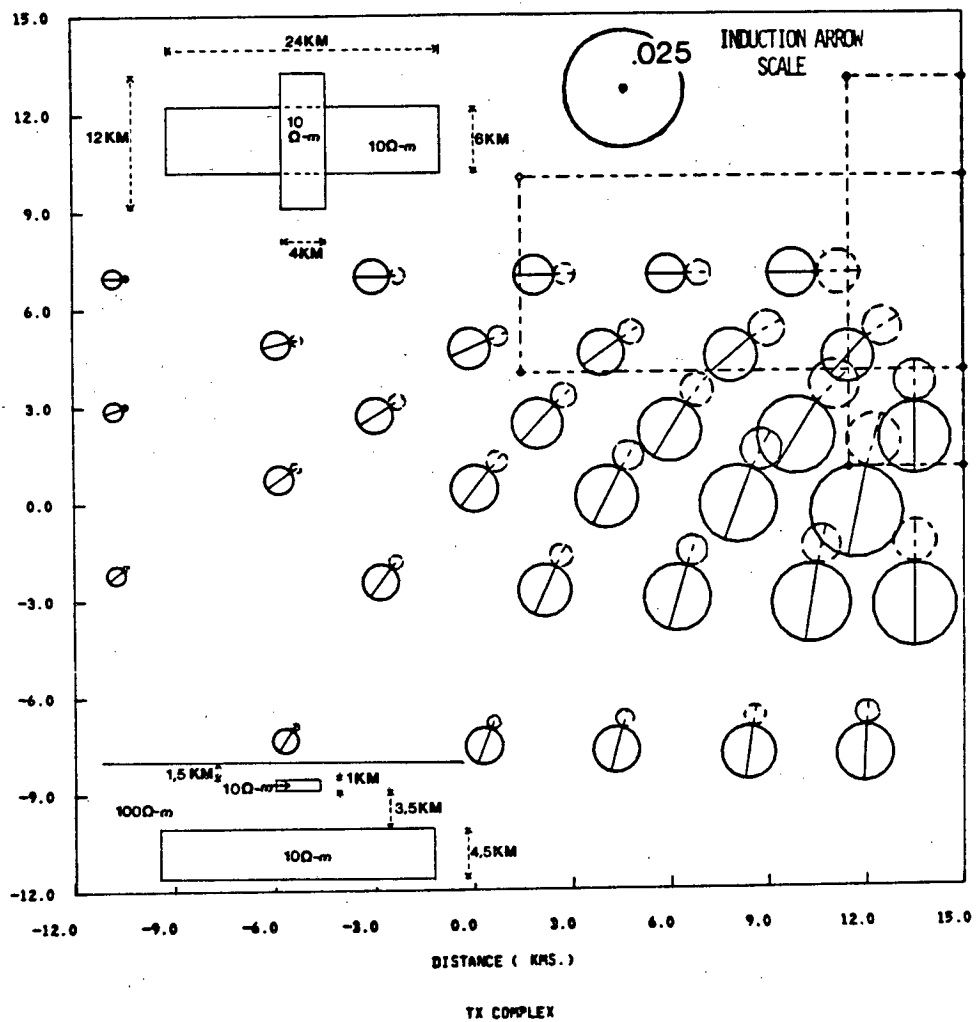


AVERAGED PRESS. IN RANGE OF .022 HZ.

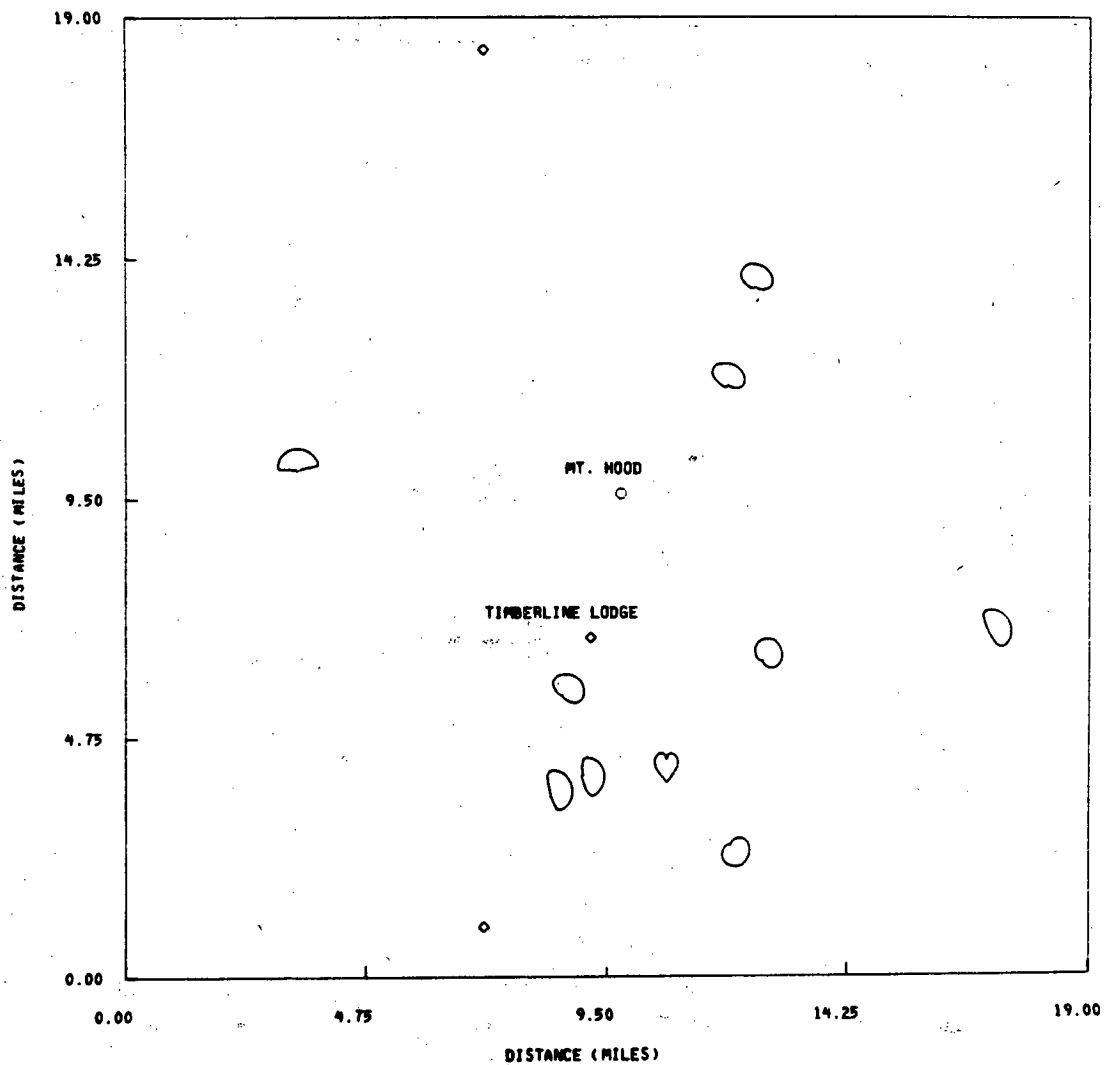


PRY PHASE OF APPARENT RESISTIVITY XY

AVERAGED FREQS. IN RANGE OF .022 HZ.

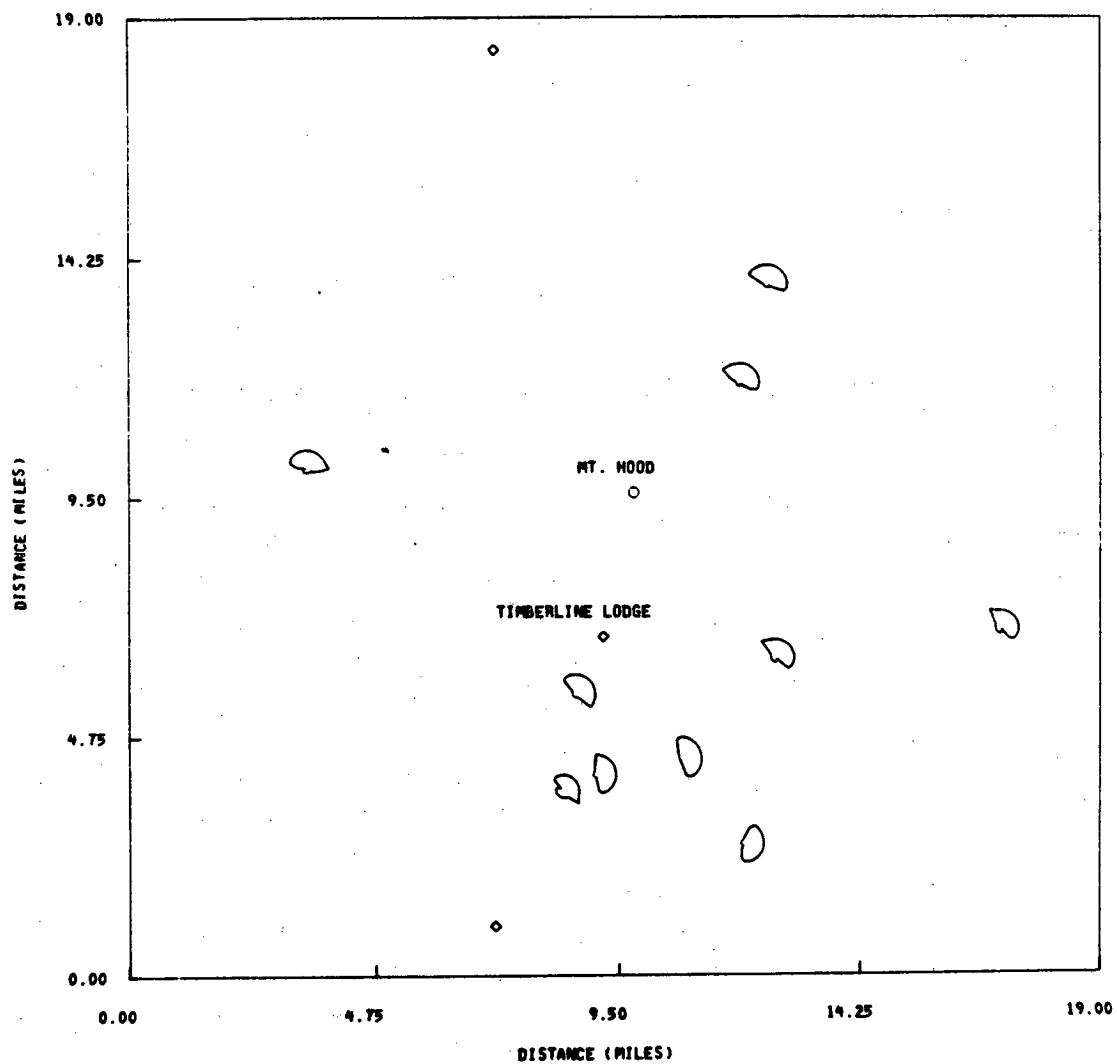


AVERAGED FREQS. IN RANGE OF .2-.03 MZ

Phase Scale  
(degrees)

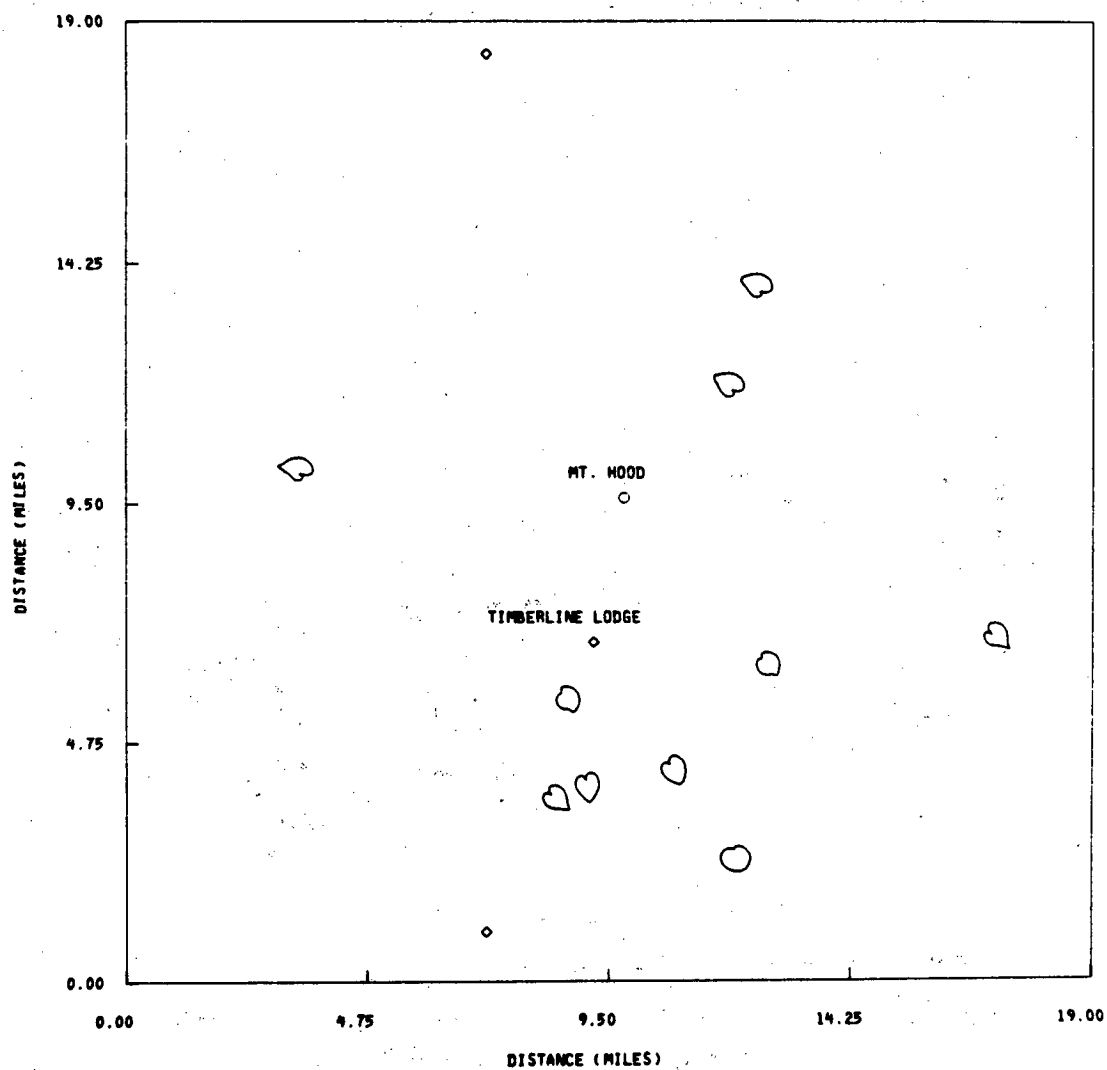
TPX TIPPER PHASE X

AVERAGED FREQS. IN RANGE OF .03-.006HZ

Phase Scale  
(degrees)

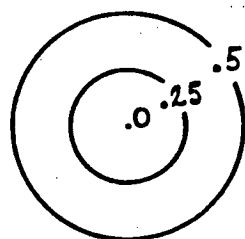
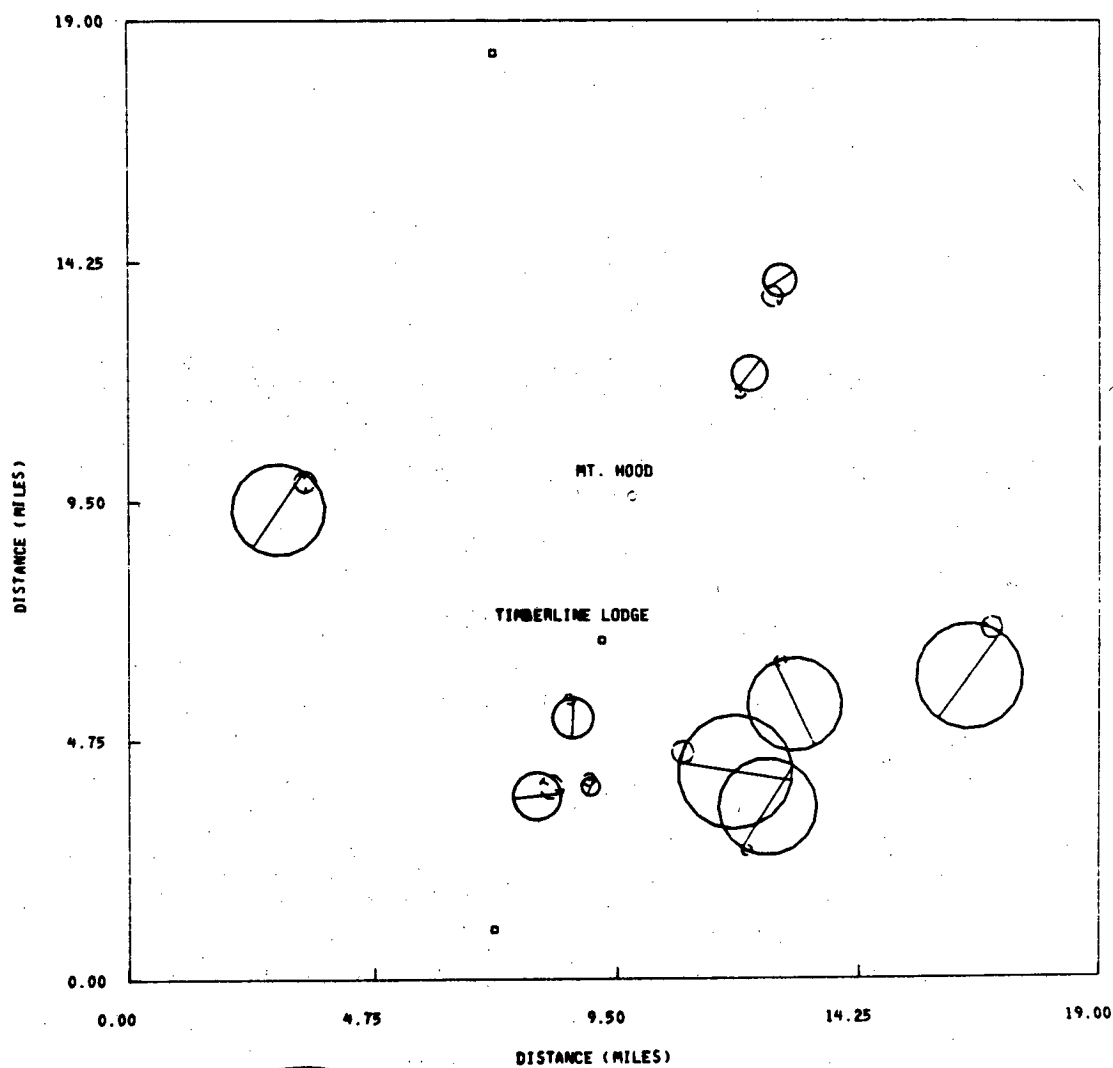
TPX TIPPER PHASE X

AVERAGED FREQS. IN RANGE OF .006-LOWHZ

Phase Scale  
(degrees)

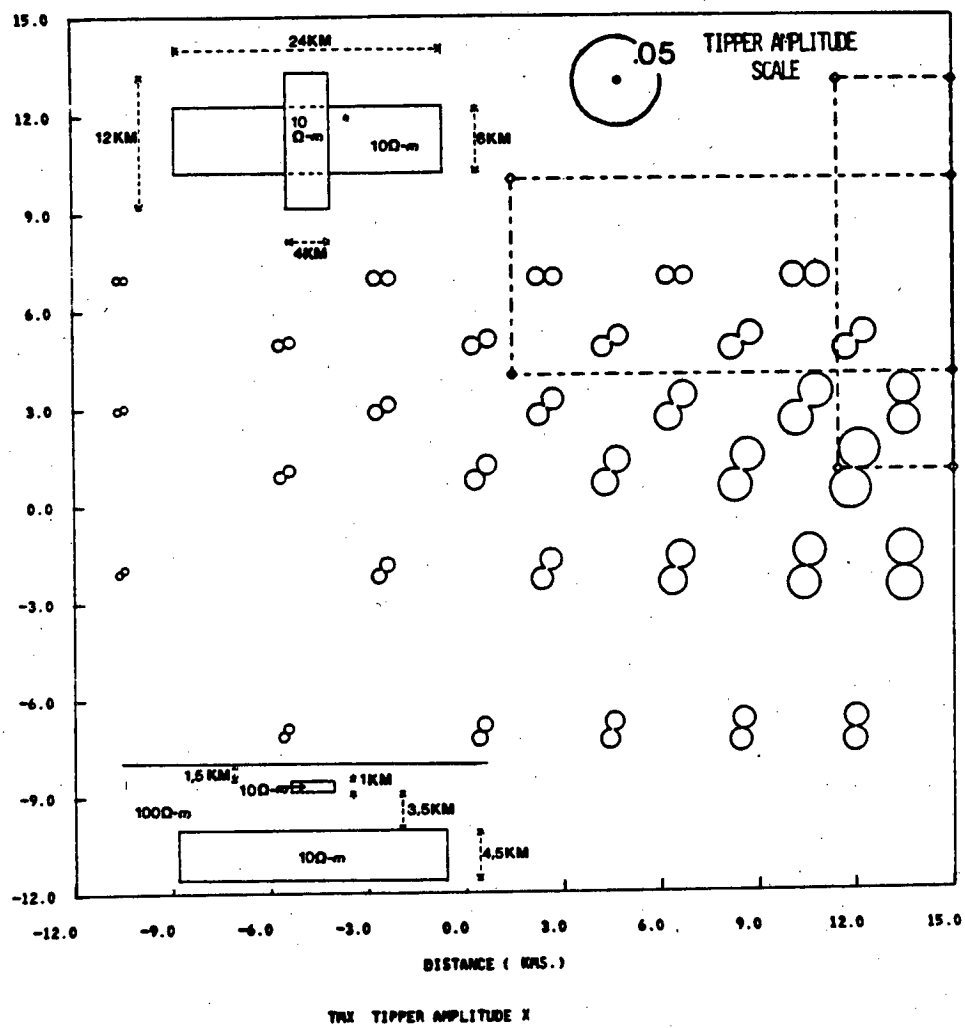
TPX TIPPER PHASE X

AVERAGED FREQS. IN RANGE OF 5.0-1.0 HZ

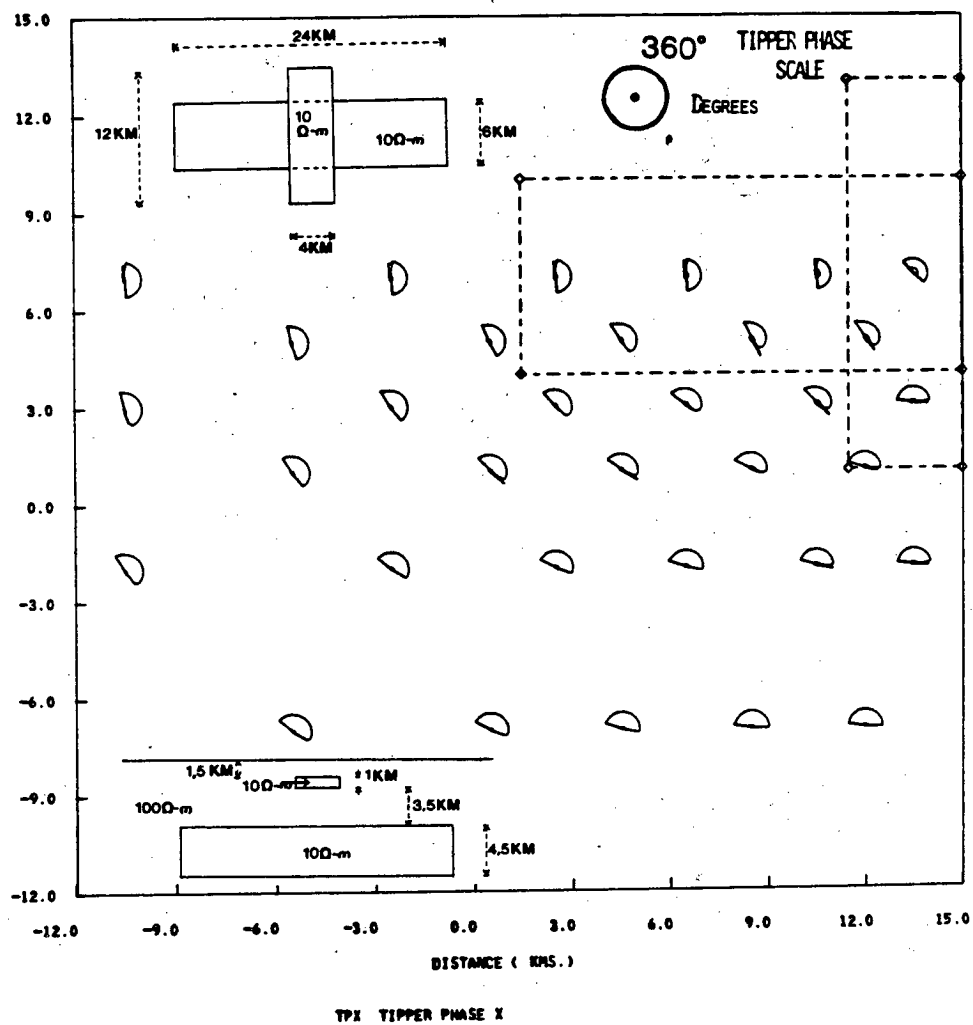


Induction Arrow  
Scale

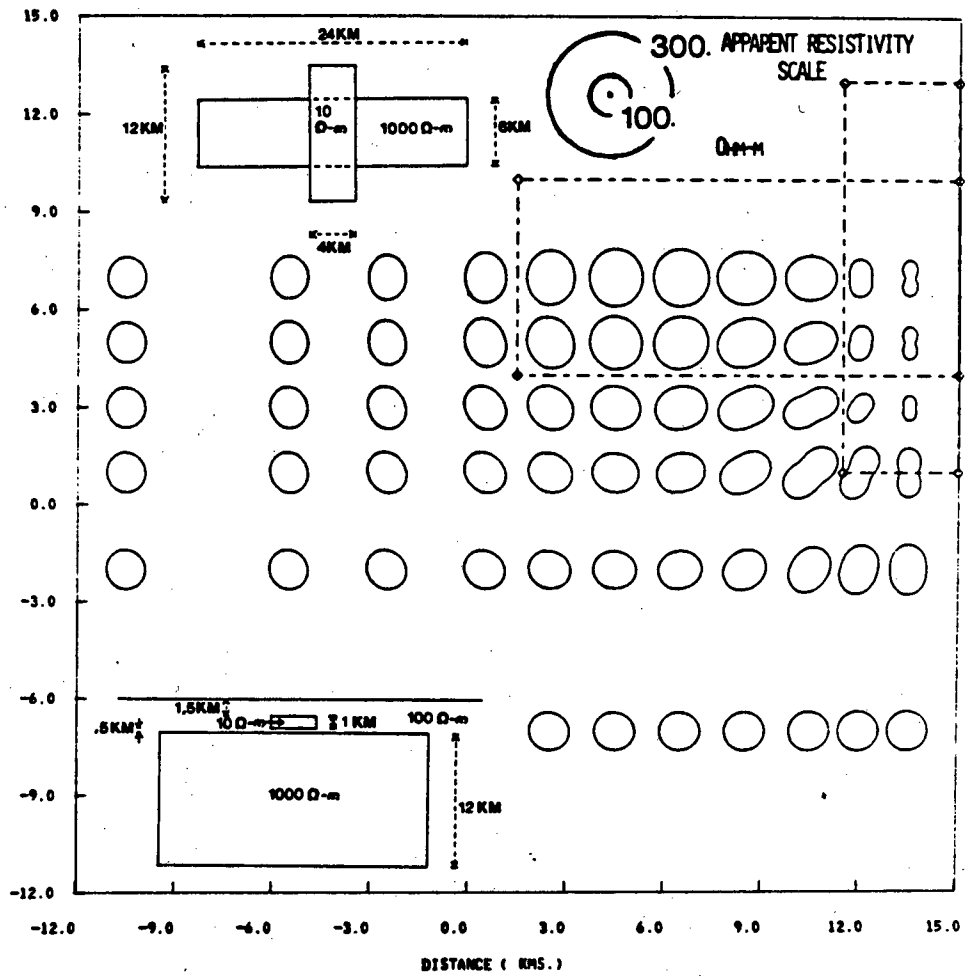
AVERAGE FREQS. IN RANGE OF .022 HZ.



AVERAGED FREQS. IN RANGE OF .022 HZ.

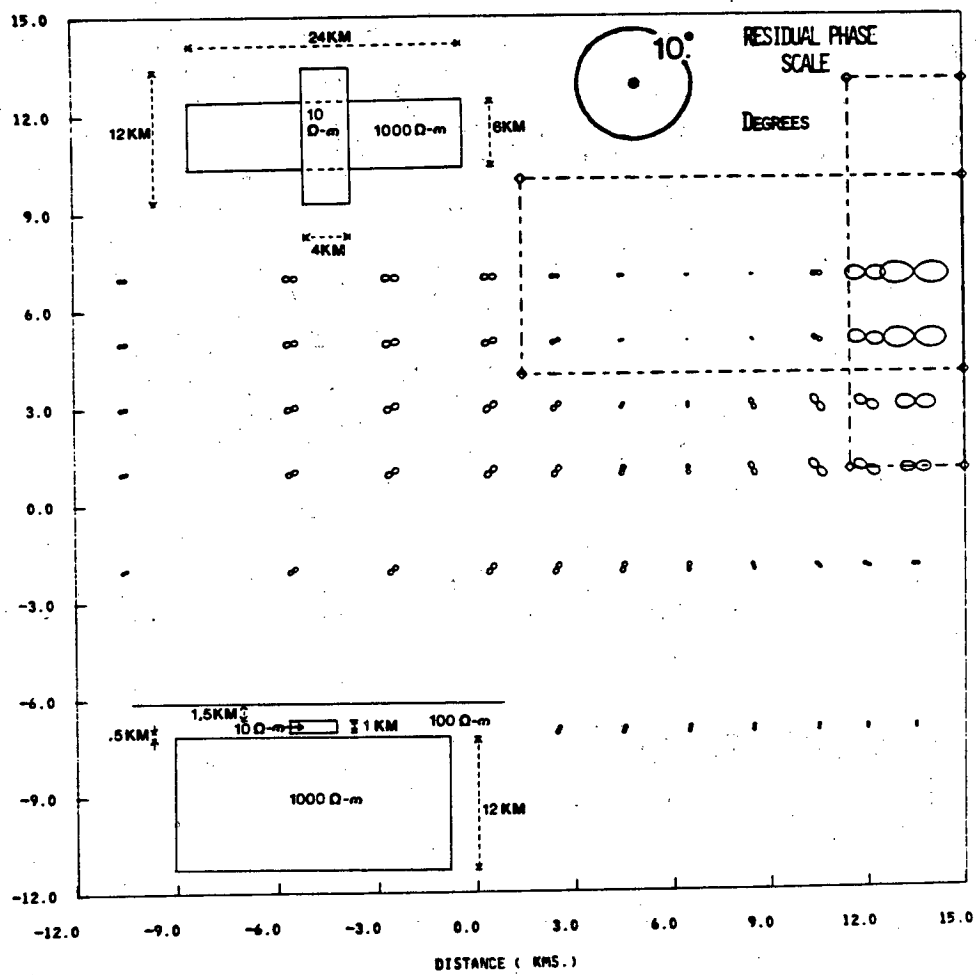


AVERAGED FREQS. IN RANGE OF .022 HZ.



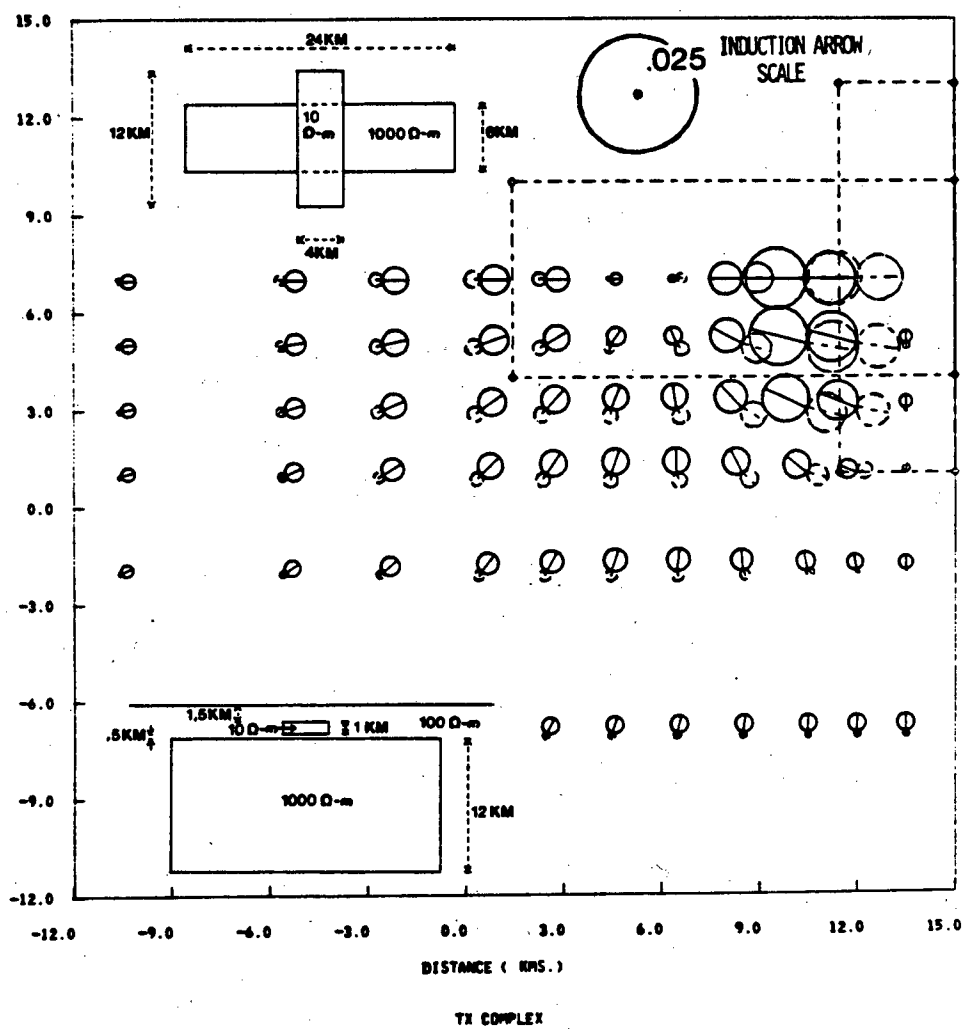
BY APPARENT RESISTIVITY BY

AVERAGED FREQS. IN RANGE OF .022 HZ.

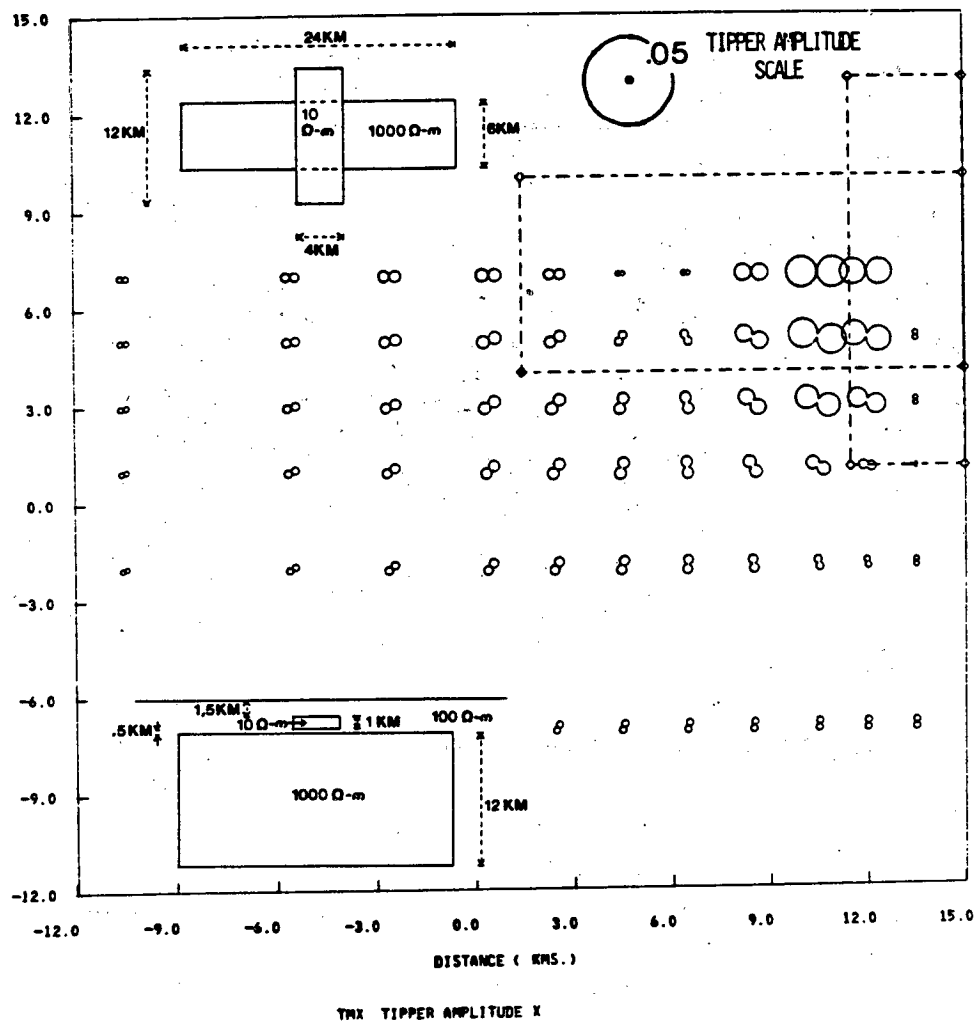


PXV PHASE OF APPARENT RESISTIVITY XV

AVERAGED PRESS. IN RANGE OF .022 HZ.

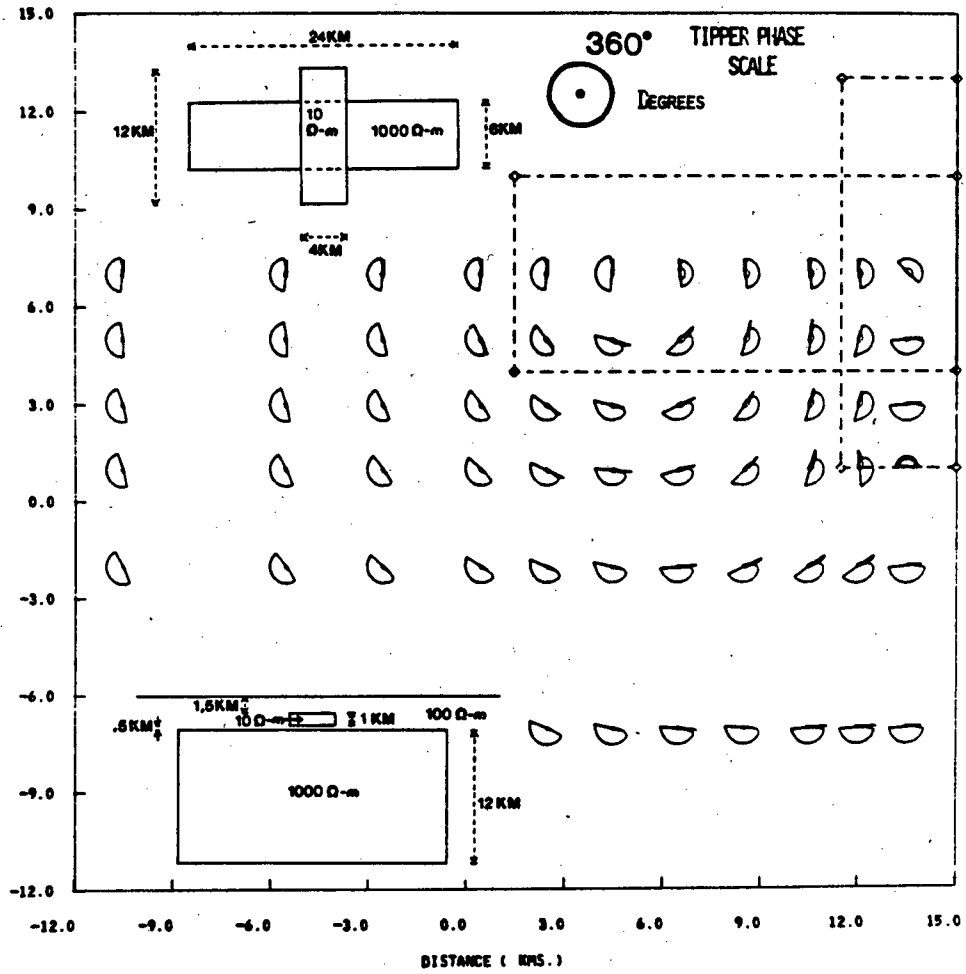


AVERAGED FREQS. IN RANGE OF .022 HZ.

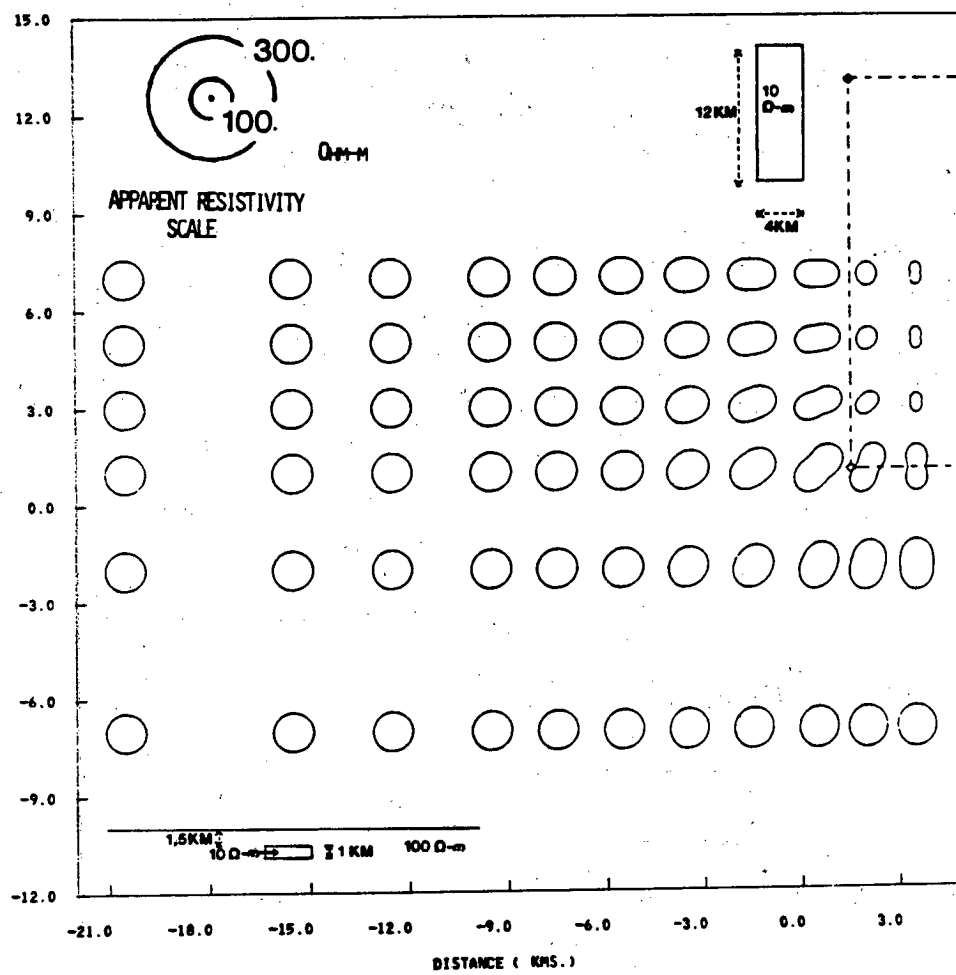


7

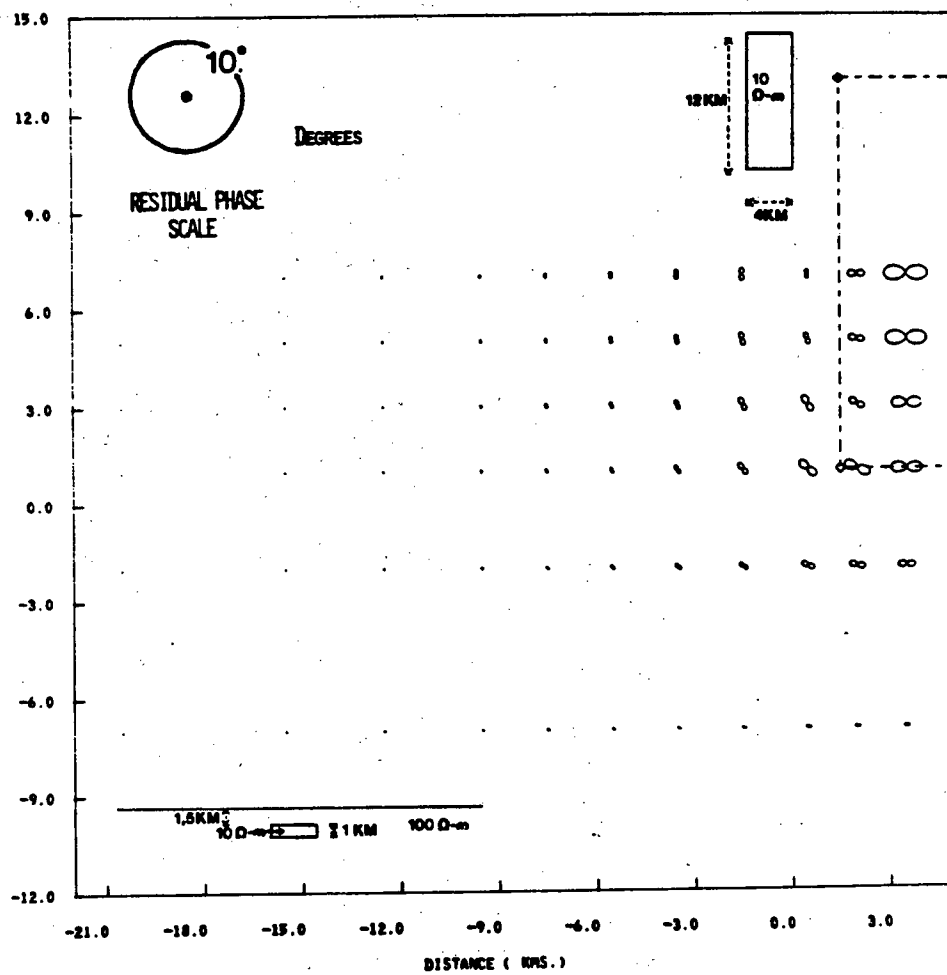
AVERAGED FREQS. IN RANGE OF .022 HZ.



AVERAGED FREQS. IN RANGE OF .022 HZ.

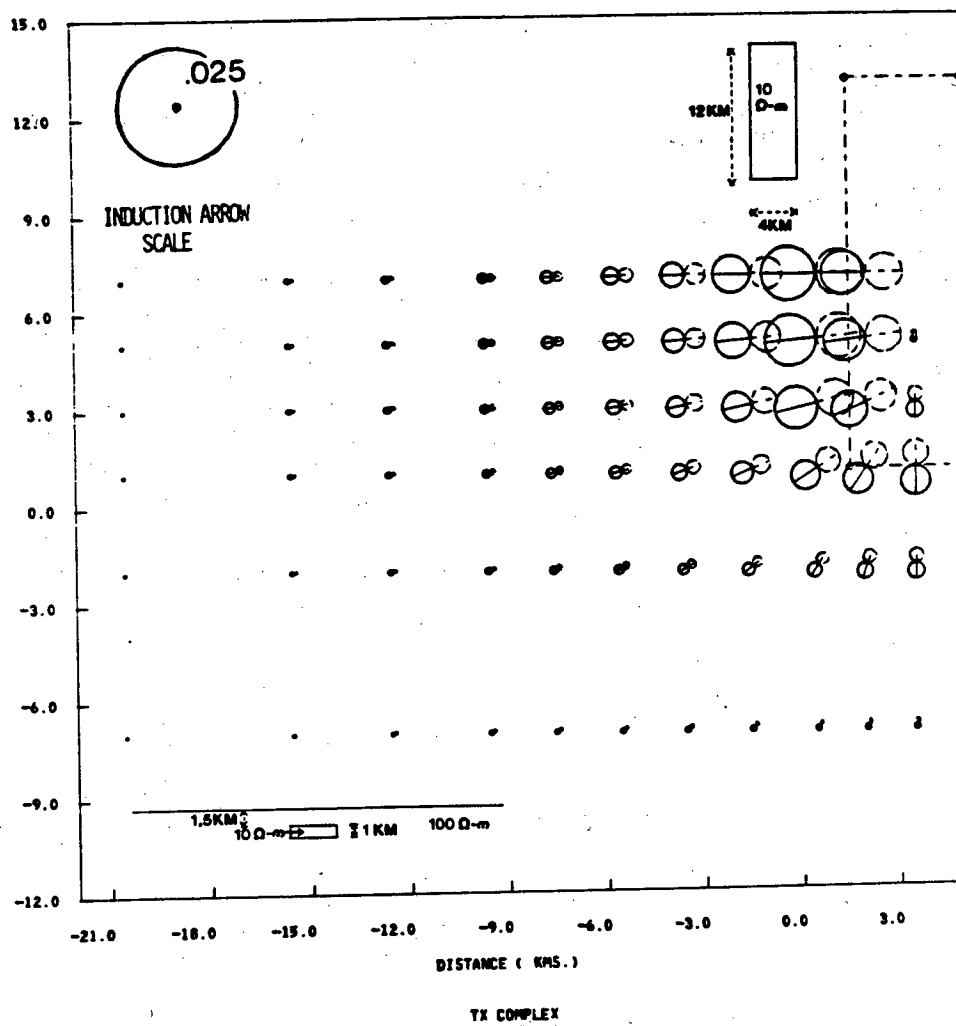


AVERAGED FREQS. IN RANGE OF .022 HZ.

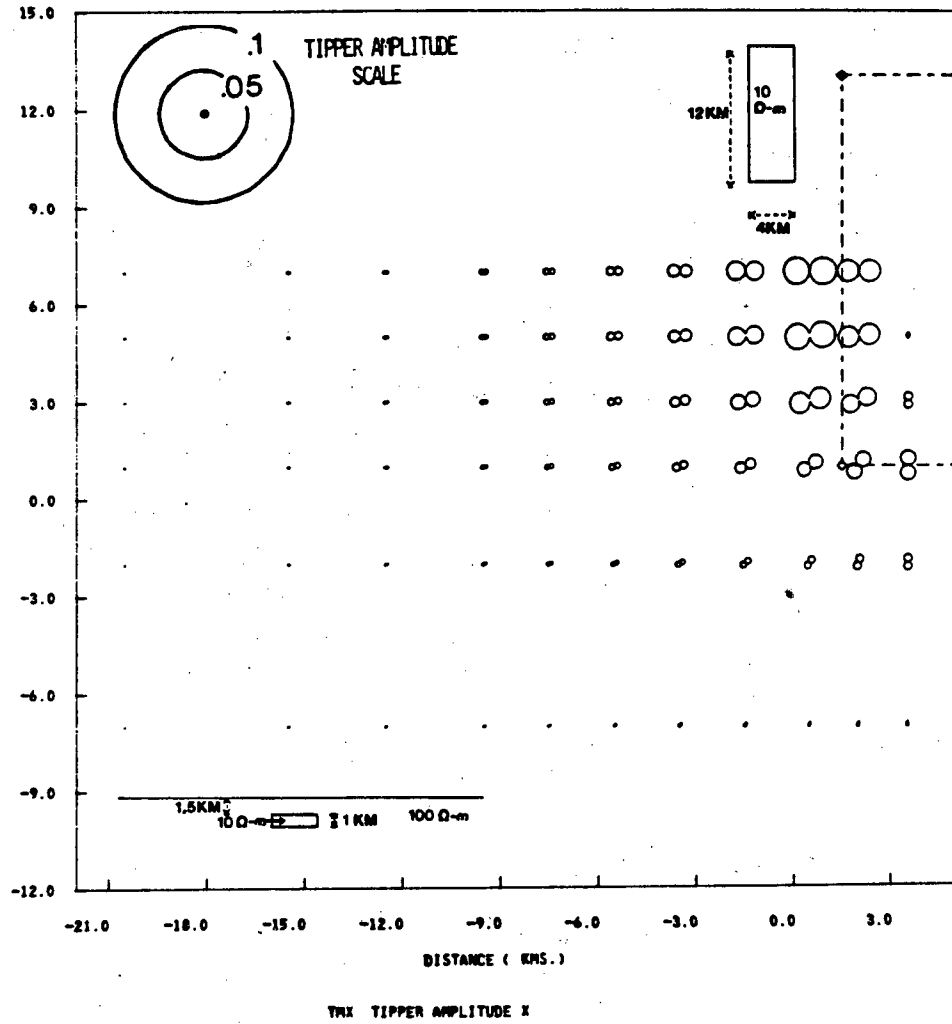


### PKV PHASE OF APPARENT RESISTIVITY XV

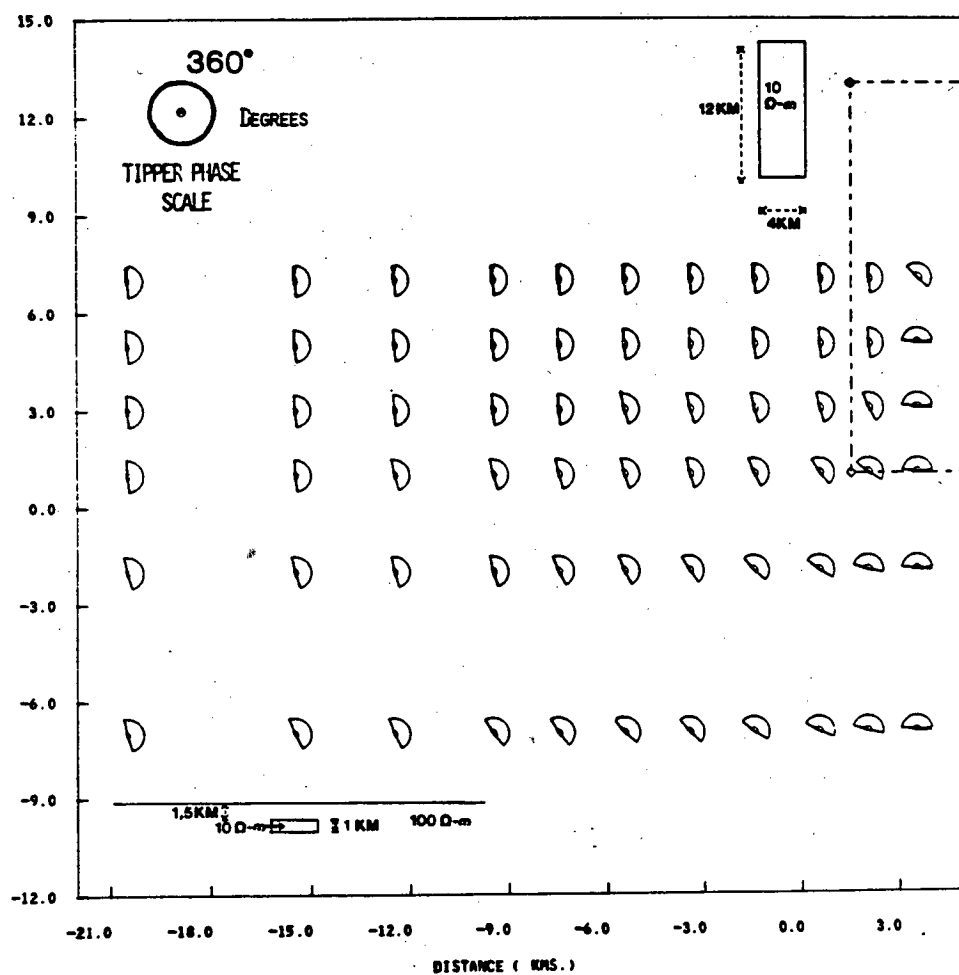
AVERAGED FREQS. IN RANGE OF .022 HZ.



AVERAGED FREQS. IN RANGE OF .022 HZ.

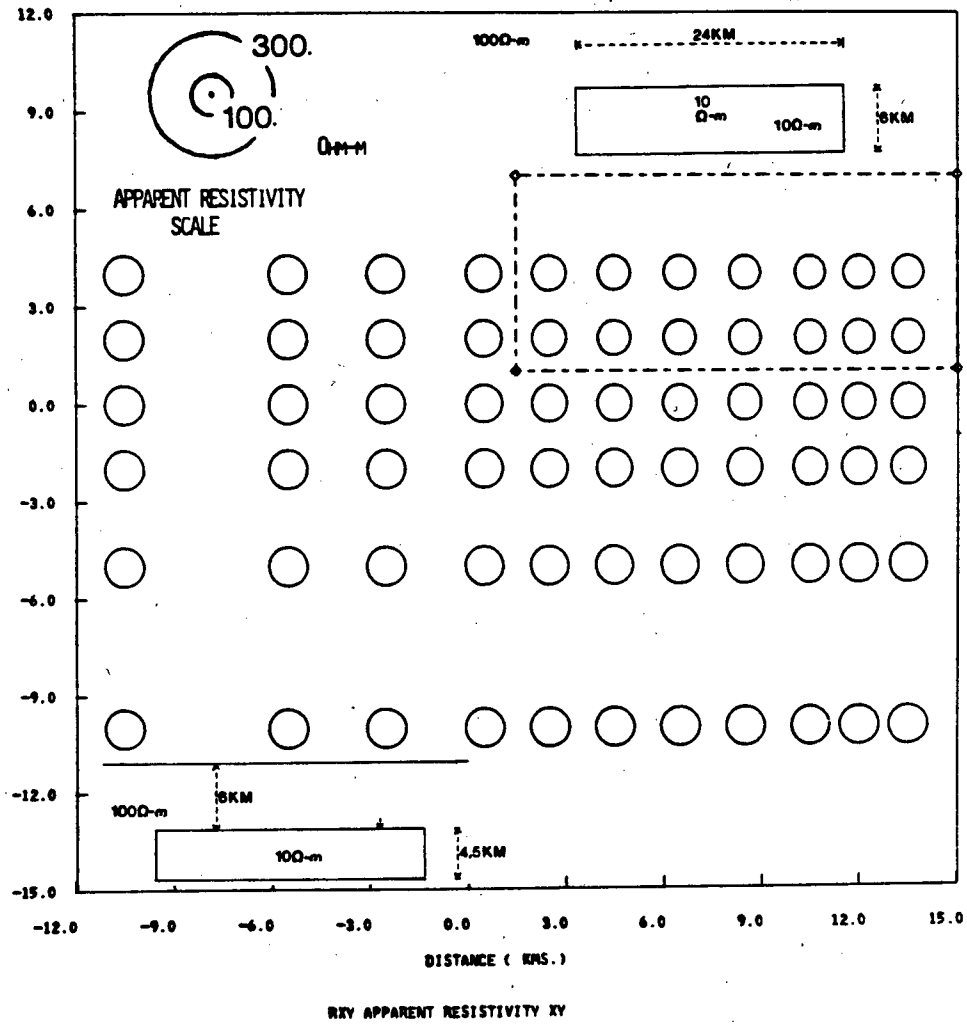


AVERAGED FREQS. IN RANGE OF .022 HZ.

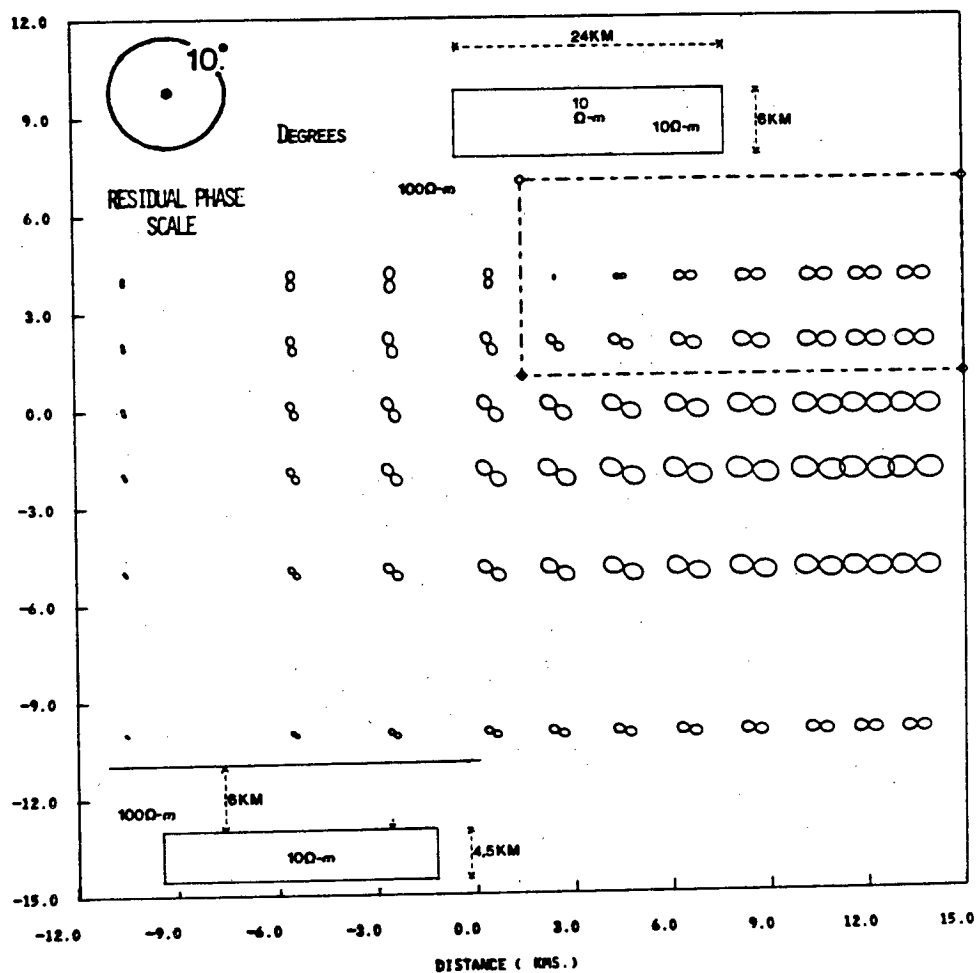


TPX TIPPER PHASE X

AVERAGED FREQS. IN RANGE OF 0.22 HZ.

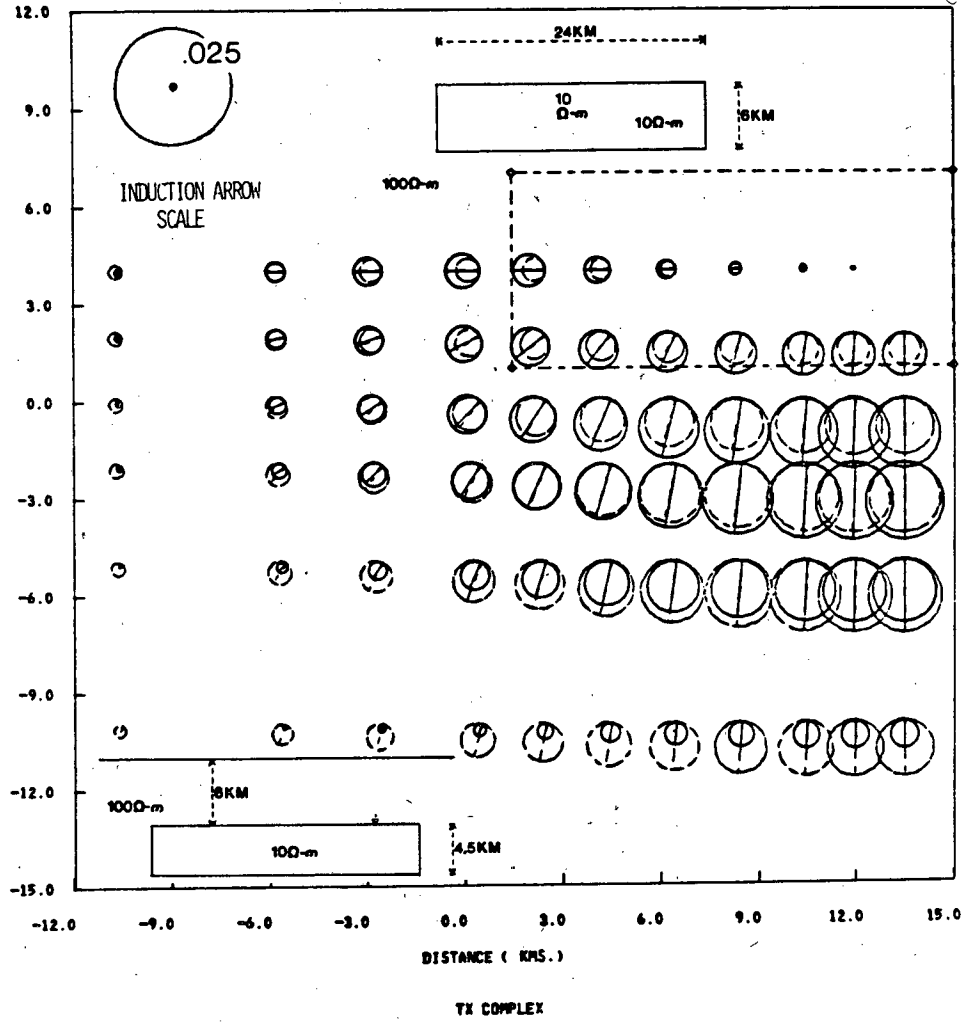


AVERAGED FREES. IN RANGE OF 0.22 HZ.

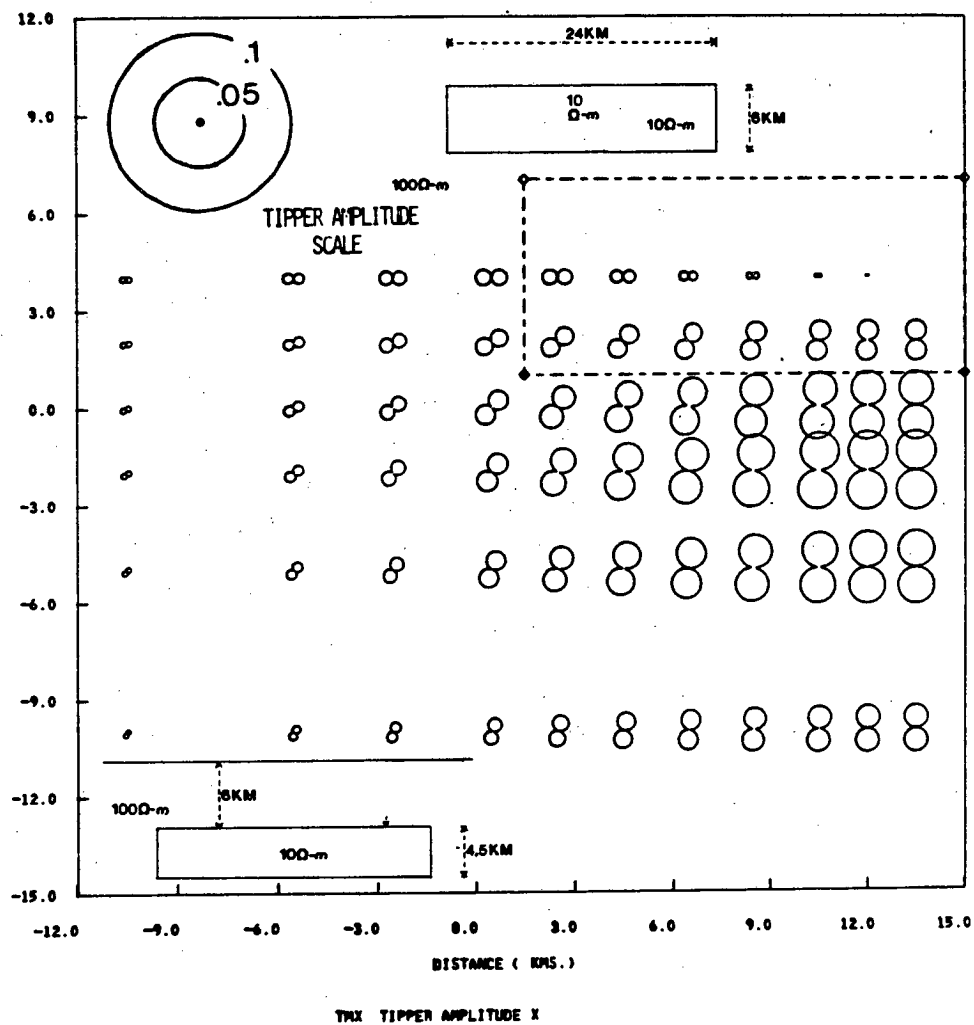


PXY PHASE OF APPARENT RESISTIVITY XY

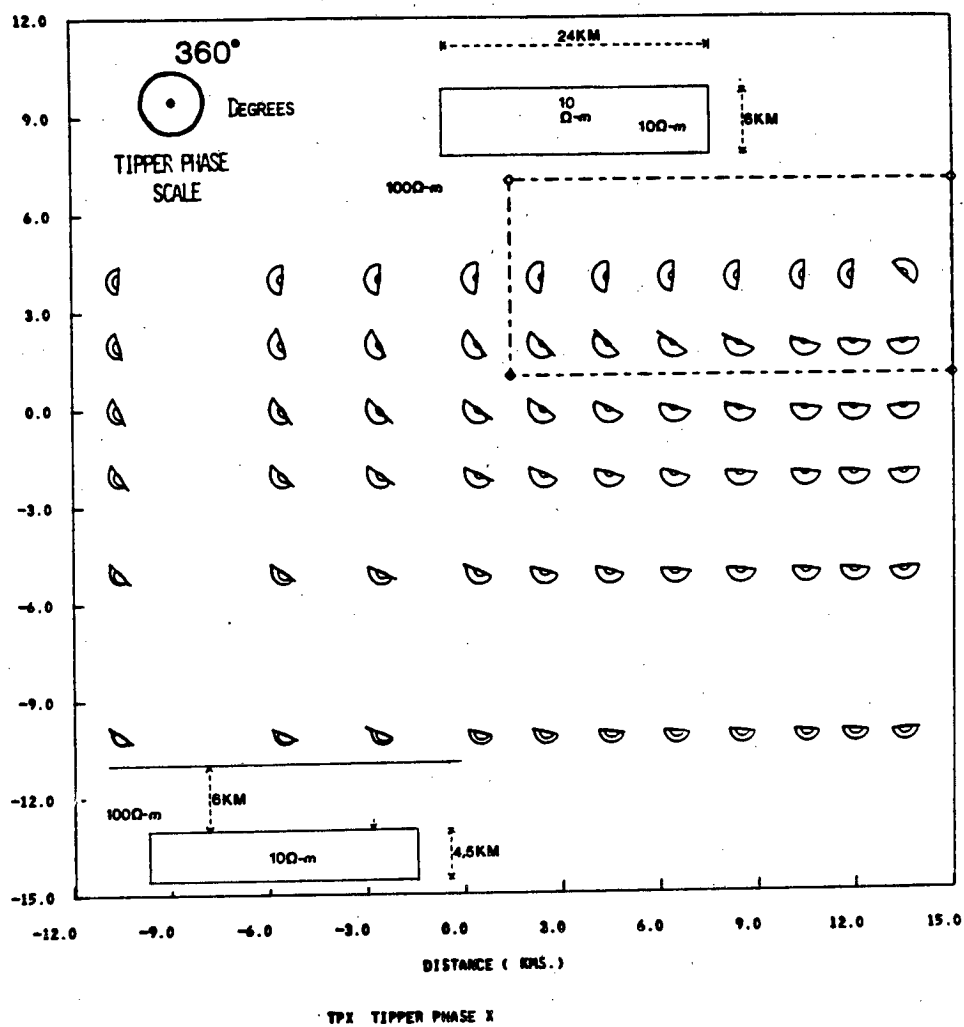
AVERAGED FREQS. IN RANGE OF 0.22 HZ.



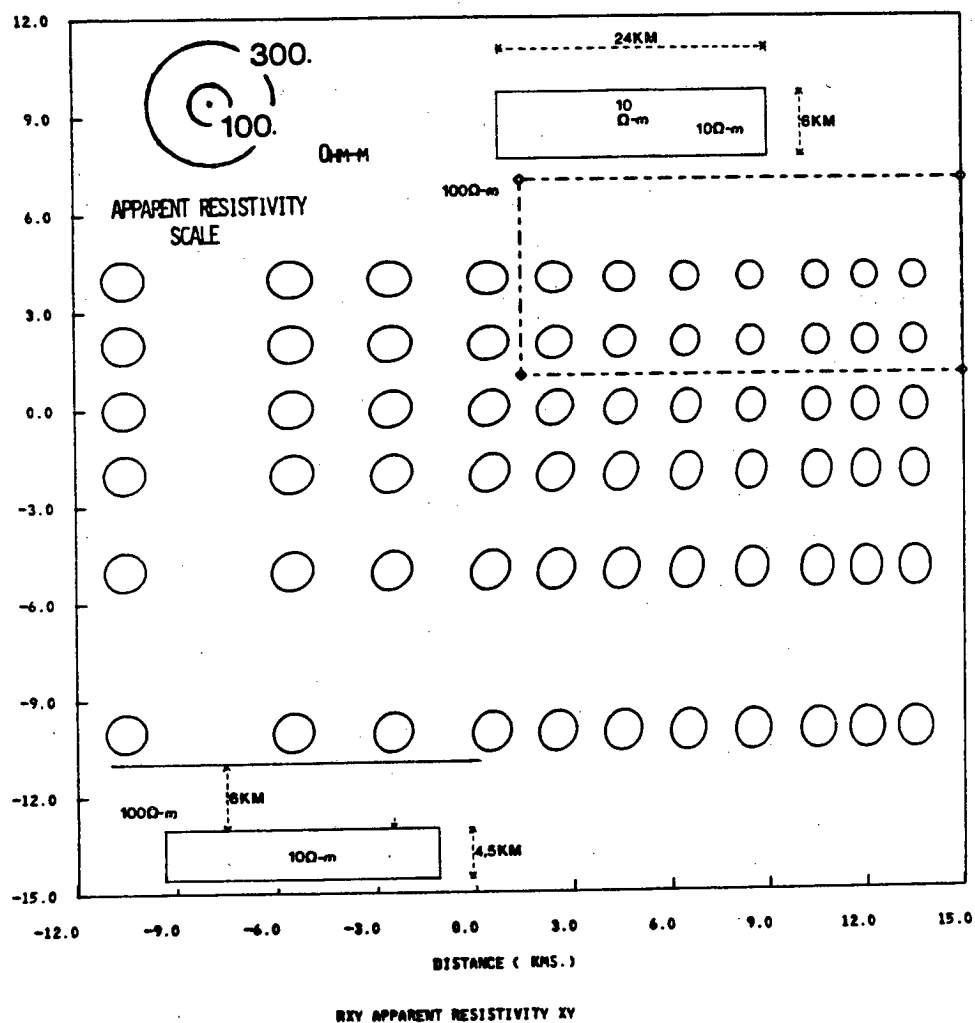
AVERAGED FREQS. IN RANGE OF 0.22 HZ.



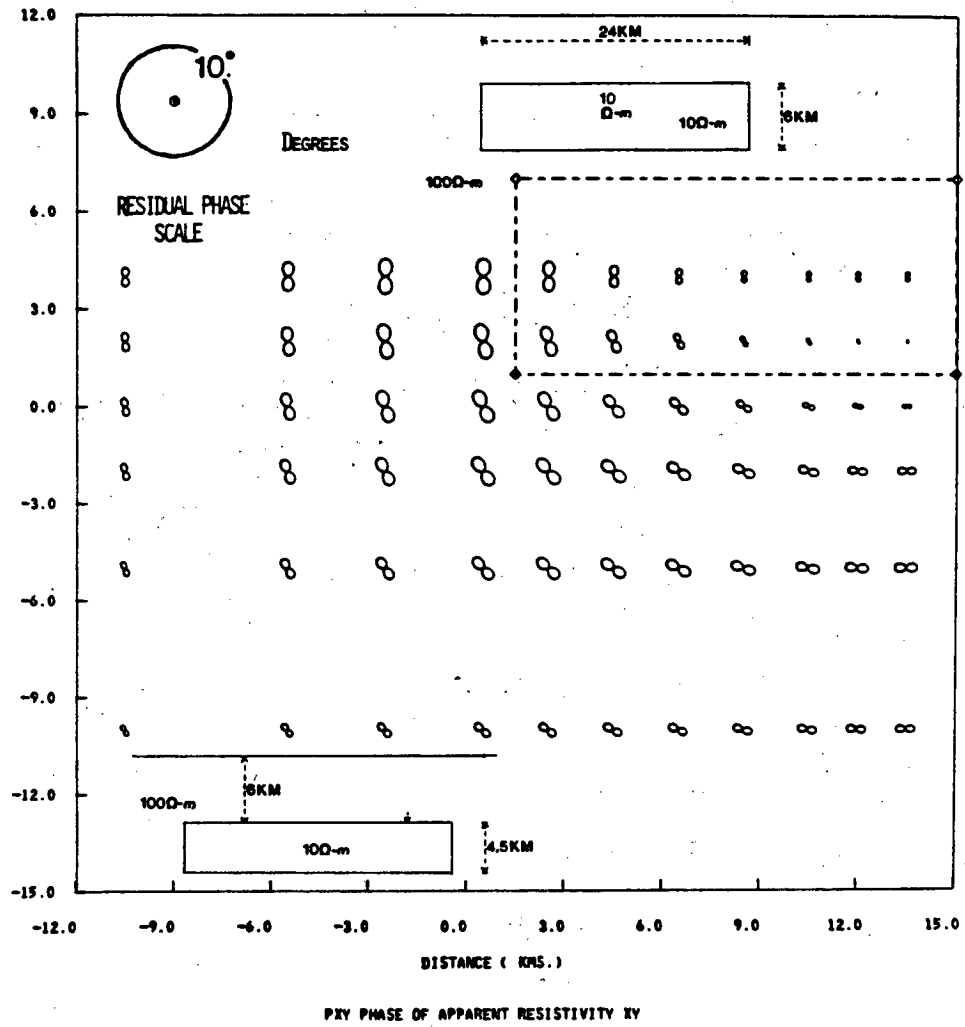
AVERAGED FREQS. IN RANGE OF 0.22 HZ.



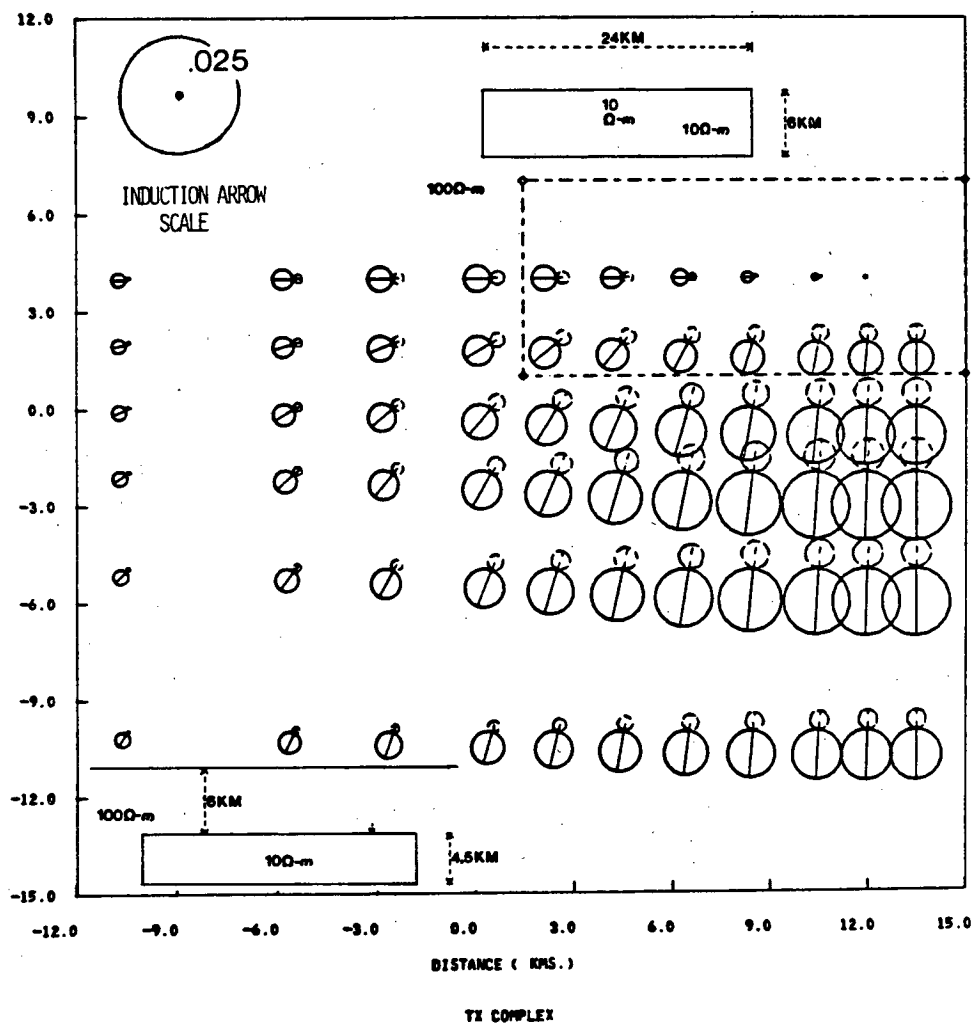
AVERAGED FREQS. IN RANGE OF .022 HZ.



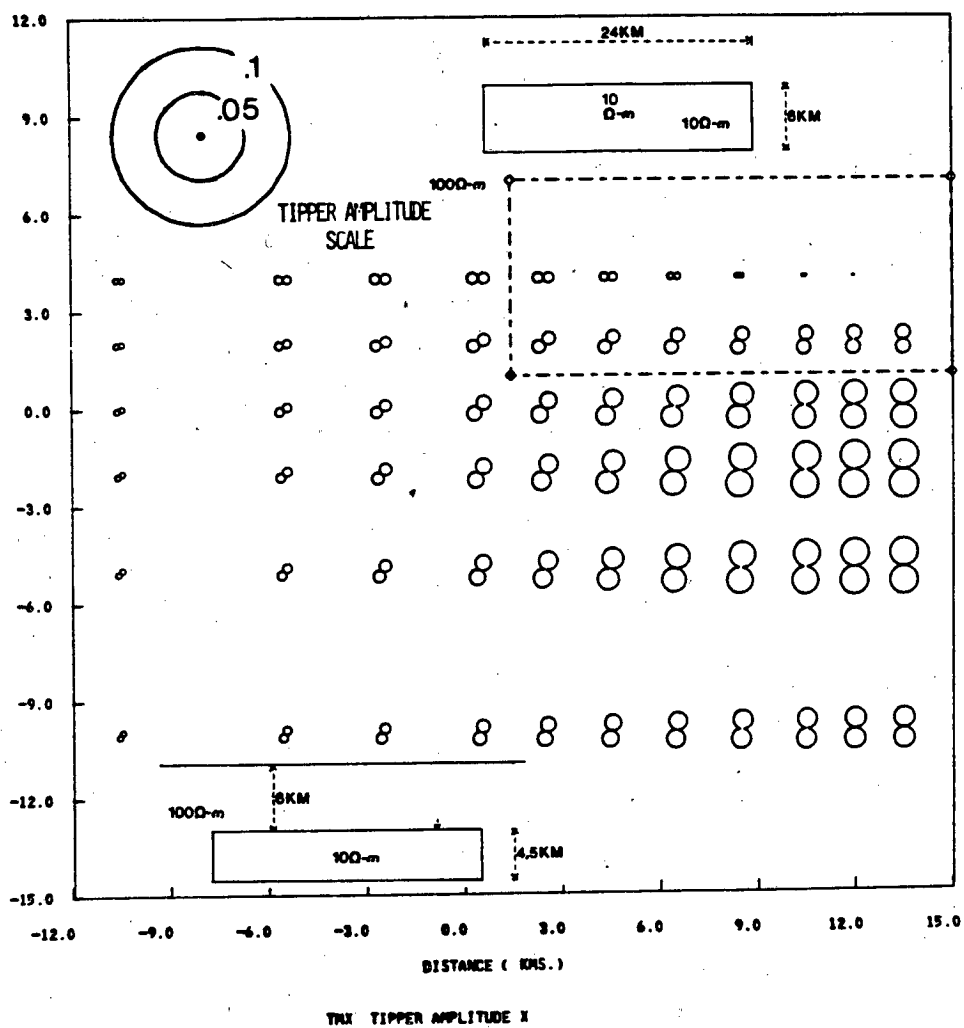
AVERAGED FREES. IN RANGE OF .022 HZ.



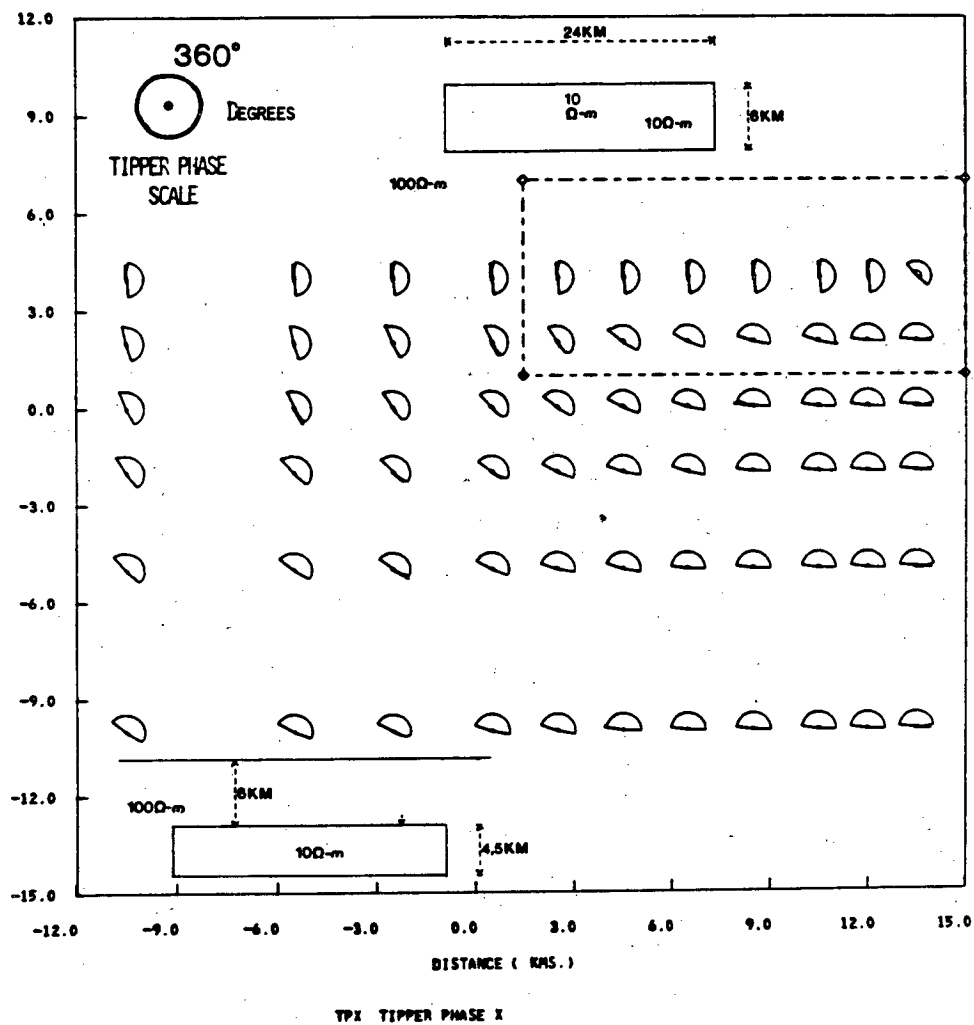
AVERAGED FREQS. IN RANGE OF .022 HZ.



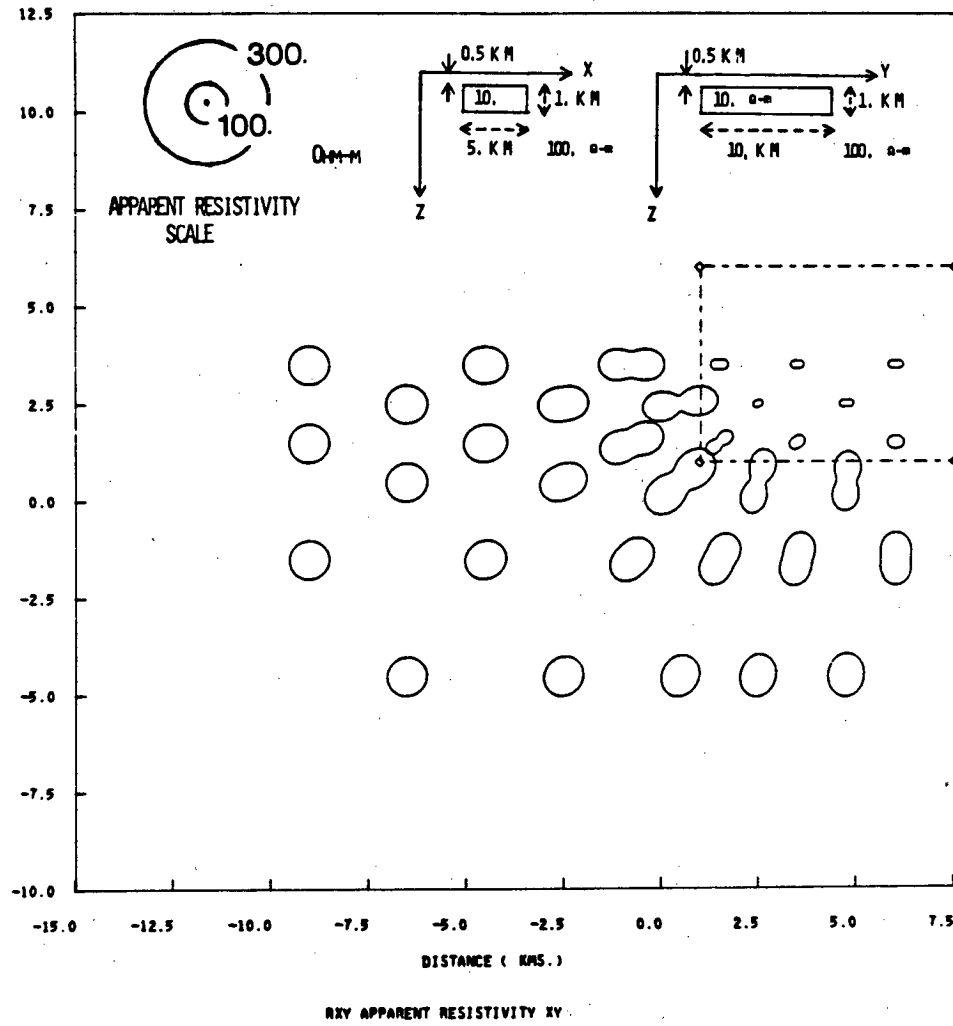
AVERAGED FREQS. IN RANGE OF .022 HZ



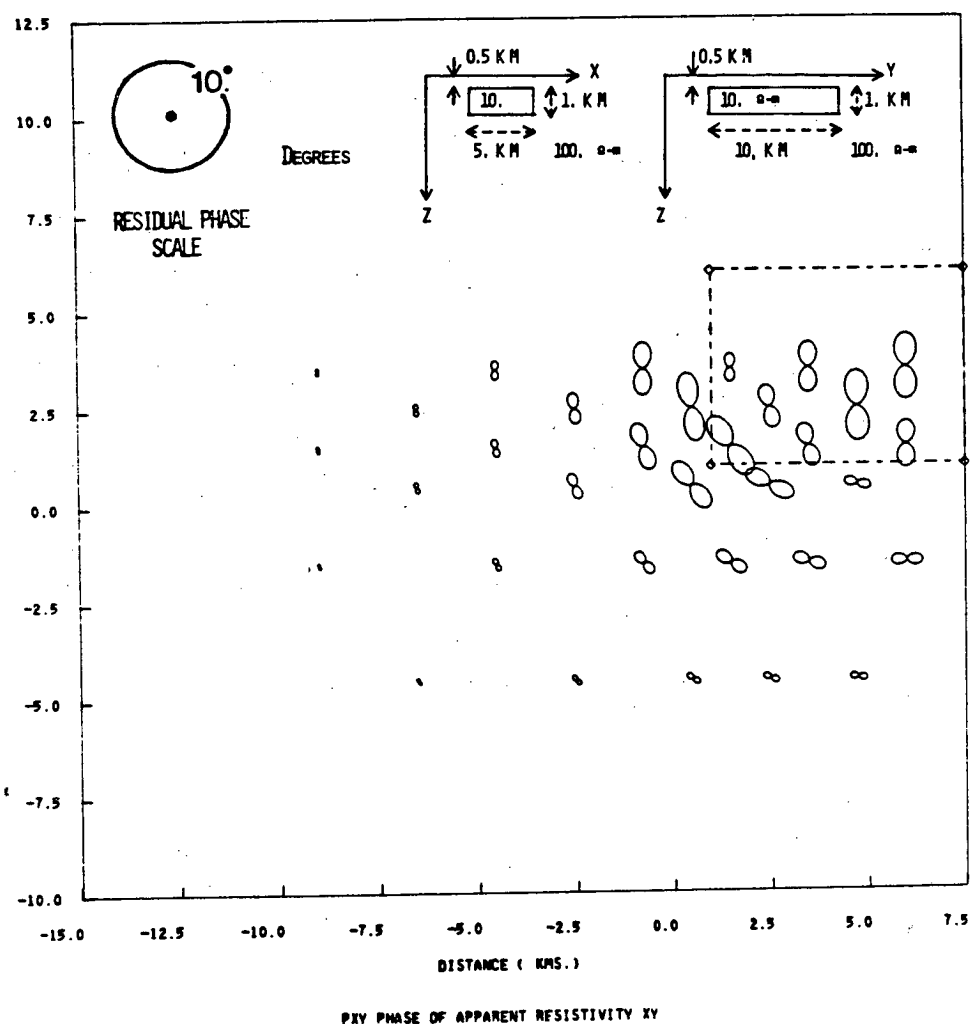
AVERAGED FREQS. IN RANGE OF .022 HZ.



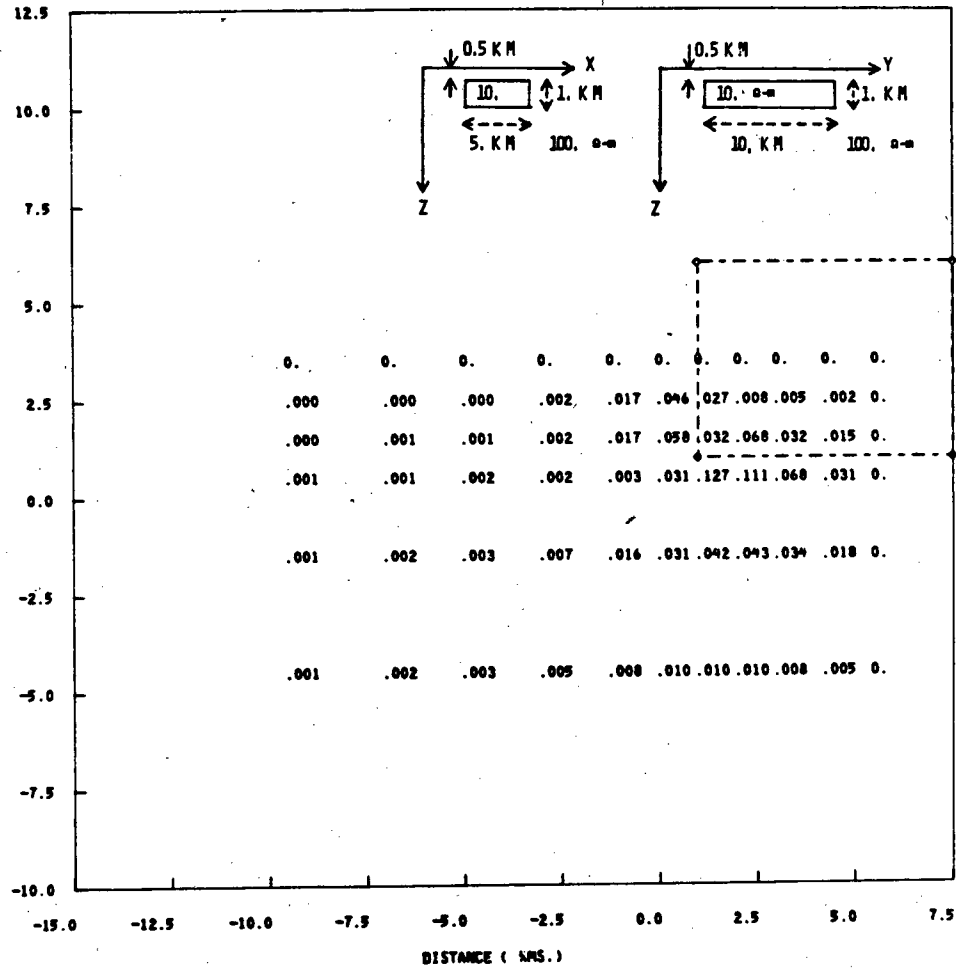
AVERAGED FREQS. IN RANGE OF 0.1 HZ.



AVERAGED FREQS. IN RANGE OF 0.1 HZ.

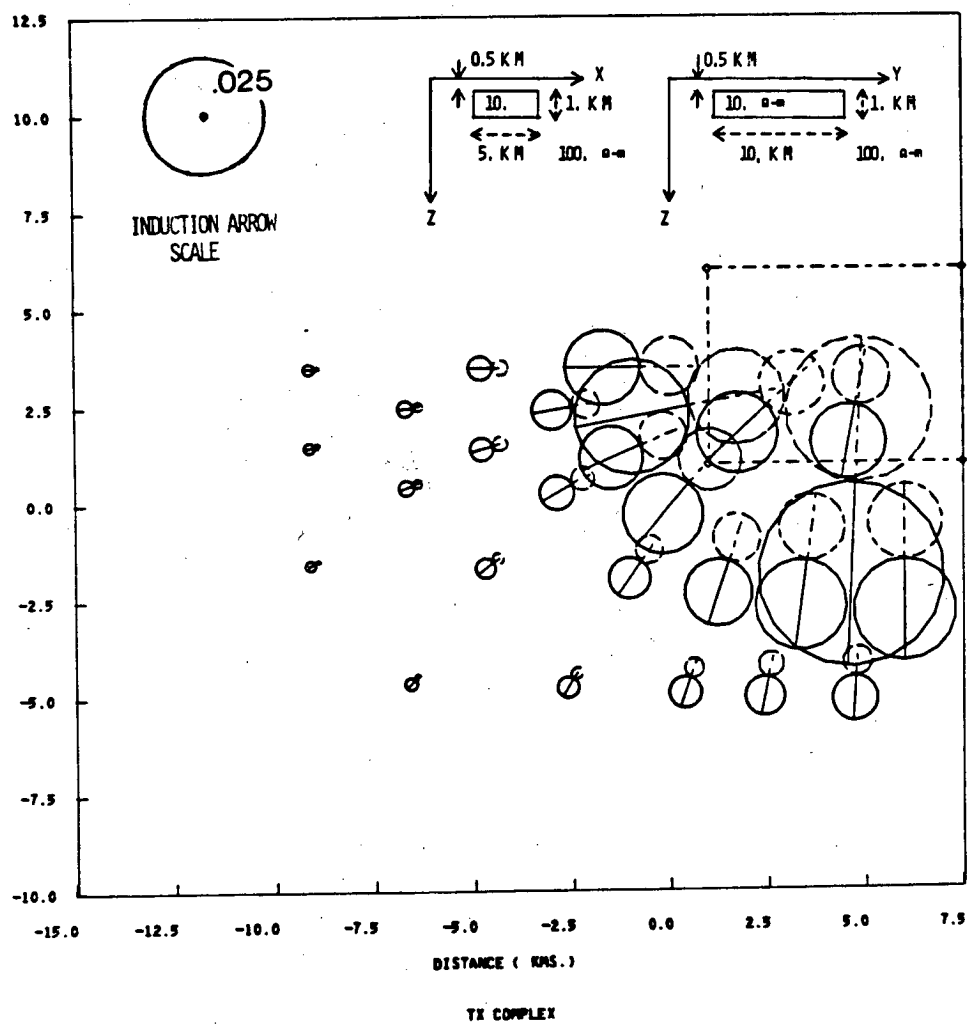


AVERAGED FREQS. IN RANGE OF 0.1 HZ.

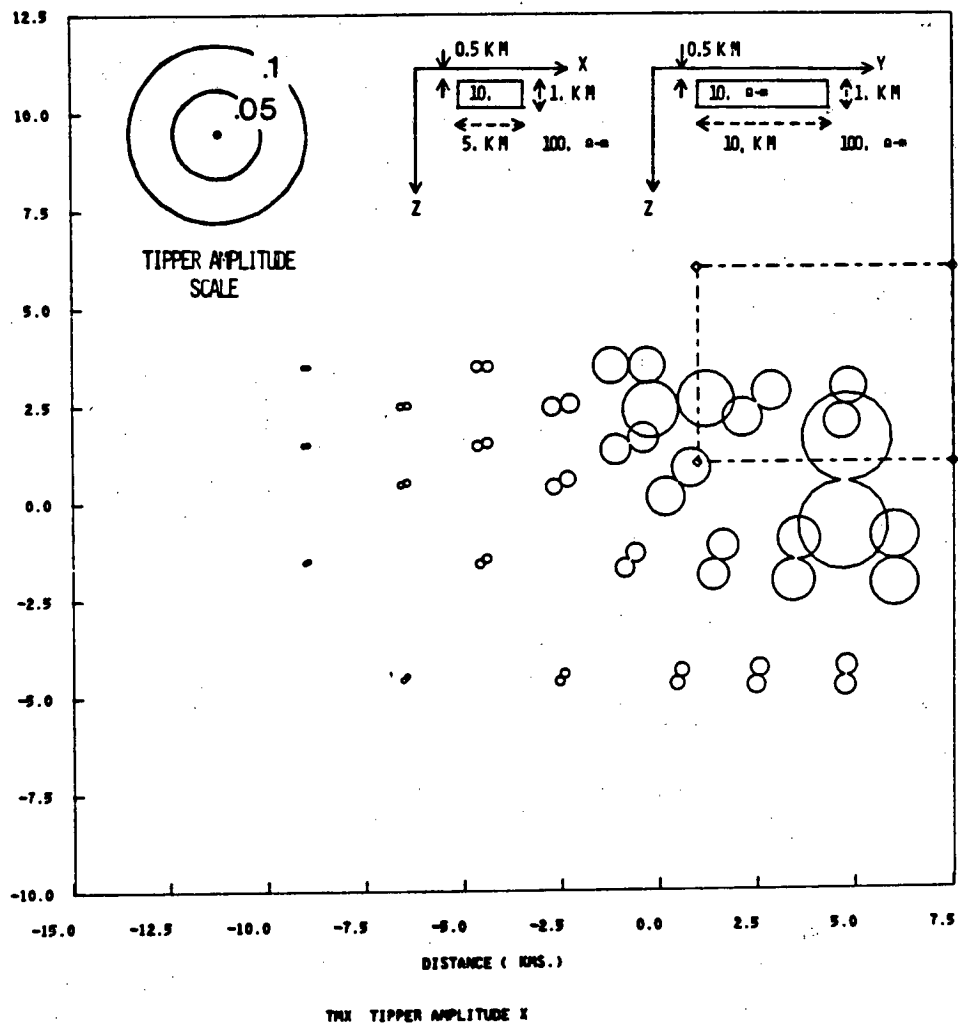


$$SKEW = ABS((ZXI + ZYI) / (ZXY - ZYX))$$

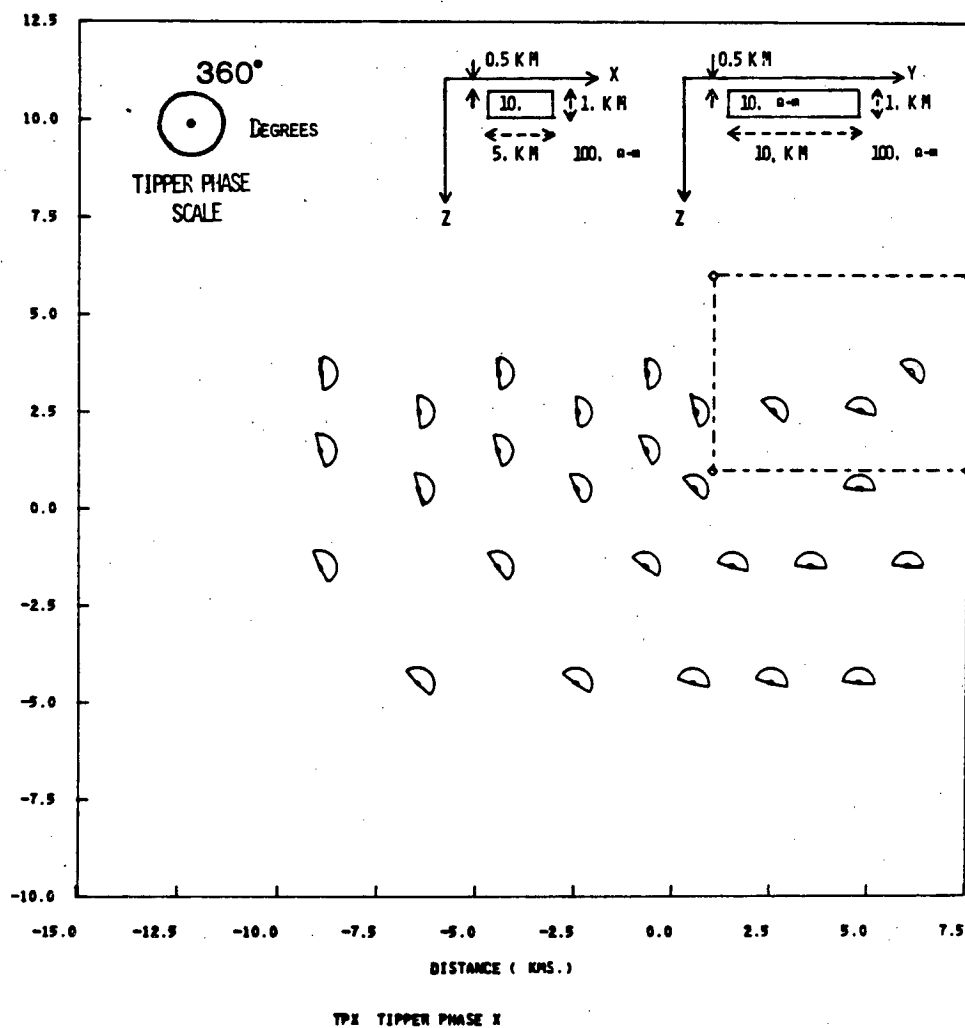
AVERAGED FREES. IN RANGE OF 0.1 HZ.



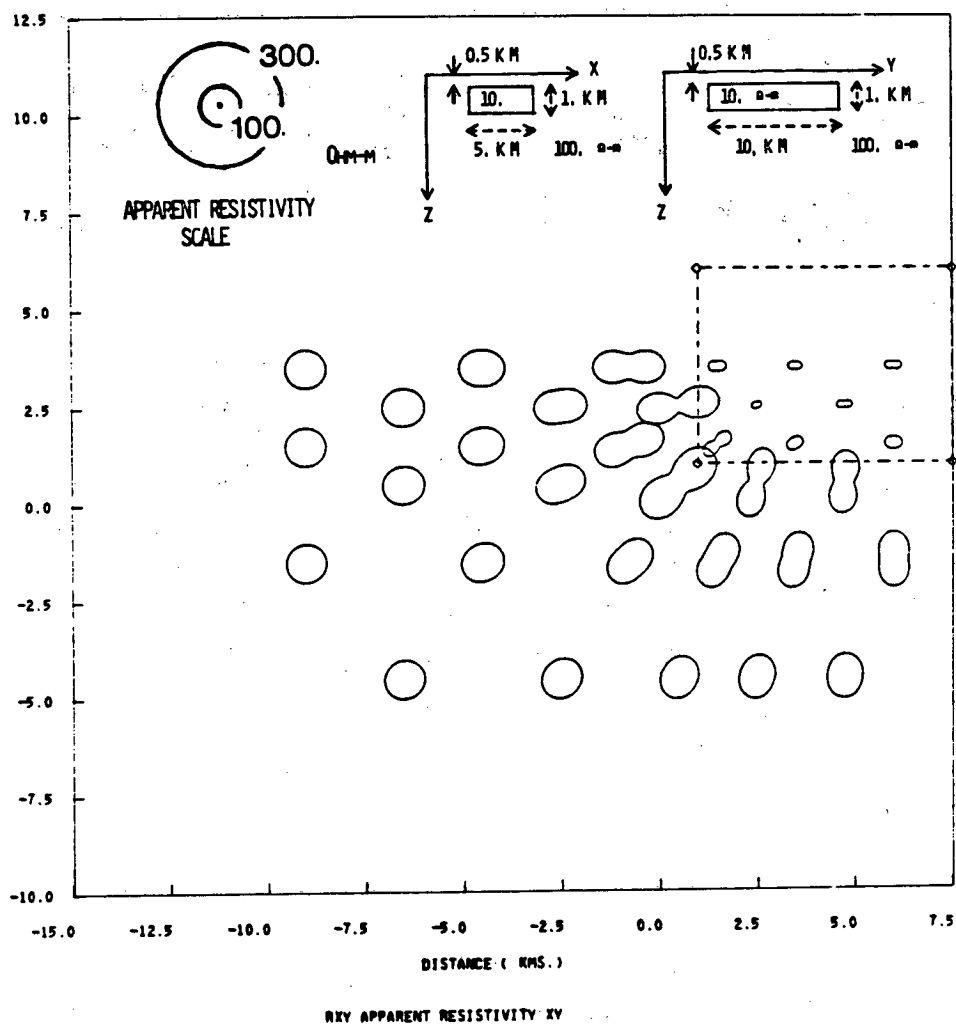
AVERAGED FREQS. IN RANGE OF 0.1 HZ.



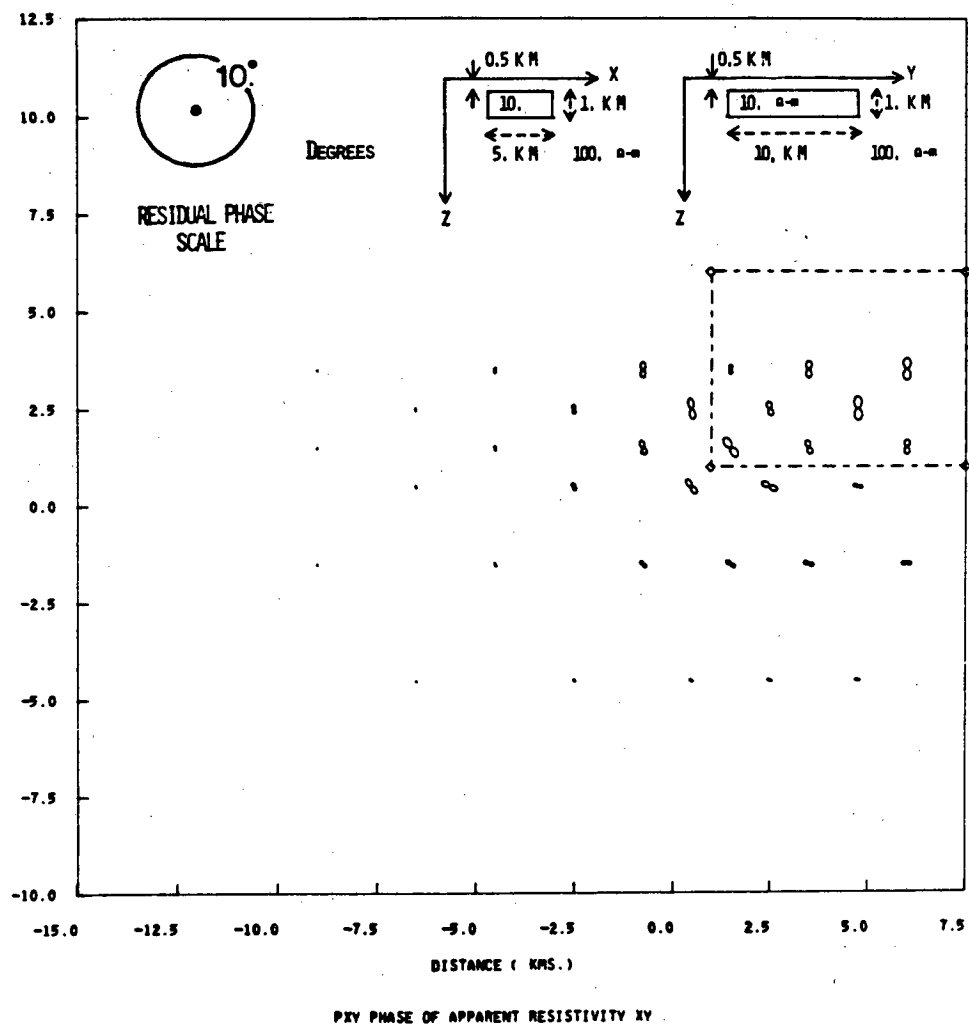
AVERAGED FREQS. IN RANGE OF 0.1 HZ.



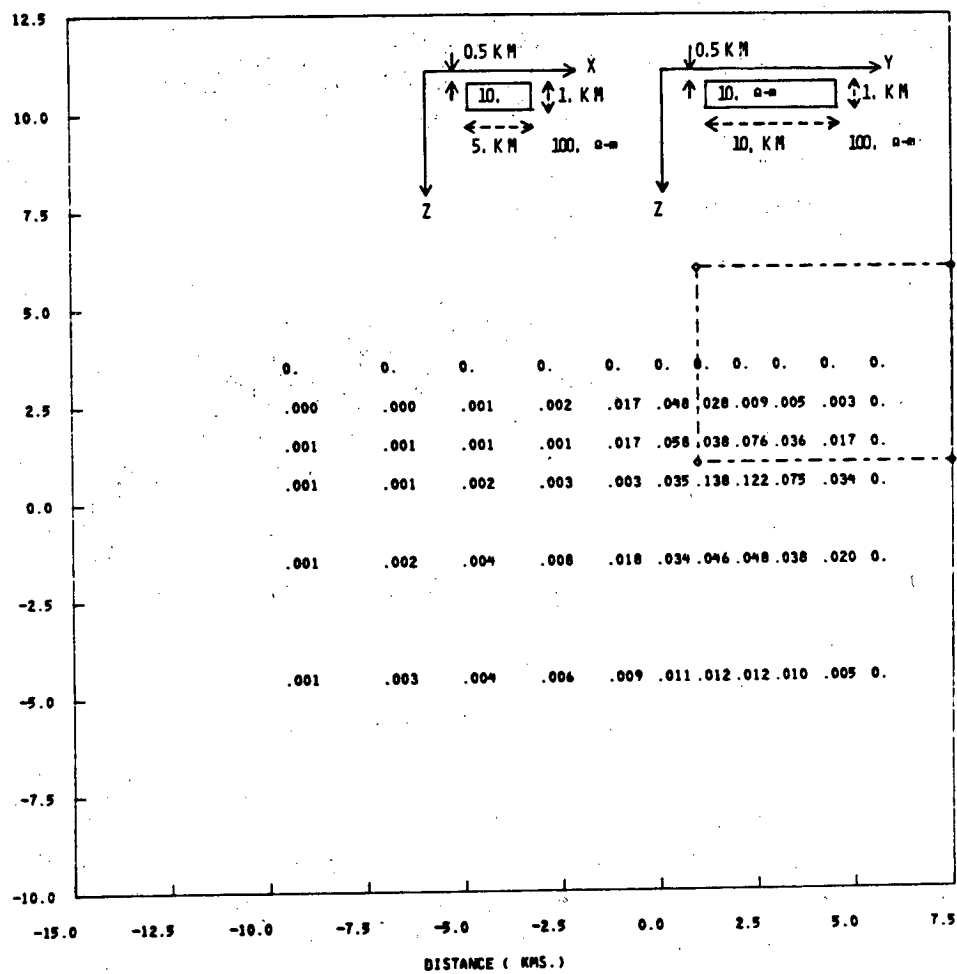
AVERAGED FREQS. IN RANGE OF 0.01 MZ.



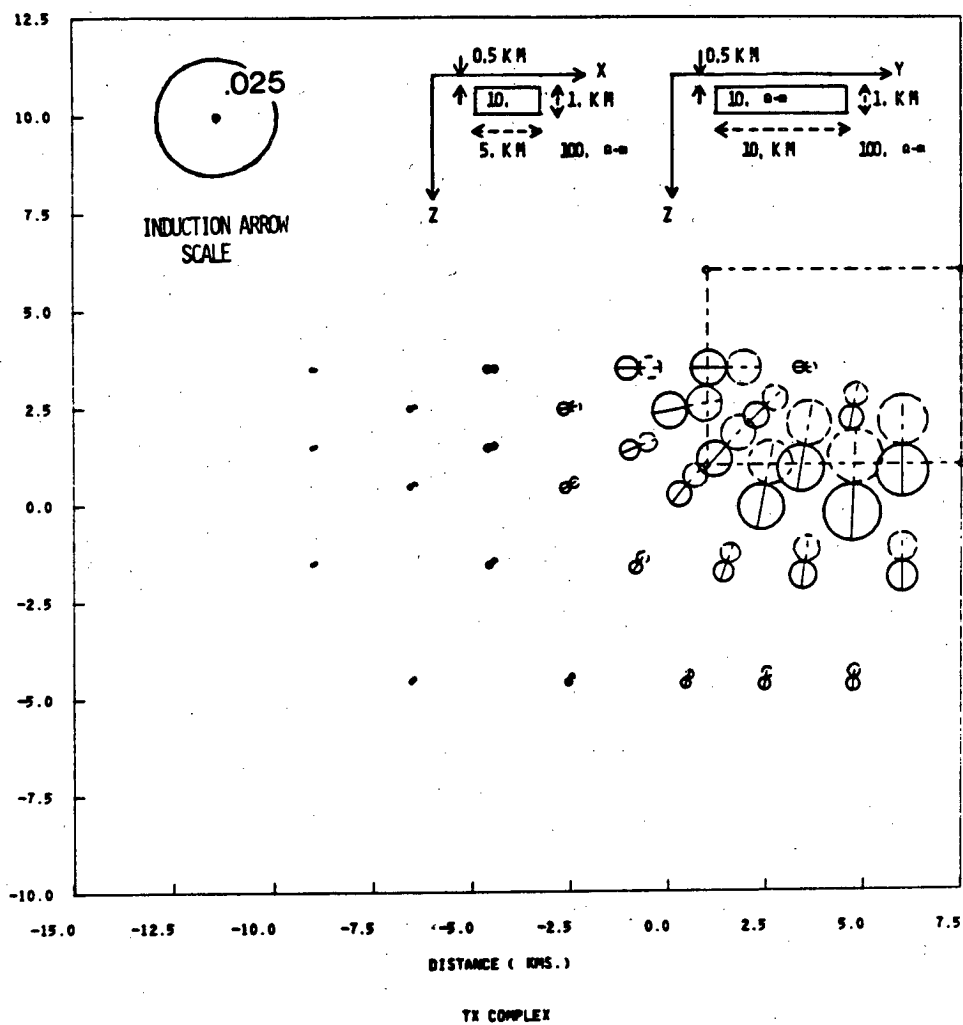
AVERAGED FREQS. IN RANGE OF 0.01 HZ.



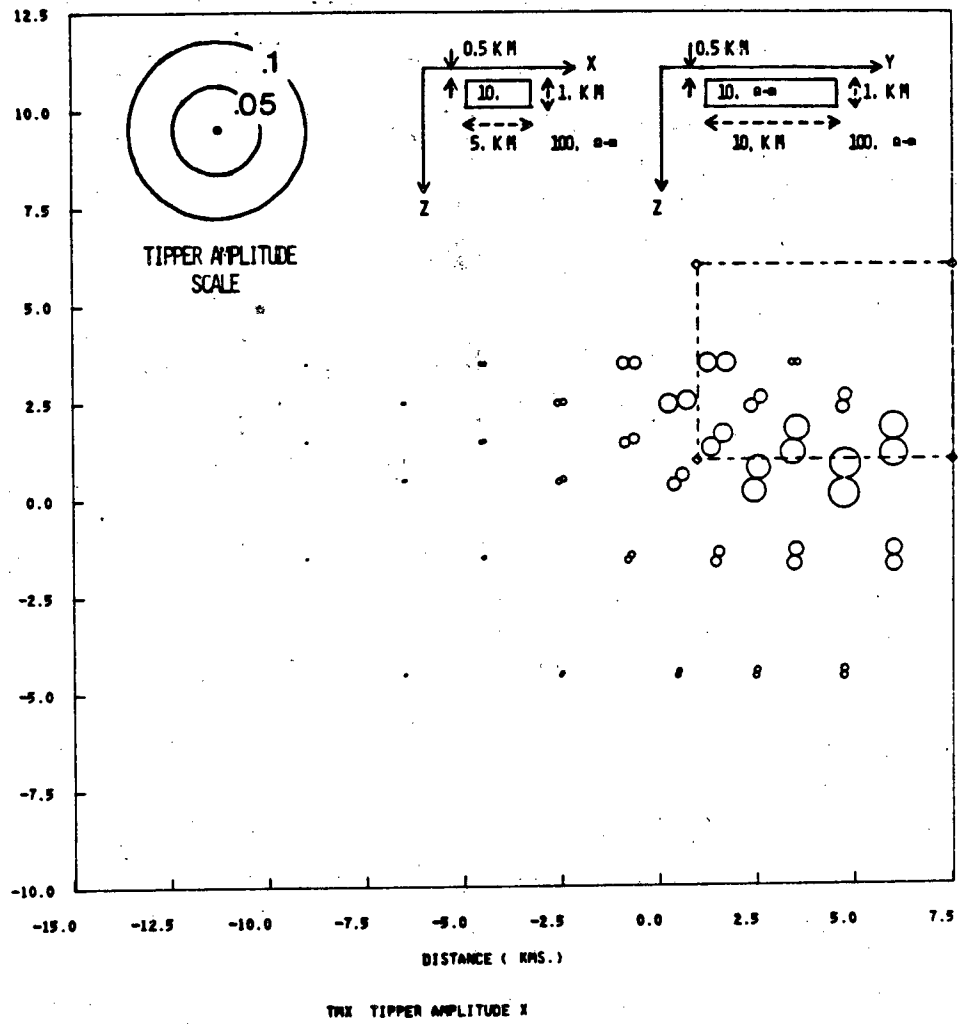
AVERAGED FREQS. IN RANGE OF 0.01 HZ.



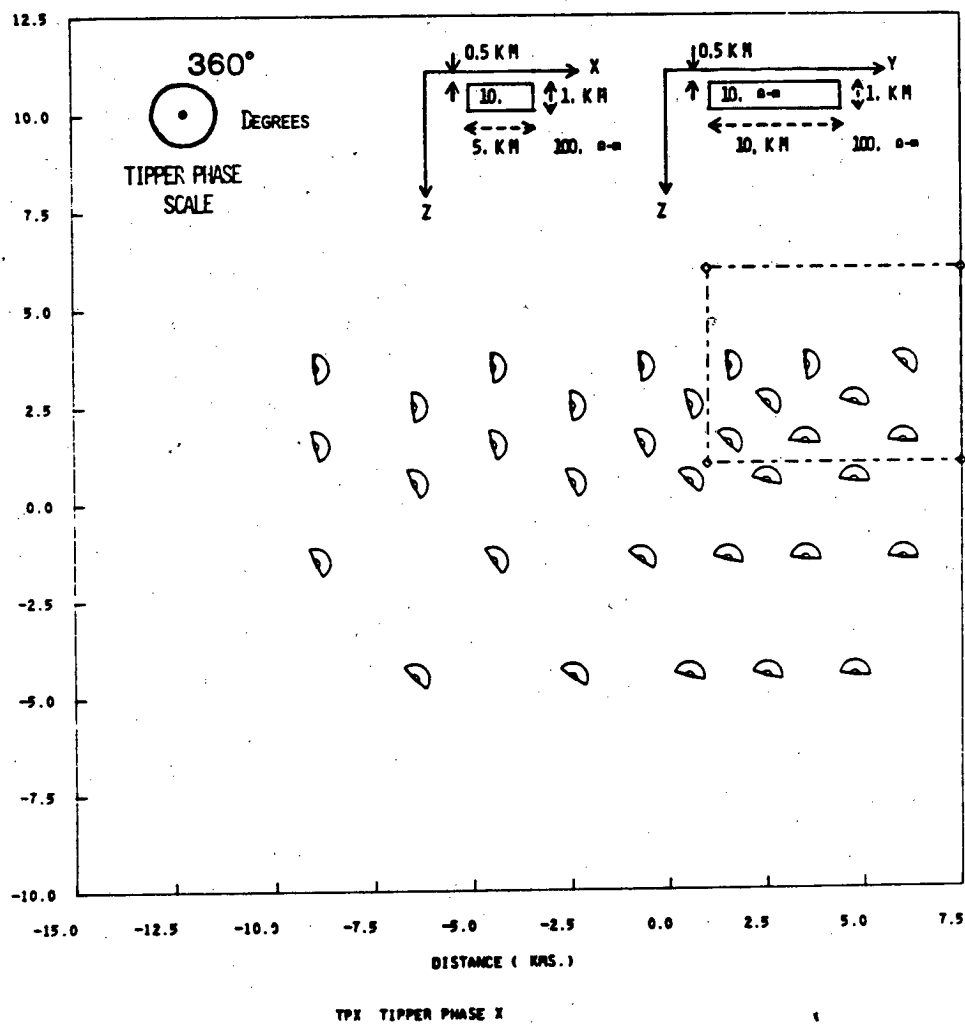
AVERAGED FREQS. IN RANGE OF 0.01 HZ.



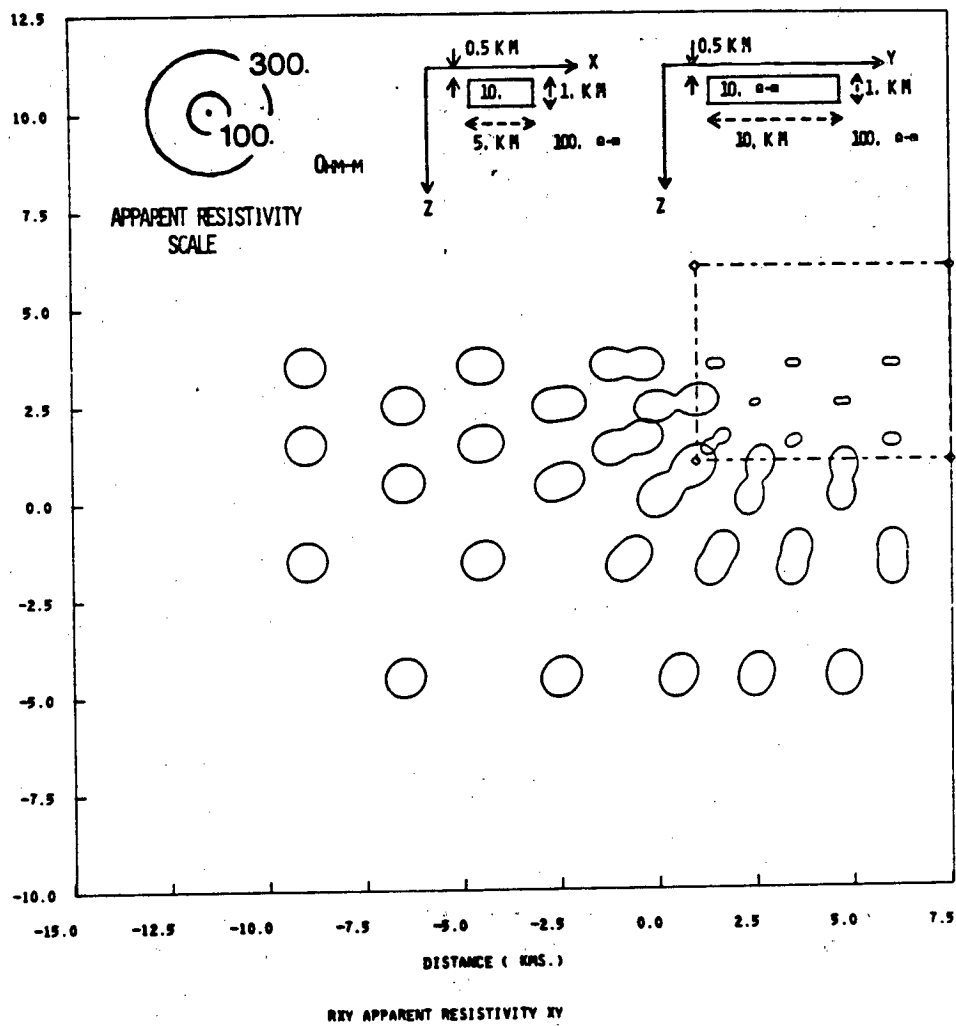
AVERAGED FREQS. IN RANGE OF 0.01 HZ.



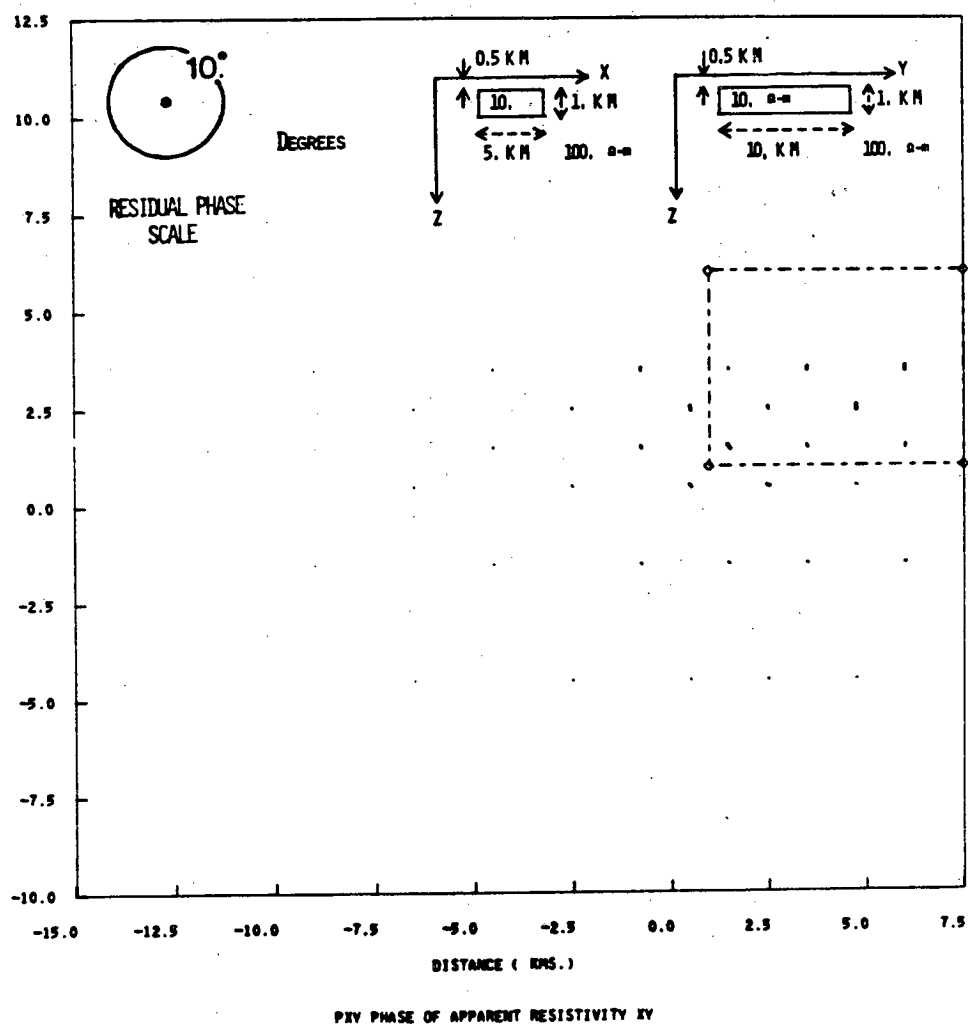
AVERAGED FREQS. IN RANGE OF 9.01 HZ.



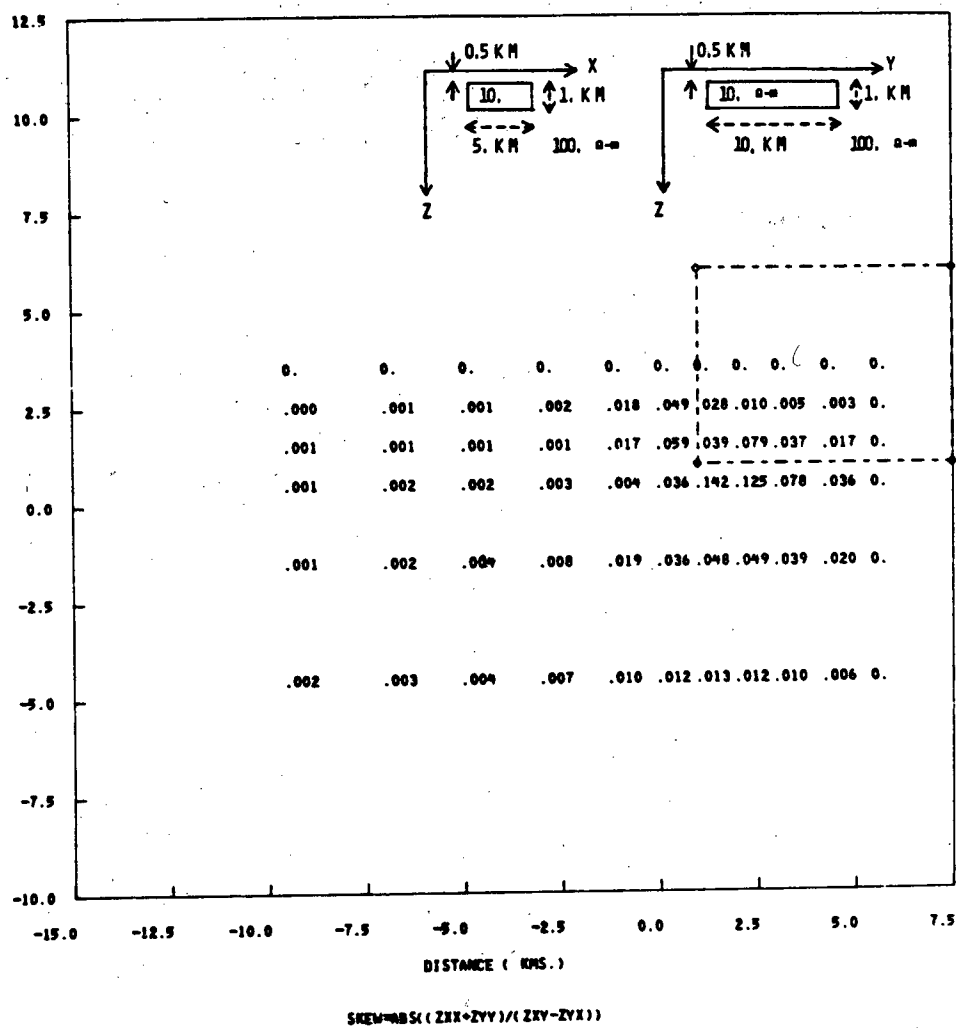
AVERAGED FREQS. IN RANGE OF .001 HZ.



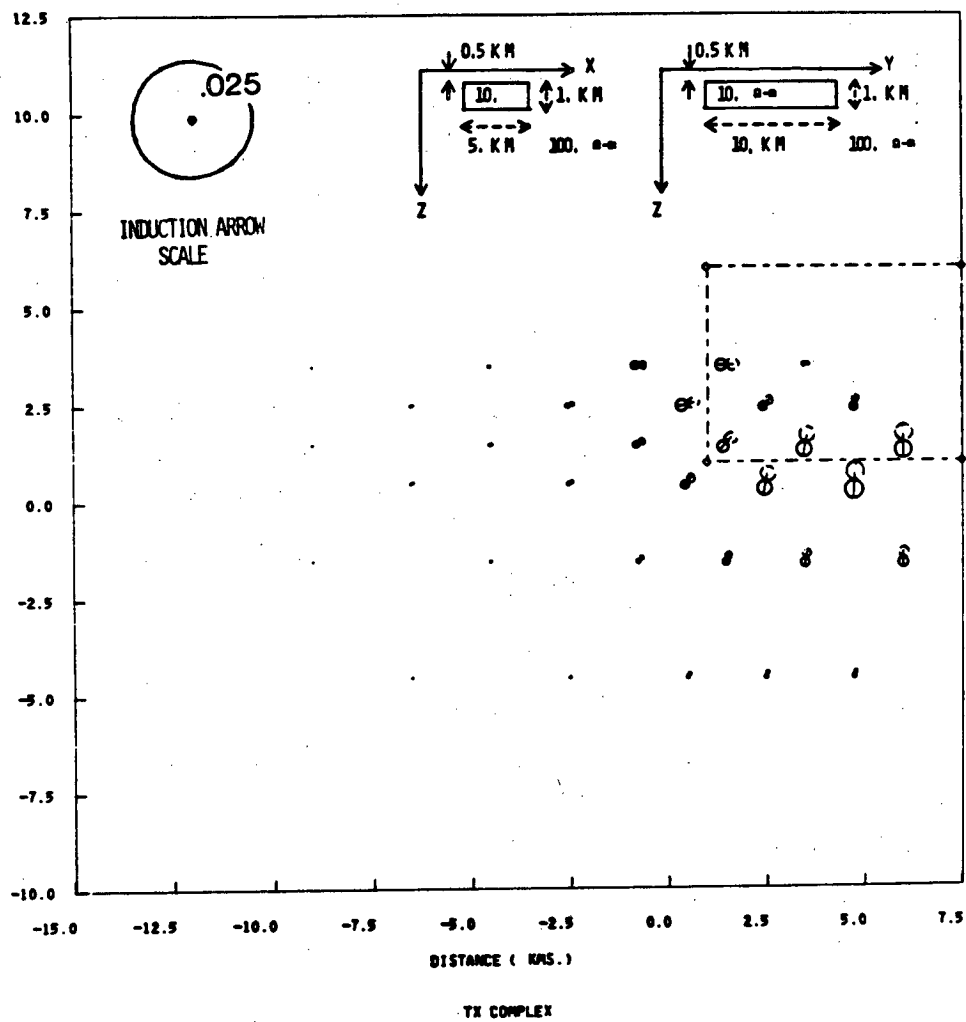
AVERAGED FREQS. IN RANGE OF .001 HZ.



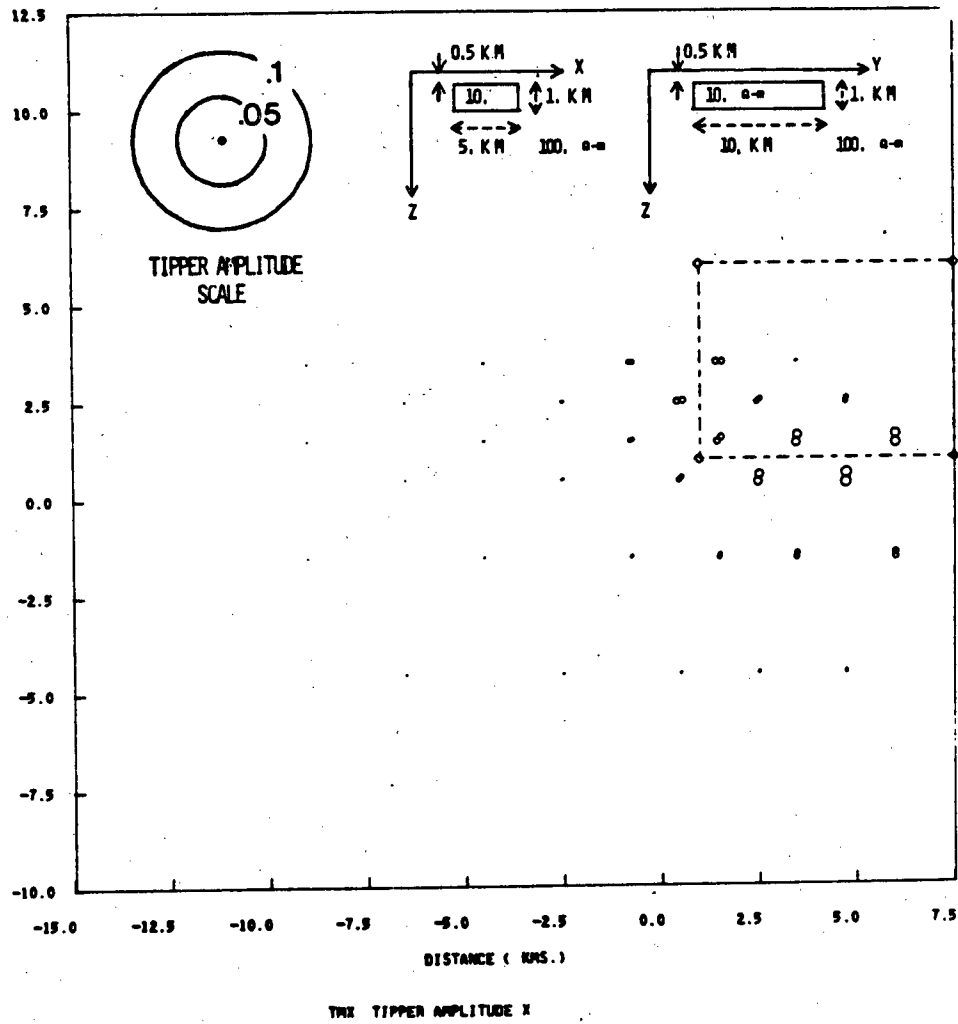
AVERAGED PRESS. IN RANGE OF .001 HZ.



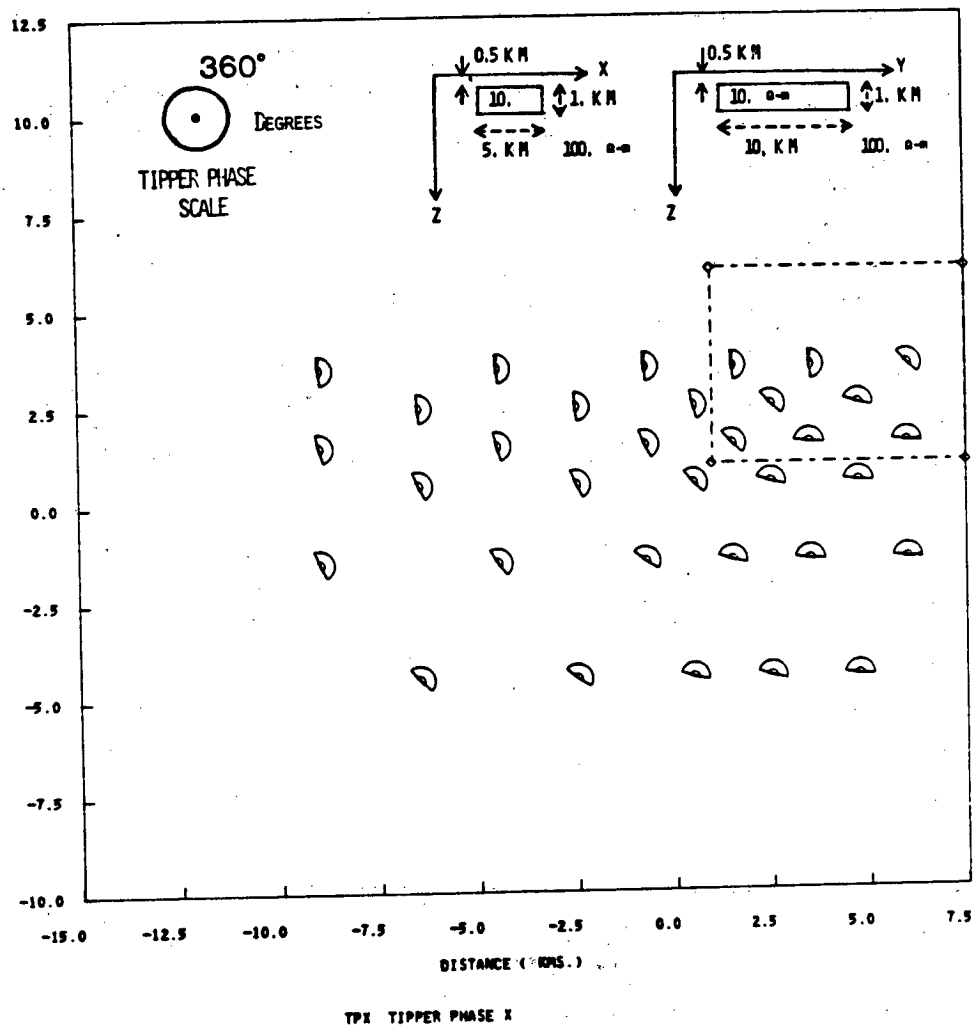
AVERAGED FREQS. IN RANGE OF .001 HZ.



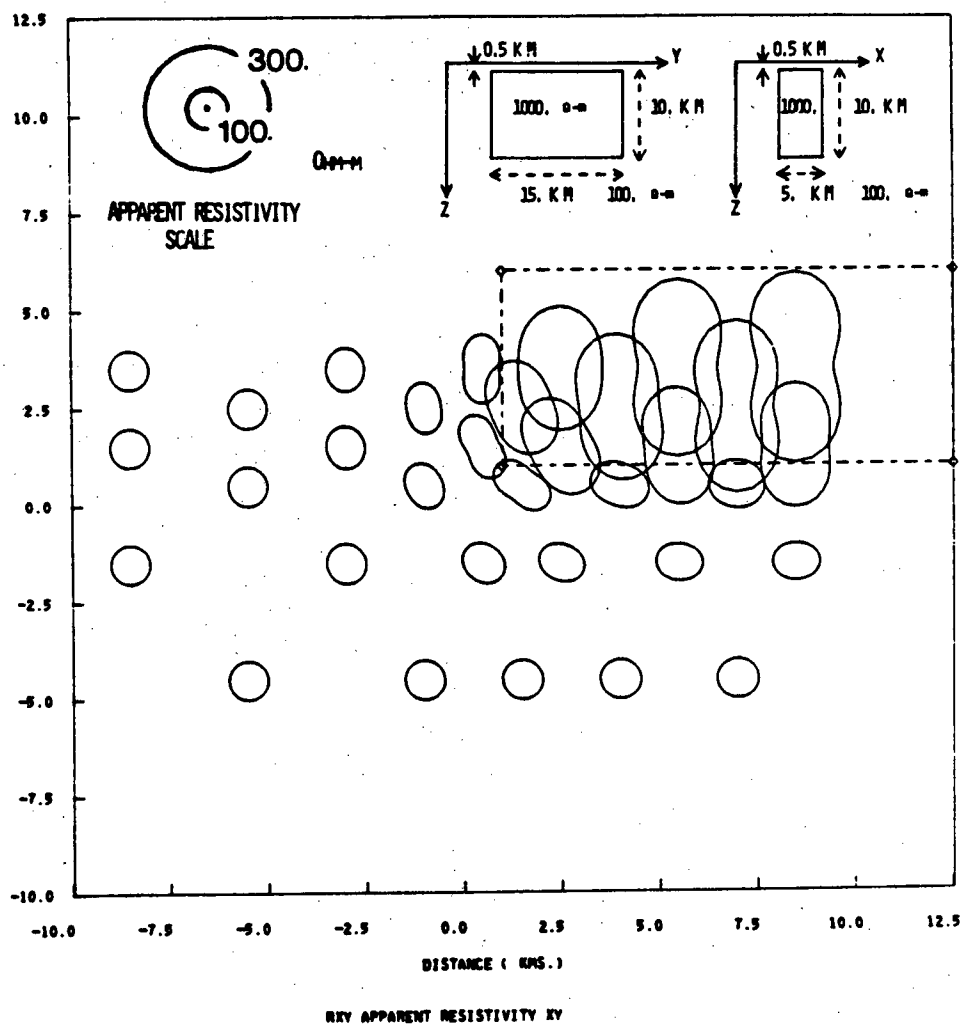
AVERAGED PRESS. IN RANGE OF .001 HZ.



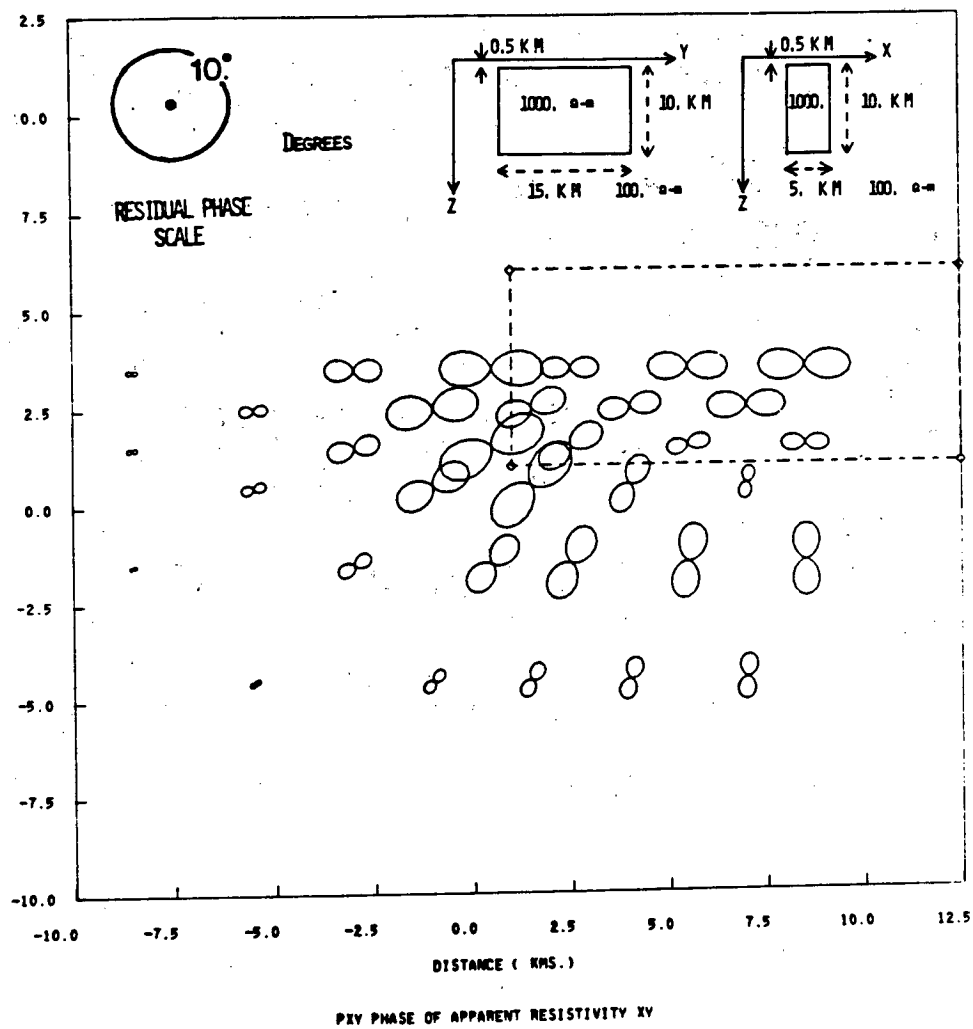
AVERAGED FREQS. IN RANGE OF .001 HZ.



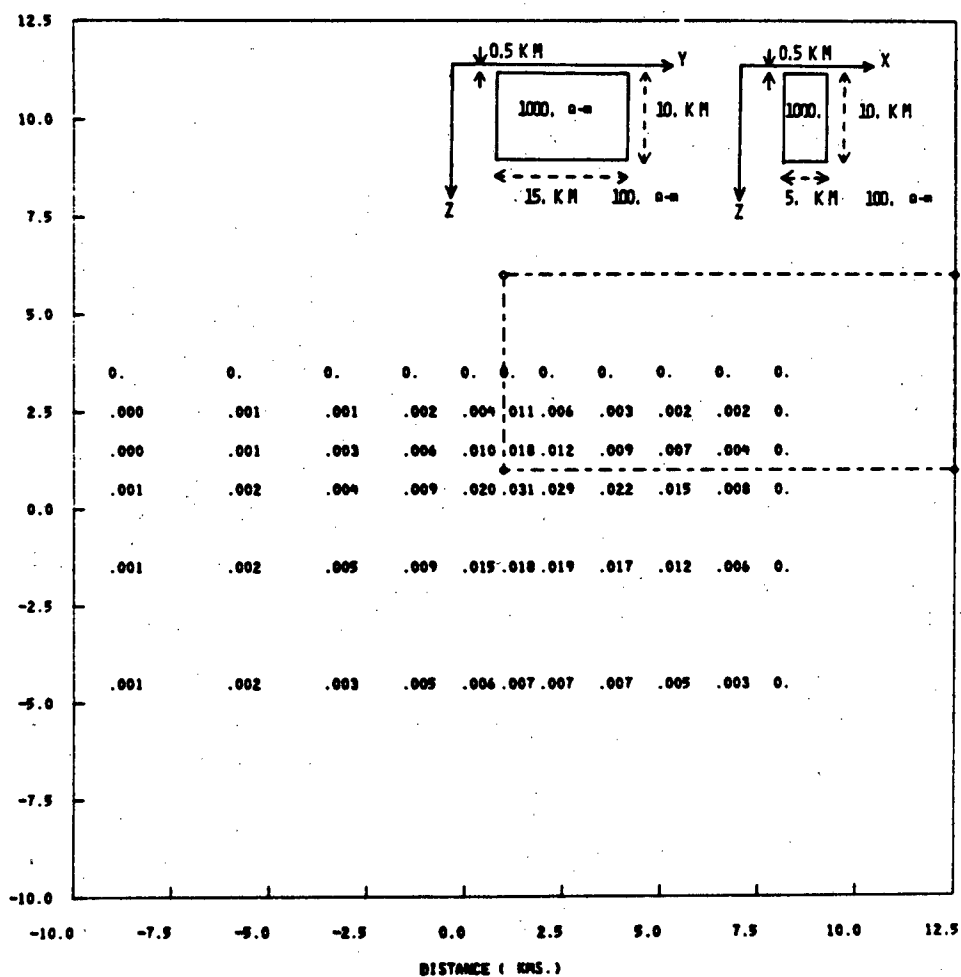
AVERAGED FREQS. IN RANGE OF 1.0 HZ.



AVERAGED FREQS. IN RANGE OF 1.0 HZ.

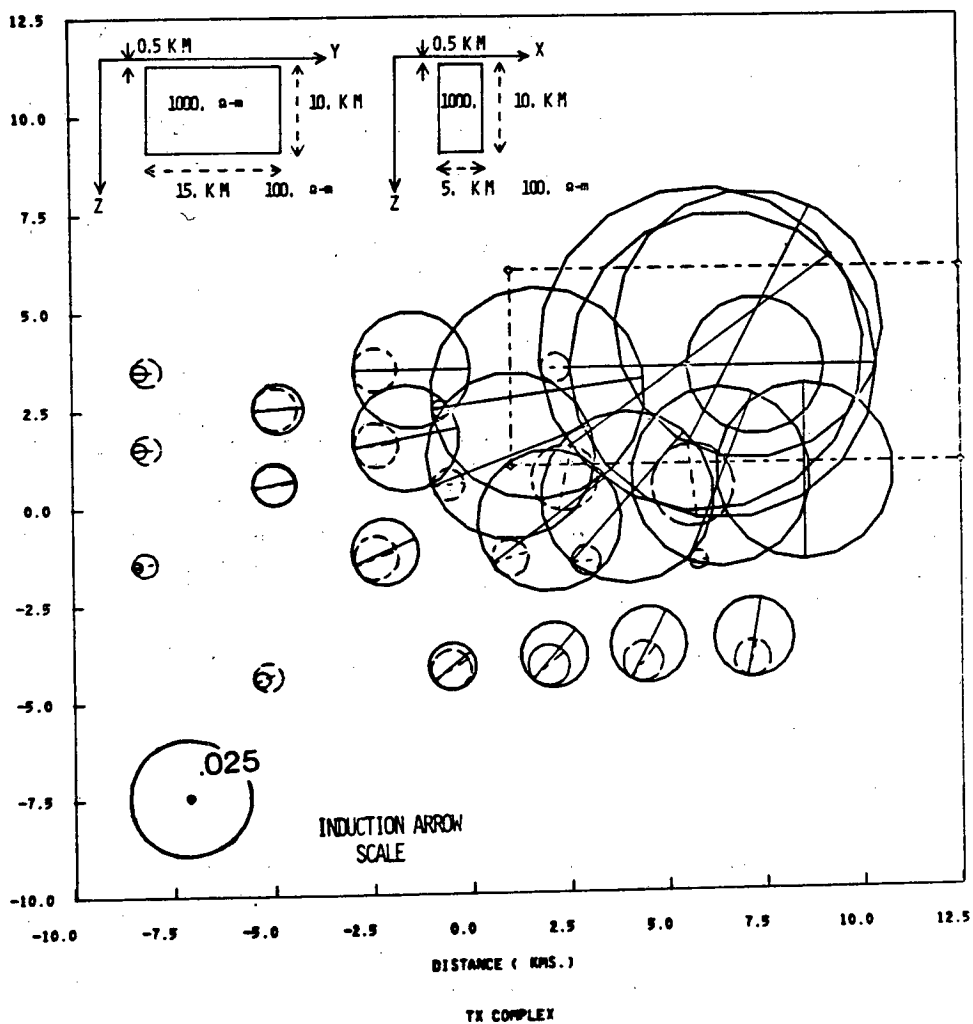


AVERAGED FREQS. IN RANGE OF 1.0 HZ.

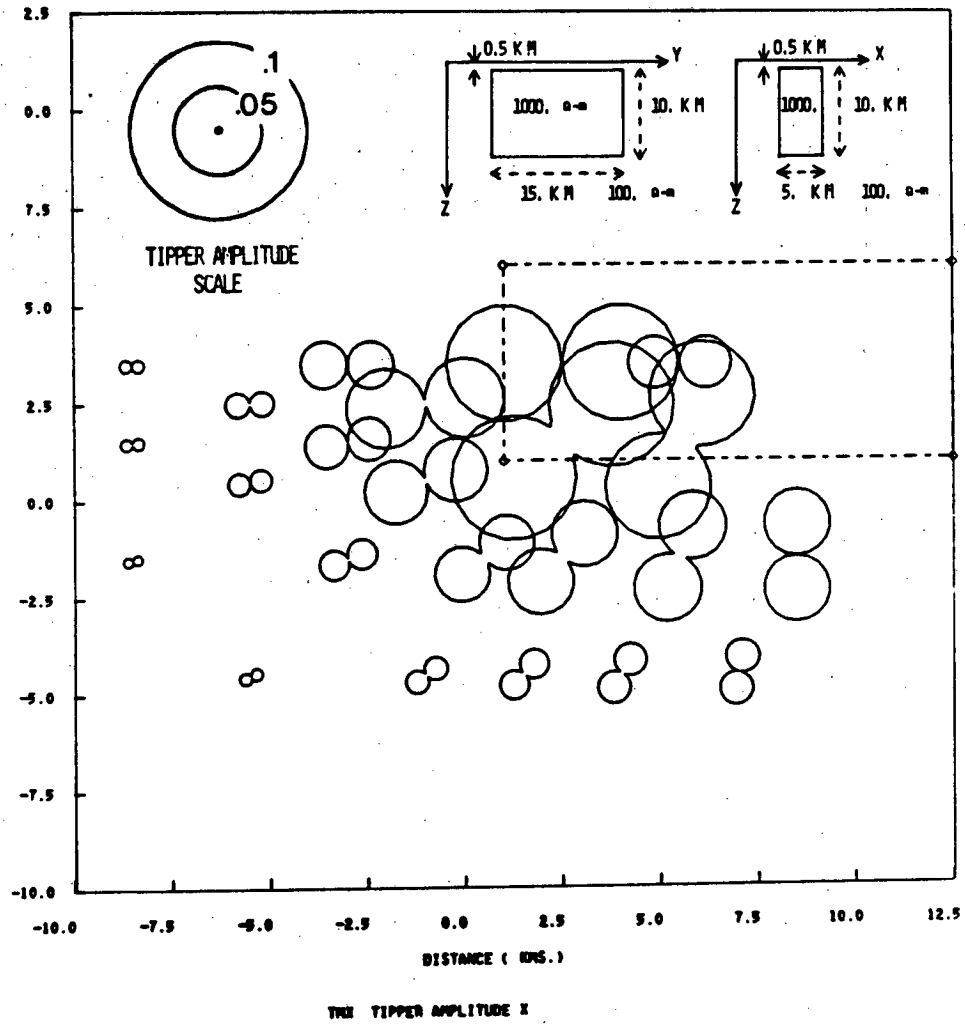


$$SKEW = \frac{ZXX - ZYY}{(ZXX - ZYY)}$$

AVERAGED FREES. IN RANGE OF 1.0 HZ.

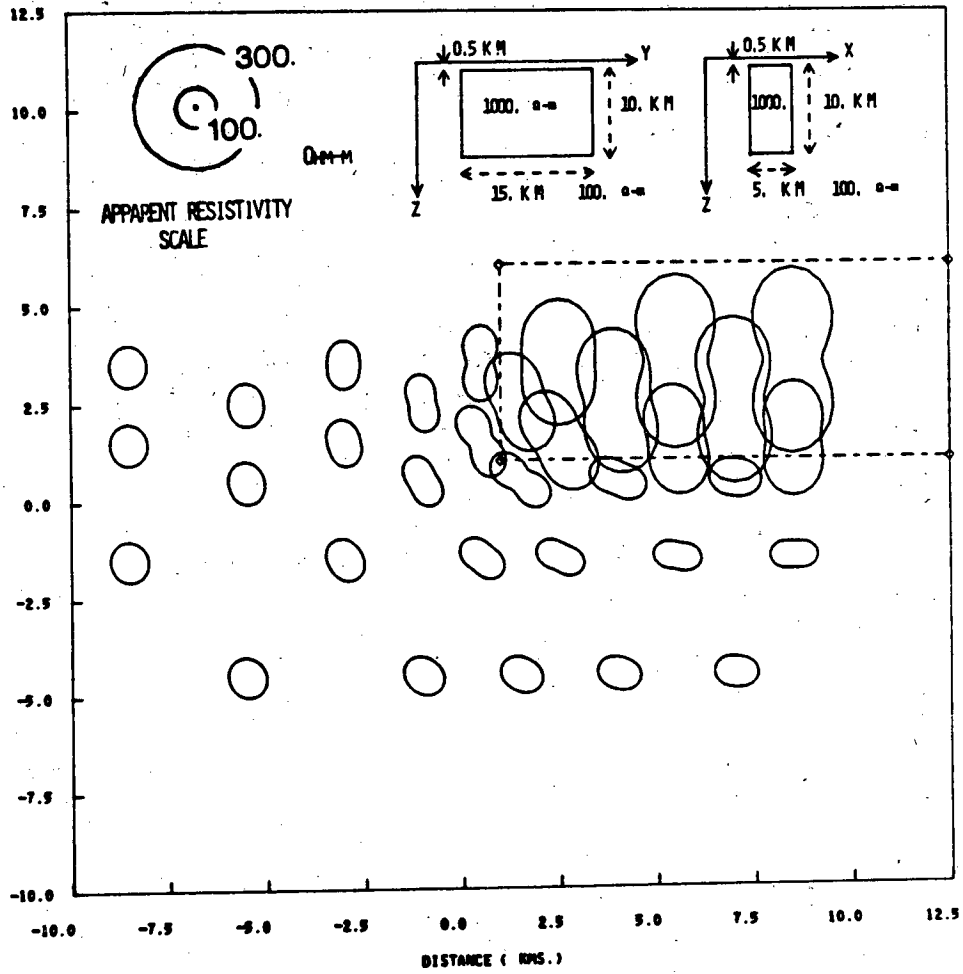


AVERAGED PRESS. IN RANGE OF 1.0 HZ.



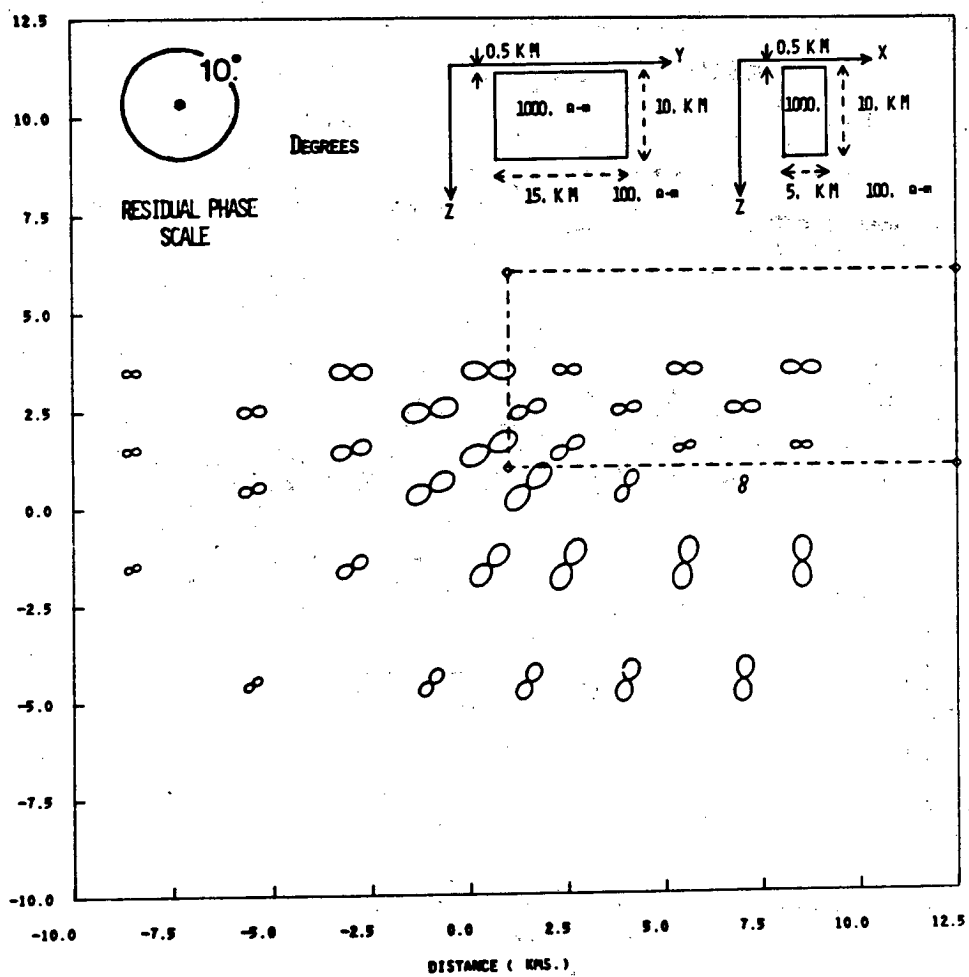


AVERAGED FREES. IN RANGE OF 0.1 HZ.

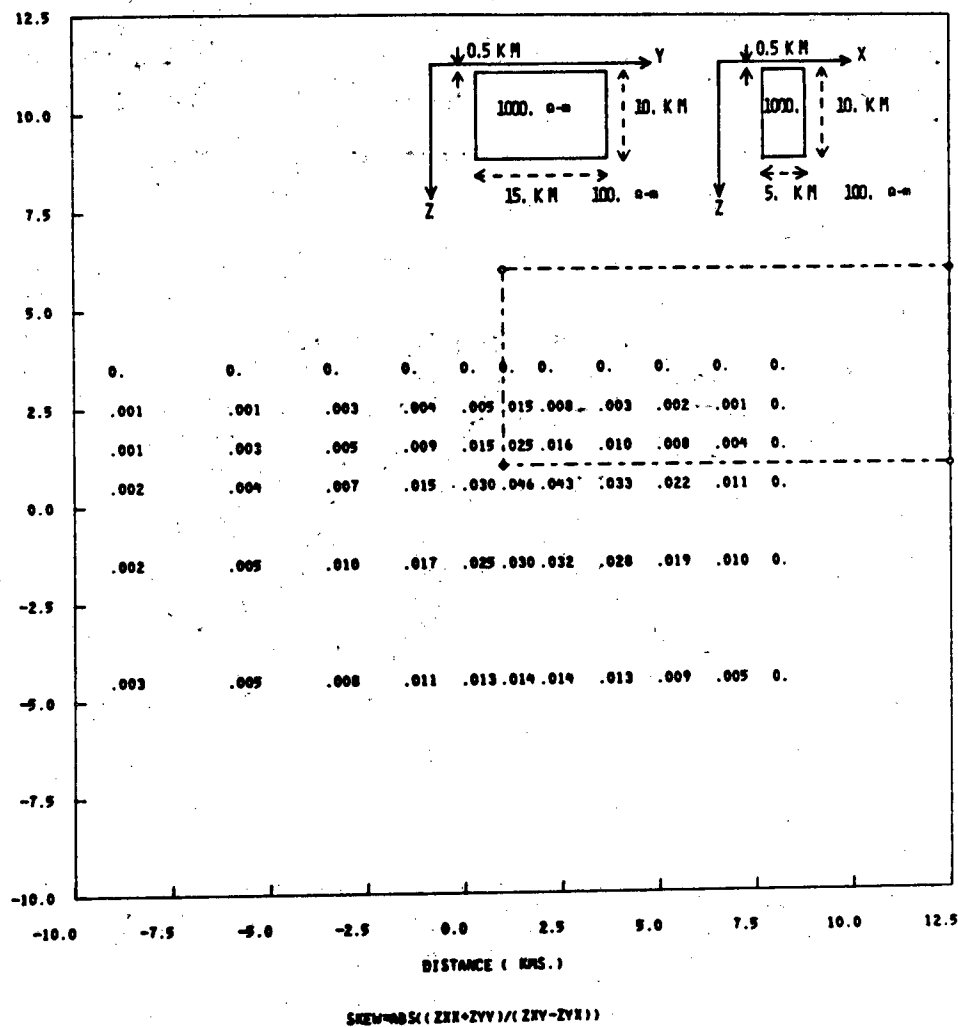


REV APPARENT RESISTIVITY XY

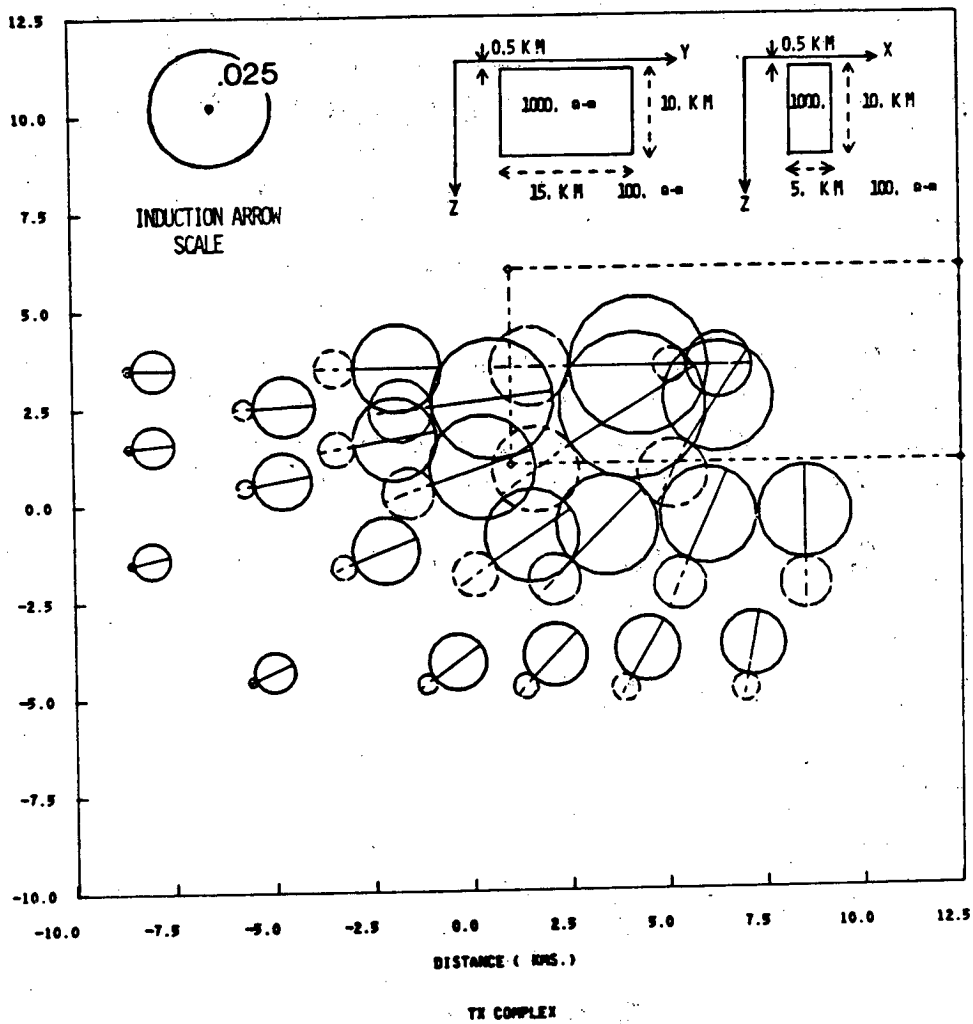
AVERAGED FREQS. IN RANGE OF 0.1 HZ.



AVERAGED FREQS. IN RANGE OF 0.1 HZ.

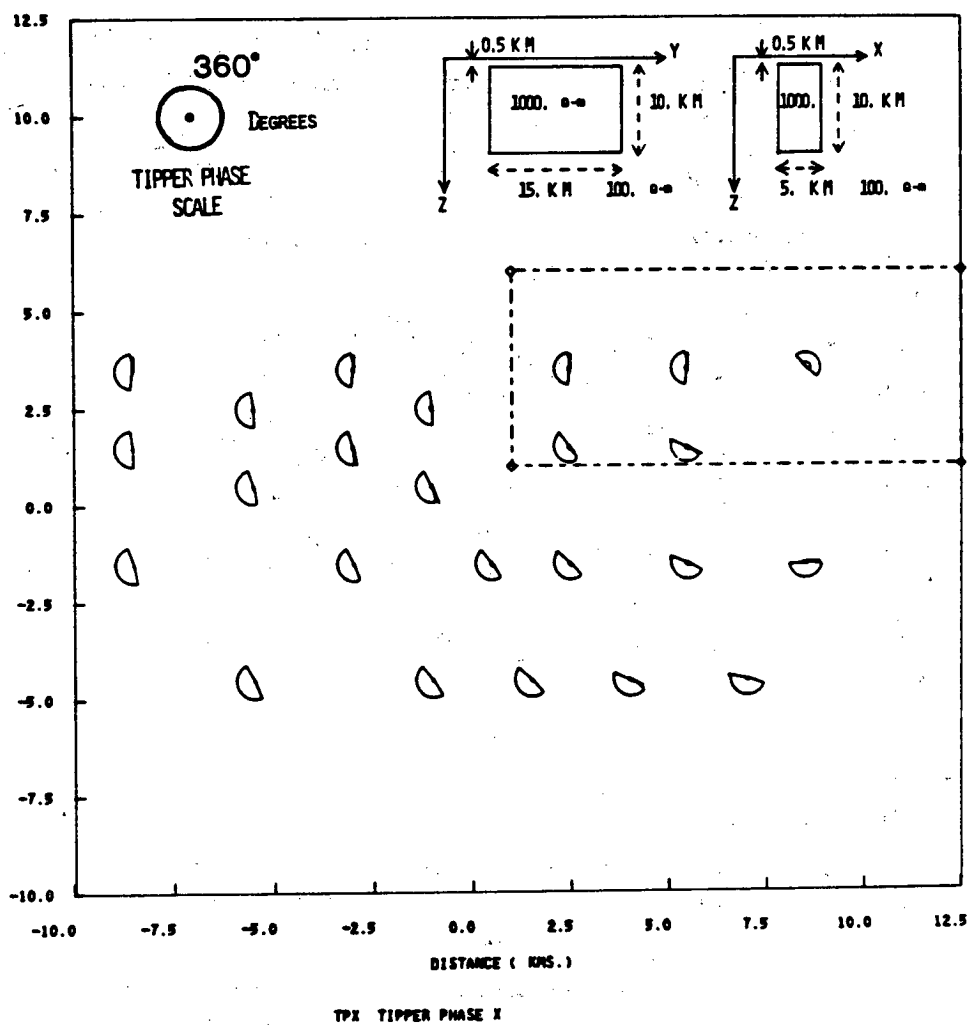


AVERAGED FREQS. IN RANGE OF 0.1 HZ.

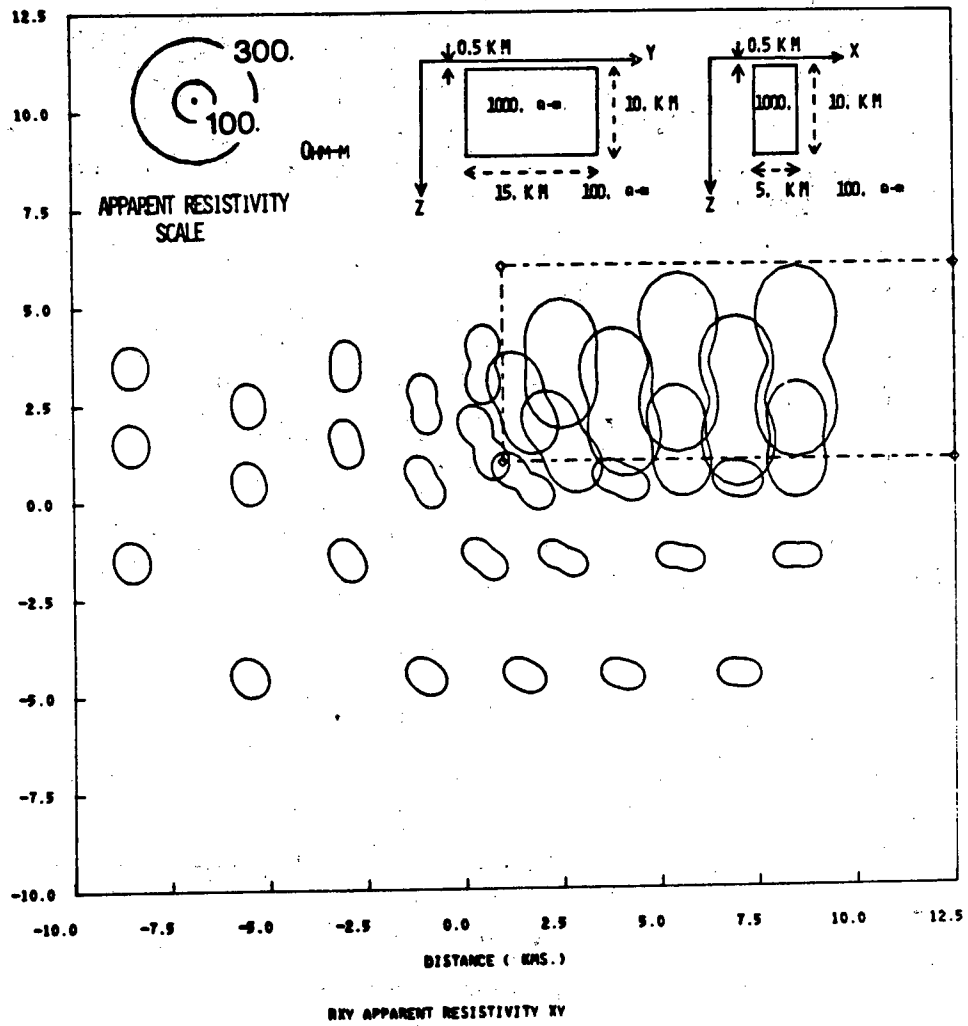




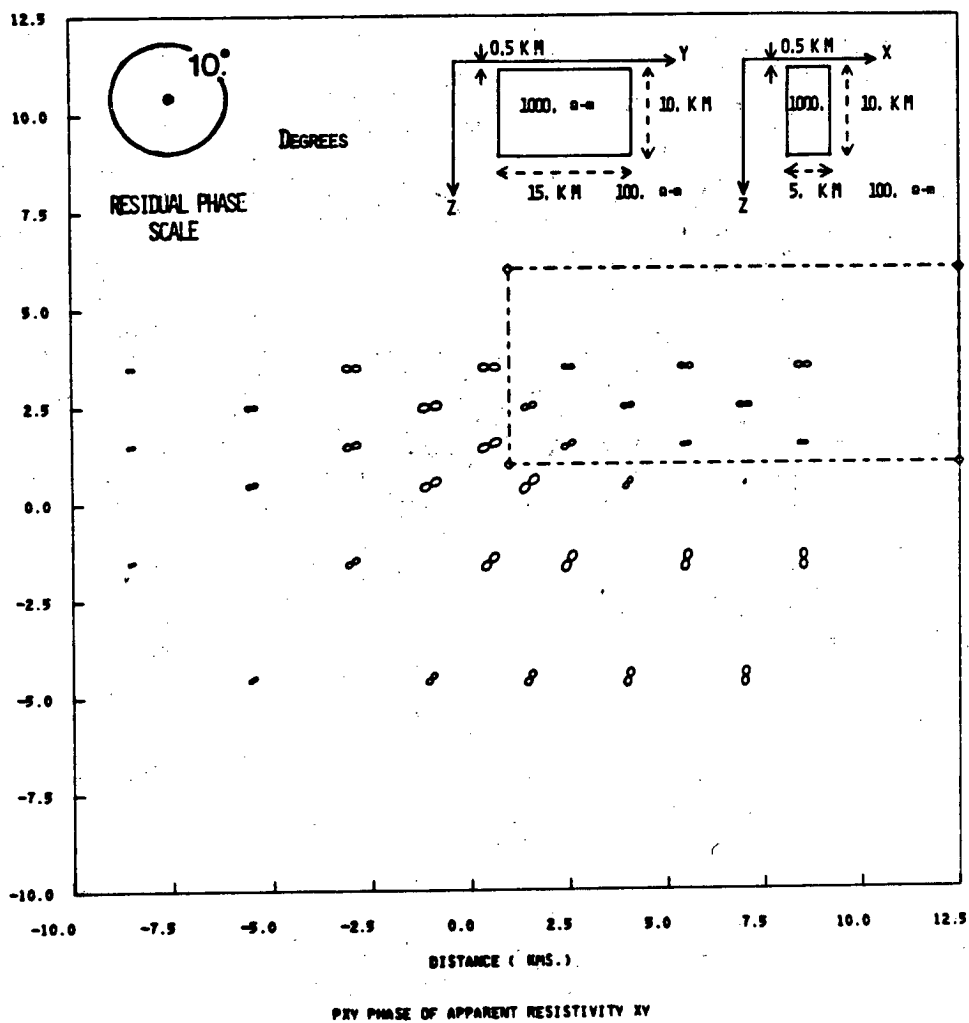
AVERAGED FREQS. IN RANGE OF 0.1 HZ.



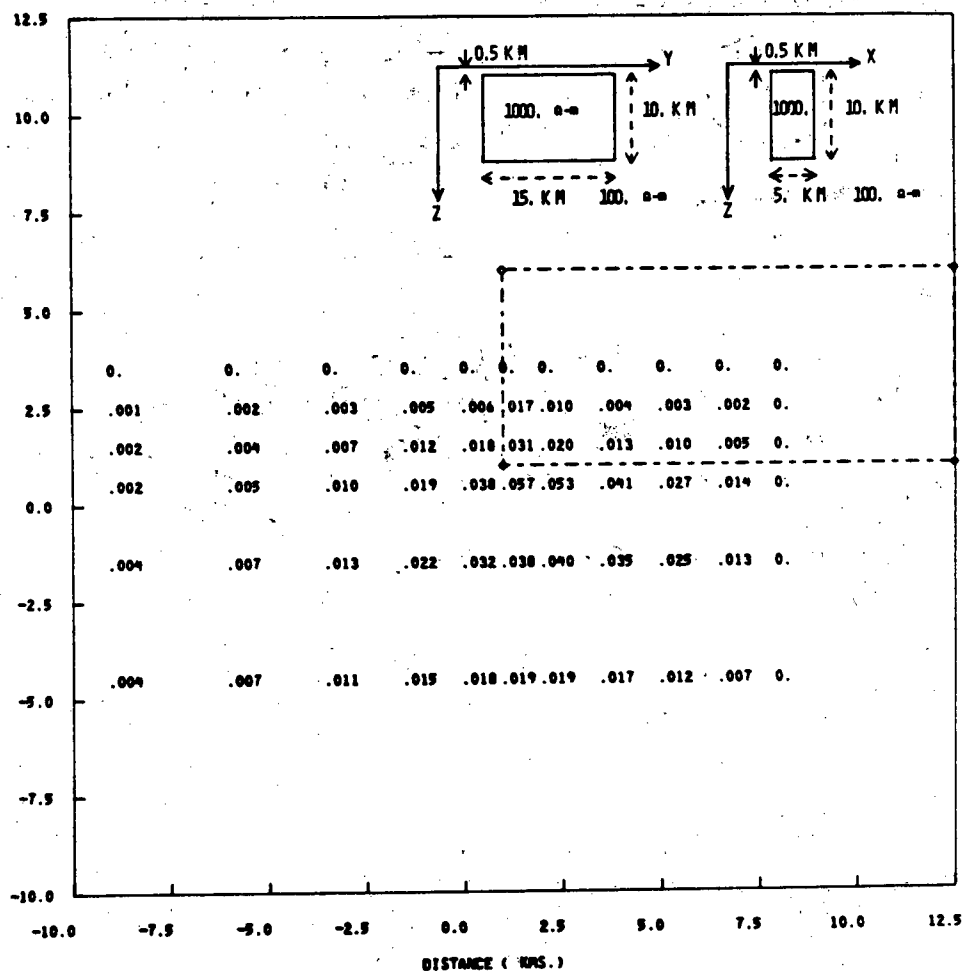
AVERAGED FREDS. IN RANGE OF 0.01 HZ.



AVERAGED PRESS. IN RANGE OF 0.01 HZ.

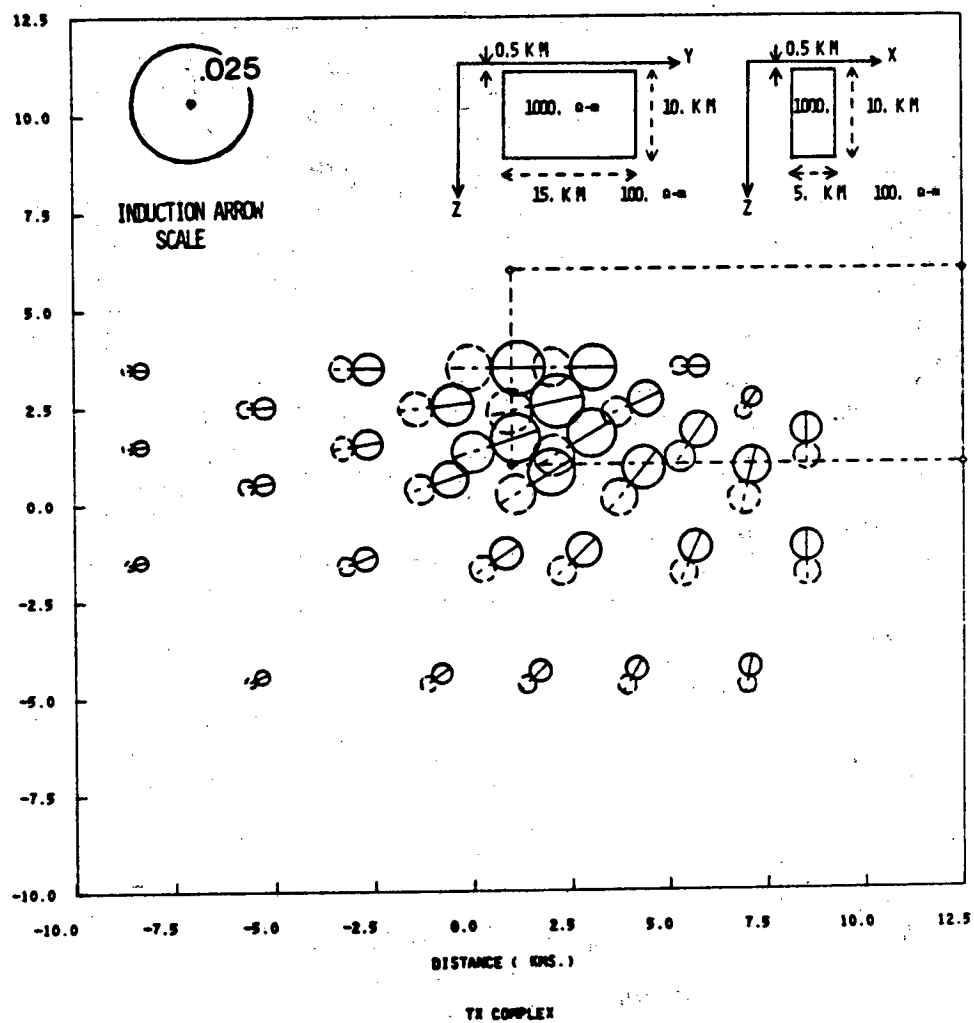


AVERAGED FREQS. IN RANGE OF 0.01 HZ.

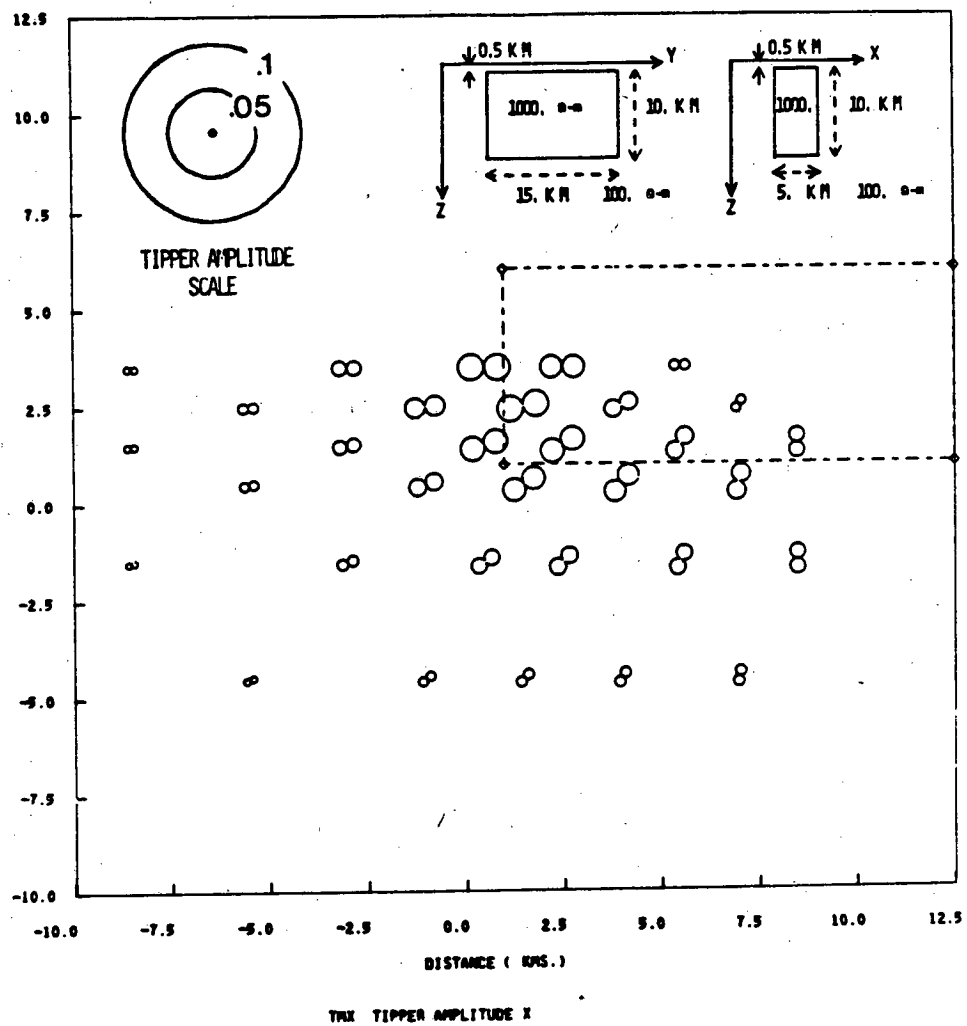


SKEWNESS (  $ZHX+ZVY$  ) / (  $ZHY-ZVX$  )

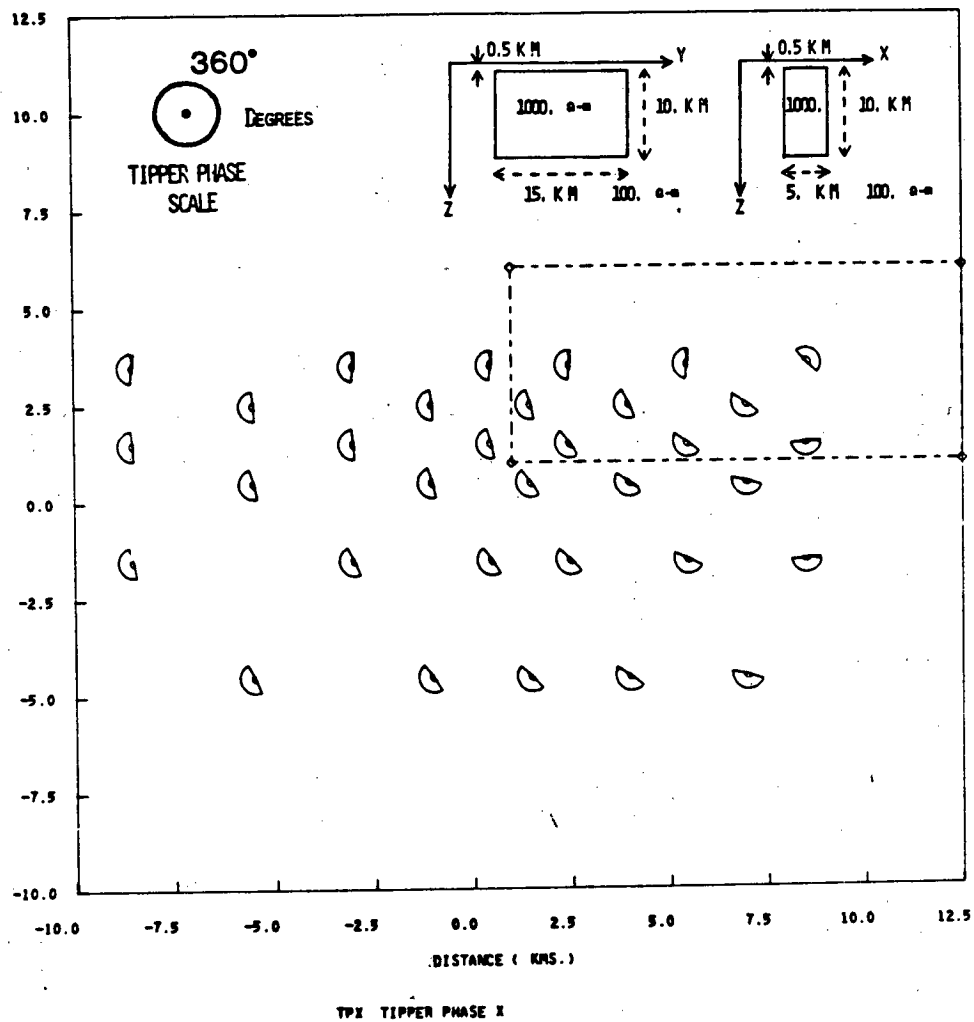
AVERAGED FREQS. IN RANGE OF 0.01 HZ.



AVERAGED FREES. IN RANGE OF 0.01 HZ.



AVERAGED FREQS. IN RANGE OF 0.01 HZ.



This report was done with support from the Department of Energy. Any conclusions or opinions expressed in this report represent solely those of the author(s) and not necessarily those of The Regents of the University of California, the Lawrence Berkeley Laboratory or the Department of Energy.

Reference to a company or product name does not imply approval or recommendation of the product by the University of California or the U.S. Department of Energy to the exclusion of others that may be suitable.

TECHNICAL INFORMATION DEPARTMENT  
LAWRENCE BERKELEY LABORATORY  
UNIVERSITY OF CALIFORNIA  
BERKELEY, CALIFORNIA 94720